

UNIVERSITÄT ZU LÜBECK

From the Institute of Chemistry and Metabolomics

of the University of Lübeck

Director: Prof. Dr. rer. nat. Thomas Peters

"Investigation into Substrate Binding and Structural Dynamics of Human Blood Group A and B Glycosyltransferases by NMR Spectroscopy"

Dissertation

for Fulfillment of

Requirements

for the Doctoral Degree

of the University of Lübeck

from the Department of Natural Sciences

Submitted by

Felix Friedemann Flügge

from Meschede

Lübeck 2018

First referee: Prof. Dr. rer. nat. Thomas Peters

Second referee: Prof. Dr. rer. nat. Christian Hübner

Date of oral examination: July 10th, 2018

Approved for printing. Lübeck, February 6th, 2019

Abstract

Human α-(1→3)-N-acetylgalactosaminyltransferase GTA, and α-(1→3)-galactosyltransferase GTB catalyze the last step in the biosynthesis of the blood group A and B antigens, respectively. GTA and GTB are highly homologous retaining glycosyltransferases, for which many mechanistic details are still under debate. Here, methyl-TROSY NMR experiments offer new tools for the functional analysis of the 70 kDa homodimeric catalytic domains of GTA and GTB. Spectral assignment of the methyl groups is a prerequisite for the application of methyl-TROSY studies into protein structures, dynamics and interactions. In this thesis a structure-guided assignment approach is described, which relies on 4D methyl-methyl NOESY experiments, lanthanide-induced pseudocontact shifts (PCSs) and high-resolution crystal structures yielding the complete assignment of all 97 Ala, Ile (δ1), Leu (δ2), Met and Val (δ2) $^{13}C^{1}H_3$-labeled methyl groups in GTA and GTB. Furthermore, NOEs and PCSs confirm the exclusive formation of homodimers in solution, and reveal delicately balanced conformational states of the enzymes dependent on the metal ion cofactor.

The methyl group assignments are the basis for detailed NMR-based protein-ligand interaction studies. For the first time, the binding kinetics of donor and acceptor substrates are quantitatively determined by line shape analysis and magnetization exchange experiments. The investigations reveal that the mutual cooperativity of donor and acceptor substrate binding is balanced by their binding on- and off-rates. Significant deviations from diffusion-controlled binding on-rates suggest a complex binding mechanism with large energetic barriers. NMR chemical shift perturbation (CSP) experiments reveal allosteric interactions and highlight that substrate binding is intrinsically linked to conformational reorientations. GTA and GTB have characteristic mobile loops covering the active site upon substrate binding, and leading from an “open” apo state over the donor-bound “semi-closed” conformation to the donor- and acceptor-bound “closed” conformation. The CSPs are correlated with the transitions between these major states. The lifetime of the closed protein conformation is estimated from the off-rates of the ligands from ternary complexes. The exchange between open and closed forms of the enzyme occurs on a timescale of hundreds of milliseconds to seconds. Of note, a single amino acid substitution of Trp^{181} with Met or Glu leads to significantly higher on- and off-rates, indicating a decoupling of ligand binding and conformational transition, and an elimination of cooperativity of substrate binding. For the first time, negative mutual cooperativity has been observed for the binding of products of the glycosyltransferase reaction, UDP and blood group B trisaccharide, suggesting that the enzymes employ the same, yet to be discovered allosteric networks for catalysis of glycosyltransfer and for promotion of egress of products. Furthermore, substrate and analog binding to GTA, GTB and a GTA/GTB hybrid with dual specificity appears with significantly differing binding kinetics. These differences are related to substrate discrimination mechanisms.

In summary, this work provides detailed insights into the mode of substrate binding and associated protein dynamics of the biologically relevant human blood group A and B glycosyltransferases. The studies have uncovered novel aspects of allosteric control of these enzymes by their substrates and products yielding important insights into the catalytic mechanism.

Zusammenfassung

Die α-(1→3)-N-Acetylgalactosaminyltransferase GTA und α-(1→3)-Galactosyltransferase GTB katalysieren jeweils den letzten Schritt in der Biosynthese der humanen AB0 Blutgruppenantigene A und B. Sie sind hoch homologe konfigurationserhaltende Glycosyltransferasen (GTs), deren enzymatischer Mechanismus noch nicht vollständig aufgeklärt ist. Für NMR-basierte funktionelle Untersuchungen der 70 kDa großen Homodimere der katalytischen Domänen von GTA und GTB stellt die Methyl-TROSY Technik ein ideales Werkzeug dar. Die spektrale Zuordnung der Methylgruppen ist dabei eine Grundvoraussetzung, um detaillierte Analysen von Proteinstrukturen, -dynamiken und -interaktionen zu ermöglichen. Hier wird eine strukturbasierte Zuordnungsstrategie entwickelt, die auf 4D Methyl-Methyl NOESY Experimenten, Lanthanoid-induzierten *pseudocontact shifts* (PCSs) und hoch aufgelösten Kristallstrukturen basiert. Bemerkenswerterweise wurden so alle 97 Ala, Ile (δ1), Leu (δ2), Met und Val (γ2) $^{13}C^{1}H_{3}$-markierten Methylgruppen in GTA und GTB zugeordnet. Die generierten NOE- und PCS-Daten bestätigen die postulierte Homodimerisierung in Lösung und offenbaren abhängig von dem Metallionen-Cofaktor sensibel ausbalancierte konformationelle Zustände.

Die Zuordnung der Methylgruppen ist die Basis für detaillierte Untersuchungen von Protein-Ligand-Wechselwirkungen mit Hilfe der NMR Spektroskopie. Zum ersten Mal werden kinetische Daten zur Bindung von Donor- und Akzeptorsubstraten und deren Analoga quantitativ erhoben. Dafür werden Analysen der Signalkonturen in Titrationsspektren, sowie Magnetisierungsaustauschexperimente durchgeführt. Die Untersuchungen offenbaren eine wechselseitige Kooperativität zwischen Donor- und Akzeptorsubstraten, die durch Assoziations- und Dissoziationsraten gesteuert wird. Die Assoziationsraten sind signifikant kleiner als für einen diffusionskontrollierten Prozess erwartet werden kann. Dies deutet auf einen komplexen Bindungsmechanismus hin, der durch hohe energetische Barrieren charakterisiert ist. Die assoziierten Veränderungen chemischer Verschiebungen (*chemical shift perturbations: CSPs*) decken spezifische allosterische Effekte auf und untermauern, dass die Substratbindung eng mit konformationellen Umorientierungen im Protein verknüpft ist. GTA und GTB haben charakteristische flexible Regionen, die in Abhängigkeit von den Substraten das aktive Zentrum entweder zugänglich machen oder es über den Substraten verschließen. Folglich durchleben die GTs einen Übergang von einem „offenen" ligandenfreien Zustand über eine Donor-gebundene „halb-geschlossene" Konformation hin zu der „geschlossenen" Konformation in Gegenwart von Donor- und Akzeptorsubstrat. Die CSPs können mit Übergängen zwischen diesen Zuständen korreliert werden. Die Lebensdauer des geschlossenen Zustands kann über die Dissoziationsraten der Liganden vom ternären Komplex abgeschätzt werden. So können quantitative Aussagen über die Austauschraten zwischen offener und geschlossener Konformation gemacht werden. Dieser Prozess muss sich im Bereich von mehreren Hundert Millisekunden bis hin zu Sekunden abspielen. Interessanterweise führt

ein einzelner Aminosäureaustausch von Trp^{181} zu Glu oder Met dazu, dass Ligandenbindung und Konformationsänderungen weitestgehend entkoppelt werden und die Kooperativität gewissermaßen „ausgeschaltet“ wird. Dies äußert sich in signifikant erhöhten Assoziations- und Dissoziationsraten der Liganden.

Zum ersten Mal wird eine negative wechselseitige Kooperativität zwischen der Bindung von Produkten der Glycosyltransferasereaktion, UDP und Blutgruppe B Trisaccharid, beobachtet. Dies deutet darauf hin, dass die Enzyme dasselbe allosterische Netzwerk für die Katalyse des Glycosyltransfers und für die Förderung der Produktdissoziation nutzen. Außerdem binden GTA, GTB und ein GTA/GTB Hybridenzym mit dualer Substratspezifität die analysierten Substrate und Analoga mit unterschiedlicher Bindungskinetik. Diese Unterschiede geben Hinweise auf Mechanismen, wie die Enzyme zwischen natürlichen Substraten und enzymatisch inaktiven Liganden diskriminieren.

Somit liefert diese Arbeit detaillierte Einblicke in den Modus der Substratbindung und der gekoppelten Proteinbewegungen in den biologisch relevanten humanen Glycosyltransferasen. Die Studien legen neue Aspekte der allosterischen Kontrolle von GTA und GTB durch ihre Substrate und Produkte offen, die wichtige Rückschlüsse auf den katalytischen Mechanismus erlauben.

Content

Abstract V

Zusammenfassung VII

Content X

Abbreviations XV

List of tables XIX

List of figures XXI

List of appendix tables XXV

List of appendix figures XXIX

1 Introduction 1

1.1 Glycobiology 1

1.2 Glycosyltransferases 2

1.3 Human blood group A and B glycosyltransferases 5

1.3.1 The ABO histo-blood group system 5

1.3.2 Structural features and substrate binding 7

1.4 NMR Spectroscopy 14

1.4.1 Methyl labeling and methyl-TROSY experiments 15

1.4.2 Chemical exchange in proteins 15

1.4.3 Paramagnetic NMR 17

2 Objectives 21

3 Methods 25

3.1 Protein expression 25

3.1.1 Bacterial system and plasmid 25

3.1.2 Growth media 25

3.1.3 Cloning of single site mutants 27
3.1.4 Plasmid DNA preparation 28
3.1.5 Preparation of electrocompetent *E.coli* cells 28
3.1.6 Transformation of *E.coli* cells by electroporation 29
3.1.7 Preparation of *E.coli* glycerol stocks 29
3.1.8 Synthesis of unlabeled protein 29
3.1.9 Synthesis of labeled protein in D_2O 29
3.2 Protein purification and NMR sample preparation 30
3.2.1 Cell Lysis 30
3.2.2 Cation exchange chromatography 30
3.2.3 Affinity chromatography 31
3.2.4 Dialysis and buffer exchange 31
3.3 Analytics of protein purification 32
3.3.1 SDS-PAGE 32
3.3.2 Spectrophotometric protein quantification 33
3.3.3 Activity assay 33
3.4 NMR spectroscopy 34
3.4.1 HMQC-NOESY experiments 35
3.4.2 Paramagnetic labeling and pseudocontact shift analysis 35
3.4.3 NMR-monitored titration experiments and line shape analysis 36
3.4.4 ZZ exchange experiments 37
4 Results 41
4.1 Assignment of AILMV $^{13}CH_3$-methyl resonances in methyl-TROSY spectra 41
4.1.1 Identification of residue types 43

4.1.2 Initial assignment with methyl-methyl NOESY 46

4.1.3 Lanthanide-induced PCSs for assignment completion 51

4.1.4 Transfer of assignments to GTA and AAGlyB 59

4.1.5 Structural implications from PCSs and NOE correlations.....62

4.2 Ligand interaction studies 66

4.2.1 Donor substrate binding induced chemical shift perturbations in GTB 66

4.2.2 2D NMR line shape analysis of donor substrate titration data.....71

4.2.3 Acceptor substrate binding induced chemical shift perturbations in GTB 74

4.2.4 2D NMR line shape analysis of acceptor substrate titration data.....78

4.2.5 Combined donor and acceptor binding-induced chemical shift perturbations in GTB 81

4.2.6 2D NMR line shape analysis of titration data leading from the binary to the ternary binding complex.....94

4.2.7 Investigating slow chemical exchange with the ZZ-exchange experiment 98

4.2.8 Substrate analog binding to GTA and AAGlyB..... 100

4.2.9 Substrate analog binding to W181M and W181E mutants 105

5 Discussion..... 111

5.1 Evaluation of the methyl group assignment strategy..... 111

5.2 Ligand binding and conformational transitions 115

5.2.1 Donor substrate and analog binding by GTB 115

5.2.2 Comparative analysis of donor substrate and analog binding by GTA, GTB, AAGlyB and GTB Trp^{181} mutants 117

5.2.3 Acceptor substrate and analog binding by GTB..... 119

5.2.4 Positive cooperativity of ligand binding and the associated protein dynamics 121

5.2.5 Implications from different ternary binding complexes 124

5.2.6 Product release 126

5.2.7 The role of the metal ion cofactor 127

5.2.8 Comparison with LgtC NMR studies 129

6 Summary and Outlook 133

Appendix 139

Material and equipment 139

Chemicals 141

Chemical shifts of methyl resonances of GTA 143

Chemical shifts of methyl resonances of GTB 145

Chemical shifts of methyl resonances of AAGlyB 149

NOE correlations 151

Pseudocontact shifts 158

Chemical shifts in presence of ligands 161

Chemical shifts of methyl resonances of GTB Trp^{181} mutants 177

Line shape analysis fitting results 181

Donor analog titrations with GTB 181

Acceptor substrate and analog titrations with GTB 193

Donor analog titrations with acceptor substrate- or analog-saturated GTB 211

Acceptor substrate and analog titrations with donor analog-saturated GTB 252

Ligand titrations with GTA 264

Ligand titrations with AAGlyB 273

Ligand titrations with GTB Trp^{181}mutants 288

Pulse programs ... 313
Methyl-TROSY ... 313
3D NOESY HMQC ... 315
4D HMQC NOESY HMQC ... 318
ZZ-exchange auto experiment ... 321
ZZ-exchange cross experiment ... 324
Literature ... 329
Curriculum Vitae ... 343
Acknowledgment ... 347

Abbreviations

µ	micro
1D	one-dimensional
2D	two-dimensional
3D	three-dimensional
3DD	H-disaccharide 3-deoxy derivative (α-L-Fuc*p*-(1→2)-3-deoxy-β-D-Gal*p*-O-octyl)
4D	four-dimensional
aa	amino acid
Amp	ampicillin
Carb	carbenicillin
CSA	chemical shift anisotropy
CSP	chemical shift perturbation
CV	column volume
Da	Dalton
dpm	disintegrations per minute
dsDNA	double stranded DNA
DSS	4,4-dimethyl-4-silapentane-1-sulfonic acid
d_x	number of introduced deuterons
E.coli	*Escherichia coli*
EDTA	ethylenediaminetetraacetic acid
ESI-MS	electrospray ionization mass spectrometry
f.c.	final concentration
FID	free induction decay
g	gram
Gal	galactose
GalNAc	N-acetylgalactosamine
Glc	glucose
GlcNAc	N-acetylglucosamine

GT	glycosyltransferase
GTA	human blood group A α-(1→3)-N-acetylgalactosaminyltransferase
GTB	human blood group B α-(1→3)-galactosyltransferase
h	hour
H-dis	H-disaccharide (α-L-Fuc*p*-(1→2)-β-D-Gal*p*-O-octyl)
HMQC	Heteronuclear Multiple-Quantum Correlation
HSQC	Heteronuclear Single-Quantum Correlation
H-tris	H-trisaccharide
IPTG	isopropyl β-D-1-thiogalactopyranoside
ITC	isothermal titration calorimetry
k	kilo
k_{cat}	catalytic turnover rate constant
K_d	dissociation constant
K_m	Michaelis constant
k_{off}	off-rate constant
k_{on}	on-rate constant
L	liter
LgtC	lipopolysaccharide α-(1→4)-galactosyltransferase C from *Neisseria meningitidis*
m	milli
M	molar (mol/L)
mol	mole
MW	molecular weight
MWCO	molecular weight cut-off
n	nano
NMR	nuclear magnetic resonance
NOE	nuclear Overhauser effect/enhancement
NOESY	Nuclear Overhauser Enhancement SpectroscopY
NUS	non-uniform sampling
OD_{600}	optical density at 600 nm

p	pico
PCR	polymerase chain reaction
PCS	pseudocontact shift
PDB	protein data bank (www.rcsb.org)
pH*	the pH meter reading without correction for isotope effects
ppm	parts per million
PRE	paramagnetic relaxation enhancement
R_1	longitudinal relaxation rate
R_2	transversal relaxation rate
RDC	residular dipolar coupling
rms	root mean square
rpm	rounds per minute
RT	room temperature
s	second
SDS-PAGE	sodium dodecyl sulfate polyacrylamide gel electrophoresis
SPR	surface plasmon resonance
STD NMR	saturation transfer difference NMR
T_1	longitudinal relaxation time
T_2	transversal relaxation time
TCEP	tris(2-carboxyethyl)phosphine
TROSY	Transverse Relaxation Optimized SpectroscopY
U	enzyme unit
UDP	uridine 5'-diphosphate
U-labeled	uniformly labeled
UV/Vis	ultraviolet/visible light
wt	wild-type
α3GalT	bovine α-(1→3)-galactosyltransferase

Amino acids

Ala	A	Alanine
Arg	R	Arginine
Asn	N	Asparagine
Asp	D	Aspartic acid
Cys	C	Cysteine
Gln	Q	Glutamine
Glu	E	Glutamic acid
Gly	G	Glycine
His	H	Histidine
Ile	I	Isoleucine
Leu	L	Leucine
Lys	K	Lysine
Met	M	Methionine
Phe	F	Phenylalanine
Pro	P	Proline
Ser	S	Serine
Thr	T	Threonine
Trp	W	Tryptophan
Tyr	Y	Tyrosine
Val	V	Valine

List of tables

Table 3.1: List of H_2O-based *E.coli* nutrient media (1 L).....26

Table 3.2: D_2O-based *E.coli* M9 minimal media for starter and main cultures.....27

Table 3.3: Quantity of precursor or aa used to selectively label/unlabel methyl groups. 27

Table 3.4: Mutagenic primers. 28

Table 3.5: Lysis buffer.....30

Table 3.6: Cation exchange chromatography buffers 31

Table 3.7: Affinity chromatography buffers.....31

Table 3.8: NMR spectroscopy buffers. 32

Table 3.9: SDS-PAGE buffers.....32

Table 3.10: SDS polyacrylamide gels.....33

Table 3.11: Activity assay buffer and stock mix.....34

Table 4.1: $\Delta\chi$ tensor parameters derived with *Numbat* from proton PCSs of the tentatively assigned resonances. 56

Table 4.2: Final magnetic susceptibility tensors derived with *Numbat* from fitting ^{1}H PCSs of A, I, L, M and V methyl groups using the "ensemble" structure.....63

Table 4.3: Q factors derived from measured and expected PCSs of $\Delta\chi$ tensor fits to different structural models.....65

Table 4.4: Thresholds and numbers of significantly perturbed resonances by binding of different ligands in the donor binding site. 67

Table 4.5: Fitted two-state ligand binding model parameters for the interaction of GTB with different donor analogs.....72

Table 4.6: Thresholds and numbers of significantly perturbed resonances by binding of different ligands in the acceptor binding site.....75

Table 4.7: Fitted two-state ligand binding model parameters for the interaction of GTB with different acceptor analogs. 78

Table 4.8: Thresholds and numbers of significantly perturbed resonances by combined binding of donor and acceptor analogs. 83

Table 4.9: Fitted two-state ligand binding model parameters for transitions from the binary to the ternary binding complex. 95

Table 4.10: Rate constants determined in the ZZ-exchange experiment. 99

Table 4.11: Specific activities of GTA, GTB and AAGlyB using UDP-Gal or UDP-GalNAc as donor substrates. 100

Table 4.12: Comparison of donor substrate analog binding parameters of GTA, GTB and AAGlyB. 103

Table 4.13: Comparison of binding parameters of UDP and H-dis to GTB wt, W181E and W181M. 107

List of figures

Figure 1.1: General folds of the catalytic domain of nucleotide-sugar-dependent GTs. 2

Figure 1.2: Proposed mechanisms of glycosyl transfer reactions catalyzed by inverting (**a**) and retaining (**b** and **c**) enzymes.....4

Figure 1.3: Final step in the biosynthesis of blood group A and B antigens. 5

Figure 1.4: The six subtypes of the ABO blood group antigens. 6

Figure 1.5: Topology of GTA and GTB. 7

Figure 1.6: Crystal structures of GTB in absence and presence of substrates. 8

Figure 1.7: Overlay of the open (light grey) and closed (dark grey) conformation of GTA/GTB... 10

Figure 3.1: Plasmid map of pCWΔlac coding for -10 GTB.....25

Figure 4.1: Sequence-specific assignment strategy of AILMV methyl groups in GTB. 42

Figure 4.2: Distribution of the relevant methyl bearing amino acids in the primary and quaternary structure of GTB.....43

Figure 4.3: Superposition of 2D [^{13}C, ^{1}H]-HMQC spectra of differently methyl-labeled GTB samples. 44

Figure 4.4: Evaluation of incorporation efficiencies in the AIL^{proS}MV^{proS} labeling scheme.....46

Figure 4.5: Example of a NOE cluster of spatially neighboring amino acids.....48

Figure 4.6: Intermolecular NOEs at the homodimer interface.....50

Figure 4.7: NOE correlations between Leu^{132} and Ala^{350} suggest the orientation of the C-terminal loop in the open conformation. 51

Figure 4.8: Crystal structure (PDB entry 2RJ8) showing the coordination of the manganese ion in the active site of GTB.....52

Figure 4.9: Methyl-TROSY spectra of AIL^{proS}MV^{proS} GTB in the diamagnetic and paramagnetic state. 54

Figure 4.10: "Ensemble structure" for Δχ tensor fitting. 55

Figure 4.11: Sequence-specific resonance assignments of all AIL^{proS}MV^{proS} methyl groups in GTB. 57

Figure 4.12: Example of Val pro-R methyl group assignment. 58

Figure 4.13: Sequence-specific resonance assignments of Leu and Val pro-R methyl groups in GTB. 59

Figure 4.14: Sequence-specific resonance assignments of all AIL^{proS}MV^{proS} methyl groups in GTA and AAGlyB. 60

Figure 4.15: Chemical shift deviations between apo-GTA, apo-GTB and apo-AAGlyB. 61

Figure 4.16: PCS isosurfaces (created with *Numbat* and *PyMOL*) of the anisotropic magnetic susceptibility tensors and correlations of experimental versus calculated PCSs for (**a**) Cerium, (**b**) Europium and (**c**) Praseodymium. 64

Figure 4.17: Differences of calculated Pr^{3+}-induced PCSs obtained from different structural models. 65

Figure 4.18: Residue specific CSPs observed during ligand binding in the donor binding site.. 68

Figure 4.19: Correlation between crystal structure methyl displacements and NMR CSPs of methyl resonances induced by UDP binding. 69

Figure 4.20: Residue specific chemical shift deviations observed between donor-saturated states. 70

Figure 4.21: Line shape analysis of HMQC-based UDP titration data. 73

Figure 4.22: Line shapes of resonances corresponding to residues of the internal loop during UDP titration. 74

Figure 4.23: Residue specific CSPs observed during ligand binding in the acceptor binding site... 76

Figure 4.24: Residue specific CSPs observed during binding of different H-trisaccharide antigens. 77

Figure 4.25: Line shape analysis of HMQC-based H-dis titration data. 79

Figure 4.26: Different exchange regimes associated with binding of different H-tris types revealed by line shape analysis of titration data. 80

Figure 4.27: Combined residue specific CSPs observed during ligand binding in the donor and acceptor binding site. 82

Figure 4.28: Residue specific CSPs observed during UDP binding to apo-GTB (top) or H-dis-saturated GTB (bottom). 84

Figure 4.29: Residue specific CSPs observed during H-dis binding to apo-GTB (top) or UDP-saturated GTB (bottom). 84

Figure 4.30: UDP/H-dis and UDP/B-tris binding induces similar chemical shift deviations. 86

Figure 4.31: Differences between UDP-Gal/3DD and UDP-Glc/3DD binding induced CSPs. ..87

Figure 4.32: Differences between UDP-GlcNAc/3DD and UDP-Gal/3DD binding-induced CSPs. 88

Figure 4.33: Differences between UDP-Gal/3DD and UDP-GalNAc/3DD binding induced CSPs. 90

Figure 4.34: Residue specific CSPs observed during binding of different H-trisaccharide antigens and UDP....92

Figure 4.35: Correlation of CSPs in GTB between UDP- and H-trisaccharide type II-saturated and UDP- and other H-trisaccharide- and H-disaccharide-saturated states. 93

Figure 4.36: Comparison of CSPs induced by UDP and H-dis binding, employing Mg^{2+} (grey bars) or La^{3+} (black bars) as cofactor. 94

Figure 4.37: Line shape analysis of HMQC-based UDP titration data recorded in presence of excess amounts of H-dis. 96

Figure 4.38: Line shape analysis of HMQC-based H-dis titration data recorded in presence of saturating amounts of UDP. 97

Figure 4.39: Normalized peak intensities of the direct correlation signals corresponding to Ile^{123}, Leu^{173} (proS), Met^{186} and Ile^{192} methyl groups in the ZZ-exchange experiment. 99

Figure 4.40: Residue specific CSPs observed during nucleotide sugar binding to GTA (blue bars), GTB (black bars) and AAGlyB (red bars). 101

Figure 4.41: Correlation of CSPs induced by binding of UDP-GalNAc or UDP to AAGlyB. ...102

Figure 4.42: Residue specific CSPs observed during nucleotide sugar and 3DD binding to GTA (blue bars), GTB (black bars) and AAGlyB (red bars). 104

Figure 4.43: Weighted Euclidean distances between signal positions in spectra of wt GTB and mutants W181E and W181M. 105

Figure 4.44: Comparison of ligand binding-induced CSPs in GTB wt (open bars) and W181E (black bars) and W181M (grey bars) mutants. 106

Figure 5.1: Donor binding site of GTB identified by significant CSPs. 115

Figure 5.2: Acceptor binding site of GTB identified by significant CSPs. 119

Figure 5.3: Significantly perturbed sites in the ternary binding complex. 121

Figure 5.4: Kinetics of the transitions between different states induced by UDP and H-dis binding to wt GTB. 123

Figure 5.5: Comparison of crystal structures of GTB (**a**, PDB entry 2RJ7) and LgtC (**b**, 1G9R). 129

List of appendix tables

Tab. 1: List of devices....139

Tab. 2: List of disposables....140

Tab. 3: List of chemicals....141

Tab. 4: ^{1}H and ^{13}C chemical shifts of all assigned methyl groups of apo-GTA in a 2D [$^{13}C^{1}H$]-HMQC spectrum.....143

Tab. 5: ^{1}H and ^{13}C chemical shifts of all assigned methyl groups of apo-GTB in a 2D [$^{13}C^{1}H$]-HMQC spectrum.....145

Tab. 6: ^{1}H and ^{13}C chemical shifts of all assigned methyl groups of apo-AAGlyB in a 2D [$^{13}C^{1}H$]-HMQC spectrum.....149

Tab. 7: List of NOE peak positions in the 4D methyl-methyl NOESY spectrum recorded with AIL^{proS}MV^{proS} methyl-labeled GTB in D_2O phosphate NMR buffer at 950 MHz ^{1}H frequency and 298 K.....151

Tab. 8: List of experimental and calculated ^{1}H PCSs....158

Tab. 9: Chemical shifts of the AIL^{proS}MV^{proS} methyl resonances of GTB in complex with donor substrates and analogs.....161

Tab. 10: Chemical shifts of the AIL^{proS}MV^{proS} methyl resonances of GTB in complex with 3DD, H-dis and B-tris.....163

Tab. 11: Chemical shifts of the AIL^{proS}MV^{proS} methyl resonances of GTB in ternary binding complexes.....165

Tab. 12: Chemical shifts of the AIL^{proS}MV^{proS} methyl resonances of GTA in complex with donor substrate and analogs.....168

Tab. 13: Chemical shifts of the AIL^{proS}MV^{proS} methyl resonances of GTA in ternary binding complexes.....170

Tab. 14: Chemical shifts of the AIL^{proS}MV^{proS} methyl resonances of AAGlyB in complex with donor substrates and analogs.....172

Tab. 15: Chemical shifts of the AIL^{proS}MV^{proS} methyl resonances of AAGlyB in ternary binding complexes. 174

Tab. 16: Chemical shifts of the IL^{proS}MV^{proS} methyl resonances of apo-GTB W181E and in binary and ternary binding complexes. 177

Tab. 17: Chemical shifts of the IL^{proS}MV^{proS} methyl resonances of apo-GTB W181M and in binary and ternary binding complexes. 179

Tab. 18: Line shape analysis results of the titration of GTB with UDP. 182

Tab. 19: Line shape analysis results of the titration of GTB with UDP-Glc. 185

Tab. 20: Line shape analysis results of the titration of GTB with UDP-GalNAc. 188

Tab. 21: Line shape analysis results of the titration of GTB with UDP-GlcNAc. 191

Tab. 22: Line shape analysis results of the titration of GTB with H-dis. 193

Tab. 23: Line shape analysis results of the titration of GTB with 3DD. 195

Tab. 24: Line shape analysis results of the titration of GTB with B-tris. 198

Tab. 25: Line shape analysis results of the titration of GTB with H-tris type I. 200

Tab. 26: Line shape analysis results of the titration of GTB with H-tris type II. 202

Tab. 27: Line shape analysis results of the titration of GTB with H-tris type III. 204

Tab. 28: Line shape analysis results of the titration of GTB with H-tris type IV. 206

Tab. 29: Line shape analysis results of the titration of GTB with H-tris type V. 207

Tab. 30: Line shape analysis results of the titration of GTB with H-tris type VI. 209

Tab. 31: Line shape analysis results derived from the UDP titration to H-dis-saturated GTB. 212

Tab. 32: Line shape analysis results derived from the UDP titration to B-tris-saturated GTB. 216

Tab. 33: Line shape analysis results derived from the UDP titration to H-tris type I saturated GTB. 219

Tab. 34: Line shape analysis results derived from the UDP titration to H-tris type II saturated GTB. 224

Tab. 35: Line shape analysis results derived from the UDP titration to H-tris type III saturated GTB. 229

Tab. 36: Line shape analysis results derived from the UDP titration to H-tris type IV saturated GTB. 234

Tab. 37: Line shape analysis results derived from the UDP titration to H-tris type V saturated GTB. 238

Tab. 38: Line shape analysis results derived from the UDP titration to H-tris type VI saturated GTB. 244

Tab. 39: Line shape analysis results derived from the UDP-Glc titration to 3DD-saturated GTB.. 250

Tab. 40: Line shape analysis results derived from the H-dis titration to UDP-saturated GTB. 253

Tab. 41: Line shape analysis results derived from the H-tris type I titration to UDP-saturated GTB. 256

Tab. 42: Line shape analysis results derived from the H-tris type II titration to UDP-saturated GTB. 258

Tab. 43: Line shape analysis results derived from the 3DD titration to UDP-Glc-saturated GTB.. 261

Tab. 44: Line shape analysis results derived from the UDP-Gal titration to GTA. 265

Tab. 45: Line shape analysis results derived from the UDP-Glc titration to GTA.....268

Tab. 46: Line shape analysis results derived from the UDP-GlcNAc titration to GTA. 271

Tab. 47: Line shape analysis results derived from the UDP titration to AAGlyB. 274

Tab. 48: Line shape analysis results derived from the UDP-Gal titration to AAGlyB. 278

Tab. 49: Line shape analysis results derived from the UDP-Glc titration to AAGlyB.....282

Tab. 50: Line shape analysis results derived from the UDP-GlcNAc titration to AAGlyB. 286

Tab. 51: Line shape analysis results derived from the H-dis titration to GTB W181E.....289

Tab. 52: Line shape analysis results derived from the UDP titration to GTB W181E.....292

Tab. 53: Line shape analysis results derived from the UDP titration to H-dis-saturated GTB W181E. 296

Tab. 54: Line shape analysis results derived from the H-dis titration to GTB W181M. 300

Tab. 55: Line shape analysis results derived from the UDP titration to GTB W181M. 304

Tab. 56: Line shape analysis results derived from the UDP titration to H-dis-saturated GTB W181M. 309

List of appendix figures

Fig. 1: Overlay of experimental (blue) and fitted (red) line shapes of the titration of GTB with UDP. 181

Fig. 2: Overlay of experimental (blue) and fitted (red) line shapes of the titration of GTB with UDP-Glc. 184

Fig. 3: Overlay of experimental (blue) and fitted (red) line shapes of the titration of GTB with UDP-GalNAc. 187

Fig. 4: Overlay of experimental (blue) and fitted (red) line shapes of the titration of GTB with UDP-GlcNAc. 190

Fig. 5: Overlay of experimental (blue) and fitted (red) line shapes of the titration of GTB with H-dis. 193

Fig. 6: Overlay of experimental (blue) and fitted (red) line shapes of the titration of GTB with 3DD. 195

Fig. 7: Overlay of experimental (blue) and fitted (red) line shapes of the titration of GTB with B-tris. 197

Fig. 8: Overlay of experimental (blue) and fitted (red) line shapes of the titration of GTB with H-tris type I.....200

Fig. 9: Overlay of experimental (blue) and fitted (red) line shapes of the titration of GTB with H-tris type II. 202

Fig. 10: Overlay of experimental (blue) and fitted (red) line shapes of the titration of GTB with H-tris type III.....204

Fig. 11: Overlay of experimental (blue) and fitted (red) line shapes of the titration of GTB with H-tris type IV. 205

Fig. 12: Overlay of experimental (blue) and fitted (red) line shapes of the titration of GTB with H-tris type V. 207

Fig. 13: Overlay of experimental (blue) and fitted (red) line shapes of the titration of GTB with H-tris type VI. 209

Fig. 14: Overlay of experimental (blue) and fitted (red) line shapes of the UDP titration to H-dis-saturated GTB. 211

Fig. 15: Overlay of experimental (blue) and fitted (red) line shapes of the UDP titration to B-tris-saturated GTB. 215

Fig. 16: Overlay of experimental (blue) and fitted (red) line shapes of the UDP titration to H-tris type I saturated GTB. 219

Fig. 17: Overlay of experimental (blue) and fitted (red) line shapes of the UDP titration to H-tris type II saturated GTB. 224

Fig. 18: Overlay of experimental (blue) and fitted (red) line shapes of the UDP titration to H-tris type III saturated GTB. 229

Fig. 19: Overlay of experimental (blue) and fitted (red) line shapes of the UDP titration to H-tris type III saturated GTB. 233

Fig. 20: Overlay of experimental (blue) and fitted (red) line shapes of the UDP titration to H-tris type V saturated GTB. 238

Fig. 21: Overlay of experimental (blue) and fitted (red) line shapes of the UDP titration to H-tris type VI saturated GTB. 244

Fig. 22: Overlay of experimental (blue) and fitted (red) line shapes of the UDP-Glc titration to 3DD-saturated GTB. 249

Fig. 23: Overlay of experimental (blue) and fitted (red) line shapes of the H-dis titration to UDP-saturated GTB. 252

Fig. 24: Overlay of experimental (blue) and fitted (red) line shapes of the H-tris type I titration to UDP-saturated GTB. 255

Fig. 25: Overlay of experimental (blue) and fitted (red) line shapes of the H-tris type II titration to UDP-saturated GTB. 258

Fig. 26: Overlay of experimental (blue) and fitted (red) line shapes of the 3DD titration to UDP-Glc-saturated GTB. 261

Fig. 27: Overlay of experimental (blue) and fitted (red) line shapes of the UDP-Gal titration to GTA. 264

Fig. 28: Overlay of experimental (blue) and fitted (red) line shapes of the UDP-Glc titration to GTA. 267

Fig. 29: Overlay of experimental (blue) and fitted (red) line shapes of the UDP-GlcNAc titration to GTA. 270

Fig. 30: Overlay of experimental (blue) and fitted (red) line shapes of the UDP titration to AAGlyB. 274

Fig. 31: Overlay of experimental (blue) and fitted (red) line shapes of the UDP-Gal titration to AAGlyB. 278

Fig. 32: Overlay of experimental (blue) and fitted (red) line shapes of the UDP-Glc titration to AAGlyB. 282

Fig. 33: Overlay of experimental (blue) and fitted (red) line shapes of the UDP-GlcNAc titration to AAGlyB.....285

Fig. 34: Overlay of experimental (blue) and fitted (red) line shapes of the H-dis titration to GTB W181E. 288

Fig. 35: Overlay of experimental (blue) and fitted (red) line shapes of the UDP titration to GTB W181E. 291

Fig. 36: Overlay of experimental (blue) and fitted (red) line shapes of the UDP titration to H-dis-saturated GTB W181E. 296

Fig. 37: Overlay of experimental (blue) and fitted (red) line shapes of the H-dis titration to GTB W181M. 300

Fig. 38: Overlay of experimental (blue) and fitted (red) line shapes of the UDP titration to GTB W181M. 304

Fig. 39: Overlay of experimental (blue) and fitted (red) line shapes of the UDP titration to H-dis-saturated GTB W181M.....309

1 Introduction

1.1 Glycobiology

Besides proteins, lipids and nucleic acids, glycans represent another important class of functional biomolecules. They serve as structural scaffolds like cellulose or chitin, or as energy storage, such as glycogen or starch. Yet, glycans also fulfill more versatile functions. Most proteins that traverse the secretory pathway of eukaryotic cells are glycosylated. The glycosylation regulates protein folding and degradation, and modulates protein interactions (Caramelo and Parodi 2015; Lamriben et al. 2016; Parodi et al. 2017; Varki and Gagneux 2017). In addition, the lipids of the outer leaflet of the plasma membrane are decorated with sugar structures. Protein- and lipid-linked polysaccharides build a dense meshwork on the surface of the cell that is called glycocalyx. Besides representing a substantial physical barrier, the glycoconjugates mediate information exchange e.g. in intrinsic cell-cell and cell-matrix, or extrinsic cell-microbe recognition processes (Varki and Gagneux 2017; Varki and Sharon 2017).

Glycans are complex structures, whose diversity arises from an often highly branched composition. Theoretically, each monosaccharide can be connected via an α- or a β-glycosidic linkage to any free hydroxyl position on another mono-, oligo- or polysaccharide, allowing a nearly infinite number of possible structures (Prestegard et al. 2017). However, signaling functions of glycans require specific sets of sugar structures that are presented on different cell types of a multicellular organism. Since the biosynthesis of glycans is not template-driven, an alternative mechanism must guide their architecture. Glycosyltransferases (GTs) and glycosidases are responsible for the elongation and truncation of glycans, respectively. The activity of one enzyme yields a product, which is the preferred substrate of the subsequent enzyme. Thus, the coordinated action of GTs and glycosidases during trafficking of proteins and lipids in the secretory pathway determines the set of presented glycan structures (Dube and Bertozzi 2005; Berg et al. 2007; Rini and Esko 2017). Two major types of protein glycosylation are distinguished. In N-glycosylation, a sugar is linked via an N-glycosidic bond to an asparagine side chain, while in O-glycosylation, serine or threonine side chains serve as aglycons. N-glycosylation begins in the lumen of the endoplasmic reticulum (ER) and is continued in the Golgi apparatus. O-glycosylation is restricted to the Golgi vesicles (Berg et al. 2007; Brockhausen and Stanley 2017; Stanley et al. 2017; Varki et al. 2017a).

Alterations in a cell's glycosylation pattern are often accompanied with severe diseases like muscular dystrophies, rheumatoid arthritis or cancer (Christiansen et al. 2014; Freeze et al. 2017a, b, c; Varki et al. 2017b). In viral and bacterial infections, the interactions between pathogen and host organism are largely mediated by glycans, including histo-blood group antigens, and glycan-binding receptors (Heggelund et al. 2017; Szymanski et al. 2017). Furthermore, pathogenic bacteria evade the immune system through molecular mimicry of host glycan structures (Secundino et al. 2016). Therefore, the field of glycobiology offers a variety of potential therapeutic targets (Hinou and Nishimura 2009). These examples illustrate

the importance of a comprehensive understanding of glycoconjugates, and of the enzymes involved in their biosynthesis.

1.2 Glycosyltransferases

Glycosyltransferases catalyze the transfer of a sugar residue from a specific donor substrate to a specific acceptor substrate, which involves the formation of a specific glycosidic bond. The donor substrate is an activated mono- or oligosaccharide, containing a nucleoside phosphate or lipid phosphate leaving group. Acceptors are most commonly other carbohydrates, but also proteins, lipids and nucleic acids, as well as small organic molecules (Lairson et al. 2008; Rini and Esko 2017).

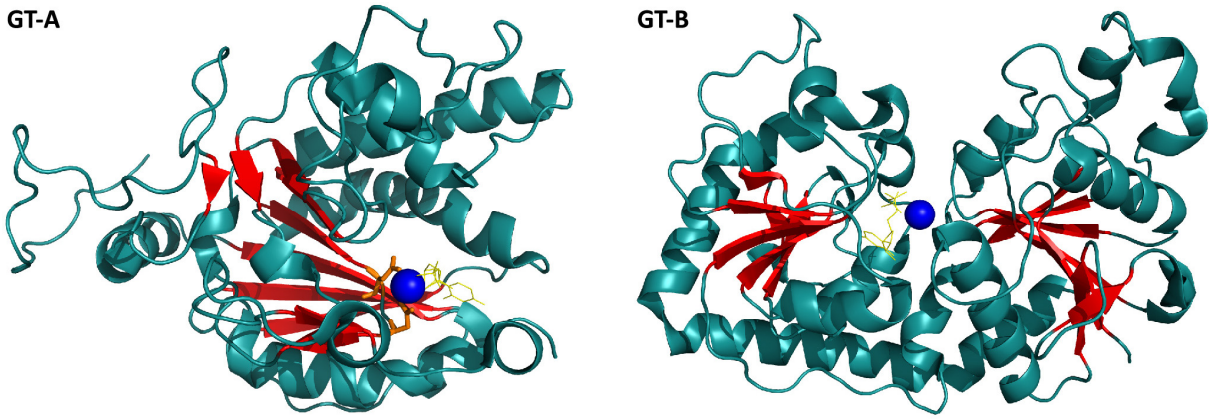


Figure 1.1: General folds of the catalytic domain of nucleotide-sugar-dependent GTs. The GT-A fold is represented by the catalytic domain of the human blood group A glycosyltransferase (PDB entry 3SXE), and the GT-B fold by the bacteriophage T4 β-glucosyltransferase (PDB entry 1JG7). The DXD motif of the GT-A enzyme is highlighted as orange sticks. Donor substrates are shown as yellow sticks and metal ions as blue spheres.

According to amino acid sequence similarities, GTs have been classified into nearly 100 different families in the Carbohydrate-Active EnZymes database (CAZy: http://www.cazy.org) (Campbell et al. 1997; Coutinho et al. 2003; Cantarel et al. 2009). However, the catalytic domains of enzymes that use sugar nucleotides as donor substrates appear in just two major folds: GT-A and GT-B (compare Fig. 1.1) (Lairson et al. 2008). GT-A enzymes are defined by two tightly associated Rossmann-fold domains (topology β/α/β/α/β). Usually, a "DXD" (Asp-any residue-Asp) metal-binding motif coordinates a divalent cation, which is crucial for activity (Lairson et al. 2008). GT-A enzymes display flexible loops that are located near the active site, and whose motions are linked to substrate binding and catalysis (Ramakrishnan et al. 2004; Yazer and Palcic 2005). In contrast, GT-B enzymes consist of two flexibly associated Rossmann folds that face each other. The active site is located within the resulting cleft between the domains, and the activity of GT-B enzymes is generally metal ion independent (Guerin et al. 2007; Lairson et al. 2008). The majority of GTs of the eukaryotic secretory pathway is membrane bound. Commonly, the C-terminal catalytic domain is linked via a stem region to the membrane spanning anchor and a short cytosolic N-terminal tail. This modular set-up is typical for type II

transmembrane proteins (Paulson and Colley 1989; Varki et al. 2017a). Enzymes that use lipid-linked sugar donors are described to adopt a lysozyme-like fold, or to be integral membrane proteins, representing a third type of fold, named GT-C fold (Lovering et al. 2007; Lairson et al. 2008; Chung et al. 2013; Rini and Esko 2017).

Besides sequence similarities and structural features, GTs are also classified by the stereoselectivity of the catalyzed reaction (Fig. 1.2). The anomeric configuration of the product is either retained or inverted with respect to the donor substrate. Thus, the enzymes are classified as retaining or inverting GTs. Interestingly, there is no correlation between general fold (GT-A or GT-B) and catalytic mechanism (retaining or inverting) (Lairson et al. 2008). Inverting enzymes are believed to employ a single displacement S_N2-like mechanism. The hydroxyl group of the acceptor substrate is deprotonated by a general base and attacks the anomeric carbon of the donor sugar from one side, while the nucleotide (or lipid phosphate) leaves from the other (Lairson et al. 2008). The mechanistic details of retaining enzymes are less clear. Under debate are a double displacement S_N2-like mechanism with a covalent glycosyl-enzyme intermediate, and a front-side (front-face) single displacement mechanism that can proceed in a concerted manner (S_Ni: "internal return" nucleophilic substitution) via an oxocarbenium ion-like transition state, or stepwise (S_Ni-like) via a short-lived oxocarbenium-phosphate ion pair intermediate (Fig 1.2) (Lairson et al. 2008; Ardèvol and Rovira 2015; Ardèvol et al. 2016). The double displacement mechanism requires an adequately positioned nucleophile in the active site of the enzyme. So far such a nucleophile is only described for members of the GT family 6: human blood-group A and B glycosyltransferases (GTA and GTB: Glu^{303}), mammalian α-1,3-galactosyltransferase (α3GalT: Glu^{317}) and a bacterial glycosyltransferase from *Bacteroides ovatus* (BoGT6a: Glu^{192}) (Boix et al. 2001; Patenaude et al. 2002; Pham et al. 2014). The double-displacement mechanism is supported by chemical rescue studies, where covalent β-glycosyl azide derivatives are generated by an α3GalT E317A mutant from UDP-α-D-Gal and the exogenous nucleophile azide (Monegal and Planas 2006). Theoretical quantum mechanics/molecular mechanics (QM/MM) studies on the α3GalT reaction indicate that Glu^{317} is indeed essential for catalysis, but double displacement and front-face mechanism are both feasible (Gómez et al. 2013). Yet, the combination of QM/MM and molecular dynamics (MD) calculations suggest that GTs with a putative nucleophile operate exclusively by a double displacement mechanism (Rojas-Cervellera et al. 2013). In the case of GTA and GTB a covalent glycosyl-enzyme intermediate could be detected by mass spectrometry with an E303C mutant (Soya et al. 2011). Theoretical QM/MM calculations suggest that the covalent adduct is not stable enough to be observed in the wildtype (wt) enzyme (Bobovská et al. 2015). However, clear experimental evidence for the wildtype glycosyl-enzyme intermediate that would prove the double-displacement mechanism is still lacking (Ardèvol et al. 2016). Furthermore, most characterized GTs do not possess an obvious nucleophile candidate. Such GTs may rather operate via the front-face mechanism, where the nucleophilic hydroxyl group of the acceptor directly attacks the anomeric carbon of the donor sugar from the same side as the leaving group departs. Strong experimental and theoretical support for the front-side mechanism is provided by kinetic isotope

effect studies on the GT-B-fold trehalose-6-phosphate synthase (OtsA) (Lee et al. 2011), QM/MM calculations on the GT-A-fold lipopolysaccharyl-α-1,4-galactosyltransferase C (LgtC) (Gómez et al. 2012), and a combination of structural, chemical, enzymatic, MD and QM/MM calculations on the GT-A-fold glucosyl-3-phosphoglycerate synthase (GpgS) (Albesa-Jové et al. 2015). In summary, the current hypothesis is that there is no canonical mechanism for retaining GTs. The majority may follow a front-face mechanism, and only enzymes with an appropriately positioned carboxylate residue may utilize the double displacement mechanism (Ardèvol et al. 2016).

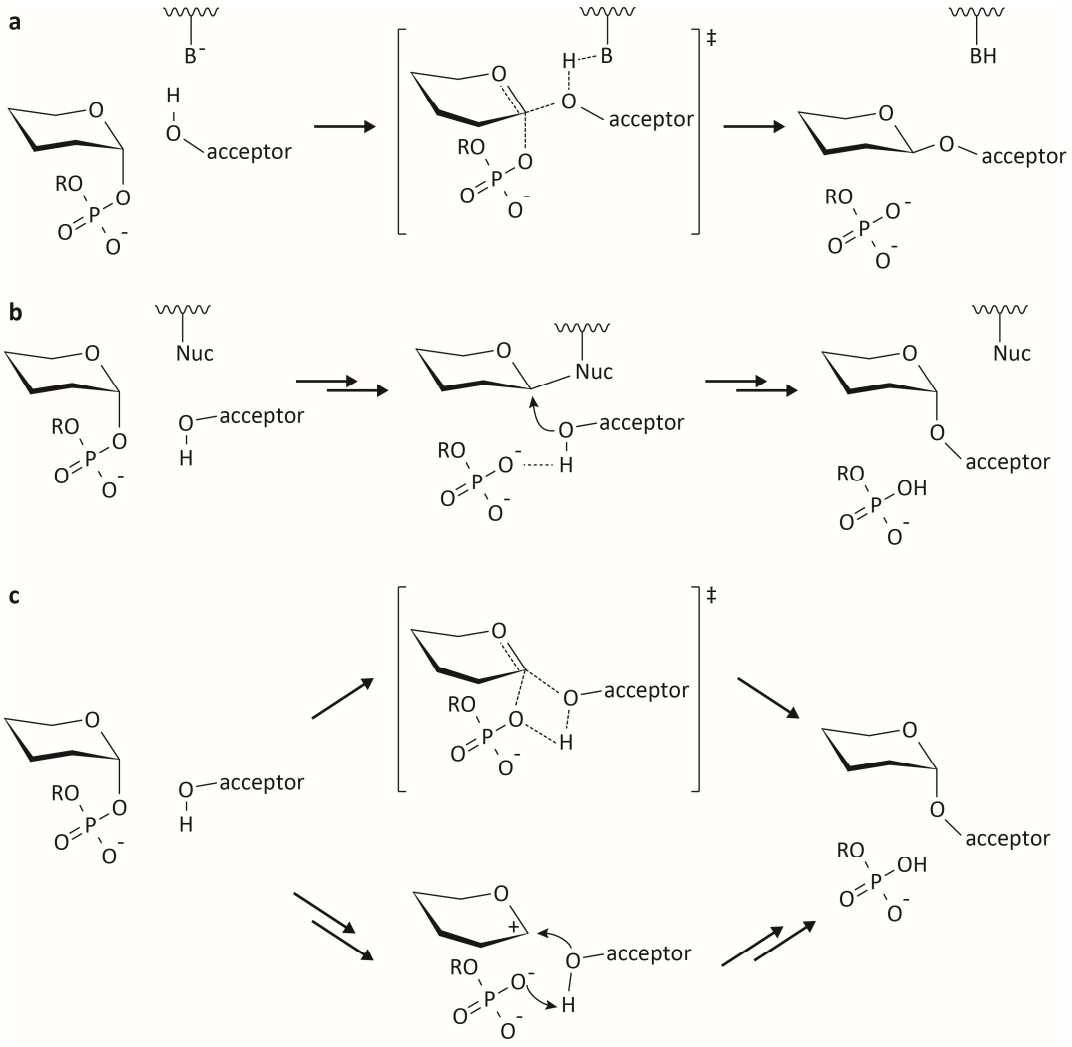


Figure 1.2: Proposed mechanisms of glycosyl transfer reactions catalyzed by inverting (**a**) and retaining (**b** and **c**) enzymes. (**a**) Inverting GTs utilize an enzymatic base-catalyzed direct-displacement S_N2-like mechanism involving a single oxocarbenium ion-like transition state. Retaining GTs may either follow a double displacement mechanism (**b**), where an enzymatic catalytic nucleophile forms a covalent intermediate with the transferred sugar, or a front-face mechanism (**c**), where leaving group departure and nucleophilic attack of the acceptor occur on the same side of the donor sugar. The front-face mechanism may follow a concerted one-step reaction (S_Ni; top) via an oxocarbenium ion-like transition state, or a stepwise reaction (S_Ni-like; bottom), in which a short-lived ion pair intermediate is formed. Substituents of the donor sugar are omitted for clarity.

1.3 Human blood group A and B glycosyltransferases

1.3.1 The ABO histo-blood group system

Discovered over a century ago by Karl Landsteiner (Landsteiner 1900), and extended by Alfred von Decastello and Alfredo Sturli (Decastello and Sturli 1902), today the ABO histo-blood group system is one of the most important antigenic classification systems in transfusion and transplantation medicine. The system is defined by four major blood types called A, B, O and AB, and bases on three different antigens (A, B and H (O)) and the respective antibodies against the A and B antigens (anti-A and anti-B). Morgan and Watkins allocated the ABH antigens to glycan structures (Watkins and Morgan 1957; Morgan and Watkins 1959, 1969). Soon after these discoveries the enzymatic basis for the biosynthesis of the A and B antigens was established (Tuppy and Staudenbauer 1966; Kobata et al. 1968a, b). The glycans are covalently linked to proteins and lipids on the surface of erythrocytes and diverse human cell types, but are also found on secreted glycoproteins and –lipids, as well as free oligosaccharides in human sera (Morgan and Watkins 1969; Finne et al. 1978; Järnefelt et al. 1978; Krusius et al. 1978; Finne 1980). In 1990, Yamamoto et al. discovered the genetic basis of the ABO histo-blood group system (Yamamoto et al. 1990a). The A, B and O genes are all found in the same gene locus and inherited according to the Mendelian laws with A and B genes being codominant. The A and B genes that encode for the functional glycosyltransferases differ only in a few bases. A frame-shift mutation in the recessive O gene yields an inactive gene product.

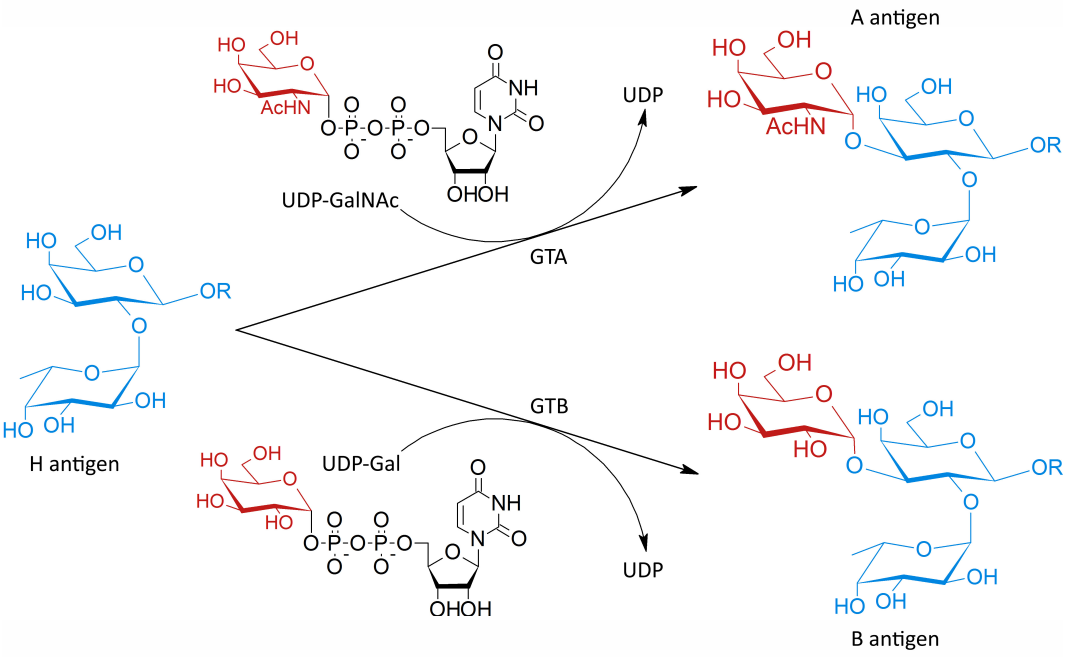


Figure 1.3: Final step in the biosynthesis of blood group A and B antigens.
GTA transfers *N*-acetyl-α-D-galactosamine (GalNAc) and GTB α-D-galactose (Gal) from an UDP-activated donor substrate to the H antigen core structure to give the A and B antigens.

The enzymes responsible for the last step in the biosynthesis of A and B antigens are named human blood group A (GTA) and B (GTB) glycosyltransferases. GTA is an α-(1→3)-N-acetylgalactosaminyltransferase and GTB an α-(1→3)-galactosyltransferase (Fig. 1.3). Both enzymes utilize the same core structure as acceptor substrate, the H (O) antigen. The H antigen (H-dis) is a disaccharide consisting of L-fucose and D-galactose, while the A and the B antigens are defined as trisaccharides containing the disaccharide H antigen with an additional α-(1→3)-linked D-N-acetylgalactosamine or D-galactose residue, respectively. The ABO antigens can be further divided into six different subtypes according to the peripheral disaccharide core structures on which the ABH determinants are synthesized (type I-VI) (Yamamoto 2004; Meloncelli and Lowary 2010). In humans the type I–VI antigens are presented as N- or O-linked glycoproteins, glycolipids, or as free oligosaccharides (Stellner and Hakomori 1974; Yamamoto 2004; Milland and Sandrin 2006). The H trisaccharide subtypes are summarized in Fig. 1.4.

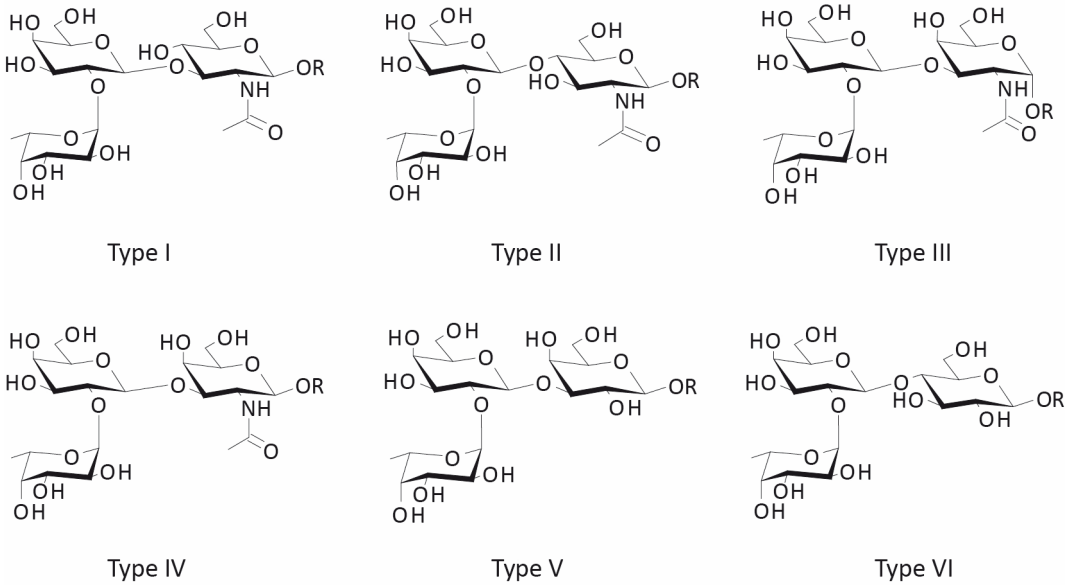


Figure 1.4: The six subtypes of the ABO blood group antigens. Shown are the different H trisaccharides: HA-β-(1→3)-β-D-Glc*p*NAc (type I), HA-β-(1→4)-β-D-Glc*p*NAc (type II), HA-β-(1→3)-α-D-Gal*p*NAc (type III), HA-β-(1→3)-β-D-Gal*p*NAc (type IV), HA-β-(1→3)-β-D-Gal*p* (type V) and HA-β-(1→4)-β-D-Glc*p* (type VI).

Anti-A and anti-B IgM antibodies are formed in the early phase of the development of the adaptive immune system and are believed to be directed against carbohydrates of bacterial cell walls and other naturally occurring non-human carbohydrate antigens. In carriers of A or B antigens, the formation of anti-A or anti-B antibodies is prevented by recognition of "self" by the immune system (Storry and Olsson 2009).

1.3.2 Structural features and substrate binding

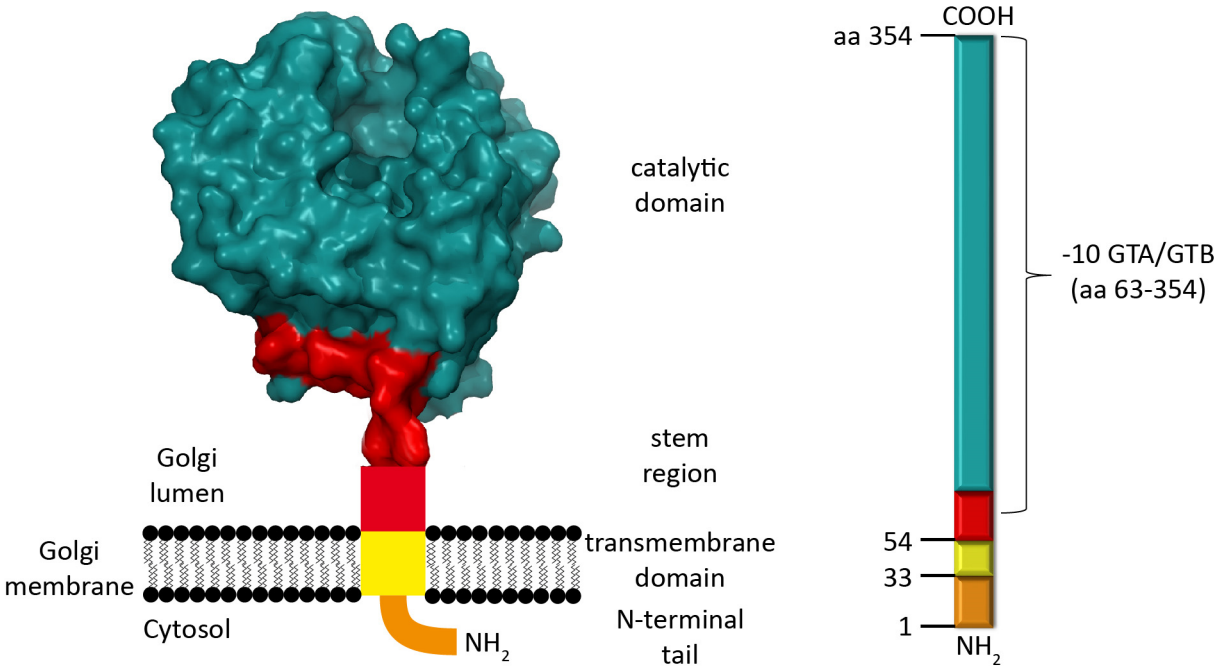


Figure 1.5: Topology of GTA and GTB.Here, all investigations are based on a functional, truncated form of the luminal soluble part of GTA/GTB (-10 GTA/GTB).

Human GTA and GTB are single-pass type II membrane proteins, active in the Golgi apparatus of the cell (Paulson and Colley 1989). Each comprises 354 aas with an overall molecular weight of about 41 kDa (Yamamoto et al. 1990b). Topologically, they are characterized by a short cytosolic N-terminal tail, a transmembrane anchoring domain and a luminal stem region connecting the anchor with the large catalytic C-terminal domain (Fig. 1.5). Through proteolytic cleavage, the C-terminal catalytic part can be released into body fluids, providing active soluble enzymes (Nagai et al. 1978a, b; Paulson and Colley 1989). Structural and functional investigations are typically based on truncated recombinant enzymes like the -10 GTB construct (aa 63-354) with comparable characteristics to the naturally occurring circulating forms (Seto et al. 1995; Marcus et al. 2003). The construct consists of the whole luminal soluble part minus ten residues on the N-terminal side of the stem region. Size exclusion chromatography and X-ray crystallography provided initial evidence for the formation of homodimers for recombinant as well as plasma-isolated enzymes (Nagai et al. 1978a, b; Patenaude et al. 2002; Alfaro et al. 2008). Electrospray ionization mass spectrometry (ESI-MS) finally proved the extremely tight but non-covalent formation of homodimers in solution at ambient temperature and neutral pH. Under these conditions, the monomeric form is not observable and therefore, considering the high sensitivity of mass spectrometry, practically not existent. Furthermore, ESI-MS data demonstrated the thermodynamic equivalency of the two active sites of the homodimer where donor and acceptor substrates can bind (Shoemaker et al. 2007, 2008; Soya et al. 2009).

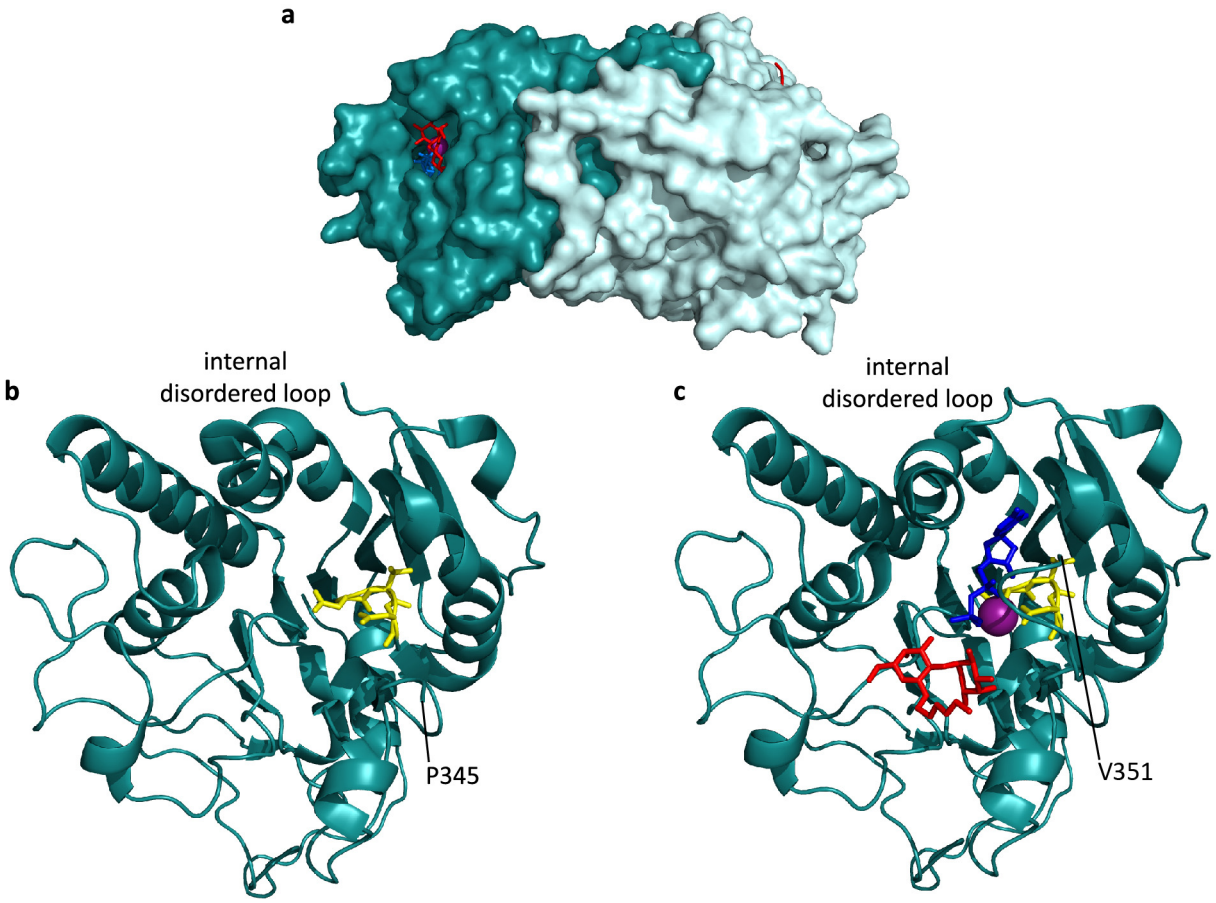


Figure 1.6: Crystal structures of GTB in absence and presence of substrates. (**a**) The -10 GTB construct appears as a homodimer in the crystal structures (PDB entry 2RJ8). (**b**) In absence of ligands, aa 177-180 of the internal disordered loop and C-terminal aa 346-354 show low electron density due to high flexibility (PDB entry 2RIT). (**c**) aa 177-179, Q182 and aa 347-351 are resolved in the structure with bound donor analog (UDP, blue) and acceptor substrate (H antigen disaccharide, red) (PDB entry 2RJ8). The DXD motif is highlighted in yellow, the manganese ion in purple. The last resolved aa at the C-terminus is P345 in absence of ligands, and V351 in presence of UDP and H-dis.

The soluble recombinant enzymes are structurally very well described (Fig. 1.6) (Patenaude et al. 2002; Letts et al. 2006; Persson et al. 2007; Alfaro et al. 2008; Schuman et al. 2010; Johal et al. 2014; Gagnon et al. 2015, 2017; Blackler et al. 2017). GTA and GTB show the classical GT-A fold with a Rossmann-type fold nucleotide-donor binding domain closely abutting the acceptor binding domain, and a wide central cleft containing the active site (Patenaude et al. 2002; Lairson et al. 2008). Like most GT-A fold proteins they possess a conserved DXD motif ($Asp^{211}Val^{212}Asp^{213}$), coordinating a divalent metal ion (Mn^{2+}/Mg^{2+}). This cofactor is critical for binding of the nucleotide-donor through interactions with the pyrophosphate group (Patenaude et al. 2002). Importantly, the cofactor binds only in presence of donor substrate, too (Shoemaker et al. 2008).

Although using different donor substrates, GTA and GTB differ only in four aas: Arg/Gly^{176}, Gly/Ser^{235}, Leu/Met^{266} and Gly/Ala^{268} (Yamamoto and Hakomori 1990). Systematic mutagenesis studies with hybrid GTA/GTB enzymes, employing all 16 combinations of these critical residues, revealed their unexpected roles (Yamamoto and Hakomori 1990; Seto et al. 1997, 1999). In these studies a simplifying nomenclature distinguishing the chimeric enzymes was introduced based on the status of the four critical residues (GTA = AAAA; GTB = BBBB). Kinetic characterization of the BAAA hybrid (GTA R176G) revealed residue 176 to affect enzyme turnover (Seto et al. 1997; Alfaro et al. 2008). Surprisingly, residues 235 and 266 have been shown to significantly modulate acceptor binding although GTA and GTB use the same acceptor substrates (Letts et al. 2006). Only two of the four critical residues, dominantly Leu/Met266 and to a minor extent Gly/Ala268, have a significant influence on donor-selection specificity (Yamamoto and Hakomori 1990; Yamamoto and McNeill 1996; Seto et al. 1999).

Some of the unexpected features of the critical residues can be rationalized on a structural basis. NMR spectroscopy and X-ray crystallography revealed that UDP-Gal binds in a high energy "tucked under" ("folded-back") conformation to GTB and AABB chimeric enzymes. The adoption of this conformation is believed to be required for catalysis (Angulo et al. 2006; Alfaro et al. 2008; Gagnon et al. 2015). Only critical residues 266 and 268 are positioned in the nucleotide-sugar binding site (Patenaude et al. 2002). The larger side chains of Met^{266} and Ala^{268} in GTB readily accommodate binding of UDP-Gal in the tucked under conformation but prohibit the same for UDP-GalNAc through steric clashes with the N-acetylic group (Alfaro et al. 2008; Wagner et al. 2015). The binding conformation of UDP-GalNAc is not known. However, the tucked under conformation in the wider GTA binding site is feasible as shown by computational modeling. Crystal structures of the AAGlyB chimeric enzyme (GTA L266G, G268A) in presence of UDP-GalNAc derivatives reveal two alternative, potentially productive conformations for the sugar residue, explaining the GalNAc-transferase activity of AAGlyB (Wagner et al. 2015). However, the substrate discrimination mechanism of GTA remains elusive. There is no steric hindrance for binding of the smaller UDP-Gal to the wider GTA binding cleft. High flexibility of the galactose moiety in GTA structures, whereas the same is fully ordered in GTB, suggest an incapability of GTA to stabilize UDP-Gal in the catalytically active conformation (Gagnon et al. 2015). Naturally occurring *cis*-active enzymes, capable of producing both A and B antigens with mutations apart from the four critical amino acids, further highlight the delicate balance of the donor recognition mechanism (Marcus et al. 2003; Persson et al. 2007).

A striking feature of GTA and GTB are two mobile polypeptide regions, the internal disordered loop (aa 177-195) and the C-terminal tail (aa 345-354), which are directly involved in donor and acceptor binding (Fig. 1.7) (Patenaude et al. 2002; Alfaro et al. 2008). According to our current understanding, substrate binding employs three conformational states (Alfaro et al. 2008). GTA and GTB adopt an "open" conformation in the absence of both substrates or in the presence of acceptor only. The flexible loops are disordered, potentially due to mutual repulsive positive charges of Lys^{179}, Arg^{180} and Lys^{124} side chains (Persson et al. 2007; Johal et al. 2014), and the substrate binding sites are exposed to solvent.

Donor substrate binding induces the transition to a "semi-closed" conformation with the internal loop orienting towards the ligand and partially occluding the active site. The negative charge of the nucleotide may counterbalance the electrostatic repulsion between the basic residues 179, 180 and 124 (Alfaro et al. 2008; Johal et al. 2014). The presence of both substrates is a prerequisite for ordering of parts of the C-terminal tail, which is facilitated by direct hydrogen bonds to the α-L-Fuc*p* of the acceptor and to the pyrophosphate of the donor substrate. This "closed" conformation is further stabilized through a cation-π-interaction between the side chains of Trp^{181} and Arg^{352}. It is the only direct contact between internal loop and C-terminal tail. Base-modified UDP-Gal and UDP-GalNAc analogs, acting as competitive GT inhibitors, block this stacking interaction (Pesnot et al. 2010; Jørgensen et al. 2013; Wagner et al. 2015), reflecting the importance of the formation of the fully closed state for catalytic activity.

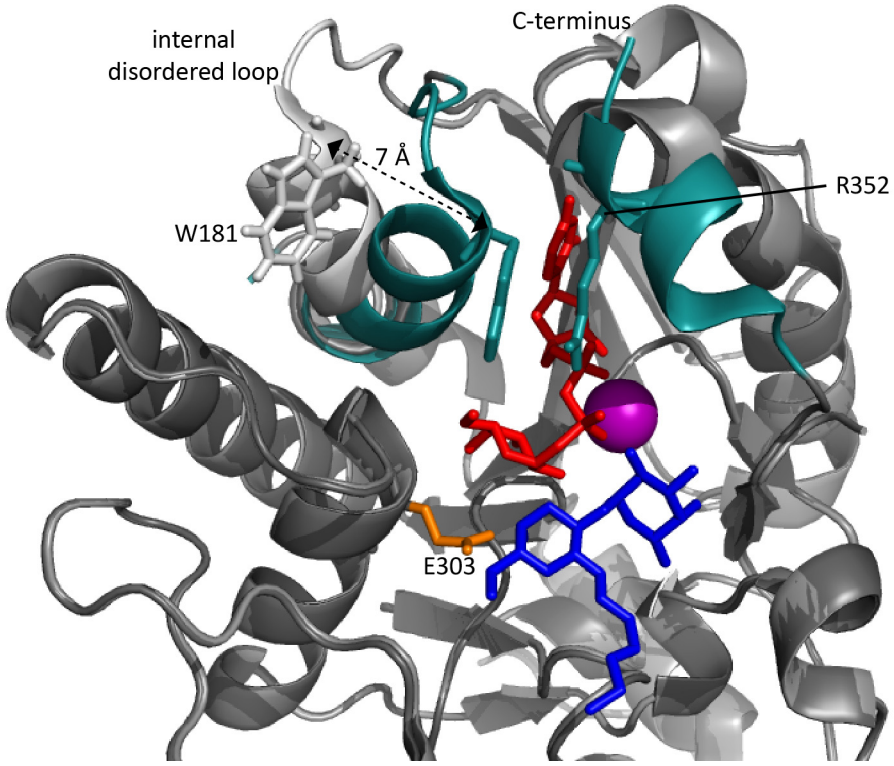


Figure 1.7: Overlay of the open (light grey) and closed (dark grey) conformation of GTA/GTB. The most flexible regions highlighted in cyan (closed state) are only resolved in crystal structures of the AABB chimeric enzyme (PDB entries 3IOH (open), 2RJ7 (closed)). The C-terminal tail is only visible in the closed conformation. The internal disordered loop moves by ca. 7 Å between open and closed conformation. The closed conformation is locked via a stacking interaction between Trp^{181} and Arg^{352}. Glu^{303} (orange sticks) likely acts as a catalytic nucleophile. Donor (red) and acceptor (blue) substrate are represented as sticks. The metal ion is shown as a sphere (purple).

So far, nothing is known about the time scales, on which transitions between the open, the semi-closed, and the closed conformation occur. However, the critical residue Arg/Gly^{176} located near the internal loop is known to significantly influence enzyme kinetics. The largely increased turnover rate of the single

mutant BAAA in comparison to GTA might be the consequence of faster product release and substrate exchange due to higher flexibilities of internal and C-terminal loops (Seto et al. 1997; Alfaro et al. 2008). This idea is supported by the crystal structures of the chimeric enzymes ABBB and AABB, which show lower thermal motion in the flexible regions than GTB (Alfaro et al., 2008).

The substrate binding process has been extensively studied through interactions with several substrate and product analogs. The acceptor glycan is covalently linked to lipids or proteins in nature. However, interaction studies are typically performed with truncated forms of the acceptor. The minimal motif that is necessary for efficient catalysis, and common to all types of H antigens is the H antigen disaccharide (α-L-Fuc*p*-(1⟶2)-β-D-Gal*p*-OR) (Watkins 1991; Lowary and Hindsgaul 1994). Enzyme kinetics with type I (α-L-Fuc*p*-(1⟶2)-β-D-Gal*p*-(1⟶3)-β-D-GlcNAc*p*-OR) and II (α-L-Fuc*p*-(1⟶2)-β-D-Gal*p*-(1⟶4)-β-D-GlcNAc*p*-OR) H-trisaccharides (Fig. 1.4) report on significantly decreased activities compared to the disaccharide, mainly due to elevated K_M values. GTA and GTB both show higher specificity constants for type II compared to type I H trisaccharides, which may be reflected *in vivo* (Letts et al. 2006).

Enzyme-catalyzed hydrolysis of the native donor substrates is a major drawback in functional studies. This can be understood as a glycosyl transfer reaction to water, and indicates that the acceptor substrate is not required for cleavage of the glycosidic bond (Zhang et al. 2001; Sindhuwinata et al. 2010). Importantly, the donor analogs UDP-Glc and UDP-GlcNAc do not undergo enzymatic hydrolysis, reflecting their inactivity in transfer reactions, and approving them as alternatives for the natural substrates (Soya et al. 2009). Binding of the donor substrate is mainly mediated by the nucleotide moiety. Therefore, UDP is a suitable donor analog (Blume et al. 2006). Recent efforts to generate non-hydrolysable donor analogs employed substitution of the anomeric oxygen by carbon. However, the corresponding donor analogs did not adopt the folded-back conformation, limiting their usability in mechanistic studies (Gagnon et al. 2015).

Initial enzyme kinetic investigations proposed a step-wise ordered binding mechanism with binding of donor substrate together with the metal cofactor preceding acceptor binding (Kamath et al. 1999). Significantly longer lifetimes of the donor-enzyme complex compared to the acceptor-enzyme complex support these findings (Angulo et al. 2006). In contrast to the closely related bovine α3GalT, GTA and GTB bind the acceptor with reasonable affinity in absence of the donor, too (Boix et al. 2002; Shoemaker et al. 2008; Sindhuwinata et al. 2013). On the other hand, acceptor binding is significantly enhanced in presence of the donor in a positive cooperative manner (Shoemaker et al. 2008). Furthermore, mutual cooperativity is also observed for the donor substrate, showing increased affinities in presence of the acceptor (Sindhuwinata et al. 2010, 2013). Apart from direct hydrogen bonds between donor and acceptor, positive cooperativity may partly be attributed to interactions between enzyme and substrates that are only formed in the closed state. At the same time, the formation of the closed state relies on the presence of both substrates (Alfaro et al. 2008). This is consistent with thermodynamic signatures from ITC experiments, in which donor and acceptor analogs show more favorable binding enthalpies in

presence of the respective other ligand. The entropic contribution is however more unfavorable, potentially due to higher order of the enzymes' flexible regions in the closed state (Sindhuwinata et al. 2013).

Interaction studies with the UDP-Gal or UDP-GalNAc epimers UDP-Glc and UDP-GlcNAc, respectively, gave insights into the mechanism of stereoselectivity. The sugar epimers are transferred with very low efficiency by GTA and GTB, despite the high similarity to the natural donors (Seto et al. 1999). Comparison of the specificity constants (k_{cat}/K_m) reveal a more than 4000 times higher specificity towards the natural substrate (Seto et al. 1999, 2000). However, the epimers bind with comparable affinities as the natural donors and show similar binding epitopes (Blume et al. 2006; Soya et al. 2009). UDP-Glc is even capable of binding in the same bioactive folded-back conformation as UDP-Gal (Angulo et al. 2006; Gagnon et al. 2015). Angulo et al. proposed a "molecular tweezers" mechanism where the promotion to the transition state requires interactions between sugar and enzyme, which are not formed by Glc-O4 (Angulo et al. 2006). Recent crystallographic data demonstrate a higher organization of internal and C-terminal loop in presence of UDP-Gal. Closure of the internal loop is hindered by the different position of the epimeric 4-OH group, which sterically clashes with the γ-OH group of Ser^{185} in the closed conformation. The inability to reach the catalytically active closed state might allow epimer discrimination (Gagnon et al. 2015).

The process of product release is a matter of ongoing studies in order to advance mechanistic understanding. New crystal structures of GTA and GTB in presence of the A (α-L-Fuc*p*-(1⟶2)-[α-D-GalNAc*p*-(1⟶3)]-β-D-Gal*p*-OR) and B (α-L-Fuc*p*-(1⟶2)-[α-D-Gal*p*-(1⟶3)]-β-D-Gal*p*-OR) trisaccharides suggest a steric clash between UDP and the transferred sugar, leading to a disordered active site and destabilizing product binding (Gagnon et al. 2017). The authors propose that UDP and product glycan cannot bind at the same time and UDP is ejected first, in agreement with the double displacement mechanism. However, crystallographic data were not obtained in presence of UDP and the kinetics of product release remain unresolved.

GTA and GTB are retaining GTs, whose transfer mechanism is still under debate. Different mechanisms have been proposed as described in detail in section 1.2. Glu^{303}, located in a strained double turn motif (aa 298-303) in the active site, has been identified as a key residue to distinguish between the mechanisms. It may either act as a catalytic nucleophile (double-displacement), stabilize the oxocarbenium ion-like intermediate and assist leaving group departure (S_Ni-like; front-face stepwise), or stabilize the transition state (S_Ni; front-face concerted) (Blackler et al. 2017). Evidence for the double-displacement mechanism was provided by ESI-MS experiments with Glu303Cys mutants, detecting covalent glycosyl-enzyme intermediates (Soya et al. 2011). Recent structural and kinetic investigations, employing systematic Glu^{303} substitutions demonstrate that nucleophilicity is more important than preservation of the active site architecture, pointing in the direction of a double-displacement mechanism (Blackler et al. 2017). However, residual activities of the mutants cannot exclude a specific mechanism, and may rather suggest that different mechanistic pathways can be followed (Hurtado-

Guerrero and Davies 2012; Blackler et al. 2017). According to hybrid QM/MM calculations, a double displacement and a front-face attack are equally feasible in the enzymatic catalysis, too (Bobovská et al. 2015).

1.4 NMR Spectroscopy

Nuclear magnetic resonance (NMR) spectroscopy is a versatile biophysical method for the investigation of the dynamic structure and interaction of molecules. The resonance frequencies of nuclear spins in a strong magnetic field allow conclusions on their detailed chemical environments. For the analysis of proteins, the most interesting nuclei are the spin ½ nuclei ^{1}H, ^{13}C and ^{15}N, and the spin 1 nucleus ^{2}H. By exploitation of these nuclei in modern labeling techniques, it is possible to bring probes to nearly every desired position in a protein without interfering with its native structure and dynamics. In an NMR experiment a sample is placed in a strong magnetic field (B_0). Spin ½ nuclei, which can be regarded as small magnetic dipoles, split into two energy states. The dipoles preferentially align with the magnetic field and build up a bulk magnetization parallel to the vector of the magnetic field (defined as z-axis) reflected by overpopulation over the high energy β state. This bulk magnetization caused by a single type of nuclei (e.g. ^{1}H) can now be rotated towards the x,y-plane by a magnetic field that is oriented perpendicular to B_0. This is achieved with the help of electromagnetic radiation in the range of radiofrequencies that meet exactly the resonance frequency of the nuclei and induce transitions between α and β states. The resonance frequency depends on the gyromagnetic ratio γ of the nucleus and the applied static magnetic field B_0. Each spin precesses at a characteristic rate that depends on the local magnetic field defined by local chemical structure, solvent composition etc. This precession induces a time-dependent current in the receiver coil which gives rise to the observable free induction decay (FID). Fourier transformation translates this time-dependent FID into the frequency domain to give the NMR spectrum. For a comprehensive introduction into the theoretical background of NMR the reader is referred to the literature (Keeler 2010).

When the perturbing temporary magnetic field is switched off, the spins will return to their equilibrium state in a process called relaxation. Longitudinal relaxation characterized by the time constant T_1 describes the recovery of magnetization in z direction. In this process the absorbed energy of the spins is transferred to the surrounding in form of thermal motion. The transversal relaxation is the process of dephasing of spins in the x,y-plane and is characterized by the time constant T_2. This process is responsible for the exponential decay of the FID and directly connected with the line width (λ) of the signal in the NMR spectrum ($R_2 = 1/T_2 \approx \lambda/2$). Responsible for relaxation are local magnetic field fluctuations originating from rotational molecular motions. For spin ½ nuclei the main relaxation mechanisms are dipole-dipole interactions between spins (mainly protons) and chemical shift anisotropy (CSA). The latter takes into account that orbitals of molecular bonds are not isotropically oriented around a nucleus. Therefore, the orientation of the molecule relative to B_0 during its tumbling motion in solution varies the local magnetic field experienced by a nucleus and contributes to its relaxation. The velocity of rotational diffusion of molecules is described by the correlation time (τ_c). Large proteins show rapid transversal relaxation due to their long correlation times in the range of ns, and the large number of dipole-dipole interactions that arise from the large number of protons. This leads to line-broadening and disappearance of signals. Besides the improvement of the spectrometer

hardware, several isotope labeling techniques and specialized NMR pulse programs contributed to largely overcome these problems.

1.4.1 Methyl labeling and methyl-TROSY experiments

In a 2D [^{13}C,^{1}H]-HMQC (Heteronuclear Multiple-Quantum Correlation) experiment proton-carbon multiple quantum states are generated and evolve with the carbon frequency during t_1. The MQ states are transferred back to observable proton magnetization that is detected in time t_2 under conditions of broadband ^{13}C decoupling. The spectra show cross signals at the resonance frequencies of both nuclei (Keeler 2010). Interestingly, the standard [^{13}C,^{1}H]-HMQC pulse sequence gives rise to the methyl-TROSY (Transverse Relaxation Optimized SpectroscopY) effect (Ollerenshaw et al. 2003; Tugarinov et al. 2003). Thus, [^{13}C,^{1}H]-HMQC and methyl-TROSY are used interchangeably throughout this thesis. In brief, methyl-TROSY NMR relies on the rapid rotation of methyl groups around their threefold axis in slowly tumbling macromolecules, leading to the separation of rapidly and slowly relaxing single and multiple quantum transitions. Magnetization is transferred between the slowly relaxing transitions to give rise to spectra with high sensitivity. (Ollerenshaw et al. 2003; Kay 2011). The sensitivity is additionally increased by depletion of the surrounding protons. By specific $^{13}C^{1}H_3$ methyl-labeling within a perdeuterated background, macromolecular complexes with molecular weights much larger than 100 kDa can be analyzed (Sprangers and Kay 2007; Sprangers et al. 2007; Rosenzweig and Kay 2014; Wiesner and Sprangers 2015).

Protocols for the introduction of $^{13}C^{1}H_3$ methyl groups into every methyl bearing amino acid are available. Selectively labeled metabolic precursors are developed for the labeling of Ile, Val and Leu residues (Gardner and Kay 1997; Goto et al. 1999; Tugarinov and Kay 2004; Gans et al. 2010). The methyl groups of Ala, Met and Thr residues are usually labeled by direct addition of the selectively labeled amino acids (Gelis et al. 2007; Isaacson et al. 2007; Ayala et al. 2009; Velyvis et al. 2012).

Compared to [^{1}H,^{15}N]-TROSY-HSQC spectra, methyl-TROSY experiments have the advantage of higher sensitivity, of less crowded spectra, and of not being dependent on unfolding/refolding procedures that are often required to re-protonate buried amides. However, there is no standard strategy for the assignment of methyl groups. This procedure can be challenging and time-consuming.

1.4.2 Chemical exchange in proteins

In NMR spectroscopy, chemical exchange processes between at least two distinguishable states directly affect the resonance positions, intensities and linewidths in the spectra (Kleckner and Foster 2011; Palmer 2014). Consequently, chemical exchange phenomena are the basis for plenty of experiments to study protein motions on time-scales from ps to s, which comprise processes like ligand binding, allosteric regulation, catalysis and protein folding (Korzhnev et al. 2004, 2010; Neudecker et al. 2009; Chan et al. 2013). In the simplest model ($A \underset{k_A}{\overset{k_B}{\rightleftharpoons}} B$), where the respective nucleus occupies just two different

states (A and B), these states are characterized by two individual resonance frequencies ν_A and ν_B. The appearance of the corresponding NMR spectrum depends on the difference of these frequencies ($\Delta\nu = |\nu_A - \nu_B|$), the total exchange rate ($k_{ex} = k_A + k_B$; with k_A: $B \rightarrow A$ and k_B: $A \rightarrow B$), and the relative population of the individual states ($p_A = \frac{k_A}{k_A+k_B}$ and $p_B = \frac{k_B}{k_A+k_B}$). Three major time regimes are distinguishable. When the exchange rate is much lower than the chemical shift difference ($k_{ex} << \Delta\nu$), the system is in the limit of slow chemical exchange, where each state gives rise to a distinct spectrum. Relative intensities correspond to the respective populations (p_A and p_B). With increasing k_{ex} into the range of $\Delta\nu$ ($k_{ex} \approx \Delta\nu$), the exchange process contributes more and more to transverse relaxation. Thus, the resonances are strongly exchange-broadened, which can result in a complete disappearance of signals. This occurs in the intermediate exchange regime. In the fast chemical exchange regime, k_{ex} is much larger than $\Delta\nu$ ($k_{ex} >> \Delta\nu$). Only one single signal is observed at the population-weighted average frequency of both states (Kleckner and Foster 2011).

A typical example for chemical exchange is the interaction of a ligand with a protein. In a protein-monitored ligand binding event, the on- (k_{on}) and off-rate (k_{off}) of the ligand define the exchange rate ($k_{ex} = k_{on}[L] + k_{off}$). In the course of an NMR-monitored ligand titration, both the population of the two exchanging states, and their exchange rate (as a consequence of a changing ligand concentration) are shifted. If the exchange process is fast on the NMR timescale throughout the titration (large off-rate), the resonance progressively moves from the position of the ligand free to the position of the ligand bound state. In the limit of slow chemical exchange, two separated resonances corresponding to the free and bound states are detected with intensities that depend on the population of the ligand bound state. In the intermediate exchange regime, a more complex behavior is observed. Neither chemical shift nor intensity are linearly related to the extent of binding (Kovrigin 2012). Thus, only a profound analysis that considers peak positions, intensities and line-widths of all titration points at the same time can accurately extract information on exchange rates and dissociation constants of the investigated system.

Line shape analysis of NMR signals is a powerful method to derive site-specific kinetic and thermodynamic information on chemical exchange processes. Typically, such an analysis is based on NMR-monitored ligand titrations. Historically, line shapes were first derived from one dimensional spectra, or as cross-sections from two dimensional spectra, and fitted to the McConnel equations, which describe NMR signals that are subject to chemical exchange (McConnell 1958; London 1993; Günther et al. 2002). However, the application of 1D NMR titrations to proteins is not practical due to the degeneracy of chemical shifts. The method of extraction of cross-sections from two dimensional spectra suffers from the dependency on normalization due to differential relaxation of the states in both dimensions, which introduces random and systematic errors in the analysis. Recently, the direct quantum mechanical simulation of experiments was introduced for fitting of two dimensional NMR titration data with the program *TITAN* (Waudby et al. 2016). The program calculates the evolution of magnetization throughout the pulse sequence. Thus, *TITAN* can fully account for differential relaxation of states, and an error-prone normalization is not necessary. The method has been adapted to the

[^{13}C,^{1}H]-HMQC experiment. Line shape analysis can even be applied to more complex exchange processes involving intermediate states like in the induced-fit or conformational selection binding model (Mittag et al. 2004; Agafonov et al. 2014; Shinya et al. 2017).

Slow chemical exchange events can also be probed by two-dimensional exchange spectroscopy (Farrow et al. 1994). Domain movements, as well as ligand binding and release are processes that are observed in the time window of slow chemical exchange (Sahu et al. 2007; Religa et al. 2010). The zz-exchange experiment requires at least two detectable signals corresponding to the two exchanging states. In the zz-exchange experiment spins are first labeled with their respective chemical shifts according to their current state. Then, magnetization is stored in z-direction for a fixed exchange time. During this period, spins exchange between states. At the end of the exchange time, some of the spins have switched the state. The resulting spectra show the auto signals for spins that remain in the same state during evolution and detection period. Cross signals arise at mixed frequency positions for spins that are observed in different states during the evolution and detection period. Kinetic information can be extracted from build-up curves that are generated by acquisition of a series of zz-exchange experiments with varying exchange times (Li and Palmer 2009; Kleckner and Foster 2011). A modification of this strategy is introduced by Kloiber et al. The strategy is based on the combination of two complementary experiments, where the first frequency labeling period and the exchange delay are interchanged. Consequently, two types of spectra are generated, one with and one without resolving exchange cross peaks. The extraction of exchange rates from the intensities of the auto signals in both types of spectra is more reliable, as systematic errors caused by differential relaxation of the states are avoided (Kloiber et al. 2011).

1.4.3 Paramagnetic NMR

Paramagnetic species are defined by unpaired electrons that align with an external magnetic field. Typical sources of unpaired electrons comprise nitroxide radicals, certain divalent metal ions, such as Mn^{2+} or Fe^{3+}, and most trivalent ions of the lanthanide series of chemical elements (Liu et al. 2014). In an NMR experiment, paramagnetic species severely affect the behavior of spins, even if paramagnetic center and nuclear probe are separated by a large distance. Thus, paramagnetic NMR plays an important role in the structural and dynamical characterization of macromolecules by site-specific labeling with paramagnetic probes. The most commonly used paramagnetic effects comprise paramagnetic relaxation enhancement (PRE), pseudocontact shifts (PCSs) and residual dipolar couplings (RDCs) (Liu et al. 2014). PRE induced line-broadening relies on the Solomon and Curie spin mechanism that both contribute to transversal relaxation and show an r^{-6} distance dependency. While all paramagnetic species induce PRE, PCSs and RDCs are restricted to those species with an anisotropic magnetic susceptibility tensor (χ-tensor). All paramagnetic lanthanide ions except Gd^{3+} have anisotropic χ-tensors. In order to allow the determination of RDCs and PCSs, the orientation of the anisotropic paramagnetic label has to be adequately fixed with respect to the investigated molecule. Dipolar couplings that are usually

cancelled by the random orientation of molecules in solution state NMR become observable, as the metal ions induce a weak molecular alignment with the magnetic field. PCSs are chemical shift changes caused by through-space interactions between the unpaired electrons and the investigated spins. PCSs show a long-ranging r^{-3} distance dependency with measurable effects at distances of up to 40 Å (Su and Otting 2010). However, PCSs are also dependent on the orientation of the nuclear spin relative to the anisotropic χ-tensor. It is common practice to decompose the χ-tensor in an isotropic and an anisotropic part, resulting in the Δχ-tensor. The Δχ-tensor is described by an axial ($\Delta\chi_{ax} = \chi_z - (\chi_x + \chi_y)/2$) and a rhombic component ($\Delta\chi_{rh} = \chi_x - \chi_y$), and has the same principal axes as the χ-tensor (x, y, z) that originates in the paramagnetic center. The magnitude of the chemical shift change ($\Delta\delta^{PCS}$) between the paramagnetic sample and a diamagnetic reference can be calculated according to the following equation:

$$\Delta\delta^{PCS} = 1/(12\pi r^3)[\Delta\chi_{ax}(3\cos^2\theta - 1) + 1.5\Delta\chi_{rh}\sin^2\theta\cos^2\varphi] \quad (1.1)$$

where r, θ and φ are the spherical polar coordinates of the nucleus relative to the principal axes of the Δχ-tensor (Otting 2010; Liu et al. 2014). Thus, PCSs represent particularly valuable structural restraints that can be used for spectral assignment and structure determination (Allegrozzi et al. 2000; Schmitz et al. 2012; Pan et al. 2016; Lescanne et al. 2017). Furthermore, PCSs are exploited to characterize protein-protein and protein-ligand interactions, as well as protein dynamics (Pintacuda et al. 2007; Tang et al. 2007; Keizers et al. 2010)

2 Objectives

Glycoconjugates contribute to diverse biological functions (Varki 1993; Varki and Gagneux 2017). Changes in glycosylation patterns are directly linked to diseases like cancer and chronic inflammations (Dube and Bertozzi 2005; Christiansen et al. 2014; Freeze et al. 2017b; Varki et al. 2017b). Glycans also serve as attachment factors for pathogens. For instance, human blood group antigens are recognized by various viruses and bacteria (Harrington et al. 2004; Heggelund et al. 2017). Glycans are exploited as therapeutics, e.g. vaccines or carbohydrate mimics (Kwan and Withers 2011; Seeberger and Cummings 2017), and may have a huge therapeutic potential. The biosynthesis of glycans is achieved by cascades of highly specific glycosyltransferases (GTs) also recognized as therapeutic targets. However, specific inhibition or modulation of GTs turned out to be complicated. To overcome this challenge, it will be very important to better understand the mechanisms used by these enzymes.

Here, the human blood group glycosyltransferases GTA and GTB are investigated to reveal their mode of operation. Many details have already been revealed from crystal structures and ligand-interaction studies focusing on thermodynamics (Alfaro et al. 2008; Sindhuwinata et al. 2013). However, there is a lack of kinetic data describing substrate binding and associated protein dynamics. Solution state NMR spectroscopy offers various experiments for the analysis of protein dynamics. In order to gain site-specific information on intermolecular interactions, and to reveal allosteric sites, the assignment of the resonances is required. In former studies, it was attempted to assign the backbone resonances (Sindhuwinata 2012; Grimm 2015; Weissbach 2016). However, the slow rotational tumbling and internal molecular dynamics of GTA and GTB hampered the assignment. Only a small number of side chain resonances of Trp, Ile and Met residues could be sequence-specifically allocated (Flügge 2014; Weissbach 2016; Grimm et al. 2017).

Thus, a major goal is to obtain a more detailed picture of the enzymes. For that reason, $^{13}C^{1}H_3$-methyl labels are introduced into the side chains of all Ala, Ile, Leu, Met and Val residues, which are evenly and densely distributed throughout the enzymes. As the assignment of nearly 100 residues by point mutation is not feasible, an alternative assignment strategy is required. Here, I used information from NOE correlations between neighboring methyl groups and lanthanide-induced PCSs in a structure-based approach for assignment. It is known that paramagnetic metal ions can be introduced into the natural metal binding site of GTA and GTB (Grimm et al. 2017). However, for the measurement of PCSs, the experimental conditions have to be optimized. Apart from being instrumental for the assignment strategy, NOEs and PCSs are explored to deliver important structural insights, too.

NMR-monitored ligand titrations are rich sources of structural, mechanistic, thermodynamic and kinetic information on biomolecular interactions. Ligand binding-induced chemical shift perturbations (CSPs) report on ligand binding sites and allosterically affected regions. The appearance of the spectra in a ligand titration is determined by the exchange rate between free and bound, open and closed or

differently characterized states. The resonance line shapes report on the timescale of the exchange process. Therefore, a systematic protein-based line shape analysis facilitates quantification of thermodynamics and kinetics of the respective binding event. Here, I use in-depth binding studies of different donor and acceptor substrates and analogs to GTA, GTB and the AAGlyB chimeric enzyme to reveal common and distinctive behavior of the enzymes. This can deliver new insights into the binding modes, and reveal mechanisms for substrate discrimination. Former studies revealed exchange processes in the slow time regime (Flügge 2014; Weissbach et al. 2018). Besides line shape analysis, the ZZ-exchange experiment is ideally suited to quantify exchange processes on this time-scale.

Finally, ligand binding studies are also applied to Trp^{181} mutants of GTB. This residue is located on the tip of the internal disordered loop and locks the protein in the closed state via a cation-π interaction to Arg^{352} of the C-terminal domain. Substitutions of Trp^{181} with Met or Glu are hypothesized to either weaken or strengthen this interaction. Thus, significant effects on protein dynamics and ligand binding kinetics are expected to be observed for these Trp-mutants.

The most important goals of the protein-ligand interaction studies are:

- insights into substrate discrimination mechanisms
- the identification of allosteric effects important for catalysis
- the kinetic quantification of the binding processes and the associated protein dynamics

3 Methods

3.1 Protein expression

3.1.1 Bacterial system and plasmid

The high efficiency transformation strain *E.coli* K12 DH5α (genotype: *fhuA2 lac(del)U169 phoA glnV44 Φ80' lacZ(del)M15 gyrA96 recA1 relA1 endA1 thi-1 hsdR17)* is used for cloning. *E. coli* K12 BL21 cells (F- *ompT hsd*SB(rB-mB-) *gal dcm*) serve as expression systems for recombinant glycosyltransferases.

The plasmid encodes for aa 64-354 of the entire human glycosyltransferase sequence. The DNA sequence has been optimized to match codon usage in *E. coli.* The N-terminal transmembrane region and ten aas of the stem region of GTA/GTB are not encoded and are replaced by a six aa sequence (MAIGEF). Because of N-terminal methionine excision, the N-terminus of the recombinant protein is formed by the Ala residue in this sequence. Back counting from the encoded catalytic domain, this is residue 58.

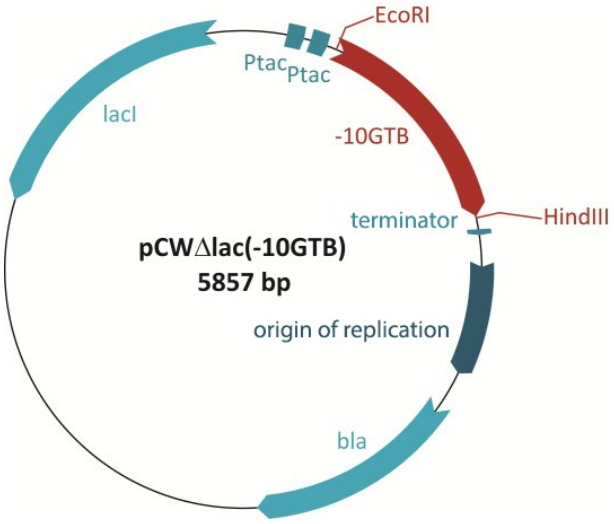


Figure 3.1: Plasmid map of pCWΔlac coding for -10 GTB. The Ptac promotor (-35 region trp promotor + -10 region lac promotor) precedes the -10 GTB (or GTA) and terminator sequence. The bla gene ensures selection by coding for the β-lactamase, responsible for ampicillin resistance. The lacI sequence encodes the lac repressor, inhibited by IPTG to induce expression.

3.1.2 Growth media

For preparation of D_2O based media, salts and glucose are dissolved in D_2O and lyophilized to remove residual exchangeable protons. 100x vitamin D_2O stocks contain riboflavin (0.01 mg/mL), D-biotin, choline chloride (0.1 mg/mL), folic acid (0.1 mg/mL), nicotinamide (0.1 mg/mL), D-pantothenic acid (0.1 mg/mL), pyridoxal hydrochloride (0.1 mg/mL), thiamine hydrochloride (0.1 mg/mL), myo-inositol

(0.2 mg/mL) and NaCl (8.5 mg/mL). 1000x trace metal D_2O stocks contain $CaCl_2$ (20 mM), $FeCl_3$ (100 mM), $MnCl_2$ (10 mM), $ZnSO_4$ (10 mM), $CoCl_2$ (2 mM), $CuCl_2$ (2 mM), $NiSO_4$ (2 mM), Na_2MoO_4 (2 mM), H_3BO_3 (2 mM) and EDTA (17 mM). Heat-sensitive components and D_2O containing solutions are sterilized by filtration (0.22 µm). All other solutions are autoclaved at 121°C for 20 min.

Table 3.1: List of H_2O-based *E.coli* nutrient media (1 L).

Medium	Quantity	Additives
Luria-Bertani (LB) medium (pH 7)	10 g	Tryptone
	5 g	Yeast extract
	10 g	NaCl
	ad 1000 mL	H_2O
LB agar plates (pH 7)	10 g	Tryptone
	5 g	Yeast extract
	10 g	NaCl
	ad 1000 mL	H_2O
	15 g	Agar
Super Optimum Broth (SOB) medium	20 g	Tryptone
	5 g	Yeast extract
	0.6 g	NaCl
	0.2 g	KCl
	Sterile addition immediately before inoculation:	
	5 mL	$MgCl_2$ (2 M)
Super Optimum Broth with Catabolite repression (SOC) medium	Based on SOB medium	
	3.6 g	glucose
Terrific Broth (TB) medium (optimized for GTB expression)	12 g	Tryptone
	24 g	Yeast extract
	4 ml	Glycerol
	6 g	Na_2HPO_4
	3 g	KH_2PO_4
	1 g	NH_4Cl
	0,5 g	NaCl
	ad 1000 ml	H_2O
	Sterile addition immediately before inoculation:	
	1 ml	1 M $MgSO_4$
	1 ml	0.1 M $CaCl_2$
	0,5 ml	10 mg/ml thiamine
	10 ml	20% glucose
	20 ml	20% casamino acids
	1 ml	100 mg/ml Amp

For deuteration of the Ile-precursor (2-ketobutyric acid-4-^{13}C-3,3-d_2), 72 mg of 2-ketobutyric acid-4-^{13}C are dissolved in 200 ml D_2O containing 0.73 g K_2HPO_4 anhydrate. The pH* is adjusted to 10.5 using NaOD. The solution is incubated overnight at 45°C in a round bottom flask in an oil bath. The flask is closed with a rubber plug, and a cannula is added for ventilation. NaH_2PO_4 is added until a pH* of 7.4 is reached. The success of the deuteration is checked by ^{1}H-NMR spectroscopy. The deuterated precursors are stored at -20°C.

Table 3.2: D_2O-based *E.coli* M9 minimal media for starter and main cultures.

	Starter culture (50 mL)	Main culture (500 mL)	Final concentration
Na_2HPO_4	445 mg	4.45 g	8.9 g/L
KH_2PO_4	340 mg	3.4 g	6.8 g/L
NaCl	25 mg	250 mg	0.5 g/L
$(NH_4)_2SO_4$	165 mg	-	3.3 g/L
$(^{15}NH_4)_2SO_4$	-	1.65 g	3.3 g/L
D-glucose	200 mg	-	4.0 g/L
D-glucose d_7	-	1.5 g	3.0 g/L
$MgSO_4$ (1 M)	165 µL	1.65 mL	3.3 mM
Trace metal mix (1000x)	50 µL	500 µL	1x
Thiamine (20 mg/ml)	50 µL	500 µL	20 mg/L
Vitamin mix (100x)	500 µL	5 mL	1x
Carbenicillin (100 mg/ml)	50 µL	500 µL	100 mg/L

Table 3.3: Quantity of precursor or aa used to selectively label/unlabel methyl groups.

Labeled methyl group	Used amino acid/ molecular precursor	Quantity
Alanine (Cβ)	L-alanine-3-^{13}C-2-d	0.4 g/L
	Succinate-d_4	2.5 g/L
Isoleucine (Cδ^1)	2-ketobutyric acid-4-^{13}C-3,3-d_2	72 mg/L
Leucine (Cδ^2)/	DLAM-LV^{proS}	8 vials per liter
Valine (Cγ^2)	2-hydroxy-2-(^{13}C-methyl)-3-oxo-4-d_3 butanoate	
Leucine (Cδ^1, Cδ^2)/	2-keto-3-(methyl-d_3)-3-d-4-^{13}C butanoate	120 mg/L
Valine (Cγ^1, Cγ^2)		
Methionine (Cε)	L-Methionine-(methyl-^{13}C)	100 mg/L
Leucine unlabeling	L-Leucine-d_{10}	80 mg/L

3.1.3 Cloning of single site mutants

Met or Glu are substituted for Trp^{181} following the QuickChange Site-Directed Mutagenesis protocol (Strategene). Mutagenic PCR primers are purchased from Eurofins. The plasmid pCWΔlac vector encoding for wt -10 GTB is isolated from E.coli BL21 expression cells by mini-preparation, using the

QIAprep Spin Miniprep Kit (Qiagen). The plasmid is amplified by *Pfu* DNA Polymerase (Promega) in a PCR (initial denaturation at 95°C for 5 min followed by 18 cycles at 95°C for 50 s, 60°C for 1 min, 68°C for 6 min, and a final extension at 68°C for 10 min) and the parental DNA is digested with *DpnI* for 60 min at 37°C. The *DpnI*-treated plasmids are transformed into *E.coli* DH5α cells and plated on LB-agar plates containing 100 µg/mL ampicillin (Amp). Isolated clones are picked and grown over night in 10 mL of LB Amp (100 µg/mL) media at 37°C. Plasmids are purified by mini-preparation, and mutations are verified by nucleotide sequencing (LGC genomics). The sequencing mix contains 100 ng/µL plasmid DNA and 5 pmol/µL sequencing primer (forward: 5'-ACA GGA TCC ATC GAT GCT TAG G-3'; reverse: 5'-CAG ATC TGC TCA TGT TTG ACA GC-3'). The plasmid is introduced into *E.coli* BL21 expression cells. The cells are plated onto LB agar plates containing 100 µg/mL ampicillin, and isolated clones are picked for glycerol cultures.

Table 3.4: Mutagenic primers. Substituted nucleotides are marked in red.

Mutation	Mutated codon	Direction	Primer sequence
W181M	TGG → ATG (bp 373-375)	Forward	5'-GAAGTGGGCGCCTACAAACGTATG CAGGACGTTTCCATGCGTC-3'
		Reverse	5'-GACGCATGGAAACGTCCTGCATAC GTTTGTAGGCGCCCACTTC-3'
W181E	TGG → GAA (bp 373-375)	Forward	5'-GAAGTGGGCGCCTACAAACGTGAA CAGGACGTTTCCATGCGTCG-3'
		Reverse	5'-CGACGCATGGAAACGTCCTGTTCA CGTTTGTAGGCGCCCACTTC-3'

3.1.4 Plasmid DNA preparation

Plasmid DNA is isolated from transformed *E.coli* cells using the QIAprep Spin Miniprep Kit (Qiagen). The respective clone is inoculated into 10 mL LB medium containing ampicillin (100 µg/mL) and incubated over night at 37°C. The cells are harvested by centrifugation at 8,000 x g for 5 min at RT. The plasmid DNA is isolated following the kit protocol, and eluted with 50 µL of H_2O. The DNA concentration is determined by UV absorbance at 260 nm employing a NanoDrop™ UV/Vis spectrometer (OD_{600}=1 equals 50µg/µL double stranded DNA (dsDNA)).

3.1.5 Preparation of electrocompetent *E.coli* cells

E.coli DH5α or BL21 cells are inoculated into 5 mL of SOB medium (without Mg^{2+}) and incubated over night at 37°C. The overnight culture is transferred into 250 mL of SOB medium, and incubated at 37°C until an optical density at 600 nm (OD_{600}) of 0.6-0.8 is reached. The cells are harvested by centrifugation at 2600 x g for 10 min at 4°C. The cell pellet is washed two times in sterile 10% glycerol. Finally, the cells

are resuspended in sterile 10% glycerol and transferred into cryo cups in 100 µL aliquots and rapidly frozen in liquid nitrogen. The aliquots are stored at -80°C.

3.1.6 Transformation of *E.coli* cells by electroporation

100 µL aliquots of electrocompetent *E.coli* cells are thawed on ice, 10 ng of plasmid DNA are added, and the suspension is applied into an electroporation cuvette. DNA uptake is induced by a short voltage pulse of 1.75 kV (400 Ω, 25 µF). 1 mL of SOC medium is added and the cells are incubated for 1 h at 37°C in a shaking thermomixer at 500 rpm. The cells are harvested by centrifugation at 4000 x g for 2 min and resuspended in 200 µL of LB medium containing Amp (100 µg/mL). 50 and 150 µL of the suspension are plated onto two LB Amp agar plates and incubated overnight at 37°C. Isolated clones are picked for plasmid DNA preparation and analyzed by nucleotide sequencing (LGC genomics).

3.1.7 Preparation of *E.coli* glycerol stocks

E.coli Bl21 cells transformed with plasmid DNA containing the verified aa substitution are plated onto LB Amp agar plates and grown overnight at 37°C. Isolated clones without satellites are picked, and incubated in 5 mL of LB Amp medium at 37°C to an OD_{600} of one. 250 µL of sterile 80% glycerol are added to 1 mL of this suspension to reach a final glycerol concentration of 16%. The glycerol stocks are rapidly frozen in cryo cups in liquid nitrogen and stored at -80°C.

3.1.8 Synthesis of unlabeled protein

The glycerol clone of interest is inoculated into 50 mL of optimized TB medium and incubated in a 250 mL baffled shake flask overnight at 30°C and 230 rpm. The overnight culture is used to inoculate a scale-up culture with a start OD_{600} of 0.05, and further incubated in a baffled shake flask at 30°C and 230 rpm. Gene expression is induced by addition of IPTG to a final concentration of 1 mM, when an OD_{600} of 0.6-0.8 is reached. The incubation is continued for 20-24 h at 30°C. Cells are harvested by centrifugation at 5000 x g and 4°C for 20 min. The cell pellet is either stored at -20°C, or resuspended in lysis buffer and stored at -80°C after rapid freezing in liquid nitrogen.

3.1.9 Synthesis of labeled protein in D_2O

E.coli BL21 cells, containing the plasmid with the gene of interest are inoculated into 50 mL of TB rich medium and grown until an optical density at 600 nm (OD_{600}) >1 is reached. Carbenicillin (Carb) (100 µg/mL) is used as selecting agent throughout the expression. Cells for inoculation of 50 mL 100% D_2O-based M9 minimal medium with a start OD_{600} of 0.1 are harvested by centrifugation, and excessive TB medium is removed. This starter culture is grown overnight at 37°C with agitation. The next morning, the cells from the starter culture are harvested by centrifugation (3000 x g, 2 min) and inoculated into 50 mL of 99.85% D_2O-based M9 minimal medium for protein synthesis. Exchangeable

protons of Na_2HPO_4, KH_2PO_4, $(^{15}NH_4)_2SO_4$, and of D-glucose-d_7 are removed by lyophilization before use. The pH* is adjusted to 7.2. The expression culture is grown at 37°C with agitation, and successively increased to 4/5 of the final culture volume. When an OD_{600} of 0.5 is reached, the culture is increased to its final volume of 0.5 L with M9 minimal medium containing the desired labeled precursors and amino acids. GT expression is induced 1 h after addition of labeled precursors using 1 mM (f.c.) IPTG. After incubation overnight at 37°C with agitation, the cells are harvested by centrifugation (5000 x g, 20 min, 4°C), when the maximal cell density is reached (OD_{600} of 4-5). The cell pellet is either directly used for protein purification, or stored at -20°C.

3.2 Protein purification and NMR sample preparation

Wild type and mutant GTs are purified from *E.coli* lysates by successive chromatography on SP Sepharose FF (GE Healthcare) and UDP-Hexanolamine Sepharose, following previously published protocols with critical modifications, as indicated below (Seto et al. 2000; Marcus et al. 2003; Sindhuwinata et al. 2010; Grimm et al. 2017). Column chromatography is performed with an Äkta FPLC system. The buffers are filtered (0.45 µm) and degassed before usage.

3.2.1 Cell Lysis

The cell pellet is resuspended in freshly prepared lysis buffer. The cell suspension is repeatedly passed through a French Pressure cell at 25,000 psi, and the cell debris are removed by ultracentrifugation at 110,000 x g and 4°C for 1 h.

Table 3.5: Lysis buffer

Lysis buffer (50 mL)	50 mM	MOPS (pH 7)
	1 mM	EDTA
	5 mM	β-mercaptoethanol
	1 tablet	Protease inhibitor

3.2.2 Cation exchange chromatography

Wild type and mutant GTs have a positive net charge at neutral pH and bind to the negatively charged sulfopropyl groups of the SP Sepharose FF (GE Healthcare) column material. A column packed with 75 mL of SP Sepharose is preequilibrated with at least three column volumes (CV) of wash buffer. The cytosolic fraction of the *E.coli* cell lysates is filtered (0.8 µm) and applied to the column. Proteins and other cytosolic components that do not bind to the column material are removed with a continuous flow of wash buffer until a stable UV absorbance at 280 nm is reached. The GTs are eluted applying a linear ionic strength gradient (0-100% elution buffer over 500 mL). The eluate is collected in fractions of 10 mL and checked for GTs by SDS-PAGE. The fractions containing the GTs are pooled. A constant flow-rate

of 1 mL/min is applied in all steps. The column material is successively regenerated with three CVs of 8 M urea, H_2O, 2 M NaCl, H_2O, 1 M NaOH, H_2O, 30% isopropanol, H_2O and 30% ethanol, respectively, and stored in 30% ethanol at 4°C.

Table 3.6: Cation exchange chromatography buffers

SP sepharose wash buffer	50 mM	MOPS (pH 7)
	5 mM	β-mercaptoethanol
SP sepharose elution buffer	50 mM	MOPS (pH 7)
	500 mM	NaCl
	5 mM	β-mercaptoethanol

3.2.3 Affinity chromatography

Wild type and mutant GTs bind exclusively in presence of divalent manganese ions to UDP-hexanolamine-functionalized sepharose column material. Therefore, $MnCl_2$ (5 mM f.c.) is added to the pooled elution fractions of the ion exchange chromatography. The combined fractions are applied to a preequilibrated column, packed with 10 mL of the UDP-functionalized sepharose. The column is rinsed with wash buffer until a stable UV absorbance at 280 nm is reached. The GTs are eluted with an EDTA-containing buffer, which removes the Mn^{2+} ions and weakens the interaction to the column material. The eluate is collected in fractions of 4 mL, and fractions containing GTs are combined. A constant flow-rate of 0.4 mL/min is applied during all steps. The column material is successively regenerated with 10-20 CVs of 8 M urea, H_2O and 30% ethanol, respectively, and stored in 30% ethanol at 4°C.

Table 3.7: Affinity chromatography buffers

UDP hexanolamine sepharose wash buffer	50 mM	MOPS (pH 6.7)
	500 mM	NaCl
	5 mM	$MnCl_2$
	5 mM	β-mercaptoethanol
UDP hexanolamine sepharose elution buffer	50 mM	MOPS (pH 6.7)
	500 mM	NaCl
	20 mM	EDTA
	5 mM	β-mercaptoethanol

3.2.4 Dialysis and buffer exchange

GTs are concentrated with Amicon Ultra-4 Centrifugal Filter Units (Millipore, MWCO 10 kDa) to a final volume of < 500 µL. The exchange into the desired NMR buffer is performed in Zellu/Trans Mini-Dialyzer membranes (Roth, MWCO 12 kDa) with a sample-to-dialysate ratio of 1:15. The reservoir

buffer is replaced at least five times until EDTA concentrations are < 0.1 µM. The protein samples are stored at 4°C until they are used for NMR experiments.

Table 3.8: NMR spectroscopy buffers. The buffers are prepared in 100% D_2O. The Bis-tris buffer is used in all experiments involving lanthanide ions. The phosphate buffer is the standard buffer for all other NMR experiments.

Phosphate buffer	35 mM	Na_2DPO_4/NaD_2PO_4 (pH* 6.8)
	50 mM	NaCl
	5 mM	$MgCl_2$
	1 mM	TCEP-d_{16}
	0.1 mM	DSS-d_6
Bis-tris buffer	30 mM	Bis-tris-d_{19} (pH* 6.4)
	80 mM	NaCl
	1 mM	TCEP-d_{16}
	0.1 mM	DSS-d_6

3.3 Analytics of protein purification

3.3.1 SDS-PAGE

Protein purification procedures are checked with sodium dodecyl sulfate polyacrylamide gel electrophoresis (SDS-PAGE). 10 µL of 2 x loading buffer are added to 10 µL of protein sample. The proteins are denatured at 85°C for 15 min, and loaded onto an acrylamide gel with 6% (v/v) stacking and 12% (v/v) separation gels. 5 µL of a molecular weight marker are loaded, too. The proteins are separated by a voltage of 90 V in a separation chamber filled with 1 x electrode buffer. The gel is stained with GelCode Blue Stain Reagent for >1 h, and the background is destained with H_2O overnight. For documentation, gels are dried under vacuum at 80°C for 1 h.

Table 3.9: SDS-PAGE buffers

1x electrode buffer	6 g/L	TRIS HCl
	28.8 g/L	glycine
	1 g/L	SDS
2x loading buffer:	180 mM	TRIS HCl (pH 6.8)
	12% (v/v)	glycerol
	3% (w/v)	SDS
	5% (v/v)	β-mercaptoethanol
	1 mg/mL	bromphenol blue
	0.3 g/mL	urea

Table 3.10: SDS polyacrylamide gels

	Separation gel (12%)	Stacking gel (6%)
Rotiphorese® Gel 30	4 mL	1 mL
1.5 M Tris, pH 6.8		1,25 mL
1.5 M Tris, pH 8.8	2,5 mL	
H_2O	3,2 mL	2,58 mL
10% (w/v) SDS	100 µL	50 µL
87% (v/v) Glycerol	200 µL	100 µL
20% (w/v) ammonium persulfate	50 µL	25 µL
TEMED	10 µL	10 µL

3.3.2 Spectrophotometric protein quantification

The UV absorbance of the protein samples is determined with a NanoDrop™ spectrometer using the corresponding buffer as a blank. Wild type GT concentrations are determined according to the Lambert-Beer law ($A=\varepsilon_{280}\ c\ d$) by UV absorbance at 280 nm with a theoretical molar extinction coefficient (ε_{280}) of 52,370 $M^{-1}cm^{-1}$, which proofed to be a reasonable estimate from findings of an amino acid analysis. Similarly, theoretical molar extinction coefficients are the basis for the determination of mutant GT concentrations, too (GTB W181M, W181E: ε_{280} = 46,870 $M^{-1}cm^{-1}$).

3.3.3 Activity assay

The enzymatic activity is analyzed, using the radiochemical assay of Palcic et al., 1988. GTB (GTA) transfers a uniformly [^{14}C]-radiolabeled galactose (GalNAc) from the donor UDP-Gal (UDP-GalNAc) to the acceptor H disaccharide (H-Dis-octyl: α-L-Fuc*p*-(1→2)-β-D-Gal*p*-O-octyl). Hydrophobic interactions of the octyl moiety to a reversed phase C-18 SepPak® cartridge in water allow the isolation of the trisaccharide reaction product, which can be quantified by liquid scintillation counting. The reaction is performed under conditions, where the formation of the product depends linearly on the incubation time, which applies, when substrate turnover stays below 10%.

The GTs are prediluted to a concentration of 300-500 ng/mL with 1 x A/B buffer. 4 µL of the prediluted GT sample are added to 1 µL 10 x A/B buffer and 5 µL of donor/acceptor stock mix, and incubated for 10 min at 37°C. The reaction is stopped by addition of 170 µL H_2O (4°C). The reaction mixture is applied to a water-preequilibrated SepPak® cartridge. Excessive radioactive donor substrate is removed with two times 2 mL H_2O. The radioactively labeled reaction product is eluted with three times 2 mL of methanol. After addition of 6 mL scintillation mix, the radioactive reaction product is quantified using a liquid scintillation counter.

The specific activity is determined, according to the following equation:

$$specific\ Activity\ (U/mg) = \frac{(A_{sample} - A_{blank}) \times n_{UDP-Gal}}{(A_{sample} - A_{blank}) \times t \times V_{sample} \times c_{protein}} \quad (3.1)$$

It considers the measured activity of the sample (A_{sample} in dpm), and the background radiation of a blank without GT activity (A_{blank}) set to 100 dpm by default. Besides the radiolabeled donor, the reaction mix contains regular (cold) UDP-Gal (UDP-GalNAc), too. The total amount of the provided UDP-Gal (UDP-GalNAc) in the mix is given by $n_{UDP\text{-}Gal}$ in µmol. V_{sample} is the sample volume (mL) and $c_{protein}$ is the GT concentration (mg/mL) of the prediluted protein sample. t is the incubation time (10 min). One U of activity is defined as the amount of enzyme that catalyzes the conversion of one µmol of substrate to product per min (Kamath et al. 1999).

Table 3.11: Activity assay buffer and stock mix. The stock mix contains either UDP-Gal (GTB) or UDP-GalNAc (GTA).

10 x A/B buffer	500 mM	MOPS (pH 7.0)
	200 mM	$MnCl_2$
	10 mg/ml	BSA
donor/acceptor stock mix	992 µM (4.96 nmol in 5 µL)	H-Dis-octyl
	532 µM (2.66 nmol in 5 µL)	UDP-Gal (UDP-GalNAc)
	786 Bq (0.065 nmol in 5 µL)	UDP-u-^{14}C-Gal (UDP-u-^{14}C-GalNAc)

3.4 NMR spectroscopy

Unless stated otherwise, the experiments are performed on a Bruker Avance III 500 MHz NMR spectrometer equipped with a TCI cryogenic probe. Topspin 3.1, 3.2 and 3.5 are used for data acquisition and processing. 2D [^{13}C,^{1}H] HMQC spectra that are recorded in the course of NMR-monitored ligand titrations are processed with NMRPipe (Delaglio et al. 1995). All experiments are performed at 298 K, and chemical shifts are referenced to 2,2-dimethyl-2-silapentane-d_6-5-sulfonic acid (DSS-d_6, Sigma-Aldrich) as external standard.

The protein samples are treated according to the buffer exchange scheme described above. The Bis-tris buffer is used in all experiments involving lanthanide ions. The phosphate buffer is the standard buffer for all other NMR experiments. Before use, aggregates are removed by filtration employing 0.5 mL centrifugal filter devices (0.22 µm) at 5,000 x g for 5 min. Final protein concentrations are determined by UV absorbance at 280 nm with the NanoDrop™ spectrometer. All experiments are recorded with sample volumes ranging from 150 to 190 µL in a 3 mm NMR tube.

3.4.1 HMQC-NOESY experiments

The 4D methyl-methyl HMQC-NOESY-HMQC spectrum (Tugarinov et al. 2005) is recorded with a 440 µM AIL^{proS}MV^{proS} $^{13}CH_3$-methyl-labeled uniformly deuterated GTB sample at the Utrecht NMR facility SONNMRLSF on a 950 MHz NMR machine equipped with a cryoprobe system. The experiment is recorded with a mixing time of 400 ms using 32% non-uniform sampling (NUS) with 10154 complex NUS data points in a grid of 52 (^{13}C) × 92 (^{1}H) × 52 (^{13}C) points in the indirect dimensions. 1024 data points are collected in the direct proton dimension. The points in each indirect dimension are linear-predicted, and the time-domain data in all dimensions are apodized with a cosine window function and zero filled prior to Fourier transformation. The spectrum is processed with Topspin 3.5 pl 6 on a Mac-Book Pro running Yosemite 10.10.5 using Multi-Dimensional Decomposition (MDD, Bruker).

3D [^{1}H,^{13}C,^{1}H] NOESY HMQC spectra (Fesik and Zuiderweg 1988) are acquired with IMV-, ILMV- and AIL^{proS}MV^{proS}-labeled protein samples (~200-400 µM) with 8 scans, and 194 × 48 data points in the indirect and 1024 points in the direct dimension, and a mixing time of 400 ms. The points in each indirect dimension are linear-predicted, and the time-domain data in all dimensions are apodized with a cosine window function and zero filled prior to Fourier transformation.

The spectra are analyzed with CcpNmr Analysis (Vranken et al. 2005), and NOE correlations are picked manually. NOE correlations and chemical shifts are used as restraints in the first round of the automated assignment procedure.

3.4.2 Paramagnetic labeling and pseudocontact shift analysis

PCSs are measured from 2D [^{13}C,^{1}H] HMQC spectra (Tugarinov et al. 2003) recorded with samples of ILMV-, IL^{proS}MV^{proS}-, and AIL^{proS}MV^{proS} $^{13}CH_3$-methyl-labeled uniformly deuterated GTB (~100 µM). The experiments are performed in Bis-tris-d_{19} buffer with pH* 6.4. The spectra are acquired with 1024 (^{1}H) and 256 (^{13}C) data points and 32 scans, and processed with a cosine window function and zero filling prior to Fourier transformation.

Lanthanide ion binding to the natural metal binding site is facilitated by concurrent addition of UDP and H-dis. UDP, H-dis and lanthanide ions are independently dissolved in NMR buffer and adjusted to pH* 6.4. First, the H-disaccharide is added in saturating amounts (~10 fold excess) to the GTB solution. Subsequently, UDP and lanthanide ions are added in equimolar ratios never exceeding their solubility product until resonances of the UDP-free state vanished entirely (~8 fold excess).

PCSs are measured as differences between peak positions in the NMR spectra recorded with GTB in the paramagnetic and diamagnetic state. Importantly, each set of methyl-TROSY spectra of GTB in the diamagnetic and paramagnetic state is recorded with the same protein batch split into the required number of samples. La^{3+} serves as diamagnetic reference. Ce^{3+}, Eu^{3+} and Pr^{3+} are exploited as paramagnetic probes.

Because of the low digital resolution in the carbon dimension, only proton PCSs are used for Δχ tensor refinement with *Numbat* (Schmitz et al. 2008). The experimental PCS value is treated as the average of the PCSs of the three ^{1}H nuclei belonging to each methyl group in the structure. The structural model used for Δχ tensor refinement is described in detail in the results section. The Δχ tensor parameter errors are estimated from the standard deviations in a Metropolis Monte Carlo error analysis with 1000 samplings and random omission of 20% of the PCSs in each sampling. Q factors are determined as the root mean square deviation between experimental and calculated PCSs divided by the root mean square of the experimental PCSs (Cornilescu et al. 1998; Schmitz et al. 2012):

$$Q = rms(PCS_i^{calc} - PCS_i^{exp})/rms(PCS_i^{exp}) \quad (3.2)$$

Experimental and predicted PCSs are used as further restraints in the automated assignment procedure.

3.4.3 NMR-monitored titration experiments and line shape analysis

Titration experiments are performed with AIL^{proS}MV^{proS} methyl-labeled GTA, GTB and AAGlyB. The same stock of D_2O-based phosphate buffer (pH* 6.8) is used for dissolving the ligands, as well as for the buffer exchange of the protein. The pH* of the ligand stock solutions is carefully readjusted to 6.8. Ligand working solutions are generated as dilutions of the ligand stock solution with protein solution, in order to provide a largely constant protein concentration during the titration. The protein concentration at the start of the titration is determined by UV absorbance at 280 nm. At each titration step, 2D [^{13}C,^{1}H]-HMQC experiments are recorded with 8 scans using 1024 (^{1}H) and 256 (^{13}C) complex data points. The spectra are processed with 4 Hz (^{1}H) and 8 Hz (^{13}C) exponential line broadening and zero filling to 512 complex points in the indirect dimension using *NMRPipe* (Delaglio et al. 1995).

Peak positions are followed using *CcpNmr Analysis* (Vranken et al. 2005). Ligand binding-induced chemical shift perturbations (CSPs) are calculated as weighted Euclidean distances (Δδ) between peak positions in the spectrum recorded with the highest ligand concentration, and the positions in the spectrum recorded for the apo state (Williamson 2013):

$$\Delta\delta = \sqrt{\Delta\delta_H^2 + (0.18\Delta\delta_C)^2} \quad (3.3)$$

The weighting factor of 0.18 is estimated from the observed ^{13}C chemical shift range of ca. 17 ppm and of the ^{1}H shift range of ca. 3 ppm.

The processed 2D [^{13}C,^{1}H] HMQC spectra of each titration point are imported into *MATLAB* 2015a (The MathWorks, Inc., Natick) for analysis with *TITAN* (Waudby et al. 2016). All data are fitted to a two-state ligand binding model, respectively:

$$P + L \underset{k_{off}}{\overset{k_{on}}{\rightleftharpoons}} PL$$

Several peaks are selected for global fitting, in order to describe the common interaction event more accurately. Chemical shifts and linewidths of the apo state are determined using only the first spectrum (absence of ligand). These parameters are hold constant for the remainder of the fitting session. Peak positions of the bound state and linewidths of all states as well as the dissociation constant (K_d) and the off-rate (k_{off}) of the ligand are fitted using the entire dataset. The bootstrap residual resampling procedure provided within *TITAN* is applied for estimation of parameter uncertainties in 200 runs.

3.4.4 ZZ exchange experiments

Two sets of 2D longitudinal exchange experiments are recorded using previously described pulse sequences (Farrow et al. 1995; Kloiber et al. 2011). In one set of experiments the ^{13}C frequency labeling precedes the mixing time. In the second set of experiments the order of frequency labeling and mixing time is interchanged. The experiments are performed on a Bruker Avance I spectrometer, operating at a proton frequency of 700 MHz, and equipped with a TXI cryogenic probe. The spectra are recorded with ILMV methyl-labeled GTB (465 µM) in presence of saturating amounts of H-dis (1.5 mM), and half-saturating concentrations of UDP (250 µM). The mixing times range from 10 to 600 ms. For normalization, a set of reference spectra is acquired, where the mixing time is set to 0. Data are acquired with 48 scans and a recycle delay of 2.7 s, using 1024 (^{1}H) and 256 (^{13}C) complex data points. The spectra are processed with a cosine window function and zero filled to 2048 x 512 real points.

The peak intensities of the direct correlation signals in both sets of spectra (with/without frequency labeling) are extracted using *CcpNmr analysis* (Vranken et al. 2005), and normalized with the peak intensities observed in the spectra with 0 mixing time, respectively. The normalized intensities are transferred to *Origin* (OriginLab, Northampton, MA) and are globally and simultaneously fitted to equations describing a two-site exchanging system (Kloiber et al. 2011). In the frequency-labeled experiment, the time dependency of the direct correlation peaks is given by (Farrow et al. 1995; Palmer et al. 2001):

State A: $$\frac{M_{AA}(t)}{M_{AA}(0)} = \frac{1}{\lambda_1 - \lambda_2}[(a_{22} + \lambda_1)e^{\lambda_1 t} - (a_{22} + \lambda_2)e^{\lambda_2 t}] \quad (3.4)$$

State B: $$\frac{M_{BB}(t)}{M_{BB}(0)} = \frac{1}{\lambda_1 - \lambda_2}[(a_{11} + \lambda_1)e^{\lambda_1 t} - (a_{11} + \lambda_2)e^{\lambda_2 t}]$$

The time dependencies of the normalized intensities of the direct correlation peaks in the experiment without frequency labeling are given by (Kloiber et al. 2011):

State A: $$\frac{M_A(t)}{M_A(0)} = \frac{1}{\lambda_1 - \lambda_2}[(a_{22} - a_{21} + \lambda_1)e^{\lambda_1 t} - (a_{22} - a_{21} + \lambda_2)e^{\lambda_2 t}] \quad (3.5)$$

State B: $$\frac{M_B(t)}{M_B(0)} = \frac{1}{\lambda_1 - \lambda_2}[(a_{11} - a_{12} + \lambda_1)e^{\lambda_1 t} - (a_{11} - a_{12} + \lambda_2)e^{\lambda_2 t}]$$

$M_{AA}(t)$, $M_{BB}(t)$, $M_A(t)$ and $M_B(t)$ are the magnitudes of the direct correlation peaks corresponding to states A and B at time point t. The intensities are normalized with the respective magnitudes of the direct

correlation peaks at the start of the mixing period, $M_{AA}(0)$, $M_{BB}(0)$, $M_A(0)$, and $M_B(0)$. $\lambda_{1,2}$ is described by the following equation:

$$\lambda_{1,2} = 1/2[-(a_{11} + a_{22}) \pm \sqrt{(a_{11} - a_{22})^2 + 4a_{12}a_{21}}]$$

with $a_{11} = k_{AB}+R_1^A$; $a_{22} = k_{BA}+R_1^B$; $a_{12} = -k_{BA}$, and $a_{21} = -k_{AB}$. Parameters k_{AB} and k_{BA} represent the microscopic kinetic rate constants describing the interconversion between states A and B. R_1^A and R_1^B are the longitudinal relaxation rates of states A and B.

Because of the normalization, the longitudinal relaxation and kinetic rate constants can be extracted without line-broadening distortions from the four direct correlation peaks by simultaneous fitting of (3.4) and (3.5) to the experimental data. Consequently, the results are independent of the peak integration method, i.e. intensities can be used (Kloiber et al. 2011).

4 Results

4.1 Assignment of AILMV $^{13}CH_3$-methyl resonances in methyl-TROSY spectra

In high molecular weight, slowly tumbling systems, $^{13}C^1H_3$-labeled methyl groups within a deuterated background have superior spectroscopic properties in comparison to the commonly used $^1H^{15}N$-labeled backbone amides, due to rapid rotation of their three equivalent protons around the symmetry axes (Tugarinov et al. 2003; Kay 2011). 2D [^{13}C,^1H]-HMQC experiments exploit the favorable relaxation properties known as methyl-TROSY effect (Ollerenshaw et al. 2003; Tugarinov et al. 2003). Today, protocols are available for the selective introduction of $^{13}C^1H_3$-labels into every methyl containing amino acid of a protein, recombinantly expressed in *E.coli*.

Protocols for the individual and simultaneous labeling of Ala, Ile, Leu, Met and Val methyl groups are adapted to the investigated GTs. Methyl-labeled α-ketoisovalerate and acetolactate are used as amino acid precursors for Leu and Val residues (Tugarinov and Kay 2004; Gans et al. 2010). Acetolactate serves the stereospecific introduction of methyl probes into Leu/Val pro-S sites. Ile δ1 methyl labeling is achieved with specifically isotope-enriched α-ketobutyrate (Goto et al. 1999). Supplementation of growth media with methyl-labeled Ala and Met extends the labeling scheme to these amino acids (Gelis et al. 2007; Isaacson et al. 2007; Ayala et al. 2009; Stoffregen et al. 2012). Pyruvate is the deaminase reaction product of Ala, and is central to several amino acid metabolic pathways. Therefore, growth media are additionally supplemented with deuterated succinate to prevent isotope scrambling from methyl-labeled Ala (Ayala et al. 2009).

The sequence-specific assignment of methyl resonances that is required for more detailed functional, e.g. binding studies is still challenging to achieve. So far, only sparse backbone assignments are available in the case of GTA and GTB (Grimm 2015; Weissbach 2016). Therefore, pulse schemes that transfer magnetization between side chain methyl groups and backbone amides or carbonyls (Tugarinov and Kay 2003a) are not helpful here. Alternatively, single amino acid substitutions can be employed in a systematic manner (Amero et al. 2011). Unfortunately, even conservative single-site mutations can lead to an almost complete inhibition of the GTs' synthesis in *E.coli* (Grimm 2015; Weissbach 2016).

Here, another methyl group assignment strategy is followed (see Fig. 4.1). Because of the high sequence similarity of GTA and GTB, most NMR experiments are performed with GTB, and the assignments are subsequently transferred to GTA. The strategy is based on crystallographic structure data, methyl-methyl NOEs, and lanthanide-induced PRE and PCSs. At first, samples with different $^{13}CH_3$-methyl labeling patterns are generated for the stereospecific identification of residue types. The 4D methyl-methyl NOESY experiment with $AIL^{proS}MV^{proS}$ $^{13}CH_3$-methyl-labeled GTB reports on spatially neighbored residues. The software tool *MAP-XSII* (Xu and Matthews 2013) serves automatic assignment of methyl groups based on the observed NOEs and chemical shift predictions that are derived with the

programs *CH3Shift* (Sahakyan et al. 2011) and *SHIFTX2* (Han et al. 2011). High-resolution crystal structures of the GTB homodimer with added hydrogens are required by all programs (Alfaro et al. 2008; Gagnon et al. 2015). Metropolis Monte Carlo samplings are applied, and only resonances consistently assigned to the same residue are propagated as initial tentative assignments. Lanthanide ions as paramagnetic probes, binding in the enzyme's natural metal binding site, deliver additional spatial information. For each lanthanide, initial approximate Δχ tensor parameters are calculated with *Numbat* (Schmitz et al. 2008) on the basis of PCSs of the tentatively assigned residues and different protein models. This program delivers for each lanthanide a set of predicted PCSs, depending on the respective Δχ tensors. In a second round, experimental and calculated PCSs are added to the input files used by *MAP-XSII*, leading to the assignment of all AIL^{proS}MV^{proS} $^{13}CH_3$-methyl resonances. 3D methyl-methyl NOESY experiments with ILMV methyl-labeled GTB allows the additional assignment of a number of LV pro-R methyl groups.

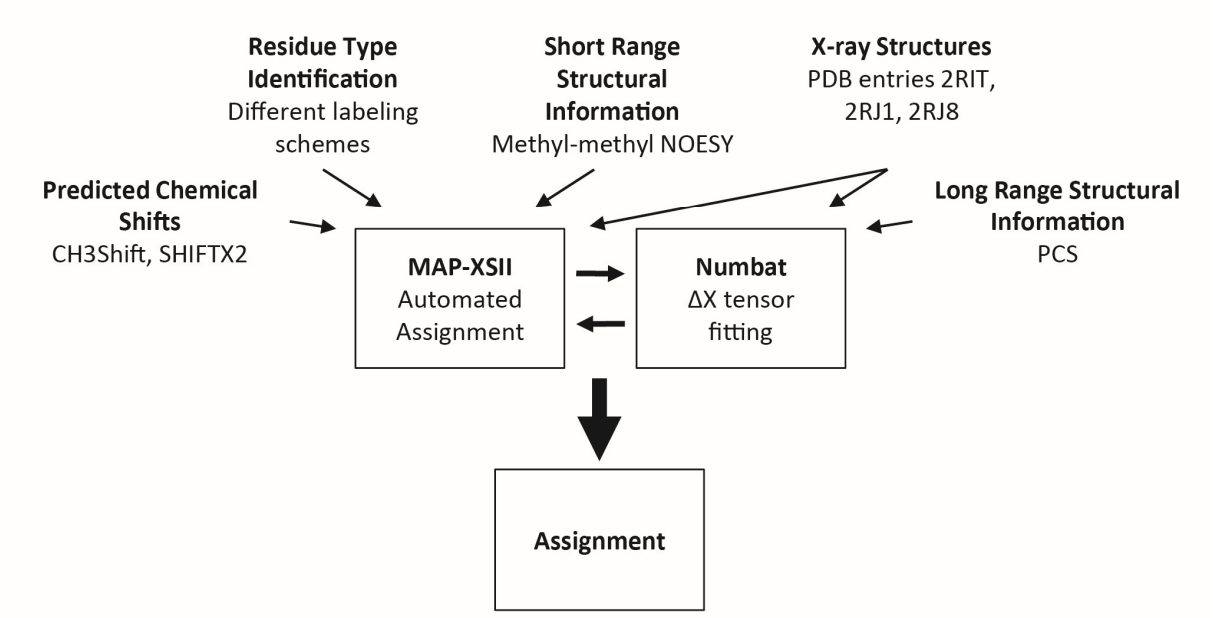


Figure 4.1: Sequence-specific assignment strategy of AILMV methyl groups in GTB. Central to the strategy are two software tools, MAP-XSII and Numbat, requiring spatial information from NOEs chemical shifts and PCSs as well as crystal structures. Numbat is necessary for Δχ tensor fitting and MAP-XSII serves automatic assignment. Detailed information are provided in the main text.

Some resonances were already assigned in former studies with the help of site-directed mutagenesis (Weissbach 2016; Grimm et al. 2017). Previously assigned residues comprise Ile^{123}, Ile^{192}, Met^{142}, Met^{186}, Met^{189}, Met^{191}, Met^{288}, Met^{289} and Val^{351} (prochirality not clear). It is worth noting that this information is not used as a starting point, but as a verification of the assignment. Additionally, assignments could be readily transferred from GTB to GTA. The expected differences in methyl-TROSY spectra, induced by the four critical residues, also support the assignment.

4.1.1 Identification of residue types

Methyl groups of different amino acid types show residue-specific ^{13}C and ^{1}H chemical shifts. Thus, the respective resonances show up in distinct regions of 2D [^{13}C,^{1}H]-HMQC spectra. This knowledge can guide the identification of the residue type, but usually further experiments are needed due to overlapping chemical shift distributions. All Ala, Ile (δ1), Leu (δ1 (pro-R) and δ2 (pro-S)), Met, and Val (γ1 (pro-R) and γ2 (pro-S)) methyl groups are $^{13}CH_3$-labeled, summing up to a total of 156 $^{13}CH_3$-methyl groups to be assigned. Amino acids with labeled methyl groups constitute 27% of the polypeptide sequence and distribute over all regions of the enzyme (see Fig.4.2).

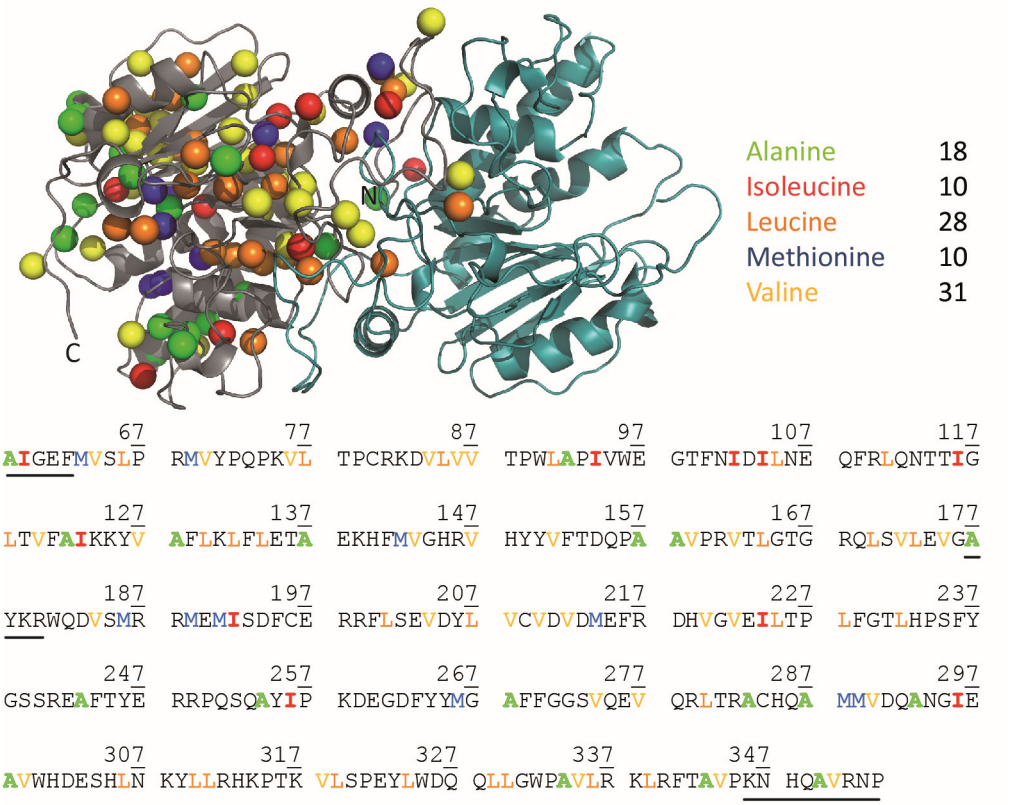


Figure 4.2: Distribution of the relevant methyl bearing amino acids in the primary and quaternary structure of GTB. The aa sequence of the recombinant GTB construct with a numbering that relates to the residue positions in the native protein sequence including the N-terminal membrane anchor. Flexible regions including the N- and C-terminus as well as the internal loop are not observable in crystal structures. These domains are modeled in the protein structure of the GTB homodimer (PDB entry 2RIT) using the web server ModLoop. One monomer is colored in grey the other one in cyan. The carbons of the methyl groups of one monomer are highlighted as spheres in the same color scheme used in the primary sequence. For clarity, only the pro-S methyl groups of Leu and Val residues are shown. Total numbers of the relevant amino acid types are provided on the right.

The amino acid type identification is based on five differentially methyl-labeled GTB samples. Specifically, I-, M-, IMV-, ILMV- and AIL^{proS}MV^{proS} $^{13}CH_3$-methyl-labeled and otherwise deuterated

molecules are generated. Despite the common metabolic precursor, decoupling of Leu from Val methyl labeling is achieved by Leu-selective unlabeling in the IMV sample (Atreya and Chary 2001). Briefly, saturation of culture media with unlabeled Leu inhibits incorporation of the methyl label into Leu residues. Samples with individual labeling of Ile and Met residues (I, M) were available from previous studies (Grimm 2015; Weissbach 2016). All other samples are synthesized and purified as described in sections 3.1 and 3.2. The quality of the batches is checked by SDS-PAGE and a radiochemical activity assay (see section 3.3).

Comparison of the methyl-TROSY spectra of the differently labeled samples in most cases allows a straightforward assignment of each cross peak to an amino acid type, as illustrated in figure 4.3. In some regions of the spectra, signal picking is complicated by signal overlap. Regarding Met residues, this was already solved in a previous study by ligand titrations (Weissbach 2016). In the case of Leu/Val residues, stereospecifically labeled samples dramatically improve the separation of signals.

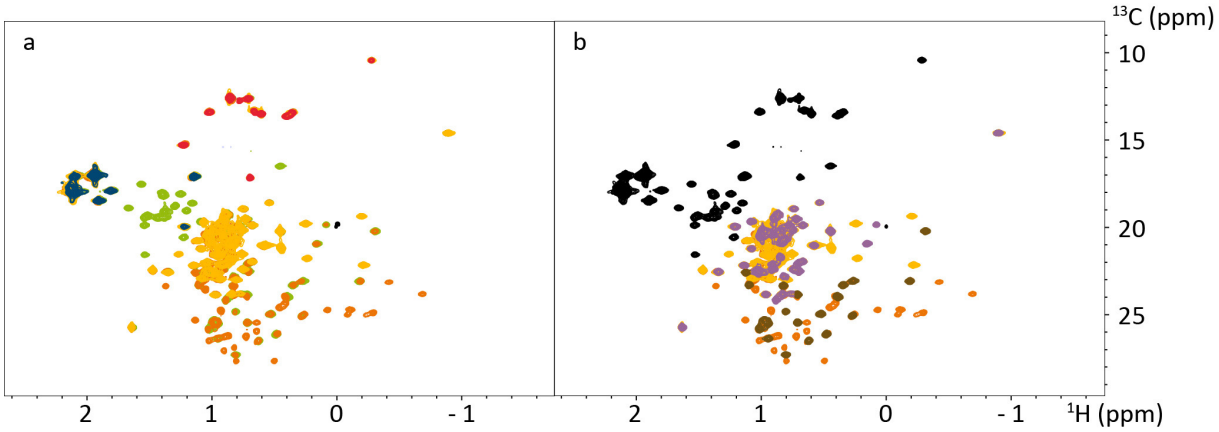


Figure 4.3: Superposition of 2D [^{13}C, ^{1}H]-HMQC spectra of differently methyl-labeled GTB samples. (**a**) Identification of amino acid types. The HMQC spectrum of each sample is allocated to a distinct color (I red, M blue, IMV yellow, ILMV orange and AIL^{proS}MV^{proS} green). Because of the order of the spectra in the superposition, the amino acid types can be identified from the color of the top layer of each resonance (Ala green, Ile red, Leu orange, Met blue, Val yellow). (**b**) The prochirality of Leu and Val methyl groups is easily identified when overlaying the spectra of the IMV, ILMV and AIL^{proS}MV^{proS} labeled GTB (Val pro-R yellow, Val pro-S purple, Leu pro-R orange, Leu pro-S olive). For clarity resonances of other amino acid types are shown in black. All spectra are acquired at 298 K at 500 MHz ^{1}H frequency with varying protein concentrations between 100 and 400 µM.

All new simultaneous labeling schemes have been successfully established, showing methyl labeling at all desired sites. The addition of deuterated succinate to prevent Ala scrambling leads to increased cell densities in the *E.coli* cultures owing to the extra carbon source. A maximum OD_{600} of 4-5 is reached with Ala labeling and an OD_{600} of 3 without. Consequently, protein yields are increased in batches with Ala labeling from 10-14 mg/L to 16-20 mg/L of culture volume. Spectra of AIL^{proS}MV^{proS}-labeled GTB show the expected number of signals for each residue type. An additional, low intensity Ile signal also found in all other Ile-labeled samples likely arises because of incomplete N-terminal Met excision.

Therefore, this signal is assigned to Ile^{59} in molecules with Met^{58} present. The resonance of Met^{58} is not observable, likely due to overlap with other Met signals. Crowded spectral regions caused by chemical shift degeneracy of Leu and Val methyl groups and their high abundance are the reason that only 25 of 28 Leu and 30 of 31 Val pro-R methyl resonances are unambiguously located in spectra of IMV- and ILMV-labeled GTB. Leu-specific unlabeling in IMV-labeled GTB is also successful. Even at noise level, no Leu signals are observed.

For evaluation of the established labeling schemes, incorporation efficiencies of methyl labels into all desired aa types are estimated on basis of signal intensities (see Fig. 4.4 a, b). No differences are detected in IMV- and ILMV-labeled samples. The differing average intensities in the first sample of AIL^{proS}MV^{proS} GTB (Fig. 4.4 a) indicate an unequal incorporation efficiency into the different residue types. On average, Ala signals are the most intense. Leu and Val signals are the least intense with only ca. one third of the Ala average intensity. However, signal intensities are not only dependent on the incorporation efficiency, but also e.g. on solvent exposure and local flexibility. This is reflected in significantly higher signal intensities of the flexible and exposed N-terminal and C-terminal residues.

Furthermore, close inspection of 2D methyl-TROSY spectra near noise level reveal scrambling of the Ala label into undesired sites (see Fig. 4.4 c, d). Small signals are showing up in the region where Ile γ2 signals are expected. Similarly, labels are also introduced into Leu δ1 (pro-R) and Val γ1 (pro-R) positions. Since the metabolic pathways of all three amino acids are closely connected to pyruvate as a common precursor, the origin of the label is likely Ala (Ayala et al. 2009). The finding that scrambling is not observed in absence of Ala labeling confirms this hypothesis. Amino acids with isotope labels originating from Ala scrambling compete with aas with isotope labels originating from the provided metabolic precursor, directly indicating a reduced incorporation efficiency into the desired sites of Ile, Leu and Val residues.

In a second labeling attempt, where metabolic precursor concentrations of Ile and Leu/Val are increased, the average signal intensities of all residue types are almost identical (see Fig. 4.4 b). Only Ile signals are on average slightly less intense. This is mainly due to the signal intensities of neighboring residues Ile^{116} and Ile^{224} located in the hydrophobic core of the protein. Scrambling of Ala labels is still observed in this sample, indicating that a 100% labeling efficiency is not reached. However, signals of Ile γ2, Leu δ1 and Val γ1 are just above noise and intensities are less than 5% of the signal intensities of Ile δ1, Leu δ2 and Val γ2. Consequently, an interference in methyl-methyl NOESY and other following experiments is not expected. In summary, the AIL^{proS}MV^{proS} labeling scheme, as well as the IMV (Leu unlabeling) and ILMV labeling schemes are successfully established and optimized for GTB.

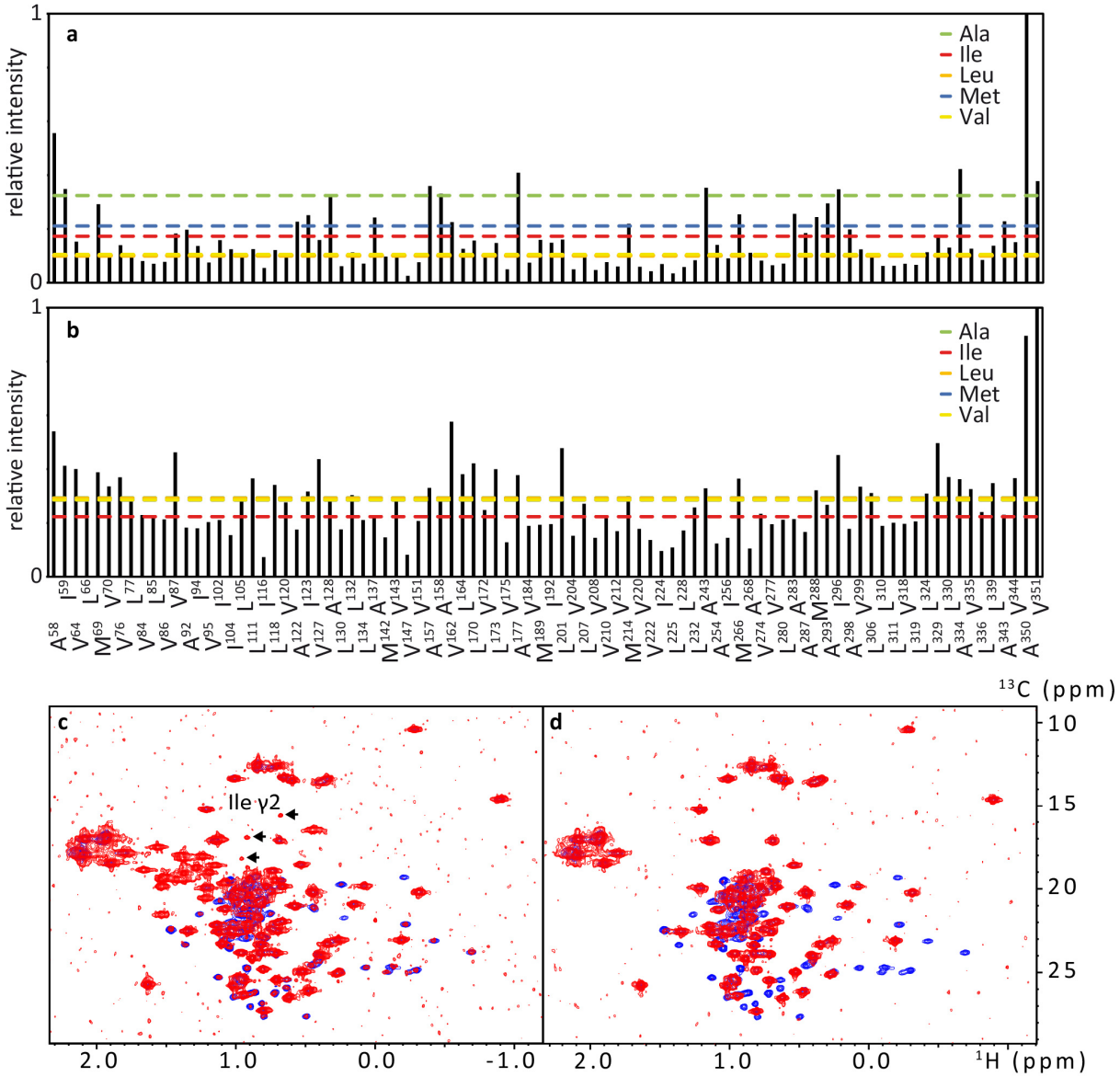


Figure 4.4: Evaluation of incorporation efficiencies in the AIL^{proS}MV^{proS} labeling scheme. (**a**) Relative intensities of all non-overlapping signals of AIL^{proS}MV^{proS} GTB are represented as bars. The average intensity of each aa type is shown as a dashed line. On average Ala residues are three times more intense than Leu/Val residues and two times more intense than Ile residues, indicating different incorporation efficiencies for different aa types. (**b**) This is largely overcome by increased precursor concentrations in a second labeling attempt. (**c**) The overlay of 2D methyl-TROSY contour plots of AIL^{proS}MV^{proS} (red), cut at noise level, and ILMV (blue) GTB show scrambling of isotope label originating from Ala. (**d**) This is not observable in the superposition of IL^{proS}MV^{proS} (red) and ILMV (blue) GTB spectra. Scrambling results in incorporation into Ile γ2 (arrows), Leu δ1 (pro-R) and Val γ1 (pro-R) positions.

4.1.2 Initial assignment with methyl-methyl NOESY

In NMR experiments, magnetization transfer through space, known as nuclear Overhauser effect (NOE), delivers spatial information. The NOE is inversely dependent to the sixth power of the distance

between the nuclei. Therefore, in methyl-methyl NOESY experiments, magnetization is only measurably transferred between closely neighboring methyl groups. The structure-based approach for methyl group assignment makes use of the known three dimensional distribution of the methyl groups in the quaternary structure of the GTB homodimer. This leads to unique methyl group "clusters". A unique cluster contains sets of aas, whose methyl groups are close enough to be linked through NOEs. The aa composition of individual clusters is unique. Because of this uniqueness, it is possible to achieve a resonance assignment by matching of the structurally predicted and experimentally determined NOE correlations. The assignment procedure greatly benefits from increasing the number of labeled aa types. On the one hand, the density of labeled methyl probes is increased, and therefore more NOE connectivities are expected. On the other hand, more types of aas with methyl label improve the chances for unique clusters.

A drawback of the increased number of methyl labels are crowded spectra. This is overcome by the acquisition of a 4D ^{13}C-resolved HMQC-NOESY-HMQC experiment with AIL^{proS}MV^{proS} GTB. The application of a four-dimensional NMR experiment has the advantage of superior separation of peaks. NOE correlations are easily and unambiguously allocated to the corresponding resonances, despite chemical shift degeneracies, particularly in the proton dimension. The labeling scheme provides the maximal methyl probe density with a minimal crowding of signals. In this regard, the stereoselective Leu/Val labeling is especially advantageous, as the spectral crowding is minimized, the number of possible assignment solutions is reduced, and a higher sensitivity is reached. Furthermore, several 3D (^{1}H, ^{13}C, ^{1}H) HMQC-NOESY experiments are acquired with IMV, ILMV and AIL^{proS}MV^{proS} GTB, which are helpful in extending the assignment to Leu/Val pro-R methyl groups and benefit from the √2 higher sensitivity compared to 4D experiments (Tugarinov et al. 2005).

Average distances between proton mean positions of AIL^{proS}MV^{proS} methyl groups are calculated using self-written Python scripts. The X-ray crystallographic structure of the apo-GTB homodimer (PDB entry 2RIT) is used as structural model for calculation of distances, chemical shift predictions and the automated assignment process. Because of local disorder, three regions with lacking electron density have to be modelled into the structure. These regions consist of the four N-terminal residues including the methyl bearing amino acids Ala^{58} and Ile^{59}, the eight C-terminal residues including Ala^{350} and Val^{351}, as well as the internal disordered loop of four amino acids, including Ala^{177}. The web server *ModLoop* (Fiser and Sali 2003) is used to fill the gaps, and *Maestro* (Schrödinger, LLC, NY 2015) is used for hydrogen rebuilding. 376 NOEs, including 18 intermolecular NOEs between the monomers, are expected to be observed for AIL^{proS}MV^{proS} methyl-labeled GTB homodimers, employing a cut-off distance of 8 Å. In the 4D methyl-methyl NOESY experiment 269 NOE correlations between 97 labeled methyl groups are detected. The experiment is recorded with a 440 µM AIL^{proS}MV^{proS} GTB sample on a 950 MHz NMR machine equipped with a cryoprobe system, using non-uniform sampling and a mixing time of 400 ms. Phosphate buffer in 100% D_2O with pH* 6.8 and a temperature of 298 K are chosen for the experiment.

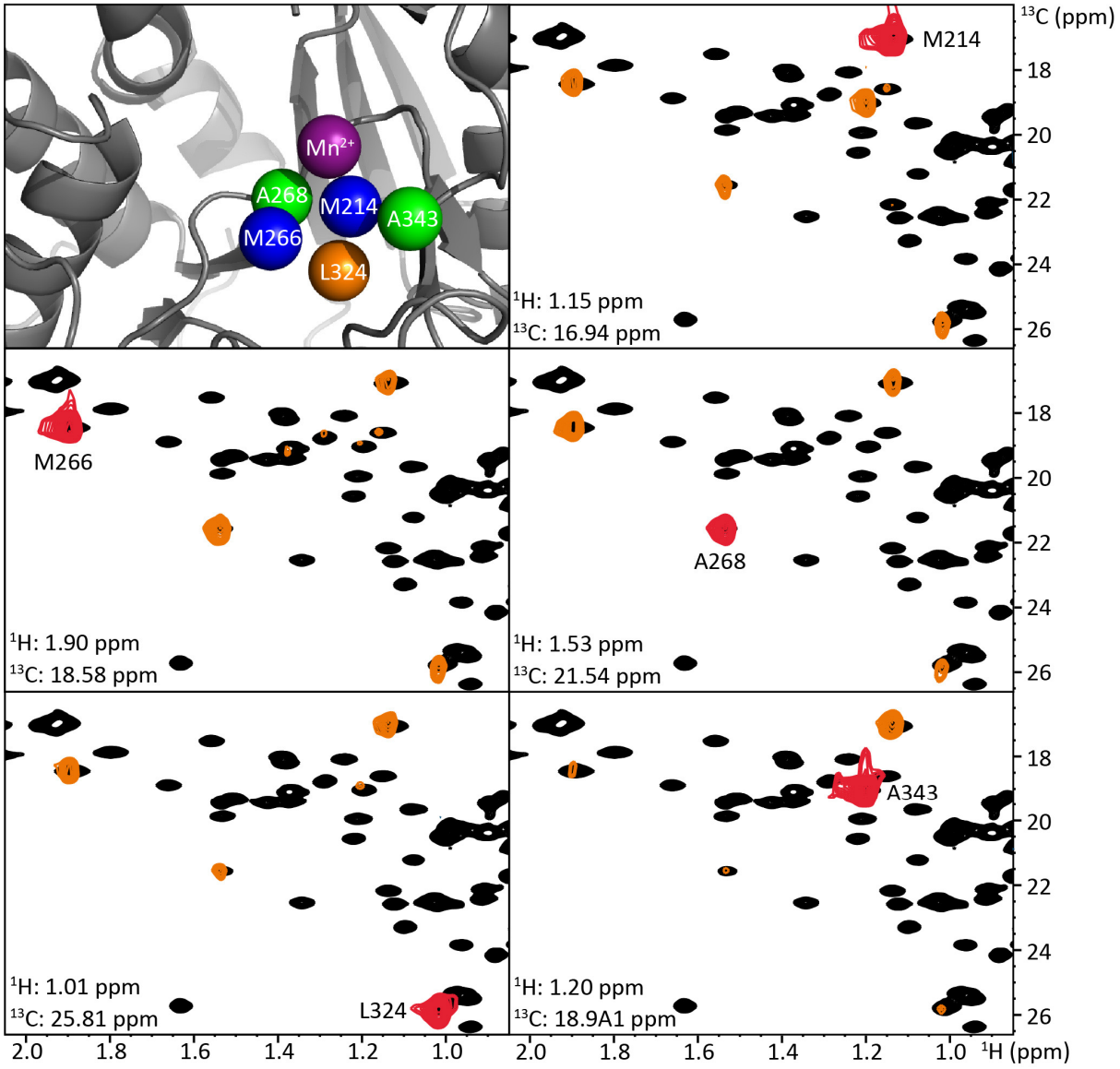


Figure 4.5: Example of a NOE cluster of spatially neighboring amino acids. The arrangement of the respective residues in the GTB crystal structure (PDB entry 2RIT) is provided on the top left panel. Methyl carbons and metal ion are represented as spheres. The cluster comprises the critical residues Met^{266} and Ala^{268}, responsible for donor substrate specificity. All residues are spatially close to the metal binding site with distances ranging from 3.6 Å (Met^{214}) to 7.2 Å (Leu^{324}). Overlays of 2D [^{13}C, ^{1}H]-planes of the 4D methyl-methyl HMQC-NOESY-HMQC experiment (orange, red) and the 2D [^{13}C, ^{1}H]-HMQC spectrum (black) recorded with AIL^{proS}MV^{proS} GTB are provided on the top right to bottom right panels. The ^{1}H and ^{13}C frequencies of the selected planes are given on the bottom left of each panel. The corresponding diagonal resonances at these positions are highlighted in red and labeled with the assigned residue. NOE signals are shown in orange. All resonances of this cluster show NOE correlations to each other. Sequence-specific information can only be gained through further connectivities to Val344.

The protein batch used results from the first AIL^{proS}MV^{proS} labeling attempt with differing label incorporation efficiencies for each aa type. However, the high protein concentration and high magnetic

field strength facilitates detection of NOE connectivities in the incompletely labeled molecules. The NOE correlation peaks are manually picked using *CcpNmr Analysis* (Vranken et al. 2005). An example of a NOE cluster, where all methyl groups involved show NOE correlations to each other, is illustrated in figure 4.5.

The automated assignment of AIL^{proS}MV^{proS} methyl peaks is based on NOE correlations, chemical shifts and the structural model of the GTB homodimer described above. To restrict assignment solutions to Leu/Val pro-S methyl groups, all Leu/Val pro-R methyl groups are removed from the structure employing a self-written Python script. The program *MAP-XSII* (Xu and Matthews 2013) matches the structure-based NOE and chemical shift predictions with the experimental data, and generates initial assignments in multiple parallel samplings in a Metropolis Monte Carlo optimization procedure. The chemical shift predictions are derived with the software tools *CH3Shift* (Sahakyan et al. 2011) and *SHIFTX2* (Han et al. 2011), using the structure of the apo-GTB homodimer (see above). *CH3Shift* is specifically designed for the assignment of methyl groups, and considers factors like ring current, magnetic anisotropy, electric field, rotameric type, dihedral angle and interatomic distances for predictions. *SHIFTX2* calculates all ^{1}H, ^{13}C and ^{15}N chemical shifts by utilizing advanced machine learning based on a database of a training set of proteins, and takes surface accessibility, temperature and pH into account.

For an initial assignment, twenty Metropolis Monte Carlo tests are run with a cut-off distance of 7.5 Å and a weighting of chemical shift to NOE information of 0.2. All samplings reach comparable scores and 81 out of 97 peaks are consistently assigned to the same residue. From these 81 suggestions, 78 remained unaffected in the final assignment. Although sequence-specific information on two Ile and eight Met resonances is already available from former studies (Weissbach 2016; Grimm et al. 2017), this is not used as a restriction in the Metropolis Monte Carlo testing. Both Ile residues as well as four of the eight Met residues are correctly allocated in the initial assignment. Three of the remaining Met residues are not consistently assigned to one respective residue in all twenty runs. This is not surprising, since the resonances of Met^{63} and Met^{191}, as well as the peaks of Met^{186} and Met^{289} overlap in the 2D methyl-TROSY spectrum. The resonance of Met^{288} is consistently assigned to Met^{186}, despite a negative NOE score.

Interesting observations are intermolecular NOE correlations between neighboring methyl groups of Val^{76} of one monomer and Leu^{85}, Ile^{94} and Leu^{232} of the other monomer (see Figure 4.6). Intramolecular distances between the methyl carbons of Val^{76} and the same three residues are greater than 18 Å, respectively. Intermolecular NOEs can also be observed between Leu^{77} and Val^{84}, Val^{335} and Leu^{336}, as well as between Leu^{91} and Val^{95} and Leu^{105}. These observations prove the homodimerization of GTB under the experimental conditions.

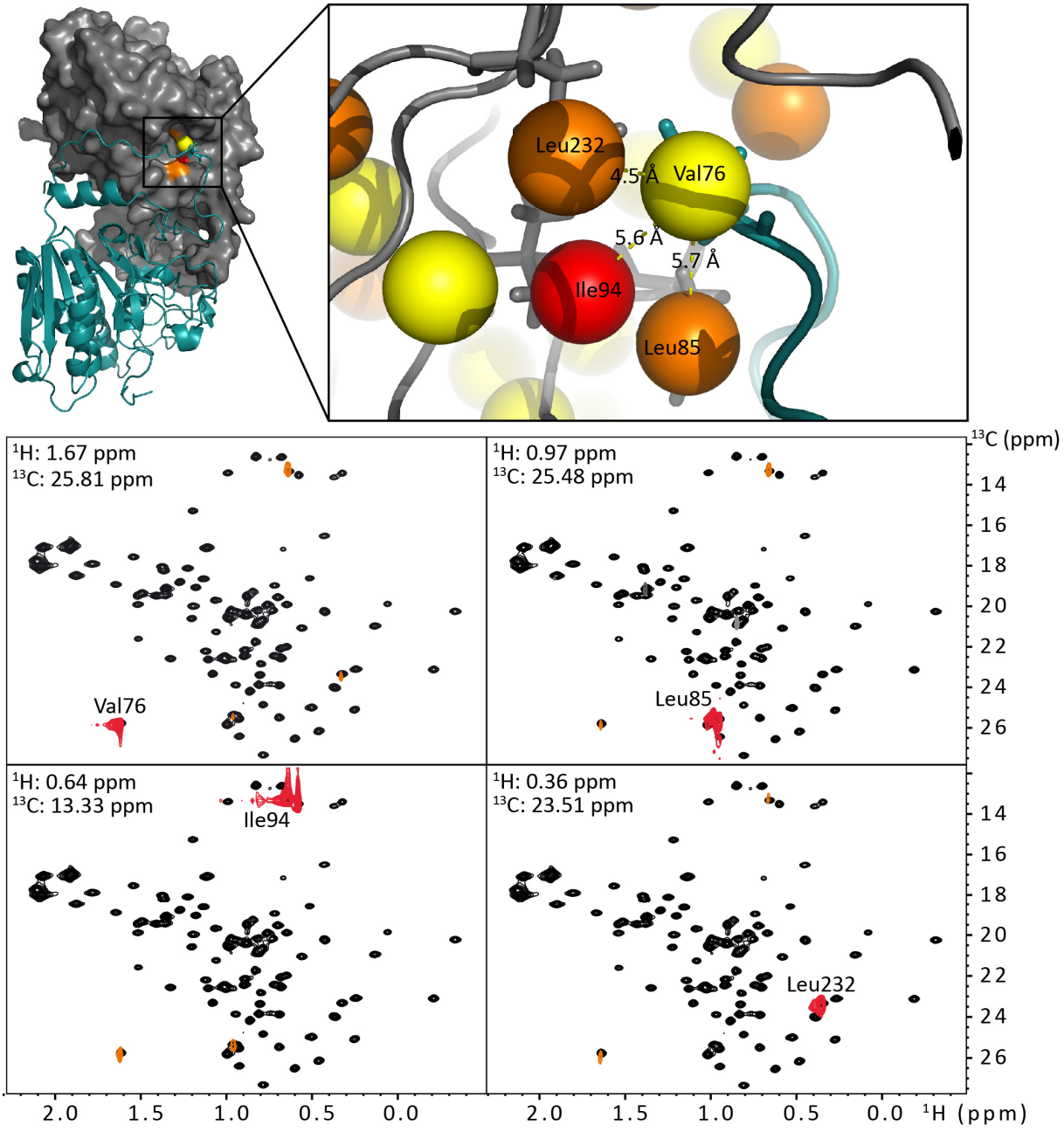


Figure 4.6: Intermolecular NOEs at the homodimer interface. The top panel shows the crystal structure of the homodimer (PDB entry 2RIT) with one monomer represented as ribbons (cyan) and the other one as molecular surface (grey). The scale-up reports on distances between the methyl carbons of the involved residues. Val^{76} is part of monomer A (cyan), while the other three residues belong to monomer B (grey). Overlays of 2D [^{13}C, ^{1}H]-planes of the 4D methyl-methyl NOESY experiment (orange, red) and the 2D [^{13}C, ^{1}H]-HMQC spectrum (black) recorded with AIL^{proS}MV^{proS} GTB are provided on the panels below. The ^{1}H and ^{13}C frequencies of the selected F3/F4 planes are given on the top left of each panel. The corresponding diagonal resonances at these positions are highlighted in red and labeled with the assigned residue. NOE signals are shown in orange. Val^{76} shows NOE correlations to all three residues and vice versa.

Furthermore, NOE correlations between Leu^{132} and Ala^{350} indicate the unknown orientation of the nine C-terminal aas in the open conformation (see figure 4.7), reporting on a positioning of Ala^{350} in close proximity to Leu^{132}. This necessitates a reorientation of the C-terminal residues in comparison to the closed state, leaving the active site accessible for donor and acceptor substrates.

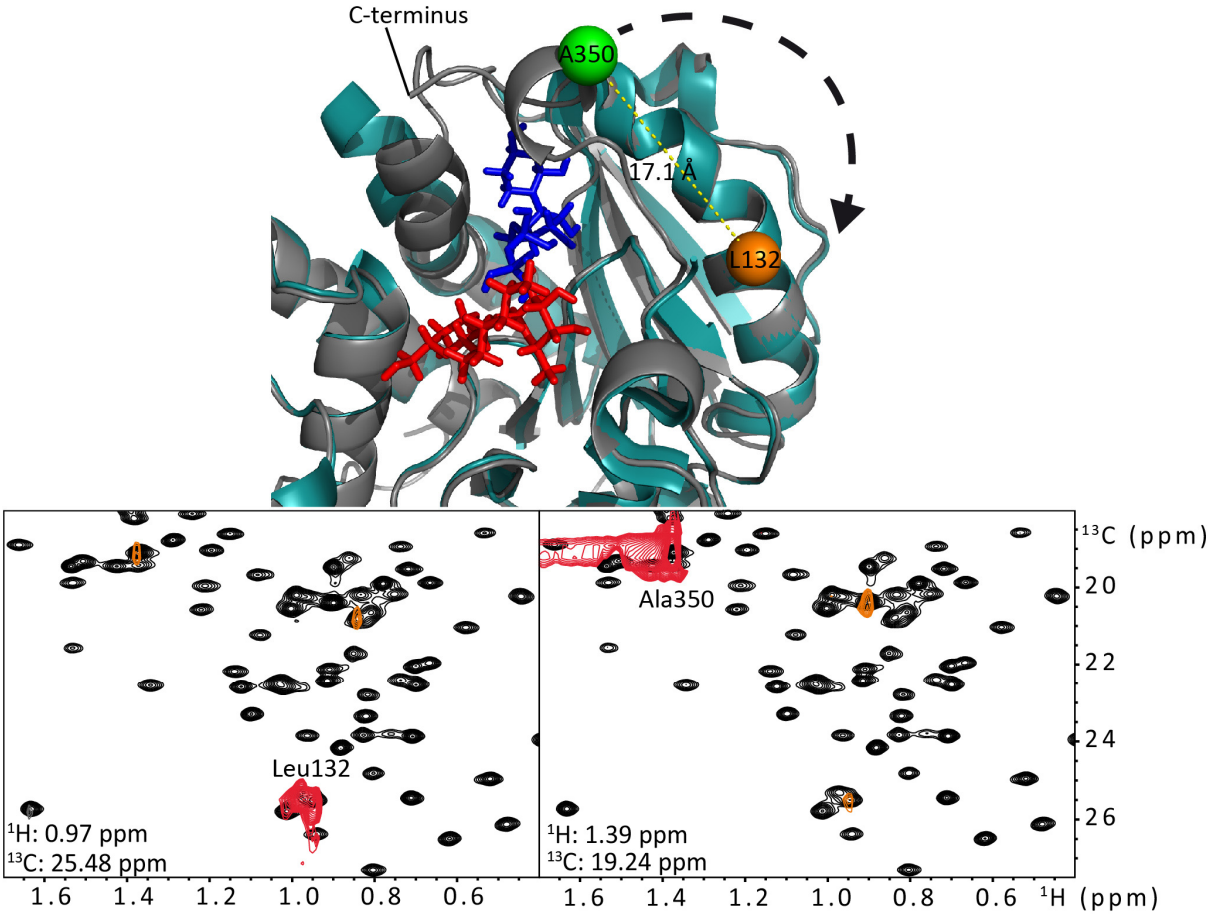


Figure 4.7: NOE correlations between Leu^{132} and Ala^{350} suggest the orientation of the C-terminal loop in the open conformation. The nine C-terminal residues of GTB are only resolved in the closed (grey, PDB entry 2RJ1) and not in the open conformation (cyan, PDB entry 2RIT), in the superposition of crystal structures. In the closed state, Leu^{132} and Ala^{350} are separated by a distance of ca. 17 Å. Overlays of 2D [^{13}C, ^{1}H]-planes of the 4D methyl-methyl NOESY experiment (NOEs: orange, auto peaks: red) and the 2D [^{13}C, ^{1}H]-HMQC spectrum (black) reveal NOE correlations between the methyl groups of these residues, demonstrating that the C-terminus occupies a conformation orienting Ala^{350} towards Leu^{132}. This orientation leaves the active site accessible for the substrates (stick representation). The ^{1}H and ^{13}C frequencies of the selected planes are given on the bottom left of each panel.

4.1.3 Lanthanide-induced PCSs for assignment completion

GTA and GTB are metal-dependent enzymes necessitating divalent manganese or magnesium ions to accommodate donor substrate binding. The replacement of natively used divalent metal ions by lanthanides (Ln^{3+}) is reported for several metalloproteins (Allegrozzi et al. 2000; Pintacuda et al. 2004),

despite their additional charge, different atomic radii and different preference in coordination number. The substitution with lanthanide ions is favorable because of their magnetically anisotropic nature, allowing measurement of pseudocontact shifts (PCSs) in paramagnetic NMR. PCSs depend on the position of the nuclear spin relative to the $\Delta\chi$ tensor originating in the metal ion and deliver valuable long ranging spatial information used e.g. for protein structure refinement (Allegrozzi et al. 2000) or resonance assignment (Pintacuda et al. 2004; John et al. 2007; Pan et al. 2016). However, in studies reported, lanthanide binding is either accommodated by a high affinity binding site in the protein, or by an artificial lanthanide binding tag, covalently bound to the protein. Furthermore, in the case of a DNA polymerase, the active site contains two Mn^{2+} ions that are replaced by a single lanthanide ion (Pintacuda et al. 2004).

In GTA and GTB, only one Mn^{2+} ion is coordinated by the conserved DXD motif in the active site (Patenaude et al. 2002), as illustrated in figure 4.8. Additionally, the pyrophosphate group of the donor nucleotide participates in coordination of the metal ion (Alfaro et al. 2008). ESI-MS data even suggest that metal binding does not occur in absence of the donor substrate (Soya et al. 2009). Binding of La^{3+}, Gd^{3+}, Dy^{3+} and Yb^{3+} in presence of UDP is shown by surface plasmon resonance (SPR) and NMR in previous studies (Grimm 2015; Grimm et al. 2017). However, PCSs could not be determined, potentially due to different possible orientations of the lanthanide ions in the metal binding site, inducing multiple resonances for each investigated spin system.

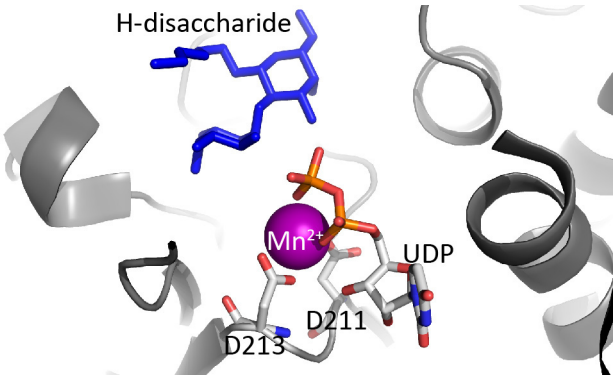


Figure 4.8: Crystal structure (PDB entry 2RJ8) showing the coordination of the manganese ion in the active site of GTB. Two Asp residues and the pyrophosphate group of the donor nucleotide coordinate the metal. A water molecule (not shown) captures the sixths position. The H-disaccharide is not in direct contact with the metal ion.

Furthermore, homodimerization of GTB causes the presence of two neighboring paramagnetic centers. The distance between the two manganese ions in the crystal structure is about 56 Å. Depending on the used lanthanide, PCSs are observable as far as 40 Å from the metal position. Thus, the lanthanides have to be chosen with care. An extensive overlap of the magnetic anisotropy spheres from both centers complicates $\Delta\chi$ tensor fitting and subsequently resonance assignment. Since PCSs are inversely proportional to the third power of the distance between nucleus and lanthanide, weaker paramagnetic ions should be chosen for PCS measurement. This is also advantageous, because the metal binds in the

center of the monomer. Paramagnetic relaxation enhancement (PRE), an effect always accompanying paramagnetic species, would hamper PCS measurement if the lanthanide is strongly paramagnetic. All these considerations necessitate a sensitive optimization of experimental conditions.

Since lanthanide phosphate salts tend to have low solubility products, and lanthanide ions are quite sensitive towards pH above 8, the buffering system is chosen carefully. The experiments are performed in Bis-Tris-d_{19} buffer in 100% D_2O with pH* 6.4 at 298 K. As lanthanide binding requires the presence of a donor substrate, it is crucial to add UDP as a donor substrate analog. However, precipitation of UDP and lanthanide ions is observed, when concentrations exceed ca. 4 mM each. Therefore, UDP and lanthanide ions are added in equimolar ratios never exceeding their solubility product. In order to keep the excess of UDP and lanthanide as low as possible, and to reach a higher residence time of the lanthanide in the metal binding site, the H-disaccharide (H-dis) is added, too. A positive cooperative binding effect between UDP and H-dis is described (Sindhuwinata et al. 2010), and the presence of the H-dis is thought to increase the affinity of UDP and thereby of the lanthanide ion.

PCSs are measured as differences between peak positions in NMR spectra recorded of the desired molecule in the paramagnetic and diamagnetic state. Therefore, the diamagnetic state is an important reference, which should be as close to the paramagnetic sample as possible. However, peak positions are directly perturbed by binding of UDP and H-dis, which are required to accommodate lanthanide complexation. Thus, the ideal choice of a diamagnetic reference is a protein sample with the same ligand concentrations as in the paramagnetic state. As the coordination chemistry of all lanthanides is similar, and differs from coordination of Mg^{2+} ions, a diamagnetic lanthanide is the best reference metal ion.

In order to establish the ideal conditions for PCS measurement, UDP, H-dis and lanthanide ions are separately dissolved in the NMR buffer and adjusted to pH* 6.4. Differentially labeled protein samples ($AIL^{proS}MV^{proS}$, $IL^{proS}MV^{proS}$, ILMV) with concentrations of ca. 100 µM are generated. Importantly, each set of methyl-TROSY spectra of GTB in the diamagnetic and paramagnetic state is recorded with the same protein batch split into the required number of samples. La^{3+} serves as the diamagnetic reference. Ce^{3+}, Eu^{3+} and Pr^{3+} are exploited as paramagnetic probes to induce PCSs. The rather weak paramagnetic effect of these metals is favorable for the reasons mentioned above. For the same reasons, further trials with Dy^{3+} and Yb^{3+} proved these metals as unfeasible for PCS measurements in this system (data not shown).

First, the acceptor substrate is added to GTB in a tenfold excess. Subsequently, the H-dis saturated GTB sample is titrated with UDP and the respective lanthanide ion in equimolar quantities. Interestingly, the UDP and Ln^{3+} binding associated chemical exchange is slow on the NMR timescale. These phenomena are discussed in detail in chapter 4.2. It needs to be emphasized that in the limit of slow chemical exchange, peak positions are no longer dependent on the degree of saturation with ligands. In a system, where close to 100% saturation of binding sites can only be reached with a large excess of UDP and Ln^{3+}, this is critical to accurately measure PCSs. UDP and Ln^{3+} are added until resonances of the UDP-free state vanish entirely, which is achieved with an eight-fold excess of the

ligands. Methyl-TROSY spectra of AIL^{proS}MV^{proS} labeled GTB in presence of H-dis, UDP and diamagnetic and paramagnetic lanthanide ions are presented in figure 4.9. It is evident that all peaks of residues within a sphere of about 9 Å around the metal binding site, including the resonances of the NOE cluster described in figure 4.5 are broadened beyond detection due to PRE. This demonstrates that binding of the metal occurs at the expected position. A disadvantage of the weak paramagnetism of the employed lanthanides is the rather small induced PCSs. In the ^{13}C dimension, PCSs are error prone because they are on the order of the spectral resolution for a large number of residues. Therefore, only shifts in the ^{1}H dimension are used for $\Delta\chi$ tensor refinement in the next step.

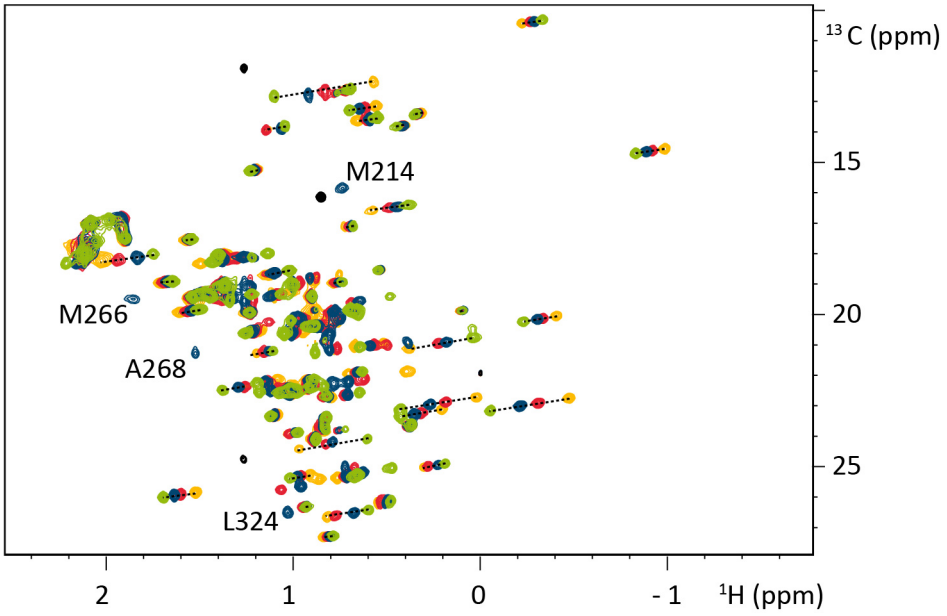


Figure 4.9: Methyl-TROSY spectra of AIL^{proS}MV^{proS} GTB in the diamagnetic and paramagnetic state. Superposition of 2D [^{13}C, ^{1}H]-HMQC spectra acquired with ca. 100 µM AIL^{proS}MV^{proS} labeled GTB in presence of saturating amounts of H-disaccharide, UDP and four different metal ions (La^{3+} blue, Ce^{3+} red, Eu^{3+} green, Pr^{3+} yellow). La^{3+} is used as the diamagnetic reference. PCSs, induced by Ce^{3+}, Eu^{3+} and Pr^{3+}, are apparent as altered resonance positions relative to the diamagnetic reference, indicated by dashed lines. Some peaks vanish in presence of the paramagnetic metal ions due to PRE. The mutagenesis and NOE-based assignment of these peaks to residues close to the DXD motif confirms Ln^{3+} binding at the expected site. Methyl groups beyond 9 Å from the metal position are detectable due to the weakly paramagnetic nature of the chosen metal ions. Spectra are acquired at 298 K and 500 MHz ^{1}H frequency. Resonances corresponding to ligands are colored black.

Tracking of signals from the position in the ligand-free to the position in the ligand-bound spectrum, as well as from the position in the diamagnetic to the position in the respective paramagnetic spectrum is performed manually with *CcpNmr Analysis* (Vranken et al. 2005). The stereospecifically labeled samples ease the analysis in the crowded LV region. However, not all PCSs can be determined because of PRE and signal overlaps. 69 (Ce^{3+}), 68 (Eu^{3+}) and 70 (Pr^{3+}) of the 81 resonances, tentatively assigned by NOE experiments, can be unambiguously located in the paramagnetic spectra. PCSs of these

resonances are used as a starting point for fitting of magnetic susceptibility tensors with the help of *Numbat* (Schmitz et al. 2008).

Numbat is designed to determine Δχ tensors based on PCSs of assigned resonances. For that purpose, eight variables have to be determined, which comprise the three Cartesian coordinates of the lanthanide position, three angles relating Δχ tensor and molecular orientation, and the axial and rhombic anisotropy parameters (Schmitz et al. 2008). Obviously, the software requires a structural model. This demands some prior considerations in the case of GTB. It is well established that GTB undergoes conformational transition upon substrate binding (Alfaro et al. 2008; Gagnon et al. 2015). When donor and acceptor substrate are present, the enzyme tends to adopt a closed state, where the disordered internal loop and C-terminus move towards the active site. Which conformation is adopted, when Ln^{3+} is substituted for the natively used Mn^{2+} is not clear. Therefore, an "ensemble structure" (see Fig. 4.10) is generated by combining the X-ray structures of the open (PDB entry 2RIZ) and closed state (PDB entries 2RJ1 and 2RJ8). Furthermore, homodimerization delivers two metal binding sites, and thus two paramagnetic centers. Only one tensor is fitted by the software on basis of a monomer structure. However, some residues of the N-terminus, close to the dimer interface, get closer to the metal binding site of the respective other monomer. This is addressed by substitution of the positions of residues 63-79 by those of the other monomer.

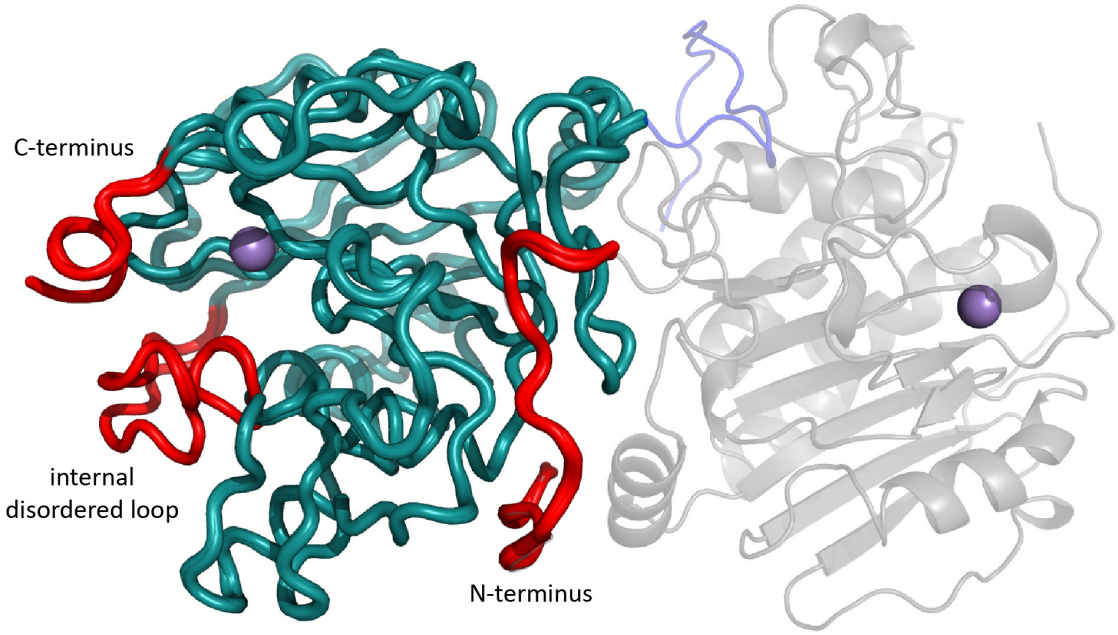


Figure 4.10: "Ensemble structure" for Δχ tensor fitting. The model (cyan tubes) is generated from X-ray structures of the open (PDB entry 2RIZ) and closed state (PDB entries 2RJ1 and 2RJ8). Important regions are highlighted in red. The C-terminus is only observable in the closed state. Two different conformations of the internal disordered loop are considered. As the N-terminal residues 63-79 get closer to the metal binding site of the other monomer (transparent cartoon), their positions (transparent blue) are replaced by those of the other monomer (red). Metal ions are displayed as spheres.

Proton PCSs of the previously tentatively assigned resonances are used for Δχ tensor refinement on basis of the "ensemble structure". The tensors are independently fitted for each Ln^{3+}. The tensor center is neither fixed nor predefined to the metal position in the structure. Nevertheless, the coordinates of the tensor center are fitted very close to the expected position (<1Å), which is the center of the manganese ion in the crystal structure. With the exception of the imprecisely determined γ angle of the tensor orientation of Ce^{3+}, there are no significant differences from the final Δχ tensor determinants derived from PCSs of all assigned resonances. The fitting results are summarized in table 4.1. It is important to note that PCSs of Ala^{350} and Val^{351} are excluded in the fits that lead to the parameters summarized in this table. These residues are removed from tensor fitting due to large differences between observed and expected PCSs introducing declining fit qualities. As the assignment of the resonance of Val^{351} is additionally confirmed by site-directed mutagenesis, this discrepancy can be attributed to an alternative major orientation of the flexible C-terminus that is not observed in the crystal structures.

Table 4.1: Δχ tensor parameters derived with *Numbat* from proton PCSs of the tentatively assigned resonances. All parameters are free and the tensors are calculated independently for each metal ion. The errors correspond to the standard deviation in 1000 Metropolis Monte Carlo approaches with random selection of 80% of PCS data for tensor fitting. For comparison, the position of the manganese ion in the crystal structure is indicated in the last line.

	Tensor	**ΔX_{ax} (10^{-32} m^3)**	**ΔX_{rh} (10^{-32} m^3)**	**Coordinates of tensor center (Å)**			**Orientation of tensor axes (°)**		
				X	Y	Z	α	β	γ
	Ce^{3+}	0.857 (±0.018)	0.143 (±0.012)	15.266 (±0.120)	16.138 (±0.134)	4.458 (±0.183)	66.1 (±1.0)	44.8 (±0.8)	187.3 (±50.6)
	Eu^{3+}	-1.510 (±0.043)	-0.798 (±0.035)	14.621 (±0.176)	16.328 (±0.255)	4.349 (±0.194)	69.2 (±1.2)	42.6 (±1.5)	40.6 (±1.9)
	Pr^{3+}	2.608 (±0.051)	1.092 (±0.050)	14.822 (±0.110)	16.399 (±0.140)	4.541 (±0.148)	65.5 (±0.7)	49.9 (±0.7)	41.1 (±1.4)
Crystal structure (2RJ1)	Mn^{2+}	-	-	14.998	16.922	4.050	-	-	-

Based on the derived Δχ tensors, *Numbat* provides lists of expected PCSs for all methyl protons. These lists as well as lists of the experimental PCSs are now used as additional input files in a second round of automated assignment using *MAP-XSII*. The program is originally designed to use PRE rates instead of PCSs. The PRE score is calculated as the squared difference between experimental and calculated PRE rate and subtracted of the score obtained from NOE and chemical shift information (Xu and Matthews 2013). Therefore, the substitution of PCSs for PRE rates is straightforward. As PCSs are rather small, they are multiplied by a weighting factor of 10 to have a significant influence on the final assignment

score. In twenty independent assignment trials with the same NOE cut-off and chemical shift weighting factor used before, 95 of the 97 methyl signals are consistently assigned to the same residue. The remaining two resonances overlap in the spectrum of the apo state and belong to Met^{186} and Met^{289}, which already have been assigned by point mutation (Weissbach 2016; Weissbach et al. 2018). Following this strategy, all AIL^{proS}MV^{proS} methyl groups are assigned unambiguously.

It should be noted that PCS restraints alone do not give sufficient information for a complete assignment. The reason is the very similar center position and orientation of all three $\Delta\chi$ tensors, leading to degenerated information with sets of PCSs that can fit to several residues in the structure. Therefore, assignment trials with *PARAssign*, a software tool for automated assignment solely based on PCSs, have not been successful (Skinner et al. 2013; Lescanne et al. 2017).

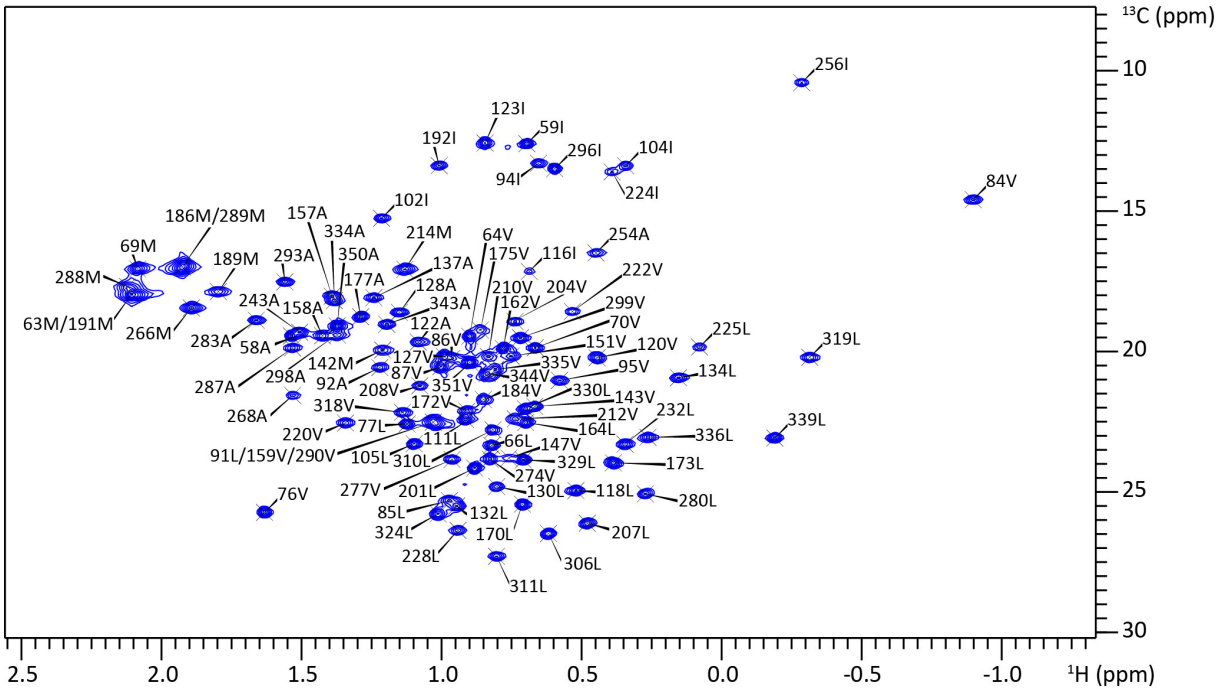


Figure 4.11: Sequence-specific resonance assignments of all AIL^{proS}MV^{proS} methyl groups in GTB. 2D methyl-TROSY spectrum of AIL^{proS}MV^{proS} labeled apo-GTB recorded in D_2O phosphate buffer pH* 6.8 at 298 K and 500 MHz ^{1}H frequency. DSS-d_6 serves as external reference. The labels indicate the assigned residues.

Further sequence-specific assignments are achieved for a number of Leu/Val pro-R methyl groups by generation of a network of NOE correlations to the previously assigned resonances. Because of the spectral crowding in the Leu/Val region, only 25 of 28 Leu and 30 of 31 Val pro-R methyl resonances are located unambiguously. 3D (^{1}H, ^{13}C, ^{1}H) HMQC-NOESY experiments acquired with ILM and ILMV methyl-labeled GTB are utilized to generate the network. However, NOE correlations between Ala and Leu/Val pro-R methyl groups are lacking in the network, since using the described labeling schemes, they are never simultaneously labeled in any GTB sample. PCSs are also determined for a number of Leu/Val pro-R methyl groups. *MAP-XSII* is again used for automated assignment. In this case, all

previously assigned resonances are used as given restriction for further assignments. However, chemical shift degeneracies and missing correlations to Ala methyl groups not labeled limit the assignment to nine Val and eleven Leu pro-R methyl resonances. In addition, seven Val and nine Leu residues are tentatively assigned. Tentative assignments are made for resonances, which are not consistently allocated to one residue, but which show a clear prevalence for it in all samplings.

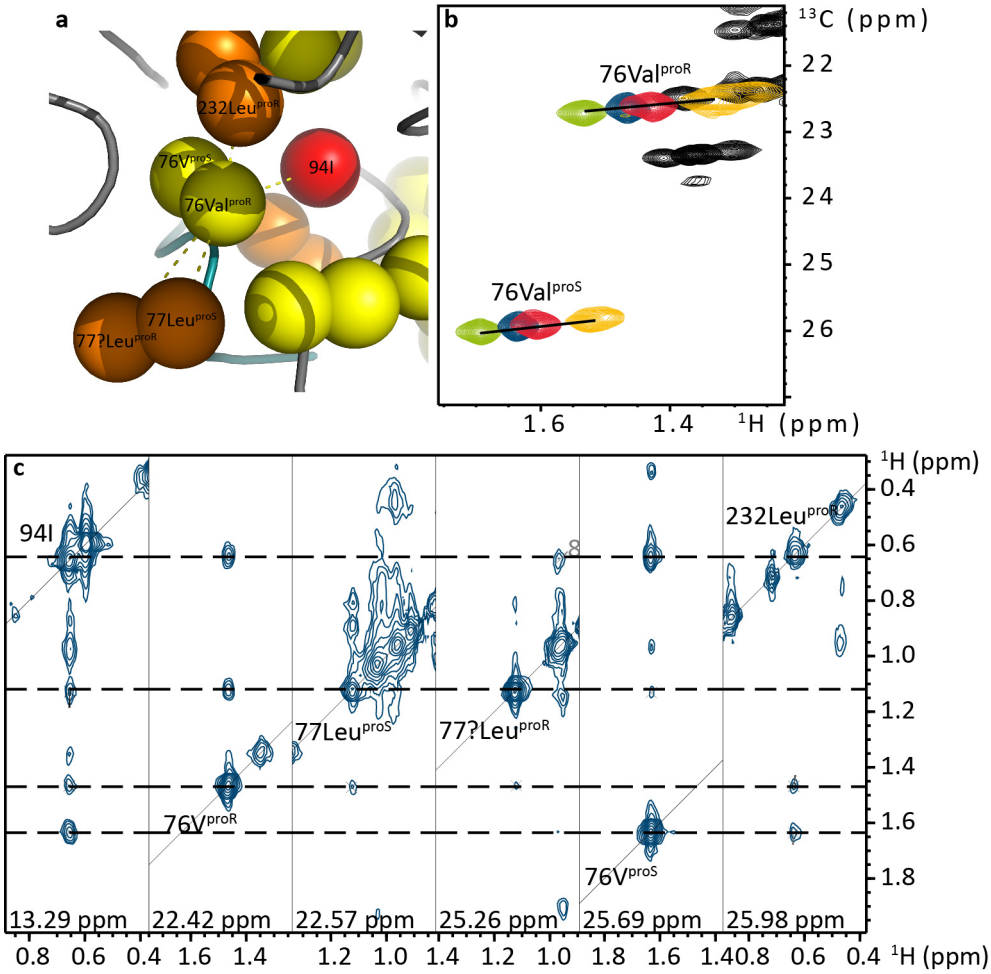


Figure 4.12: Example of Val pro-R methyl group assignment. The pro-R methyl group of Val^{76} is assigned by lanthanide induced PCSs and NOE correlations in a 3D HMQC-NOESY experiment. (**a**) The crystal structure is shown for orientation. (**b**) 2D methyl-TROSY spectra of ILMV GTB in the diamagnetic (La^{3+} blue) and paramagnetic state (Ce^{3+} red, Eu^{3+} green, Pr^{3+} yellow) reveal similar PCSs as for the already assigned pro-S methyl group. (**c**) Strips of the 3D HMQC-NOESY experiment recorded with ILMV GTB demonstrate NOE correlations between the methyl groups shown in (**a**). Diagonal signals are labeled with the assigned residue. The carbon frequency of the selected plane is displayed on the bottom of each strip. NMR experiments are performed at 298 K and 500 MHz ^{1}H frequency.

The assignment of the Val^{76} pro-R methyl resonance is exemplified in figure 4.12. Just like the pro-S methyl group (compare Fig. 4.6), the pro-R methyl group shows intermolecular NOEs to Ile^{94} and Leu^{232}. As expected, no direct NOE correlations are observable to the pro-S methyl group, as the metabolic

precursor allows labeling only at one position per molecule (either pro-R or pro-S). Further arguments that lead to the unambiguous assignment of the peak, are the chemical shift and the lanthanide induced PCSs. Both match corresponding values observed for the pro-S methyl group. All assigned Leu/Val pro-R methyl groups are summarized in figure 4.13.

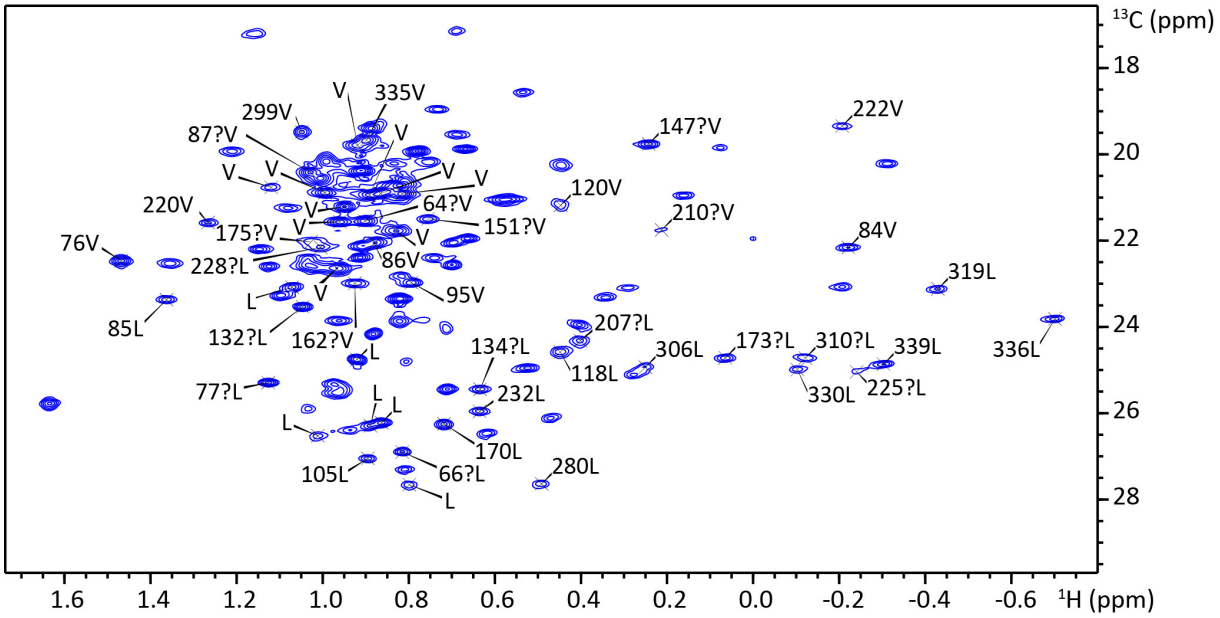


Figure 4.13: Sequence-specific resonance assignments of Leu and Val pro-R methyl groups in GTB. 2D methyl-TROSY spectrum of ILMV labeled apo-GTB zoomed in the Leu/Val region. The spectrum is recorded in D_2O phosphate buffer pH* 6.8 at 298 K and 500 MHz ^1H frequency. DSS-d_6 serves as external reference. For clarity, only pro-R methyl groups are tagged. The question mark indicates tentatively assigned peaks. Sequence-specific information is lacking for resonances without numbering.

4.1.4 Transfer of assignments to GTA and AAGlyB

Assignments from GTB can be readily transferred to spectra of AIL^{proS}MV^{proS} $^{13}CH_3$-methyl-labeled GTA (GTB G176R, S235G, M266L A268G) and AAGlyB (GTA L266G, G268A). Predominantly, peaks of the matching residues are found at approximately the same position in all three spectra. The absence of the Met^{266} peak in methyl-TROSY spectra of both "mutants", and the absence of the Ala^{268} peak in the GTA spectrum confirm these assignments (compare Fig. 4.11 and Fig. 4.14). The additional peak in the GTA spectrum can be assigned to Leu^{266}. Besides the absence and presence of resonances assigned to the critical aas, significant chemical shift deviations are observed for several additional residues. All protein samples are synthesized in the same manner and methyl spectra are recorded under identical conditions. Therefore, chemical shift perturbations can solely be attributed to the four critical aas, distinguishing GTA from GTB. The assignment of the perturbed resonances is in most cases straightforward, too, by choice of the closest resonance. The assignments are supported by similar behavior in ligand titration assays performed with the three enzymes (see section 4.2.8).

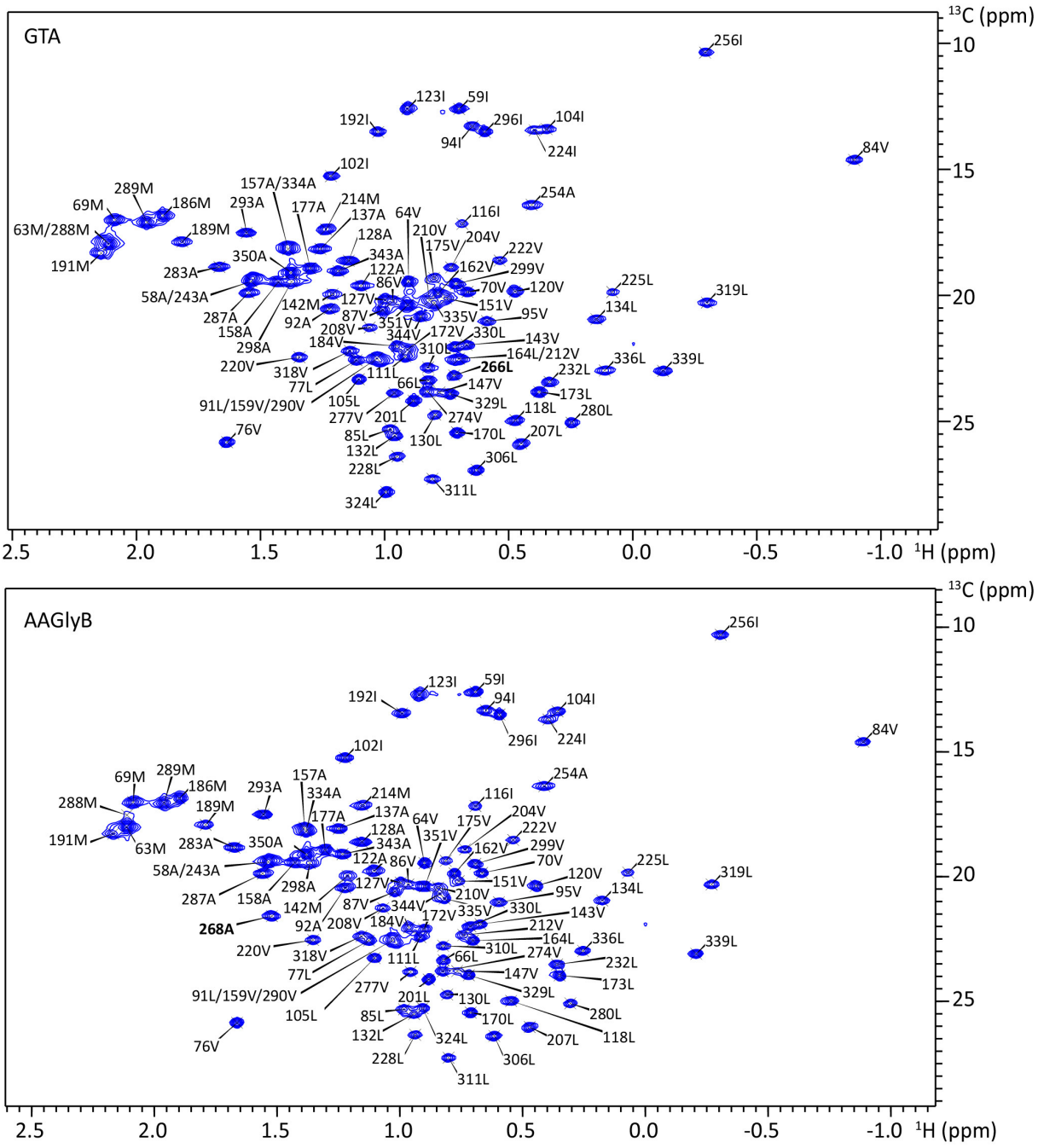


Figure 4.14: Sequence-specific resonance assignments of all AIL^{proS}MV^{proS} methyl groups in GTA and AAGlyB. 2D methyl-TROSY spectra of AIL^{proS}MV^{proS} labeled apo-GTA (top) and apo-AAGlyB (bottom) recorded in D_2O phosphate buffer pH* 6.8 at 298 K and 500 MHz ^{1}H frequency. DSS-d_6 serves as external reference. The labels indicate the assigned residues. Critical residues L^{266} and A^{268} are bold.

In order to systematically evaluate the observed deviations, weighted Euclidean distances between peak positions in 2D methyl-TROSY spectra are determined (see Fig. 4.15). The most dramatic deviations are observed for Leu^{324}, which is in contact to both critical residues 266 and 268. This explains also the significant deviations for Met^{214} and additionally of Val^{210}, Val^{212} and Leu^{306}. Chemical shifts of

residues composing the internal disordered loop (Val[175], Val[184], Met[186], Met[191]) are significantly perturbed, when comparing GTB with the two other enzymes, but essentially not, when comparing GTA and AAGlyB. Therefore, these deviations can be directly attributed to the critical residue 176, which is a Gly in GTB and an Arg in GTA and AAGlyB. However, similar chemical shift perturbations cannot be observed for Leu[329] and Leu[330], which are located in close proximity to the critical residue 235.

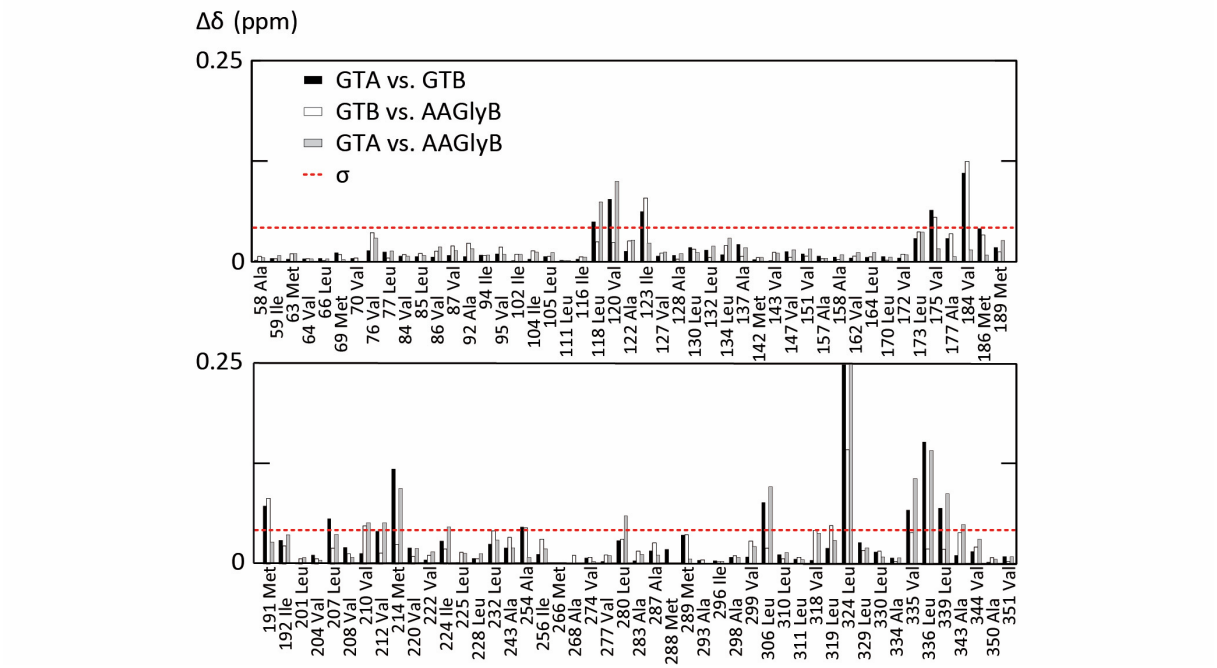


Figure 4.15: Chemical shift deviations between apo-GTA, apo-GTB and apo-AAGlyB. Summarized are the chemical shift deviations as weighted Euclidean distances between resonance positions in 2D methyl-TROSY spectra of AIL^{proS}MV^{proS}-labeled GTA, GTB and AAGlyB. A weighting factor of 0.18 for ^{13}C relative to ^{1}H chemical shifts is applied. Black bars represent chemical shift deviations between GTA and GTB, white bars represent deviations between GTB and AAGlyB and grey bars represent deviations between GTA and AAGlyB. The red dashed line represents the standard deviation (0.04 ppm) of all weighted Euclidean distances. The deviations observed for Leu[324] are 0.36 ppm (GTA vs. GTB), 0.14 ppm (GTB vs. AAGlyB) and 0.46 ppm (GTA vs. AAGlyB).

Remarkable are chemical shift deviations for residues in unexpected regions of the enzymes. The analysis reveals different chemical shifts for Val[335], Leu[336] and Leu[339], which are located in a turn structure more than 10 Å away from any critical residue. Crystal structures do not show significant differences in main chain or side chain orientations between the three enzymes. However, they reveal Leu[336] and Leu[339] to be sandwiched between Trp[325] and Trp[332], explaining their unusually upfield shifted ^{1}H frequencies. Furthermore, three positively charged residues are located nearby (Arg[337], Lys[338] and Arg[340]). In summary, all these residues contribute to a delicate magnetic environment, turning Val[335], Leu[336] and Leu[339] into sensitive reporters of small changes in this environment. The chemical shift deviations are more pronounced between GTA and GTB and between GTA and AAGlyB, implying a closer resemblance of GTB and AAGlyB in this region. Likewise, significant chemical shift deviations can also

be observed for Leu^{118}, Val^{120} and Ile^{123}, partly located in the rigid β-sheet core of the enzymes. Again, deviations cannot be anticipated from the crystal structures, as the distances to any critical residue are greater than 9 Å.

4.1.5 Structural implications from PCSs and NOE correlations

Proton PCSs of all unambiguously assigned residues of GTB are used to derive final Δχ tensors. The "ensemble" structure described in figure 4.10 is utilized for the fits. The best fits are derived without restricting the lanthanide position to the metal position in the crystal structure, as shown by the smaller standard deviations in the error analysis. The tensors are very robust in the error analysis with the exception of the γ angle of the tensor orientation of Ce^{3+}. On average, PCSs induced by Ce^{3+} are the smallest, which potentially causes the poorly defined rotation angle. All tensor centers are fitted close to the metal position in the crystal structure. The results of three different fitting sessions are summarized in table 4.2.

In figure 4.16 the Δχ tensors are represented as PCS isosurfaces on the structure of the homodimer. An overlap of the Δχ tensors originating from the metal center of each monomer is minimized. Still, it is evident that some residues at the interface should simultaneously interact with the paramagnetic species of both sites. Actually, PCSs of the relevant residues (84-87) are all larger than calculated with a single paramagnetic center. The plots of calculated versus experimental PCSs allow evaluation of the fit quality (Pan et al. 2016). Q factors are determined as the root mean square deviation between experimental and calculated PCSs divided by the root mean square of the experimental PCSs (see equation 3.2) (Cornilescu et al. 1998; Schmitz et al. 2012). Q factors are also used in validation of NMR protein structure determinations from PCSs (Schmitz et al. 2012). Q factors below 20% reflect good fits. The slope of the plot should be close to one and intercepts with the y axis close to zero.

Ala^{350} and Val^{351} located in the C-terminus are excluded from the fit owing to significant deviations between experimental and calculated PCSs. Measured PCSs are much smaller than the expected ones. The C-terminus is very flexible and only observable in the crystal structure of the closed state. The differences indicate that the conformation of the C-terminus found in the crystal structure is lowly populated in solution. NOE correlations between Ala^{350} and Leu^{132} in the 4D methyl-methyl NOESY experiment show a possible alternative orientation of the C-terminus (compare Fig. 4.7). However, the experiment is recorded with an unliganded protein sample, while PCSs are measured in presence of UDP and H-dis. It is expected that the orientation of the C-terminus differs between both states, as it forms direct contacts to the ligands in the crystal structure.

Table 4.2: Final magnetic susceptibility tensors derived with *Numbat* from fitting ^{1}H PCSs of A, I, L, M and V methyl groups using the "ensemble" structure. Results of three different fits are listed. *Individual* indicates a fitting process, where all parameters are free and the tensors are calculated independently for each metal ion. *Combined* indicates a fitting process, where all parameters are free but tensors are calculated simultaneously for all metal ions sharing the same tensor centers. *Fixed metal position* indicates a fitting process, where the coordinates of the tensor center are restricted to the metal position in the X-ray structure. The errors correspond to the standard deviation in 1000 Metropolis Monte Carlo approaches with random selection of 80% of PCS data for tensor fitting. For comparison, the position of the Mn^{2+} ion in the crystal structure is indicated in the last line.

	Tensor	**ΔX_{ax} (10^{-32} m^3)**	**ΔX_{rh} (10^{-32} m^3)**	**Coordinates of tensor center (Å)**			**Orientation of tensor axes (°)**		
				X	Y	Z	α	β	γ
Individual	Ce^{3+}	0.822 (±0.010)	0.147 (±0.011)	15.325 (±0.131)	16.357 (±0.102)	4.250 (±0.120)	67.3 (±0.9)	44.8 (±0.7)	8.5 (±37.9)
	Eu^{3+}	-1.452 (±0.032)	-0.746 (±0.022)	14.769 (±0.123)	16.244 (±0.191)	4.009 (±0.151)	68.9 (±1.1)	40.7 (±1.0)	42.1 (±1.7)
	Pr^{3+}	2.593 (±0.034)	1.076 (±0.045)	14.878 (±0.097)	16.375 (±0.095)	4.495 (±0.086)	65.6 (±0.6)	49.6 (±0.4)	41.0 (±1.2)
Combined	Ce^{3+}	0.832 (±0.015)	0.164 (±0.022)	14.915 (±0.076)	16.359 (±0.079)	4.274 (±0.082)	65.9 (±1.1)	44.8 (±0.6)	15.0 (±24.4)
	Eu^{3+}	-1.467 (±0.031)	-0.712 (±0.025)	14.915 (±0.076)	16.359 (±0.079)	4.274 (±0.082)	68.2 (±0.9)	40.7 (±0.8)	42.2 (±1.6)
	Pr^{3+}	2.547 (±0.038)	1.083 (±0.050)	14.915 (±0.076)	16.359 (±0.079)	4.274 (±0.082)	65.9 (±0.7)	49.1 (±0.5)	41.5 (±1.3)
Fixed metal position	Ce^{3+}	0.809 (±0.016)	0.184 (±0.022)	14.998	16.922	4.050	66.5 (±1.2)	46.4 (±0.6)	15.7 (±11.0)
	Eu^{3+}	-1.394 (±0.054)	-0.727 (±0.030)	14.998	16.922	4.050	69.1 (±1.1)	43.1 (±0.9)	38.9 (±2.4)
	Pr^{3+}	2.381 (±0.044)	1.043 (±0.049)	14.998	16.922	4.050	65.9 (±0.7)	50.4 (±0.6)	39.2 (±1.8)
Crystal structure (2RJ1)	Mn^{2+}	-	-	14.998	16.922	4.050	-	-	-

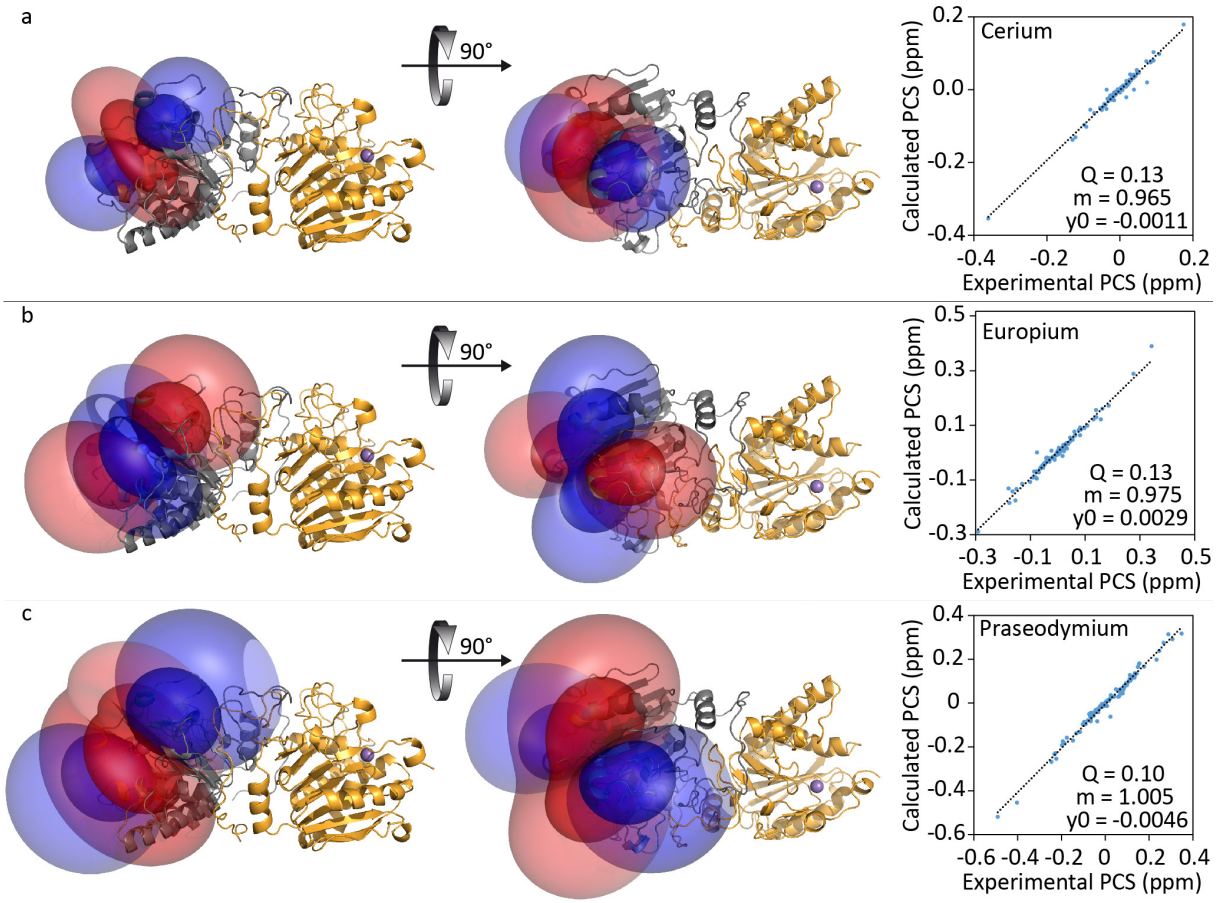


Figure 4.16: PCS isosurfaces (created with *Numbat* and *PyMOL*) of the anisotropic magnetic susceptibility tensors and correlations of experimental versus calculated PCSs for (**a**) Cerium, (**b**) Europium and (**c**) Praseodymium. Each panel shows the crystal structure of the GTB homodimer (PDB entry 2RJ8) in cartoon representation with PCS isosurfaces contoured at ±0.02 ppm and ±0.1 ppm. Blue and red isosurfaces represent regions with positive and negative PCSs, respectively. The monomers are displayed in grey and orange. The metal position is not fixed in the calculation of the Δχ tensor. The coordinates of the tensor center fit very well the position of the metal ion in the crystal structure represented by a sphere. For further estimation of Δχ tensor quality, the correlation between observed and predicted PCSs is given on the right of each panel. Q factors (equation 3.2), slopes (m) and y-axis intercepts (y0) are indicated

In order to assess which protein state is captured in presence of UDP, H-dis and Ln^{3+}, different structural models are used for Δχ tensor refinement. Structures of the open and closed state are used independently and combined in the "ensemble" model. Residues of the C-terminus are excluded in the fits, as it is not resolved in the structure of the open conformation. Besides the C-terminus, the structures of the open and closed state differ only in the internal disordered loop. The "ensemble" structure provides for all lanthanides the best fits, as can be concluded from the Q factors (compare Tab. 4.3). Figure 4.17 points out that Q factor deviations can mainly be attributed to differently calculated PCSs in the internal loop (Val^{175}-Met^{191}). The PCSs calculated on basis of the "ensemble" structure differ from those that are independently derived on basis of either the open or the closed structure. In the case of

the "ensemble" structure, *Numbat* computes the expected PCSs as the average of those for each individual conformation. The higher quality fit indicates that the solution structure adopted in the paramagnetic NMR experiments is an average state between the open and closed conformation. This is in agreement with the semi-closed conformation, which is adopted when only donor substrate is bound. The semi-closed state is observed as an "intermediate state" between the open and closed conformation with evidence for both internal loop orientations with ca. 50% occupancy each in crystal structures of ABBB and AABB in presence of UDP. The crystal structure of GTB in presence of UDP shows high disorder in the region of the internal loop with a continuum of conformations between the two states (Alfaro et al. 2008).

Table 4.3: Q factors derived from measured and expected PCSs of Δχ tensor fits to different structural models. Tensors are fitted to the open or closed state or a combination of both structures. Residues of the C-terminus are excluded in the fitting sessions, as it is not resolved in the structure of the open conformation.

Structural model	**Q factor**		
	Ce^{3+}	Eu^{3+}	Pr^{3+}
Open conformation (PDB entries 2RIT, 2RIZ)	0.1614	0.1404	0.1299
Closed conformation (PDB entries 2RJ1, 2RJ8)	0.1288	0.1461	0.1143
"Ensemble" (PDB entries 2RIT, 2RIZ, 2RJ1, 2RJ8)	0.1283	0.1334	0.0967

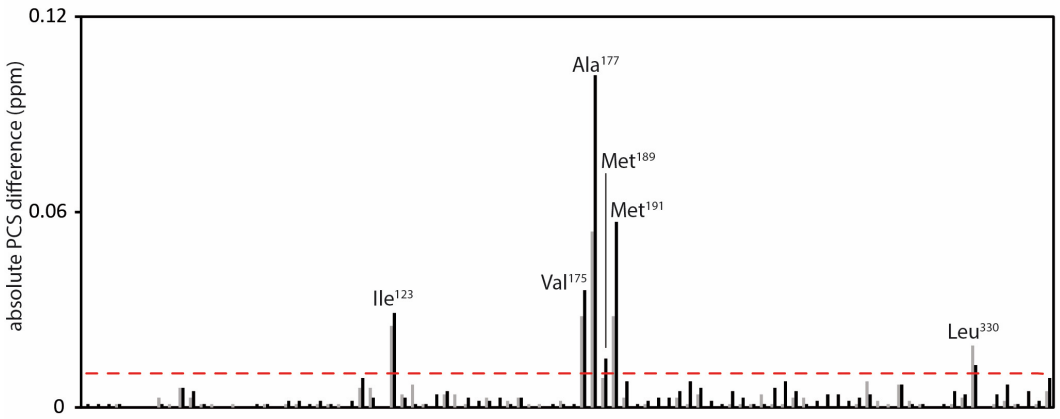


Figure 4.17: Differences of calculated Pr^{3+}-induced PCSs obtained from different structural models. The absolute differences of the calculated PCSs, derived from the open conformation (black bars) and closed conformation (grey bars) are calculated for each residue relative to the "ensemble" structure derived values. The differences are represented in sequential order. The red dashed line represents the standard deviation of all differences.

4.2 Ligand interaction studies

NMR chemical shifts are very sensitive to changes in the magnetic environment of the respective nuclei. Accordingly, changes of peak positions of protein spins upon addition of a ligand report on ligand binding sites, or on allosteric sites of structural or dynamic alterations induced by ligand binding. However, NMR titrations are even richer sources of structural, mechanistic, thermodynamic and kinetic information on biomolecular interactions. The appearance of the spectra during a titration is determined by the exchange rate between free and bound state relative to their frequency difference, and the population ratio of free versus bound state. According to this, the resonance line shapes report on the timescale of the exchange process, and the peak positions and/or intensities reflect the equilibrium populations. Therefore, a systematic line shape analysis facilitates quantification of ligand affinities, as well as quantification of ligand on- and off-rates.

This chapter summarizes interaction studies between different donor and acceptor substrate analogs and GTA, GTB and AAGlyB. Peak positions of AIL^{proS}MV^{proS} methyl groups in 2D [^{13}C, ^{1}H]-HMQC spectra recorded for the ligand saturated state reveal the ligand binding sites, as well as allosterically affected sites. Subtle deviations in the induced perturbations between different analogs give new insights into ligand binding modes. Additionally, 2D line shape analysis of ligand titration data, employing the *TITAN* software (Waudby et al. 2016), allows a quantitative evaluation of the observed interactions. The observed binding rates are related to exchange rates determined in ZZ-exchange experiments. Finally, ligand binding studies are applied to Trp^{181} mutants. This residue is located on the tip of the internal disordered loop and locks the protein in the closed state via a cation-π interaction to Arg^{352} of the C-terminal domain. Substitutions of Trp^{181} with Met or Glu are hypothesized to either weaken or strengthen this interaction. The binding studies of the mutants, as well as the ZZ-exchange experiments are executed with ILMV methyl-labeled proteins.

4.2.1 Donor substrate binding induced chemical shift perturbations in GTB

GTB solutions are titrated with different nucleotide sugars in order to shine more light on the enzyme's mode of donor substrate discrimination. Ligands comprise GTB's native donor substrate, UDP-Gal, as well as the native substrate of GTA, UDP-GalNAc, and their respective epimers UDP-Glc and UDP-GlcNAc, and the transferase product UDP. AIL^{proS}MV^{proS} methyl-labeled GTB is generated according to section 3.1. The same stock of D_2O-based 35 mM phosphate buffer (pH* 6.8) is used for dissolving the ligands, as well as exchange of the protein solution buffer. Subsequently, the pH* of the ligand stock solution is carefully readjusted to 6.8. Ligand working stocks are generated as dilutions of the ligand stocks with the protein solution, in order to provide a largely constant protein concentration during the titration. The buffer contains 50 mM NaCl to minimize ionic strength effects by the introduced nucleotide salts, and 5 mM $MgCl_2$ to accommodate binding of the nucleotide. Samples of the same protein stock (specific activity: ~12 U/mg) are used for the different titrations in 3 mm NMR tubes with

a volume ranging between 145-180 µL. The protein concentration at the start of the titration is 280 µM, as determined by UV absorbance at 280 nm. At each titration step, 2D [^{13}C, ^{1}H]-HMQC experiments are recorded at 298 K and 500 MHz proton frequency with 8 scans using 1024 (^{1}H) and 256 (^{13}C) complex data points. As GTB shows UDP-Gal hydrolysis activity, the native nucleotide sugar is added in one step to achieve the maximum concentration of 6200 µM. The spectra are processed with 4 Hz (^{1}H) and 8 Hz (^{13}C) exponential line broadening and zero filling to 512 complex points in the indirect dimension using *NMRPipe* (Delaglio et al. 1995). DSS-d_6 serves as internal reference for the chemical shifts. The reported donor substrate binding-induced chemical shift perturbations (CSPs) (see Fig. 4.18) are weighted Euclidean distances (Δδ) between peak positions in the spectrum recorded with the highest donor concentration (6200 µM) relative to the positions in the spectrum recorded with apo-GTB (equation 3.3). Peak positions are followed using *CcpNmr Analysis* (Vranken et al. 2005). The standard deviation (σ) of all Euclidean chemical shift changes is calculated independently for each ligand titration. Only shift changes greater than σ, or 2σ as highly restrictive threshold, are considered as significant.

Similar regions of the enzyme are influenced by binding of each donor substrate analog. However, CSPs are much less pronounced for UDP-GalNAc and even less pronounced for UDP-GlcNAc binding. The observed exchange rates are fast to intermediate on the NMR time scale, implying that peak positions are proportional to the degree of ligand saturation. Although using >20 times excess of donor substrates relative to the protein concentration, the size of CSPs is trivially still dependent on the ligand affinity. As determined by NMR line shape analysis and reported in the next section, UDP-GalNAc and UDP-GlcNAc bind with a one order of magnitude lower affinity to GTB than the other ligands. The usage of σ as a variable cut-off allows a comparison between the ligands. Table 4.4 summarizes the used cutoffs and the number of signals with CSPs exceeding these thresholds.

Table 4.4: Thresholds and numbers of significantly perturbed resonances by binding of different ligands in the donor binding site. σ and 2σ are given in units of ppm. The number of resonances that show larger changes than the cut-offs are indicated in brackets.

	UDP-GlcNAc	**UDP-GalNAc**	**UDP-Glc**	**UDP-Gal**	**UDP**
σ (ppm)	0.017 (22)	0.027 (23)	0.052 (24)	0.047 (24)	0.052 (25)
2σ (ppm)	0.035 (12)	0.055 (13)	0.105 (9)	0.093 (9)	0.105 (10)

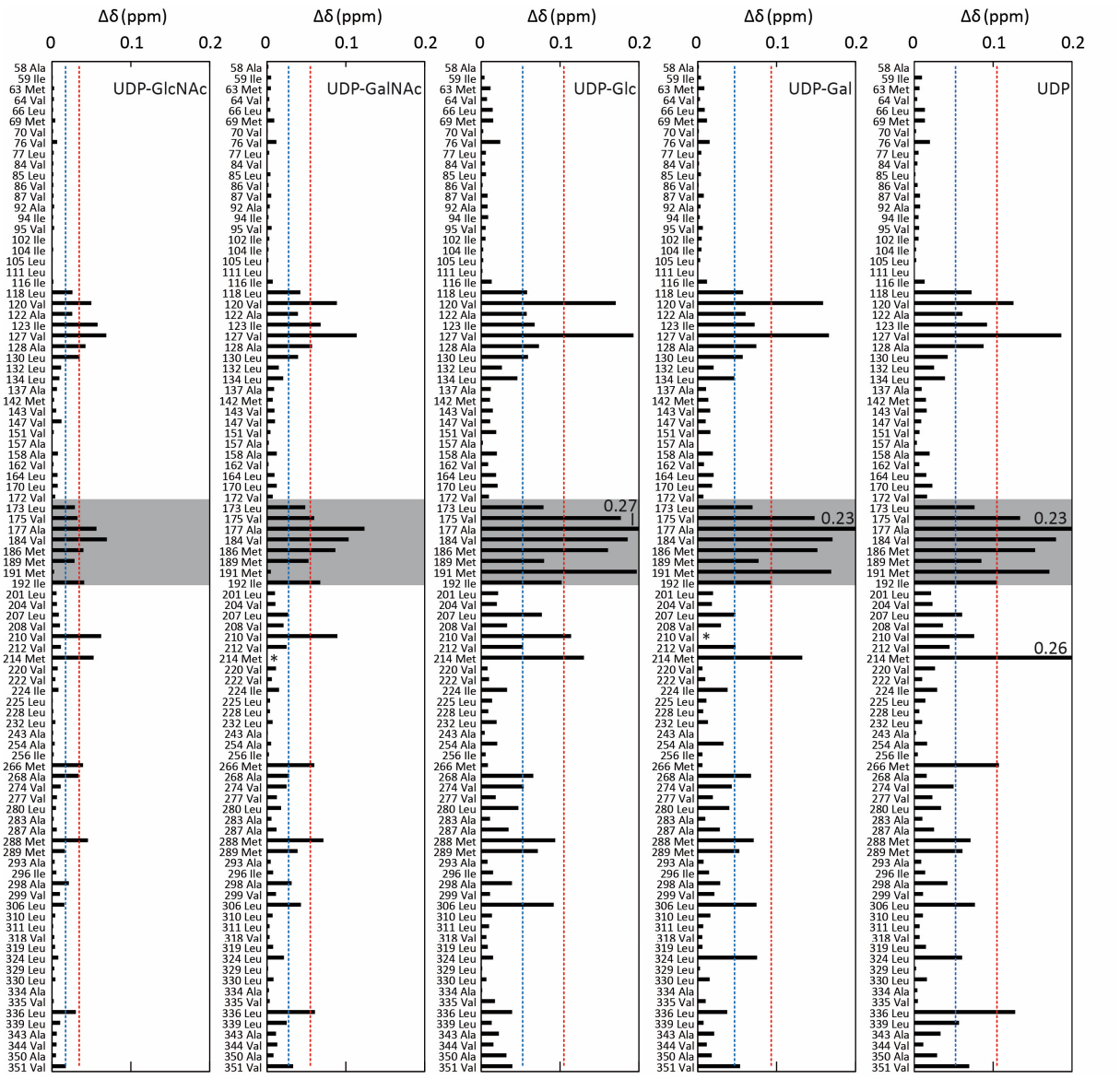


Figure 4.18: Residue specific CSPs observed during ligand binding in the donor binding site. The five panels show the weighted Euclidean distances (Δδ) between peak positions in 2D [^{13}C,^{1}H]-HMQC spectra recorded with apo-GTB and ligand-saturated GTB, respectively. Spectra are recorded with AIL^{proS}MV^{proS} GTB (270 µM) and high excess of ligands (6200 µM). Residues are listed in sequential order. The dashed lines indicate cutoffs at 1σ (blue) and 2σ (red). The internal disordered loop is highlighted in grey. Chemical shift perturbations greater than 0.2 ppm are given at the respective bars. Ambiguous CSPs are labeled with *.

As expected, the most pronounced changes (>2σ) can be observed for residues of the β3-strand-turn-α2-helix structure (residues 118-130) and the internal disordered loop (residues 173-192), which are in direct contact with the nucleotide. The largest CSPs are measured for Ala^{177} (0.27 ppm) in presence of UDP-Glc, and Met^{214} (0.26 ppm) in presence of UDP. As described earlier (compare Fig. 4.5), the methyl group of Met^{214} is located close to the metal position. Crystal structures show direct and water mediated hydrogen bonds between the nucleotide and Phe^{121} Ile^{123}, Lys^{125} and Tyr^{126} (Alfaro et al. 2008). However,

the observed changes reflect most likely not only direct contacts to the ligand, but also the transition to the semi-closed protein conformation. In order to correlate the observed CSPs to structural reorientations, methyl positions are determined in the crystal structures of apo-ABBB (PDB entry 2RIZ) and UDP-soaked ABBB (PDB entry 2RJ0). The structures are aligned using *PyMOL* version 1.3 (DeLano 2002), and the relevant methyl carbon positions are extracted using a self-written Python script. Normalized distances between methyl carbons in both structures are summarized in figure 4.19 together with normalized UDP binding-induced CSPs. A global correlation between both parameters is observable, but there are also significant differences, e.g. M^{214} as will be discussed below.

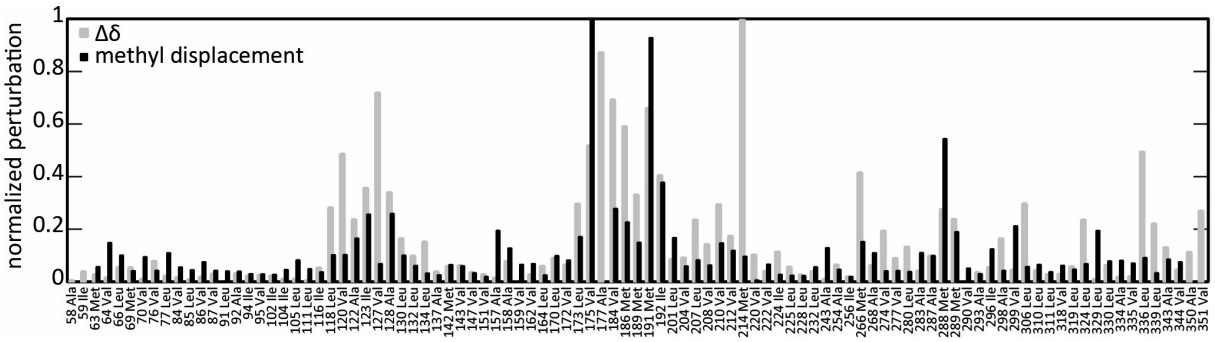


Figure 4.19: Correlation between crystal structure methyl displacements and NMR CSPs of methyl resonances induced by UDP binding. The UDP binding-induced CSPs (Δδ, grey bars) are normalized to the largest observed change (Met^{214}: 0.26 ppm) and reported in residue-specific sequential order. Methyl displacements (black bars) are determined as the distance between the position of the methyl carbon in the apo-ABBB crystal structure (PDB entry 2RIZ) and its position in the UDP-soaked structure (PDB entry 2RJ0) and normalized to the largest observed displacement (Val^{175}: 1.70 Å). Ala^{177}, Ala^{350} and Ala^{351} are not resolved in the crystal structures.

Although the CSP patterns are strikingly similar for all used donor analogs, there are also notable differences. To emphasize the differences between effects induced by different donor analogs, the peak positions in the ligand-saturated states are compared. As described above, ligand binding occurs in the fast exchange regime, and peak positions depend on the degree of saturation of GTB. Therefore, such a comparison is only useful for ligands with comparable affinities. The dissociation constants described in table 4.5 of the next section allow an estimation of the maximum extent of this effect. According to the law of mass action, a protein concentration of 270 µM and a ligand concentration of 6200 µM imply bound state populations of 97% (UDP), 91% (UDP-Gal/UDP-Glc), and 65% (UDP-GalNAc/UDP-GlcNAc). Thus, the CSPs between peak positons in spectra of the ligand-saturated states are only calculated for UDP, UDP-Gal and UDP-Glc. The results are reported in figure 4.20. The zoomed regions in the 2D [^{13}C,^{1}H] HMQC spectra show chemical shift changes of Ile^{123}, Ile^{192} and Ala^{268} into different directions upon addition of the respective ligand. This demonstrates that different peak positions in the ligand-saturated states are not an artifact, due to varying degrees of saturation but a result of altered binding effects induced by the individual ligands. The differences between nucleotide sugar- and UDP-

saturated states are larger (σ: 0.024 ppm) than differences between the UDP-Gal- and UDP-Glc-saturated states (σ: 0.012 ppm).

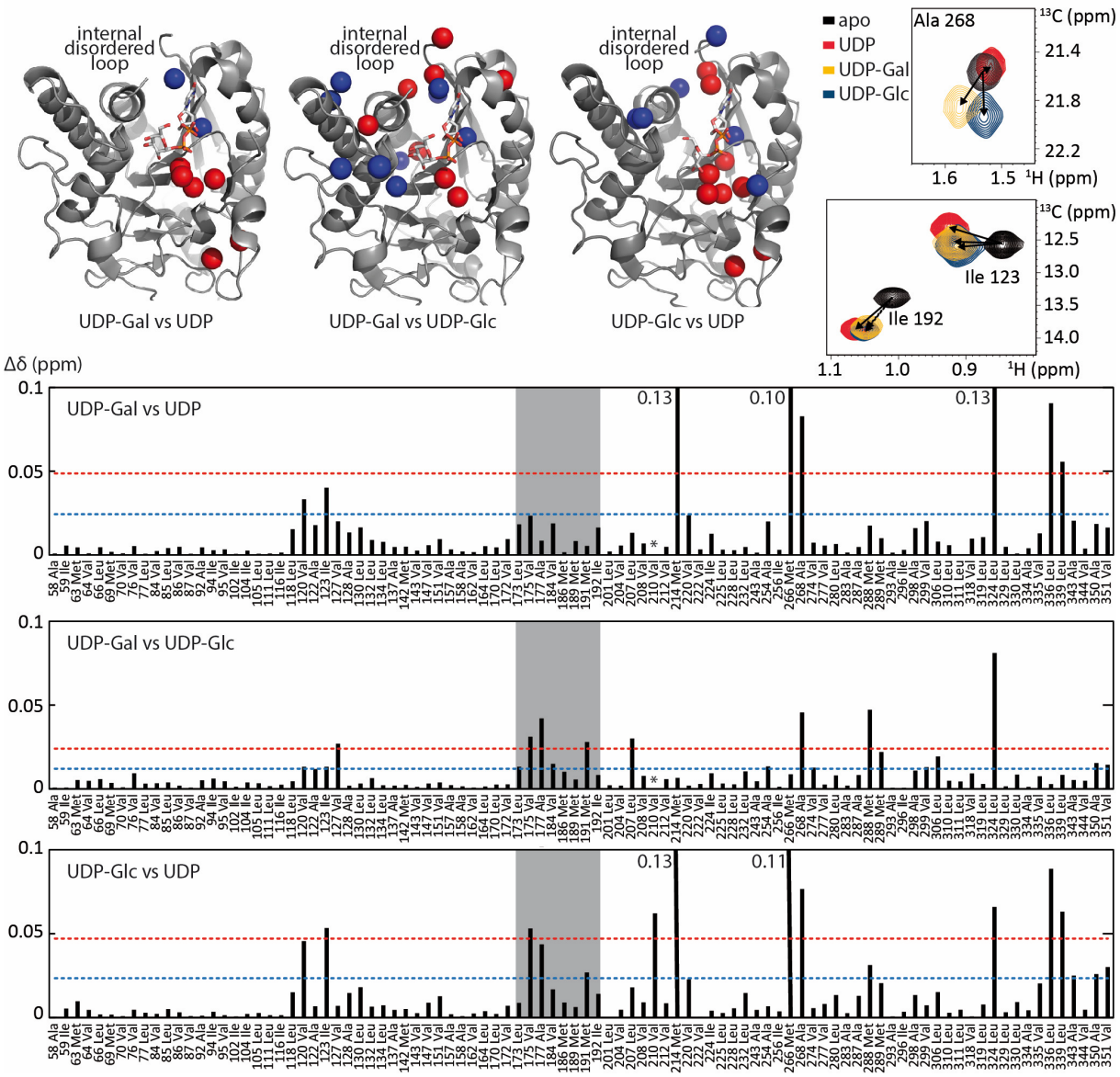


Figure 4.20: Residue specific chemical shift deviations observed between donor-saturated states. The three bottom panels show the weighted Euclidean distances between peak positions in 2D [^{13}C,^{1}H]-HMQC spectra recorded with UDP-Gal, UDP-Glc and UDP-saturated GTB, respectively. The dashed lines indicate cutoffs at 1σ (blue) and 2σ (red). The internal disordered loop is highlighted in grey. Chemical shift perturbations greater than 0.1 ppm are indicated at the respective bars. Ambiguous CSPs are labeled with *. The crystal structures on the top show the location of the methyl carbons of significantly perturbed (σ and 2σ) residues in the same color code (PDB entries 2RJ7, 5C4D). The positions of peaks of Ile^{123}, Ile^{192} and Ala^{268} in spectra recorded with apo (black), UDP- (red), UDP-Gal- (yellow) and UDP-Glc-saturated (blue) GTB illustrate perturbations into different directions.

The differences observed between UDP-Gal and UDP can be understood as differences between educt and product. The most pronounced differences (Δδ>2σ) are observed for Met^{214}, critical residues Met^{266}

and Ala[268], and Leu[324], which are all located in the active site. Significant differences are also observed for Leu[336] and Leu[339] located in a remote region more than 15 Å away from the sugar moiety. Comparison with figure 4.18 shows that these residues are only significantly perturbed in the UDP-saturated state.

Different peak positions in spectra of UDP-Gal- and UDP-Glc-saturated GTB emphasize regions in the enzyme that are potentially involved in the selection mechanism between the epimers. Again, Ala[268] and Leu[324] show significant deviations. They are located close to the sugar moiety. The other significantly perturbed peaks correspond to residues of the internal disordered loop or residues abutting this loop. Furthermore, also methyl labels of the C-terminus appear at different positions in the spectra recorded in presence of the respective nucleotide sugars. An influence of donor binding on the C-terminus in absence of an acceptor substrate has not been described so far. The C-terminus remains disordered in all nucleotide- or nucleotide sugar-soaked crystal structures. Residues of the internal disordered loop, of regions close-by, and of the C-terminus are also affected as seen from a comparison of peak positions of the UDP-Glc- and of the UDP-saturated state. Therefore, differences in these regions can be traced back to the Glc moiety.

4.2.2 2D NMR line shape analysis of donor substrate titration data

Titration data are acquired with UDP, UDP-Glc, UDP-GlcNAc and UDP-GalNAc. The UDP-Gal hydrolysis activity does not allow a line shape analysis with the native donor substrate. The processed 2D [^{13}C,^{1}H] HMQC spectra (compare section 4.2.1) of each titration point are imported into *MATLAB* for analysis with *TITAN* (Waudby et al. 2016). All data are fitted to a two-state ligand binding model, respectively:

$$P + L \underset{k_{off}}{\overset{k_{on}}{\rightleftharpoons}} PL$$

Several peaks are selected for global fitting, in order to describe the common interaction event more accurately. Chemical shifts and linewidths of the apo state are determined using only the first spectrum (absence of donor substrate). These parameters are hold constant for the remainder of the fitting session. Peak positions of the bound state and linewidths of all states, as well as the dissociation constant (K_d) and the off-rate (k_{off}) of the ligand are fitted using the entire dataset. The bootstrap residual resampling procedure provided within *TITAN* is applied for estimation of parameter uncertainties in 200 runs.

The fits of the UDP titration data are visualized in figure 4.21. 19 residues are selected for the fit and the resonances are tracked in seven titration steps. The fits of the other titrations are provided in the appendix. All resonances are found in the fast to intermediate exchange time regime. The three dimensional visualizations of the global fits are shown exemplarily for the resonances of Ile[192], Met[214] and Leu[336]. They report on the high quality of the fit. Binding parameters and uncertainties are listed in table 4.5.

Table 4.5: Fitted two-state ligand binding model parameters for the interaction of GTB with different donor analogs. The dissociation rate and off-rate are derived from the fits using *TITAN*. The on-rate is calculated on basis of these parameters ($K_d = k_{off}/k_{on}$). The uncertainties are determined by bootstrapping using residual resampling with 200 replicas.

	K_d (μM)	k_{on} ($M^{-1}s^{-1}$)	k_{off} (s^{-1})
UDP	161 ± 3	1.51 x 10^6	244 ± 7
UDP-Glc	598 ± 7	3.66 x 10^5	219 ± 4
UDP-GalNAc	3370 ± 60	1.46 x 10^5	493 ± 15
UDP-GlcNAc	3300 ± 110	1.85 x 10^5	610 ± 50

The observed affinities follow a previously described tendency (UDP > UDP-Gal/UDP-Glc > UDP-GalNAc/UDP-GlcNAc) (Blume et al. 2006). As reported for other enzymes (Fersht 1999; Tugarinov and Kay 2003b), the on-rate is significantly lower than expected for diffusion-controlled association (~10^8-10^9 $M^{-1}s^{-1}$). Such deviations are indicative for a complex binding mechanism, where high activation barriers limit the entry of the donor substrate into the binding site. High activation barriers can be due to structural rearrangements in the protein, as well as in the ligand. Both types of rearrangement have been described for GTB and its ligands. GTB undergoes the transition from the open to semi-closed conformation upon donor substrate binding (Alfaro et al. 2008). UDP-Gal and UDP-Glc adopt the tucked-under conformation, when they are bound to GTB (Angulo et al. 2006; Gagnon et al. 2015).

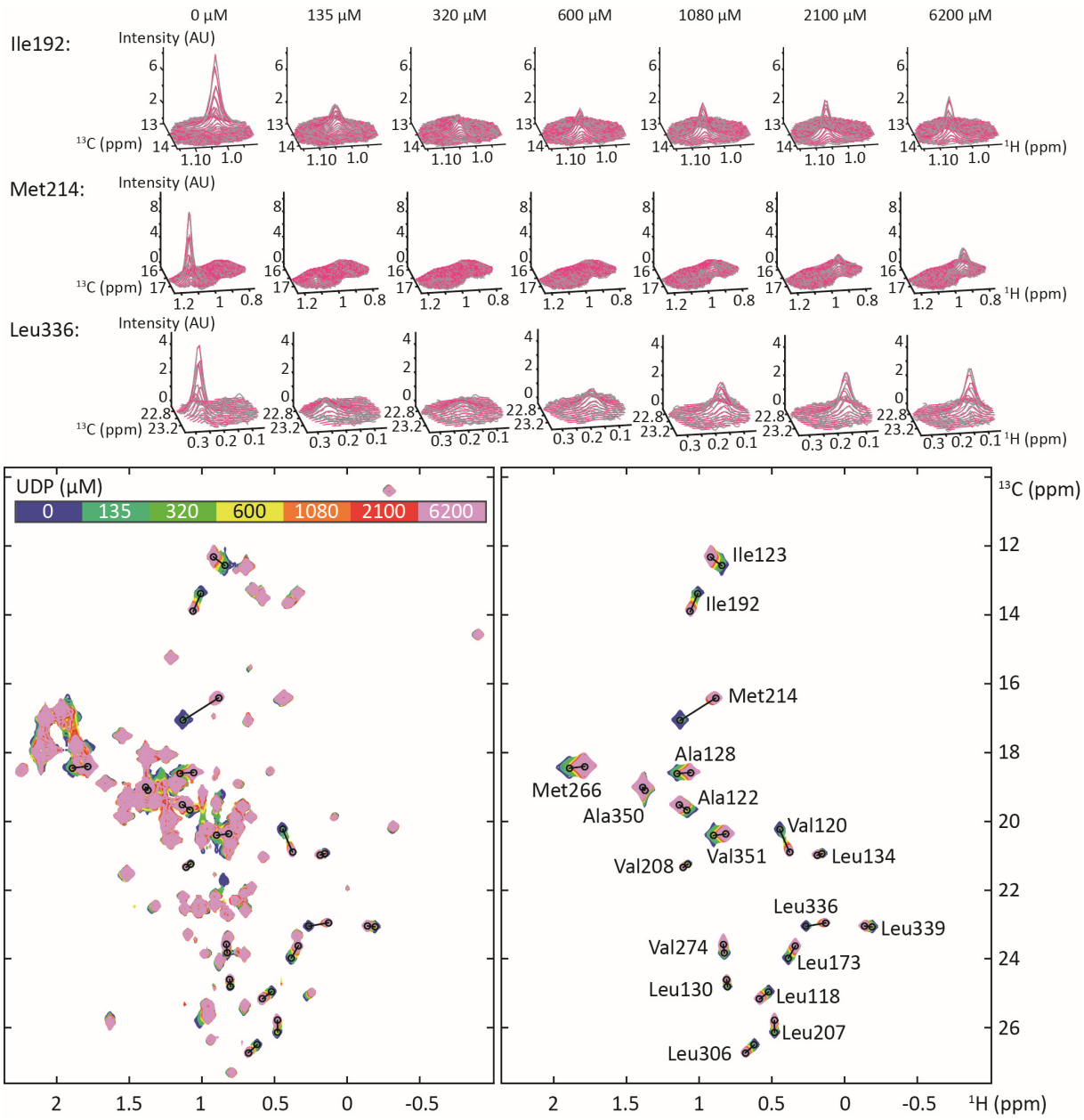


Figure 4.21: Line shape analysis of HMQC-based UDP titration data. The bottom panels show the observed (left) and fitted (right) 2D [^{13}C,^{1}H]-HMQC spectra of 280 µM AIL^{proS}MV^{proS} GTB upon titration with UDP. 19 resonances are selected for a global fit. The overlays of fitted (red) and observed (grey) spectra provided on the top visualize the exchange process for 3 of the 19 resonances in a 3D plot.

The line shapes of resonances corresponding to residues of the internal loop suggest a complex binding mechanism, too (see Fig. 4.22). These resonances are not included in the global fit to the two state binding mechanism. However, fitting to a more complex binding mechanism (e.g. induced-fit) does not deliver reasonable estimates because of signal overlap and extensive exchange broadening. It should be noted that all resonances are mainly perturbed in the ^{13}C dimension. Since carbon chemical shifts of methyl groups are more sensitive to local methyl group rotamer distribution than to through-space

interactions with e.g. charged groups or phenyl rings (Williamson 2013), the CSPs are very likely due to methyl group reorientation associated with the transition from the open to semi-closed protein conformation. The correlation between CSPs and methyl reorientations in crystal structures (compare Fig. 4.19) leads to the same hypothesis. Comparable line shapes can also be observed upon titration with the other donor analogs. The observed exchange broadening in the fully saturated state is in accordance with findings in crystal structures, where the internal loop is more disordered in presence of a donor substrate (Alfaro et al. 2008; Gagnon et al. 2015).

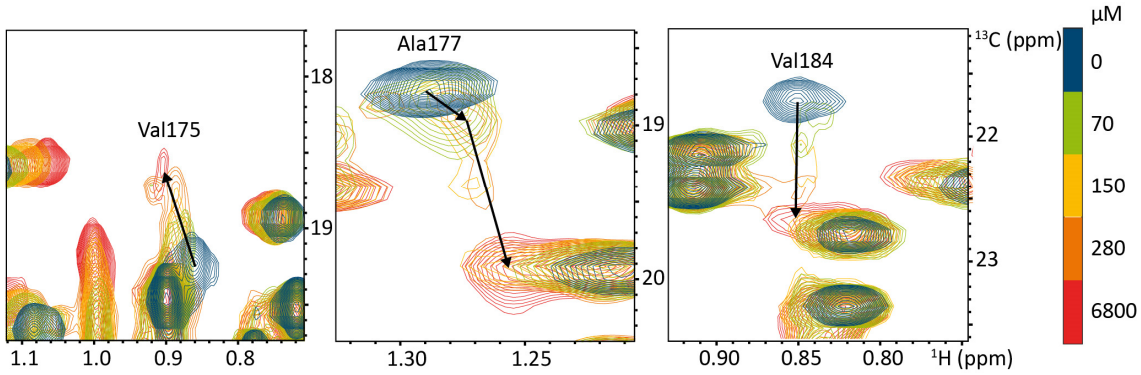


Figure 4.22: Line shapes of resonances corresponding to residues of the internal loop during UDP titration. Shown are overlays of 2D [^{13}C,^{1}H]-HMQC spectra of 195 µM AIL^{proS}MV^{proS} GTB upon titration with UDP. The spectra are color coded with the UDP concentrations indicated on the right. All resonances show complex line shapes with significant exchange broadening in the fully saturated state. The trajectories are from a second UDP titration with a GTB sample where labeling efficiency is comparable for all aa types.

4.2.3 Acceptor substrate binding induced chemical shift perturbations in GTB

Interactions between GTB and several acceptor analogs are analyzed based on ligand-induced CSPs. Used ligands comprise the H antigen disaccharide (H-dis; α-L-Fuc*p*-(1→2)-β-D-Gal*p*-O-octyl) and its 3-deoxy-Gal derivative (3DD), as well as the transferase product of GTB, the B antigen trisaccharide (B-tris; α-D-Gal*p*-(1→3)-[α-L-Fuc*p*-(1→2)]-β-D-Gal*p*-O-octyl). Furthermore, GTB is titrated with all six types of H antigen trisaccharides (H-tris). The protein and ligand solutions are prepared as described in section 4.2.1 with the same buffer system. For the titrations with H-dis, 3DD and B-tris, the same protein stock solution is used with a concentration of 280 µM. For all H-tris titrations, the protein concentration of the commonly used stock solution is 195 µM. These concentrations are determined by UV absorbance at 280 nm using a NanoDrop spectrometer. At each titration step, 2D [^{13}C, ^{1}H]-HMQC experiments are recorded at 298 K and 500 MHz proton frequency with 8 scans using 1024 (^{1}H) and 256 (^{13}C) complex data points. The spectra are processed with 4 Hz (^{1}H) and 8 Hz (^{13}C) exponential line broadening and zero filling to 512 complex points in the indirect dimension using *NMRPipe* (Delaglio et al. 1995). DSS-d_6 serves as internal reference for the chemical shifts. CSPs are calculated for spectra recorded with GTB

in the absence of any ligand and in the presence of the highest ligand concentration. As described before, σ and 2σ serve as cut-off values to select the significantly perturbed resonances.

Table 4.6: Thresholds and numbers of significantly perturbed resonances by binding of different ligands in the acceptor binding site.σ and 2σ are given in units of ppm. The number of resonances showing greater changes than the cut-offs are indicated in brackets.

	H-dis	**3DD**	**B-tris**	**H-tris I**	**H-tris II**	**H-tris III**	**H-tris IV**	**H-tris V**	**H-tris VI**
σ (ppm)	0.032 (9)	0.031 (14)	0.032 (7)	0.012 (9)	0.042 (9)	0.009 (13)	0.005 (24)	0.020 (9)	0.023 (11)
2σ (ppm)	0.064 (7)	0.062 (7)	0.063 (5)	0.025 (6)	0.083 (4)	0.018 (7)	0.011 (7)	0.040 (7)	0.047 (8)

The induced CSPs are summarized in figure 4.23 (H-dis, 3DD and B-tris) and figure 4.24 (H-tris). CSPs are on average smaller than the observed effects induced by donor analogs. Moreover, less residues are significantly perturbed. These findings indicate a more locally restricted binding event, agreeing with crystal structures, which show no conformational transition upon acceptor binding, if the donor substrate is absent. When comparing the resonances with the most pronounced CSPs, a common binding motif can be identified for all acceptor analogs. Common to all ligands are shift changes for Met^{214}, Met^{266}, Val^{299}, Leu^{324}, Leu^{329}, Leu^{330} (not B-tris), Leu^{336} and Leu^{339}. Most of these residues are anticipated from the crystal structures, since they are located in the acceptor binding site. However, significant CSPs for Leu^{329} and Leu^{330} come as a surprise, as they are located more than 10 Å away from the acceptor position.

As described above, fast exchange phenomena complicate the analysis of differences between the ligands, when a full saturation of binding sites is not reached. However, H-dis, 3DD and B-tris show comparable affinities (see section 4.2.4). Differences between these ligands are reported in figure 4.23 as differences between peak positions in the spectra recorded with the highest ligand concentrations. Deviations occur mainly for residues of the common binding motif (>2σ). Crystal structures show a van der Waals contact between critical residue Met^{266} and the α-Gal moiety of the B-trisaccharide (Gagnon et al. 2017), which explains differences at this site. Smaller deviations (σ<Δδ<2σ) show up at locations further away from the binding site and might partially be artifacts of different saturation degrees. It is, however, worth noting that residues of the internal disordered loop or of the C-terminus are not influenced by binding of any ligand, indicating that the protein adopts in all cases the open conformation and that the α-Gal moiety of the B-trisaccharide does not interact or sterically interfere with residues of these domains, either.

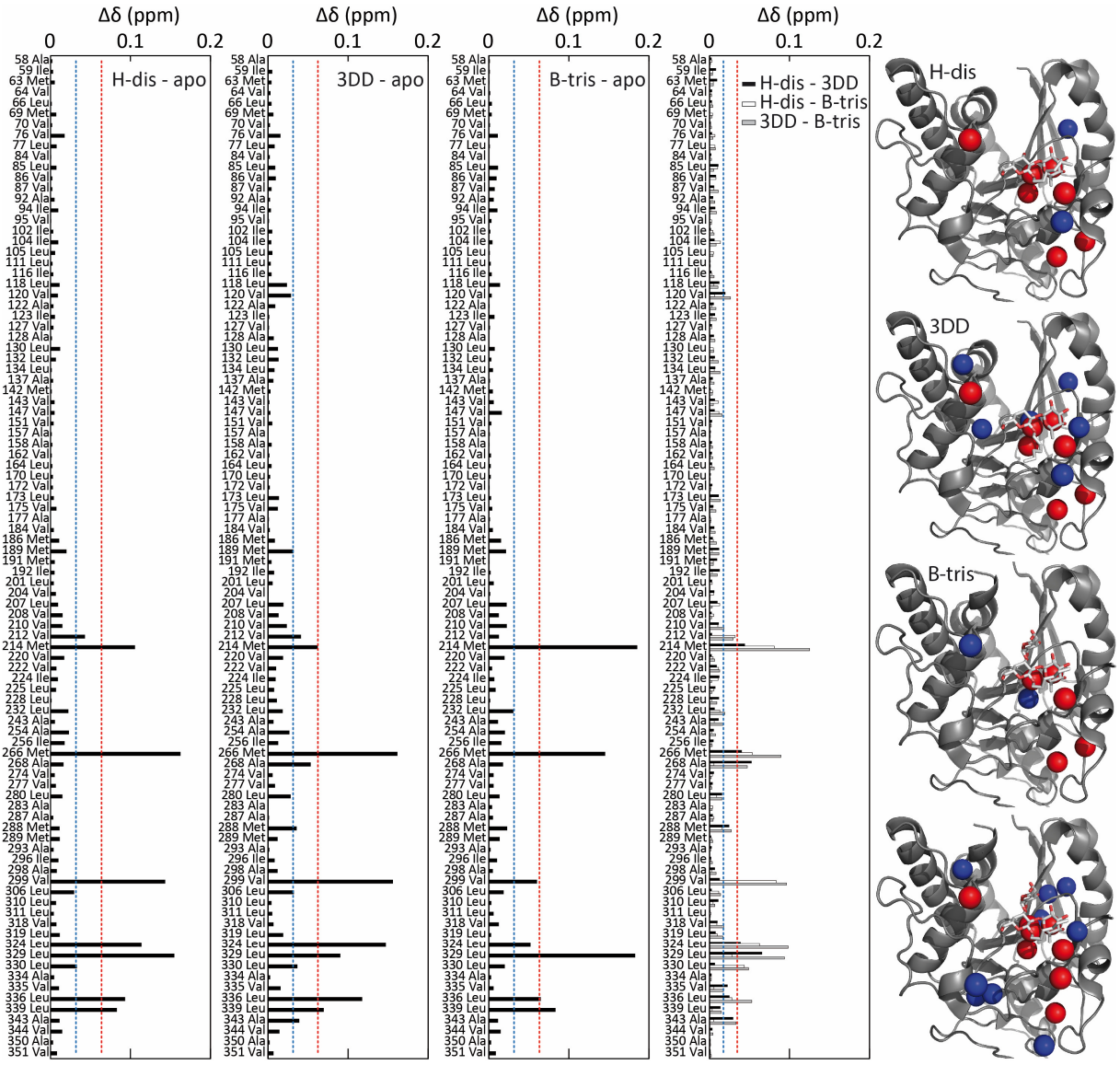


Figure 4.23: Residue specific CSPs observed during ligand binding in the acceptor binding site. The three left panels show the weighted Euclidean distances between peak positions in 2D [^{13}C,^{1}H]-HMQC spectra recorded with apo-GTB and ligand-saturated GTB, respectively. Spectra are recorded with AIL^{proS}MV^{proS} GTB (270 µM) and excess of ligand (1120 µM). Residues are listed in sequential order. The fourth panel shows Euclidean distances between peak positions in the spectra of each ligand saturated state. The dashed lines indicate cutoffs at 1σ (blue) and 2σ (red). The crystal structures on the right show the location of the methyl carbons of significantly perturbed residues in the same color code for H-dis (PDB entry 2RIY), 3DD (PDB entry 2RJ7) and B-tris (PDB entry 5TJN). The crystal structure on the bottom summarizes all differences between the three ligands in correspondence with the fourth panel.

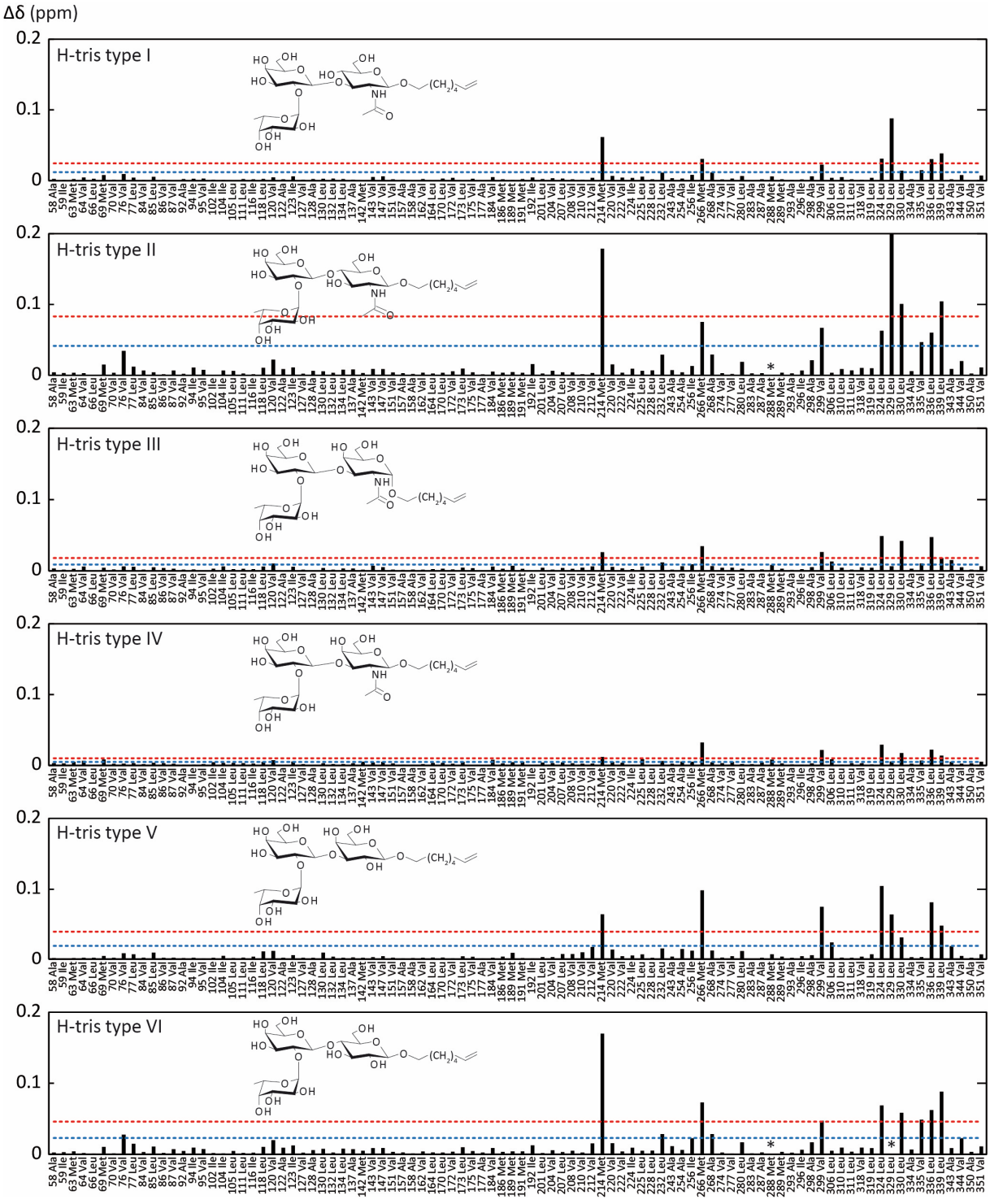


Figure 4.24: Residue specific CSPs observed during binding of different H-trisaccharide antigens. Shown are the weighted Euclidean distances between peak positions in 2D [^{13}C,^{1}H]-HMQC spectra recorded with apo-GTB and GTB in presence of H-trisaccharide antigens, respectively. Spectra are recorded with AIL^{proS}MV^{proS} GTB (180 µM) and excess of ligand (3120 µM). Residues are listed in sequential order. The dashed lines indicate cut-offs at 1σ (blue) and 2σ (red).

A comparison of the different types of H-trisaccharides based on the peak positions in the spectra recorded with the highest ligand concentration is not reasonable, as they show significantly differing affinities (see section 4.2.4).The largest CSPs can be observed for H-tris type II, while in the case of H-tris type III and IV, the peaks are found at almost the same position as in the spectrum of apo-GTB. Trivially, these findings correlate well with the determined affinities. A detailed analysis of differences between the trisaccharides based on CSPs is reported in section 4.2.5, where the presence of UDP shifts the binding process into the preferable slow exchange regime.

4.2.4 2D NMR line shape analysis of acceptor substrate titration data

Titration data are acquired with all ligands described in the previous section. The processed 2D [^{13}C,^{1}H] HMQC spectra (compare section 4.2.1) of each titration point are imported into *MATLAB* for analysis with *TITAN*. All data are fitted to a two-state ligand binding model, respectively. Several peaks are selected for global fitting, in order to describe the common interaction event more accurately. Chemical shifts, linewidths and the binding model parameters (K_d and k_{off}), as well as uncertainties of parameters are determined analogously to section 4.2.2.

The fits of the H-dis titration data are visualized in figure 4.25. Eight residues are selected for the fit and the resonances are tracked in seven titration steps. The fits of the other titrations are provided in the appendix. In the H-dis titration all resonances are found in the fast exchange time regime. The three-dimensional visualizations of the global fits are shown exemplarily for the resonances of Met^{214} and Leu^{339}. Binding parameters and uncertainties are listed in table 4.7.

Table 4.7: Fitted two-state ligand binding model parameters for the interaction of GTB with different acceptor analogs. The dissociation constants and off-rates are derived from the fits using *TITAN*. The on-rates are calculated on basis of these parameters ($K_d = k_{off}/k_{on}$). The uncertainties are determined by bootstrapping using residual resampling with 200 replicas. Values in brackets are considered as unreliable, as the maximum concentration is on the order of the determined K_d value.

	K_d (µM)	k_{on} ($M^{-1}s^{-1}$)	k_{off} (s^{-1})
H-dis	164 ± 4	1.9 x 10^7	3100 ± 300
3DD	420 ± 8	7.9 x 10^6	3300 ± 200
B-tris	264 ± 4	1.1 x 10^7	2900 ± 100
H-tris type I	(3200 ± 100)	(5.0 x 10^5)	(1600 ± 200)
H-tris type II	291 ± 6	7.2 x 10^5	210 ± 7
H-tris type III	(2900 ± 200)	(2.3 x 10^5)	(700 ± 100)
H-tris type IV	-	-	-
H-tris type V	1270 ± 20	2.0 x 10^6	2600 ± 200
H-tris type VI	318 ± 5	1.1 x 10^6	340 ± 10

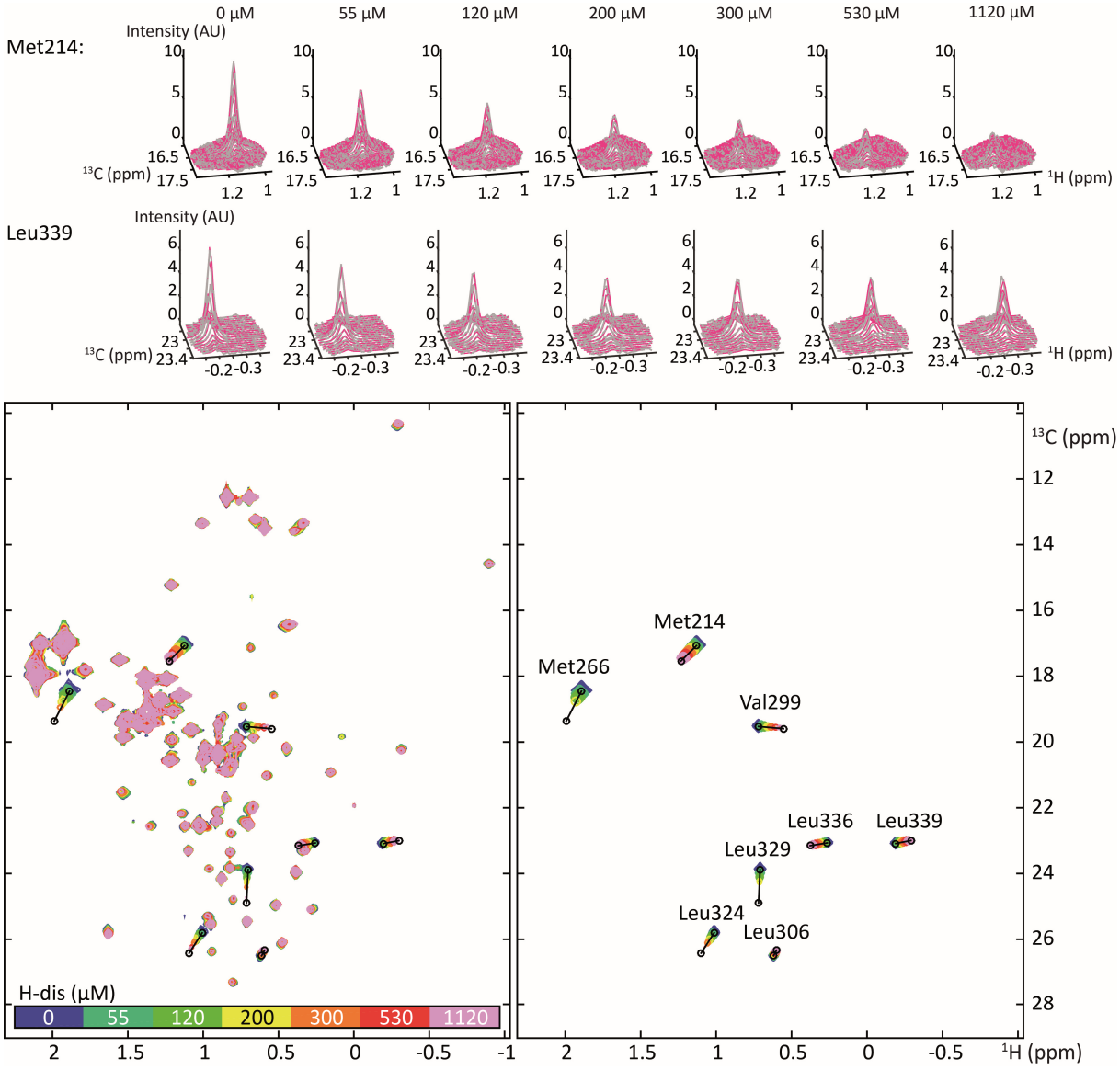


Figure 4.25: Line shape analysis of HMQC-based H-dis titration data. The bottom panels show the observed (left) and fitted (right) 2D [^{13}C,^{1}H]-HMQC spectra of 280 µM AIL^{proS}MV^{proS} GTB upon titration with H-dis. 8 resonances are selected for a global fit. The overlays of fitted (red) and observed (grey) spectra provided on the top visualize the exchange process for 2 of the 8 resonances in a 3D plot.

The binding parameters of H-dis, 3DD and B-tris are fairly similar with an on-rate of ca. $1{\cdot}10^{7}$ $M^{-1}s^{-1}$ and an off-rate of ca. 3000 s^{-1}. Although still one order of magnitude smaller than any diffusion-controlled association, the binding of these ligands is considerably faster than the association of the donor analogs (compare Tab. 4.5). This implies a lower energetic barrier, which can reflect different characteristics of the ligands (nucleotides are charged), or differences in the required structural transitions. It has been shown that in contrast to the donor substrate, H-dis binds in a conformation that predominates also in solution (Angulo et al. 2006). Furthermore, no structural transitions are observed

in the protein upon binding of just the acceptor substrate (Alfaro et al. 2008). It is also worth noting that the α-Gal moiety of the B-trisaccharide has no significant effect on binding, when compared with the parameters of H-dis. These ligands are the product and educt of the transferase reaction, and the findings are in agreement with recent structural data revealing that contacts are in both cases mainly established via β-Gal and α-Fuc (Gagnon et al. 2017).

The presence of an additional sugar at the non-reducing end of the H antigen core motif (H-dis) has no effect on the binding characteristics. However, the identity of the sugar at the reducing end and the linkage type dramatically influence association, as well as dissociation of the H-tris types. Compared with the H-dis, the association of all H-tris types is about one order of magnitude slower. The association rate is, however, comparable between the different types. Therefore, ligand affinity is mainly dependent on the dissociation rate that differs dramatically between the H-tris types. For H-tris I, III and IV the induced CSPs are very small and the affinity is extremely weak. Thus, a reasonable estimation of the binding parameters by line shape analysis is not possible. The highest affinities are observed for H-tris II and VI, being the only trisaccharides with a (1→4)-linkage to the reducing end sugar. The linkage type has a more pronounced effect than the identity of the sugar. However, the N-acetyl group of the reducing end sugar of H-tris I (β-GlcNAc), III (α-GalNAc) and IV (β-GalNAc) seems to have a negative effect on the binding affinity when compared with H-tris V (β-Gal). In crystal structures, the N-acetyl groups of β-GlcNAc of H-tris I ((1→3)-linkage) and II ((1→4)-linkage) are oriented in different directions (PDB entries 1ZJ2 and 1ZJ3), explaining why the functional group does not influence binding of H-tris II.

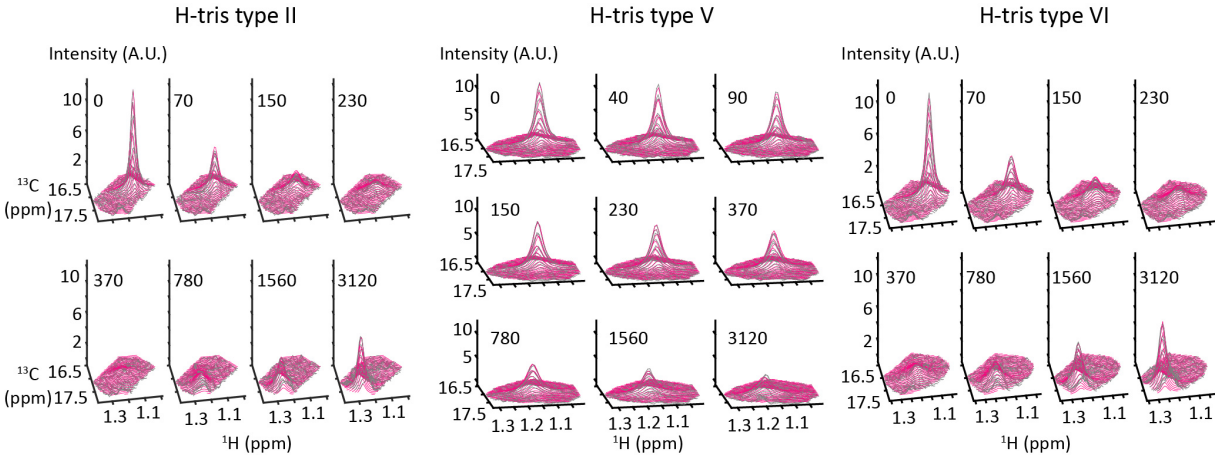


Figure 4.26: Different exchange regimes associated with binding of different H-tris types revealed by line shape analysis of titration data. Shown are overlays of the observed (grey) and fitted (red) spectra of the H-tris II, V and VI titrations for Met^{214}. The binding process is in the intermediate exchange regime for H-tris II and VI and fast for H-tris V. UDP concentrations are indicated in units of μM. Eight or nine titration points are recorded. All calculated spectra are derived from global fitting sessions involving at least seven additional residues, respectively.

Only H-tris II, V and VI are adequate binders for a line shape analysis. The smaller association rate constants compared to H-dis suggest higher energetic barriers for the trisaccharides, potentially as a result of structural reorientations of the reducing end sugar. Three dimensional visualizations of the

resonance of Met^{214} upon titration with the trisaccharides reveal the differing exchange regimes of the binding processes (Fig. 4.26). Although binding of H-tris type V is one order of magnitude weaker than that of H-dis, the line shapes of these titrations bear the closest resemblance (compare Fig. 4.25 and Fig. 4.26).

4.2.5 Combined donor and acceptor binding-induced chemical shift perturbations in GTB

X-ray crystallography has revealed a transition to a closed protein conformation, if donor and acceptor substrates are bound to GTB (Alfaro et al. 2008). The closed conformation is believed to be catalytically active. Therefore, it is of particular importance to investigate GTB in presence of both substrates to retrieve insights into the enzyme's mechanism for donor and acceptor discrimination, product release, etc. Interactions between GTB and several pairs of donor and acceptor analogs are analyzed on basis of ligand-induced CSPs and line shape analysis of titration data (see next section). Used are the ligands described above. However, not every combination of donor and acceptor analog is reasonable. UDP is used in combination with H-dis, all H-tris types and B-tris. The combination of UDP and B-tris is of particular interest, as these are the products of the transferase reaction. Binding of the nucleotide sugars is only investigated in combination with 3DD, as the lacking OH prevents the enzymatic reaction from taking place.

The protein and ligand solutions are prepared as described in section 4.2.1 with the same buffer system. Protein concentrations are determined by UV absorbance at 280 nm using a NanoDrop spectrometer. The protein is saturated with one substrate and the respective other one is titrated into this solution, while keeping concentrations of the protein and the first substrate as constant as possible. There are two directions for this process. The donor substrate can be kept constant, and the donor bound protein is titrated with the acceptor substrate or vice versa. Irrespective of the order of the titrations (donor first or acceptor first), the resonances appear at the same positions in the spectra of the ternary binding complex, when the same combination of ligands is used. This clearly illustrates the thermodynamic equivalence of the binding pathways.

At each titration step, 2D [^{13}C,^{1}H]-HMQC experiments are recorded at 298 K and 500 MHz proton frequency with 8 scans using 1024 (^{1}H) and 256 (^{13}C) complex data points. The spectra are processed with 4 Hz (^{1}H) and 8 Hz (^{13}C) exponential line broadening and zero filling to 512 complex points in the indirect dimension using *NMRPipe*. DSS-d_6 serves as internal reference for the chemical shifts. CSPs are calculated as differences of peak positions in the spectra recorded with apo-GTB, and with GTB in presence of the highest ligand concentrations. These CSPs are illustrated in figure 4.27 and figure.4.34. As described before, σ and 2σ serve as cut-off values to select the significantly perturbed resonances, and they are summarized in table 4.8. Regardless of the combination of ligands, all binding processes are observed in the slow exchange regime. Therefore, peak positions are no longer dependent on the degree

of saturation, and a systematic analysis of correlations between CSPs induced by different combinations of substrates is possible.

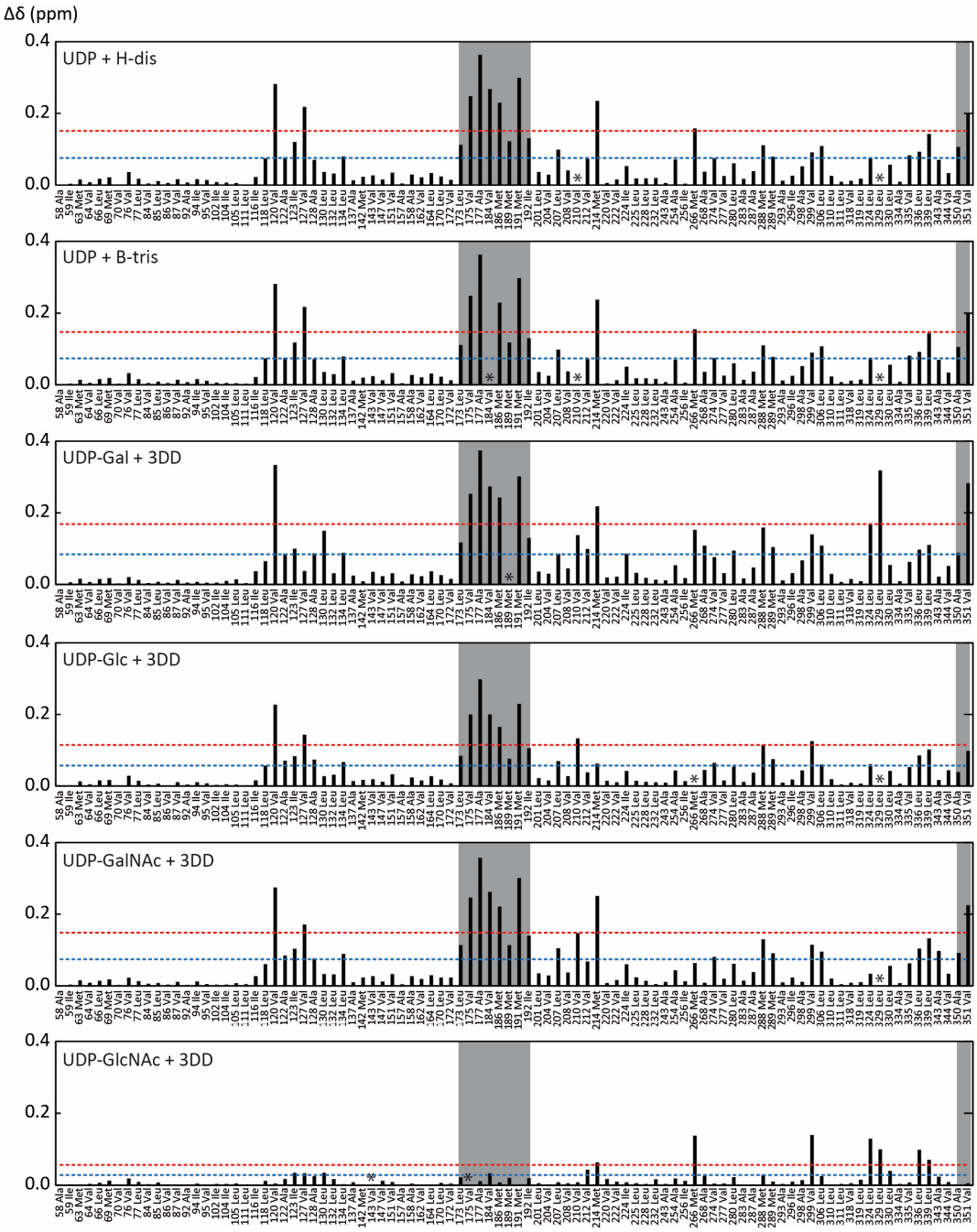


Figure 4.27: Combined residue specific CSPs observed during ligand binding in the donor and acceptor binding site. The six panels show the weighted Euclidean distances between peak positions in 2D [^{13}C,^{1}H]-HMQC spectra recorded with apo-GTB and ligand-saturated GTB, respectively. Spectra are recorded with AIL^{proS}MV^{proS} GTB (260 µM) and high excess of ligands. Ambiguous CSPs are indicated by *.The dashed lines indicate cut-offs at 1σ (blue) and 2σ (red). The internal disordered loop and residues of the C-terminus are highlighted in grey.

Owing to the UDP-Gal hydrolysis activity of GTB, UDP-Gal and 3DD are directly added to reach their maximum concentrations. However, hydrolysis of UDP-Gal forms UDP, competing with UDP-Gal for the donor binding site. In spectra recorded in presence of UDP-Gal/3DD, two sets of resonances are observable for a number of residues, corresponding to either UDP-Gal/3DD or UDP/3DD-bound GTB. These states are in slow chemical exchange and easily distinguishable by overlaying the spectrum with the spectrum of the UDP/H-dis-saturated state. As the hydrolysis reaction is rather slow, repeated recording of HMQC spectra over time allows additionally the tracking of decreasing and increasing signal intensities connected to the hydrolysis of UDP-Gal to UDP.

Table 4.8: Thresholds and numbers of significantly perturbed resonances by combined binding of donor and acceptor analogs. σ and 2σ are given in units of ppm. The number of resonances showing greater changes than the cut-offs are indicated in brackets.

	UDP H-dis	**UDP B-tris**	**UDP-Gal 3DD**	**UDP-Glc 3DD**	**UDP-GalNAc 3DD**	**UDP-GlcNAc 3DD**
σ (ppm)	0.076 (26)	0.074 (26)	0.084 (31)	0.057 (27)	0.076 (27)	0.028 (14)
2σ (ppm)	0.151 (10)	0.147 (9)	0.168 (10)	0.114 (10)	0.152 (9)	0.056 (7)

The observed Euclidean distances are generally larger than for the previously described interactions. With the exception of the combination of UDP-GlcNAc and 3DD, the CSP patterns induced by all other combinations of donor and acceptor substrates and analogs are strikingly similar, indicating a largely homologous binding event. About 40% of all residues have $\Delta\delta > 0.05$ ppm (UDP-Glc/3DD ~30%; UDP-GlcNAc/3DD ~10%), and the sheer number of perturbed residues is evidence for a conformational change. The most pronounced CSPs are observed for resonances corresponding to residues of the β3-strand-turn-α2-helix structure (residues 118-130), and of the internal disordered loop (residues 173-192), residues close to the metal binding site (Met^{214}, Met^{266}) and residues of the C-terminus (Ala^{350}, Val^{351}). The perturbed regions comprise residues that are also influenced in separated titrations with donor and acceptor substrates, as reported above (Fig. 4.18, 4.23, 4.24). However, the observed effects by simultaneous binding of both substrates are more than the simple sum of CSPs of the separated binding events of donor and acceptor analog.

This becomes clearer, by comparing the CSPs induced by UDP binding to apo-GTB or to H-dis-saturated GTB (Fig. 4.28), and more evident by comparing H-dis binding to apo-GTB or UDP-saturated GTB (Fig. 4.29). In this case, the Euclidean distances are calculated relative to the peak positions in the original state, which are the spectra recorded of apo GTB or H-dis-saturated GTB for the UDP titrations, and of apo-GTB and UDP-saturated GTB for the H-dis titrations.

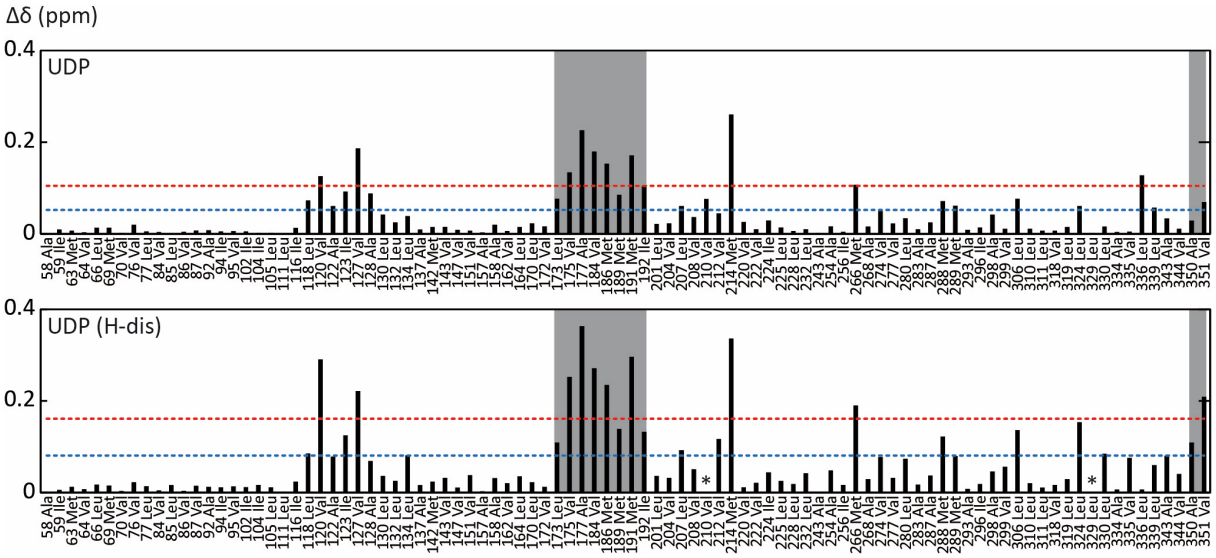


Figure 4.28: Residue specific CSPs observed during UDP binding to apo-GTB (top) or H-dis-saturated GTB (bottom). The top panel shows the weighted Euclidean distances between peak positions in 2D [^{13}C, ^{1}H]-HMQC spectra recorded with apo-GTB and UDP-saturated GTB. The bottom panel shows the weighted Euclidean distances between peak positions in the spectra recorded with H-dis-saturated-GTB and UDP-/H-dis-saturated GTB. Spectra are recorded with AIL^{proS}MV^{proS} GTB and high excess of ligands. Ambiguous CSPs are indicated by *.The dashed lines indicate cut-offs at 1σ (blue) and 2σ (red). The internal disordered loop and residues of the C-terminus are highlighted in grey.

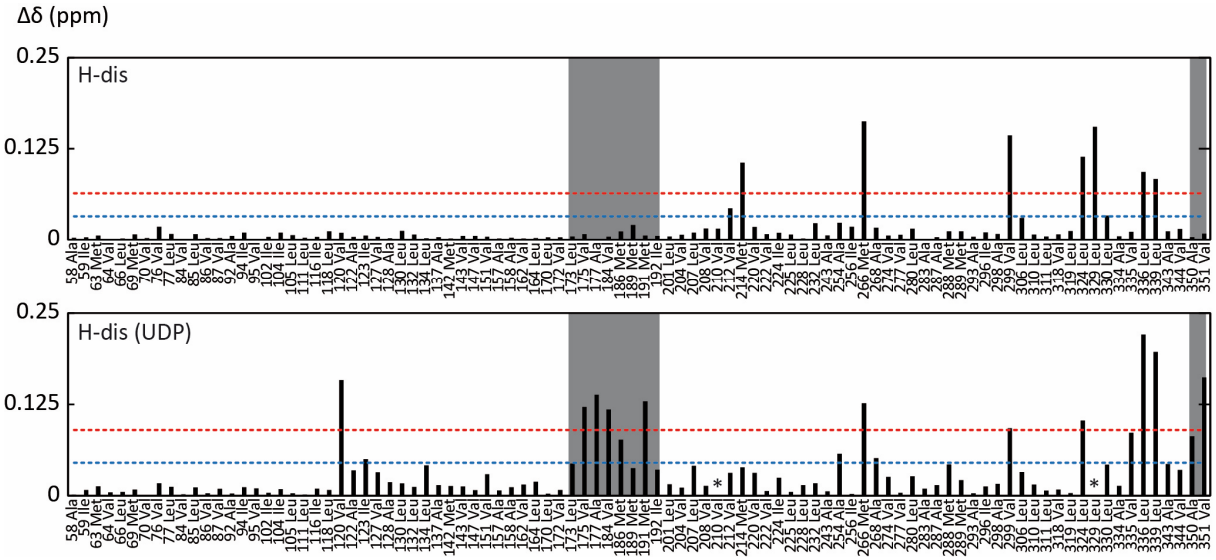


Figure 4.29: Residue specific CSPs observed during H-dis binding to apo-GTB (top) or UDP-saturated GTB (bottom). The top panel shows the weighted Euclidean distances between peak positions in 2D [^{13}C,^{1}H]-HMQC spectra recorded with apo-GTB and H-dis-saturated GTB. The bottom panel shows the weighted Euclidean distances between peak positions in the spectra recorded with UDP-saturated-GTB and UDP-/H-dis-saturated GTB. Spectra are recorded with AIL^{proS}MV^{proS} GTB and high excess of ligands. Ambiguous CSPs, cut-offs, and internal disordered loop and C-terminus are indicated as described in the caption of the previous figure.

UDP binding perturbs the same regions of the enzyme, regardless of binding to apo-GTB or H-dis-saturated GTB. However, CSPs are generally much larger in presence of H-dis. The CSPs observed upon H-dis binding to UDP-saturated GTB, reveal regions that are not influenced in absence of the donor substrate. In particular, peaks corresponding to residues of the disordered internal and C-terminal loop are only perturbed upon H-dis binding in presence of UDP, very likely reflecting the transition from the semi-closed to the closed protein conformation.

Besides the combination of UDP-GlcNAc/3DD, all other ligand saturated states show strikingly similar CSP patterns. Especially remarkable is the high similarity between the UDP/H-dis- and the UDP/B-tris-saturated states as summarized in figure 4.30. The deviations between peak positions in spectra of both states are below 0.01 ppm for all residues, and therefore on the order of the spectral resolution. The perfect correlation of CSPs between both states are indicative of a common interaction motif for educt (H-dis) and product (B-tris). The presence of the additional α-D-Gal moiety does not induce significant CSPs. Furthermore, these data show undoubtedly that GTB binds UDP and B-tris not only at the same time, but also in the same overall protein conformation. This is in contrast to a recently published hypothesis on product release (Gagnon et al. 2017). The authors propose a steric clash between the β-phosphate and the donated product sugar, which induces a disordered active site and weakens product binding. In particular, the steric clash is thought to prohibit simultaneous occupation of the active site by both substrates. However, this assumption is only based on crystal structures of binary complexes between GTB and UDP, or GTB and B-tris.

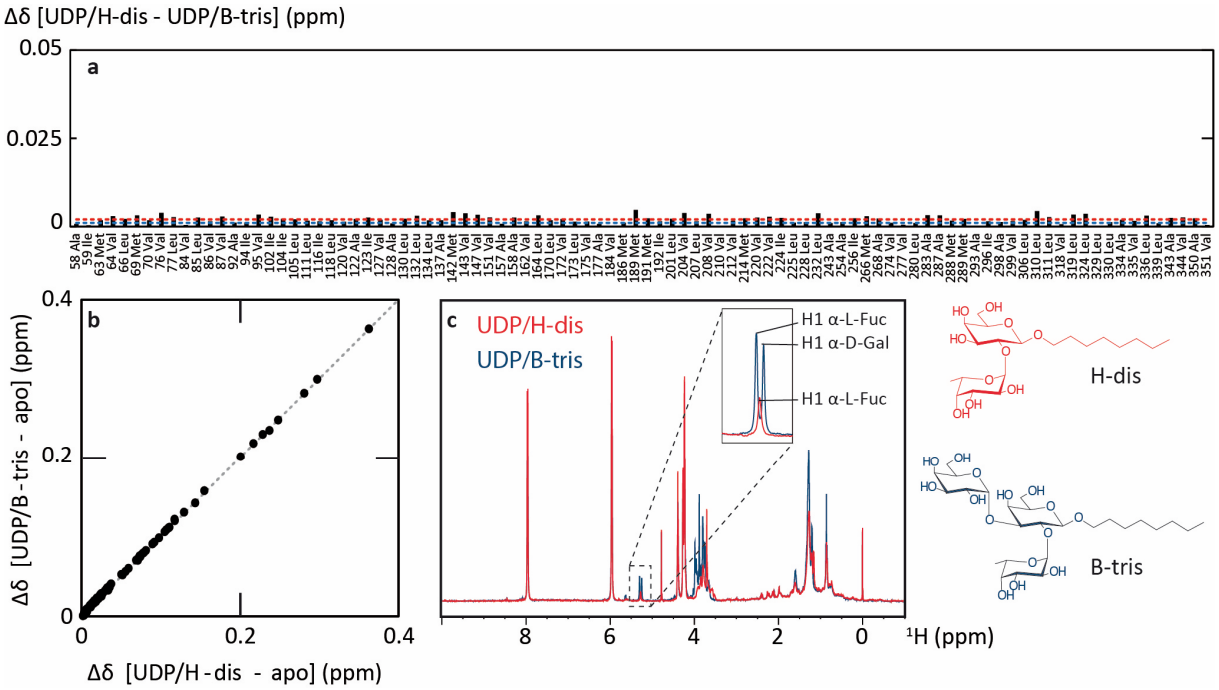


Figure 4.30: UDP/H-dis and UDP/B-tris binding induces similar chemical shift deviations. (**a**) Residue specific deviations between signal positions in 2D [^{13}C,^{1}H]-HMQC spectra recorded with UDP/H-dis- and UDP/B-tris-saturated GTB. Deviations are below 0.01 ppm for all peaks. (**b**) Correlation of chemical shift perturbations in GTB between UDP/H-dis- and UDP/B-tris-saturated states relative to the apo state. Each dot corresponds to a methyl group. All methyl groups show highly similar perturbations in both ligand bound states indicated by a perfect linearity. (**c**) The proton NMR spectrum of AIL^{proS}MV^{proS} GTB in presence of saturating amounts of UDP/H-dis (blue) and UDP/B-tris (red) demonstrates the integrity of the acceptor substrates as revealed by the close-up of the anomeric protons.

The differences between the spectra of UDP-Gal/3DD- and UDP-Glc/3DD-bound GTB are summarized in figure 4.31. There is a correlation of CSPs in GTB between both states. However, CSPs are generally larger in the presence of the native donor substrate (Fig. 4.31 b). Significant deviations are observable for residues corresponding to the internal disordered and C-terminal loop, and residues abutting these structures. Likewise, residues of the nucleotide sugar binding site show changed CSPs. Like the differences observed in absence of the acceptor analog (Fig. 4.20), these data suggest that the different orientation of the OH-group of the nucleotide sugar directly influences the orientation and mobility of the internal loop.

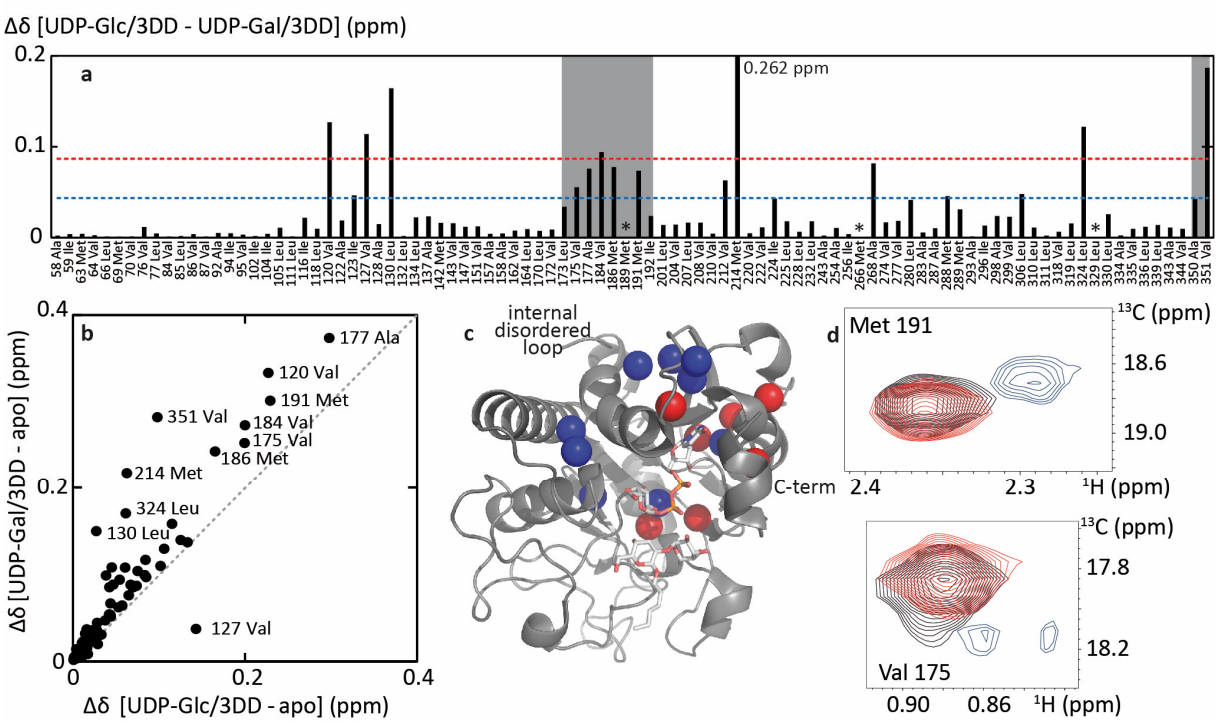


Figure 4.31: Differences between UDP-Gal/3DD and UDP-Glc/3DD binding induced CSPs. (**a**) Residue specific deviations between signal positions in 2D [^{13}C,^{1}H]-HMQC spectra recorded with UDP-Gal/3DD- and UDP-Glc/3DD-saturated AIL^{proS}MV^{proS} GTB. Ambiguous CSPs are indicated by *.The dashed lines indicate cut-offs at 1σ (blue) and 2σ (red). CSPs greater than 0.2 ppm are indicated. The internal disordered loop and residues of the C-terminus are highlighted in grey. (**b**) Correlation of CSPs in GTB between UDP-Gal/3DD- and UDP-Glc/3DD-saturated states relative to the apo state. Each dot corresponds to a methyl group. CSPs are more pronounced for UDP-Gal/3DD as indicated by the deviation from a +1 slope of the linear regression. (**c**) Methyl groups showing significant deviations between both saturated states are highlighted in the crystal structure (PDB entry 2RJ7; 1σ: blue; 2σ: red). UDP-Gal and 3DD are shown as sticks. (**d**) shows overlays of the spectral regions of Val^{175} and Met^{191}. The spectra are acquired in presence of UDP/H-dis (black), UDP-Gal/3DD (red) and UDP-Glc/3DD (blue). Signals are exchange-broadened in presence of UDP-Glc/3DD.

Furthermore, the resonances corresponding to residues of the internal loop are extensively exchange-broadened in the spectrum acquired with UDP-Glc/3DD-saturated GTB as exemplified for Val^{175} and Met^{191} (Fig. 4.31 d). This is not observable for UDP-Gal/3DD- or UDP/H-dis-saturated GTB, and indicates a higher disorder in the UDP-Glc/3DD-saturated state. The peak location between the resonances of apo-GTB (open) and the UDP-Gal/3DD-bound (closed) state suggests that the disorder is due to a conformational exchange between the open and closed conformation.

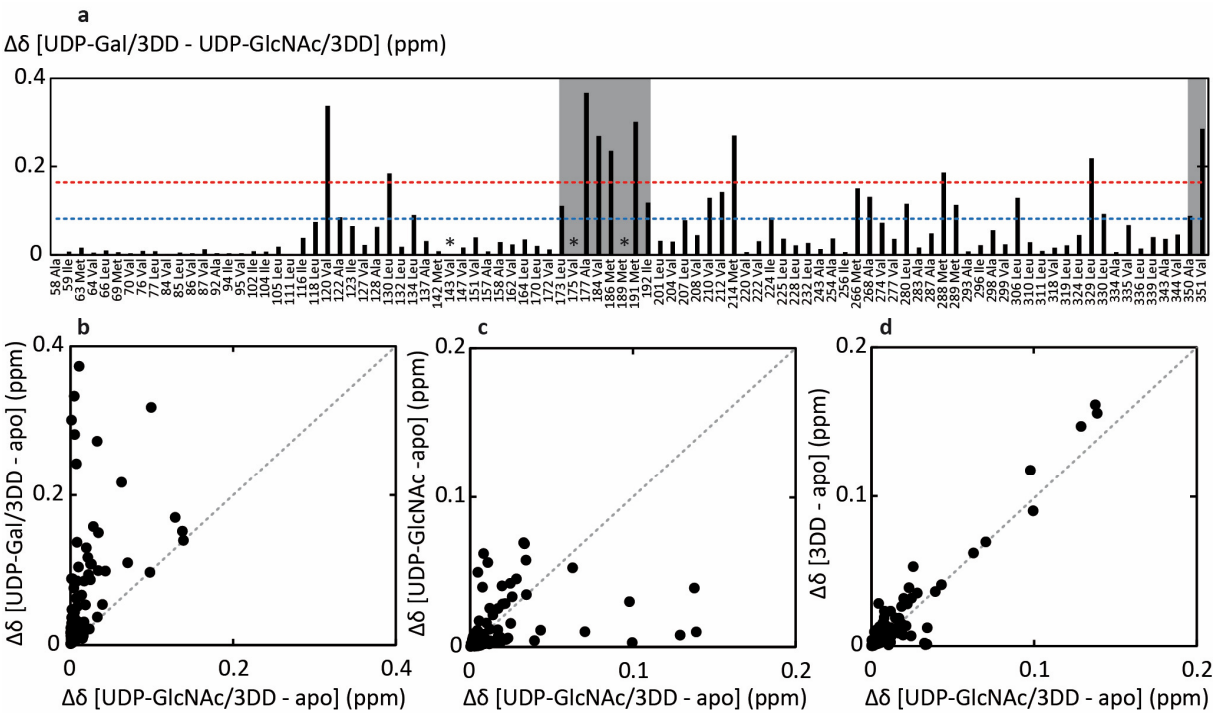


Figure 4.32: Differences between UDP-GlcNAc/3DD and UDP-Gal/3DD binding-induced CSPs. **(a)** Residue specific deviations between signal positions in 2D [^{13}C,^{1}H]-HMQC spectra recorded with UDP-Gal/3DD- and UDP-GlcNAc/3DD-saturated AIL^{proS}MV^{proS} GTB. Ambiguous CSPs are indicated by *.The dashed lines indicate cut-offs at 1σ (blue) and 2σ (red). The internal disordered loop and residues of the C-terminus are highlighted in grey. (**b-d**) Correlation of CSPs in GTB between UDP-Gal/3DD- and UDP-GlcNAc/3DD-saturated states (**b**), UDP-GlcNAc- and UDP-GlcNAc/3DD-saturated states (**c**) and 3DD- and UDP-GlcNAc/3DD-saturated states relative to the apo state. Each dot corresponds to a methyl group. The dramatic deviations from the linear regression with a +1 slope indicate differing binding effects in (**b**) and (**c**). In contrast, (**d**) reports on high similarities between the 3DD and UDP-GlcNAc/3DD-saturated states, suggesting that UDP-GlcNAc does not bind to GTB in presence of the acceptor substrate.

The most apparent deviation from the common binding mode shared by all other combinations of ligands is observed for UDP-GlcNAc/3DD. As shown in figure 4.27, significant CSPs are particularly lacking in regions associated with nucleotide binding. CSPs are rather small and only seven residues have $\Delta\delta > 0.05$ ppm. A more systematic analysis of the UDP-GlcNAc/3DD binding process is summarized in figure 4.32 in comparison with the native donor substrate UDP-Gal and 3DD. The large deviations between peak positons in spectra of UDP-GlcNAc/3DD- and UDP-Gal/3DD-saturated GTB are on the order of the CSPs observed for UDP-Gal/3DD-saturated GTB relative to apo-GTB (Fig. 4.32 a). The UDP-GlcNAc/3DD binding-induced CSPs do not correlate well with UDP-Gal/3DD or UDP-GlcNAc binding-induced CSPs (Fig. 4.32 b, c). However, there is a correlation between the UDP-GlcNAc/3DD- and the 3DD-bound state (Fig. 4.32 d). These findings report on the inability of the enzyme to bind UDP-GlcNAc and 3DD at the same time. In presence of both ligands, binding of 3DD

(higher affinity) precludes binding of UDP-GlcNAc. Moreover, conformational changes observable for the other combinations of ligands are excluded, too.

GTB discriminates also between UDP-Gal and UDP-GalNAc, which is the natural substrate of GTA. Line shape analysis reveals similar affinities for UDP-GalNAc and UDP-GlcNAc (section 4.2.2). However, the mode of binding of these ligands in presence of 3DD is strikingly different for both substrates as revealed by CSPs (Fig. 4.27). Figure 4.33 compares the UDP-GalNAc/3DD-bound state with the UDP-Gal/3DD-bound state. As mentioned above, UDP-Gal is hydrolyzed by GTB on a time scale of hours, allowing the observation of the UDP-Gal/3DD-bound state (Fig. 4.33 d). The superposition of the spectrum acquired with UDP-GalNAc/3DD-saturated GTB and the spectrum acquired with UDP-Gal/3DD-saturated GTB after ca. 10 h of incubation at 25°C (Fig. 4.33 e), where UDP-Gal is largely hydrolyzed to UDP indicates that UDP-GalNAc is hydrolyzed, too. The signal positions match perfectly the UDP/3DD-saturated state. As a result of product inhibition 1D proton spectra suggest that UDP-GalNAc is largely intact (data not shown). However, the large difference in the affinities between UDP and UDP-GalNAc does not allow the observation of the UDP-GalNAc/3DD-saturated state of GTB. Therefore, figure 4.33 describes differences between the UDP-Gal/3DD- and the UDP/3DD-saturated states.

Different to the combinations UDP-Glc/3DD (Fig. 4.31) and UDP-GlcNAc/3DD (Fig.4.32), there is a clear correlation of CSPs between the UDP/3DD- and the UDP-Gal/3DD-bound states that is reflected by a slope of a linear regression of +1 (Fig. 4.33 b). This indicates a common binding mode for UDP-Gal and UDP in the ternary binding complex. In particular, there are no significant deviations between CSPs of residues of the internal disordered loop, suggesting a similar orientation of this domain in both states. As expected, the resonances of the critical residues Met^{266} and Ala^{268} located adjacent to the sugar position show up at significantly different positions in the spectra of both states. The neighboring residues Met^{214}, Leu^{324}, and Ala^{343} show substantial deviations from the linear correlation of CSPs between both states. Interestingly, also residues of the β3-strand-turn-α2-helix structure (residues 120, 123, 127 and130) show different CSPs in both states. This region of the enzyme is known to interact with the nucleotide, but is located more than 12 Å away from the sugar moiety. This suggests a subtle alteration of the nucleotide base orientation.

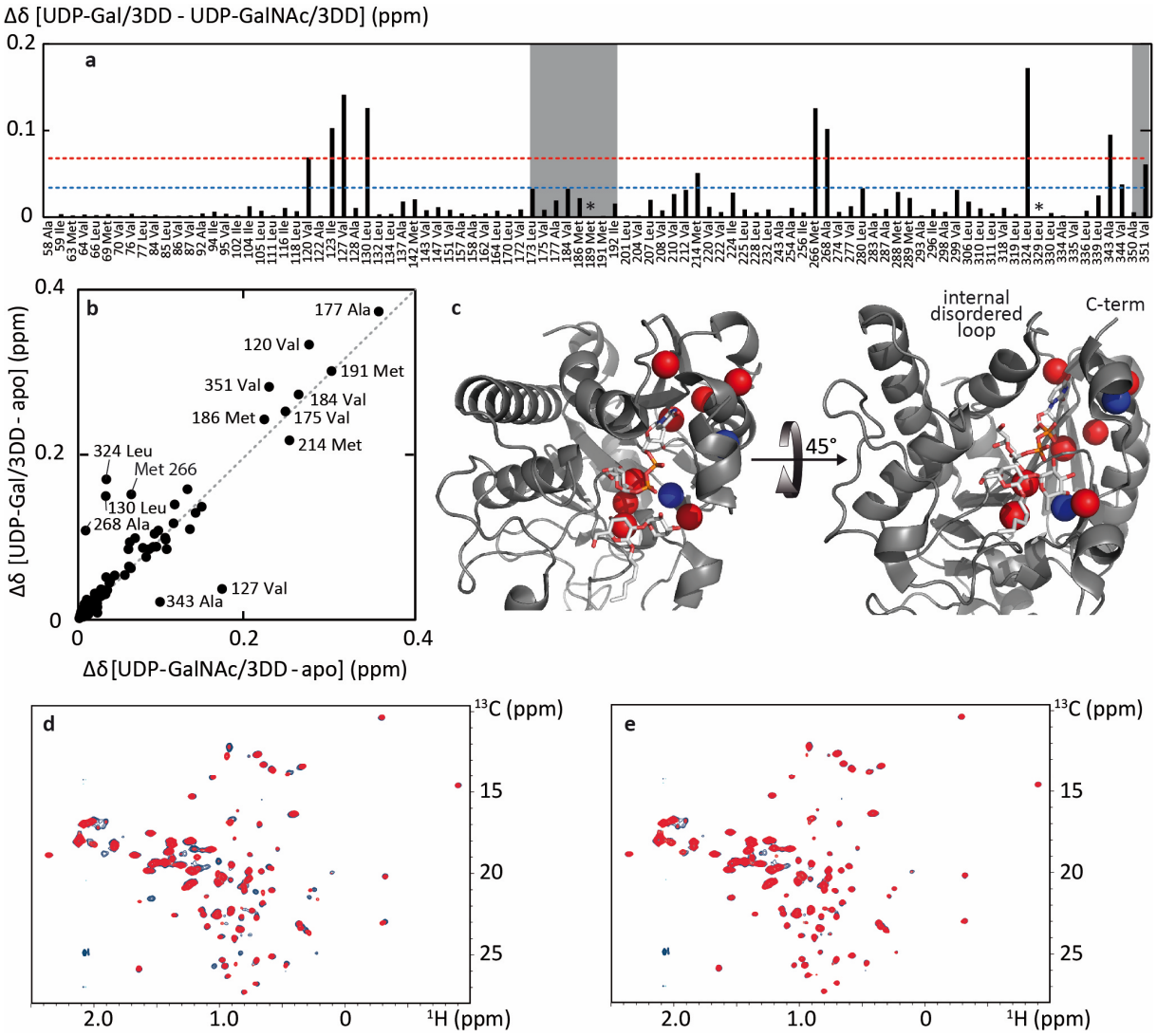


Figure 4.33: Differences between UDP-Gal/3DD and UDP-GalNAc/3DD binding induced CSPs. (**a**) Residue specific deviations between signal positions in 2D [^{13}C,^{1}H]-HMQC spectra recorded with UDP-Gal/3DD- and UDP-GalNAc/3DD-saturated AIL^{proS}MV^{proS} GTB. Ambiguous CSPs are indicated by *.The dashed lines indicate cut-offs at 1σ (blue) and 2σ (red). The internal disordered loop and residues of the C-terminus are highlighted in grey. (**b**) Correlation of CSPs in GTB between UDP-Gal/3DD- and UDP-GalNAc/3DD-saturated states relative to the apo state. Each dot corresponds to a methyl group. The rough compliance with a linear regression with a +1 slope indicates similar binding effects in both states. (**c**) Methyl groups showing significant deviations between both saturated states are highlighted in the crystal structure (PDB entry 2RJ7; 1σ: blue; 2σ: red). UDP-Gal and 3DD are shown as sticks. (**d**) Superposition of 2D [^{13}C, ^{1}H]-HMQC spectra recorded with UDP-Gal/3DD- (red) and UDP-GalNAc/3DD-saturated (blue) AIL^{proS}MV^{proS} GTB. (**e**) shows the same as in (**d**) but the spectrum of the UDP-Gal/3DD-saturated GTB is recorded after ~10 h of incubation at 25°C, highlighting the hydrolysis of UDP-Gal.

Line shape analysis reveals significant differences between the affinities of GTB for the different H-tris types (section 4.2.4). To mimic the Michaelis complex, UDP is titrated into GTB solutions with excess concentrations of the respective H-tris. In all cases, binding of UDP is slow on the NMR time scale. CSPs as differences between peak positions in spectra of the apo-state and of the UDP/H-tris-saturated states are summarized in figure 4.34. Unlike reported in figure 4.24, the CSP patterns are very similar for all UDP/H-tris combinations. Furthermore, UDP/H-dis (and UDP/B-tris) binding induces also very similar CSPs in GTB. The high similarity between all states is visualized in figure 4.35 as correlation plots between the CSPs of the UDP/H-tris type II-saturated and all other UDP/H-tris or UDP/H-dis saturated states. A perfect correlation is observable between all states. Only three resonances are observed to deviate significantly from the linear correlation of CSPs (Leu^{329}, Leu^{330} and Leu^{339}). Different CSPs are expected for Leu^{329} and Leu^{330}, as these residues are located close to the discriminating reducing end sugar of the trisaccharide (see crystal structures in Fig. 4.35). Different binding effects, induced by different reducing end sugars, are transmitted to Leu^{339}, which is located further away from the acceptor binding site. Despite these small differences, the CSP data indicate that GTB adopts the same overall conformation in presence of UDP and each acceptor analog, reflecting that each H-tris type is a substrate of the transferase reaction.

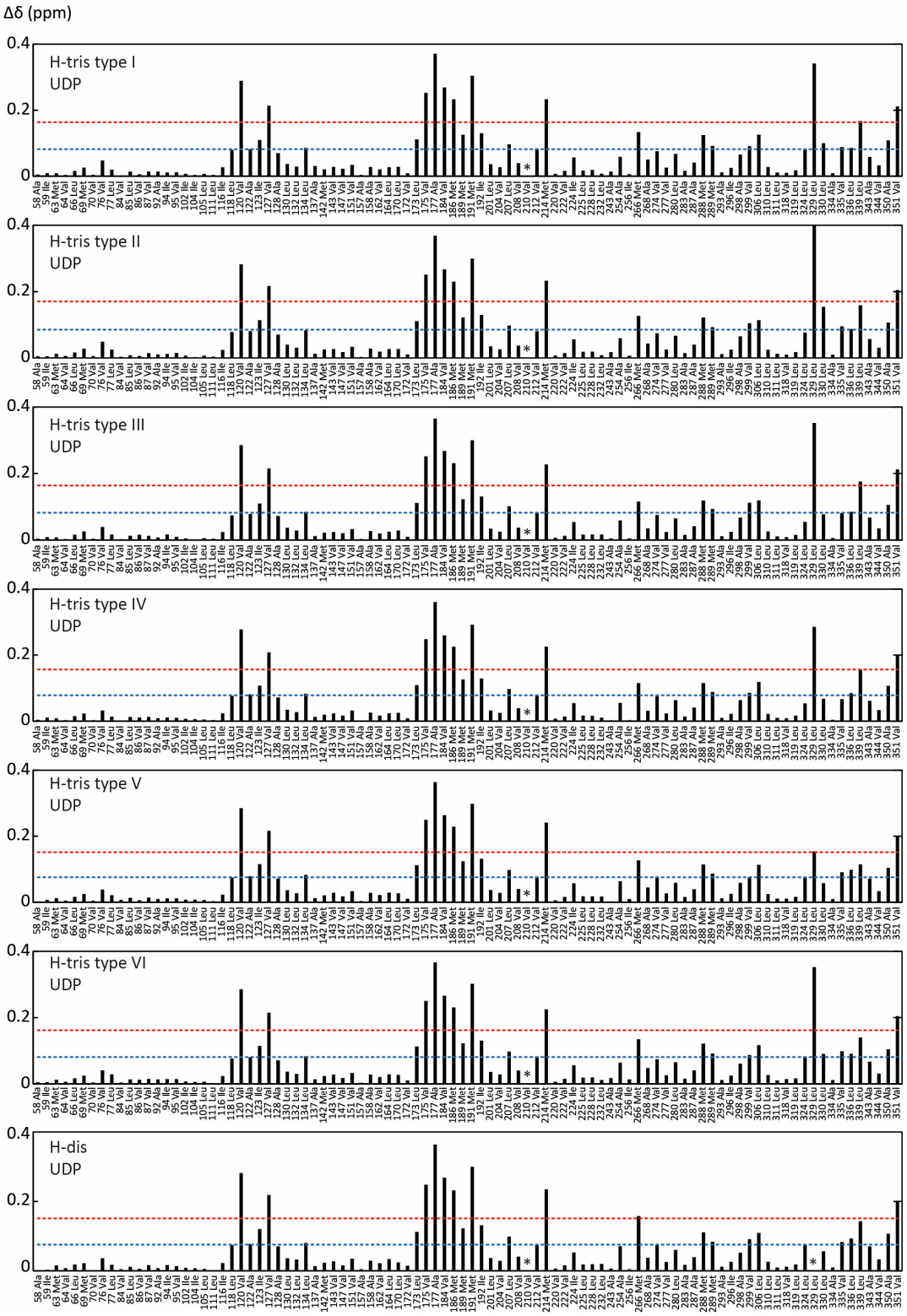


Figure 4.34: Residue specific CSPs observed during binding of different H-trisaccharide antigens and UDP. Shown are the weighted Euclidean distances between peak positions in 2D [^{13}C, ^{1}H]-HMQC spectra recorded with apo-GTB, and GTB in presence of UDP and H-trisaccharide antigens, respectively. Spectra are recorded with AIL^{proS}MV^{proS} GTB (180 µM) and excess of UDP (6800 µM) and H-trisaccharide antigens (3120 µM). Residues are listed in sequential order. The dashed lines indicate cut-offs at 1σ (blue) and 2σ (red)

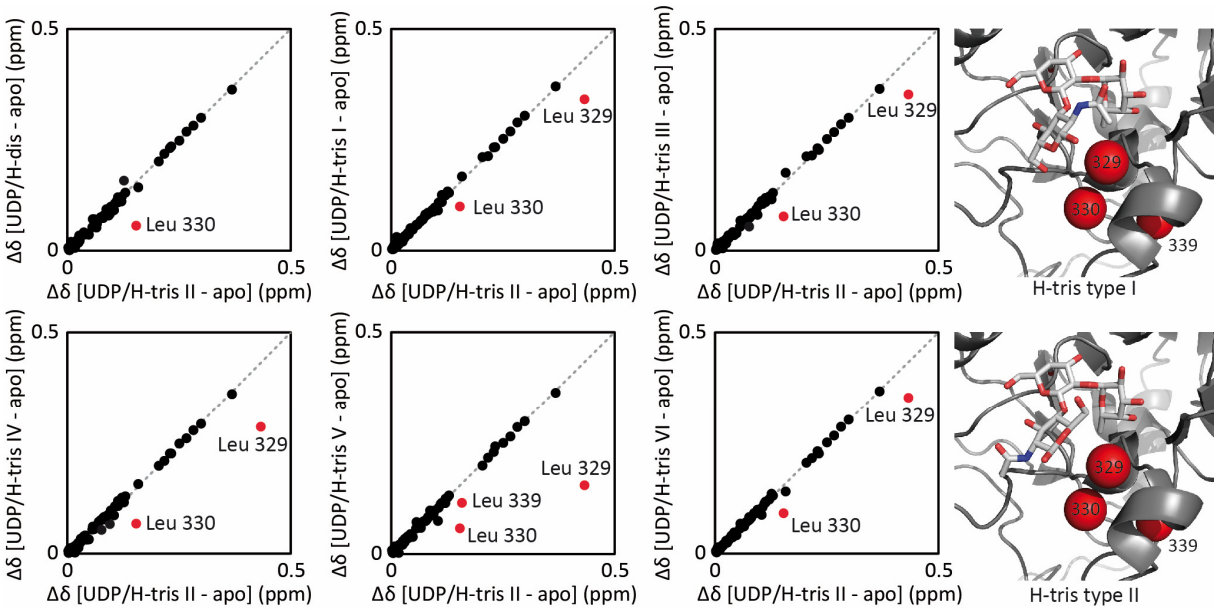


Figure 4.35: Correlation of CSPs in GTB between UDP- and H-trisaccharide type II-saturated and UDP- and other H-trisaccharide- and H-disaccharide-saturated states.CSPs are determined relative to the apo state, respectively. Each dot corresponds to a methyl group. All methyl groups show highly similar perturbations in both ligand bound states indicated by a perfect linearity with a +1 slope. Signals showing deviations from linearity are marked in red, if differences in CSPs are greater than 0.04 ppm. The crystal structures on the right (PDB entry 1ZJ2, 1ZJ3) show the different orientations of the reducing end GlcNAc of type I and II H-trisaccharides in contact with Leu^{329} and Leu^{330}.

As described in section 4.1.3, it is necessary to add H-dis as well as UDP in order to adequately complex lanthanide ions in the metal binding site. The choice of the metal ion cofactor has a significant influence on the observed CSPs upon UDP and H-dis binding, as highlighted in figure 4.36. UDP binding in presence of La^{3+} and H-dis is accompanied with large CSPs. The largest effect ($\Delta\delta > 0.5$ ppm) could be observed for Met^{214}. The extent is rather unusual, but can be explained by its localization close to the metal binding site. Further significant changes can be observed for the β-strand-turn-α-helix structure (residues 118-130) and internal disordered loop (residues 173-192) in direct contact to UDP. However, CSPs of resonances corresponding to residues of the internal loop are significantly larger, when employing Mg^{2+} as cofactor. Furthermore, chemical shifts of Ala^{350} and Val^{351} are not significantly perturbed in presence of La^{3+}, which indicates that the C-terminus remains disordered in the presence of lanthanide ions. This is in agreement with the observed PCSs of these residues (compare section 4.1.3). Besides the additional charge and different preferred coordination numbers (Mg^{2+}: 6 vs. Ln^{3+}: 9), an obvious difference between Mg^{2+} (0.65 Å) and Ln^{3+} (0.98-1.20 Å) is the ion radius (Su and Otting 2010). It should be noted that the spectra are acquired with slightly different buffer conditions, due to the incompatibility of lanthanide ions and phosphate salts. Also the used ligand concentrations vary between the samples because of this incompatibility. However, regardless of the employed cofactor,

binding of UDP to GTB in presence of H-dis occurs in the limit of slow chemical exchange. Therefore, peak positions are not dependent on the degree of saturation.

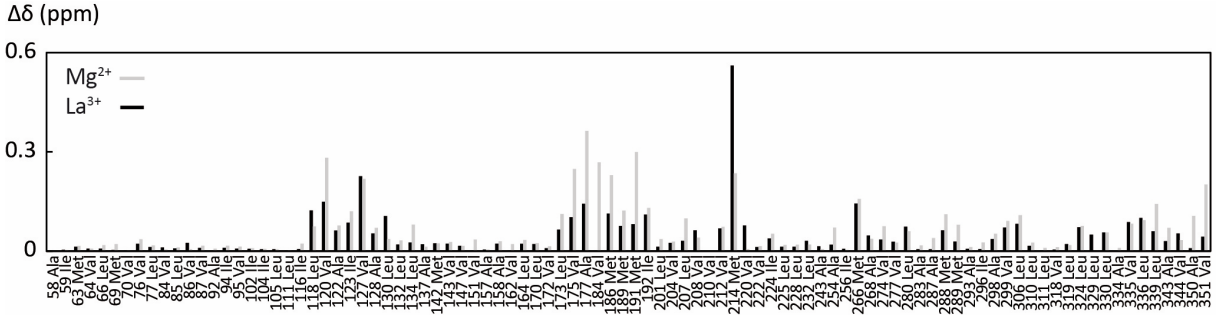


Figure 4.36: Comparison of CSPs induced by UDP and H-dis binding, employing Mg^{2+} (grey bars) or La^{3+} (black bars) as cofactor.Shown are two sets of weighted Euclidean distances between peak positions in 2D [^{13}C, ^{1}H]-HMQC spectra recorded with AIL^{proS}MV^{proS} apo-GTB, and AIL^{proS}MV^{proS} GTB in presence of UDP and H-dis, and either Mg^{2+} or La^{3+}.

4.2.6 2D NMR line shape analysis of titration data leading from the binary to the ternary binding complex

To mimic formation of the Michaelis complex (ternary binding complex), titration data are acquired with several donor and acceptor analogs in presence of saturating amounts of the respective other substrate. For the donor site, binding of UDP and UDP-Glc is analyzed. H-dis, 3DD, B-tris and all H-tris are investigated for the acceptor site. The processed 2D [^{13}C,^{1}H] HMQC spectra (compare section 4.2.1) of each titration point are imported into *MATLAB* for analysis with *TITAN*. All data are fitted to a two-state ligand binding model, respectively. Several peaks are selected for global fitting, in order to describe the common interaction event more accurately. Chemical shifts, linewidths and the binding model parameters (K_d and k_{off}), as well as parameter uncertainties are determined analogous to section 4.2.2.

An example of a donor titration fit is visualized in figure 4.37 for UDP binding to H-dis-saturated GTB. The respective fit of an H-dis titration into an UDP-saturated GTB solution is summarized in figure 4.38. In each case, several residues are selected for the fit and the resonances are tracked in eight titration steps. The fits of the other titrations are provided in the appendix. Binding parameters and uncertainties are listed in table 4.9. All binding processes comply reasonably well with the two-state model.

Strikingly, the presence of the first ligand appears to enhance the affinity of the second ligand (compare Tab. 4.5, 4.7 and 4.9). This positive cooperativity is observed in all cases with the exception of UDP binding to B-tris saturated GTB. It is worth noting that these ligands are the products of the transferase reaction and a negative cooperativity is reasonable, in order to provide an accessible active site for a further catalytic cycle.

Table 4.9: Fitted two-state ligand binding model parameters for transitions from the binary to the ternary binding complex. The dissociation constant and off-rate are derived from the fits using *TITAN*. The on-rate is calculated on basis of these parameters ($K_d = k_{off}/k_{on}$). The uncertainties are determined by bootstrapping using residual resampling with 200 replicas. Indicated in brackets is the respective ligand that is provided in a fixed excess concentration throughout the titration.

	K_d (μM)	k_{on} ($M^{-1}s^{-1}$)	k_{off} (s^{-1})
Donor			
UDP (H-dis)	103 ± 2	2.5 x 10^4	2.6 ± 0.3
UDP (B-tris)	660 ± 10	2.8 x 10^4	18 ± 1
UDP (H-tris I)	38 ± 1	5.8 x 10^4	2.2 ± 0.2
UDP (H-tris II)	6 ± 1	2.8 x 10^5	1.7 ± 0.3
UDP (H-tris III)	29 ± 1	1.2 x10^5	3.6 ± 0.5
UDP (H-tris IV)	65 ± 2	1.9 x 10^5	12 ± 1
UDP (H-tris V)	31 ± 1	1.2 x 10^5	3.4 ± 0.3
UDP (H-tris VI)	32 ± 1	6.9 x 10^4	2.2 ± 0.2
UDP-Glc (3DD)	580 ± 10	8.6 x 10^4	50 ± 2
Acceptor			
H-dis (UDP)	28 ± 1	2.5 x 10^5	6.9 ± 0.4
H-tris I (UDP)	44 ± 2	<2.3 x 10^4	<1
H-tris II (UDP)	10 ± 1	1.7 x 10^5	1.7 ± 0.5
3DD (UDP-Glc)	120 ± 10	3.3 x 10^6	390 ± 20

For UDP in combination with H-dis and all H-tris, the line shape analysis reveals dissociation rates in the range of ms to s, reflected by slow exchange binding phenomena. The off-rate of UDP is two orders of magnitude lower than observed in the binary binding complex. Although the affinities are enhanced in the ternary binding complex with respect to the binary binding complex, they are still observed in the μM range. The conflict between slow dissociation rates and just intermediate affinities can only be explained by a complex binding mechanism responsible for low on-rates. Actually, the observed binding on-rates are dramatically lower than bimolecular diffusion-controlled on-rates. This is in agreement with the hypothesis of the transition from the open to the closed protein conformation associated with binding of UDP to acceptor-saturated GTB, or of acceptor to the UDP-saturated enzyme. It is also thinkable that the low on-rates of UDP binding are due to an ordered binding mechanism, where UDP associates only to acceptor-free active sites. Interestingly, UDP shows identical on-rates to H-dis- or B-tris-saturated GTB, implying that in both cases the same complex binding mechanism applies. One

order of magnitude faster off-rates of UDP in presence of B-tris reflect most likely weakened interactions to the enzyme.

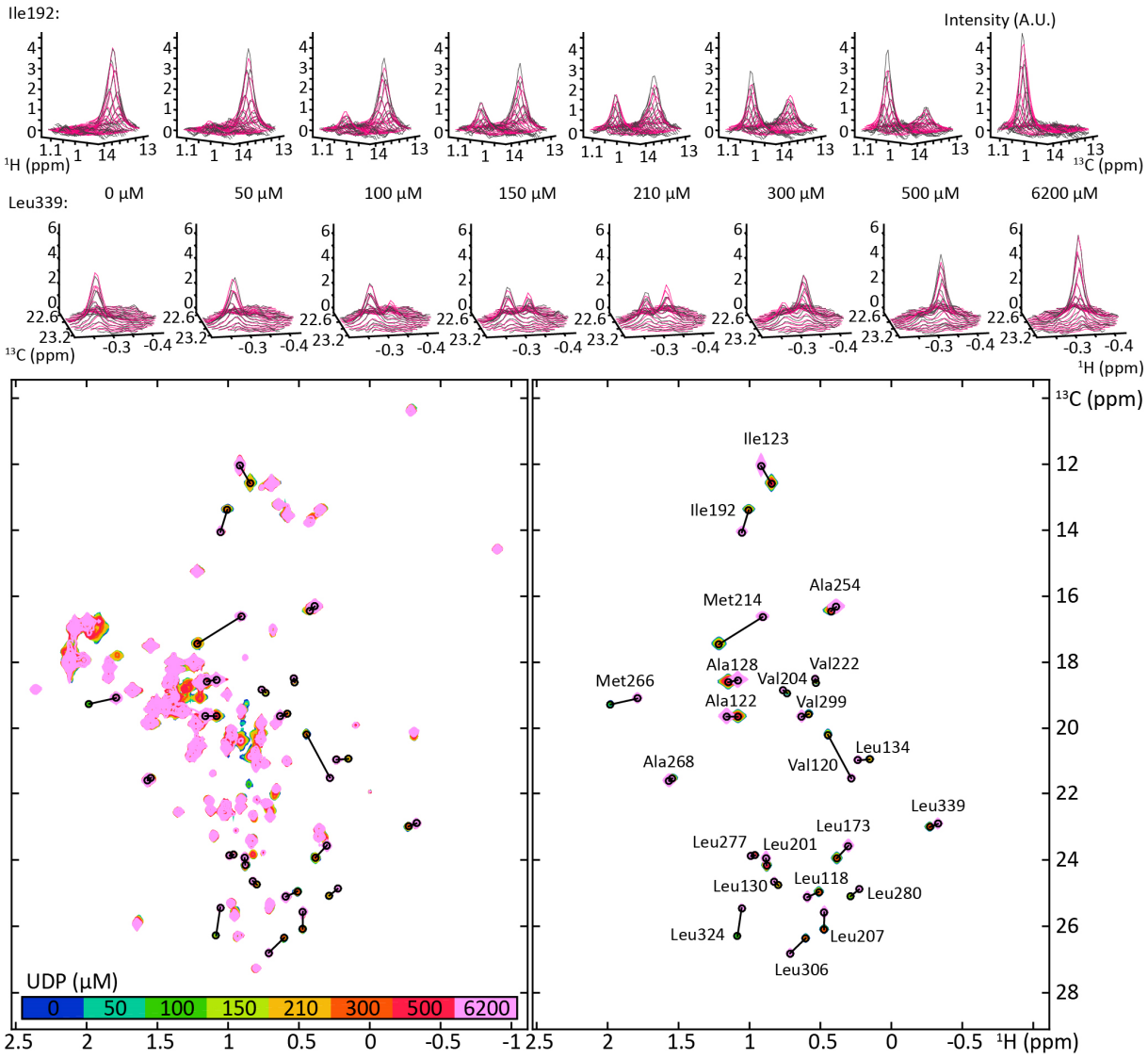


Figure 4.37: Line shape analysis of HMQC-based UDP titration data recorded in presence of excess amounts of H-dis. The bottom panels show the observed (left) and fitted (right) 2D [^{13}C,^{1}H]-HMQC spectra of 280 µM AIL^{proS}MV^{proS} GTB upon titration with UDP. The H-dis concentration is 1120 µM. 23 resonances are selected for a global fit. The overlays of fitted (red) and observed (grey) spectra provided on the top visualize the exchange process for 2 of the 23 resonances in a 3D plot.

UDP binding in presence of the different types of H-trisaccharides is observed with comparable parameters. However, these data should be treated with care, as some of the trisaccharides are weak binders (see Tab. 4.7) and therefore saturating conditions at the start of the titrations are not reached.

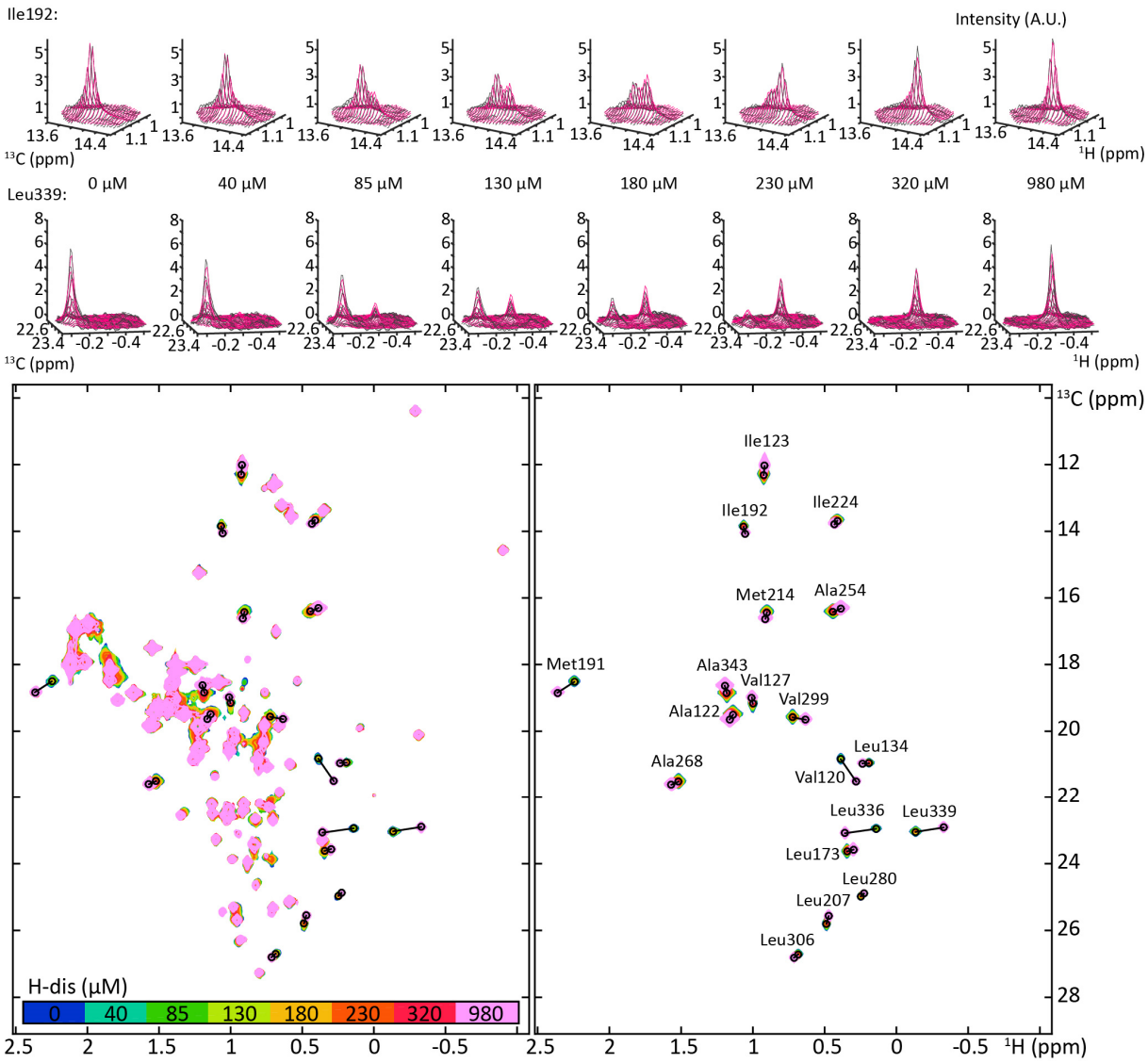


Figure 4.38: Line shape analysis of HMQC-based H-dis titration data recorded in presence of saturating amounts of UDP. The bottom panels show the observed (left) and fitted (right) [^{13}C,^{1}H]-HMQC spectra of 280 µM AIL^{proS}MV^{proS} GTB upon titration with H-dis. The UDP concentration is 6200 µM. 19 resonances are selected for a global fit. The overlays of fitted (red) and observed (grey) spectra provided on the top visualize the exchange process for 2 of the 19 resonances in a 3D plot.

H-dis and H-tris dissociation from the ternary binding complex occurs almost three orders of magnitude slower than from the binary binding complex. Low off-rates in combination with intermediate affinities in the µM range necessitate again low on-rates, potentially reflecting the transition from the semi-closed to the closed protein conformation in a complex binding process. It is worth noting that the significant differences in the binding affinities between H-tris type I and II are largely attenuated in presence of UDP from one order of magnitude to a factor of four.

Binding parameters are also determined for the ternary binding complex comprising GTB, UDP-Glc and 3DD. Interestingly, the affinity of UDP-Glc is only marginally higher in the ternary binding

complex. However, binding rates are shifted with ca. four times slower dissociation from the ternary complex than from the binary complex (compare Tab. 4.5 and 4.9). Binding of 3DD occurs with higher affinity in presence of UDP-Glc. The off-rate from the ternary complex is one order of magnitude faster than from the binary complex (compare Tab. 4.7 and 4.9). Remarkable is the one order of magnitude higher on-rate with respect to the association of H-dis to UDP-bound GTB, implying a lower energetic barrier.

4.2.7 Investigating slow chemical exchange with the ZZ-exchange experiment

In the last section, several binding processes are observed in the limit of slow chemical exchange. As slow chemical exchange implies only weak line broadening, the investigated binding events are at the limits of the accessibility of the line shape analysis. The ZZ-exchange experiment allows quantification of slow exchange rates between two (or more) exchanging species on time scales ranging from ~0.5 to ~50 s^{-1} (Kloiber et al. 2011). Interconversion between the states occurs during a variable mixing time, where magnetization is stored in z direction. To avoid errors resulting from differential line broadening effects, two sets of spectra are recorded, where the order of chemical shift evolution and mixing time is interchanged. T1 relaxation and exchange rates can be extracted from the two direct correlation signals in the frequency-labeled and non-frequency-labeled experiment. UDP titrations at H-dis saturating conditions reveal slow chemical exchange with two observable signals. The ZZ-exchange experiment is applied at half-saturating concentrations of UDP, where both states are equally populated. The sample contains 465 µM ILMV methyl-labeled GTB, 1.5 mM H-dis and 250 µM UDP. A series of two times seven 2D spectra are recorded at 300 K and 700 MHz proton frequency with mixing times ranging between 10 to 600 ms. For normalization, a set of reference spectra is acquired, where the mixing time is set to 0. Data are acquired with 48 scans, using 1024 (^{1}H) and 256 (^{13}C) complex data points. The spectra are processed with a cosine window function and zero filled to 2048 x 512 real points. DSS-d_6 serves as internal reference for the chemical shifts.

Four residues are selected for the analysis, as the frequencies of both states differ in both dimensions. The peak intensities of the direct correlation signals in both sets of spectra (with/without frequency labeling) are extracted using CcpNmr analysis (Vranken et al. 2005), and normalized with the peak intensities observed in the spectra with 0 mixing time, respectively. The normalized intensities are transferred to Origin (OriginLab, Northampton, MA) and globally fitted to equations 3.4 and 3.5, describing a two-site exchanging system (Kloiber et al. 2011). The fits are shown in figure 4.39 and the extracted exchange rates are summarized in table 4.10.

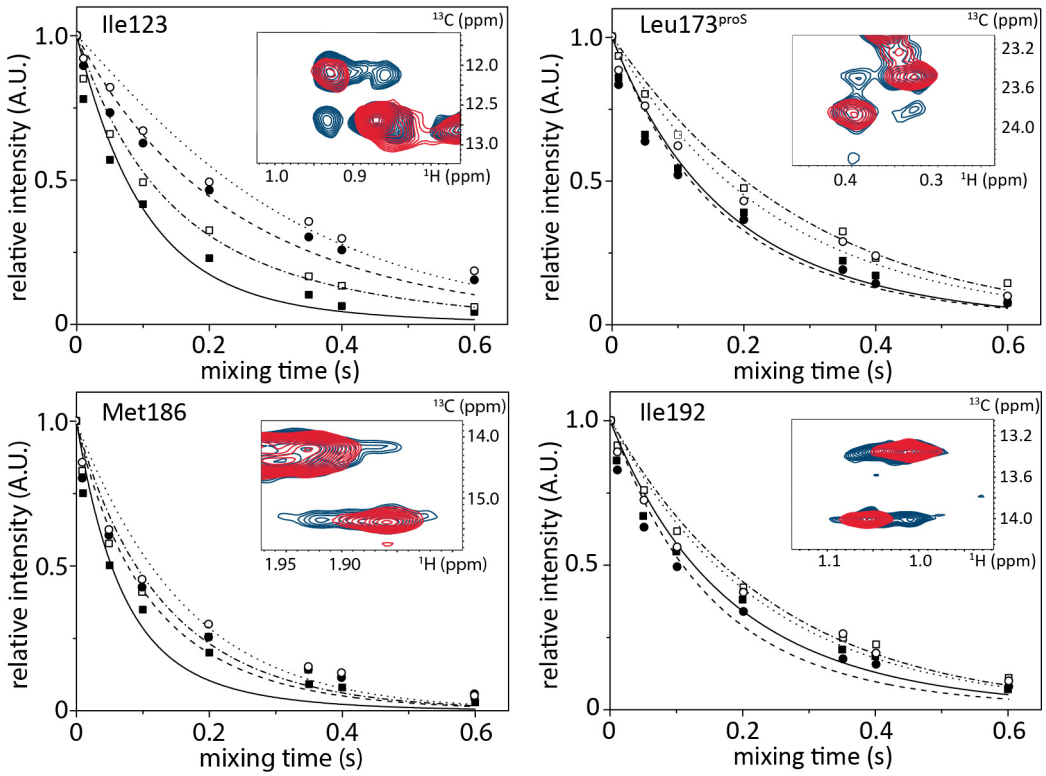


Figure 4.39: Normalized peak intensities of the direct correlation signals corresponding to Ile[123], Leu[173] (proS), Met[186] and Ile[192] methyl groups in the ZZ-exchange experiment. The intensities are plotted in dependence of the mixing time (··○·· A, --●-- AA, ·-□·- B, –■– BB). A and B correspond to the direct correlation signals in the non-frequency-labeled spectra, and AA and BB to those in the frequency-labeled spectra. Equations 3.4 and 3.5, which describe the time dependency of the direct correlation peaks in a two-site exchanging system are globally fitted to the intensities of the four residues with shared exchange rates. The inserts show zooms of the respective methyl group region in 2D [^{13}C,^{1}H] correlation spectra with (blue) and without (red) frequency-labeling during t1 at 200 ms mixing time.

Table 4.10: Rate constants determined in the ZZ-exchange experiment. Shown are the longitudinal relaxation rates of the indicated methyl groups in the binary (GTB/H-dis: **A**) and ternary binding complex (GTB/H-dis/UDP: **B**), as well as the shared exchange rates between the states.

		Ile[123]	Leu[173]	Met[186]	Ile[192]
R_1 (s^{-1})	A	2.4 ± 0.4	4.2 ± 0.4	6.3 ± 0.6	4.6 ± 0.5
	B	5.0 ± 0.7	3.3 ± 0.4	8.6 ± 0.9	3.8 ± 0.4
k_{AB} (s^{-1})			**2.0 ± 0.5**		
k_{BA} (s^{-1})			**2.5 ± 0.6**		

The here determined exchange rates match very well those of the line shape analysis (compare Tab.4.9: UDP (H-dis). The rate k_{BA} describes the transition from the ternary to the binary binding complex,

comparable with the off-rate in the line shape analysis. The determined values are almost identical (2.6 vs. 2.5 s^{-1}). An analogous comparison of k_{on} and k_{AB} is not that straightforward, as the association rate is dependent on the concentrations of both binding partners. However, multiplication of the line shape analysis derived pseudo-first-order rate constant k_{on} with the ligand concentration (250 µM) delivers a transition rate that is in the range of k_{AB} (6.3 vs. 2 s^{-1}).

4.2.8 Substrate analog binding to GTA and AAGlyB

Despite their high homology, GTA, GTB and AAGlyB show astonishingly different substrate specificities. Responsible for substrate specificity are mainly residues 266 and 268. AAGlyB is in this respect of particular interest, as it shows a dual Gal and GalNAc transferase activity. This chapter compares CSPs induced by binding of different nucleotide sugars to the three enzymes. The protein and ligand solutions are prepared as described in section 4.2.1 with the same buffer system. Protein concentrations are determined by UV absorbance at 280 nm using a NanoDrop spectrometer. The specific activities of GTA, GTB and AAGlyB, employing either UDP-Gal or UDP-GalNAc, are determined in a parallel assay for all three enzymes and are summarized in table 4.11.

Table 4.11: Specific activities of GTA, GTB and AAGlyB using UDP-Gal or UDP-GalNAc as donor substrates.

	GTA	**GTB**	**AAGlyB**
UDP-Gal (U mg^{-1})	0	5	2
UDP-GalNAc (U mg^{-1})	11	0	1

At each titration step, 2D [^{13}C,^{1}H]-HMQC experiments are recorded at 298 K and 500 MHz proton frequency with 8 scans using 1024 (^{1}H) and 256 (^{13}C) complex data points. The spectra are processed with 4 Hz (^{1}H) and 8 Hz (^{13}C) exponential line broadening and zero filling to 512 complex points in the indirect dimension using NMRPipe. DSS-d_6 serves as internal reference for the chemical shifts. CSPs are calculated as differences in peak positions in the spectra recorded of the apo state of GTA or AAGlyB, and in presence of the highest ligand concentrations, respectively. A comparative summary of donor analog-induced CSPs in GTA, GTB and AAGlyB is shown in figure 4.40.

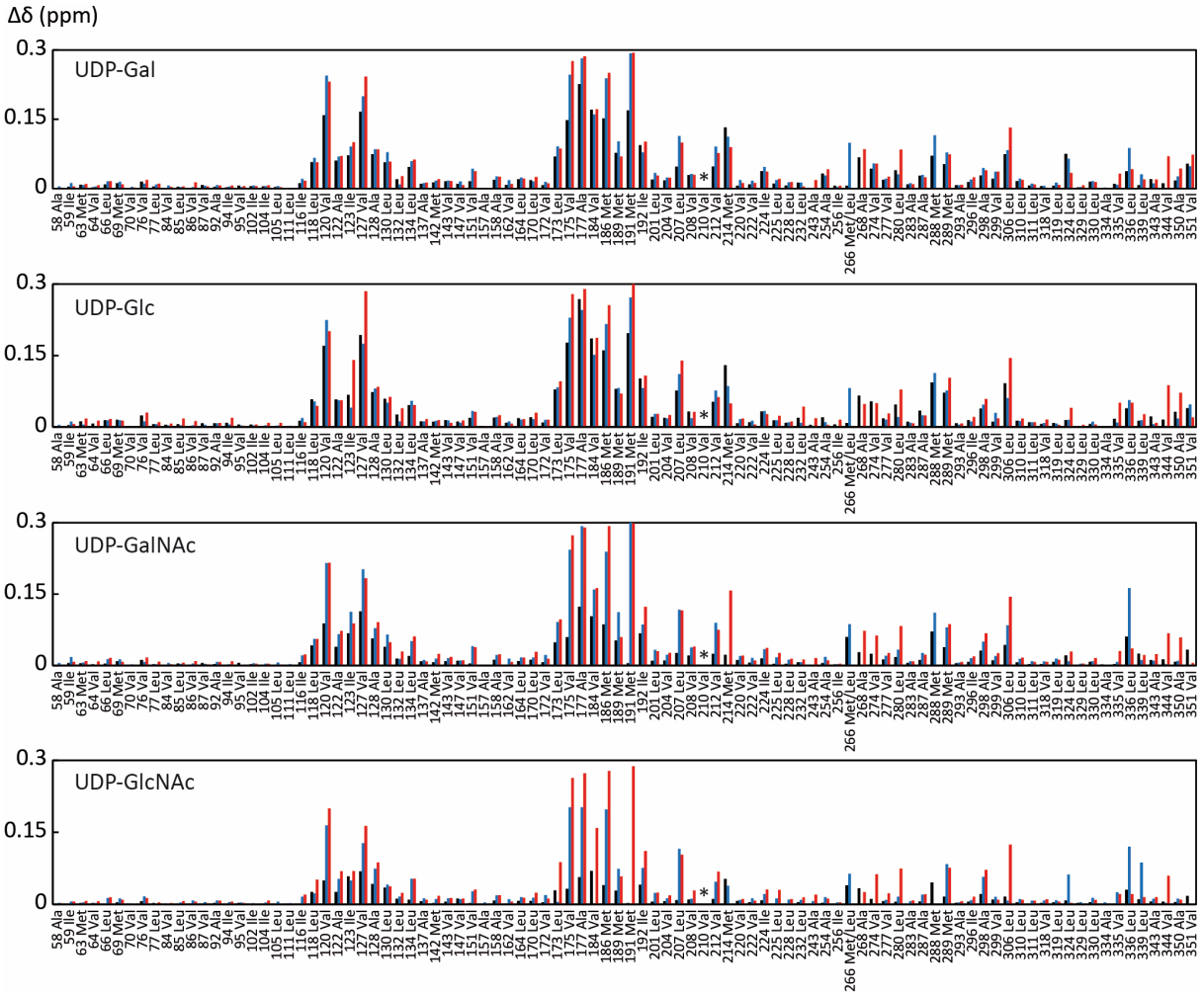


Figure 4.40: Residue specific CSPs observed during nucleotide sugar binding to GTA (blue bars), GTB (black bars) and AAGlyB (red bars). The four panels show the weighted Euclidean distances (Δδ) between peak positions in 2D [^{13}C, ^{1}H]-HMQC spectra recorded of the apo-state and the ligand-saturated state, respectively. Spectra are recorded with AIL^{proS}MV^{proS} methyl labeled proteins (GTA: ~120 µM; GTB: ~270 µM; AAGlyB ~120 µM) and high excess of ligands (GTA and AAGlyB: 6900 µM excess concentration; GTB: 6200 µM excess concentration). Residues are listed in sequential order. Ambiguous CSPs are labeled with *.

The CSP patterns induced by UDP-Gal and UDP-Glc binding are strikingly similar among the three enzymes. Binding of UDP-GalNAc and UDP-GlcNAc show, however, significant differences between GTB on the one hand and GTA and AAGlyB on the other hand. CSPs are generally larger in GTA and AAGlyB. As shown in table 4.12, this complies with the observed higher affinities of these sugar nucleotides for GTA and AAGlyB, and is a consequence of only partial saturation of GTB's binding sites at the highest ligand concentration. The long side chain of Met^{266} interferes with binding of any nucleotide sugar bearing an N-acetylic group in position 2 of the sugar.

Because of the rapid hydrolysis of UDP-GalNAc, this substrate is added in one step to protein solutions of GTA and AAGlyB. However, no differences in peak positions can be observed between spectra of the

UDP- and UDP-GalNAc-saturated states (see Fig. 4.41). This demonstrates that the hydrolysis is too fast for NMR studies of UDP-GalNAc binding to GTA and AAGlyB. Importantly, GTB shows only very slow UDP-GalNAc hydrolysis activity, allowing such studies. GTA and AAGlyB hydrolyze UDP-Gal adequately slowly allowing a several step NMR titration, too.

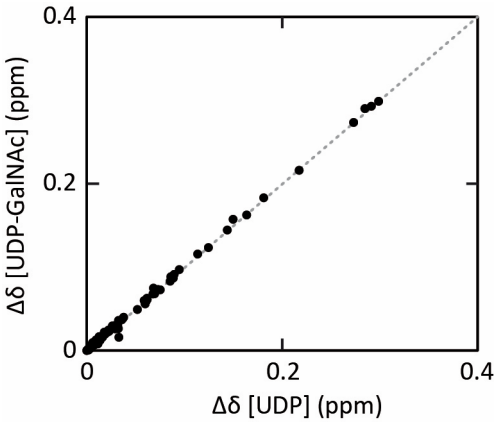


Figure 4.41: Correlation of CSPs induced by binding of UDP-GalNAc or UDP to AAGlyB. Each dot represents a methyl resonance.

Line shape analysis allows the estimation of binding parameters of the donor analogs to GTA and AAGlyB (see Tab. 4.12). Because of the rapid hydrolysis, the binding parameters of UDP-GalNAc cannot be determined. However, GTA and AAGlyB show a one order of magnitude higher affinity for UDP-GlcNAc than GTB, suggesting a similar relation for UDP-GalNAc. Clear tendencies can be concluded from the comparison of affinities in table 4.12: UDP > UDP-Gal, UDP-Glc > UDP-GalNAc, UDP-GlcNAc and AAGlyB > GTA > GTB. The first tendency correlates the affinity with the size of the ligands, while the second tendency correlates the affinity with the size of the binding site. Interestingly, binding of UDP-GlcNAc to GTA and AAGlyB occurs with comparable affinities, but binding of UDP-Gal/UDP-Glc to AAGlyB is significantly stronger than to GTA.

As anticipated, also binding associated exchange rates differ between the enzymes. Full sets of parameters are only available for binding of UDP-Glc and UDP-GlcNAc. Association of UDP-Glc occurs with comparable rates to GTA and GTB. However, association of UDP-Glc to AAGlyB is one order of magnitude slower, indicating significantly higher energetic barriers. The dissociation of the binary binding complex comprising UDP-Glc is one order of magnitude slower from AAGlyB compared with GTA or GTB. In contrast, association and dissociation of UDP-GlcNAc are comparable for GTA and AAGlyB. In summary, there is a tendency for higher exchange rates in GTB, intermediate exchange rates in GTA, and lower exchange rates in AAGlyB.

Table 4.12: Comparison of donor substrate analog binding parameters of GTA, GTB and AAGlyB. The parameters describing UDP-Gal binding to AAGlyB are indicated in brackets, as slow hydrolysis of UDP-Gal occurs during the titration introducing a systematic error.

	GTA			GTB			AAGlyB		
	K_d (µM)	k_{on} ($M^{-1}s^{-1}$)	k_{off} (s^{-1})	K_d (µM)	k_{on} ($M^{-1}s^{-1}$)	k_{off} (s^{-1})	K_d (µM)	k_{on} ($M^{-1}s^{-1}$)	k_{off} (s^{-1})
UDP	-	-	-	161 ± 3	$1.5x10^6$	243 ± 7	37 ± 1	$1.8x10^5$	6.8 ±0.4
UDP-Gal	237 ± 4	$2.7x10^5$	64 ± 2	-	-	-	(64 ± 1)	($8.3x10^4$)	(5.3 ± 0.2)
UDP-Glc	375 ± 6	$2.1x10^5$	78 ± 2	598 ± 7	$3.6x10^5$	219 ± 4	39 ± 1	$<3x10^4$	<1
UDP-GalNAc	-	-	-	3370 ± 60	$1.5x10^5$	493 ± 15	-	-	-
UDP-GlcNAc	374 ± 13	$5.9x10^4$	22 ± 2	3300 ± 110	$1.9x10^5$	610 ± 50	297 ± 9	$7.5x10^4$	22 ± 1

After saturation with donor analogs, 3DD is titrated into the protein solution to mimic the Michaelis (ternary) complex. Unfortunately, addition of 3DD to GTA and AAGlyB leads to visual precipitation of protein in the samples. While resonance positions of the ternary complex, and therefore CSPs can still be determined with high accuracy, protein precipitation introduces large errors in the line shape analysis. This precludes a reasonable estimation of binding parameters of any acceptor substrate to GTA or AAGlyB in this setup. The CSPs of different ternary binding complexes relative to the apo state are reported in figure 4.42.

UDP-GalNAc is rapidly hydrolyzed by the GTs. Thus, the UDP-GalNAc/3DD-saturated states cannot be observed. Instead, the data obtained represent the UDP/3DD-saturated state of the GTs. Hydrolysis of UDP-Gal is also significantly accelerated in presence of 3DD. In the case of GTB and AAGlyB, two sets of signals are observed. One set corresponds to the UDP-Gal/3DD saturated state, the other set to the UDP/3DD-saturated state. They are unambiguously identified by superposition with spectra of the UDP/H-dis-saturated state and by changing intensities with time due to hydrolysis of UDP-Gal. In GTA, only one set of signals is observed, which can be assigned to the UDP/3DD-bound state. Therefore, the UDP-GalNAc/3DD-bound state is not observable for any enzyme, and the UDP-Gal/3DD-bound state is only observable for GTB and AAGlyB.

The most striking differences in the CSP patterns are observed for the UDP-GlcNAc/3DD-saturated state. UDP-GlcNAc and 3DD cannot bind to GTB at the same time. However, the larger active sites of GTA and AAGlyB provide enough space for simultaneous binding of both substrate analogs. The CSPs in GTA and AAGlyB indicate that both enzymes undergo also a conformational transition from the open to the closed protein conformation.

All other CSP patterns are very similar among GTA, GTB and AAGlyB. Residues attracting attention are Leu^{336} and Leu^{339} located rather remote from the active site. As pointed out in figure 4.15, the peaks of these residues appear at similar positons in the apo state of GTB and AAGlyB, while the resonances of GTA are shifted relative to these positions. Here, the CSPs of Leu^{336} and Leu^{339} induced by UDP-Gal/3DD (UDP/3DD in the case of GTA), UDP-Glc/3DD and UDP/3DD are significantly larger in GTA than in GTB or AAGlyB. As the chemical shifts of both residues show shared properties in GTB and AAGlyB, but different behaviors in GTA, Leu^{336} and Leu^{339} may sense dynamic effects involved in the UDP-Gal discrimination mechanism.

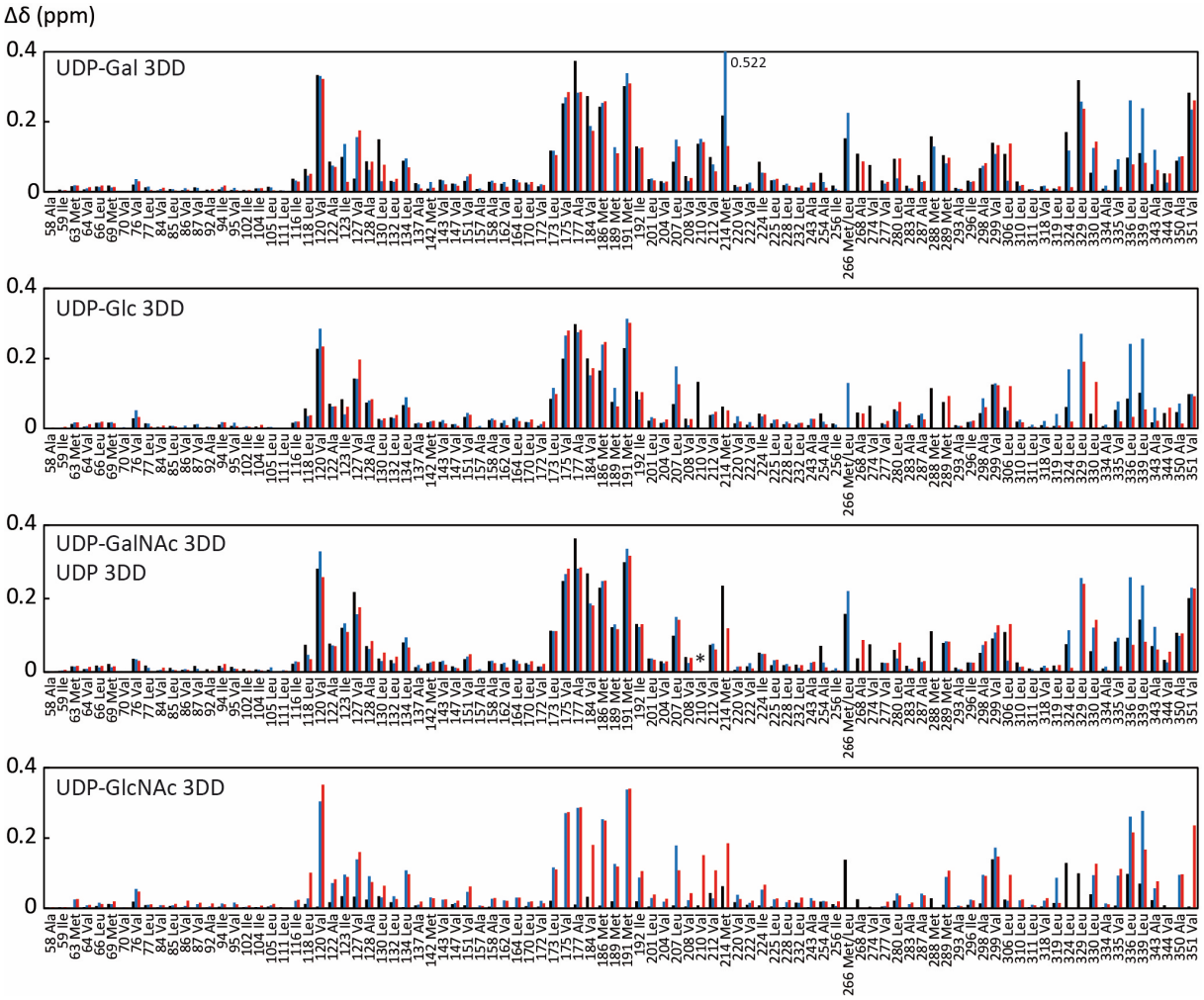


Figure 4.42: Residue specific CSPs observed during nucleotide sugar and 3DD binding to GTA (blue bars), GTB (black bars) and AAGlyB (red bars).The four panels show the weighted Euclidean distances (Δδ) between peak positions in 2D [^{13}C, ^{1}H]-HMQC spectra recorded of the apo-state and the ligand-saturated state, respectively. Spectra are recorded with AIL^{proS}MV^{proS} methyl labeled proteins (GTA: ~120 µM; GTB: ~270 µM; AAGlyB ~120 µM) and high excess of ligands. Residues are listed in sequential order. Ambiguous CSPs are labeled with *. The third panel reports CSPs induced by UDP/3DD binding, as the UDP-GalNAc/3DD-bound state is not observable due to the rapid hydrolysis of UDP-GalNAc to UDP. In the first panel the reported CSPs in GTA correspond to the UDP/3DD-bound state, too.

4.2.9 Substrate analog binding to W181M and W181E mutants

Trp[181] has a unique function in GTA and GTB, as it is involved in the only direct contact between internal disordered loop and C-terminus via a cation-π interaction with Arg[352]. The interaction has a crucial role in stabilization of the closed protein state. Therefore, modification of the interaction strength will likely be reflected by altered exchange rates between open and closed conformations. This chapter summarizes ligand titration data of UDP and H-dis binding to W181E and W181M mutants. Substitution of Trp with Glu is hypothesized to stabilize the closed conformation by formation of an ionic bonding. On the other hand, substitution with Met is meant to disrupt the interaction. Julian Revenstorff synthesized ILMV methyl-labeled protein samples and performed NMR titrations in his bachelor thesis. These titration data are used for exploration of CSPs and line shape analysis, and compared with the findings of the GTB wildtype (wt) investigations. Pro-R Leu/Val methyl groups are excluded from the CSP analysis as well as Ala methyl groups, as they are either not isotopically labeled in the wt or in the mutants. Because of signal overlaps in the Leu/Val region, a small number of pro-S methyl groups are excluded, too.

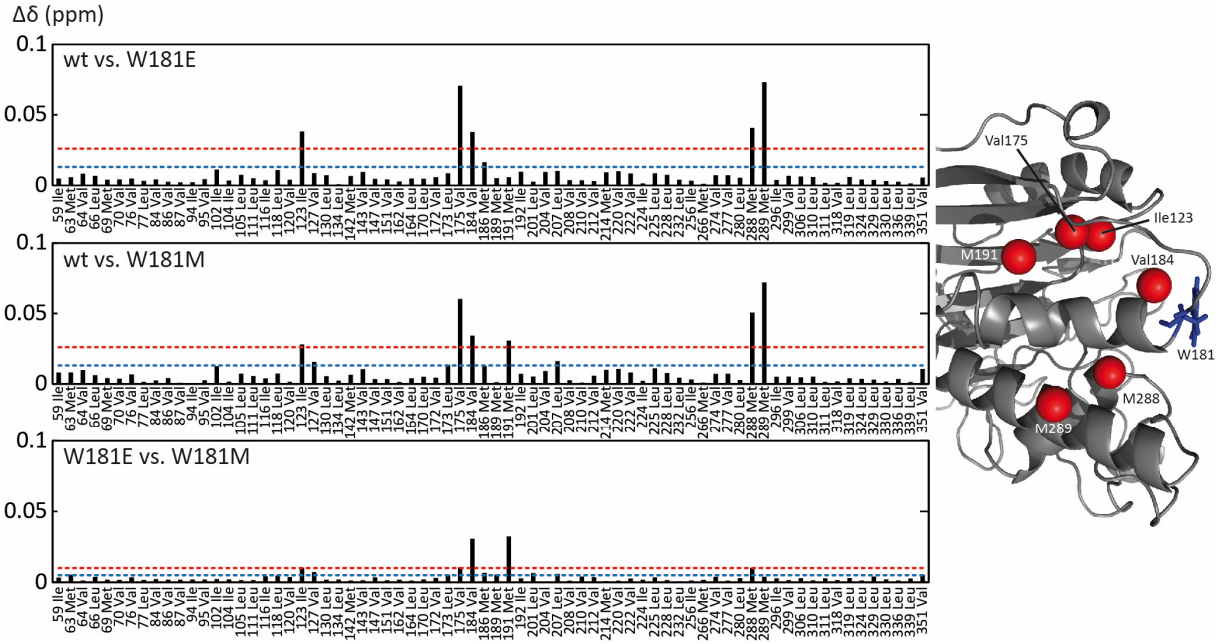


Figure 4.43: Weighted Euclidean distances between signal positions in spectra of wt GTB and mutants W181E and W181M. Signal positions are determined in 2D [^{13}C, ^{1}H]-HMQC spectra of the apo states. GTB mutants are ILMV methyl-labeled. The dashed lines indicate cut-offs at 1σ (blue) and 2σ (red). Carbons of methyl groups that show larger differences than 2σ are highlighted as red spheres in the crystal structure on the right. Blue sticks show the location of Trp[181].

Peak positions in 2D [^{13}C,^{1}H]-HMQC spectra of the apo state of GTB wt and both mutants are comparable. Figure 4.43 summarizes the differences between peak positions in the apo state. The standard deviation of the observed differences is in all cases on the order of the spectral resolution.

However, some resonances exceed the 2σ cut-off and are considered as significant. All resonances exceeding this threshold are assigned to residues of the internal disordered loop, or to residues located next to this domain (Met^{288}, Met^{289}). Both mutations perturb a similar set of residues. The only significant differences are observed for Val^{184} and Met^{191}, which is only perturbed in the W181M mutant. In the case of GTB W181M an additional resonance is expected for Met^{181}. Unfortunately, the resonance overlaps with the peak of Met^{69}, precluding its exploitation in the line shape analysis.

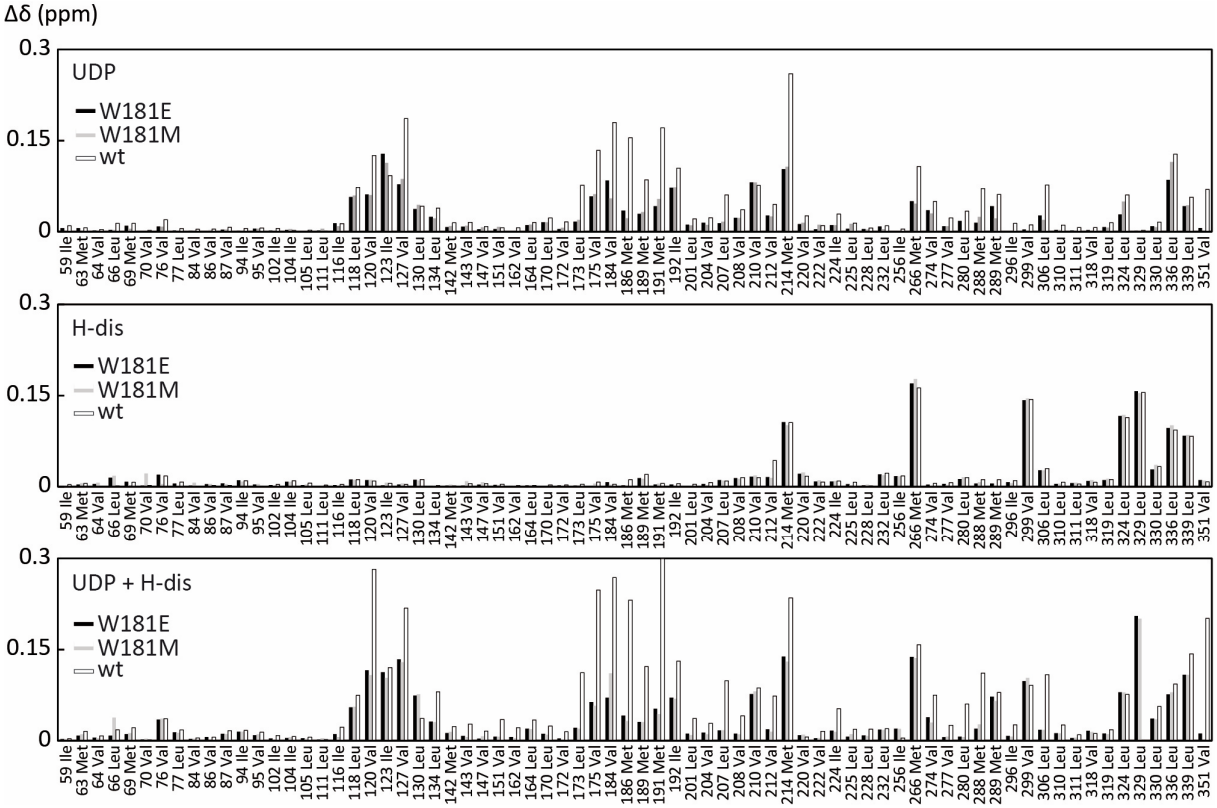


Figure 4.44: Comparison of ligand binding-induced CSPs in GTB wt (open bars) and W181E (black bars) and W181M (grey bars) mutants. The three panels show the weighted Euclidean distances (Δδ) between peak positions in 2D [^{13}C, ^{1}H]-HMQC spectra recorded of the apo-state and the ligand-saturated state (UDP: top; H-dis: center; UDP + H-dis: bottom), respectively. Spectra of the mutants are recorded with ILMV methyl-labeled proteins (W181E ~100 µM; W181M ~200 µM) and high excess of ligands (UDP: 5 mM; H-dis: 1.4 mM). Residues are listed in sequential order.

Ligand titrations are performed with UDP and H-dis, and the induced CSPs are summarized in figure 4.44. Binding of the acceptor substrate in the absence of the donor analog is observed with the same CSP patterns in GTB wt and mutants. This is expected, as acceptor binding in absence of donor is not connected to a conformational transition. However, significant differences in the CSP patterns can be observed for UDP binding, and more pronounced for the ternary binding complex. The most striking differences are observed for residues of the internal disordered loop (residues 173-192), where CSPs are significantly larger in GTB wt than in the mutants. As the internal loop undergoes a transition from the

open to semi-closed state upon binding of UDP, and a transition from the open to closed state upon binding of UDP and H-dis, these findings indicate that these transitions are incomplete in the mutants. The CSP patterns of both mutants are strikingly similar in all states. In contrast to expectations, the data suggest that ionic bonding between Glu^{181} and Arg^{352} is not present. The substitution rather leads to a similar disruption of the interaction between disordered loop and C-terminus as in the W181M mutant.

During storage, GTB W181M is quantitatively truncated on the N- and C-terminal site by a protease impurity apparently only present in this protein batch. The absence of methyl signals indicate that on the N-terminal site residues 58 to 64 or 65 are cut off. On the C-terminal site, only the resonance of Val^{351} is lacking, indicating a proteolytic cleavage between Val^{344} and Val^{351}. Besides small CSPs observed for residues located close to the N- and C-terminus, the vast majority of signals resides at the positon of the non-cleaved form, indicating a preserved overall protein conformation. This truncated protein form is only used in the titration with UDP (without H-dis). The CSP pattern induced by UDP binding is highly similar to the pattern observed for W181E, suggesting a similar binding mode, where the lacking residues do not have a crucial role.

Table 4.13: Comparison of binding parameters of UDP and H-dis to GTB wt, W181E and W181M. The binding parameters are derived by line shape analysis of NMR titration data. Line shapes of more than eight resonances are analyzed in a global fitting session applying a two-state binding model.

	GTB wt			**GTB W181E**			**GTB W181M**		
	K_d (µM)	k_{on} ($M^{-1}s^{-1}$)	k_{off} (s^{-1})	K_d (µM)	k_{on} ($M^{-1}s^{-1}$)	k_{off} (s^{-1})	K_d (µM)	k_{on} ($M^{-1}s^{-1}$)	k_{off} (s^{-1})
UDP	161 ± 3	$1.5 \cdot 10^6$	243 ± 7	738 ± 6	$2.3 \cdot 10^6$	1700 ± 70	890 ± 10	$1.2 \cdot 10^6$	1050 ± 60
UDP (H-dis)	103 ± 2	$2.5 \cdot 10^4$	2.6 ± 0.3	499 ± 4	$1.3 \cdot 10^6$	650 ± 10	486 ± 7	$1.1 \cdot 10^6$	560 ± 10
H-dis	164 ± 4	$1.9 \cdot 10^7$	3100 ± 280	35 ± 1	$3.7 \cdot 10^7$	1290 ± 30	216 ± 4	$7.0 \cdot 10^6$	1520 ± 60

The line shape analysis of the titration data delivers exciting insights into the binding modes (see Tab. 4.13). The experimental and fitted line shapes are provided in the appendix. UDP shows a lower affinity towards the W^{181} mutants, which is the result of an accelerated off-rate, observed almost one order of magnitude higher than in GTB wt. Association of UDP occurs with comparable rates in wt and mutant GTB in the absence of acceptor. These findings suggest weakened interactions between mutant enzymes and UDP cause the differences in the affinities. However, in crystal structures the sidechain of Trp^{181} is not directly interacting with the nucleotide. The induced CSPs suggest that the internal disordered loop does not occupy the same conformation in wt and mutant enzymes, which likely influences the dissociation rate of UDP. The H-dis binding parameters are comparable for all three enzymes. Fast association and dissociation rates are observed.

Particularly exciting are the binding parameters, describing the formation of the ternary binding complex. A small increase in the UDP affinity can be observed in presence of the H-dis, for GTB wt as well as for the two mutants. This can partly be attributed to decreased dissociation rates. However, in the case of GTB wt, the dissociation is decelerated by two orders of magnitude, when the acceptor is present. In the two mutants, the dissociation of the ternary binding complex is only ca. two times slower than the dissociation of the binary binding complex. On the other hand, the on-rate of UDP to GTB wt is almost two orders of magnitudes lower, when the enzyme is saturated with the acceptor, while the on-rates of UDP to the mutants remain largely unchanged. As alluded to above, the slow association rates to GTB wt indicate a high energetic barrier, which can likely be attributed to the conformational transitions from the open to the closed state. The two orders of magnitude higher on-rates of the binding event to GTB W181M and W181E suggest that this conformational transition does not occur in the mutants. This is in agreement with the CSP patterns described in the bottom panel of figure 4.43, which show significant differences for residues of the internal loop and the C-terminus.

5 Discussion

5.1 Evaluation of the methyl group assignment strategy

A structure-guided strategy is introduced for the assignment of all AIL^{proS}MV^{proS}, and a number of L^{proR}V^{proR} methyl groups in GTB, making use of selective labeling schemes, methyl-methyl NOESY and lanthanide-induced PCSs. The assignment is supported by several single site mutants, and by all ligand titration data. However, the assignment process is rather complex and critical steps will be discussed in this section.

Five differentially labeled protein samples are sufficient, in order to unambiguously assign each resonance to a residue type. The expression yields depend on the used labeling scheme. Succinate, preventing scrambling of the Ala methyl label, increases the expression yields significantly. The unequal label incorporation efficiencies in the first AIL^{proS}MV^{proS} methyl-labeled GTB batch report on a depletion of other metabolic precursor molecules during protein synthesis. By increasing the concentrations of the metabolic precursor molecules, comparable incorporation efficiencies are reached for all residue types. However, low intensity signals at the positions of the pro-R methyl groups of Leu and Val, and Ile $C\gamma^2$ indicate a depletion of the provided succinate, and residual label scrambling. The undesired methyl labels clearly originate from the provided labeled Ala, as they are not observed in spectra of GTB samples without Ala labeling. The reason for the observed residual label scrambling is most likely the prolonged expression time at 37°C in comparison to analogous examples from the literature (Ayala et al. 2009; Proudfoot et al. 2016). However, the expression time and the provided temperature also affect expression yields, and the introduced labeling protocol is a compromise between expression yields and label incorporation efficiencies. Furthermore, the low intensity signals do not interfere with any subsequent conclusions in this thesis, as their intensity is below 5% of the intensity of the desired methyl labels. Therefore, the introduction of the AIL^{proS}MV^{proS} methyl labeling protocol for GTB is successful. Further successfully introduced labeling schemes comprise ILMV and IMV methyl labeled samples. In the latter, a complete suppression of Leu labeling is achieved by addition of unlabeled Leu.

The 4D methyl-methyl NOESY experiment is recorded with an AIL^{proS}MV^{proS} methyl-labeled GTB sample at a high magnetic field strength, and with a high protein concentration. However, the protein batch showed an unequal label incorporation efficiency into the desired residue types. Nevertheless, 269 of the 376 expected NOE correlations (cut-off: 8Å) are detected. The relation is comparable to other examples from the literature (Xu and Matthews 2013). The observability of an NOE correlation depends not only on the distance between two methyl groups. This makes the definition of a single threshold difficult and reduces the meaning of the exact number of “expected” NOE correlations. However, the experiment suffers from the unequal label incorporation efficiencies. In particular NOE correlations between Leu and Val methyl groups show lower intensities. The average intensities of Leu/Val cross peaks are only about 1/3 of the intensity of Ala resonances. Consequently, NOE correlations between

Leu and Val residues are expected to occur with about 1/9 of the signal intensity of an NOE correlation between two Ala residues. The detection of such NOE correlations between Leu and Val residues is attributed to the high protein concentration. Thus, a repetition of the experiment with the second protein batch, where label incorporation efficiencies are comparable for all aa types, will likely produce higher quality spectra at lower protein concentrations. The estimation that each pair of two Leu/Val residues is just in 1/9 of all molecules simultaneously labeled, reports on usable protein concentrations as low as about 50 μM.

Despite the labeling efficiency problem, the 4D HMQC NOESY HMQC experiment alone delivers >80% correct assignments. *MAP-XS II* is used for the automated assignment process (Xu and Matthews 2013). The developers of the program claim that they could reproduce ~95% of previously published assignments in three different protein samples. Cross-checking assignments between different runs largely decreases the probability of incorrect assignments. Only resonances that are invariably allocated to the same residue in all runs, are subsequently used for further steps in the assignment process. However, incorrect assignments cannot be completely precluded, but are certainly minimized by the successive usage of PCSs as additional structural restraints.

The usage of stereoselectively Leu/Val methyl labeled GTB samples in the NOESY experiment, and the discrimination between Leu and Val residues by Leu specific unlabeling reduce the possible assignment solutions dramatically. To restrict assignments to Leu/Val pro-S methyl groups, their pro-R methyl groups are deleted from the structural model. This step is only reasonable in high resolution crystal structures (as used here), providing sufficient electron density to clearly discriminate between pro-R and pro-S methyl groups. However, while the crystal structure reports on the lowest energetic conformation, a rotation of Leu and Val sidechains in solution is surely anticipated. Therefore, the pro-R and pro-S methyl groups can occupy quite similar positons and will consequently show quite similar NOE correlation patterns. Thus, even if the electron density in the crystal structure does not provide enough information to unambiguously distinguish between pro-R and pro-S, the deletion of in part wrongly allocated pro-R methyl groups from the structure is not expected to introduce significant errors. On the other hand, the deletion halves the number of possible Leu/Val methyl groups for the assignment, as a stereoselective restriction is not provided within *MAP-XS II*.

The high resolution crystal structure of the apo-GTB homodimer (PDB entry 2RIT) is used as structural model. The output results of *MAP-XS II* depend on the reliability of the structural model. As electron density is lacking in several regions of the crystal structure, these domains are modeled. The solution conformation of the C-terminus deviates from the model, as the NOE correlations between Ala^{350} and Leu^{132} clearly indicate. These NOE correlations provide the first evidence for the orientation of the C-terminal region in the open and semi-closed state, as these residues are not resolved in any crystal structure. The modeled N-terminal region is most likely not the main conformation adopted in solution, either, as can be concluded from NOE correlations between Ala^{58} and Met^{63}. However, as the N-terminal residues are an artificial product of the cloning procedures, their actual orientation is

considered less important. Other than in the cases of the N- and C-terminus, the orientation of the internal disordered loop is restricted at two sites. However, a NOE correlation between the methyl groups of Met^{186} and Ile^{123}, separated by a distance of ~14 Å, and both additionally assigned by point mutation, and resolved in the original crystal structure, questions the orientation of the internal loop in the model, too. In the closed protein conformation, both methyl groups are separated by an even larger distance, indicating that the crystal structures might not report on all possible orientations of the internal loop.

Besides these questionable regions, the model is robust. In particular, the intermolecular NOE correlations prove the exclusive existence of GTB in the homodimeric form. An exchange between monomeric and dimeric forms is excluded, since only one set of signals is observed for residues at the dimeric interface. Such an exchange process is expected in the limit of slow chemical exchange, as the sheer sum of interactions leads to a high affinity binding event, and consequently low off-rates. However, an exchange process in the limit of fast chemical exchange can be excluded, too. A fast chemical exchange process is observed in low affinity interactions, where off-rates are fast. Yet peaks of residues at the interface are found at the same location in all methyl-TROSY spectra, regardless of the used protein concentration. These findings are in agreement with previously published ESI-MS data, which also suggest that GTB exists exclusively as a very stable homodimer in solution (Soya et al. 2009).

Lanthanide-induced PCSs are used as structural restraints to verify the NOE-based assignments, and to assign further methyl resonances. The natural metal binding site is exploited for tagging with the paramagnetic metal ions. GTB binds its metal ion cofactor, however, only in presence of the donor substrate, as shown by ESI-MS (Shoemaker et al. 2008). Similarly, lanthanide binding is only observed in presence of a donor substrate analog. Moreover, the acceptor substrate H-dis is added, as its presence increases the affinity of UDP and the metal ion cofactor in a positive cooperative manner. Thus, binding of the lanthanides (and UDP) occurs in the regime of slow chemical exchange. This is an important observation, as the signal positions are not dependent on the degree of saturation, which is a prerequisite for the accurate measurement of PCSs. As the used lanthanide ions are only weakly paramagnetic, the induced PCSs are rather small. Therefore, PCSs induced in the carbon dimension, where the shifts are on the order of the spectral resolution, are not suitable as structural restraints. Yet proton PCSs are determined accurately enough to calculate the $\Delta\chi$-tensors of all three lanthanides. The plausibility of the determined $\Delta\chi$-tensors is documented by the fitted metal ion positions. Furthermore, the tensors are quite robust in the error analysis provided within *Numbat*, where $\Delta\chi$-tensors are reconstructed with 80% of the PCS data randomly selected in 1000 runs. The Q-factors indicate a good compliance of experimental and calculated PCSs throughout the enzyme, too. Exceptions are the observed PCSs of Ala^{350} and Val^{351} of the C-terminus, suggesting that the closed protein state with an ordered C-terminus is not reached. This observation may, however, not be generalized. The comparison of CSPs induced by UDP and H-dis binding in presence of La^{3+} and Mg^{2+} suggests that the metal ion cofactor has a significant influence on the adopted protein conformation. Particularly, Ala^{350} and Val^{351} are only significantly

perturbed employing Mg^{2+} as cofactor. Also residues of the internal disordered loop show larger perturbations in presence of Mg^{2+}. The comparison of Q-factors derived with Δχ-tensor fits to different structural models provides evidence that the internal disordered loop adopts a conformation between the open and closed state in presence of the lanthanides. In summary, these findings can be interpreted as GTB adopting a state resembling the semi-closed conformation in presence of the lanthanides, and the closed conformation in presence of Mg^{2}. The incapability to reach the catalytically active state also explains why almost no transferase activity is observed employing lanthanides as cofactors (Grimm 2015). While the divalent Mg^{2+}/Mn^{2+} ions require only six coordination sites, eight to nine coordination sites are needed to complex the trivalent Ln^{3+} ions (Su and Otting 2010). Furthermore, lanthanides show larger ionic radii: 0.98-1.20 Å (Ln^{3+}) vs. 0.65 Å (Mg^{2+}) or 0.78 Å (Mn^{2+}). Also the additional charge of the lanthanide ions may interfere with the formation of the closed state. An electrostatic repulsion between Lys^{179}, Arg^{180} and Arg^{188} of the internal loop and Lys^{346} and Arg^{352} of the C-terminus is thought to hold the enzyme in the open state, which is overcome by binding of the negatively charged nucleotide donor (Alfaro et al. 2008). The extra positive charge may be responsible for residual mutual repulsions. 4D methyl-methyl NOESY spectra recorded with GTB in presence of UDP, H-dis and Mg^{2+} or La^{3+} will provide more structural information. Such experiments should certainly be performed in the future.

More importantly, the high quality of the Δχ-tensor fits allows the usage of PCSs as further structural restraints in the assignment process. NOE and PCS data are combined to complete the assignment of $AIL^{proS}MV^{proS}$ methyl groups. In multiple assignment trials, all peaks are consistently assigned to the same residues by *MAP-XS II,* using both types of structural restraints. This cross-checking largely decreases the probability of wrong assignments. Even if single assignments remain false, the wrongly assigned methyl group most likely locates closely to the real one. Several assignments are supported by independent data from amino acid substitutions. Additionally, the observed CSPs induced by ligand binding support the assignment. The CSP patterns highlight the expected regions of the enzyme, which comprise residues in the active site, directly interacting with the ligands, but more importantly also the dynamic domains, reorienting upon ligand binding. Thus, the assignment of all $AIL^{proS}MV^{proS}$ methyl groups is considered highly reliable. Also some Leu/Val pro-R methyl groups are assigned. However, the signal crowding in their spectral region impeded a full assignment. If the complete assignment of Leu/Val pro-R methyl groups will be desired in the future, the preparation of stereoselectively labeled samples is recommended.

The assignments of $AIL^{proS}MV^{proS}$ methyl groups are also transferred to GTA and AAGlyB. Although no assignment-targeted experiments are performed with these enzymes, the assignments are reliable. Chemical shift deviations between GTA, GTB and AAGlyB are mainly observed for the expected resonances, corresponding to residues located close to the “mutation" sites.

Importantly, neither NOE nor PCS data alone deliver enough information for a complete assignment. Owing to the very similar center position and orientation of all three Δχ tensors, the information of the PCS data is degenerated, involving sets of PCSs that can fit to several residues in the structure. Therefore,

trials with *PARAssign* (Skinner et al. 2013; Lescanne et al. 2017), a software tool for automated assignment solely based on PCSs, are not successful. However, introduction of a second artificial lanthanide binding site, or binding of a lanthanide chelating ligand can deliver $\Delta\chi$ tensors that differ in position and orientation of the tensors described here. The combined information of all PCSs would likely be sufficient for the assignment of the vast majority of signals. Yet the structure-based assignment strategy introduced here is very successful and very robust. Moreover, the success and the robustness are particularly attributed to the combined exploitation of NOE and PCS data.

5.2 Ligand binding and conformational transitions

The methyl group assignments obtained with the introduced strategy allow detailed functional investigations of GTA and GTB, which are discussed in this section. NMR titrations document binding of donor and acceptor substrate analogs and reveal their binding sites. More importantly, the observations also indicate conformational transitions, which are correlated with the exchange events between the open, semi-closed and closed protein state found in crystal structures. Line shape analysis allows for the first time a quantitative estimation of the coupled exchange process of ligand binding and conformational transition. The results are compared with NMR observations of the Lipooligosaccharide α-1,4-galactosyltransferase (LgtC) from *Neisseria meningitides*. Like GTB, LgtC uses a retaining mechanism for the transfer of α-galactose from the sugar donor UDP-Gal.

5.2.1 Donor substrate and analog binding by GTB

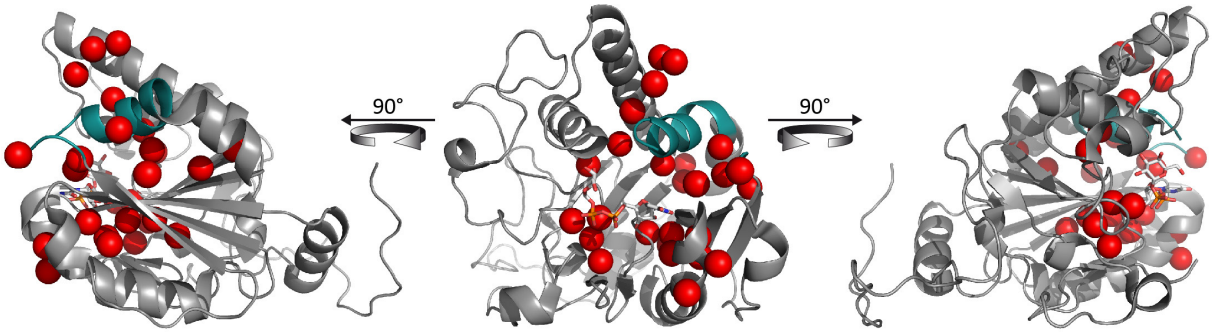


Figure 5.1: Donor binding site of GTB identified by significant CSPs. Highlighted in red are carbons of methyl groups in GTB (PDB entry 5C1L) that show CSPs >σ upon nucleotide (sugar) binding. UDP-Gal is shown in stick representation. The internal disordered loop is emphasized in cyan.

Donor substrate binding requires the presence of a metal ion cofactor. GTB does not bind the metal ion in absence of the nucleotide sugar as shown by ESI-MS data (Shoemaker et al. 2008). Based on these findings, it is clear that binding of the cofactor and donor substrate occurs simultaneously. The prior binding of the metal ion by the nucleotide sugar is a process that is imperceptible in the protein-based NMR experiments. Yet, the association of the nucleotide sugar/metal ion complex to the protein is surely

decelerated, if binding of the metal ion by the nucleotide sugar is rate limiting. The provided excess amounts of the metal ion, however, ensure a fast formation of the nucleotide sugar/metal ion complex. Thus, in the following discussions, the binding of donor substrate and analogs is referred to the simultaneous binding of nucleotide (sugar) and metal ion.

The similar CSP patterns among all used donor analogs indicate a common interaction mode with GTB. A large amount of ca. 25% of all resonances are significantly perturbed (>σ), and the CSPs can be correlated with methyl group displacements between crystal structures of the open and semi-closed state. Consequently, most of the observed CSPs are not exclusively caused by direct contacts to the ligand, but rather reflect conformational transitions. Thus, the interaction has to comprise two events that are kinetically and thermodynamically coupled: the association/dissociation of the ligand, and the conformational exchange. However, the binding event can be described by the simplest model of bimolecular interactions, which is the two-state binding model. Binding of the ligand and conformational exchange cannot be separated in the NMR data, and the quantitative estimations of k_{on} and k_{off} from the line shape analysis reflect the sum of both events.

Binding parameters are derived from a global fit employing several residues located in different regions of the enzyme. As the line shapes of all resonances are equally well fitted, the parameters describe a global transition in the enzyme. The determined affinities of the donor analogs are comparable to those described in former studies, following the tendency: UDP > UDP-Gal/UDP-Glc > UDP-GalNAc/UDP-GlcNAc (Blume et al. 2006; Sindhuwinata et al. 2013). The N-acetylic group decreases the affinity by a factor of ca. 5, reflecting its steric clash with Met^{266} and Ala^{268} in the tucked under conformation described for UDP-Gal/UDP-Glc.

For the first time, kinetic parameters of the interaction of GTB with donor substrate analogs are determined. The kinetic data reveal off-rates in the range of ca. 200-600 s^{-1}. In combination with the intermediate to low affinities (~200-3300 M) of the ligands, these observations indicate low on-rates that are not diffusion-controlled (~10^8-10^9 $M^{-1}s^{-1}$). This is an observation that is common to other enzymes, too (Fersht 1999; Tugarinov and Kay 2003b; Masterson et al. 2008). The low on-rates support the hypothesis of a complex binding mechanism involving the conformational transition of the internal disordered loop. This is in agreement with the large CSPs in this region of the enzyme. Furthermore, the line shapes of resonances corresponding to residues of the internal loop are indicative of a complex binding mechanism, too. These resonances are mainly shifted in the carbon dimension, which supports the idea that the perturbations are caused by conformational reorientations in the enzyme rather than direct contacts to the ligand. Although fitting to a more complex three-state binding model is not successful, the “hooked” peak shift of the methyl group of Ala^{177} clearly demonstrates a two-step mechanism.

Significant CSPs are also observed for Val^{351} located in the C-terminus. The C-terminus is not resolved in any crystal structure of the apo state or of the binary binding complex. Therefore, the CSPs are the first evidence for an interaction between the C-terminus and the nucleotide (sugar) in absence of the

acceptor substrate. This suggests that the transition to the semi-closed conformation does not only involve a reorientation of the internal loop, but also a reorientation of the C-terminus, which is supposed to only participate in the formation of the closed state (Alfaro et al. 2008). Therefore, the semi-closed conformation may not be understood as a single defined state, but rather as a continuum of states between the open and closed conformation.

Subtle yet significant chemical shift deviations are observed between the UDP-, UDP-Gal- and UDP-Glc-saturated states. Differences between UDP-Gal and UDP reflect differences between the educt and the product of the transferase reaction. Besides obvious differences close to the sugar position, differing positions of peaks corresponding to Leu^{336} and Leu^{339} are not anticipated from the crystal structure. Yet these residues are sandwiched by two Trp residues, and so sensitive reporters of subtle deviations in their environment. Different distributions of the conformational energy in the UDP and UDP-Gal saturated states may be the source of the significant deviations.

Chemical shift deviations between the UDP-Glc and UDP-Gal saturated states potentially report on residues involved in the epimer selection mechanism. The deviations between both states are rather small. Yet, it is interesting to note that residues of the internal loop or residues abutting this region show chemical shift deviations. This is in accordance with recent crystallographic data (Gagnon et al. 2015), which report on higher disorder in the internal loop in presence of UDP-Glc.

Despite different affinities, the off-rate of UDP-Glc and UDP are identical. Therefore, the association of UDP-Glc must be associated with a higher energetic barrier. As both ligands induce comparable CSP patterns, the difference in the association rate is rather associated with a structural rearrangement in the nucleotide sugar than in the protein. UDP-Glc undergoes the transition from the solution conformation to the bound tucked under conformation, which is of course not necessary in the case of UDP (Angulo et al. 2006; Gagnon et al. 2015).

5.2.2 Comparative analysis of donor substrate and analog binding by GTA, GTB, AAGlyB and GTB Trp^{181} mutants

While wt GTB is the main target in the protein-based NMR experiments, ligand interaction studies are also performed with GTA, AAGlyB and Trp^{181} mutants of GTB. An important observation is the enzyme-catalyzed hydrolysis of the donor substrates. The hydrolysis reaction can be understood as the transferase reaction to a water molecule, confirming the functional integrity of the enzymes during the NMR experiments. Importantly, the hydrolysis of UDP-GalNAc is much faster than the hydrolysis of UDP-Gal, which has been described before (Soya et al. 2009; Sindhuwinata et al. 2010). This is particularly evident for AAGlyB, which utilizes both substrates with equal efficiency in the real transferase reaction (Yamamoto et al. 2001; Jørgensen et al. 2013). The GalNAc moiety may more readily adopt the catalytic conformation in the bound state due to its larger size, while the Gal moiety samples unproductive orientations. This explains why the chemical shifts of the UDP-GalNAc saturated state are

identical to those of the UDP saturated state, but differ significantly from those of the UDP-Gal saturated state.

Nucleotide (sugar) binding induces comparable CSP patterns in all investigated "mutants". However, there are also significant differences observable. In GTB, binding of UDP-GalNAc and UDP-GlcNAc is impeded by the steric clash of the N-acetylic group with Met^{266} and Ala^{268} (Alfaro et al. 2008; Wagner et al. 2015). The wider active sites of GTA and AAGlyB allow binding of these ligands, indicated by much larger CSPs, and one order of magnitude higher affinities. However, also UDP-Glc and UDP-Gal bind with higher affinity to GTA and AAGlyB than to GTB. There is a correlation between the affinity and the size of the ligand (UDP > UDP-Gal/UDP-Glc > UDP-GalNAc/UDP-GlcNAc), as well as a correlation between the affinity and the size of the binding site (GTB < GTA < AAGlyB). Since the nucleotide moiety is mainly responsible for the affinity (Blume et al. 2006), those correlations suggest a loss of conformational entropy upon binding by restricting the sugar flexibility. In the wider active site of AAGlyB, the orientation of the sugar is not that restricted as in the narrow active site of GTB. Moreover, a narrower active site will restrict the motion of larger sugars more severely than those of smaller sugars. This is in agreement with conclusions from crystallographic data showing full electron density of UDP-Gal (UDP-C-Gal) in the active site of GTB, but absent density of the sugar moiety in GTA structures (Gagnon et al. 2015).

The kinetic parameters reveal a clear trend for higher exchange rates in GTB, intermediate exchange rates in GTA, and lower exchange rates in AAGlyB. This is already qualitatively perceptible in the exchange phenomena observed during the NMR titrations, spanning the (intermediate) fast regime in GTB to the slow regime of chemical exchange in AAGlyB. Both the on- and off-rates are affected. Although the conformational entropy of the sugar moiety likely contributes to the Gibbs free energy, the observation that exchange rates are dramatically affected in the case of UDP, too, necessitates a second modulating effect. Crystal structures revealed a correlation between the identity of critical residue 176 and the order of the internal loop (Alfaro et al. 2008). Structures containing Arg^{176}, which is found in GTA, show significantly more order than structures containing Gly^{176} found in GTB. A higher order implies a longer lifetime of the semi-closed state. As in the semi-closed state the reorientation of the internal loop towards the active site restricts the dissociation of the donor substrate, this is in agreement with lower dissociation rates.

Remarkably, binding of UDP-GlcNAc to GTA and AAGlyB occurs with comparable affinities, but binding of UDP-Gal and UDP-Glc to AAGlyB is significantly stronger than to GTA. This is reflected by the kinetic profiles of the binding events. The on- and off-rate of UDP-GlcNAc are largely identical for GTA and AAGlyB. Yet, UDP-Gal and UDP-Glc show one order of magnitude longer residence times in the binary complex with AAGlyB than with GTA. From crystal structures it is concluded that the selectivity of GTA against UDP-Gal may depend on the inability to stabilize the B-donor in a catalytically active conformation due to GTA's wider binding site (Gagnon et al. 2015). However, the binding cleft of AAGlyB is even wider than that of GTA, and it shows reasonable transferase activity employing the

B-donor. The longer lifetime of UDP-Gal in the active site of AAGlyB may allow a higher probability to reach the catalytically active conformation. Crystal structures of AAGlyB in presence of a base-modified UDP-Gal derivative reveal the tucked under conformation in the binary binding complex (Jørgensen et al. 2013). The methyl group of critical residue Ala^{268}, which is also found in GTB may support the adoption of the tucked under conformation.

Binding of UDP to the Trp^{181} mutants of GTB provides further interesting insights. The stacking interaction between Trp^{181} and Arg^{352} is the only direct contact between the internal loop and C-terminus in the closed conformation. Importantly, the sidechain of Trp^{181} does not form direct contacts to the nucleotide. The W181E and W181M GTB mutants are designed to either strengthen or weaken the interaction between internal loop and C-terminus. However, the CSP patterns as well as the thermodynamic and kinetic parameters of the UDP binding event indicate highly similar effects in both mutants. The affinity of UDP towards the mutants is decreased by a factor of ca. 5. The association rates are comparable to those observed for wt GTB, and are ca. two orders of magnitude lower than bimolecular diffusion-controlled rates. As discussed above, this is in agreement with an induced conformational transition in the enzymes, which is likely the reorientation of the internal disordered loop towards the active site. However, the off-rate is almost one order of magnitude larger in the mutants than in wt GTB. A shorter lifetime of the semi-closed state is likely the reason for the increased dissociation rates. This is also in agreement with the observed CSP patterns, which show significantly larger CSPs in the internal loop for wt GTB than for the mutants. Furthermore, this indicates that the interaction between Trp^{181} and Arg^{352} is transiently formed in absence of the acceptor substrate, too, which is likely responsible for the increased lifetime. The observations show that a salt bridge is not formed, when substituting Trp^{181} with a Glu residue. Most likely, the side chain of Glu^{181} cannot adopt a conformation that brings the negatively charged carboxylic group in contact with the positively charged side chain of Arg^{352}.

5.2.3 Acceptor substrate and analog binding by GTB

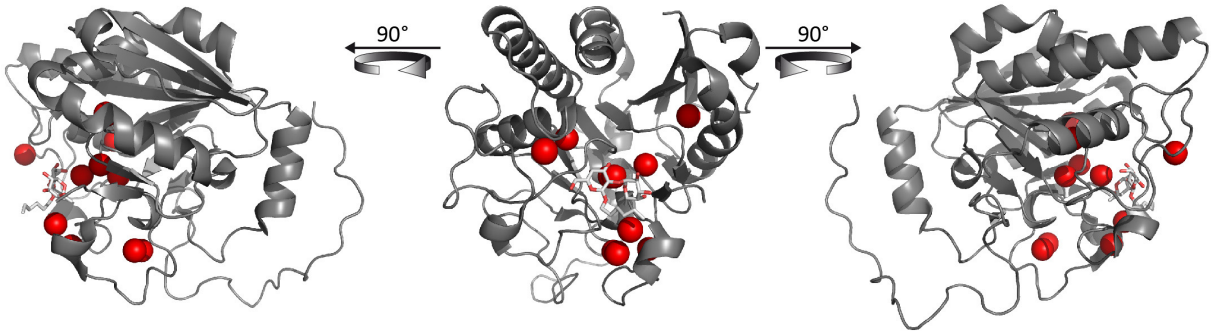


Figure 5.2: Acceptor binding site of GTB identified by significant CSPs. Highlighted in red are carbons of methyl groups in GTB (PDB entry 2RIY) that show CSPs >σ upon acceptor binding. The H-dis is shown in stick representation.

From enzyme kinetics, it is concluded that acceptor substrate binding succeeds donor substrate binding in the catalytic cycle of the GTs (Kamath et al. 1999). However, the enzymes do bind acceptor substrates in absence of the donor substrate, too. The binary binding complexes of GTB with the H-dis, the 3-deoxy-Gal H-dis derivative (3DD), all described types of H-tris, and the B-trisaccharide are investigated.

The binding parameters of H-dis, 3DD and B-tris are very similar. The on-rate is ca. $1 \cdot 10^7$ $M^{-1}s^{-1}$ and the off-rate is ca. 3000 s^{-1}. Their observed affinities comply with described data derived with alternative techniques (Soya et al. 2009; Sindhuwinata et al. 2013). Although still one order of magnitude smaller than any diffusion-controlled association, the binding of these ligands is considerably faster than the association of the donor analogs. This implies a lower energetic barrier, which can reflect different characteristics of the ligands, or differences in the required structural transitions in the protein. It has been shown that in contrast to the donor substrate, H-dis binds in a conformation that predominates in solution, too (Angulo et al. 2006). Furthermore, GTB retains the open conformation in presence of the H-dis (Alfaro et al. 2008). This is in agreement with the observed CSP patterns. Donor substrate binding induces significant CSPs in ca. 25% of all methyl groups, indicating a global conformational transition that correlates with the observed transition in the crystal structures. Only ca. 10% of all methyl groups are significantly perturbed upon acceptor binding, suggesting a more locally restricted binding event. Remarkably, residues of the internal loop and of the C-terminus are not influenced by acceptor binding, which demonstrates that the enzyme retains the open conformation.

Acceptor binding occurs with one order of magnitude higher on- and off-rates than donor binding. This is in agreement with previous estimates derived by STD NMR (Angulo et al. 2006). Moreover, the significant longer lifetime of the donor binary complex may explain, why donor substrate binding precedes acceptor binding in the catalytic cycle. However, the binding parameters of the interactions with the H-trisaccharides indicate that the on-off-kinetics of the disaccharide are artificially increased. Compared with the H-dis, the association of all H-tris types is ca. one order of magnitude slower. Major conformational transitions on the protein side are not responsible for the lower on-rates, as documented by the highly similar CSP pattern. Therefore, the higher energetic barrier is more likely attributed to the orientation of the trisaccharides' reducing end sugar, adopting a different conformation in the bound state than in solution.

Although all different types of H-tris are described as potential acceptor substrates (Meloncelli and Lowary 2010), their affinities differ dramatically. Only H-tris II, V and VI are adequate binders for a line shape analysis. The other H-tris induce only very small CSPs. It is evident that the linkage type has a significant influence on the affinity. The (1→4)-linkage (type II, VI) is clearly preferred over the (1→3)-linkage (type I, II, IV, V). The dissociation rates of type II and VI antigens are reduced by one order of magnitude in comparison with the H-dis, indicating that the reducing end sugar forms direct contacts to the enzyme. However, crystal structures of GTB soaked with type I and II trisaccharides provide evidence for direct hydrogen bonds between Ser^{235} and the reducing end sugar of type I, but not of type II antigens (Letts et al. 2006). Yet the off-rate of the type I antigen is comparable to that of the H-dis.

This conflict reflects the complexity of the investigated interactions. The observed differences in the affinities for H-tris I and II are in agreement with enzyme kinetic data reporting on differing K_M values on the same order of magnitude (Letts et al. 2006).

5.2.4 Positive cooperativity of ligand binding and the associated protein dynamics

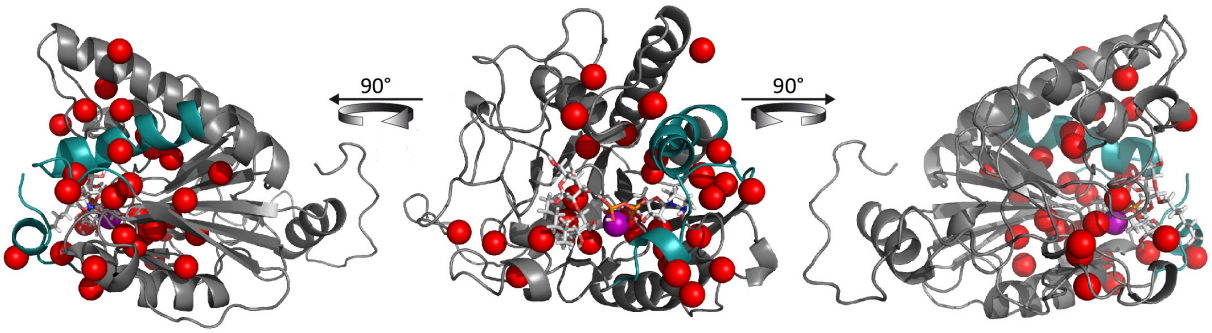


Figure 5.3: Significantly perturbed sites in the ternary binding complex. Highlighted in red are carbons of methyl groups in GTB (PDB entry 2RJ1) that show CSPs >σ upon UDP and H-dis binding. The ligands are shown in stick representation. The internal disordered loop and C-terminus are emphasized in cyan.

The investigations of the ternary binding complex, comprising the enzyme, the nucleotide sugar/metal ion and the acceptor substrate are of particular importance. The interplay of three binding partners immediately raises the question of the validity of the employed two-state binding model. Yet the excess amounts of the first ligand provide a system for the second ligand titration that can be adequately described by a two-state model. This is obviously not true, if binding of the ligands has a specific order. In the case of GTB, the Theorell-Chance mechanism suggests that donor binding precedes acceptor binding (Kamath et al. 1999). Therefore, the donor substrate cannot bind to an acceptor-loaded enzyme. Upon titration of a donor substrate under saturating conditions of the acceptor substrate, the enzyme has to traverse through different states to reach the ternary binding complex (compare Fig. 5.2). The donor binds only to the free form of the enzyme, which has a low abundance in presence of saturating amounts of the acceptor. Afterwards, the donor-enzyme complex will rapidly bind another acceptor substrate. Predicting the associated line shapes of such a complex transition is not straightforward, and depends on the associated kinetics. The quality of the fits employing a two-state mechanism, however, suggests that the donor substrate may enter the acceptor-loaded active site. This might only be true for the investigated pairs of ligands and not for the natural substrates.

The similar CSP patterns among all used donor acceptor pairs indicate a common interaction mode with the GTs. A large amount of ca. 40% of all resonances have $\Delta\delta > 0.05$ ppm, and ca. 30% of all resonances are significantly perturbed (>σ) relative to the apo state. As anticipated from crystal structures, the CSPs can be correlated with transitions between the major states of the enzyme, which

are the open and the closed state. Like discussed above for the binary binding complex with the donor analogs, the formation of the ternary binding complex starting from the binary binding complex has to comprise two events that are kinetically and thermodynamically coupled: the association/dissociation of the second ligand(s), and the conformational exchange.

As the interplay between three binding partners is rather complex, it is reasonable to first focus on the simplest system, comprising GTB, UDP and the H-dis. The findings agree perfectly with the proposed main protein states concluded from the crystal structures. UDP binding induces either the transition from the open to the semi-closed conformation (absence of H-dis), or the transition from the open to the closed conformation (presence of H-dis). The NMR titrations reveal CSPs in the same regions of the enzyme, regardless of binding to apo-GTB or H-dis-saturated GTB. However, CSPs are generally much larger in presence of H-dis (σ = 0.05 vs. 0.08 ppm), which is in agreement with the idea of the semi-closed state as a continuum of conformations between the open and closed state (Alfaro et al. 2008). H-dis binding induces no conformational transition in absence of the donor, while GTB undergoes the transition from the semi-closed to the closed conformation, when H-dis binds to the UDP-saturated enzyme. The CSPs observed upon H-dis binding to UDP-saturated GTB, reveal regions that are not influenced in absence of the donor substrate. In particular, peaks corresponding to residues of the internal disordered loop, and of the C-terminus are only perturbed upon H-dis binding in presence of UDP.

Importantly, binding of the first ligand appears to enhance the affinity of the second ligand, regardless of the order of the titration. This is in agreement with previously published data derived with orthogonal techniques (Shoemaker et al. 2008; Sindhuwinata et al. 2010, 2013). The affinity of UDP is enhanced by a factor of ~1.6 in presence of the H-dis. H-dis binding is even ca. six times stronger in presence of UDP. This is accompanied with a profound redistribution of the associated energetic landscape, as indicated by the on-off kinetics. The on-rate of UDP to the H-dis saturated enzyme is decelerated by a factor of ca. 60. The same factor is observed for the association of H-dis to the UDP-saturated enzyme. The on-rates in presence of the respective other ligand are far from any diffusion-controlled association. This clearly indicates high energetic barriers, which reflect the major structural rearrangements that occur upon binding. Of particular interest are the observed shifts in the off-rates, indicating the lifetime of the ternary binding complex. The off-rates of donors and acceptors converge in the ternary complexes. The off-rate of UDP is ca. 100 times higher from the binary binding complex than from the ternary binding complex. H-dis dissociates almost 400 times faster from the binary binding complex. It is evident that the rearrangement of the internal loop and of the C-terminus in the closed state prevents the exit of the ligands. Therefore, it is very likely that the long lifetime of the ternary binding complex in the range of 0.1-1 s reflects the lifetime of the closed protein state on the same time scale. The kinetic insights into the interactions of GTB with UDP and H-dis are summarized in a mechanistic model in figure 5.4.

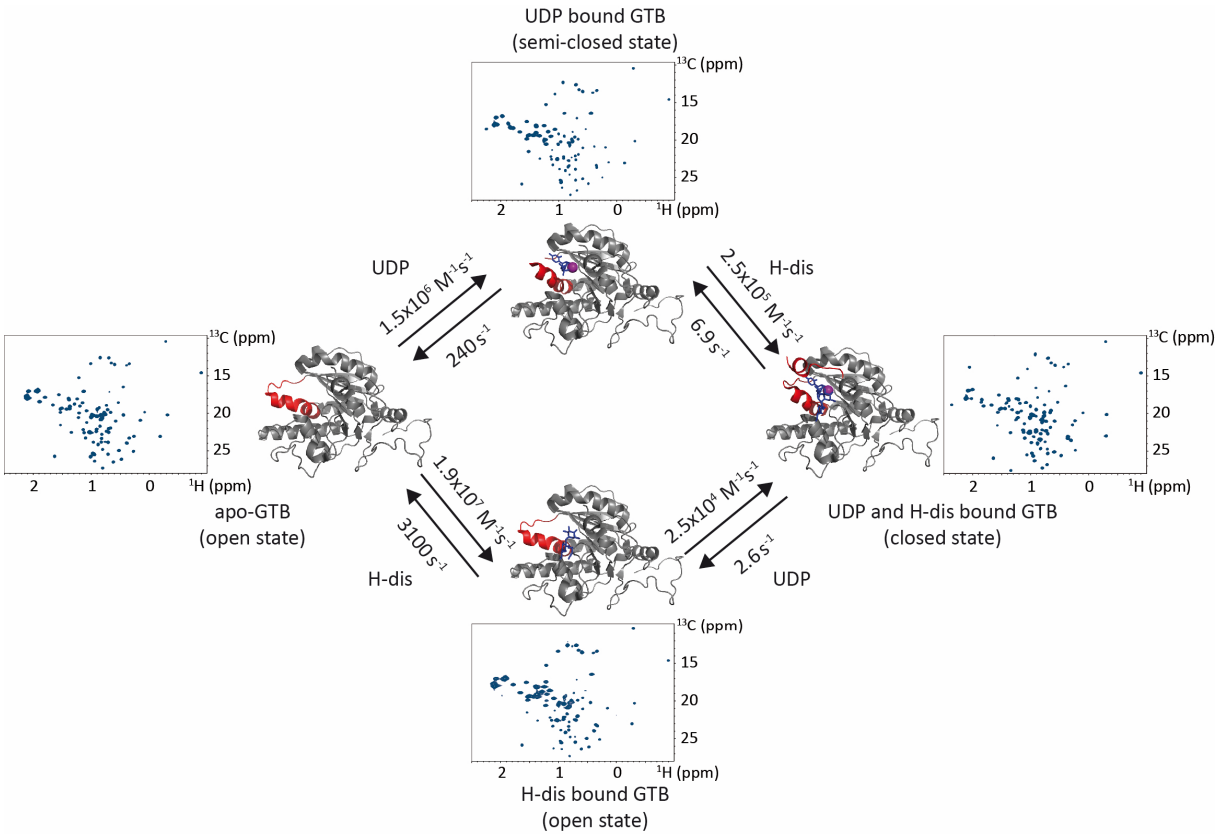


Figure 5.4: Kinetics of the transitions between different states induced by UDP and H-dis binding to wt GTB. Shown are the 2D [^{13}C, ^{1}H] HMQC spectra and crystal structures of apo GTB (left, PDB entry 2RIZ) and UDP- (upper, 2RJ0), H-dis- (lower, 2RJ6) and UDP/H-dis-bound (right, 2RJ1) GTB. The internal and C-terminal loop are highlighted in red to emphasize the conformational transitions between the major states: open, semi-closed and closed

Magnetization transfer experiments are employed to prove the timescale of the slow exchange between the two major conformational states (open and closed) of GTB. To provide a system, in which both conformational states are equally populated, GTB is saturated with the acceptor substrate, and UDP is added at half-saturating concentrations. The analyzed transition reflects the exchange process between the binary and ternary complex described on the lower right side of the mechanistic model in figure 5.2. Four residues are selected for the analysis as the frequencies of both states differ in both dimensions. The residues are either part of the internal disordered loop (Met^{186}, Ile^{192}), or located adjacent to this domain (Ile^{123}, Leu^{173}). Also in this setup, ligand binding and conformational exchange cannot be separated, and the determined kinetics describe the coupled process. Importantly, the ZZ-exchange experiment supports the exchange rates determined by the line shape analysis. The observed rate (2.5 s^{-1}) of the transition from the ternary to the binary binding complex matches perfectly the off-rate reported in figure 5.2. The transition from the binary to the ternary binding complex is observed with a rate of ca. 2 s^{-1}. This rate is obviously dependent on the concentration of the protein-acceptor complex and on the nucleotide concentration. To compare the rate with the pseudo-first-order rate constant reported in

figure 5.2, the latter is multiplied by the UDP concentration (250 µM) provided in the ZZ-exchange experiment. This rule of thumb estimation suggests that the transition from the binary to the ternary complex is three times faster (ca. 6 s^{-1}). Despite the disregarded protein concentration, the timescale matches reasonably well, too.

It is worth noting that the timescale of the suggested lifetime of the closed state (k_{off}: 2.6 s^{-1}) is on the order of the turnover rate described for GTB (k_{cat}: 5.1 s^{-1}) (Marcus et al. 2003). The deviation of a factor of two can easily be explained by different experimental temperatures (25°C vs. 37°C), and by the destabilization of the closed conformation by the reaction products. The process of product release is discussed below. In summary, the transition between open and closed protein state is likely the rate limiting step in the catalytic cycle.

In an attempt to modulate the stability of the closed conformation, the Trp^{181} mutants are designed. The kinetic profiles of the mutants are particularly exciting. The on-rates of the UDP association to the apo-state or to the binary binding complex are identical, suggesting that the energetic profiles of the binary and the ternary binding complex are highly similar. The high energetic barriers deduced from low on-rates to wt GTB are not observed. In wt GTB, they likely reflect transitions between the major conformational states. Therefore, the mutation largely decouples the association/dissociation of the ligand from the structural reorientations. This is in agreement with the induced CSP patterns. In contrast to wt GTB, the induced CSPs of the combined UDP and H-dis interaction with the mutants reflect the simple sum of the binding effects observed in the individual binary complexes. The off-rates indicate lifetimes of the ternary binding complex in the range of 0.1-2 ms, which is three orders of magnitude shorter than the lifetime of the ternary binding complex comprising wt GTB. The transition between the open and closed protein conformation occurs most likely on the same timescale (0.1-2 ms) in the mutants. The short lifetime of the closed state may also explain why the catalytic activity of the mutants is almost completely lost. Despite the destabilization of the closed conformation, the positive cooperativity between the ligands is not fully decoupled in the mutants. UDP binding is still stronger in presence of the H-dis. Hydrogen bonds between the β-phosphate of the nucleotide and OH groups of the acceptor sugars may explain the residual cooperativity (Alfaro et al. 2008).

5.2.5 Implications from different ternary binding complexes

Besides UDP and H-dis, binding of a number of further combinations of donor and acceptor substrates to GTB is investigated. Furthermore, the studies involved also ternary complexes with GTA and AAGlyB. In all cases a positive cooperativity can be identified.

The CSP patterns induced by the combined binding of UDP and each H-tris are largely identical to the pattern induced by UDP and H-dis, indicating that GTB adopts in all cases the same conformation. As this conformation likely represents the catalytically active closed state, this suggests that all H-tris types can serve as acceptor substrate in the transferase reaction. H-tris I is identified as a weak binder in absence of UDP. However, it shows a comparable affinity as the H-dis in the ternary binding complex.

The off-rates of UDP or the H-tris from the ternary binding complex indicate a comparable lifetime of the closed state as in complex with UDP and H-dis. These data suggest that GTB binds even "poor" acceptor substrates by locking them in the active site through the adoption of the closed conformation. The identity of the reducing-end sugar has no significant influence on the stability of the closed conformation, as expected from the crystal structures.

Of particular interest is the ternary complex comprising GTB, UDP-Gal and 3DD. The hydrolysis activity precluded kinetic investigations. However, the induced CSPs deliver exciting insights into this important complex. Like observed in crystal structures (Alfaro et al. 2008), UDP-Gal and 3DD simultaneously occupy the active site of GTB. The UDP-Gal/3DD-bound state, yet, differs from the UDP/3DD-bound state as is clearly perceptible from two sets of signals for a few residues, which change in relative intensity with ongoing hydrolysis of UDP-Gal. These findings allow a number of conclusions. The ternary binding complex comprising UDP and H-dis is a good model for the analysis of the transition between the major protein states, but more subtle conformational rearrangements that are most likely associated with the catalytic activity are not resolved. As two sets of signals are observable, the exchange between the UDP/3DD- and UDP-Gal/3DD-bound states is slow on the NMR timescale. However, the hydrolysis of UDP-Gal occurs on timescales of hours, implying that not every binding event results in a hydrolyzed molecule. Nevertheless, the hydrolysis proves the functional integrity of GTB in the NMR experiments.

As UDP-Glc is not hydrolyzed by GTB, the thermodynamics and kinetics of the binding events that lead to the ternary complex can be determined. The observed off-rates of UDP-Glc and 3DD describe a lifetime of the ternary binding complex in the range of 2-20 ms, which is significantly shorter than the lifetime of the ternary binding complex comprising UDP and H-dis (0.1-1 s). Since the lifetime of the ternary binding complex is most likely determined by the life time of the closed state, these findings indicate a more unstable closed state in presence of UDP-Glc and 3DD. This agrees with the observed CSP pattern. The CSPs induced by UDP-Glc/3DD and UDP-Gal/3DD show a correlation, but the signals are stronger shifted in presence of the natural substrate. Importantly, signals corresponding to residues of the internal disordered loop are considerably exchange broadened in the fully saturated state, which is not observed in presence of UDP/H-dis or UDP-Gal/3DD. An exchange process on the order of the lifetime of the closed conformation (50-400 Hz) will likely match the difference of the chemical shifts of both states and is therefore a potential source for the exchange broadening. These findings are in agreement with crystal structures, which also indicate a higher disorder in the internal loop and C-terminus in complex with UDP-Glc than with UDP-Gal (Gagnon et al. 2015). Therefore, GTB discriminates between the epimers by a destabilization of the closed state, induced by the epimeric position of the 4-OH group of the nucleotide sugar.

The most striking difference between the ternary complexes comprising either GTA, GTB or AAGlyB can be observed in presence of UDP-GlcNAc and 3DD. The CSP pattern indicates that UDP-GlcNAc and 3DD cannot occupy the active site of GTB at the same time. Consequently, GTB does not reach the

closed state in presence of UDP-GlcNAc. This is different to GTA and AAGlyB, whose active sites provide enough space for the two ligands. The observed CSPs induced by UDP-GlcNAc/3DD binding clearly indicate the transition to the closed conformation for GTA and AAGlyB. Unfortunately, a similar analysis of the ternary complexes comprising UDP-GalNAc and 3DD is not possible, as UDP-GalNAc is too rapidly hydrolyzed. However, GTB will likely not be able to bind UDP-GalNAc and 3DD at the same time, either, and consequently not reach the closed state in presence of these ligands. This explains, how GTB discriminates between UDP-Gal and UDP-GalNAc.

However, how GTA discriminates between its natural substrate UDP-GalNAc and the B-donor remains however elusive. Striking differences in the CSP patterns between the B active enzymes GTB and AAGlyB on the one hand, and GTA on the other hand are observed for Leu^{336} and Leu^{339}. The peaks of these residues appear at similar positons in the apo state of GTB and AAGlyB, while the resonances of apo GTA are shifted relative to these positions. UDP-Glc/3DD or UDP/3DD binding induces significantly larger CSPs in GTA than in GTB or AAGlyB at this site. Yet these residues are located more than 10 Å away from any critical residue, discriminating between GTA and GTB, and even further away from the nucleotide sugar. As the chemical shifts of both residues show shared properties in GTB and AAGlyB, but different behaviors in GTA, Leu^{336} and Leu^{339} may sense dynamic effects involved in the UDP-Gal discrimination. Because of the hydrolysis of UDP-Gal, spectra recorded of GTA in presence of UDP-Gal and 3DD reveal only the UDP/3DD-bound state. Therefore, a direct comparison of the UDP-Gal/3DD bound states of all three enzymes is not possible. From crystal structures it is concluded that the selectivity of GTA against UDP-Gal may depend on the inability to stabilize the B-donor in a catalytically active conformation (Gagnon et al. 2015). Further experiments are needed to prove this hypothesis, but it is supported by the observations of the binary binding complexes described above.

5.2.6 Product release

UDP and B-trisaccharide represent the products of the transferase reaction catalyzed by GTB. The mechanism by which GTA and GTB release their reaction products is not resolved. Initial enzyme kinetic data proposed the Theorell-Chance mechanism that predicts only binary enzyme-substrate complexes (Kamath et al. 1999). This mechanism necessitates the release of UDP before the oligosaccharide product is formed. However, the authors admit that their data cannot fully rule out a simple ordered mechanism, in which a ternary binding complex comprising enzyme, donor and acceptor is allowed. In recent crystallographic studies, structures of the binary binding complexes comprising either GTB and UDP, or GTB and B-trisaccharide were generated (Gagnon et al. 2017). From a steric clash between the donated product sugar residue of the B-trisaccharide and the β-phosphate of the UDP donor in a superposition of both structures, the authors conclude that the products cannot simultaneously occupy the active site of GTB. They claim that their data provide evidence for the Theorell-Chance mechanism comprising only binary enzyme-substrate complexes.

This supports the double displacement mechanism, which, unlike the S_Ni mechanism, does not rely on the presence of UDP in the active site subsequent to the sugar transfer.

Protein observed NMR titrations with UDP and B-trisaccharide, partly contradict the conclusions of those studies. The CSP pattern induced by UDP and B-trisaccharide binding is identical to the CSP pattern induced by UDP and H-dis binding. This not only clearly proves that UDP and B-tris can and do occupy the active site of GTB at the same time, but also that GTB adopts the same protein conformation as in presence of UDP and H-dis. However, in contrast to the observed positive cooperativity between UDP and H-dis binding, between UDP and B-trisaccharide a negative cooperativity is identified. UDP binding to B-tris-saturated GTB is almost four times weaker than in the binary binding complex. This is reasonable, as it provides an avenue for an accessible active site in a further catalytic cycle. Interestingly, the on-rate of UDP binding to the B-tris-saturated enzyme is on the order of the on-rate to the H-dis-saturated enzyme. This indicates that in both cases a similarly high energetic barrier has to be overcome, which likely is the major conformational transition to the closed state. The off-rate of UDP from the ternary binding complex comprising the B-tris is, however, one order of magnitude faster than from the ternary binding complex comprising the H-dis. This likely correlates with the lifetime of the closed state, which is destabilized in presence of the B-tris.

The discrepancy between the proposed steric clash of UDP and B-tris, and the observed simultaneous binding of both ligands suggests that either UDP or B-tris adopts a conformation in the ternary binding complex that differs from the conformation in the binary binding complex. For instance, a reorientation of the β-phosphate of UDP would accompany a weakening of the interaction to the metal ion, which can explain the lower affinity in presence of the B-tris.

Mechanistic conclusions should be carefully evaluated. The observed simultaneous occupation of the active site by UDP and B-tris does not give any evidence for the Theorell-Chance or the double displacement mechanism. However, the data cannot disprove these mechanisms either. Structures of the ternary binding complex involving the donor substrate UDP-Gal and the acceptor analog 3DD, yet further question the Theorell-Chance mechanism. There is simply no structural justification that UDP has to leave the active site before the acceptor substrate can enter. Furthermore, the presence of the nucleotide is explicitly needed to reach the closed state, which is believed to be catalytically active. In summary, these considerations suggest that the enzyme undergoes a simpler “concentration-weighted” random sequential binding mechanism, where the donor sugar binds more likely before the acceptor substrate binds, and UDP is not necessarily released prior to acceptor binding and product release. Importantly, this is also in agreement with the initial enzyme kinetic data.

5.2.7 The role of the metal ion cofactor

The presence of a metal ion cofactor is mandatory for donor binding. Either Mg^{2+} or Ln^{3+} are utilized in the reported NMR studies. Lanthanides are rare earth metals with a low water solubility, and thus play

only minor roles in biology (Pol et al. 2014). Importantly, Ln^{3+} ions do not compete with Mg^{2+}/Mn^{2+} in humans. Therefore, the assembled system, consisting of GTB, UDP/Ln^{3+} and H-dis is highly artificial. Nevertheless, significant conclusions are drawn from the analysis of this complex. It is important to note that the choice of the metal ion influences the CSPs induced by UDP and H-dis binding. Significant differences are particularly observed in the internal disordered loop, indicating changes in its orientation in dependence of the metal ion. Also the C-terminus has to adopt a different conformation in presence of Ln^{3+} than reported in the crystal structures, as shown by the observed PCSs. All these findings suggest that the closed protein conformation is not reached, employing lanthanide ions as cofactors. However, binding of UDP/Ln^{3+} still occurs in the limit of slow chemical exchange. This contrasts with the observations from the GTB Trp^{181} mutants, where the destabilization of the closed state leads to a shift into the fast exchange regime. GTB potentially adopts an alternative conformation in presence of Ln^{3+}, where the cation-π interaction between Trp^{181} and Arg^{352} is still formed. However, it raises the question of the validity of the Mg^{2+}-mediated complexes, too. Since GTB shows significantly higher donor affinities and activities in presence of Mn^{2+} than Mg^{2+} (Blume et al. 2006; Sindhuwinata et al. 2013), it is obvious that differences between these metal ions exist. Yet, the strong paramagnetic character of Mn^{2+} precludes its usability in NMR-monitored ligand interaction studies. Calorimetric data show e.g. a ~18 times higher affinity of UDP in presence of Mn^{2+} than in presence of Mg^{2+} in the ternary binding complex with H-dis (Sindhuwinata et al. 2013). Trivially, this must be connected with shifts in the associated kinetics. A decrease of the off-rate (2.6 s^{-1}) by a factor of 18 means a lifetime of the ternary binding complex in the range of several seconds. Such long lifetimes are surely not anticipated in the cell. Therefore, Mg^{2+}, which shows >1000 times higher intracellular concentrations than Mn^{2+}, is potentially utilized as cofactor *in vivo*, too (Blume et al. 2006).

5.2.8 Comparison with LgtC NMR studies

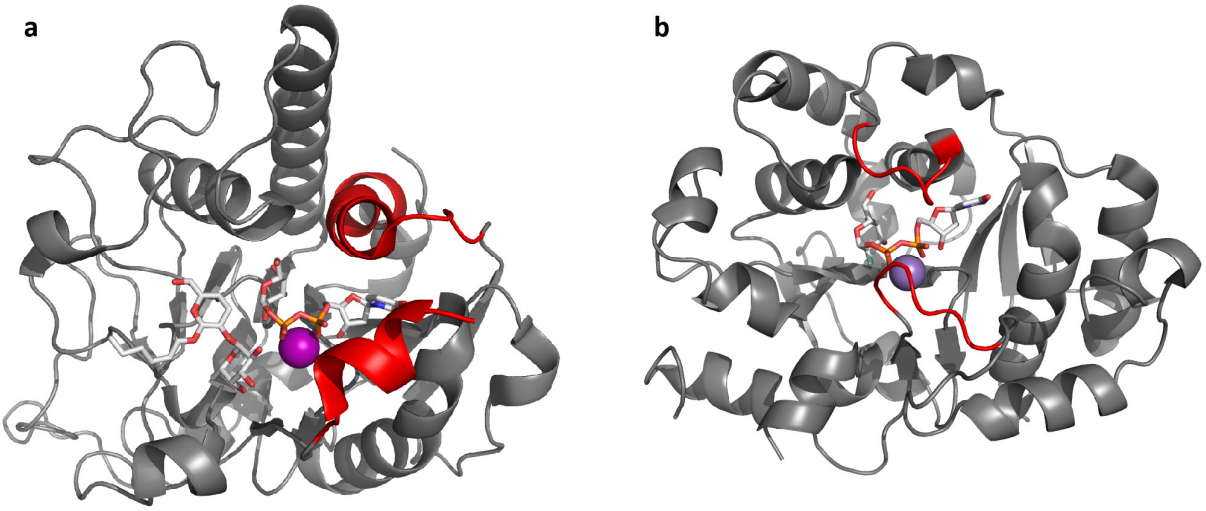


Figure 5.5: Comparison of crystal structures of GTB (**a**, PDB entry 2RJ7) and LgtC (**b**, 1G9R). (**a**) shows the ternary binding complex, comprising GTB, UDP-Gal/Mn^{2+} and 3DD. (**b**) shows LgtC in complex with UDP-2FGal/Mn^{2+}. Despite major structural differences, both enzymes employ two loop structures (highlighted in red) that shield the bound donor sugar from water.

Like GTB, the Lipooligosaccharide α-1,4-galactosyltransferase (LgtC) from *Neisseria meningitides* uses a retaining mechanism for the transfer of α-galactose from the sugar donor UDP-Gal. Yet the monomeric LgtC belongs to the GT family 8 (GTB: family 6), and consists of an N-terminal domain, containing the active site, and a C-terminal domain, mediating membrane attachment. Despite these structural differences, similar major states are proposed for LgtC and GTB, which are the open state in absence of the substrates, and the closed state, which LgtC reaches already in the binary binding complex with the nucleotide sugar (Persson et al. 2001). Furthermore, LgtC is a rare example of GTs, for which NMR data are available (Chan et al. 2012, 2013). As observed for GTB, Mg^{2+}/Mn^{2+} is required for the enzymatic activity, and binds simultaneously with the sugar nucleotide to LgtC (Chan et al. 2012). NMR-monitored titration experiments with UDP-2-deoxy-2-fluorogalactose (UDP-2FGal) reveal substrate binding in the slow-exchange regime, despite an only modest affinity in the range of ~20 µM. This reflects relatively slow on- and off-kinetics, and the authors deduce that conformational transitions are rate-limiting. The ligand interaction data of the human GTs allow similar conclusions.

Methyl-TROSY spectra of Ile-δ1 methyl-labeled LgtC in absence of ligands reveal two interchanging states for many of the labeled residues (Chan et al. 2013). The authors conclude that apo-LgtC exists in an equilibrium of open and closed states that interconvert on time scales of seconds. Binding of the donor sugar shifts the conformational equilibrium towards the closed state. Moreover, the subsequent binding of the acceptor substrate does not significantly perturb the conformation adopted in the binary complex. These observations contrast with the findings of the investigations of the human GTs. Methyl-

TROSY spectra recorded of GTB, GTA and AAGlyB in absence of the substrate reveal only one major state. Even at a low temperature of 275 K, only one set of signals is detected (Grimm et al. 2017). Therefore, LgtC and GTB (GTA) must follow different binding mechanisms. The LgtC data indicate a conformational selection mechanism with a pre-existing conformational isomerization in absence of the ligands. The observations of the human GTs rather suggest that the classical induced-fit mechanism applies, where conformational isomerization is only possible in presence of the ligands. However, the timescale of the transition between open and closed conformation is for both enzymes largely the same, and the interchange occurs in the range of high ms-s, respectively.

LgtC, which lacks an obvious nucleophile candidate, most likely follows a "front side attack" S_Ni mechanism (Lee et al. 2011). Methyl-TROSY relaxation dispersion experiments reveal an additional layer of dynamics in LgtC, which is correlated with movements of a catalytic loop containing the DXD motif. Importantly, these motions are damped in a covalent glycosyl-enzyme intermediate of an LgtC Q189E mutant, which suggests that the motions are linked with its enzymatic mechanism. In GTA/GTB Glu^{303} is identified as a potential nucleophile for a double displacement mechanism. However, Glu^{303} may also be involved in an S_Ni-like mechanism, or stabilize the transition state in an orthogonal associative reaction (Lairson et al. 2008; Schuman et al. 2013; Bobovská et al. 2015; Blackler et al. 2017). There is theoretical and experimental evidence for each of these mechanisms. The observation that LgtC and GTB follow different binding mechanisms support the idea that they may also exploit different enzymatic mechanisms. So far motions in the µs-ms time regime are not detected in GTA or GTB, employing Ile or Met residues as probes (Weissbach 2016; Grimm et al. 2017). The additional assignments of Ala, Leu and Val resonances will however allow more detailed investigations in the future.

6 Summary and Outlook

The analysis of high molecular weight systems by NMR spectroscopy remains a major challenge. The slow rotational tumbling and internal molecular dynamics hampered spectral backbone assignments of GTA and GTB in former studies (Sindhuwinata 2012; Grimm 2015; Weissbach 2016). These limitations have been overcome by an extensive exploitation of methyl labels as NMR active probes. The first part of this thesis summarizes a structure-guided assignment strategy, which makes use of state-of-the-art NMR techniques, such as 4D methyl-methyl NOESY experiments and paramagnetic NMR. Remarkably, the resonances of all Ala, Ile, Leu pro-S, Met and Val pro-S methyl groups in GTA and GTB were assigned. Therefore, the successful efforts deliver for the first time detailed site-specific dynamic insights into the glycosyltransferases. It is worth noting that the methyl groups of the analyzed amino acids are well distributed throughout the whole enzyme, including the active site and important structural domains like the internal disordered loop and the C-terminus. Therefore, an additional assignment of Thr methyl groups and of the remaining pro-R methyl groups of Leu and Val is certainly straightforward from the existing assignments, but will most likely not deliver significant extra information that is not provided by the assigned residues. However, labeling schemes for Thr and pro-R Leu/Val methyl groups are available and can be adapted to the glycosyltransferases (Proudfoot et al. 2016).

The assignment of the methyl groups is of course the most important achievement from the methyl-methyl NOESY and paramagnetic experiments. However, these experiments delivered also important structural insights into GTB. The intermolecular NOEs prove the exclusive existence of homodimers in solution. Furthermore, there is evidence for the orientation of the C-terminus in the open conformation of GTB, which is not observable in the crystal structures. PCSs suggest that the major orientation of the internal and C-terminal loop in presence of the lanthanides differs from the orientation in presence of Mg^{2+}. For further structural investigations, the 4D methyl-methyl NOESY experiment should be repeated with GTB adopting the closed conformation, e.g. in presence of saturating amounts of UDP/Mg^{2+} and H-dis. The presence of NOE correlations between key residues can prove the transition to the closed conformation. Covalent introduction of a lanthanide binding tag or binding of a lanthanide chelating ligand can deliver further structural restraints to improve the available models. Furthermore, it may be possible to derive backbone assignments on basis of the here reported $\Delta\chi$ tensors, when combined with datasets from a second paramagnetic center with alternative center position and tensor orientation.

The methyl group assignments are the basis for detailed functional analysis of the GTs by NMR-monitored ligand interaction studies. The line shape analysis and ZZ-exchange experiment deliver for the first time insights into the binding kinetics of donor and acceptor substrates. The large deviation of the on-rates from the limit of bimolecular diffusion-controlled interactions suggests that large energetic barriers have to be overcome. The observed CSPs indicate that ligand binding is intrinsically tied to conformational reorientations, which can be correlated with transitions between the major states

observed in crystal structures, too. Following this argumentation, the lifetime of the closed protein conformation can be estimated from the off-rates of the ligands from the ternary binding complex. The exchange between open and closed form of the enzyme is placed into the timescale of high milliseconds to seconds. This is an important result, as the lifetime of the closed state is on the order of the turnover rate, and may therefore be rate-limiting in the catalytic cycle. Remarkably, the single amino acid substitution of Trp^{181} with Met or Glu leads to significantly higher on- and off-rates, indicating that the process of ligand binding is largely decoupled from the conformational transitions in the enzyme. This is further supported by the observed CSP patterns that show significantly larger shifts in the relevant regions in wt GTB. Moreover, it indicates the catalytic importance of the cation-π interaction between Trp^{181} and Arg^{352}, which is further supported by the conservation of the two amino acids among different members of the GT family 6 (Flügge 2014).

The observation of a negative cooperativity between binding of the transferase products UDP and B-trisaccharide provides evidence for the product release mechanism. The one order of magnitude faster release of UDP in presence of B-tris than in presence of H-dis indicates a destabilization of the closed protein state. This supports the release of the ligands and provides an avenue for a free active site in a succeeding catalytic cycle. Furthermore, the findings also contradict a recently published hypothesis that UDP and B-trisaccharide cannot occupy the active site at the same time (Gagnon et al. 2017). The observation of the simultaneous binding of UDP and B-tris to GTB, adopting the closed protein state questions the proposed Theorell-Chance mechanism for substrate binding, which supports the double displacement enzymatic reaction mechanism.

In order to shine more light on the donor substrate discrimination mechanisms of the GTs, several binary and ternary binding complexes are analyzed. The data provide evidence that the discrimination between the epimers UDP-Gal and UDP-Glc can be attributed to a destabilization of the catalytically active closed conformation. This is supported by crystallographic data that show higher disorder in the internal and C-terminal loop in presence of UDP-Glc (Gagnon et al. 2015). The discrimination between UDP-Gal and UDP-GalNAc by GTB is mediated by a steric clash of the N-acetyl group with the critical residues Met^{266} and Ala^{268}. Because of the hydrolysis of UDP-GalNAc, there is only indirect evidence from UDP-GlcNAc complexes that the acetyl group prohibits the simultaneous binding of UDP-GalNAc and the acceptor oligosaccharide. Trivially, UDP-GlcNAc is discriminated against by the same mechanism in GTB.

Furthermore, significantly different kinetics can be observed between GTA, AAGlyB and GTB regarding donor analog binding. The differences can be partially attributed to the critical residue 176, which has been described to modulate the order of the internal loop in crystal structures. Moreover, this study shows that the size of the active site and the size of the ligand contribute to the lifetime of the bound state, too. Recent crystallographic studies have revealed different orientations of the sugar moiety of the nucleotide donor in the active sites of GTA and GTB (Gagnon et al. 2015). The sugar moiety is disordered in the wider active site of GTA, which likely enhances the entropic contribution to the Gibb's

free energy of binding. Importantly, the lifetime of UDP-Gal in the binary binding complex with AAGlyB is one order of magnitude longer than in complex with GTA. This may provide sufficient time for UDP-Gal to adopt the catalytically active tucked under conformation, and may explain the dual specificity of the AAGlyB chimeric enzyme. The enzymatic hydrolysis of the donor substrates UDP-Gal and UDP-GalNAc, which is accelerated in presence of the acceptor analog 3DD, partially hampered the determination of the ternary binding complexes. Therefore, direct comparisons between these complexes with GTA, AAGlyB and GTB are not available. This is certainly a major objective of future studies. Band-selective optimized flip angle short transient (SOFAST) HMQC experiments allow the recording of high quality spectra in a few seconds (Schanda et al. 2005; Amero et al. 2009). Alternatively, the proposed catalytic nucleophile Glu^{303} can be substituted with a non-nucleophilic residue like Ala. This may prevent not only the transferase reaction, but also the hydrolysis to take place. Moreover, such a mutant would be of interest as it allows the determination of intermolecular NOEs, and thus the distance between the anomeric proton of the sugar moiety and the methyl group of the introduced Ala residue.

The assignment of all $AIL^{proS}MV^{proS}$ methyl groups allows also more extensive investigations into further layers of molecular dynamics. Methyl-TROSY-based relaxation dispersion experiments focusing on Ile and Met residues revealed no significant dynamics in the µs-ms time regime (Weissbach 2016; Grimm et al. 2017). However, the higher occurrence of Ala, Leu and Val methyl groups in GTB will provide a more detailed view, representing all regions of the enzyme. Furthermore, chemical exchange saturation transfer (CEST) experiments can be exploited to probe for the closed protein state in absence of ligands (Bouvignies and Kay 2012; Vallurupalli et al. 2012, 2017; Long et al. 2013; Rennella et al. 2015), and stress the hypothesis, if GTB follows the induced-fit mechanism or the conformational-selection mechanism, which is observed for LgtC.

The GTs sample multiple conformations during their catalytic cycles. Ligand binding shifts the population of the conformations, and NMR CSPs are sensitive reporters of these changes. Relationships between different enzyme-ligand complexes and allosteric networks can be revealed by the CHEmical Shift Covariance Analysis (CHESCA) (Selvaratnam et al. 2011; Boulton et al. 2014). A systematic comparison of chemical shifts between two reference samples (e.g. active and inactive) and a perturbed sample (e.g. mutation) can be used to draw dynamics-function relationships in the CHEmical Shift Projection Analysis (CHESPA) (Selvaratnam et al. 2012; Akimoto et al. 2015). The COordiNated Chemical Shifts bEhavior (CONCISE) analysis allows the quantification of population shifts associated with ligand titrations (Cembran et al. 2014; Xu et al. 2017). On basis of the substantial amount of titration data, all of these statistical methods can be used to map the energetic landscapes of the GTs, revealing the information flow that drives the changes of populations of protein states.

In summary, this work provides detailed insights into the mode of substrate binding and the associated dynamics in human model glycosyltransferases. The assignment of all $AIL^{proS}MV^{proS}$ methyl groups provides an avenue for versatile prospective investigations by NMR spectroscopy. All of this will

contribute to understand the enzymatic mechanism, and allow the targeted modulation of glycosyltransferase activities *in vitro* and *in vivo*.

Appendix

Material and equipment

Tab. 1: List of devices

Autoclave	Laboklav	SHP Steriltechnik AG
Balances	Adventurer™	Ohaus
	KERN GJ 610-2M	Kern
	MC 210 S	Sartorius
Centrifuges	Ultracentrifuge, Rotor 45 Ti	Beckman Coulter
	Sorvall RC 5B Plus, Rotor GS3	Du Pont
	Universal 320 R	Hettich Zentrifugen
	Heraeus Pico 17	Thermo Scientific
	minispin	Eppendorf
	Centrifuge 5810	Eppendorf
	Centrifuge 5415D	Eppendorf
FPLC devices	ÄKTA purifier	GE Healthcare
	Column XK 16/20 + adaptor	Pharmacia Biotech
	Column XK 26/40 + adaptor	Pharmacia Biotech
	Detector Uvicord SII	Pharmacia Biotech
	Fraction collector SuperFrac™	Pharmacia Biotech
	Recorder Rec 112, Rec 10	Pharmacia Biotech
Electroporator	MicroPulser™	BioRad
French press cell disrupter	French-Pressure Cell Press, French Pressure Cell 40K, Rapid Fill Kit	Thermo IEC
Gel dryer	Model 543	Bio-Rad
Incubator	Innova 4330	New Brunswick Scientific
Liquid scintillation counter	Wallac 1409 Liquid Scintillation Counter	Wallac
Freeze-dryer	ALPHA 1-2 LD plus	Christ
NMR spectrometer	Bruker Avance III 500 with TCI cryogenic probe	Bruker
	Bruker Avance I 700 with TXI cryogenic probe	Bruker
	Utrecht NMR facility; 950 MHz NMR machine equipped with a cryogenic probe	Bruker
Peristaltic pump	Econo Pump	Bio-Rad
pH meter	pH 330	WTW
Photometer	MRX TC microplate reader	Dynex Technologies

	NanoDrop 1000	peqlab
	V550 UV/VIS	Jasco
Pipettes	Eppendorf Reference	Eppendorf
	Eppendorf Research	Eppendorf
Power supply	Power Pac 300	Bio-Rad
Ultra-pure water system	Ultra Clear	SG Wasseraufbereitung und Regenerierstation GmbH
Sample changer	SampleXpress	Bruker
SDS-PAGE devices	Mini-PROTEANÒ 3	Bio-Rad
Thermomixer	Thermomixer 5436 comfort	Eppendorf
	Thermomixer Thermostat 5320	
	Thermomixer Thermostat plus	
Vacuum chamber	Baker	J.T. Baker
Vacuum controller	B161	Büchi
Vacuum pump	Duo 5	Pfeiffer

Tab. 2: List of disposables

3 mm NMR tubes for Bruker MATCH holder	Hilgenberg
Amicon centrifugal ultrafilter (10.000 MWCO)	Millipore
Cannulas	B. Braun Melsungen
Cryo tube	Sarstedt
Cuvettes, disposable	Sarstedt
Durapore membrane, PVDF, 0.45 µm	Millipore
Dialysis cassettes, Slide-A-Lyzer, 10 kDa	Thermo Scientific
Electroporation Cuvettes Gene Pulser/MicroPulser	BioRad
Pipette tips, epT.I.P.S.	Eppendorf
Polyethylen vials and cap, 20 mL (for liquid scintillation counting)	Zinsser Analytic
Quick Change II Site-Directed Mutagenesis Kit	Agilent Technologies
Reaction tubes, 0.5 mL, 1.5 mL, 2 mL	Eppendorf
Rotilabo filter 0.22 µM (sterile)	Roth
Rotilabo filter 0.8 µM	Roth
Rotilabo microtest plate	Roth
Sep-Pak® Vac Rc (100mg) C18-Cartridges	Waters
SnakeSkin Pleated Dialysis Tubing (10.000 MWCO)	Pierce
SP Sepharose™ Fast Flow (FF)	GE Healthcare
Stericup® & Steritop™, 500 mL, 0.22 µM	Millipore
Syringes (sterile)	B. Braun Melsungen
Tube 15 ml (sterile)	Starstedt
Tube 50 ml (sterile)	Starstedt
UDP-hexanolamine-sepharose	W. Hellebrandt

Ultrafree®-MC Centrifugal Filter Devices, PVDF, 0.22 µm, 0.5 mL	Millipore
Vivaspin 500 filter unit (10.000 MWCO)	Satorius, stedim biotech
ZelluTrans Mini-Dialyzer (12.000 MWCO)	Roth

Chemicals

Tab. 3: List of chemicals

2-Keto-4-^{13}C-butyrate	CortecNet
2-Keto-3-(methyl-d_3)-3-d-4-^{13}C butanoate	Euriso-Top
2-mercaptoethanol	Sigma-Aldrich
2-propanol	Merck, Roth
3DD (α-L-Fuc*p*-(1→2)-3-deoxy-β-D-Gal*p*-O-octyl)	W. Hellebrandt
Ammonium chloride ($^{15}NH_4Cl$, 99 % ^{15}N)	Euriso-Top
Ammonium chloride (NH_4Cl)	Merck
Ammonium sulfate ($(^{15}NH_4)_2SO_4$ 99% ^{15}N)	Euriso-Top
Ampicillin sodium salt	Gerbu
Bis-tris-d_{19}	Sigma-Aldrich
BME vitamin mix (100 x)	Sigma-Aldrich
Bradford reagent Bio-Rad Protein Assay	Bio-Rad
Bromphenolblue	Sigma-Aldrich
Calciumchloride dihydrate ($CaCl_2$ x 2 H_2O)	Merck
Carbenicillin disodium salt	Sigma-Aldrich
Casamino acids	Merck
Cerium(III) chloride, anhydrous ($CeCl_3$)	Sigma-Aldrich
Choline chloride	Fluka
D-Biotin (Vitamin B7, Vitamin H)	Sigma-Aldrich
Deuterium oxide (D_2O) 100 % (99,97 % d)	Euriso-Top
Deuterium oxide (D_2O) 99,85 %	Euriso-Top, CoretecNet
DLAM-LV^{ProS}	NMR-BIO
(2-Hydroxy-2-(^{13}C-methyl)-3-oxo-4-d_3 butanoate)	
D-(+)Glucose	Merck
D-Glucose-d7 (98 % 1,2,3,4,5,6,6 d7)	Sigma-Aldrich, Euriso-Top
Disodium hydrogen phosphate (Na_2HPO_4)	Merck
Disodium hydrogen phosphate dihydrate	Merck
(Na_2HPO_4 x 2 H_2O)	
DMSO	Merck
D-Pantothenic acid hemicalcium salt (Vitamin B5)	Sigma-Aldrich
DSS-d_6	Sigma-Aldrich
(2,2-dimethyl-2-silapentane-d_6-5-sulfonic acid sodium salt)	
DTT	Gerbu
EDTA disodium salt dihydrate	Roth

Ethanol	Roth
Ethanol, denatured	Büfa Chemikalien
Europium(III) chloride, anhydrous ($EuCl_3$)	Sigma-Aldrich
Folic acid (Vitamin B9, Vitamin B11, Vitamin M)	Sigma-Aldrich
GelCode® Blue Stain Reagent	Pierce
Glycerin	Roth
Glycine	Merck, Sigma-Aldrich
H-dis-octyl (α-L-Fuc*p*-(1→2)-β-D-Gal*p*-O-octyl)	W. Hellebrandt
H-trisaccharides type I-VI	P. Melloncelli, T. Lowary
IPTG	Gerbu
L-alanine-3-^{13}C-2-d	Sigma-Aldrich
L-leucine-d_{10}	CIL
L-methionine (99 % methyl ^{13}C)	Euriso-Top
Lanthanum(III) chloride, anhydrous ($LaCl_3$)	Sigma-Aldrich
Magnesium chloride hexahydrate ($MgCl_2$ x 6 H_2O)	Merck, Roth
Magnesium sulfate heptahydrate ($MgSO_4$ x 7 H_2O)	Merck
Manganese (II) chloride tetrahydrate ($MnCl_2$ x 4 H_2O)	Merck
Methanol	Büfa Chemikalien
Monopotassium phosphate (KH_2PO_4)	Merck, Roth
Monosodium phosphate dihydrate (NaH_2PO_4 x 2 H_2O)	Merck
MOPS	Gerbu
Myo-inositol	Sigma-Aldrich
Nicotinamide	Sigma-Aldrich
Praseodymium(III) chloride, anhydrous ($PrCl_3$)	Sigma-Aldrich
Protease inhibitor tablets, cOmplete, EDTA-free	Roche Diagnostics
Protein standard bovine gamma globulin	Pierce
Protein standard SDS-PAGE Molecular Weight Standards, Low Range	Bio-Rad
Pyridoxal hydrochloride	Sigma-Aldrich
Riboflavin (Vitamin B2)	Sigma-Aldrich
Rotiphorese® Gel 30 (Acrylamide:Bis-Acrylamide 37.5:1)	Roth
Succinate-d_4	CIL
SDS	Serva, Sigma-Aldrich
Sodium chloride (NaCl)	Merck, Roth
Sodium hydroxide (NaOH)	Merck
SP-Sepharose™ Fast Flow	Amersham Biosciences
Szinti Mix Aquasafe 800	Zinsser Analytik
TEMED	Sigma-Aldrich

Thiamine hydrochloride (Vitamin B_1 hydrochloride)	Sigma-Aldrich
Tris	Merck, Roth
Tris(2-carboxyethyl)phosphine-d_{16} (TCEP)	Euriso-Top
Tryptone (from casein, pancreatic digested)	MP Biomedicals, Roth
UDP disodium salt	Sigma-Aldrich
UDP hexanolamine sepharose	W. Hellebrandt
UDP-u-^{14}C-α-D-galactose lithium salt	Amersham Biosciences
UDP-u-^{14}C-N-acetyl-α-D-galactosamine lithium salt	ARC
UDP-α-D-galactose disodium salt	B. Ernst
UDP-α-D-Glucose	Sigma-Aldrich
UDP-N-acetyl-α-D-galactosamine disodium salt	Sigma-Aldrich
UDP-N-acetyl-α-D-glucosamine disodium salt	Sigma-Aldrich
Urea	GERBU
Vitamin B_{12} (Cyanocobalamine)	Sigma-Aldrich
Yeast extract SERVAbacter®	Serva

Chemical shifts of methyl resonances of GTA

Tab. 4: ^{1}H and ^{13}C chemical shifts of all assigned methyl groups of apo-GTA in a 2D [^{13}C^{1}H]-HMQC spectrum. The spectrum is recorded in D_2O phosphate NMR buffer at pH* 6.8 and 298 K. The chemical shifts are referenced with DSS-d_6.

sequence position	residue type	methyl position	1H (ppm)	13C (ppm)
58	Ala	beta	1.54	19.44
59	Ile	delta1	0.70	12.61
63	Met	epsilon	2.11	17.96
64	Val	gamma2	0.90	19.46
66	Leu	delta2	0.82	23.37
69	Met	epsilon	2.09	17.01
70	Val	gamma2	0.67	19.86
76	Val	gamma2	1.63	25.82
77	Leu	delta2	1.11	22.57
84	Val	gamma2	-0.89	14.63
85	Leu	delta2	0.98	25.30
86	Val	gamma2	0.97	20.22
87	Val	gamma2	1.01	20.58
91	Leu	delta2	1.03	22.50
92	Ala	beta	1.22	20.54
94	Ile	delta1	0.65	13.30
95	Val	gamma2	0.59	21.02
102	Ile	delta1	1.22	15.27
104	Ile	delta1	0.35	13.40

sequence position	residue type	methyl position	1H (ppm)	13C (ppm)
105	Leu	delta2	1.10	23.33
111	Leu	delta2	0.92	22.42
116	Ile	delta1	0.69	17.16
118	Leu	delta2	0.47	24.95
120	Val	gamma2	0.47	19.84
122	Ala	beta	1.09	19.62
123	Ile	delta1	0.91	12.60
127	Val	gamma2	1.00	20.18
128	Ala	beta	1.14	18.62
130	Leu	delta2	0.80	24.73
132	Leu	delta2	0.96	25.57
134	Leu	delta2	0.15	20.94
137	Ala	beta	1.26	18.16
142	Met	epsilon	1.21	19.95
143	Val	gamma2	0.67	21.96
147	Val	gamma2	0.78	23.84
151	Val	gamma2	0.75	20.12
157	Ala	beta	1.39	18.17
158	Ala	beta	1.43	19.47
159	Val	gamma2	1.03	22.50
162	Val	gamma2	0.78	19.92
164	Leu	delta2	0.70	22.51
170	Leu	delta2	0.71	25.43
172	Val	gamma2	0.91	22.15
173	Leu	delta2	0.38	23.82
175	Val	gamma2	0.80	19.31
177	Ala	beta	1.30	18.92
184	Val	gamma2	0.95	22.01
186	Met	epsilon	1.89	16.83
189	Met	epsilon	1.81	17.87
191	Met	epsilon	2.14	18.32
192	Ile	delta1	1.03	13.52
201	Leu	delta2	0.88	24.17
204	Val	gamma2	0.73	18.89
207	Leu	delta2	0.45	25.87
208	Val	gamma2	1.06	21.27
210	Val	gamma2	0.82	20.19
212	Val	gamma2	0.70	22.51
214	Met	epsilon	1.24	17.38
220	Val	gamma2	1.34	22.45
222	Val	gamma2	0.54	18.62
224	Ile	delta1	0.40	13.45
225	Leu	delta2	0.08	19.87
228	Leu	delta2	0.95	26.38
232	Leu	delta2	0.34	23.43

sequence position	residue type	methyl position	1H (ppm)	13C (ppm)
243	Ala	beta	1.54	19.44
254	Ala	beta	0.41	16.41
256	Ile	delta1	-0.29	10.37
266	Leu	delta2	0.72	23.17
274	Val	gamma2	0.83	23.80
277	Val	gamma2	0.96	23.87
280	Leu	delta2	0.25	25.05
283	Ala	beta	1.67	18.87
287	Ala	beta	1.55	19.90
288	Met	epsilon	1.54	19.44
289	Met	epsilon	1.96	17.10
290	Val	gamma2	1.03	22.50
293	Ala	beta	1.56	17.52
296	Ile	delta1	0.60	13.52
298	Ala	beta	1.37	19.46
299	Val	gamma2	0.71	19.54
306	Leu	delta2	0.63	26.92
310	Leu	delta2	0.82	22.85
311	Leu	delta2	0.81	27.28
318	Val	gamma2	1.14	22.20
319	Leu	delta2	-0.30	20.28
324	Leu	delta2	0.99	27.79
329	Leu	delta2	0.74	23.90
330	Leu	delta2	0.72	22.03
334	Ala	beta	1.39	18.17
335	Val	gamma2	0.80	20.30
336	Leu	delta2	0.11	22.98
339	Leu	delta2	-0.12	23.00
343	Ala	beta	1.19	19.04
344	Val	gamma2	0.85	20.84
350	Ala	beta	1.38	19.10
351	Val	gamma2	0.91	20.37

Chemical shifts of methyl resonances of GTB

Tab. 5: ^{1}H and ^{13}C chemical shifts of all assigned methyl groups of apo-GTB in a 2D [$^{13}C^{1}H$]-HMQC spectrum. Tentatively assigned residues are labeled with a question mark. The spectrum is recorded in D_2O phosphate NMR buffer at pH* 6.8 and 298 K. The chemical shifts are referenced with DSS-d_6.

sequence position	residue type	methyl position	tentative	^{1}H (ppm)	^{13}C (ppm)
58	Ala	beta		1.54	19.45
59	Ile	delta1		0.70	12.60

sequence position	residue type	methyl position	tentative	^{1}H (ppm)	^{13}C (ppm)
63	Met	epsilon		2.11	17.96
64	Val	gamma1	?	0.90	21.55
64	Val	gamma2		0.90	19.46
66	Leu	delta1	?	0.82	26.90
66	Leu	delta2		0.82	23.34
69	Met	epsilon		2.09	17.06
70	Val	gamma1		-	-
70	Val	gamma2		0.67	19.87
76	Val	gamma1		1.47	22.47
76	Val	gamma2		1.63	25.73
77	Leu	delta1	?	1.13	25.29
77	Leu	delta2		1.13	22.60
84	Val	gamma1		-0.22	22.16
84	Val	gamma2		-0.90	14.59
85	Leu	delta1		1.36	23.37
85	Leu	delta2		0.97	25.31
86	Val	gamma1		0.88	22.05
86	Val	gamma2		0.96	20.25
87	Val	gamma1	?	1.03	20.42
87	Val	gamma2		1.00	20.54
91	Leu	delta1		-	-
91	Leu	delta2		1.03	22.52
92	Ala	beta		1.22	20.57
94	Ile	delta1		0.65	13.30
95	Val	gamma1		0.79	22.97
95	Val	gamma2		0.58	21.03
102	Ile	delta1		1.21	15.26
104	Ile	delta1		0.34	13.39
105	Leu	delta1		0.90	27.05
105	Leu	delta2		1.10	23.28
111	Leu	delta1		-	-
111	Leu	delta2		0.91	22.42
116	Ile	delta1		0.69	17.15
118	Leu	delta1		0.45	24.58
118	Leu	delta2		0.52	24.95
120	Val	gamma1		0.45	21.18
120	Val	gamma2		0.45	20.22
122	Ala	beta		1.08	19.66
123	Ile	delta1		0.85	12.58
127	Val	gamma1		-	-
127	Val	gamma2		0.99	20.19
128	Ala	beta		1.15	18.61
130	Leu	delta1		-	-
130	Leu	delta2		0.80	24.81
132	Leu	delta1	?	1.05	23.53

sequence position	residue type	methyl position	tentative	^{1}H (ppm)	^{13}C (ppm)
132	Leu	delta2		0.95	25.50
134	Leu	delta1	?	0.63	25.45
134	Leu	delta2		0.15	20.93
137	Ala	beta		1.24	18.08
142	Met	epsilon		1.21	19.95
143	Val	gamma1		-	-
143	Val	gamma2		0.67	21.96
147	Val	gamma1	?	0.24	19.76
147	Val	gamma2		0.76	23.80
151	Val	gamma1	?	0.76	21.50
151	Val	gamma2		0.75	20.17
157	Ala	beta		1.39	18.03
158	Ala	beta		1.43	19.44
159	Val	gamma1		-	-
159	Val	gamma2		1.03	22.52
162	Val	gamma1	?	0.93	22.99
162	Val	gamma2		0.78	19.90
164	Leu	delta1		-	-
164	Leu	delta2		0.70	22.53
170	Leu	delta1		0.72	26.25
170	Leu	delta2		0.71	25.44
172	Val	gamma1		-	-
172	Val	gamma2		0.91	22.13
173	Leu	delta1	?	0.07	24.72
173	Leu	delta2		0.39	23.96
175	Val	gamma1	?	1.03	22.03
175	Val	gamma2		0.86	19.23
177	Ala	beta		1.29	18.77
184	Val	gamma1		-	-
184	Val	gamma2		0.85	21.71
186	Met	epsilon		1.93	16.99
189	Met	epsilon		1.80	17.87
191	Met	epsilon		2.11	17.96
192	Ile	delta1		1.01	13.38
201	Leu	delta1		-	-
201	Leu	delta2		0.88	24.15
204	Val	gamma1		-	-
204	Val	gamma2		0.74	18.93
207	Leu	delta1	?	0.40	24.32
207	Leu	delta2		0.48	26.12
208	Val	gamma1		-	-
208	Val	gamma2		1.08	21.22
210	Val	gamma1	?	0.21	21.75
210	Val	gamma2		0.83	20.18
212	Val	gamma1		-	-

sequence position	residue type	methyl position	tentative	^{1}H (ppm)	^{13}C (ppm)
212	Val	gamma2		0.74	22.40
214	Met	epsilon		1.13	17.07
220	Val	gamma1		1.27	21.58
220	Val	gamma2		1.34	22.55
222	Val	gamma1		-0.21	19.34
222	Val	gamma2		0.53	18.57
224	Ile	delta1		0.39	13.61
225	Leu	delta1	?	-0.24	25.04
225	Leu	delta2		0.08	19.84
228	Leu	delta1	?	1.01	22.16
228	Leu	delta2		0.94	26.37
232	Leu	delta1		0.64	25.96
232	Leu	delta2		0.35	23.30
243	Ala	beta		1.51	19.31
254	Ala	beta		0.45	16.49
256	Ile	delta1		-0.29	10.43
266	Met	epsilon		1.89	18.45
268	Ala	beta		1.53	21.56
274	Val	gamma1		-	-
274	Val	gamma2		0.83	23.83
277	Val	gamma1		-	-
277	Val	gamma2		0.96	23.85
280	Leu	delta1		0.49	27.64
280	Leu	delta2		0.27	25.07
283	Ala	beta		1.66	18.89
287	Ala	beta		1.53	19.87
288	Met	epsilon		2.12	17.69
289	Met	epsilon		1.92	16.86
290	Val	gamma1		-	-
290	Val	gamma2		1.03	22.52
293	Ala	beta		1.56	17.52
296	Ile	delta1		0.60	13.49
298	Ala	beta		1.37	19.41
299	Val	gamma1		1.05	19.48
299	Val	gamma2		0.72	19.51
306	Leu	delta1		0.25	24.93
306	Leu	delta2		0.62	26.48
310	Leu	delta1	?	-0.12	24.72
310	Leu	delta2		0.82	22.79
311	Leu	delta1		-	-
311	Leu	delta2		0.80	27.29
318	Val	gamma1		-	-
318	Val	gamma2		1.14	22.17
319	Leu	delta1		-0.43	23.12
319	Leu	delta2		-0.32	20.21

sequence position	residue type	methyl position	tentative	^{1}H (ppm)	^{13}C (ppm)
324	Leu	delta1		-	-
324	Leu	delta2		1.01	25.78
329	Leu	delta1		-	-
329	Leu	delta2		0.71	23.86
330	Leu	delta1		-0.10	24.99
330	Leu	delta2		0.70	22.04
334	Ala	beta		1.38	18.19
335	Val	gamma1		0.90	19.67
335	Val	gamma2		0.81	20.64
336	Leu	delta1		-0.70	23.82
336	Leu	delta2		0.26	23.06
339	Leu	delta1		-0.30	24.86
339	Leu	delta2		-0.19	23.08
343	Ala	beta		1.20	19.03
344	Val	gamma1		-	-
344	Val	gamma2		0.84	20.78
350	Ala	beta		1.37	19.09
351	Val	gamma1		-	-
351	Val	gamma2		0.90	20.39

Chemical shifts of methyl resonances of AAGlyB

Tab. 6: ^{1}H and ^{13}C chemical shifts of all assigned methyl groups of apo-AAGlyB in a 2D [^{13}C^{1}H]-HMQC spectrum. The spectrum is recorded in D_2O phosphate NMR buffer at pH* 6.8 and 298 K. The chemical shifts are referenced with DSS-d_6.

sequence position	residue type	methyl position	^{1}H (ppm)	^{13}C (ppm)
58	Ala	beta	1.54	19.42
59	Ile	delta1	0.69	12.60
63	Met	epsilon	2.11	18.02
64	Val	gamma2	0.90	19.46
66	Leu	delta2	0.82	23.35
69	Met	epsilon	2.09	17.02
70	Val	gamma2	0.67	19.86
76	Val	gamma2	1.66	25.86
77	Leu	delta2	1.13	22.56
84	Val	gamma2	-0.89	14.59
85	Leu	delta2	0.98	25.32
86	Val	gamma2	0.97	20.32
87	Val	gamma2	1.02	20.60
91	Leu	delta2	1.03	22.58
92	Ala	beta	1.22	20.45
94	Ile	delta1	0.65	13.34

sequence position	residue type	methyl position	^{1}H (ppm)	^{13}C (ppm)
95	Val	gamma2	0.60	21.03
102	Ile	delta1	1.22	15.24
104	Ile	delta1	0.36	13.38
105	Leu	delta2	1.10	23.26
111	Leu	delta2	0.92	22.43
116	Ile	delta1	0.69	17.17
118	Leu	delta2	0.55	24.99
120	Val	gamma2	0.45	20.37
122	Ala	beta	1.10	19.76
123	Ile	delta1	0.92	12.70
127	Val	gamma2	1.00	20.25
128	Ala	beta	1.15	18.62
130	Leu	delta2	0.81	24.73
132	Leu	delta2	0.94	25.51
134	Leu	delta2	0.18	20.96
137	Ala	beta	1.25	18.08
142	Met	epsilon	1.21	19.97
143	Val	gamma2	0.67	21.91
147	Val	gamma2	0.77	23.79
151	Val	gamma2	0.76	20.19
157	Ala	beta	1.39	18.04
158	Ala	beta	1.43	19.42
159	Val	gamma2	1.03	22.58
162	Val	gamma2	0.78	19.87
164	Leu	delta2	0.70	22.57
170	Leu	delta2	0.71	25.45
172	Val	gamma2	0.90	22.12
173	Leu	delta2	0.35	23.96
175	Val	gamma2	0.81	19.37
177	Ala	beta	1.30	18.95
184	Val	gamma2	0.96	22.04
186	Met	epsilon	1.90	16.86
189	Met	epsilon	1.79	17.93
191	Met	epsilon	2.17	18.28
192	Ile	delta1	0.99	13.46
201	Leu	delta2	0.88	24.13
204	Val	gamma2	0.73	18.91
207	Leu	delta2	0.47	26.03
208	Val	gamma2	1.07	21.27
210	Val	gamma2	0.84	20.44
212	Val	gamma2	0.74	22.34
214	Met	epsilon	1.15	17.15
220	Val	gamma2	1.35	22.54
222	Val	gamma2	0.54	18.53
224	Ile	delta1	0.39	13.70

sequence position	residue type	methyl position	^{1}H (ppm)	^{13}C (ppm)
225	Leu	delta2	0.07	19.84
228	Leu	delta2	0.94	26.35
232	Leu	delta2	0.36	23.52
243	Ala	beta	1.54	19.42
254	Ala	beta	0.41	16.37
256	Ile	delta1	-0.31	10.31
268	Ala	beta	1.52	21.58
274	Val	gamma2	0.83	23.80
277	Val	gamma2	0.96	23.82
280	Leu	delta2	0.31	25.08
283	Ala	beta	1.67	18.83
287	Ala	beta	1.56	19.88
288	Met	epsilon	?	?
289	Met	epsilon	1.96	17.07
290	Val	gamma2	1.03	22.58
293	Ala	beta	1.56	17.51
296	Ile	delta1	0.59	13.50
298	Ala	beta	1.37	19.46
299	Val	gamma2	0.69	19.49
306	Leu	delta2	0.62	26.39
310	Leu	delta2	0.82	22.77
311	Leu	delta2	0.80	27.26
318	Val	gamma2	1.16	22.39
319	Leu	delta2	-0.27	20.31
324	Leu	delta2	0.91	25.28
329	Leu	delta2	0.72	23.95
330	Leu	delta2	0.71	21.99
334	Ala	beta	1.38	18.19
335	Val	gamma2	0.82	20.88
336	Leu	delta2	0.25	22.98
339	Leu	delta2	-0.21	23.10
343	Ala	beta	1.23	19.10
344	Val	gamma2	0.84	20.69
350	Ala	beta	1.38	19.13
351	Val	gamma2	0.90	20.40

NOE correlations

Tab. 7: List of NOE peak positions in the 4D methyl-methyl NOESY spectrum recorded with AIL^{proS}MV^{proS} methyl-labeled GTB in D_2O phosphate NMR buffer at 950 MHz ^{1}H frequency and 298 K. This list is the basis for the automated assignment using *MAP-XSII*.

^{1}H (ppm)	^{13}C (ppm)	^{1}H (ppm)	^{13}C (ppm)
0.81	27.40	-0.28	10.30

^{1}H (ppm)	^{13}C (ppm)	^{1}H (ppm)	^{13}C (ppm)
1.94	16.88	0.86	12.59
2.10	17.97	0.86	12.48
0.87	19.25	0.86	12.40
2.11	17.89	0.70	12.46
1.54	19.38	0.70	12.52
1.64	25.81	0.66	13.22
0.98	25.40	0.66	13.23
1.23	20.77	0.68	13.26
1.01	20.39	0.68	13.31
1.14	22.46	0.68	13.34
1.15	22.23	0.66	13.07
1.80	17.88	1.02	13.30
0.50	26.15	1.02	13.33
2.13	17.84	1.03	13.32
2.09	17.02	0.35	13.34
1.22	19.94	0.40	13.58
0.69	17.03	0.40	13.57
0.09	19.77	0.40	13.62
-0.30	20.30	0.39	13.54
1.13	22.63	-0.92	14.48
0.82	20.82	-0.91	14.59
0.97	20.25	-0.91	14.58
0.54	18.60	1.23	15.25
1.10	23.28	1.24	15.25
-0.28	10.36	0.45	16.53
1.38	19.40	0.46	16.48
1.54	19.91	0.46	16.44
1.93	17.00	0.46	16.42
2.13	17.63	1.95	16.95
1.80	17.87	1.96	16.95
0.85	12.44	1.95	16.94
1.57	17.57	1.95	16.97
1.54	19.88	1.96	16.99
1.04	22.51	1.95	16.89
0.35	13.30	2.11	17.01
0.83	23.41	2.11	17.04
1.90	18.40	1.15	17.03
1.54	21.59	1.15	17.00
1.20	19.01	1.15	17.06
0.84	20.78	1.12	17.15
1.02	25.85	1.15	17.03
0.40	13.40	0.69	17.19
1.22	19.93	0.69	17.11
1.93	16.93	1.58	17.53
1.03	22.49	1.58	17.54
1.93	16.96	2.14	17.64

^{1}H (ppm)	^{13}C (ppm)	^{1}H (ppm)	^{13}C (ppm)
1.80	17.85	2.15	17.62
1.54	19.84	2.11	17.73
1.02	13.28	2.13	17.87
0.95	26.47	2.13	17.93
0.28	25.17	2.15	17.72
1.01	13.31	1.82	17.84
0.28	25.15	1.81	17.89
0.62	26.54	1.81	17.90
2.13	17.60	1.82	17.88
1.94	16.99	1.81	17.88
0.85	12.52	2.13	17.94
0.70	12.58	2.13	17.90
0.90	19.45	2.14	17.93
1.43	19.48	1.40	17.96
0.16	20.93	1.26	18.01
0.53	25.06	1.25	18.01
0.81	20.71	1.41	18.25
1.13	17.03	1.91	18.46
1.54	21.58	1.91	18.44
1.20	18.98	1.91	18.52
1.02	25.85	1.91	18.43
0.99	20.19	1.16	18.58
0.91	20.37	1.16	18.55
1.43	19.50	1.16	18.65
1.22	15.23	0.54	18.58
2.11	17.95	1.68	18.91
1.54	19.74	1.68	18.94
0.83	23.98	0.74	18.91
0.48	26.17	0.75	18.93
1.14	17.01	1.21	18.98
1.90	18.35	1.20	18.99
1.53	21.56	1.20	18.92
1.02	25.83	1.20	18.96
0.85	20.89	1.20	18.96
0.90	20.46	1.39	19.06
0.95	25.53	1.38	19.09
0.85	12.51	0.88	19.20
2.11	17.97	0.89	19.36
0.70	12.55	1.57	19.51
2.11	17.93	1.56	19.54
0.45	16.48	1.39	19.45
0.60	13.37	1.39	19.36
1.93	17.01	1.39	19.34
2.13	17.72	1.38	19.39
1.15	18.58	1.44	19.42
1.09	19.67	1.44	19.52

^{1}H (ppm)	^{13}C (ppm)	^{1}H (ppm)	^{13}C (ppm)
0.99	20.21	1.44	19.48
1.03	22.63	1.45	19.47
1.00	20.33	1.38	17.90
1.40	17.96	1.45	19.48
2.11	17.93	0.91	19.50
0.83	23.42	0.92	19.51
0.45	20.22	1.10	19.63
0.81	24.89	1.10	19.65
0.74	22.49	1.10	19.61
1.00	20.21	1.10	19.63
1.42	19.54	1.10	19.72
0.85	12.41	1.09	19.67
0.75	20.27	1.07	19.91
1.66	18.87	1.55	19.89
1.93	16.97	1.54	19.88
2.13	17.67	1.55	19.82
1.37	19.34	1.54	19.97
0.69	17.00	0.08	19.89
1.21	19.91	0.08	19.89
2.09	17.02	0.69	19.90
0.16	20.91	0.77	20.07
1.25	18.13	0.78	19.87
0.72	25.50	0.78	20.05
0.70	22.57	0.78	19.92
0.69	17.05	1.22	19.93
0.40	13.59	1.22	19.91
0.08	19.81	1.21	19.95
1.08	21.21	1.22	19.95
1.43	19.46	1.02	20.28
1.15	18.57	1.00	20.21
1.09	19.67	1.01	20.24
1.04	22.54	1.01	20.52
0.52	25.11	0.86	20.22
0.45	20.23	0.78	20.25
0.76	20.18	0.45	20.21
1.09	19.65	0.45	20.23
0.81	24.87	0.45	20.26
0.53	25.01	0.45	20.24
0.74	22.46	0.45	20.26
1.25	18.03	0.53	25.05
0.84	20.17	0.54	25.10
0.45	20.23	0.53	25.08
0.59	21.02	-0.31	20.20
0.39	13.39	-0.30	20.23
1.38	19.12	0.92	20.45
1.14	22.21	1.24	20.56

^{1}H (ppm)	^{13}C (ppm)	^{1}H (ppm)	^{13}C (ppm)
2.11	17.93	1.23	20.57
0.66	13.22	1.23	20.63
0.66	13.18	1.02	20.48
0.27	23.18	0.81	20.69
-0.89	14.54	0.82	20.58
1.13	22.61	0.82	20.60
1.39	18.19	0.82	20.60
0.95	25.60	0.84	20.83
1.14	17.12	0.86	20.83
-0.31	20.28	0.58	20.98
1.25	18.03	0.15	20.92
0.78	19.96	0.16	21.01
1.22	19.91	1.10	21.27
0.40	13.45	1.06	21.30
1.90	18.42	1.55	21.58
1.13	17.04	1.55	21.57
1.02	25.85	1.56	21.58
2.09	17.92	0.86	21.74
0.85	12.43	0.87	21.80
1.93	16.96	0.88	21.84
0.86	19.20	0.86	21.84
0.87	21.86	0.89	19.28
0.86	21.75	0.85	12.38
0.71	23.91	0.69	22.12
0.72	25.49	0.92	22.16
1.02	22.65	0.93	22.16
1.23	20.59	1.16	22.19
0.35	23.33	1.15	22.22
0.66	13.24	1.15	22.20
1.09	19.62	0.74	22.45
0.78	19.89	0.71	22.56
0.45	20.24	0.74	22.47
0.81	24.86	0.74	22.53
1.24	18.02	0.72	22.56
0.81	20.63	1.14	22.63
1.93	16.87	1.04	22.50
1.57	17.52	1.05	22.48
1.43	19.54	1.03	22.60
1.02	22.69	1.11	19.58
1.09	19.77	1.03	22.76
0.99	20.20	1.03	22.54
0.72	25.47	1.04	22.61
1.03	22.57	0.72	25.46
0.91	22.19	0.73	25.53
0.78	19.93	0.72	25.48
0.75	20.19	0.72	25.50

^{1}H (ppm)	^{13}C (ppm)	^{1}H (ppm)	^{13}C (ppm)
0.92	22.47	0.91	19.51
0.90	19.54	0.93	22.53
0.82	23.36	0.93	22.59
2.11	17.93	0.82	22.87
0.81	20.63	0.27	23.17
-0.18	23.16	0.27	23.12
0.26	23.13	-0.20	23.22
1.22	15.28	1.11	23.42
0.54	18.59	1.11	23.37
2.09	17.03	0.83	23.40
0.90	19.54	0.83	23.46
0.35	13.32	1.11	23.35
0.66	13.23	0.36	23.39
1.64	25.88	0.35	23.42
1.15	22.26	0.34	23.39
0.48	26.19	1.00	23.86
0.83	23.85	1.01	23.87
0.97	23.84	0.81	23.88
0.48	26.16	0.83	23.85
0.75	18.90	0.84	23.88
0.70	22.10	0.71	23.85
1.09	19.66	0.82	24.84
1.03	22.60	0.83	24.81
1.44	19.53	0.83	24.81
0.99	20.25	0.83	24.97
0.45	20.22	0.81	24.85
1.80	17.89	0.27	25.11
2.12	17.85	0.28	25.16
0.97	23.78	0.30	25.43
0.66	13.28	0.98	25.43
1.64	25.80	0.98	25.42
0.84	20.82	0.96	25.57
1.38	19.14	0.97	25.54
1.90	18.45	1.02	25.85
1.14	16.99	1.02	25.84
1.54	21.55	1.04	25.79
1.21	18.90	1.02	25.86
0.98	25.41	1.67	25.77
0.66	13.25	1.66	25.81
0.35	23.45	1.66	25.84
1.15	22.25	1.67	25.77
1.12	22.54	1.64	25.87
0.83	23.87	0.50	26.21
0.74	18.95	0.49	26.23
0.97	23.85	0.47	26.13
1.01	13.29	0.49	26.12

^{1}H (ppm)	^{13}C (ppm)	^{1}H (ppm)	^{13}C (ppm)
2.11	17.93	0.96	26.47
0.97	23.87	0.97	26.47
0.82	22.87	0.95	26.46
1.80	17.88	0.63	26.51
-0.28	10.30	0.82	27.41
1.54	19.57	2.11	18.00
0.86	21.80	2.12	17.90
1.09	19.71	0.84	12.44
1.39	17.93	1.02	20.23
1.02	22.76	1.40	17.88
0.92	22.21	1.03	22.67
0.70	22.57	0.70	25.46
0.16	20.89	0.72	22.70
0.70	22.51	0.17	20.90
0.72	25.52	0.17	20.98
0.16	21.14	0.73	25.41
0.81	24.95	0.16	20.85
1.09	19.77	0.76	20.08
0.76	20.21	0.15	20.94
0.82	23.39	1.11	23.32
1.04	22.56	0.59	20.95
0.59	21.12	1.05	22.57
1.01	20.56	1.03	22.55
1.21	19.94	0.77	23.88
0.92	22.51	0.84	23.37
1.64	25.84	1.15	22.53
-0.90	14.62	0.96	20.22
0.66	13.31	0.94	20.33
0.97	20.24	1.01	20.55
1.04	22.59	1.15	23.14
1.01	20.54	1.23	20.55
0.92	22.16	0.77	20.13
0.75	20.32	0.90	21.98
2.09	17.99	1.01	13.36
0.28	25.24	1.01	13.32
0.27	25.20	1.67	18.91
0.45	16.52	1.54	19.73
1.20	18.97	0.84	20.86

Pseudocontact shifts

Tab. 8: List of experimental and calculated ^{1}H PCSs. The PCSs are measured as differences of the peak positions between diamagnetic reference (La^{3+}) and paramagnetic sample (Ce^{3+}, Eu^{3+}, Pr^{3+}), respectively. The calculated PCSs are derived from Numbat on basis of the fitted Δχ-tensors.

sequence position	residue type	methyl position	Ce^{3+} exp. (ppm)	Ce^{3+} cal. (ppm)	Eu^{3+} exp. (ppm)	Eu^{3+} cal. (ppm)	Pr^{3+} exp. (ppm)	Pr^{3+} cal. (ppm)
63	Met	epsilon	-0.008	-0.004	-0.001	0.001	-0.009	-0.004
64	Val	gamma1	-0.007	-0.007	-0.001	0.006	-	-0.012
64	Val	gamma2	-0.004	-0.006	0.004	0.006	-0.013	-0.011
66	Leu	delta1	-0.003	-0.005	-0.001	0.004	-0.001	-0.007
66	Leu	delta2	-0.004	-0.004	0.002	0.003	-0.007	-0.006
69	Met	epsilon	-0.001	-0.002	0.000	0.003	-0.002	-0.003
70	Val	gamma1	-	-0.002	-0.023	0.007	-	-0.007
70	Val	gamma2	-0.002	-0.004	0.004	0.01	-0.008	-0.012
76	Val	gamma1	0.039	0.040	-0.069	-0.072	0.135	0.136
76	Val	gamma2	0.032	0.030	-0.058	-0.053	0.111	0.11
77	Leu	delta1	0.030	0.028	-0.054	-0.045	0.105	0.096
77	Leu	delta2	0.038	0.033	-0.061	-0.057	0.117	0.11
84	Val	gamma1	0.033	0.032	-0.064	-0.058	0.115	0.103
84	Val	gamma2	0.031	0.026	-0.058	-0.049	0.099	0.082
85	Leu	delta1	0.018	0.012	-0.039	-0.024	0.069	0.044
85	Leu	delta2	0.017	0.015	-0.040	-0.029	0.068	0.055
86	Val	gamma1	0.026	0.019	-0.048	-0.038	0.083	0.061
86	Val	gamma2	0.021	0.013	-0.041	-0.027	0.080	0.044
87	Val	gamma1	0.016	0.009	-0.042	-0.02	0.064	0.033
87	Val	gamma2	0.016	0.008	-0.040	-0.018	0.059	0.029
91	Leu	delta2	-	0.005	0.018	-0.012	-	0.019
92	Ala	beta	0.007	0.001	-0.030	-0.02	0.040	0.029
94	Ile	delta1	0.025	0.020	-0.050	-0.041	0.087	0.072
95	Val	gamma1	0.027	0.025	-0.063	-0.055	0.084	0.072
95	Val	gamma2	0.020	0.020	-0.053	-0.049	0.070	0.064
102	Ile	delta1	0.008	0.009	-0.019	-0.019	0.012	0.014
104	Ile	delta1	0.007	0.005	-0.007	-0.011	0.017	0.011
105	Leu	delta1	0.007	0.009	-0.025	-0.021	0.024	0.022
105	Leu	delta2	0.003	0.006	-0.018	-0.015	0.016	0.015
111	Leu	delta2	-0.005	0.000	0.007	0	-0.015	-0.004
116	Ile	delta1	-0.009	-0.007	0.011	0.009	-0.036	-0.03
118	Leu	delta2	-0.054	-0.050	0.157	0.122	-0.232	-0.233
120	Val	gamma1	-0.081	-0.055	-	0.165	-	-0.19
120	Val	gamma2	-0.122	-0.131	0.343	0.39	-0.403	-0.454
122	Ala	beta	0.038	0.000	0.064	0.064	0.113	0.11
123	Ile	delta1	0.092	0.080	-0.180	-0.131	0.348	0.317
127	Val	gamma2	0.047	0.049	-0.012	-0.026	0.112	0.128
128	Ala	beta	-0.006	0.001	0.081	0.064	-0.021	-0.017
130	Leu	delta2	-0.031	-0.032	0.186	0.172	-0.175	-0.158
132	Leu	delta2	-0.130	-0.138	0.276	0.289	-0.491	-0.519

sequence position	residue type	methyl position	Ce^{3+} exp. (ppm)	Ce^{3+} cal. (ppm)	Eu^{3+} exp. (ppm)	Eu^{3+} cal. (ppm)	Pr^{3+} exp. (ppm)	Pr^{3+} cal. (ppm)
134	Leu	delta2	-0.039	-0.042	0.141	0.13	-0.198	-0.192
137	Ala	beta	-0.036	0.000	0.131	0.122	-0.228	-0.229
142	Met	epsilon	-0.004	-0.002	-0.003	-0.006	-0.028	-0.023
143	Val	gamma2	-0.006	-0.006	0.021	0.023	-0.053	-0.058
147	Val	gamma2	-0.014	-0.012	0.031	0.028	-0.070	-0.06
151	Val	gamma2	-0.024	-0.025	0.097	0.09	-0.103	-0.097
157	Ala	beta	0.009	0.011	-0.001	-0.004	0.026	0.032
158	Ala	beta	0.017	0.024	0.002	-0.006	0.049	0.063
162	Val	gamma2	-0.022	-0.028	0.082	0.092	-0.115	-0.132
164	Leu	delta2	-0.018	-0.020	0.062	0.062	-0.090	-0.096
170	Leu	delta2	-0.011	-0.012	0.054	0.047	-0.055	-0.05
172	Val	gamma2	-0.004	-0.003	0.028	0.029	-0.015	-0.015
173	Leu	delta2	-0.016	-0.008	0.004	0.018	0.000	0
175	Val	gamma2	0.037	0.041	-	-0.075	0.154	0.179
177	Ala	beta	0.046	0.054	-0.077	-0.095	0.156	0.181
186	Met	epsilon	0.018	-0.021	0.024	0.021	0.024	-0.062
189	Met	epsilon	-0.098	-0.097	0.084	0.084	-0.194	-0.174
191	Met	epsilon	0.074	0.020	-0.054	-0.055	0.133	0.116
192	Ile	delta1	-0.070	-0.064	0.026	0.03	-0.073	-0.05
201	Leu	delta2	-0.009	-0.009	0.004	0.006	-0.012	-0.012
204	Val	gamma2	-0.021	-0.015	0.015	0.016	-0.039	-0.03
207	Leu	delta1	-0.030	-0.023	0.033	0.015	-0.036	-0.031
207	Leu	delta2	-0.034	-0.025	0.023	0.024	-0.052	-0.043
208	Val	gamma1	-0.016	-0.029	0.018	0.009	-0.037	-0.083
208	Val	gamma2	-0.026	-0.016	0.023	0.005	-0.066	-0.044
220	Val	gamma1	0.019	0.021	-0.048	-0.043	-	0.006
220	Val	gamma2	0.028	0.042	-0.086	-0.069	0.025	0.036
222	Val	gamma1	-0.003	-0.001	-0.004	-0.002	-0.005	-0.013
222	Val	gamma2	0.002	0.003	-0.009	-0.009	0.001	0
224	Ile	delta1	0.006	0.007	-0.031	-0.033	0.004	0.007
225	Leu	delta2	-0.013	-0.006	-0.006	-0.005	-0.024	-0.014
228	Leu	delta2	-0.015	-0.014	0.001	0.003	-0.014	-0.014
232	Leu	delta1	0.052	0.046	-0.090	-0.091	0.177	0.166
232	Leu	delta2	0.036	0.033	-0.072	-0.069	0.143	0.135
243	Ala	beta	0.007	-0.001	0.024	0.027	0.008	-0.013
254	Ala	beta	-0.042	-0.039	0.061	0.077	-0.132	-0.138
256	Ile	delta1	-0.023	-0.026	0.045	0.055	-0.067	-0.083
274	Val	gamma2	-0.014	-0.013	0.013	0.01	-0.028	-0.021
277	Val	gamma2	-0.032	-0.025	0.010	0.009	-0.044	-0.032
280	Leu	delta2	-0.050	-0.051	0.039	0.036	-0.080	-0.079
283	Ala	beta	-0.022	-0.022	0.022	0.019	-0.040	-0.04
287	Ala	beta	-0.025	-0.025	0.038	0.032	-0.066	-0.063
288	Met	epsilon	-0.042	-0.042	0.032	0.035	-0.096	-0.086
289	Met	epsilon	0.000	-0.008	-0.076	0.001	0.001	-0.006
293	Ala	beta	-0.004	0.000	0.006	0.006	-0.019	-0.016
296	Ile	delta1	-0.017	-0.017	0.044	0.04	-0.067	-0.076

sequence position	residue type	methyl position	Ce^{3+} exp. (ppm)	Ce^{3+} cal. (ppm)	Eu^{3+} exp. (ppm)	Eu^{3+} cal. (ppm)	Pr^{3+} exp. (ppm)	Pr^{3+} cal. (ppm)
298	Ala	beta	-0.046	-0.047	0.108	0.099	-0.187	-0.183
299	Val	gamma1	-0.050	-0.056	0.140	0.156	-0.224	-0.254
299	Val	gamma2	-0.037	-0.053	0.163	0.161	-0.246	-0.268
306	Leu	delta2	-0.092	-0.102	0.077	0.083	-0.148	-0.171
310	Leu	delta2	-0.020	-0.019	0.004	0.004	-0.014	-0.017
311	Leu	delta2	-0.012	-0.014	0.020	0.028	-0.032	-0.041
318	Val	gamma2	0.012	0.012	-0.044	-0.037	0.063	0.059
319	Leu	delta1	0.033	0.037	-0.101	-0.107	0.125	0.121
319	Leu	delta2	0.026	0.027	-0.078	-0.072	0.094	0.09
330	Leu	delta1	0.175	0.179	-0.291	-0.289	-	0.634
330	Leu	delta2	0.085	0.078	-0.130	-0.114	0.307	0.292
334	Ala	beta	0.027	0.025	-0.050	-0.045	0.086	0.079
335	Val	gamma1	0.048	0.051	-0.082	-0.09	0.149	0.165
335	Val	gamma2	0.043	0.038	-0.077	-0.068	0.134	0.122
336	Leu	delta1	0.092	0.103	-0.177	-0.184	0.288	0.314
336	Leu	delta2	0.072	0.078	-0.166	-0.142	0.246	0.238
339	Leu	delta1	0.084	0.075	-0.151	-0.133	0.234	0.198
339	Leu	delta2	0.108	0.098	-0.155	-0.175	0.266	0.275
344	Val	gamma2	-0.361	-0.354	-	0.697	-	-1.308
350	Ala	beta	-0.016	0.295	0.006	-0.091	-0.008	0.113
351	Val	gamma2	0.017	0.181	-0.047	-0.266	0.099	0.526

Chemical shifts in presence of ligands

Tab. 9: Chemical shifts of the AIL^{proS}MV^{proS} methyl resonances of GTB in complex with donor substrates and analogs.

	UDP		UDP-Glc		UDP-Gal		UDP-GalNAc		UDP-GlcNAc	
	^{1}H (ppm)	^{13}C (ppm)	^{1}H (ppm)	^{13}C (ppm)	^{1}H (ppm)	^{13}C (ppm)	^{1}H (ppm)	^{13}C (ppm)	^{1}H (ppm)	^{13}C (ppm)
58 Ala	1.54	19.45	1.54	19.45	1.54	19.45	1.54	19.45	1.54	19.45
59 Ile	0.70	12.63	0.70	12.61	0.70	12.62	0.70	12.61	0.70	12.61
63 Met	2.11	17.96	2.12	18.01	2.12	17.98	2.11	17.97	2.11	17.97
64 Val	0.91	19.47	0.91	19.45	0.90	19.47	0.90	19.46	0.90	19.47
66 Leu	0.82	23.43	0.82	23.43	0.82	23.40	0.82	23.38	0.82	23.36
69 Met	2.08	16.99	2.08	16.98	2.08	17.00	2.09	17.01	2.09	17.04
70 Val	0.67	19.87	0.67	19.87	0.67	19.87	0.67	19.88	0.67	19.88
76 Val	1.64	25.85	1.64	25.87	1.64	25.82	1.64	25.81	1.64	25.78
77 Leu	1.12	22.56	1.12	22.56	1.12	22.56	1.12	22.57	1.12	22.58
84 Val	-0.90	14.59	-0.90	14.59	-0.90	14.60	-0.90	14.60	-0.90	14.60
85 Leu	0.97	25.34	0.98	25.34	0.98	25.32	0.98	25.32	0.97	25.32
86 Val	0.97	20.23	0.96	20.24	0.96	20.25	0.97	20.25	0.97	20.25
87 Val	1.01	20.57	1.01	20.58	1.01	20.57	1.01	20.56	1.01	20.55
92 Ala	1.22	20.55	1.22	20.54	1.22	20.57	1.22	20.56	1.22	20.56
94 Ile	0.65	13.29	0.65	13.28	0.65	13.29	0.65	13.29	0.65	13.30
95 Val	0.58	21.03	0.58	21.02	0.58	21.05	0.58	21.04	0.58	21.03
102 Ile	1.22	15.27	1.22	15.27	1.22	15.26	1.22	15.26	1.22	15.26
104 Ile	0.34	13.39	0.34	13.40	0.34	13.38	0.34	13.39	0.34	13.39
105 Leu	1.10	23.29	1.10	23.30	1.10	23.28	1.10	23.29	1.10	23.30
111 Leu	0.92	22.43	0.92	22.42	0.92	22.43	0.92	22.42	0.92	22.42
116 Ile	0.69	17.08	0.68	17.08	0.69	17.08	0.69	17.11	0.69	17.14
118 Leu	0.59	25.15	0.57	25.13	0.57	25.11	0.56	25.07	0.55	25.03
120 Val	0.39	20.85	0.36	21.05	0.37	21.01	0.41	20.68	0.43	20.50
122 Ala	1.14	19.51	1.14	19.54	1.14	19.60	1.12	19.56	1.10	19.58
123 Ile	0.93	12.31	0.91	12.60	0.92	12.53	0.91	12.55	0.90	12.67
127 Val	1.00	19.16	1.00	19.12	1.00	19.27	1.00	19.56	1.00	19.81
128 Ala	1.06	18.56	1.08	18.58	1.08	18.57	1.09	18.59	1.11	18.61
130 Leu	0.81	24.59	0.81	24.49	0.81	24.50	0.81	24.60	0.80	24.62
132 Leu	0.96	25.63	0.96	25.65	0.95	25.62	0.95	25.59	0.95	25.58
134 Leu	0.19	20.96	0.20	20.95	0.20	20.97	0.18	20.95	0.16	20.94
137 Ala	1.25	18.07	1.25	18.05	1.25	18.05	1.25	18.07	1.25	18.07
142 Met	1.23	19.93	1.22	19.92	1.22	19.91	1.22	19.93	1.21	19.94
143 Val	0.66	21.90	0.66	21.90	0.66	21.89	0.66	21.93	0.67	21.95
147 Val	0.76	23.79	0.76	23.84	0.76	23.82	0.76	23.82	0.75	23.82
151 Val	0.76	20.19	0.77	20.25	0.77	20.23	0.76	20.17	0.75	20.16
157 Ala	1.39	18.05	1.39	18.04	1.39	18.03	1.39	18.04	1.39	18.03
158 Ala	1.44	19.37	1.44	19.37	1.44	19.36	1.44	19.40	1.43	19.42
162 Val	0.78	19.88	0.77	19.87	0.78	19.88	0.78	19.90	0.78	19.90
164 Leu	0.70	22.62	0.71	22.64	0.71	22.65	0.70	22.59	0.70	22.58

	UDP		UDP-Glc		UDP-Gal		UDP-GalNAc		UDP-GlcNAc	
	^{1}H (ppm)	^{13}C (ppm)	^{1}H (ppm)	^{13}C (ppm)	^{1}H (ppm)	^{13}C (ppm)	^{1}H (ppm)	^{13}C (ppm)	^{1}H (ppm)	^{13}C (ppm)
170 Leu	0.71	25.33	0.71	25.34	0.71	25.35	0.71	25.39	0.71	25.41
172 Val	0.91	22.22	0.91	22.19	0.91	22.18	0.91	22.17	0.91	22.16
173 Leu	0.34	23.63	0.33	23.65	0.33	23.72	0.36	23.74	0.37	23.83
175 Val	0.90	18.53	0.88	18.26	0.89	18.43	0.90	18.97	0.89	19.14
177 Ala	1.25	20.01	1.26	20.25	1.26	20.02	1.27	19.44	1.27	19.07
184 Val	0.85	22.72	0.87	22.75	0.87	22.67	0.83	22.29	0.82	22.06
186 Met	1.87	17.79	1.86	17.82	1.87	17.78	1.89	17.44	1.91	17.20
189 Met	1.84	18.28	1.84	18.25	1.83	18.25	1.83	18.12	1.81	18.01
191 Met	2.25	18.52	2.26	18.63	2.24	18.53	2.11	17.97	2.11	17.97
192 Ile	1.06	13.88	1.05	13.90	1.05	13.86	1.05	13.69	1.04	13.56
201 Leu	0.88	24.05	0.89	24.05	0.88	24.06	0.88	24.11	0.88	24.13
204 Val	0.76	18.90	0.76	18.89	0.76	18.90	0.75	18.94	0.74	18.95
207 Leu	0.49	25.79	0.48	25.70	0.49	25.86	0.49	25.98	0.49	26.08
208 Val	1.11	21.31	1.10	21.34	1.11	21.30	1.10	21.28	1.09	21.24
210 Val	0.90	20.36	0.95	20.12			0.92	20.23	0.88	20.38
212 Val	0.78	22.31	0.79	22.29	0.78	22.29	0.76	22.36	0.75	22.41
214 Met	0.90	16.42	1.01	16.79	1.01	16.81	1.12	16.99	1.08	16.94
220 Val	1.33	22.47	1.35	22.52	1.35	22.53	1.34	22.51	1.34	22.54
222 Val	0.53	18.54	0.53	18.53	0.54	18.54	0.54	18.56	0.53	18.57
224 Ile	0.41	13.69	0.42	13.71	0.42	13.76	0.40	13.66	0.40	13.64
225 Leu	0.10	19.90	0.09	19.91	0.09	19.89	0.09	19.87	0.08	19.86
228 Leu	0.94	26.34	0.94	26.33	0.94	26.34	0.94	26.36	0.94	26.37
232 Leu	0.35	23.35	0.37	23.32	0.36	23.35	0.35	23.34	0.35	23.33
243 Ala	1.51	19.30	1.50	19.31	1.51	19.31	1.51	19.31	1.51	19.31
254 Ala	0.44	16.42	0.44	16.42	0.42	16.41	0.45	16.46	0.45	16.48
256 Ile	-0.29	10.44	-0.28	10.46	-0.29	10.46	-0.28	10.44	-0.29	10.43
266 Met	1.79	18.40	1.90	18.41	1.89	18.43	1.83	18.40	1.86	18.36
268 Ala	1.52	21.52	1.53	21.93	1.58	21.85	1.53	21.72	1.53	21.75
274 Val	0.84	23.58	0.84	23.55	0.84	23.62	0.84	23.71	0.83	23.78
277 Val	0.99	23.86	0.98	23.90	0.98	23.88	0.98	23.86	0.97	23.85
280 Leu	0.25	24.98	0.24	24.94	0.24	24.95	0.26	25.02	0.27	25.07
283 Ala	1.67	18.90	1.67	18.89	1.67	18.89	1.67	18.90	1.66	18.90
287 Ala	1.56	19.84	1.57	19.89	1.56	19.86	1.54	19.86	1.54	19.86
288 Met	2.06	17.93	2.06	18.10	2.05	17.84	2.06	17.87	2.11	17.97
289 Met	1.98	16.79	1.99	16.84	1.97	16.84	1.96	16.89	1.94	16.96
293 Ala	1.55	17.53	1.55	17.53	1.55	17.53	1.56	17.52	1.56	17.52
296 Ile	0.59	13.54	0.59	13.56	0.59	13.55	0.59	13.52	0.59	13.51
298 Ala	1.33	19.43	1.34	19.50	1.35	19.46	1.34	19.41	1.35	19.41
299 Val	0.72	19.58	0.72	19.58	0.70	19.59	0.71	19.56	0.71	19.55
306 Leu	0.69	26.71	0.70	26.75	0.69	26.67	0.66	26.61	0.63	26.54
310 Leu	0.82	22.74	0.83	22.73	0.82	22.71	0.82	22.76	0.82	22.77
311 Leu	0.80	27.29	0.80	27.27	0.80	27.29	0.80	27.30	0.81	27.30
318 Val	1.13	22.18	1.13	22.19	1.14	22.21	1.14	22.18	1.14	22.18
319 Leu	-0.31	20.14	-0.31	20.18	-0.31	20.19	-0.31	20.18	-0.31	20.21

	UDP		UDP-Glc		UDP-Gal		UDP-GalNAc		UDP-GlcNAc	
	^{1}H (ppm)	^{13}C (ppm)	^{1}H (ppm)	^{13}C (ppm)	^{1}H (ppm)	^{13}C (ppm)	^{1}H (ppm)	^{13}C (ppm)	^{1}H (ppm)	^{13}C (ppm)
324 Leu	0.96	25.63	1.02	25.73	1.05	26.15	1.00	25.71	1.01	25.77
329 Leu	0.71	23.88	0.71	23.87	0.71	23.87	0.71	23.87	0.71	23.88
330 Leu	0.71	22.10	0.71	22.07	0.71	22.10	0.71	22.08	0.70	22.07
334 Ala	1.39	18.19	1.38	18.19	1.38	18.20	1.39	18.19	1.38	18.20
335 Val	0.81	20.65	0.81	20.76	0.81	20.72	0.81	20.66	0.81	20.68
336 Leu	0.14	22.95	0.23	23.02	0.23	23.04	0.20	23.02	0.23	23.05
339 Leu	-0.13	23.04	-0.20	23.03	-0.19	23.05	-0.17	23.05	-0.18	23.07
343 Ala	1.18	18.87	1.18	19.00	1.18	18.98	1.19	18.99	1.19	19.04
344 Val	0.84	20.86	0.85	20.88	0.85	20.85	0.85	20.87	0.84	20.84
350 Ala	1.40	18.98	1.37	18.92	1.38	19.00	1.38	19.05	1.37	19.07
351 Val	0.83	20.35	0.86	20.36	0.85	20.34	0.87	20.37	0.88	20.38

Tab. 10: Chemical shifts of the AIL^{proS}MV^{proS} methyl resonances of GTB in complex with 3DD, H-dis and B-tris.

	3DD		HA		B-tris.	
	^{1}H (ppm)	^{13}C (ppm)	^{1}H (ppm)	^{13}C (ppm)	^{1}H (ppm)	^{13}C (ppm)
58 Ala	1.54	19.45	1.53	19.45	1.54	19.46
59 Ile	0.70	12.61	0.69	12.60	0.70	12.60
63 Met	2.11	17.95	2.11	18.00	2.11	17.97
64 Val	0.90	19.46	0.90	19.48	0.90	19.48
66 Leu	0.82	23.37	0.82	23.35	0.82	23.34
69 Met	2.08	17.03	2.08	17.03	2.09	17.05
70 Val	0.67	19.89	0.67	19.89	0.67	19.88
76 Val	1.63	25.83	1.63	25.84	1.63	25.81
77 Leu	1.12	22.56	1.12	22.56	1.12	22.58
84 Val	-0.90	14.60	-0.90	14.61	-0.90	14.60
85 Leu	0.98	25.29	0.97	25.32	0.97	25.27
86 Val	0.97	20.19	0.97	20.24	0.97	20.20
87 Val	1.00	20.52	1.00	20.55	1.01	20.58
92 Ala	1.22	20.58	1.23	20.60	1.23	20.59
94 Ile	0.66	13.28	0.65	13.25	0.65	13.24
95 Val	0.58	21.04	0.58	21.04	0.58	21.03
102 Ile	1.21	15.26	1.21	15.26	1.22	15.25
104 Ile	0.34	13.39	0.34	13.38	0.35	13.39
105 Leu	1.10	23.33	1.10	23.33	1.10	23.30
111 Leu	0.91	22.41	0.91	22.42	0.91	22.42
116 Ile	0.68	17.15	0.69	17.16	0.69	17.17
118 Leu	0.50	24.95	0.51	24.97	0.51	24.94
120 Val	0.46	20.09	0.45	20.19	0.44	20.22
122 Ala	1.08	19.62	1.08	19.65	1.08	19.66
123 Ile	0.85	12.56	0.85	12.60	0.84	12.60

	3DD		HA		B-tris.	
	^{1}H (ppm)	^{13}C (ppm)	^{1}H (ppm)	^{13}C (ppm)	^{1}H (ppm)	^{13}C (ppm)
127 Val	0.99	20.19	0.99	20.21	0.99	20.20
128 Ala	1.14	18.61	1.15	18.60	1.15	18.61
130 Leu	0.80	24.76	0.80	24.77	0.80	24.79
132 Leu	0.95	25.59	0.95	25.55	0.95	25.53
134 Leu	0.15	20.93	0.15	20.95	0.16	20.95
137 Ala	1.25	18.10	1.24	18.10	1.24	18.09
142 Met	1.21	19.94	1.21	19.94	1.21	19.95
143 Val	0.67	21.96	0.67	22.00	0.67	21.94
147 Val	0.77	23.83	0.76	23.80	0.75	23.80
151 Val	0.75	20.14	0.75	20.16	0.75	20.16
157 Ala	1.39	18.03	1.39	18.03	1.39	18.03
158 Ala	1.43	19.46	1.42	19.45	1.43	19.44
162 Val	0.78	19.92	0.78	19.91	0.78	19.90
164 Leu	0.70	22.51	0.70	22.53	0.70	22.55
170 Leu	0.71	25.44	0.71	25.45	0.71	25.45
172 Val	0.91	22.15	0.91	22.15	0.91	22.14
173 Leu	0.40	23.92	0.39	23.96	0.38	23.97
175 Val	0.87	19.28	0.87	19.27	0.87	19.26
177 Ala	1.29	18.77	1.29	18.77	1.29	18.76
184 Val	0.85	21.73	0.85	21.70	0.86	21.70
186 Met	1.92	16.97	1.92	16.94	1.91	16.92
189 Met	1.77	17.78	1.78	17.82	1.78	17.83
191 Met	2.11	17.95	2.11	18.00	2.11	17.97
192 Ile	1.02	13.38	1.00	13.39	1.01	13.39
201 Leu	0.88	24.14	0.88	24.16	0.88	24.14
204 Val	0.74	18.93	0.73	18.92	0.74	18.93
207 Leu	0.47	26.04	0.47	26.09	0.47	26.04
208 Val	1.07	21.26	1.06	21.26	1.07	21.27
210 Val	0.81	20.17	0.82	20.21	0.81	20.26
212 Val	0.70	22.51	0.70	22.53	0.72	22.42
214 Met	1.18	17.32	1.21	17.45	1.28	17.66
220 Val	1.36	22.60	1.36	22.59	1.36	22.57
222 Val	0.53	18.64	0.54	18.62	0.53	18.57
224 Ile	0.40	13.56	0.40	13.63	0.39	13.57
225 Leu	0.08	19.87	0.08	19.83	0.08	19.85
228 Leu	0.95	26.41	0.94	26.38	0.94	26.38
232 Leu	0.33	23.28	0.32	23.30	0.32	23.37
243 Ala	1.51	19.29	1.50	19.31	1.50	19.31
254 Ala	0.42	16.47	0.43	16.45	0.43	16.46
256 Ile	-0.29	10.37	-0.29	10.35	-0.29	10.35
266 Met	1.94	19.31	1.98	19.23	2.01	18.97
268 Ala	1.51	21.31	1.54	21.51	1.54	21.48
274 Val	0.82	23.82	0.82	23.85	0.82	23.83
277 Val	0.96	23.84	0.96	23.86	0.96	23.85
280 Leu	0.30	25.15	0.29	25.09	0.29	25.13

	3DD		HA		B-tris.	
	^{1}H (ppm)	^{13}C (ppm)	^{1}H (ppm)	^{13}C (ppm)	^{1}H (ppm)	^{13}C (ppm)
283 Ala	1.66	18.89	1.66	18.89	1.67	18.87
287 Ala	1.53	19.86	1.53	19.88	1.54	19.85
288 Met	2.15	17.62	2.13	17.70	2.14	17.76
289 Met	1.93	17.05	1.93	17.05	1.93	17.05
293 Ala	1.56	17.52	1.56	17.52	1.56	17.52
296 Ile	0.59	13.54	0.59	13.55	0.60	13.55
298 Ala	1.37	19.48	1.37	19.45	1.37	19.43
299 Val	0.56	19.57	0.58	19.57	0.66	19.56
306 Leu	0.60	26.35	0.60	26.36	0.61	26.42
310 Leu	0.82	22.82	0.82	22.76	0.82	22.78
311 Leu	0.81	27.30	0.81	27.30	0.81	27.30
318 Val	1.14	22.14	1.15	22.18	1.15	22.24
319 Leu	-0.32	20.32	-0.31	20.28	-0.32	20.23
324 Leu	1.09	26.50	1.09	26.28	1.05	25.99
329 Leu	0.72	24.37	0.71	24.74	0.71	24.89
330 Leu	0.67	21.96	0.67	22.00	0.70	22.16
334 Ala	1.38	18.19	1.38	18.20	1.38	18.21
335 Val	0.81	20.58	0.80	20.71	0.81	20.68
336 Leu	0.38	23.16	0.36	23.12	0.33	23.10
339 Leu	-0.26	23.04	-0.27	23.01	-0.27	22.99
343 Ala	1.20	19.25	1.20	19.08	1.21	19.06
344 Val	0.85	20.88	0.85	20.87	0.85	20.87
350 Ala	1.38	19.10	1.38	19.11	1.38	19.11
351 Val	0.91	20.39	0.91	20.38	0.91	20.39

Tab. 11: Chemical shifts of the AIL^{proS}MV^{proS} methyl resonances of GTB in ternary binding complexes.

	UDP-Glc +3DD		UDP-Gal +3DD		UDP+B-tris		UDP+HA		UDP-GalNAc +3DD		UDP-GlcNAc +3DD	
	^{1}H (ppm)	^{13}C (ppm)	^{1}H (ppm)	^{13}C (ppm)	^{1}H (ppm)	^{13}C (ppm)	^{1}H (ppm)	^{13}C (ppm)	^{1}H (ppm)	^{13}C (ppm)	^{1}H (ppm)	^{13}C (ppm)
58 Ala	1.54	19.45	1.54	19.44	1.53	19.45	1.54	19.45	1.54	19.45	1.54	19.45
59 Ile	0.69	12.62	0.69	12.64	0.70	12.62	0.70	12.62	0.70	12.62	0.70	12.60
63 Met	2.12	18.02	2.12	18.02	2.12	18.02	2.12	18.02	2.12	18.02	2.11	17.97
64 Val	0.91	19.47	0.91	19.45	0.91	19.46	0.91	19.46	0.91	19.44	0.90	19.46
66 Leu	0.83	23.44	0.82	23.43	0.83	23.44	0.83	23.45	0.83	23.42	0.83	23.38
69 Met	2.08	16.98	2.08	16.97	2.08	16.96	2.08	16.95	2.08	16.98	2.08	17.00
70 Val	0.67	19.87	0.67	19.86	0.66	19.87	0.67	19.87	0.67	19.87	0.67	19.88
76 Val	1.64	25.90	1.64	25.84	1.64	25.92	1.65	25.93	1.64	25.86	1.63	25.85
77 Leu	1.12	22.51	1.13	22.52	1.13	22.50	1.13	22.49	1.13	22.52	1.12	22.55
84 Val	-0.90	14.59	-0.90	14.59	-0.90	14.60	-0.90	14.59	-0.90	14.59	-0.90	14.60
85 Leu	0.98	25.30	0.98	25.31	0.98	25.30	0.98	25.30	0.98	25.30	0.97	25.29

	UDP-Glc +3DD		UDP-Gal +3DD		UDP+B-tris		UDP+HA		UDP-GalNAc +3DD		UDP-GlcNAc +3DD	
	^{1}H (ppm)	^{13}C (ppm)	^{1}H (ppm)	^{13}C (ppm)	^{1}H (ppm)	^{13}C (ppm)	^{1}H (ppm)	^{13}C (ppm)	^{1}H (ppm)	^{13}C (ppm)	^{1}H (ppm)	^{13}C (ppm)
86 Val	0.97	20.25	0.97	20.24	0.97	20.23	0.97	20.23	0.97	20.25	0.97	20.25
87 Val	1.01	20.59	1.01	20.60	1.01	20.61	1.01	20.62	1.01	20.60	1.00	20.54
92 Ala	1.22	20.57	1.22	20.60	1.22	20.54	1.22	20.54	1.22	20.57	1.22	20.58
94 Ile	0.65	13.24	0.65	13.27	0.64	13.24	0.64	13.24	0.65	13.25	0.65	13.28
95 Val	0.59	21.03	0.58	21.04	0.59	21.00	0.59	20.98	0.58	21.02	0.58	21.04
102 Ile	1.22	15.27	1.22	15.27	1.22	15.27	1.22	15.28	1.22	15.27	1.21	15.26
104 Ile	0.34	13.38	0.34	13.36	0.35	13.40	0.35	13.40	0.35	13.39	0.34	13.39
105 Leu	1.10	23.28	1.10	23.22	1.10	23.27	1.10	23.27	1.10	23.26	1.10	23.32
111 Leu	0.91	22.42	0.91	22.41	0.91	22.42	0.92	22.42	0.91	22.40	0.91	22.41
116 Ile	0.68	17.07	0.68	16.95	0.68	17.04	0.68	17.03	0.68	17.01	0.69	17.16
118 Leu	0.57	25.09	0.58	25.08	0.59	25.12	0.59	25.12	0.58	25.09	0.51	24.98
120 Val	0.34	21.34	0.22	21.59	0.28	21.51	0.28	21.51	0.28	21.46	0.45	20.23
122 Ala	1.15	19.63	1.17	19.69	1.16	19.64	1.16	19.65	1.17	19.69	1.09	19.57
123 Ile	0.90	12.89	0.94	12.73	0.92	12.05	0.92	12.03	0.92	12.17	0.88	12.63
127 Val	1.00	19.40	1.01	20.03	1.00	18.99	1.01	18.99	1.01	19.25	0.99	20.01
128 Ala	1.08	18.57	1.07	18.52	1.08	18.54	1.08	18.54	1.08	18.54	1.13	18.61
130 Leu	0.82	24.69	0.87	25.56	0.82	24.65	0.83	24.65	0.83	24.89	0.79	24.64
132 Leu	0.96	25.69	0.96	25.68	0.95	25.68	0.96	25.69	0.95	25.69	0.94	25.61
134 Leu	0.22	20.96	0.24	21.01	0.23	20.96	0.24	20.96	0.24	20.99	0.15	20.93
137 Ala	1.25	18.02	1.23	17.96	1.24	18.02	1.24	18.01	1.24	18.03	1.25	18.10
142 Met	1.22	19.88	1.21	19.90	1.23	19.87	1.23	19.86	1.23	19.85	1.21	19.94
143 Val	0.66	21.87	0.65	21.80	0.66	21.85	0.66	21.83	0.66	21.84		
147 Val	0.76	23.79	0.75	23.73	0.76	23.79	0.75	23.79	0.76	23.77	0.75	23.82
151 Val	0.77	20.32	0.76	20.34	0.77	20.33	0.77	20.35	0.77	20.33	0.75	20.12
157 Ala	1.39	18.02	1.39	18.00	1.39	18.02	1.39	18.02	1.39	18.02	1.39	18.03
158 Ala	1.44	19.33	1.44	19.30	1.44	19.32	1.44	19.31	1.44	19.32	1.43	19.45
162 Val	0.77	19.84	0.76	19.82	0.77	19.83	0.77	19.82	0.77	19.83	0.78	19.91
164 Leu	0.71	22.69	0.70	22.74	0.70	22.71	0.71	22.72	0.70	22.70	0.70	22.55
170 Leu	0.71	25.36	0.70	25.32	0.71	25.34	0.71	25.33	0.71	25.33	0.71	25.42
172 Val	0.91	22.17	0.91	22.22	0.91	22.20	0.91	22.21	0.91	22.26	0.91	22.16
173 Leu	0.32	23.71	0.28	23.66	0.30	23.59	0.30	23.58	0.31	23.53	0.39	23.86
175 Val	0.86	18.14	0.88	17.84	0.88	17.87	0.88	17.87	0.88	17.88		
177 Ala	1.27	20.42	1.26	20.84	1.25	20.77	1.25	20.77	1.25	20.74	1.28	18.80
184 Val	0.90	22.80	0.98	23.07			0.94	23.12	0.95	23.08	0.83	21.83
186 Met	1.86	17.84	1.83	18.24	1.84	18.18	1.84	18.19	1.84	18.13	1.92	17.03
189 Met	1.84	18.23			1.85	18.46	1.85	18.48	1.84	18.45	1.78	17.84
191 Met	2.29	18.72	2.36	18.87	2.36	18.84	2.36	18.84	2.36	18.88	2.11	17.97
192 Ile	1.04	13.95	1.05	14.07	1.05	14.06	1.05	14.07	1.06	14.10	1.03	13.43
201 Leu	0.88	24.04	0.88	23.96	0.88	23.97	0.88	23.96	0.88	23.97	0.88	24.14
204 Val	0.75	18.87	0.76	18.82	0.76	18.85	0.76	18.84	0.76	18.83	0.74	18.94
207 Leu	0.47	25.74	0.47	25.65	0.47	25.58	0.47	25.58	0.47	25.55	0.48	26.09
208 Val	1.09	21.37	1.11	21.43	1.11	21.37	1.11	21.39	1.10	21.40	1.07	21.25

	UDP-Glc +3DD		UDP-Gal +3DD		UDP+B-tris		UDP+HA		UDP-GalNAc +3DD		UDP-GlcNAc +3DD	
	^{1}H (ppm)	^{13}C (ppm)	^{1}H (ppm)	^{13}C (ppm)	^{1}H (ppm)	^{13}C (ppm)	^{1}H (ppm)	^{13}C (ppm)	^{1}H (ppm)	^{13}C (ppm)	^{1}H (ppm)	^{13}C (ppm)
210 Val	0.96	20.25	0.97	20.24	0.97	20.08	0.91	20.40	0.98	20.10	0.84	20.18
212 Val	0.77	22.36	0.82	22.13	0.80	22.18	0.80	22.18	0.79	22.22	0.70	22.55
214 Met	1.16	17.37	0.92	16.91	0.91	16.62	0.91	16.62	0.89	16.66	1.18	17.32
220 Val	1.36	22.55	1.36	22.56	1.35	22.56	1.35	22.57	1.35	22.56	1.36	22.59
222 Val	0.53	18.53	0.54	18.47	0.54	18.52	0.54	18.50	0.54	18.50	0.53	18.64
224 Ile	0.42	13.75	0.46	13.90	0.43	13.79	0.43	13.80	0.44	13.76	0.40	13.57
225 Leu	0.09	19.91	0.11	19.98	0.10	19.92	0.10	19.92	0.10	19.94	0.08	19.85
228 Leu	0.94	26.32	0.93	26.29	0.93	26.29	0.93	26.28	0.94	26.31	0.94	26.39
232 Leu	0.34	23.33	0.35	23.36	0.36	23.30	0.37	23.30	0.35	23.32	0.33	23.29
243 Ala	1.50	19.31	1.50	19.32	1.50	19.31	1.50	19.31	1.50	19.32	1.51	19.30
254 Ala	0.41	16.36	0.41	16.33	0.39	16.32	0.39	16.32	0.41	16.36	0.43	16.47
256 Ile	-0.29	10.36	-0.30	10.35	-0.29	10.42	-0.29	10.43	-0.29	10.37	-0.29	10.37
266 Met			2.04	18.68	1.79	19.09	1.79	19.11	1.92	18.78	1.92	19.20
268 Ala	1.56	21.78	1.64	21.73	1.57	21.59	1.57	21.60	1.54	21.55	1.51	21.47
274 Val	0.83	23.48	0.85	23.43	0.85	23.44	0.84	23.43	0.84	23.40	0.83	23.82
277 Val	0.98	23.85	1.00	23.89	0.99	23.88	0.99	23.88	0.98	23.87	0.96	23.85
280 Leu	0.24	24.86	0.20	24.76	0.23	24.89	0.23	24.89	0.22	24.89	0.30	25.14
283 Ala	1.67	18.88	1.68	18.88	1.68	18.87	1.68	18.86	1.68	18.87	1.66	18.89
287 Ala	1.57	19.85	1.58	19.82	1.57	19.85	1.57	19.85	1.57	19.82	1.53	19.86
288 Met	2.04	18.16	1.99	18.25	2.02	17.95	2.02	17.95	2.02	18.17	2.14	17.62
289 Met	2.00	16.91	2.03	16.81	1.99	16.79	2.00	16.79	2.01	16.75	1.92	17.03
293 Ala	1.55	17.53	1.55	17.53	1.55	17.52	1.55	17.52	1.55	17.52	1.56	17.52
296 Ile	0.58	13.57	0.57	13.62	0.58	13.58	0.58	13.58	0.58	13.57	0.59	13.54
298 Ala	1.33	19.49	1.31	19.50	1.32	19.50	1.32	19.51	1.31	19.47	1.36	19.47
299 Val	0.60	19.58	0.58	19.69	0.63	19.64	0.63	19.65	0.61	19.57	0.58	19.56
306 Leu	0.67	26.66	0.72	26.76	0.71	26.80	0.71	26.81	0.70	26.79	0.61	26.37
310 Leu	0.83	22.70	0.82	22.64	0.82	22.67	0.83	22.66	0.82	22.69	0.82	22.79
311 Leu	0.80	27.29	0.80	27.28	0.80	27.27	0.80	27.26	0.80	27.28	0.81	27.30
318 Val	1.14	22.23	1.15	22.24	1.13	22.23	1.13	22.23	1.14	22.23	1.14	22.16
319 Leu	-0.31	20.22	-0.32	20.19	-0.31	20.14	-0.31	20.12	-0.32	20.17	-0.31	20.30
324 Leu	1.07	25.91	1.12	26.54	1.05	25.45	1.06	25.45	1.04	25.68	1.08	26.41
329 Leu			0.73	25.64							0.72	24.43
330 Leu	0.72	22.27	0.74	22.26	0.73	22.31	0.73	22.31	0.74	22.28	0.67	21.96
334 Ala	1.38	18.22	1.38	18.23	1.38	18.23	1.38	18.24	1.38	18.22	1.38	18.20
335 Val	0.80	20.96	0.80	21.01	0.80	21.12	0.80	21.13	0.80	21.01	0.81	20.64
336 Leu	0.35	23.08	0.36	23.07	0.36	23.10	0.36	23.08	0.37	23.08	0.36	23.15
339 Leu	-0.29	22.98	-0.30	23.04	-0.33	22.92	-0.33	22.92	-0.32	22.97	-0.26	23.02
343 Ala	1.18	19.05	1.18	19.00	1.19	18.65	1.20	18.64	1.20	18.49	1.20	19.16
344 Val	0.80	20.96	0.80	21.01	0.81	20.87	0.81	20.88	0.81	20.80	0.84	20.86
350 Ala	1.38	18.84	1.40	18.62	1.41	18.55	1.41	18.54	1.40	18.60	1.37	19.09
351 Val	0.81	20.58	0.65	21.16	0.74	21.09	0.74	21.09	0.71	21.12	0.90	20.38

Tab. 12: Chemical shifts of the AIL^{proS}MV^{proS} methyl resonances of GTA in complex with donor substrate and analogs.

	UDP-Gal		UDP-Glc		UDP-GalNAc		UDP-GlcNAc	
	^{1}H (ppm)	^{13}C (ppm)	^{1}H (ppm)	^{13}C (ppm)	^{1}H (ppm)	^{13}C (ppm)	^{1}H (ppm)	^{13}C (ppm)
58 Ala	1.54	19.42	1.54	19.42	1.54	19.41	1.54	19.43
59 Ile	0.71	12.65	0.71	12.64	0.71	12.66	0.70	12.62
63 Met	2.12	17.96	2.12	17.95	2.12	17.94	2.11	17.97
64 Val	0.91	19.46	0.90	19.45	0.90	19.46	0.90	19.44
66 Leu	0.83	23.46	0.83	23.45	0.83	23.44	0.83	23.44
69 Met	2.08	16.93	2.08	16.93	2.08	16.93	2.08	16.94
70 Val	0.66	19.84	0.66	19.85	0.67	19.84	0.66	19.85
76 Val	1.64	25.88	1.64	25.89	1.64	25.86	1.64	25.91
77 Leu	1.11	22.52	1.11	22.54	1.11	22.56	1.11	22.56
84 Val	-0.90	14.60	-0.89	14.62	-0.90	14.61	-0.89	14.62
85 Leu	0.98	25.30	0.98	25.32	0.98	25.31	0.98	25.31
86 Val	0.97	20.23	0.96	20.23	0.97	20.24	0.97	20.26
87 Val	1.01	20.60	1.01	20.60	1.01	20.59	1.01	20.60
92 Ala	1.21	20.53	1.21	20.52	1.21	20.53	1.22	20.50
94 Ile	0.64	13.28	0.64	13.28	0.64	13.29	0.64	13.29
95 Val	0.59	21.03	0.59	21.03	0.59	21.03	0.59	21.02
102 Ile	1.22	15.26	1.22	15.26	1.22	15.25	1.22	15.26
104 Ile	0.34	13.39	0.34	13.40	0.34	13.39	0.35	13.41
105 Leu	1.10	23.30	1.10	23.31	1.10	23.29	1.10	23.30
111 Leu	0.91	22.42	0.91	22.41	0.91	22.41	0.91	22.41
116 Ile	0.68	17.05	0.68	17.06	0.68	17.05	0.68	17.08
118 Leu	0.54	25.08	0.52	25.06	0.52	25.07	0.49	25.00
120 Val	0.36	21.05	0.37	20.94	0.37	20.89	0.40	20.66
122 Ala	1.16	19.67	1.15	19.59	1.16	19.62	1.15	19.56
123 Ile	0.92	12.10	0.93	12.42	0.92	11.97	0.93	12.34
127 Val	1.00	19.07	1.00	19.21	1.01	19.06	1.01	19.47
128 Ala	1.06	18.58	1.06	18.58	1.07	18.57	1.07	18.60
130 Leu	0.80	24.29	0.81	24.45	0.81	24.38	0.80	24.50
132 Leu	0.96	25.62	0.96	25.63	0.96	25.64	0.96	25.65
134 Leu	0.21	20.97	0.20	20.98	0.20	20.98	0.20	20.99
137 Ala	1.27	18.11	1.27	18.11	1.27	18.11	1.27	18.12
142 Met	1.22	19.90	1.22	19.91	1.22	19.90	1.22	19.91
143 Val	0.66	21.87	0.66	21.89	0.66	21.89	0.67	21.90
147 Val	0.76	23.84	0.77	23.87	0.77	23.86	0.77	23.85
151 Val	0.77	20.32	0.77	20.26	0.78	20.29	0.77	20.23
157 Ala	1.39	18.06	1.39	18.06	1.39	18.06	1.39	18.05
158 Ala	1.44	19.35	1.44	19.37	1.44	19.38	1.44	19.38
162 Val	0.77	19.85	0.78	19.87	0.77	19.86	0.78	19.88
164 Leu	0.70	22.64	0.70	22.59	0.70	22.60	0.70	22.59
170 Leu	0.71	25.34	0.70	25.34	0.71	25.33	0.70	25.36
172 Val	0.91	22.23	0.91	22.24	0.91	22.28	0.91	22.26
173 Leu	0.30	23.57	0.32	23.50	0.31	23.51	0.38	23.85

	UDP-Gal		UDP-Glc		UDP-GalNAc		UDP-GlcNAc	
	^{1}H (ppm)	^{13}C (ppm)	^{1}H (ppm)	^{13}C (ppm)	^{1}H (ppm)	^{13}C (ppm)	^{1}H (ppm)	^{13}C (ppm)
175 Val	0.86	17.98	0.85	18.07	0.86	18.00	0.84	18.21
177 Ala	1.27	20.48	1.27	20.27	1.27	20.54	1.27	20.03
184 Val	0.94	22.90	0.94	22.85	0.93	22.89		
186 Met	1.84	18.14	1.85	18.01	1.84	18.13	1.85	17.91
189 Met	1.86	18.36	1.86	18.26	1.88	18.38	1.85	18.22
191 Met	2.40	19.04	2.39	18.99	2.43	19.02		
192 Ile	1.04	13.95	1.05	13.96	1.04	13.99	1.05	13.93
201 Leu	0.88	23.99	0.88	24.02	0.88	23.99	0.88	24.04
204 Val	0.75	18.82	0.75	18.83	0.75	18.82	0.74	18.84
207 Leu	0.44	25.24	0.44	25.25	0.44	25.22	0.43	25.24
208 Val	1.09	21.35	1.08	21.32	1.10	21.34	1.07	21.31
210 Val								
212 Val	0.78	22.30	0.77	22.36	0.78	22.30	0.75	22.48
214 Met	1.13	17.11	1.16	17.15			1.21	17.24
220 Val	1.34	22.35	1.34	22.36	1.33	22.35	1.34	22.40
222 Val	0.54	18.52	0.54	18.54	0.54	18.53	0.54	18.55
224 Ile	0.43	13.62	0.42	13.55	0.42	13.56	0.42	13.50
225 Leu	0.10	19.93	0.09	19.92	0.10	19.92	0.09	19.91
228 Leu	0.94	26.32	0.94	26.35	0.94	26.33	0.94	26.35
232 Leu	0.33	23.50	0.33	23.48	0.34	23.47	0.33	23.48
243 Ala	1.53	19.31	1.53	19.31	1.53	19.31	1.53	19.35
254 Ala	0.39	16.31	0.41	16.36	0.39	16.34	0.42	16.38
256 Ile	-0.29	10.38	-0.29	10.38	-0.29	10.38	-0.30	10.37
266 Leu	0.66	22.76	0.66	22.86	0.65	22.87	0.68	22.90
274 Val	0.84	23.50						
277 Val	0.98	23.88	0.98	23.87	0.98	23.86	0.97	23.86
280 Leu	0.23	24.91	0.24	24.95	0.22	24.92	0.24	24.99
283 Ala	1.68	18.89	1.67	18.89	1.67	18.89	1.67	18.88
287 Ala	1.58	19.85	1.57	19.87	1.57	19.85	1.57	19.84
288 Met	2.02	17.94	2.04	18.21	2.02	17.98		
289 Met	2.00	16.74	2.01	16.79	2.00	16.72	2.03	16.90
293 Ala	1.55	17.53	1.55	17.53	1.55	17.53	1.55	17.53
296 Ile	0.58	13.59	0.59	13.56	0.58	13.57	0.59	13.55
298 Ala	1.33	19.49	1.33	19.49	1.32	19.47	1.32	19.45
299 Val	0.68	19.63	0.74	19.59	0.70	19.61	0.73	19.58
306 Leu	0.69	27.21	0.67	27.15	0.69	27.22	0.63	26.96
310 Leu	0.83	22.74	0.83	22.79	0.83	22.78	0.84	22.86
311 Leu	0.80	27.24	0.80	27.23	0.80	27.24	0.80	27.25
318 Val	1.14	22.22	1.13	22.21	1.13	22.21	1.13	22.23
319 Leu	-0.30	20.21	-0.29	20.25	-0.30	20.21	-0.29	20.29
324 Leu	1.03	28.09	1.00	27.88	1.00	27.84	0.95	27.54
329 Leu	0.73	23.90	0.74	23.91	0.73	23.90	0.73	23.91
330 Leu	0.73	22.08	0.73	22.07	0.72	22.06	0.73	22.08
334 Ala	1.39	18.17	1.39	18.17	1.39	18.16	1.39	18.18
335 Val	0.80	20.34	0.80	20.35	0.80	20.34	0.80	20.44

	UDP-Gal		UDP-Glc		UDP-GalNAc		UDP-GlcNAc	
	^{1}H (ppm)	^{13}C (ppm)	^{1}H (ppm)	^{13}C (ppm)	^{1}H (ppm)	^{13}C (ppm)	^{1}H (ppm)	^{13}C (ppm)
336 Leu	0.03	22.91	0.06	22.93	-0.05	23.01	0.23	23.09
339 Leu	-0.09	22.94	-0.11	22.94	-0.11	22.98	-0.21	22.90
343 Ala	1.18	18.98	1.19	19.02	1.18	19.04	1.19	18.98
344 Val			0.85	20.84	0.86	20.85	0.86	20.85
350 Ala	1.38	18.95	1.37	19.00	1.37	19.05	1.37	19.04
351 Val	0.86	20.34	0.86	20.35	0.91	20.36	0.91	20.36

Tab. 13: Chemical shifts of the AIL^{proS}MV^{proS} methyl resonances of GTA in ternary binding complexes.

	UDP-Gal + 3DD		UDP-Glc + 3DD		UDP-GalNAc + 3DD		UDP-GlcNAc + 3DD	
	^{1}H (ppm)	^{13}C (ppm)	^{1}H (ppm)	^{13}C (ppm)	^{1}H (ppm)	^{13}C (ppm)	^{1}H (ppm)	^{13}C (ppm)
58 Ala	1.54	19.44	1.54	19.43	1.54	19.43	1.54	19.44
59 Ile	0.70	12.62	0.70	12.62	0.70	12.62	0.70	12.61
63 Met	2.12	18.04	2.12	18.03	2.12	18.01	2.13	18.07
64 Val	0.91	19.42	0.91	19.44	0.90	19.41	0.91	19.43
66 Leu	0.83	23.43	0.83	23.46	0.83	23.43	0.83	23.46
69 Met	2.08	16.94	2.08	16.91	2.08	16.94	2.08	16.94
70 Val	0.67	19.85	0.67	19.84	0.67	19.85	0.67	19.85
76 Val	1.65	26.01	1.65	26.10	1.65	26.00	1.65	26.12
77 Leu	1.13	22.53	1.12	22.52	1.12	22.55	1.12	22.55
84 Val	-0.90	14.60	-0.89	14.65	-0.90	14.61	-0.89	14.67
85 Leu	0.98	25.32	0.98	25.33	0.98	25.31	0.98	25.34
86 Val	0.97	20.27	0.97	20.26	0.96	20.26	0.96	20.25
87 Val	1.02	20.62	1.02	20.62	1.01	20.61	1.02	20.62
92 Ala	1.22	20.51	1.22	20.51	1.22	20.52	1.22	20.51
94 Ile	0.64	13.24	0.64	13.21	0.64	13.24	0.64	13.23
95 Val	0.59	20.96	0.60	20.99	0.59	20.97	0.60	21.00
102 Ile	1.22	15.28	1.22	15.27	1.21	15.26	1.22	15.28
104 Ile	0.36	13.40	0.35	13.40	0.35	13.40	0.35	13.41
105 Leu	1.10	23.26	1.11	23.31	1.10	23.26	1.10	23.28
111 Leu	0.91	22.40	0.92	22.41	0.91	22.40	0.92	22.41
116 Ile	0.68	16.99	0.68	17.05	0.68	17.01	0.68	17.05
118 Leu	0.52	25.00	0.51	25.01	0.52	25.00	0.50	24.99
120 Val	0.30	21.39	0.34	21.24	0.30	21.39	0.33	21.32
122 Ala	1.17	19.69	1.16	19.58	1.17	19.68	1.17	19.64
123 Ile	0.91	11.84	0.92	12.38	0.92	11.86	0.92	12.07
127 Val	1.01	19.32	1.01	19.40	1.01	19.31	1.01	19.41
128 Ala	1.08	18.54	1.06	18.58	1.08	18.55	1.05	18.54
130 Leu	0.82	24.80	0.82	24.70	0.82	24.80	0.82	24.79
132 Leu	0.96	25.72	0.96	25.73	0.96	25.70	0.96	25.76
134 Leu	0.24	21.01	0.24	20.98	0.24	21.00	0.25	21.02
137 Ala	1.25	18.05	1.27	18.09	1.25	18.06	1.27	18.13

	UDP-Gal + 3DD		UDP-Glc + 3DD		UDP-GalNAc + 3DD		UDP-GlcNAc + 3DD	
	^{1}H (ppm)	^{13}C (ppm)	^{1}H (ppm)	^{13}C (ppm)	^{1}H (ppm)	^{13}C (ppm)	^{1}H (ppm)	^{13}C (ppm)
142 Met	1.22	19.82	1.22	19.85	1.22	19.82	1.23	19.81
143 Val	0.65	21.80	0.67	21.83	0.65	21.82	0.67	21.83
147 Val	0.76	23.78	0.77	23.79	0.77	23.79	0.77	23.81
151 Val	0.77	20.34	0.77	20.34	0.77	20.33	0.77	20.34
157 Ala	1.39	18.02	1.39	18.03	1.39	18.02	1.39	18.02
158 Ala	1.44	19.31	1.44	19.33	1.44	19.32	1.44	19.34
162 Val	0.77	19.81	0.77	19.82	0.77	19.82	0.77	19.83
164 Leu	0.70	22.69	0.71	22.68	0.70	22.68	0.70	22.68
170 Leu	0.70	25.32	0.70	25.34	0.70	25.32	0.70	25.33
172 Val	0.91	22.27	0.90	22.22	0.90	22.24	0.90	22.27
173 Leu	0.29	23.42	0.28	23.45	0.29	23.41	0.29	23.42
175 Val	0.86	17.86	0.84	17.85	0.86	17.87	0.86	17.84
177 Ala	1.27	20.48	1.27	20.44	1.27	20.48	1.27	20.50
184 Val	0.96	23.05	0.96	22.86	0.96	23.05		
186 Met	1.83	18.21	1.83	18.12	1.83	18.17	1.83	18.19
189 Met	1.88	18.47	1.88	18.38	1.88	18.47	1.89	18.44
191 Met	2.45	19.11	2.43	19.04	2.45	19.12	2.45	19.08
192 Ile	1.06	14.17	1.03	13.98	1.07	14.16	1.04	14.00
201 Leu	0.88	23.96	0.88	23.99	0.88	23.97	0.88	24.01
204 Val	0.75	18.77	0.74	18.79	0.75	18.78	0.74	18.79
207 Leu	0.42	25.06	0.40	24.93	0.41	25.06	0.40	24.92
208 Val	1.08	21.42	1.05	21.32	1.08	21.38	1.04	21.32
210 Val	0.97	20.02						
212 Val	0.77	22.32	0.73	22.64	0.77	22.31	0.73	22.56
214 Met	0.80	15.79			0.80	15.82		
220 Val	1.33	22.39	1.37	22.33	1.34	22.38	1.37	22.31
222 Val	0.54	18.47	0.54	18.52	0.54	18.48	0.54	18.53
224 Ile	0.45	13.57	0.43	13.50	0.44	13.54	0.44	13.56
225 Leu	0.11	19.99	0.10	19.97	0.11	19.98	0.10	19.99
228 Leu	0.93	26.28	0.93	26.31	0.93	26.30	0.94	26.32
232 Leu	0.34	23.49	0.34	23.51	0.33	23.49	0.35	23.44
243 Ala	1.50	19.33	1.50	19.32	1.50	19.32	1.50	19.33
254 Ala	0.39	16.31	0.41	16.30	0.39	16.32	0.42	16.30
256 Ile	-0.30	10.33	-0.30	10.32	-0.30	10.32	-0.29	10.33
266 Leu	0.61	22.07	0.65	22.57	0.62	22.09		
274 Val								
277 Val	0.98	23.89	0.97	23.84	0.99	23.88	0.97	23.87
280 Leu	0.21	24.94	0.22	24.83	0.21	24.95	0.22	24.86
283 Ala	1.68	18.87	1.68	18.90	1.67	18.88	1.68	18.90
287 Ala	1.57	19.81	1.59	19.80	1.57	19.82	1.59	19.81
288 Met	2.01	18.11	2.00	18.72				
289 Met	2.00	16.70			2.00	16.71	2.04	16.93
293 Ala	1.55	17.52	1.55	17.54	1.55	17.53	1.55	17.53
296 Ile	0.58	13.62	0.58	13.60	0.58	13.62	0.58	13.60
298 Ala	1.30	19.49	1.29	19.53	1.30	19.47	1.28	19.49

	UDP-Gal + 3DD		UDP-Glc + 3DD		UDP-GalNAc + 3DD		UDP-GlcNAc + 3DD	
	^{1}H (ppm)	^{13}C (ppm)	^{1}H (ppm)	^{13}C (ppm)	^{1}H (ppm)	^{13}C (ppm)	^{1}H (ppm)	^{13}C (ppm)
299 Val	0.61	19.63	0.58	19.61	0.61	19.62	0.54	19.60
306 Leu	0.64	27.08	0.60	26.68	0.64	27.08	0.64	27.02
310 Leu	0.84	22.83	0.85	22.89	0.84	22.83	0.84	22.92
311 Leu	0.81	27.23	0.80	27.22	0.81	27.24	0.80	27.22
318 Val	1.14	22.30	1.15	22.32	1.14	22.30	1.15	22.31
319 Leu	-0.30	20.25	-0.26	20.39	-0.30	20.25	-0.23	20.59
324 Leu	0.88	27.58	0.88	27.11	0.89	27.57		
329 Leu	0.76	25.32	0.76	25.39	0.76	25.31		
330 Leu	0.75	22.70			0.75	22.68	0.73	22.56
334 Ala	1.38	18.24	1.38	18.21	1.38	18.23	1.38	18.22
335 Val	0.81	20.82	0.80	20.73	0.81	20.82	0.80	20.82
336 Leu	0.37	23.10	0.35	23.14	0.37	23.09	0.37	23.18
339 Leu	-0.36	22.84	-0.37	22.73	-0.36	22.84	-0.39	22.68
343 Ala	1.21	18.39	1.20	18.72	1.21	18.37	1.19	18.73
344 Val	0.83	20.83			0.83	20.82		
350 Ala	1.41	18.58	1.38	18.71	1.41	18.58	1.40	18.59
351 Val	0.72	21.15	0.81	20.58	0.72	21.12		

Tab. 14: Chemical shifts of the AIL^{proS}MV^{proS} methyl resonances of AAGlyB in complex with donor substrates and analogs.

	UDP		UDP-Gal		UDP-GalNAc		UDP-Glc		UDP-GlcNAc	
	^{1}H (ppm)	^{13}C (ppm)	^{1}H (ppm)	^{13}C (ppm)	^{1}H (ppm)	^{13}C (ppm)	^{1}H (ppm)	^{13}C (ppm)	^{1}H (ppm)	^{13}C (ppm)
58 Ala	1.53	19.41	1.54	19.41	1.54	19.42	1.54	19.42	1.53	19.40
59 Ile	0.70	12.62	0.70	12.61	0.70	12.62	0.70	12.59	0.70	12.61
63 Met	2.12	18.02	2.12	18.05	2.12	18.04	2.12	18.10	2.12	18.03
64 Val	0.90	19.44	0.91	19.43	0.91	19.42	0.91	19.40	0.90	19.43
66 Leu	0.82	23.44	0.82	23.44	0.82	23.44	0.82	23.45	0.82	23.43
69 Met	2.08	16.96	2.08	16.97	2.09	16.97	2.08	16.94	2.09	16.98
70 Val	0.67	19.85	0.66	19.85	0.66	19.85	0.67	19.85	0.67	19.85
76 Val	1.66	25.95	1.67	25.96	1.67	25.95	1.67	26.03	1.67	25.93
77 Leu	1.12	22.52	1.12	22.51	1.12	22.52	1.12	22.52	1.12	22.55
84 Val	-0.89	14.61	-0.89	14.61	-0.89	14.60	-0.89	14.62	-0.89	14.61
85 Leu	0.98	25.36	0.99	25.34	0.99	25.35	0.99	25.41	0.98	25.36
86 Val	0.97	20.28	0.97	20.26	0.97	20.27	0.96	20.25	0.97	20.29
87 Val	1.02	20.61	1.02	20.61	1.02	20.61	1.02	20.60	1.02	20.60
92 Ala	1.21	20.43	1.22	20.44	1.22	20.43	1.22	20.42	1.22	20.43
94 Ile	0.64	13.31	0.65	13.31	0.64	13.30	0.63	13.28	0.65	13.32
95 Val	0.60	21.04	0.60	21.05	0.60	21.03	0.60	21.02	0.60	21.04
102 Ile	1.23	15.25	1.23	15.26	1.23	15.26	1.23	15.27	1.23	15.25
104 Ile	0.35	13.39	0.35	13.38	0.36	13.39	0.36	13.43	0.35	13.39

	UDP		UDP-Gal		UDP-GalNAc		UDP-Glc		UDP-GlcNAc	
	^{1}H (ppm)	^{13}C (ppm)	^{1}H (ppm)	^{13}C (ppm)	^{1}H (ppm)	^{13}C (ppm)	^{1}H (ppm)	^{13}C (ppm)	^{1}H (ppm)	^{13}C (ppm)
105 Leu	1.10	23.25	1.11	23.26	1.10	23.25	1.11	23.30	1.10	23.26
111 Leu	0.91	22.42	0.92	22.42	0.92	22.42	0.92	22.42	0.92	22.42
116 Ile	0.69	17.05	0.69	17.08	0.68	17.05	0.69	17.12	0.69	17.07
118 Leu	0.60	25.17	0.59	25.17	0.59	25.16	0.57	25.18	0.59	25.15
120 Val	0.31	21.30	0.31	21.41	0.31	21.31	0.32	21.24	0.33	21.28
122 Ala	1.18	19.72	1.18	19.74	1.18	19.71	1.15	19.60	1.17	19.71
123 Ile	0.92	12.22	0.92	12.14	0.92	12.21	0.91	11.92	0.93	12.32
127 Val	1.01	19.24	1.01	18.90	1.01	19.23	1.01	18.66	1.01	19.34
128 Ala	1.07	18.55	1.07	18.55	1.06	18.54	1.07	18.56	1.07	18.55
130 Leu	0.85	24.91	0.83	24.43	0.84	24.91	0.82	24.39	0.84	24.83
132 Leu	0.97	25.59	0.96	25.60	0.97	25.60	0.97	25.67	0.96	25.58
134 Leu	0.24	21.00	0.24	20.97	0.24	20.99	0.22	20.96	0.23	20.98
137 Ala	1.26	18.05	1.26	18.05	1.26	18.05	1.27	18.08	1.26	18.05
142 Met	1.23	19.88	1.23	19.89	1.23	19.87	1.23	19.93	1.22	19.90
143 Val	0.66	21.83	0.67	21.82	0.66	21.82	0.67	21.86	0.66	21.85
147 Val	0.76	23.79	0.76	23.80	0.76	23.80	0.76	23.84	0.76	23.78
151 Val	0.78	20.36	0.78	20.38	0.78	20.37	0.78	20.34	0.78	20.33
157 Ala	1.39	18.04	1.39	18.04	1.39	18.04	1.39	18.05	1.39	18.04
158 Ala	1.44	19.36	1.45	19.34	1.45	19.35	1.45	19.37	1.44	19.36
162 Val	0.77	19.85	0.77	19.83	0.77	19.84	0.77	19.84	0.77	19.85
164 Leu	0.71	22.66	0.71	22.69	0.71	22.66	0.71	22.66	0.71	22.64
170 Leu	0.70	25.30	0.71	25.32	0.70	25.30	0.71	25.29	0.70	25.32
172 Val	0.91	22.18	0.91	22.18	0.91	22.19	0.91	22.20	0.91	22.18
173 Leu	0.30	23.52	0.29	23.61	0.30	23.50	0.30	23.51	0.30	23.55
175 Val	0.86	17.88	0.86	17.86	0.86	17.87	0.86	17.84	0.85	17.92
177 Ala	1.27	20.52	1.27	20.53	1.27	20.55	1.26	20.54	1.27	20.45
184 Val	0.95	22.95	0.95	22.99	0.95	22.94	0.95	23.08	0.95	22.92
186 Met	1.84	18.45	1.84	18.22	1.84	18.46	1.83	18.24	1.84	18.37
189 Met	1.83	18.15	1.84	18.22	1.83	18.16	1.83	18.24	1.84	18.11
191 Met	2.43	19.04	2.43	19.03	2.43	19.04	2.44	19.07	2.42	19.04
192 Ile	1.06	14.05	1.03	13.97	1.05	14.05	1.04	13.98	1.05	13.99
201 Leu	0.88	23.97	0.88	23.97	0.88	23.96	0.88	23.98	0.88	23.99
204 Val	0.75	18.82	0.75	18.84	0.76	18.82	0.76	18.83	0.75	18.85
207 Leu	0.46	25.40	0.47	25.48	0.46	25.39	0.46	25.26	0.46	25.46
208 Val	1.10	21.38	1.09	21.36	1.10	21.40	1.09	21.39	1.09	21.37
210 Val							0.96	20.07		
212 Val	0.80	22.20	0.81	22.18	0.81	22.18	0.80	22.21	0.81	22.21
214 Met	1.01	16.93	1.06	17.03	1.00	16.93	1.14	17.42		
220 Val	1.35	22.44	1.35	22.48	1.35	22.43	1.36	22.46	1.35	22.49
222 Val	0.54	18.48	0.54	18.47	0.54	18.47	0.54	18.51	0.54	18.49
224 Ile	0.43	13.74	0.42	13.82	0.43	13.74	0.42	13.68	0.42	13.76
225 Leu	0.10	19.91	0.09	19.89	0.09	19.91	0.09	19.91	0.10	19.92
228 Leu	0.93	26.29	0.93	26.28	0.93	26.28	0.93	26.29	0.93	26.30
232 Leu	0.37	23.51	0.36	23.53	0.37	23.49	0.40	23.43	0.37	23.48

	UDP		UDP-Gal		UDP-GalNAc		UDP-Glc		UDP-GlcNAc	
	^{1}H (ppm)	^{13}C (ppm)	^{1}H (ppm)	^{13}C (ppm)	^{1}H (ppm)	^{13}C (ppm)	^{1}H (ppm)	^{13}C (ppm)	^{1}H (ppm)	^{13}C (ppm)
243 Ala	1.51	19.34	1.53	19.32	1.53	19.34	1.52	19.35	1.52	19.32
254 Ala	0.41	16.31	0.37	16.28	0.41	16.31	0.42	16.36	0.42	16.33
256 Ile	-0.31	10.31	-0.31	10.34	-0.31	10.33	-0.30	10.38	-0.31	10.33
268 Ala	1.51	21.17	1.57	21.18	1.51	21.19	1.50	21.35	1.52	21.44
274 Val	0.84	23.46	0.84	23.51	0.84	23.46	0.84	23.52	0.84	23.46
277 Val	0.98	23.86	0.98	23.89	0.98	23.87	0.98	23.93	0.98	23.85
280 Leu	0.23	24.85	0.23	24.84	0.23	24.86	0.23	24.90	0.24	24.87
283 Ala	1.68	18.87	1.68	18.88	1.68	18.87	1.68	18.87	1.68	18.87
287 Ala	1.58	19.81	1.58	19.83	1.58	19.81	1.58	19.89	1.58	19.83
288 Met	2.01	18.31	2.00	17.96	2.01	18.27	2.02	18.36	2.01	18.39
289 Met	2.01	16.68	2.00	16.73	2.01	16.69	2.05	16.75	2.02	16.84
293 Ala	1.55	17.53	1.55	17.53	1.55	17.52	1.55	17.52	1.55	17.53
296 Ile	0.58	13.57	0.58	13.61	0.58	13.57	0.58	13.60	0.58	13.56
298 Ala	1.30	19.46	1.33	19.50	1.30	19.44	1.31	19.58	1.30	19.49
299 Val	0.71	19.60	0.67	19.66	0.71	19.60	0.69	19.59	0.69	19.54
306 Leu	0.73	26.86	0.73	26.79	0.73	26.86	0.74	26.83	0.71	26.81
310 Leu	0.83	22.73	0.83	22.68	0.84	22.70	0.84	22.73	0.83	22.73
311 Leu	0.79	27.24	0.79	27.24	0.79	27.25	0.80	27.21	0.80	27.24
318 Val	1.15	22.37	1.16	22.40	1.15	22.37	1.14	22.35	1.15	22.36
319 Leu	-0.28	20.25	-0.26	20.31	-0.28	20.26	-0.27	20.29	-0.27	20.29
324 Leu	0.92	25.40	0.89	25.11	0.92	25.42	0.92	25.49	0.91	25.26
329 Leu	0.72	23.95	0.72	23.92	0.72	23.95	0.72	23.95	0.72	23.95
330 Leu	0.73	22.05	0.72	22.04	0.73	22.05	0.71	21.99	0.72	22.03
334 Ala	1.38	18.18	1.38	18.19	1.38	18.19	1.38	18.18	1.38	18.19
335 Val	0.81	21.06	0.82	21.06	0.82	21.05	0.81	21.16	0.82	21.00
336 Leu	0.22	22.91	0.21	22.92	0.22	22.91	0.21	22.87	0.23	22.94
339 Leu	-0.19	23.04	-0.19	23.05	-0.19	23.05	-0.18	23.02	-0.19	23.08
343 Ala	1.23	18.98	1.22	19.04	1.22	18.97	1.23	19.14	1.22	19.06
344 Val	0.81	21.06	0.82	21.06	0.82	21.05	0.81	21.16	0.82	21.00
350 Ala	1.43	18.90	1.38	18.89	1.42	18.89	1.38	18.72	1.38	19.08
351 Val	0.93	20.33	0.83	20.32	0.90	20.37	0.88	20.41	0.90	20.39

Tab. 15: Chemical shifts of the AIL^{proS}MV^{proS} methyl resonances of AAGlyB in ternary binding complexes.

	UDP-Gal+3DD		UDP-GalNAc+3DD		UDP-Glc+3DD		UDP-GlcNAc+3DD	
	^{1}H (ppm)	^{13}C (ppm)	^{1}H (ppm)	^{13}C (ppm)	^{1}H (ppm)	^{13}C (ppm)	^{1}H (ppm)	^{13}C (ppm)
58 Ala	1.54	19.43	1.54	19.43	1.54	19.43	1.53	19.43
59 Ile	0.69	12.62	0.70	12.62	0.70	12.61	0.70	12.61
63 Met	2.13	18.08	2.13	18.07	2.13	18.09	2.13	18.08
64 Val	0.91	19.40	0.91	19.40	0.91	19.41	0.91	19.41
66 Leu	0.83	23.45	0.83	23.44	0.83	23.46	0.82	23.44
69 Met	2.08	16.94	2.08	16.94	2.08	16.94	2.08	16.90

	UDP-Gal+3DD		UDP-GalNAc+3DD		UDP-Glc+3DD		UDP-GlcNAc+3DD	
	^{1}H (ppm)	^{13}C (ppm)	^{1}H (ppm)	^{13}C (ppm)	^{1}H (ppm)	^{13}C (ppm)	^{1}H (ppm)	^{13}C (ppm)
70 Val	0.67	19.85	0.67	19.85	0.67	19.85	0.67	19.85
76 Val	1.66	26.03	1.67	26.03	1.66	26.04	1.66	26.03
77 Leu	1.12	22.54	1.13	22.55	1.12	22.54	1.12	22.55
84 Val	-0.90	14.58	-0.90	14.58	-0.90	14.59	-0.90	14.58
85 Leu	0.99	25.34	0.99	25.33	0.99	25.35	0.99	25.34
86 Val	0.97	20.35	0.97	20.34	0.97	20.31	0.97	20.34
87 Val	1.02	20.61	1.02	20.62	1.02	20.61	1.02	20.61
92 Ala	1.22	20.48	1.22	20.46	1.22	20.45	1.22	20.46
94 Ile	0.65	13.24	0.64	13.23	0.64	13.25	0.64	13.24
95 Val	0.60	21.00	0.60	20.98	0.60	21.00	0.60	21.00
102 Ile	1.22	15.27	1.22	15.26	1.23	15.26	1.22	15.26
104 Ile	0.35	13.38	0.36	13.40	0.35	13.39	0.35	13.39
105 Leu	1.10	23.24	1.10	23.25	1.10	23.27	1.10	23.26
111 Leu	0.92	22.41	0.92	22.41	0.92	22.42	0.92	22.41
116 Ile	0.68	17.02	0.68	17.03	0.68	17.07	0.68	17.03
118 Leu	0.59	25.13	0.57	25.13	0.57	25.15	0.57	25.13
120 Val	0.22	21.63	0.27	21.45	0.30	21.39	0.27	21.44
122 Ala	1.18	19.75	1.18	19.75	1.17	19.68	1.17	19.74
123 Ile	0.94	12.59	0.92	12.10	0.93	12.36	0.92	12.11
127 Val	1.01	19.27	1.01	19.27	1.01	19.15	1.01	19.29
128 Ala	1.07	18.53	1.07	18.54	1.07	18.56	1.07	18.54
130 Leu	0.87	24.97	0.84	24.96	0.83	24.67	0.84	24.96
132 Leu	0.96	25.69	0.96	25.73	0.96	25.69	0.96	25.71
134 Leu	0.25	20.97	0.24	20.96	0.24	20.97	0.24	20.97
137 Ala	1.25	18.03	1.26	18.05	1.26	18.05	1.26	18.05
142 Met	1.21	19.91	1.23	19.85	1.23	19.89	1.23	19.84
143 Val	0.66	21.80	0.66	21.81	0.67	21.83	0.66	21.82
147 Val	0.75	23.76	0.76	23.77	0.76	23.78	0.76	23.78
151 Val	0.78	20.44	0.78	20.43	0.78	20.39	0.78	20.42
157 Ala	1.39	18.02	1.39	18.03	1.39	18.04	1.39	18.03
158 Ala	1.44	19.32	1.44	19.32	1.45	19.34	1.44	19.33
162 Val	0.77	19.82	0.77	19.83	0.77	19.83	0.77	19.83
164 Leu	0.71	22.71	0.70	22.69	0.71	22.68	0.71	22.67
170 Leu	0.70	25.31	0.70	25.30	0.70	25.31	0.70	25.32
172 Val	0.91	22.22	0.91	22.24	0.91	22.22	0.91	22.24
173 Leu	0.28	23.54	0.29	23.44	0.29	23.51	0.29	23.44
175 Val	0.86	17.81	0.86	17.83	0.86	17.84	0.86	17.83
177 Ala	1.27	20.51	1.26	20.51	1.27	20.49	1.27	20.51
184 Val	0.97	23.01	0.96	23.05	0.95	23.00	0.97	23.01
186 Met	1.83	18.24	1.83	18.19	1.83	18.19	1.83	18.18
189 Met	1.84	18.48	1.83	18.53	1.83	18.19	1.84	18.51
191 Met	2.44	19.07	2.45	19.08	2.43	19.07	2.45	19.08
192 Ile	1.05	14.07	1.06	14.08	1.04	13.97	1.06	14.08
201 Leu	0.88	23.95	0.88	23.94	0.88	23.97	0.88	23.96
204 Val	0.75	18.79	0.75	18.79	0.75	18.81	0.76	18.81

	UDP-Gal+3DD		UDP-GalNAc+3DD		UDP-Glc+3DD		UDP-GlcNAc+3DD	
	^{1}H (ppm)	^{13}C (ppm)	^{1}H (ppm)	^{13}C (ppm)	^{1}H (ppm)	^{13}C (ppm)	^{1}H (ppm)	^{13}C (ppm)
207 Leu	0.45	25.32	0.45	25.25	0.45	25.34	0.45	25.27
208 Val	1.09	21.45	1.09	21.45	1.08	21.39	1.09	21.44
210 Val	0.97	20.10	0.97	20.08			0.97	20.09
212 Val	0.79	22.19	0.80	22.18	0.79	22.28	0.80	22.22
214 Met	1.02	17.22	1.04	17.30	1.17	17.42	1.05	17.30
220 Val	1.37	22.51	1.37	22.50	1.37	22.50	1.37	22.50
222 Val	0.54	18.48	0.54	18.48	0.54	18.50	0.54	18.50
224 Ile	0.45	13.78	0.44	13.69	0.43	13.73	0.44	13.71
225 Leu	0.10	19.97	0.10	19.94	0.09	19.92	0.10	19.96
228 Leu	0.93	26.27	0.93	26.28	0.93	26.28	0.93	26.30
232 Leu	0.36	23.43	0.36	23.43	0.36	23.44	0.37	23.42
243 Ala	1.51	19.35	1.51	19.34	1.51	19.35	1.51	19.34
254 Ala	0.42	16.31	0.42	16.32	0.42	16.31	0.42	16.32
256 Ile	-0.31	10.28	-0.31	10.29	-0.30	10.30	-0.30	10.29
268 Ala	1.49	21.13	1.49	21.13	1.53	21.35	1.49	21.13
274 Val								
277 Val	0.98	23.87	0.98	23.86	0.98	23.86	0.98	23.85
280 Leu	0.23	24.81	0.24	24.87	0.24	24.86	0.24	24.86
283 Ala	1.68	18.86	1.68	18.84	1.68	18.87	1.68	18.85
287 Ala	1.58	19.78	1.58	19.77	1.58	19.82	1.58	19.80
288 Met	2.00	18.48	2.01	18.48	2.01	18.39		
289 Met	2.04	16.76	2.02	16.74	2.05	16.86	2.04	16.72
293 Ala	1.55	17.53	1.55	17.52	1.55	17.53	1.55	17.53
296 Ile	0.57	13.62	0.57	13.59	0.58	13.59	0.58	13.59
298 Ala	1.29	19.47	1.28	19.42	1.31	19.51	1.28	19.43
299 Val	0.56	19.64	0.57	19.58	0.57	19.59	0.57	19.58
306 Leu	0.72	26.86	0.72	26.81	0.71	26.79	0.72	26.81
310 Leu	0.83	22.68	0.83	22.72	0.84	22.71	0.83	22.72
311 Leu	0.80	27.24	0.80	27.25	0.80	27.24	0.80	27.24
318 Val	1.15	22.35	1.15	22.34	1.16	22.37	1.15	22.35
319 Leu	-0.28	20.26	-0.28	20.25	-0.26	20.31	-0.28	20.26
324 Leu	0.91	25.20	0.91	25.21	0.90	25.17	0.91	25.21
329 Leu	0.76	25.25	0.76	25.27	0.74	25.00	0.76	25.27
330 Leu	0.75	22.75	0.75	22.75	0.76	22.69	0.74	22.72
334 Ala	1.38	18.21	1.38	18.21	1.38	18.20	1.38	18.20
335 Val	0.81	20.92	0.81	20.96	0.81	20.98	0.81	20.92
336 Leu	0.33	23.01	0.33	22.99	0.29	22.99	0.33	23.00
339 Leu	-0.29	23.09	-0.29	23.07	-0.26	23.05	-0.29	23.06
343 Ala	1.25	18.77	1.25	18.77	1.22	19.20	1.25	18.77
344 Val	0.81	20.92	0.81	20.96	0.81	20.98	0.81	20.92
350 Ala	1.41	18.58	1.41	18.57	1.37	19.07	1.41	18.58
351 Val	0.67	21.09	0.71	21.14	0.81	20.51	0.71	21.12

Chemical shifts of methyl resonances of GTB Trp^{181} mutants

Tab. 16: Chemical shifts of the IL^{proS}MV^{proS} methyl resonances of apo-GTB W181E and in binary and ternary binding complexes.

	apo		UDP		H-dis		UDP + H-dis	
	1H	13C	1H	13C	1H	13C	1H	13C
59 Ile	0.70	12.61	0.71	12.62	0.70	12.61	0.70	12.61
63 Met	2.11	17.94	2.11	17.91	2.11	17.96	2.11	17.98
64 Val	0.89	19.41	0.89	19.40	0.89	19.42	0.89	19.40
66 Leu	0.81	23.34	0.81	23.35	0.83	23.36	0.82	23.38
69 Met	2.08	17.06	2.08	17.00	2.08	17.01	2.08	17.00
70 Val	0.66	19.86	0.66	19.86	0.67	19.87	0.67	19.87
76 Val	1.63	25.73	1.63	25.77	1.63	25.83	1.63	25.92
77 Leu	1.12	22.58	1.12	22.57	1.12	22.56	1.12	22.51
84 Val	-0.90	14.59	-0.90	14.59	-0.90	14.60	-0.90	14.60
85 Leu								
86 Val	0.96	20.25	0.96	20.25	0.96	20.23	0.96	20.21
87 Val	1.00	20.55	1.00	1H	13C	20.57	1.01	20.60
92 Ala								
94 Ile	0.65	13.30	0.65	13.30	0.65	13.24	0.65	13.22
95 Val	0.57	21.03	0.58	21.03	0.58	21.04	0.58	21.05
102 Ile	1.21	15.22	1.21	15.21	1.21	15.22	1.21	15.24
104 Ile	0.34	13.38	0.34	13.38	0.33	13.37	0.34	13.39
105 Leu	1.09	23.27	1.09	23.26	1.10	23.28	1.10	23.28
111 Leu	0.91	22.41	0.91	22.40	0.91	22.41	0.91	22.40
116 Ile	0.68	17.15	0.68	17.07	0.69	17.16	0.68	17.09
118 Leu	0.52	24.92	0.57	25.08	0.50	24.91	0.56	25.06
120 Val	0.44	20.24	0.43	20.57	0.44	20.18	0.40	20.84
123 Ile	0.84	12.78	0.87	13.47	0.84	12.79	0.86	13.39
127 Val	0.99	20.15	1.00	19.72	0.99	20.17	1.00	19.40
130 Leu	0.80	24.78	0.80	24.58	0.79	24.73	0.79	24.37
132 Leu								
134 Leu	0.16	20.95	0.18	20.96	0.15	20.95	0.19	20.95
142 Met	1.21	19.92	1.21	19.91	1.21	19.92	1.22	19.90
143 Val	0.66	21.93	0.66	21.90	0.66	21.94	0.66	21.89
147 Val	0.76	23.82	0.76	23.80	0.76	23.83	0.76	23.80
151 Val	0.75	20.16	0.75	20.14	0.75	20.16	0.74	20.17
162 Val	0.78	19.91	0.78	19.90	0.78	19.91	0.78	19.88
164 Leu	0.70	22.55	0.70	22.60	0.70	22.56	0.70	22.65
170 Leu	0.71	25.44	0.70	25.36	0.71	25.44	0.71	25.38
172 Val	0.91	22.12	0.91	22.14	0.91	22.11	0.91	22.14
173 Leu	0.39	23.96	0.39	23.88	0.39	23.95	0.38	23.87
175 Val	0.92	19.50	0.91	19.18	0.92	19.50	0.91	19.16
184 Val	0.84	21.53	0.75	21.48	0.84	21.51	0.77	21.43
186 Met	1.92	16.90	1.92	17.09	1.92	16.89	1.92	17.13
189 Met	1.80	17.87	1.80	18.03	1.79	17.83	1.79	18.02

	apo		UDP		H-dis		UDP + H-dis	
	1H	13C	1H	13C	1H	13C	1H	13C
191 Met	2.11	17.94	2.08	18.12	2.11	17.96	2.08	18.18
192 Ile	1.00	13.38	1.03	13.73	1.00	13.38	1.03	13.73
201 Leu	0.88	24.17	0.88	24.11	0.88	24.18	0.88	24.11
204 Val	0.73	18.95	0.74	18.90	0.73	18.93	0.74	18.89
207 Leu	0.47	26.11	0.47	26.03	0.46	26.07	0.47	26.02
208 Val	1.08	21.22	1.10	21.28	1.06	21.26	1.08	21.28
210 Val	0.83	20.19	0.91	20.18	0.81	20.21	0.90	20.12
212 Val	0.74	22.40	0.76	22.39	0.72	22.42	0.76	22.39
214 Met	1.14	17.11	1.04	16.87	1.22	17.49	1.23	17.67
220 Val	1.35	22.51	1.33	22.48	1.36	22.57	1.35	22.52
222 Val	0.53	18.55	0.53	18.53	0.53	18.60	0.53	18.54
224 Ile	0.39	13.60	0.40	13.65	0.40	13.63	0.40	13.67
225 Leu	0.08	19.83	0.08	19.84	0.07	19.85	0.08	19.85
228 Leu	0.93	26.37	0.93	26.35	0.94	26.36	0.93	26.33
232 Leu	0.34	23.30	0.35	23.34	0.32	23.30	0.33	23.33
256 Ile	-0.29	10.44	-0.29	10.44	-0.29	10.36	-0.29	10.34
266 Met	1.89	18.45	1.84	18.44	1.98	19.26	1.90	19.21
274 Val	0.82	23.85	0.83	23.66	0.82	23.85	0.83	23.64
277 Val	0.96	23.85	0.97	23.85	0.95	23.85	0.96	23.87
280 Leu	0.27	25.07	0.25	25.05	0.28	25.08	0.26	25.06
288 Met	2.16	17.76	2.15	17.81	2.17	17.74	2.15	17.84
289 Met	1.99	17.18	1.95	17.17	1.99	17.21	1.92	17.13
296 Ile	0.60	13.51	0.60	13.51	0.59	13.55	0.59	13.56
299 Val	0.71	19.50	0.71	19.52	0.57	19.54	0.62	19.55
306 Leu	0.62	26.48	0.64	26.53	0.60	26.35	0.63	26.46
310 Leu	0.81	22.79	0.81	22.78	0.82	22.77	0.81	22.73
311 Leu	0.80	27.30	0.80	27.30	0.81	27.30	0.81	27.29
318 Val	1.14	22.17	1.14	22.17	1.15	22.17	1.15	22.23
319 Leu	-0.32	20.21	-0.32	20.17	-0.32	20.27	-0.31	20.18
324 Leu	1.01	25.77	0.99	25.68	1.09	26.26	1.08	26.02
329 Leu	0.71	23.86	0.71	23.86	0.72	24.73	0.71	25.00
330 Leu	0.70	22.04	0.71	22.06	0.67	22.04	0.70	22.24
335 Val								
336 Leu	0.26	23.07	0.18	22.99	0.36	23.10	0.34	23.05
339 Leu	-0.19	23.09	-0.15	23.07	-0.27	23.01	-0.29	22.93
344 Val								
351 Val	0.91	20.40	0.91	20.37	0.91	20.36	0.91	20.36

Tab. 17: Chemical shifts of the IL^{proS}MV^{proS} methyl resonances of apo-GTB W181M and in binary and ternary binding complexes.

	apo		H-dis		UDP		UDP + H-dis	
	^{1}H (ppm)	^{13}C (ppm)	^{1}H (ppm)	^{13}C (ppm)	^{1}H (ppm)	^{13}C (ppm)	^{1}H (ppm)	^{13}C (ppm)
59 Ile	0.70	12.61	0.70	12.61			0.70	12.61
63 Met	2.11	17.91	2.11	17.94			2.11	17.96
64 Val	0.89	19.40	0.90	19.42			0.89	19.42
66 Leu	0.82	23.32	0.83	23.36	0.82	23.34	0.85	23.35
69 Met	2.08	17.07	2.08	17.07	2.12	17.00	2.08	17.00
70 Val	0.67	19.86	0.67	19.86	0.67	19.85	0.67	19.87
76 Val	1.63	25.71	1.63	25.83	1.63	25.77	1.63	25.91
77 Leu	1.12	22.58	1.12	22.56	1.12	22.59	1.12	22.51
84 Val	-0.90	14.59	-0.90	14.60	-0.89	14.65	-0.90	14.61
85 Leu	0.97	25.31	0.97	25.27			0.98	25.27
86 Val	0.96	20.24	0.96	20.23	0.97	20.27		
87 Val	1.00	20.54	1.00	20.56	1.00	20.53	1.01	20.60
94 Ile	0.65	13.30	0.66	13.26	0.65	13.30	0.65	13.22
95 Val	0.58	21.03	0.58	21.04	0.58	21.08	0.59	21.06
102 Ile	1.21	15.21	1.21	15.21	1.20	15.19	1.21	15.22
104 Ile	0.34	13.38	0.34	13.37	0.33	13.36	0.34	13.38
105 Leu	1.10	23.26	1.10	23.28			1.10	23.27
111 Leu	0.91	22.40	0.91	22.39	0.89	22.28	0.91	22.38
116 Ile	0.69	17.13	0.69	17.14	0.68	16.84	0.68	17.10
118 Leu	0.52	24.93	0.51	24.92	0.59	25.13	0.57	25.07
120 Val	0.45	20.23	0.45	20.17	0.43	20.59	0.41	20.80
123 Ile	0.84	12.72	0.84	12.75	0.87	13.38	0.86	13.28
127 Val	0.99	20.11	0.99	20.14	1.00	19.67	1.00	19.39
130 Leu	0.80	24.79	0.80	24.74	0.80	24.57	0.79	24.37
132 Leu	0.95	25.39	0.97	25.53			0.97	25.61
134 Leu	0.16	20.95	0.16	20.95	0.18	20.98	0.19	20.95
142 Met	1.21	19.92	1.21	19.92	1.21	19.85	1.22	19.89
143 Val	0.66	21.93	0.67	21.97	0.66	21.92	0.66	21.89
147 Val	0.76	23.83	0.77	23.82	0.75	23.78	0.76	23.81
151 Val	0.75	20.16	0.75	20.15	0.75	20.14	0.74	20.15
162 Val	0.78	19.91	0.78	19.91	0.78	19.91	0.78	19.89
164 Leu	0.70	22.55	0.70	22.56	0.70	22.60	0.71	22.65
170 Leu	0.71	25.43	0.71	25.42	0.70	25.34	0.71	25.38
172 Val	0.91	22.11	0.91	22.11	0.91	22.12	0.91	22.12
173 Leu	0.40	23.96	0.40	23.95	0.40	23.89	0.39	23.86
175 Val	0.91	19.46	0.91	19.45	0.90	19.14	0.91	19.14
177 Ala	2.06	17.07	2.07	17.07	2.08	17.17	2.08	17.16
184 Val	0.87	21.55	0.87	21.53	0.82	21.73	0.76	21.47
186 Met	1.93	16.92	1.93	16.92	1.93	17.02	1.93	17.10
189 Met	1.80	17.86	1.79	17.82	1.81	18.04	1.79	18.03
191 Met	2.08	17.98	2.08	18.01	2.04	18.11	2.04	18.14
192 Ile	1.00	13.38	1.00	13.38	1.03	13.73	1.03	13.72

	apo		H-dis		UDP		UDP + H-dis	
	^{1}H (ppm)	^{13}C (ppm)	^{1}H (ppm)	^{13}C (ppm)	^{1}H (ppm)	^{13}C (ppm)	^{1}H (ppm)	^{13}C (ppm)
201 Leu	0.88	24.14	0.88	24.14	0.87	24.04	0.88	24.09
204 Val	0.73	18.95	0.73	18.93	0.75	18.95	0.74	18.91
207 Leu	0.47	26.10	0.46	26.05	0.46	25.92	0.46	26.00
208 Val	1.08	21.22	1.07	21.26	1.11	21.24	1.08	21.27
210 Val	0.83	20.19	0.81	20.21	0.92	20.16	0.91	20.13
212 Val	0.74	22.39	0.73	22.41	0.77	22.38	0.76	22.39
214 Met	1.14	17.11	1.22	17.47	1.05	16.89	1.23	17.64
220 Val	1.35	22.51	1.37	22.57	1.33	22.46	1.36	22.52
222 Val	0.53	18.55	0.54	18.60	0.53	18.48	0.54	18.53
224 Ile	0.39	13.61	0.40	13.63	0.40	13.66	0.40	13.67
225 Leu	0.07	19.83	0.07	19.84	0.09	19.84	0.08	19.86
228 Leu	0.93	26.36	0.94	26.36	0.96	26.29	0.93	26.33
232 Leu	0.34	23.29	0.32	23.30	0.34	23.29	0.33	23.32
256 Ile	-0.28	10.44	-0.29	10.36	-0.29	10.42	-0.29	10.34
266 Met	1.89	18.45	1.98	19.30	1.85	18.43	1.91	19.20
274 Val	0.82	23.83	0.82	23.83	0.83	23.62	0.83	23.67
277 Val	0.96	23.84	0.95	23.85	0.98	23.82	0.96	23.86
280 Leu	0.27	25.08	0.29	25.10			0.27	25.06
288 Met	2.17	17.75	2.18	17.73	2.15	17.85	2.15	17.86
289 Met	1.99	17.16	1.99	17.17	1.97	17.19	1.93	17.10
296 Ile	0.60	13.52	0.59	13.55	0.60	13.49	0.60	13.56
299 Val	0.72	19.51	0.57	19.55	0.71	19.52	0.61	19.56
306 Leu	0.62	26.47	0.60	26.34	0.64	26.55	0.63	26.45
310 Leu	0.81	22.80	0.82	22.78	0.82	22.82	0.82	22.74
311 Leu	0.81	27.30	0.81	27.30	0.81	27.25	0.81	27.29
318 Val	1.14	22.17	1.15	22.18	1.12	22.17	1.15	22.23
319 Leu	-0.32	20.20	-0.31	20.27	-0.32	20.15	-0.31	20.18
324 Leu	1.01	25.77	1.09	26.27	0.97	25.58	1.08	26.02
329 Leu	0.71	23.86	0.72	24.71	0.71	23.86	0.72	24.97
330 Leu	0.70	22.04	0.67	21.97	0.71	22.07	0.70	22.24
335 Val								
336 Leu	0.26	23.07	0.36	23.11	0.14	22.98	0.34	23.06
339 Leu	-0.19	23.09	-0.27	23.01	-0.14	23.01	-0.29	22.93
344 Val								
351 Val	0.91	20.38	0.92	20.35				

Line shape analysis fitting results

Donor analog titrations with GTB

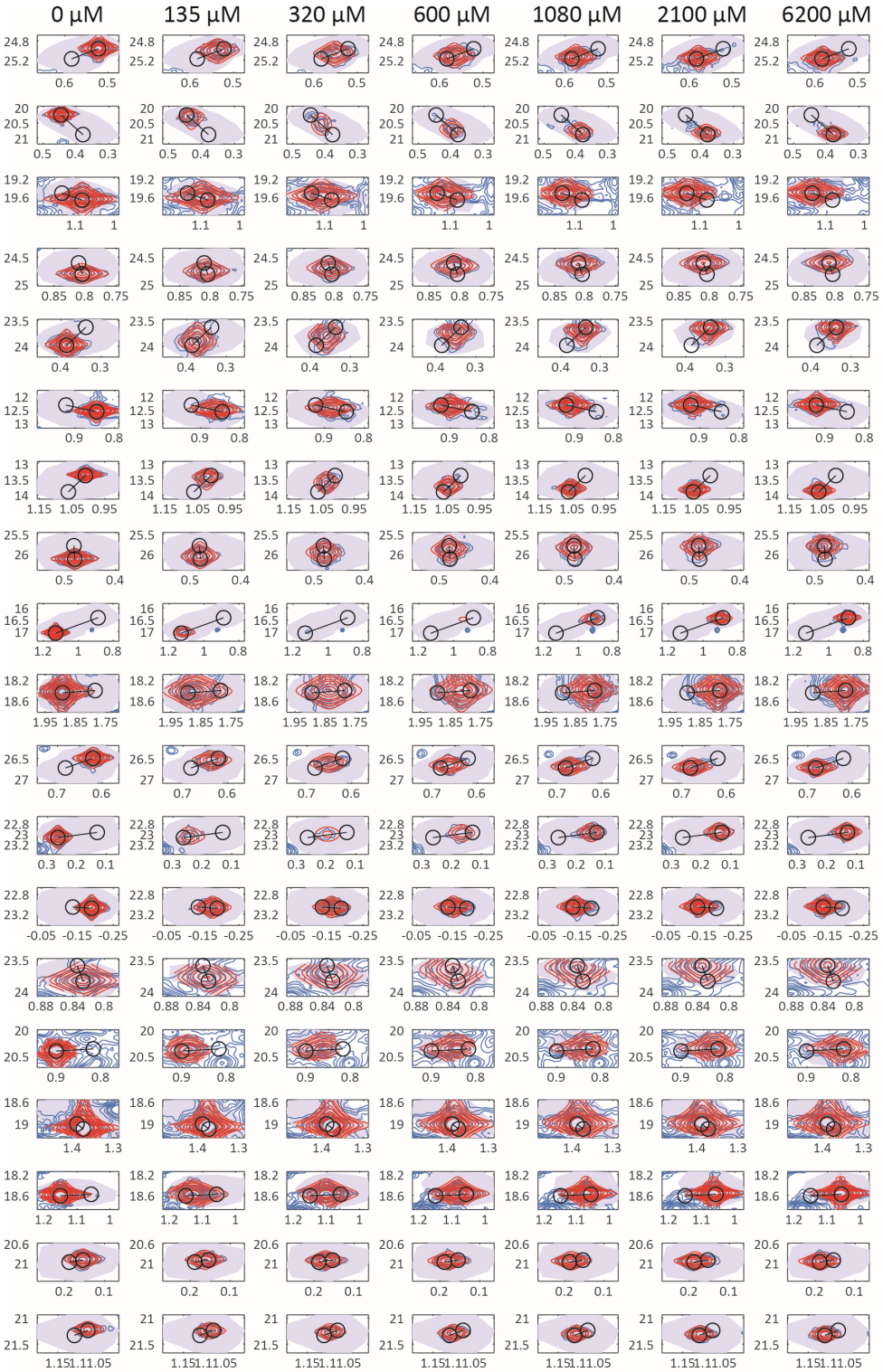


Fig. 1: Overlay of experimental (blue) and fitted (red) line shapes of the titration of GTB with UDP. Each row corresponds to one fitted residue in the same order as in the following table.

Tab. 18: Line shape analysis results of the titration of GTB with UDP.K_d is reported in units of µM. k_{off}, the transverse relaxation rates in the ^1H dimension (R2I), and the transverse relaxation rates in the ^{13}C dimension (R2S) are reported in units of s^{-1}. The chemical shifts (dI = ^1H; dS = ^{13}C) of the bound state (state 2) are reported in ppm.

Residue	Parameter	State	Fit result	Error
global	K_d		161.21	2.91
global	k_{off}		243.87	7.35
Leu118	dI	2	0.58	0.00
Leu118	dS	2	25.17	0.00
Leu118	R2I	2	40.28	2.28
Leu118	R2S	2	32.93	3.41
Val120	dI	2	0.38	0.00
Val120	dS	2	20.89	0.01
Val120	R2I	2	62.98	5.78
Val120	R2S	2	80.14	11.59
Ala122	dI	2	1.14	0.00
Ala122	dS	2	19.52	0.00
Ala122	R2I	2	64.05	1.32
Ala122	R2S	2	39.58	1.35
Leu130	dI	2	0.81	0.00
Leu130	dS	2	24.61	0.01
Leu130	R2I	2	40.34	3.97
Leu130	R2S	2	44.17	4.77
Leu173	dI	2	0.34	0.00
Leu173	dS	2	23.63	0.00
Leu173	R2I	2	36.38	1.95
Leu173	R2S	2	46.07	3.37
Ile123	dI	2	0.92	0.00
Ile123	dS	2	12.32	0.00
Ile123	R2I	2	41.17	1.38
Ile123	R2S	2	69.42	3.20
Ile192	dI	2	1.06	0.00
Ile192	dS	2	13.90	0.00
Ile192	R2I	2	44.94	2.61
Ile192	R2S	2	49.92	4.59
Leu207	dI	2	0.48	0.00
Leu207	dS	2	25.79	0.01
Leu207	R2I	2	34.38	2.54
Leu207	R2S	2	79.84	7.69
Met214	dI	2	0.89	0.00
Met214	dS	2	16.42	0.01
Met214	R2I	2	96.23	5.80
Met214	R2S	2	65.98	9.03
Met266	dI	2	1.78	0.00
Met266	dS	2	18.41	0.00
Met266	R2I	2	56.10	0.97

Residue	Parameter	State	Fit result	Error
Met266	R2S	2	51.09	1.32
Leu306	dI	2	0.68	0.00
Leu306	dS	2	26.73	0.00
Leu306	R2I	2	47.23	3.52
Leu306	R2S	2	41.83	4.92
Leu336	dI	2	0.13	0.00
Leu336	dS	2	22.97	0.01
Leu336	R2I	2	61.16	5.84
Leu336	R2S	2	34.75	5.14
Leu339	dI	2	-0.14	0.00
Leu339	dS	2	23.06	0.00
Leu339	R2I	2	42.78	1.96
Leu339	R2S	2	22.96	2.00
Val274	dI	2	0.83	0.00
Val274	dS	2	23.59	0.01
Val274	R2I	2	36.56	2.00
Val274	R2S	2	84.75	6.48
Val351	dI	2	0.82	0.00
Val351	dS	2	20.36	0.00
Val351	R2I	2	66.57	1.89
Val351	R2S	2	50.00	1.83
Ala350	dI	2	1.39	0.00
Ala350	dS	2	19.01	0.00
Ala350	R2I	2	47.32	0.37
Ala350	R2S	2	47.64	0.68
Ala128	dI	2	1.06	0.00
Ala128	dS	2	18.58	0.00
Ala128	R2I	2	40.73	0.76
Ala128	R2S	2	12.90	0.57
Leu134	dI	2	0.19	0.00
Leu134	dS	2	20.98	0.00
Leu134	R2I	2	56.29	3.99
Leu134	R2S	2	28.75	3.88
Val208	dI	2	1.11	0.00
Val208	dS	2	21.33	0.00
Val208	R2I	2	45.06	5.31
Val208	R2S	2	35.83	6.05

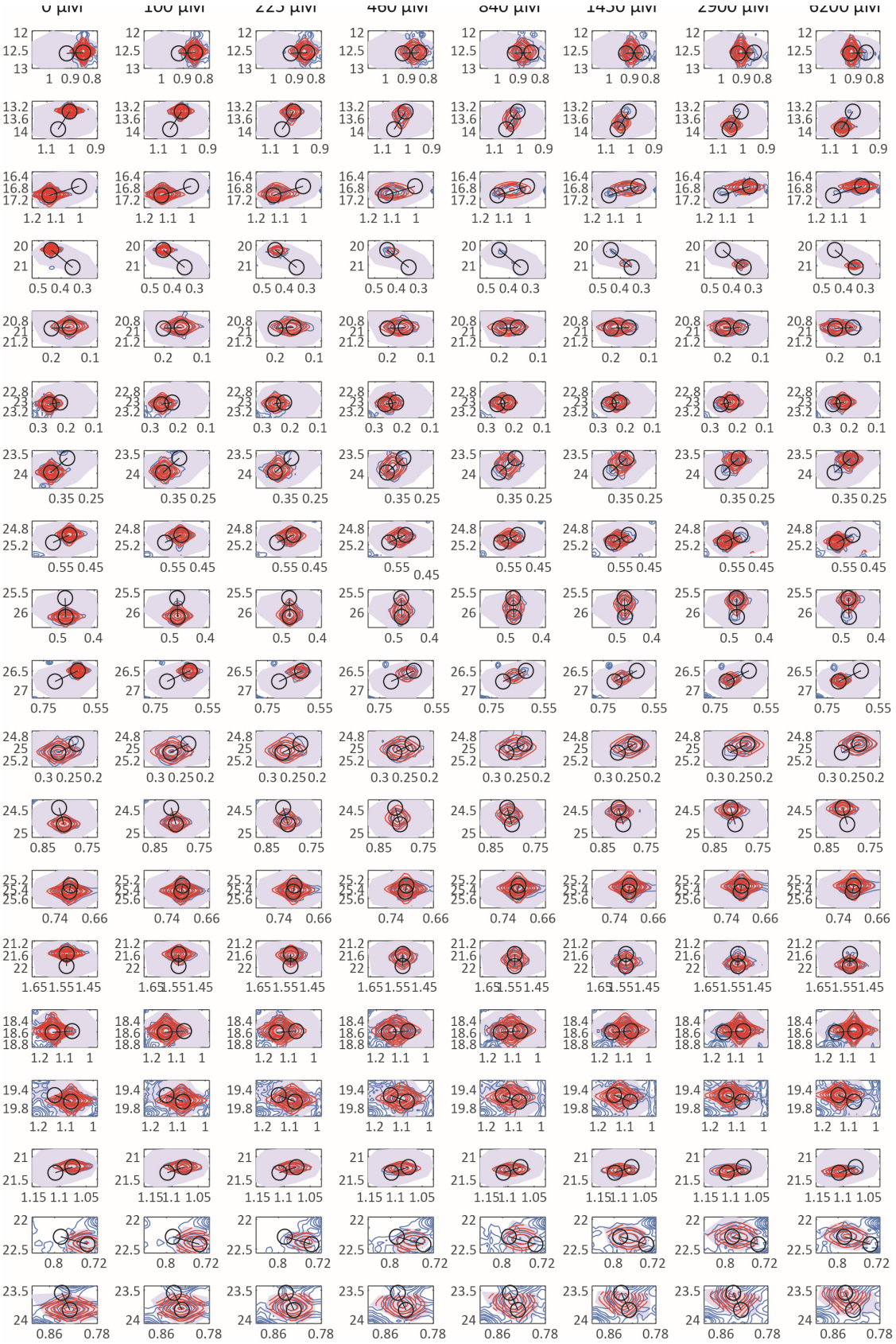


Fig. 2: Overlay of experimental (blue) and fitted (red) line shapes of the titration of GTB with UDP-Glc. Each row corresponds to one fitted residue in the same order as in the following table.

Tab. 19: Line shape analysis results of the titration of GTB with UDP-Glc.K_d is reported in units of μM. k_{off}, the transverse relaxation rates in the ^{1}H dimension (R2I), and the transverse relaxation rates in the ^{13}C dimension (R2S) are reported in units of s^{-1}. The chemical shifts (dI = ^{1}H; dS = ^{13}C) of the bound state (state 2) are reported in ppm.

Residue	Parameter	State	Fit result	Error
global	K_d		598.37	7.49
global	k_{off}		218.63	4.13
Ile123	dI	2	0.92	0.00
Ile123	dS	2	12.60	0.00
Ile123	R2I	2	34.93	0.77
Ile123	R2S	2	90.84	2.56
Ile192	dI	2	1.06	0.00
Ile192	dS	2	13.95	0.00
Ile192	R2I	2	51.03	1.91
Ile192	R2S	2	59.36	4.49
Met214	dI	2	1.00	0.00
Met214	dS	2	16.77	0.00
Met214	R2I	2	104.69	2.58
Met214	R2S	2	37.30	2.86
Val120	dI	2	0.35	0.00
Val120	dS	2	21.11	0.01
Val120	R2I	2	85.32	5.20
Val120	R2S	2	65.11	9.58
Leu134	dI	2	0.20	0.00
Leu134	dS	2	20.96	0.00
Leu134	R2I	2	60.65	2.75
Leu134	R2S	2	25.32	2.31
Leu336	dI	2	0.22	0.00
Leu336	dS	2	23.03	0.00
Leu336	R2I	2	49.21	2.09
Leu336	R2S	2	28.65	2.11
Leu173	dI	2	0.33	0.00
Leu173	dS	2	23.62	0.00
Leu173	R2I	2	40.20	1.40
Leu173	R2S	2	54.20	3.15
Leu118	dI	2	0.58	0.00
Leu118	dS	2	25.15	0.00
Leu118	R2I	2	40.41	1.58
Leu118	R2S	2	30.56	1.87
Leu207	dI	2	0.48	0.00
Leu207	dS	2	25.66	0.01
Leu207	R2I	2	33.79	1.65
Leu207	R2S	2	91.84	5.50
Leu306	dI	2	0.71	0.00
Leu306	dS	2	26.78	0.00
Leu306	R2I	2	55.83	3.34

Residue	Parameter	State	Fit result	Error
Leu306	R2S	2	45.66	5.49
Leu280	dI	2	0.24	0.00
Leu280	dS	2	24.93	0.00
Leu280	R2I	2	59.54	3.68
Leu280	R2S	2	55.36	5.64
Leu130	dI	2	0.81	0.00
Leu130	dS	2	24.46	0.00
Leu130	R2I	2	37.53	2.23
Leu130	R2S	2	34.34	4.23
Leu170	dI	2	0.71	0.00
Leu170	dS	2	25.33	0.00
Leu170	R2I	2	23.21	0.70
Leu170	R2S	2	33.46	1.45
Ala268	dI	2	1.53	0.00
Ala268	dS	2	21.96	0.00
Ala268	R2I	2	68.59	2.22
Ala268	R2S	2	71.55	3.74
Ala128	dI	2	1.07	0.00
Ala128	dS	2	18.58	0.00
Ala128	R2I	2	45.90	0.64
Ala128	R2S	2	10.99	0.48
Ala122	dI	2	1.14	0.00
Ala122	dS	2	19.53	0.00
Ala122	R2I	2	59.41	0.84
Ala122	R2S	2	32.44	0.88
Val208	dI	2	1.11	0.00
Val208	dS	2	21.36	0.00
Val208	R2I	2	43.76	3.02
Val208	R2S	2	26.96	3.26
Val76	dI	2	1.64	0.00
Val76	dS	2	25.89	0.00
Val76	R2I	2	27.67	0.80
Val76	R2S	2	43.64	1.76
Val212	dI	2	0.79	0.00
Val212	dS	2	22.29	0.01
Val212	R2I	2	91.17	4.36
Val212	R2S	2	76.27	5.24

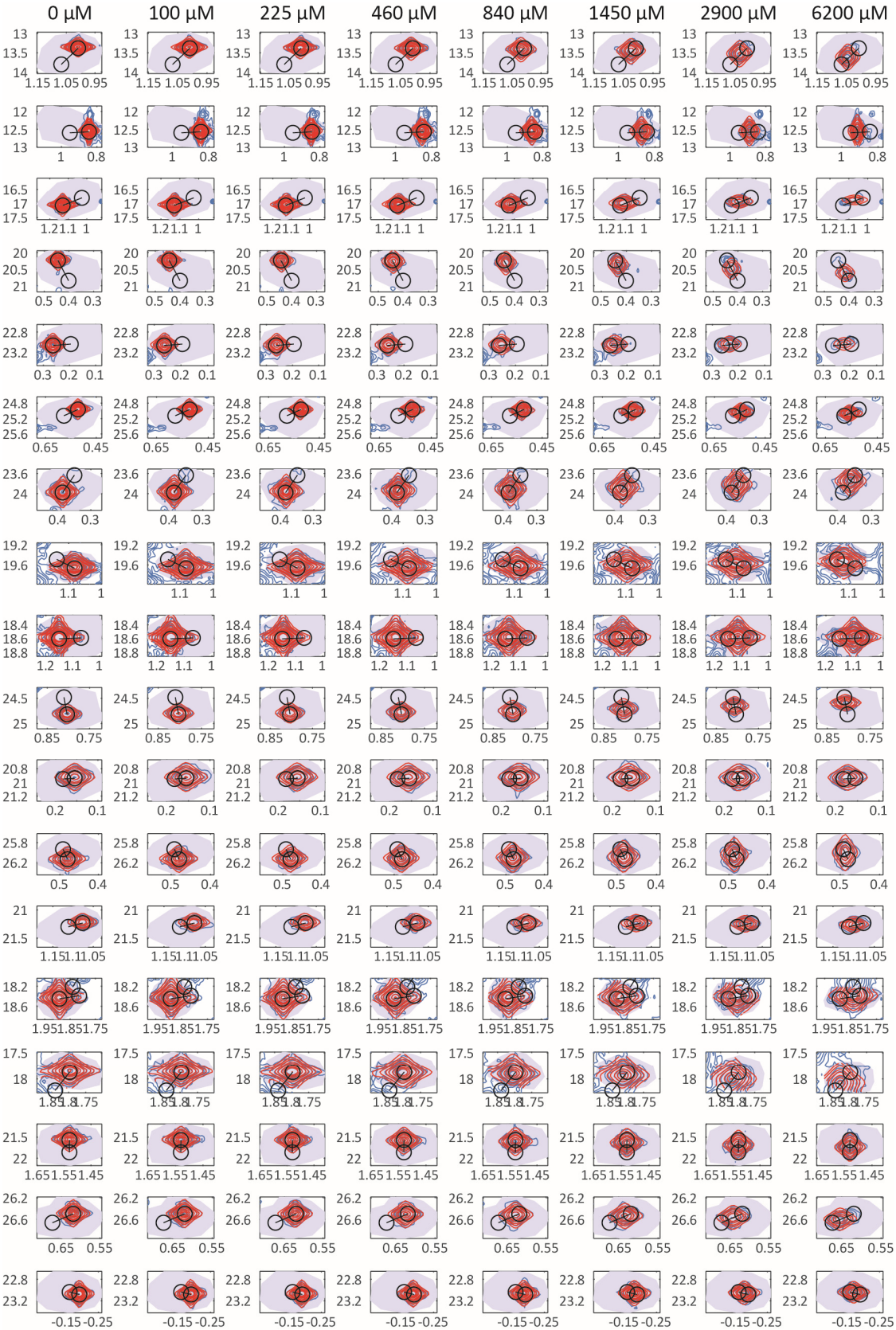


Fig. 3: Overlay of experimental (blue) and fitted (red) line shapes of the titration of GTB with UDP-GalNAc. Each row corresponds to one fitted residue in the same order as in the following table.

Tab. 20: Line shape analysis results of the titration of GTB with UDP-GalNAc.K_d is reported in units of µM. k_{off}, the transverse relaxation rates in the ^1H dimension (R2I), and the transverse relaxation rates in the ^{13}C dimension (R2S) are reported in units of s^{-1}. The chemical shifts (dI = ^1H; dS = ^{13}C) of the bound state (state 2) are reported in ppm.

Residue	Parameter	State	Fit result	Error
global	K_d		3368.93	59.90
global	k_{off}		492.61	14.49
Ile192	dI	2	1.07	0.00
Ile192	dS	2	13.80	0.01
Ile192	R2I	2	45.92	3.30
Ile192	R2S	2	92.63	8.40
Ile123	dI	2	0.95	0.00
Ile123	dS	2	12.60	0.01
Ile123	R2I	2	26.05	2.04
Ile123	R2S	2	118.58	6.68
Met214	dI	2	1.03	0.00
Met214	dS	2	16.80	0.01
Met214	R2I	2	195.52	7.72
Met214	R2S	2	55.98	10.80
Val120	dI	2	0.40	0.00
Val120	dS	2	20.85	0.02
Val120	R2I	2	81.41	6.43
Val120	R2S	2	74.87	14.71
Leu336	dI	2	0.19	0.00
Leu336	dS	2	23.04	0.01
Leu336	R2I	2	120.60	10.44
Leu336	R2S	2	61.49	13.95
Leu118	dI	2	0.58	0.00
Leu118	dS	2	25.13	0.01
Leu118	R2I	2	55.99	3.23
Leu118	R2S	2	35.04	4.21
Leu173	dI	2	0.35	0.00
Leu173	dS	2	23.63	0.01
Leu173	R2I	2	48.93	2.38
Leu173	R2S	2	51.78	5.10
Ala122	dI	2	1.14	0.00
Ala122	dS	2	19.49	0.00
Ala122	R2I	2	59.70	1.83
Ala122	R2S	2	41.81	2.38
Ala128	dI	2	1.07	0.00
Ala128	dS	2	18.59	0.00
Ala128	R2I	2	58.35	1.40
Ala128	R2S	2	7.16	1.26
Leu130	dI	2	0.81	0.00
Leu130	dS	2	24.48	0.01
Leu130	R2I	2	48.06	4.31

Residue	Parameter	State	Fit result	Error
Leu130	R2S	2	11.97	5.58
Leu134	dI	2	0.18	0.00
Leu134	dS	2	20.95	0.00
Leu134	R2I	2	58.26	4.91
Leu134	R2S	2	41.55	5.97
Leu207	dI	2	0.49	0.00
Leu207	dS	2	25.93	0.01
Leu207	R2I	2	31.36	2.98
Leu207	R2S	2	134.71	11.13
Val208	dI	2	1.11	0.00
Val208	dS	2	21.30	0.01
Val208	R2I	2	46.92	5.02
Val208	R2S	2	29.22	6.90
Met266	dI	2	1.81	0.00
Met266	dS	2	18.37	0.00
Met266	R2I	2	57.95	1.52
Met266	R2S	2	59.83	2.39
Met189	dI	2	1.84	0.00
Met189	dS	2	18.24	0.01
Met189	R2I	2	48.75	1.83
Met189	R2S	2	86.75	4.63
Ala268	dI	2	1.53	0.00
Ala268	dS	2	21.86	0.00
Ala268	R2I	2	56.85	2.66
Ala268	R2S	2	72.48	4.95
Leu306	dI	2	0.67	0.00
Leu306	dS	2	26.66	0.01
Leu306	R2I	2	56.26	3.96
Leu306	R2S	2	46.35	5.75
Leu339	dI	2	-0.16	0.00
Leu339	dS	2	23.04	0.00
Leu339	R2I	2	57.49	3.09
Leu339	R2S	2	33.36	3.18

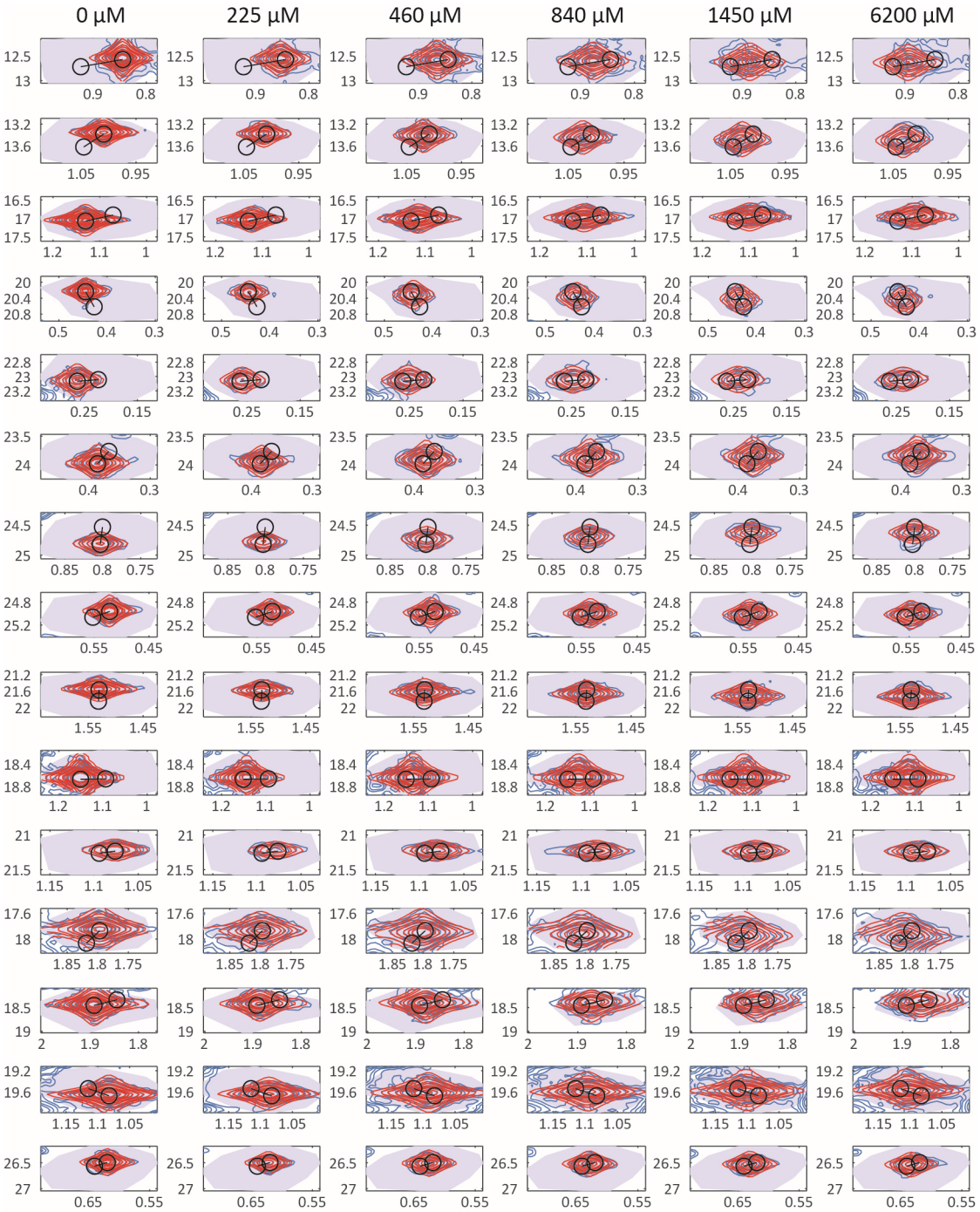


Fig. 4: Overlay of experimental (blue) and fitted (red) line shapes of the titration of GTB with UDP-GlcNAc. Each row corresponds to one fitted residue in the same order as in the following table.

Tab. 21: Line shape analysis results of the titration of GTB with UDP-GlcNAc.K_d is reported in units of μM. k_{off}, the transverse relaxation rates in the ^{1}H dimension (R2I), and the transverse relaxation rates in the ^{13}C dimension (R2S) are reported in units of s^{-1}. The chemical shifts (dI = ^{1}H; dS = ^{13}C) of the bound state (state 2) are reported in ppm.

Residue	Parameter	State	Fit result	Error
global	K_d		3301.69	107.79
global	k_{off}		609.46	47.52
Ile123	dI	2	0.92	0.00
Ile123	dS	2	12.72	0.01
Ile123	R2I	2	64.09	3.00
Ile123	R2S	2	65.85	5.14
Ile192	dI	2	1.05	0.00
Ile192	dS	2	13.62	0.01
Ile192	R2I	2	51.46	3.12
Ile192	R2S	2	78.26	5.49
Met214	dI	2	1.07	0.00
Met214	dS	2	16.91	0.00
Met214	R2I	2	90.05	2.98
Met214	R2S	2	67.87	4.29
Val120	dI	2	0.43	0.00
Val120	dS	2	20.61	0.02
Val120	R2I	2	55.32	3.70
Val120	R2S	2	120.84	12.54
Leu336	dI	2	0.22	0.00
Leu336	dS	2	23.05	0.01
Leu336	R2I	2	85.57	7.73
Leu336	R2S	2	51.33	8.13
Leu173	dI	2	0.37	0.00
Leu173	dS	2	23.77	0.01
Leu173	R2I	2	40.96	2.75
Leu173	R2S	2	55.90	4.87
Leu130	dI	2	0.80	0.00
Leu130	dS	2	24.53	0.01
Leu130	R2I	2	43.99	5.59
Leu130	R2S	2	44.13	9.45
Leu118	dI	2	0.55	0.00
Leu118	dS	2	25.06	0.00
Leu118	R2I	2	48.56	3.62
Leu118	R2S	2	40.21	4.79
Ala268	dI	2	1.53	0.00
Ala268	dS	2	21.84	0.01
Ala268	R2I	2	61.07	3.31
Ala268	R2S	2	60.83	5.35
Ala128	dI	2	1.09	0.00
Ala128	dS	2	18.60	0.00
Ala128	R2I	2	63.65	1.74

Residue	Parameter	State	Fit result	Error
Ala128	R2S	2	15.87	1.31
Val208	dI	2	1.09	0.00
Val208	dS	2	21.26	0.01
Val208	R2I	2	50.76	8.32
Val208	R2S	2	32.90	7.80
Met189	dI	2	1.82	0.00
Met189	dS	2	18.07	0.01
Met189	R2I	2	74.64	3.42
Met189	R2S	2	73.83	4.07
Met266	dI	2	1.84	0.00
Met266	dS	2	18.33	0.00
Met266	R2I	2	75.47	1.82
Met266	R2S	2	64.59	2.67
Ala122	dI	2	1.12	0.00
Ala122	dS	2	19.53	0.00
Ala122	R2I	2	64.33	1.90
Ala122	R2S	2	44.96	1.98
Leu306	dI	2	0.64	0.00
Leu306	dS	2	26.57	0.01
Leu306	R2I	2	46.30	3.76
Leu306	R2S	2	48.15	5.13

Acceptor substrate and analog titrations with GTB

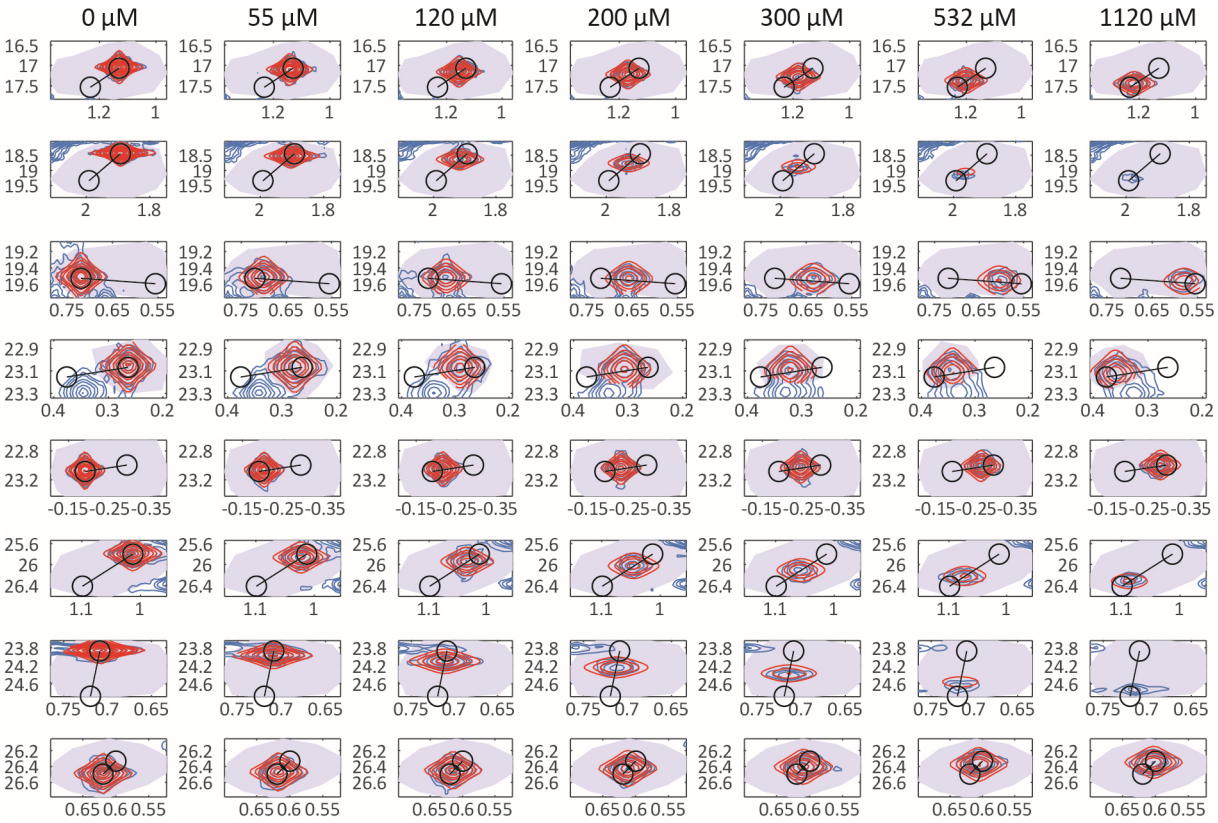


Fig. 5: Overlay of experimental (blue) and fitted (red) line shapes of the titration of GTB with H-dis.Each row corresponds to one fitted residue in the same order as in the following table.

Tab. 22: Line shape analysis results of the titration of GTB with H-dis.K_d is reported in units of µM. k_{off}, the transverse relaxation rates in the ^{1}H dimension (R2I), and the transverse relaxation rates in the ^{13}C dimension (R2S) are reported in units of s^{-1}. The chemical shifts (dI = ^{1}H; dS = ^{13}C) of the bound state (state 2) are reported in ppm.

Residue	Parameter	State	Fit result	Error
global	K_d		164.27	4.29
global	k_{off}		3097.51	281.48
Met214	dI	2	1.23	0.00
Met214	dS	2	17.54	0.00
Met214	R2I	2	99.80	1.99
Met214	R2S	2	78.16	3.10
Met266	dI	2	1.99	0.00
Met266	dS	2	19.36	0.01
Met266	R2I	2	246.42	5.67
Met266	R2S	2	168.64	13.02
Val299	dI	2	0.55	0.00
Val299	dS	2	19.60	0.01
Val299	R2I	2	103.24	4.70

Residue	Parameter	State	Fit result	Error
Val299	R2S	2	67.03	6.18
Leu336	dI	2	0.38	0.00
Leu336	dS	2	23.15	0.00
Leu336	R2I	2	51.51	2.30
Leu336	R2S	2	45.37	2.96
Leu339	dI	2	-0.29	0.00
Leu339	dS	2	23.00	0.00
Leu339	R2I	2	47.89	1.65
Leu339	R2S	2	33.44	2.06
Leu324	dI	2	1.10	0.00
Leu324	dS	2	26.42	0.01
Leu324	R2I	2	113.39	5.69
Leu324	R2S	2	106.40	9.67
Leu329	dI	2	0.72	0.00
Leu329	dS	2	24.90	0.02
Leu329	R2I	2	142.09	6.91
Leu329	R2S	2	136.74	15.13
Leu306	dI	2	0.60	0.00
Leu306	dS	2	26.33	0.00
Leu306	R2I	2	49.38	2.22
Leu306	R2S	2	41.81	2.44

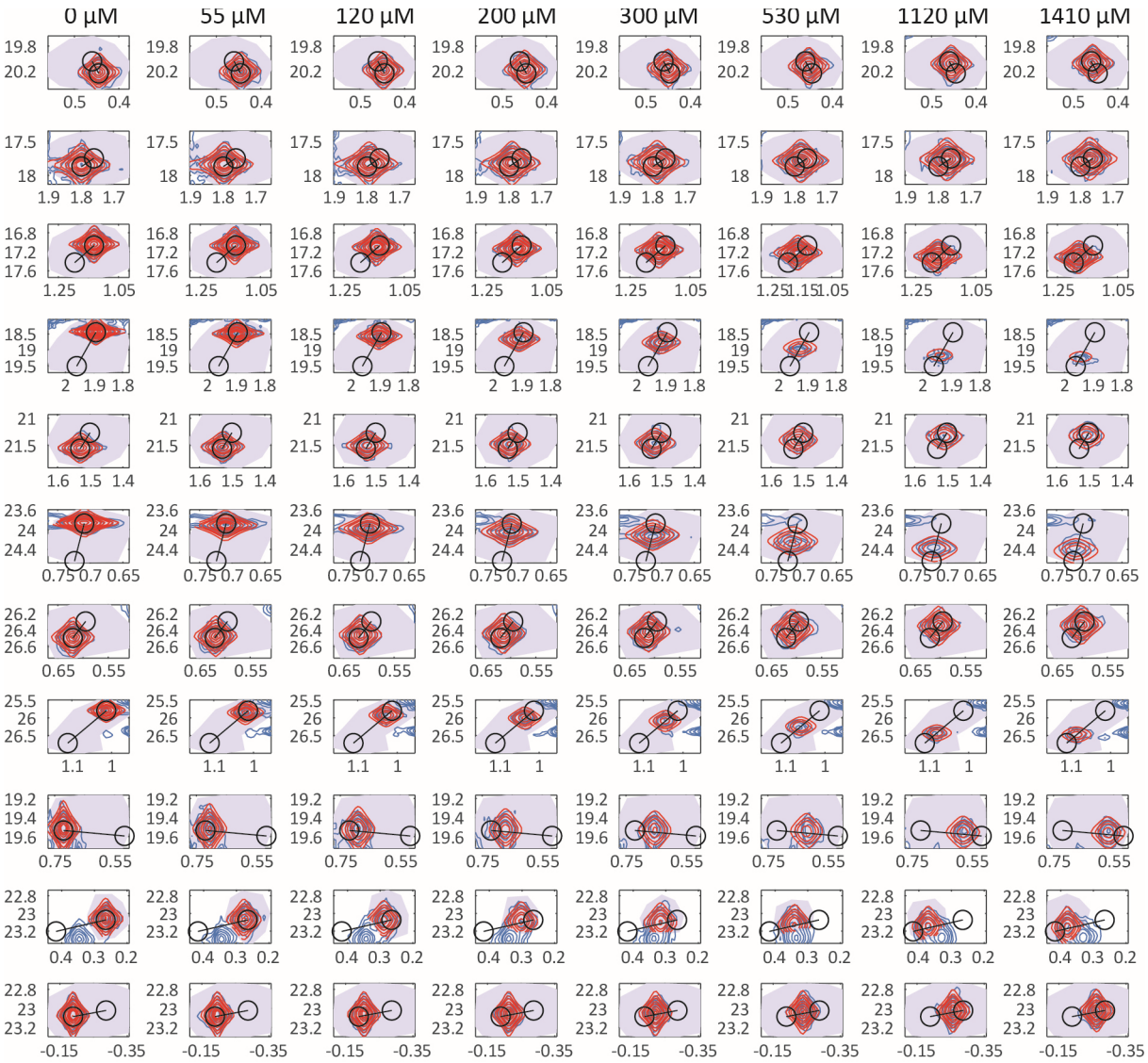


Fig. 6: Overlay of experimental (blue) and fitted (red) line shapes of the titration of GTB with 3DD.Each row corresponds to one fitted residue in the same order as in the following table.

Tab. 23: Line shape analysis results of the titration of GTB with 3DD.K_d is reported in units of µM. k_{off}, the transverse relaxation rates in the ^{1}H dimension (R2I), and the transverse relaxation rates in the ^{13}C dimension (R2S) are reported in units of s^{-1}. The chemical shifts (dI = ^{1}H; dS = ^{13}C) of the bound state (state 2) are reported in ppm.

Residue	Parameter	State	Fit result	Error
global	K_d		421.40	8.84
global	k_{off}		3346.06	209.60
Val120	dI	2	0.46	0.00
Val120	dS	2	20.04	0.00
Val120	R2I	2	43.07	1.95
Val120	R2S	2	53.47	3.22
Met189	dI	2	1.76	0.00

Residue	Parameter	State	Fit result	Error
Met189	dS	2	17.75	0.00
Met189	R2I	2	77.67	1.67
Met189	R2S	2	49.25	1.66
Met214	dI	2	1.20	0.00
Met214	dS	2	17.43	0.00
Met214	R2I	2	79.49	1.82
Met214	R2S	2	59.33	2.18
Met266	dI	2	1.96	0.00
Met266	dS	2	19.52	0.02
Met266	R2I	2	225.55	6.75
Met266	R2S	2	173.20	14.40
Ala268	dI	2	1.50	0.00
Ala268	dS	2	21.26	0.01
Ala268	R2I	2	107.76	4.81
Ala268	R2S	2	91.70	6.90
Leu329	dI	2	0.72	0.00
Leu329	dS	2	24.65	0.01
Leu329	R2I	2	86.49	4.64
Leu329	R2S	2	146.42	9.96
Leu306	dI	2	0.59	0.00
Leu306	dS	2	26.29	0.00
Leu306	R2I	2	35.58	1.77
Leu306	R2S	2	35.27	2.68
Leu324	dI	2	1.11	0.00
Leu324	dS	2	26.72	0.02
Leu324	R2I	2	106.22	6.83
Leu324	R2S	2	110.03	13.52
Val299	dI	2	0.51	0.00
Val299	dS	2	19.59	0.01
Val299	R2I	2	110.77	6.06
Val299	R2S	2	41.84	6.10
Leu336	dI	2	0.42	0.00
Leu336	dS	2	23.20	0.00
Leu336	R2I	2	49.96	2.87
Leu336	R2S	2	43.61	3.26
Leu339	dI	2	-0.29	0.00
Leu339	dS	2	23.02	0.00
Leu339	R2I	2	42.63	1.66
Leu339	R2S	2	27.64	1.90

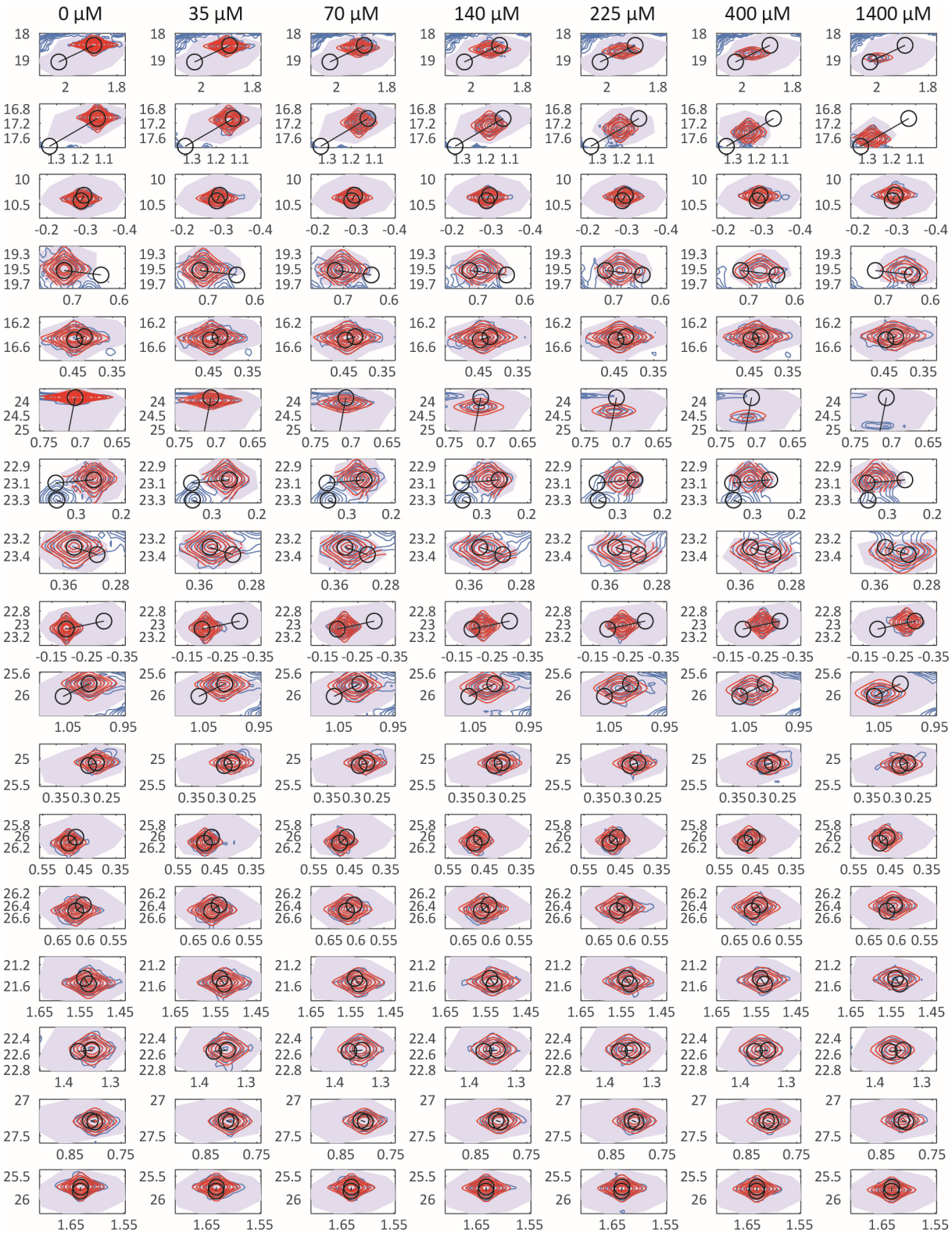


Fig. 7: Overlay of experimental (blue) and fitted (red) line shapes of the titration of GTB with B-tris. Each row corresponds to one fitted residue in the same order as in the following table.

Tab. 24: Line shape analysis results of the titration of GTB with B-tris. K_d is reported in units of µM. k_{off}, the transverse relaxation rates in the ^{1}H dimension (R2I), and the transverse relaxation rates in the ^{13}C dimension (R2S) are reported in units of s^{-1}. The chemical shifts (dI = ^{1}H; dS = ^{13}C) of the bound state (state 2) are reported in ppm.

Residue	Parameter	State	Fit result	Error
global	K_d		264.17	4.38
global	k_{off}		2940.58	91.25
Met266	dI	2	2.03	0.00
Met266	dS	2	19.07	0.01
Met266	R2I	2	211.04	4.74
Met266	R2S	2	112.41	5.95
Met214	dI	2	1.33	0.00
Met214	dS	2	17.83	0.00
Met214	R2I	2	73.69	1.78
Met214	R2S	2	61.81	3.38
Ile256	dI	2	-0.30	0.00
Ile256	dS	2	10.32	0.00
Ile256	R2I	2	56.58	2.09
Ile256	R2S	2	32.35	1.91
Val299	dI	2	0.64	0.00
Val299	dS	2	19.59	0.00
Val299	R2I	2	93.20	4.16
Val299	R2S	2	69.42	6.04
Ala254	dI	2	0.42	0.00
Ala254	dS	2	16.44	0.00
Ala254	R2I	2	94.13	2.12
Ala254	R2S	2	43.66	1.77
Leu329	dI	2	0.72	0.00
Leu329	dS	2	25.16	0.02
Leu329	R2I	2	139.81	8.03
Leu329	R2S	2	203.86	23.22
Leu336	dI	2	0.35	0.00
Leu336	dS	2	23.11	0.00
Leu336	R2I	2	43.44	1.41
Leu336	R2S	2	47.69	2.74
Leu232	dI	2	0.31	0.00
Leu232	dS	2	23.38	0.00
Leu232	R2I	2	54.45	2.53
Leu232	R2S	2	50.36	2.80
Leu339	dI	2	-0.30	0.00
Leu339	dS	2	22.96	0.00
Leu339	R2I	2	42.25	2.11
Leu339	R2S	2	28.89	2.42
Leu324	dI	2	1.06	0.00
Leu324	dS	2	26.03	0.01
Leu324	R2I	2	78.54	3.79

Residue	Parameter	State	Fit result	Error
Leu324	R2S	2	88.92	6.30
Leu280	dI	2	0.29	0.00
Leu280	dS	2	25.13	0.01
Leu280	R2I	2	56.45	3.26
Leu280	R2S	2	53.99	4.15
Leu207	dI	2	0.46	0.00
Leu207	dS	2	26.02	0.00
Leu207	R2I	2	49.98	2.23
Leu207	R2S	2	49.29	3.65
Leu306	dI	2	0.60	0.00
Leu306	dS	2	26.39	0.00
Leu306	R2I	2	46.26	2.15
Leu306	R2S	2	46.22	3.14
Ala268	dI	2	1.54	0.00
Ala268	dS	2	21.46	0.00
Ala268	R2I	2	108.97	3.67
Ala268	R2S	2	74.57	4.95
Val220	dI	2	1.37	0.00
Val220	dS	2	22.57	0.00
Val220	R2I	2	74.13	4.15
Val220	R2S	2	48.13	4.80
Leu311	dI	2	0.81	0.00
Leu311	dS	2	27.29	0.00
Leu311	R2I	2	65.80	4.55
Leu311	R2S	2	37.59	4.71
Val76	dI	2	1.63	0.00
Val76	dS	2	25.83	0.00
Val76	R2I	2	37.70	1.30
Val76	R2S	2	42.73	2.41

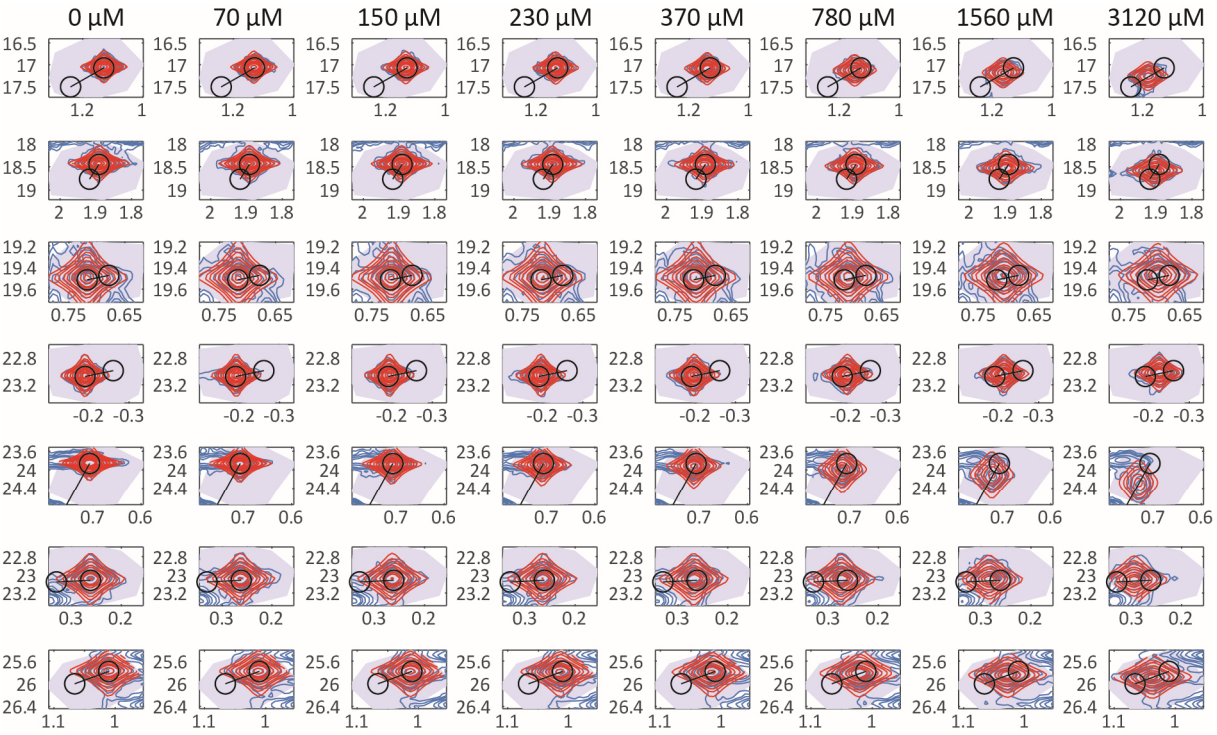


Fig. 8: Overlay of experimental (blue) and fitted (red) line shapes of the titration of GTB with H-tris type I. Each row corresponds to one fitted residue in the same order as in the following table.

Tab. 25: Line shape analysis results of the titration of GTB with H-tris type I.K_d is reported in units of µM. k_{off}, the transverse relaxation rates in the ^{1}H dimension (R2I), and the transverse relaxation rates in the ^{13}C dimension (R2S) are reported in units of s^{-1}. The chemical shifts (dI = ^{1}H; dS = ^{13}C) of the bound state (state 2) are reported in ppm.

Residue	Parameter	State	Fit result	Error
global	K_d		3220.47	138.63
global	k_{off}		1612.82	156.23
Met214	dI	2	1.24	0.00
Met214	dS	2	17.51	0.01
Met214	R2I	2	80.08	5.05
Met214	R2S	2	65.24	9.89
Met266	dI	2	1.92	0.00
Met266	dS	2	18.77	0.01
Met266	R2I	2	80.75	3.17
Met266	R2S	2	60.69	4.23
Val299	dI	2	0.68	0.00
Val299	dS	2	19.47	0.00
Val299	R2I	2	68.21	2.76
Val299	R2S	2	42.05	3.06
Leu339	dI	2	-0.26	0.00
Leu339	dS	2	22.99	0.00
Leu339	R2I	2	52.21	2.59

Residue	Parameter	State	Fit result	Error
Leu339	R2S	2	29.57	3.09
Leu329	dI	2	0.76	0.00
Leu329	dS	2	24.80	0.04
Leu329	R2I	2	80.59	3.94
Leu329	R2S	2	255.37	26.88
Leu336	dI	2	0.33	0.00
Leu336	dS	2	23.08	0.00
Leu336	R2I	2	53.75	3.60
Leu336	R2S	2	31.38	3.96
Leu324	dI	2	1.07	0.00
Leu324	dS	2	26.00	0.01
Leu324	R2I	2	65.65	3.49
Leu324	R2S	2	64.28	7.15

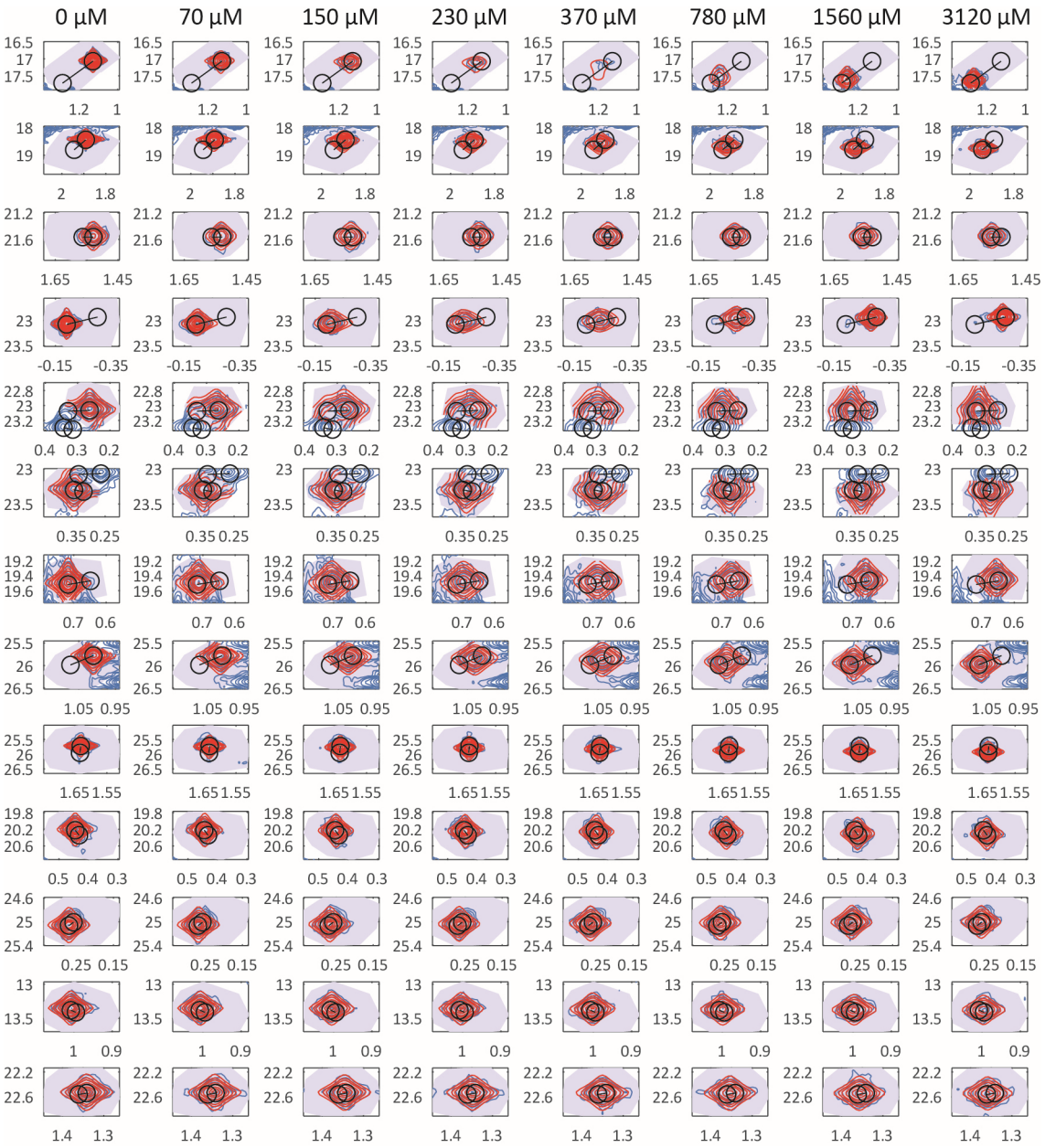


Fig. 9: Overlay of experimental (blue) and fitted (red) line shapes of the titration of GTB with H-tris type II. Each row corresponds to one fitted residue in the same order as in the following table.

Tab. 26: Line shape analysis results of the titration of GTB with H-tris type II.K_d is reported in units of µM. k_{off}, the transverse relaxation rates in the ^{1}H dimension (R2I), and the transverse relaxation rates in the ^{13}C dimension (R2S) are reported in units of s^{-1}. The chemical shifts (dI = ^{1}H; dS = ^{13}C) of the bound state (state 2) are reported in ppm.

Residue	Parameter	State	Fit result	Error
global	K_d		290.89	6.22
global	k_{off}		209.69	7.30
Met214	dI	2	1.29	0.00
Met214	dS	2	17.71	0.00

Residue	Parameter	State	Fit result	Error
Met214	R2I	2	48.18	2.26
Met214	R2S	2	51.30	4.23
Met266	dI	2	1.94	0.00
Met266	dS	2	18.80	0.00
Met266	R2I	2	82.05	2.29
Met266	R2S	2	71.59	4.13
Ala268	dI	2	1.56	0.00
Ala268	dS	2	21.57	0.01
Ala268	R2I	2	63.47	4.86
Ala268	R2S	2	49.36	6.02
Leu339	dI	2	-0.30	0.00
Leu339	dS	2	22.94	0.00
Leu339	R2I	2	36.88	1.61
Leu339	R2S	2	25.07	1.60
Leu336	dI	2	0.33	0.00
Leu336	dS	2	23.14	0.00
Leu336	R2I	2	42.09	1.28
Leu336	R2S	2	116.65	4.36
Leu232	dI	2	0.32	0.00
Leu232	dS	2	23.27	0.00
Leu232	R2I	2	45.03	1.17
Leu232	R2S	2	105.94	3.10
Val299	dI	2	0.65	0.00
Val299	dS	2	19.47	0.00
Val299	R2I	2	64.65	2.25
Val299	R2S	2	49.47	2.55
Leu324	dI	2	1.07	0.00
Leu324	dS	2	25.98	0.00
Leu324	R2I	2	48.45	1.37
Leu324	R2S	2	72.09	2.67
Val76	dI	2	1.63	0.00
Val76	dS	2	25.95	0.00
Val76	R2I	2	32.67	1.00
Val76	R2S	2	45.89	1.76
Val120	dI	2	0.43	0.00
Val120	dS	2	20.34	0.00
Val120	R2I	2	48.53	1.30
Val120	R2S	2	68.92	2.97
Leu280	dI	2	0.26	0.00
Leu280	dS	2	25.01	0.00
Leu280	R2I	2	48.45	1.74
Leu280	R2S	2	47.14	2.43
Ile192	dI	2	1.00	0.00
Ile192	dS	2	13.41	0.00
Ile192	R2I	2	57.41	2.31

Residue	Parameter	State	Fit result	Error
Ile192	R2S	2	34.93	2.37
Val220	dI	2	1.36	0.00
Val220	dS	2	22.56	0.00
Val220	R2I	2	59.99	1.94
Val220	R2S	2	47.94	2.66

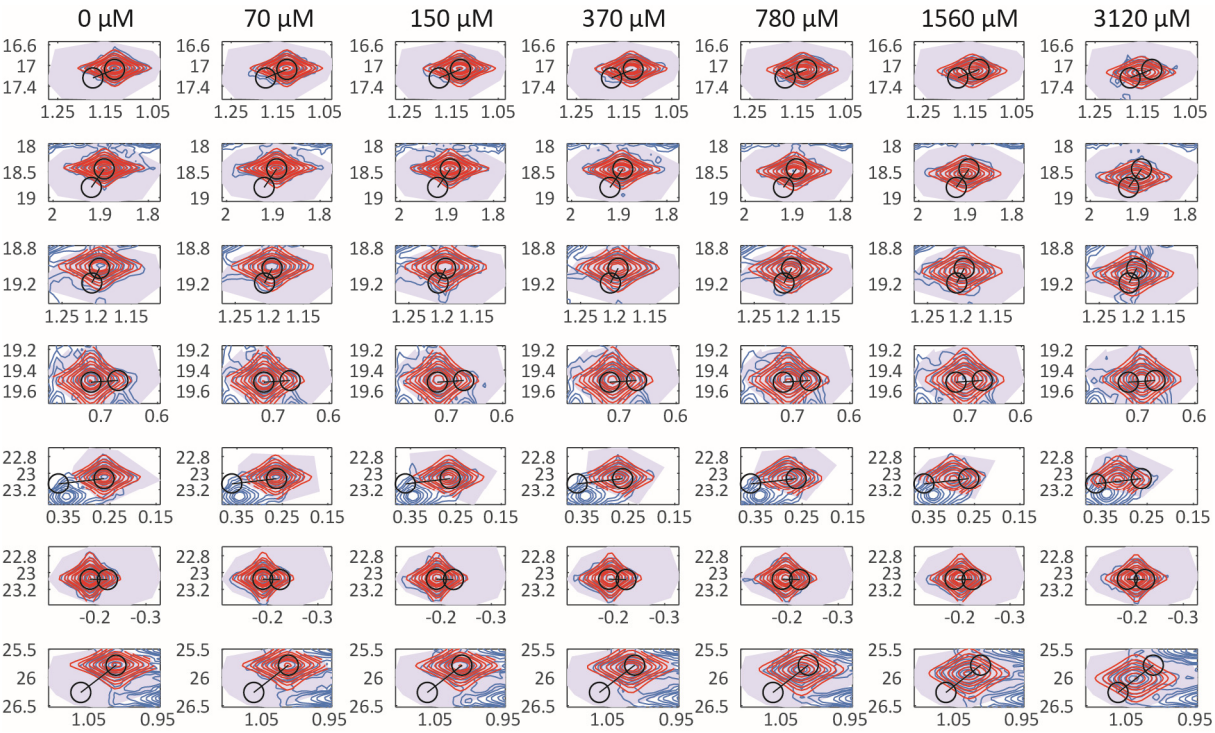


Fig. 10: Overlay of experimental (blue) and fitted (red) line shapes of the titration of GTB with H-tris type III. Each row corresponds to one fitted residue in the same order as in the following table.

Tab. 27: Line shape analysis results of the titration of GTB with H-tris type III.K_d is reported in units of µM. k_{off}, the transverse relaxation rates in the ^{1}H dimension (R2I), and the transverse relaxation rates in the ^{13}C dimension (R2S) are reported in units of s^{-1}. The chemical shifts (dI = ^{1}H; dS = ^{13}C) of the bound state (state 2) are reported in ppm.

Residue	Parameter	State	Fit result	Error
global	K_d		2934.26	195.24
global	k_{off}		684.08	103.96
Met214	dI	2	1.18	0.00
Met214	dS	2	17.24	0.01
Met214	R2I	2	86.84	6.15
Met214	R2S	2	57.61	7.52
Met266	dI	2	1.92	0.00
Met266	dS	2	18.80	0.02
Met266	R2I	2	107.10	5.10

Residue	Parameter	State	Fit result	Error
Met266	R2S	2	54.92	8.79
Ala122	dI	2	1.21	0.00
Ala122	dS	2	19.19	0.01
Ala122	R2I	2	59.42	4.46
Ala122	R2S	2	37.92	6.27
Val299	dI	2	0.67	0.00
Val299	dS	2	19.50	0.01
Val299	R2I	2	63.26	3.56
Val299	R2S	2	42.74	4.61
Leu336	dI	2	0.36	0.00
Leu336	dS	2	23.13	0.01
Leu336	R2I	2	34.53	6.27
Leu336	R2S	2	27.63	8.80
Leu339	dI	2	-0.22	0.00
Leu339	dS	2	23.08	0.00
Leu339	R2I	2	43.48	2.62
Leu339	R2S	2	29.33	3.60
Leu324	dI	2	1.06	0.00
Leu324	dS	2	26.27	0.02
Leu324	R2I	2	67.56	4.72
Leu324	R2S	2	76.20	15.40

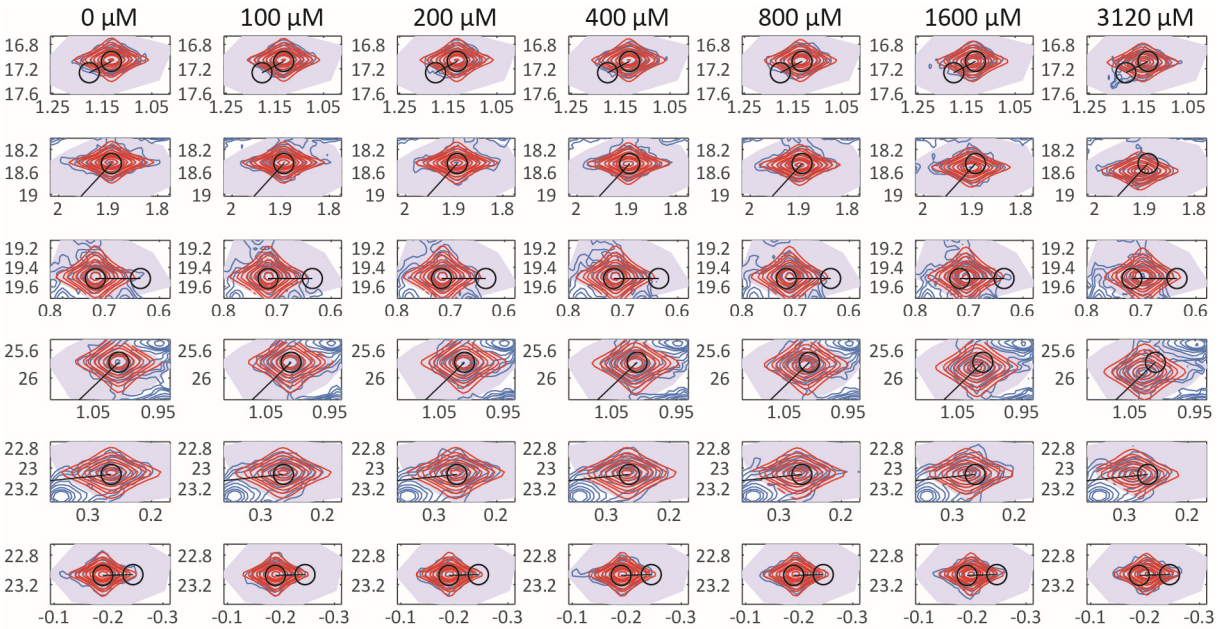


Fig. 11: Overlay of experimental (blue) and fitted (red) line shapes of the titration of GTB with H-tris type IV. Each row corresponds to one fitted residue in the same order as in the following table.

Tab. 28: Line shape analysis results of the titration of GTB with H-tris type IV.K_d is reported in units of µM. k_{off}, the transverse relaxation rates in the ^{1}H dimension (R2I), and the transverse relaxation rates in the ^{13}C dimension (R2S) are reported in units of s^{-1}. The chemical shifts (dI = ^{1}H; dS = ^{13}C) of the bound state (state 2) are reported in ppm.

Residue	Parameter	State	Fit result	Error
global	K_d		9995.92	571.10
global	k_{off}		6425.02	2847.77
Met214	dI	2	1.18	0.00
Met214	dS	2	54.83	0.45
Met214	R2I	2	46.11	0.55
Met214	R2S	2	64.84	5.82
Met266	dI	2	1.96	0.00
Met266	dS	2	19.11	0.03
Met266	R2I	2	103.67	3.97
Met266	R2S	2	71.53	14.45
Val299	dI	2	0.64	0.00
Val299	dS	2	19.52	0.00
Val299	R2I	2	60.17	3.80
Val299	R2S	2	36.16	4.81
Leu324	dI	2	1.08	0.00
Leu324	dS	2	26.40	0.03
Leu324	R2I	2	84.19	4.01
Leu324	R2S	2	93.50	14.46
Leu336	dI	2	0.37	0.00
Leu336	dS	2	23.13	0.01
Leu336	R2I	2	49.81	5.76
Leu336	R2S	2	32.99	7.05
Leu339	dI	2	-0.25	0.00
Leu339	dS	2	38.66	0.35
Leu339	R2I	2	28.18	0.42
Leu339	R2S	2	33.01	4.01

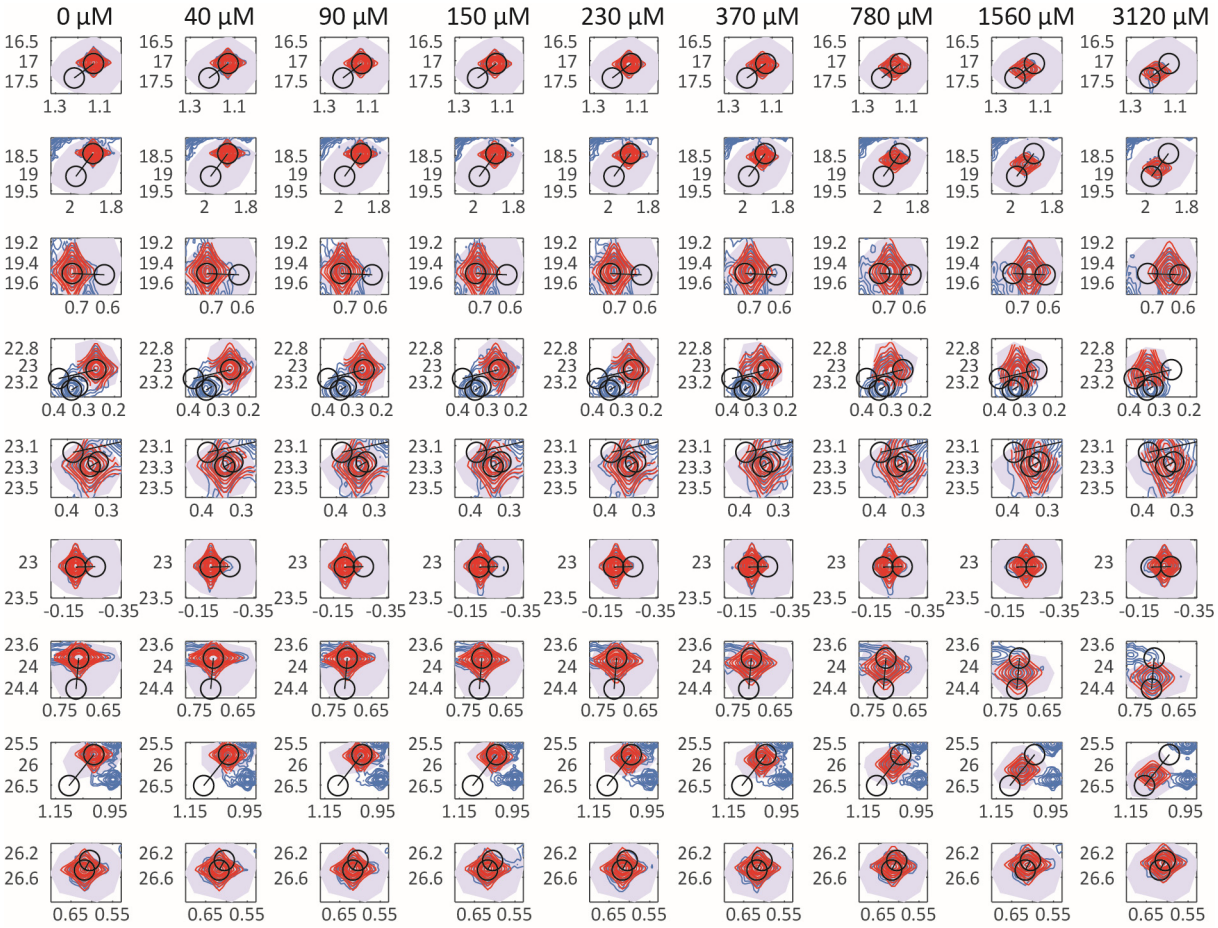


Fig. 12: Overlay of experimental (blue) and fitted (red) line shapes of the titration of GTB with H-tris type V. Each row corresponds to one fitted residue in the same order as in the following table.

Tab. 29: Line shape analysis results of the titration of GTB with H-tris type V.K_d is reported in units of µM. k_{off}, the transverse relaxation rates in the ^{1}H dimension (R2I), and the transverse relaxation rates in the ^{13}C dimension (R2S) are reported in units of s^{-1}. The chemical shifts (dI = ^{1}H; dS = ^{13}C) of the bound state (state 2) are reported in ppm.

Residue	Parameter	State	Fit result	Error
global	K_d		1269.08	20.40
global	k_{off}		2574.78	184.25
Met214	dI	2	1.21	0.00
Met214	dS	2	17.41	0.01
Met214	R2I	2	109.03	4.15
Met214	R2S	2	70.73	5.79
Met266	dI	2	1.97	0.00
Met266	dS	2	19.04	0.01
Met266	R2I	2	117.92	3.43
Met266	R2S	2	71.08	4.75
Val299	dI	2	0.62	0.00
Val299	dS	2	19.53	0.00

Residue	Parameter	State	Fit result	Error
Val299	R2I	2	62.54	2.25
Val299	R2S	2	47.27	2.65
Leu366	dI	2	0.38	0.00
Leu366	dS	2	23.21	0.00
Leu366	R2I	2	16.28	0.87
Leu366	R2S	2	60.46	1.83
Leu232	dI	2	0.33	0.00
Leu232	dS	2	23.17	0.00
Leu232	R2I	2	16.47	0.59
Leu232	R2S	2	99.11	2.38
Leu339	dI	2	-0.26	0.00
Leu339	dS	2	23.07	0.00
Leu339	R2I	2	40.80	1.39
Leu339	R2S	2	28.30	1.72
Leu329	dI	2	0.71	0.00
Leu329	dS	2	24.38	0.01
Leu329	R2I	2	74.66	2.76
Leu329	R2S	2	116.35	5.40
Leu324	dI	2	1.09	0.00
Leu324	dS	2	26.46	0.01
Leu324	R2I	2	84.18	3.08
Leu324	R2S	2	70.21	5.92
Leu306	dI	2	0.61	0.00
Leu306	dS	2	26.34	0.00
Leu306	R2I	2	37.45	1.69
Leu306	R2S	2	35.59	1.98

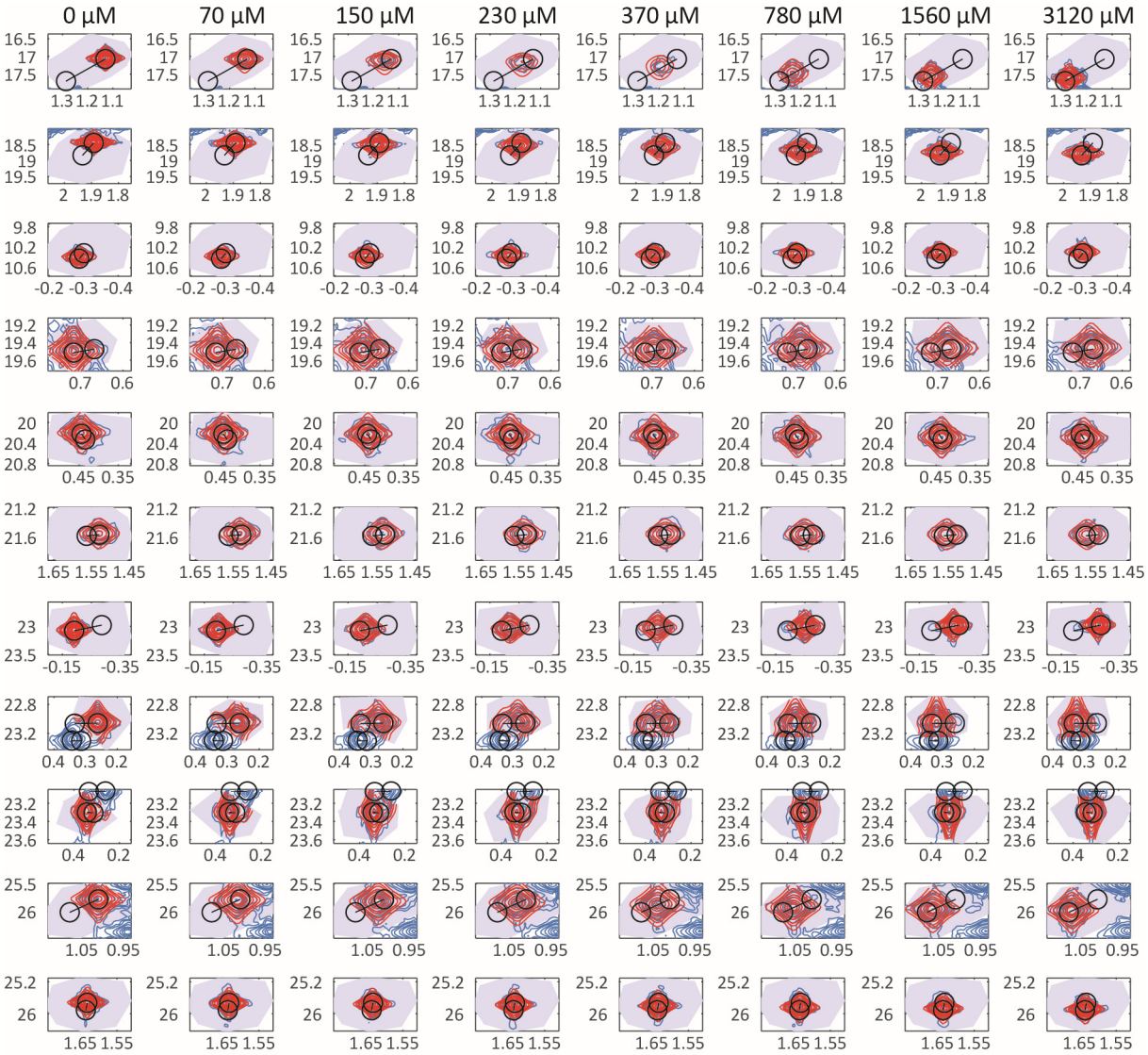


Fig. 13: Overlay of experimental (blue) and fitted (red) line shapes of the titration of GTB with H-tris type VI. Each row corresponds to one fitted residue in the same order as in the following table.

Tab. 30: Line shape analysis results of the titration of GTB with H-tris type VI.K_d is reported in units of µM. k_{off}, the transverse relaxation rates in the ^{1}H dimension (R2I), and the transverse relaxation rates in the ^{13}C dimension (R2S) are reported in units of s^{-1}. The chemical shifts (dI = ^{1}H; dS = ^{13}C) of the bound state (state 2) are reported in ppm.

Residue	Parameter	State	Fit result	Error
global	K_d		318.32	4.55
global	k_{off}		338.95	9.41
Met214	dI	2	1.28	0.00
Met214	dS	2	17.69	0.00
Met214	R2I	2	48.46	1.81
Met214	R2S	2	56.31	2.79
Met266	dI	2	1.93	0.00

Residue	Parameter	State	Fit result	Error
Met266	dS	2	18.83	0.00
Met266	R2I	2	81.87	1.75
Met266	R2S	2	60.59	2.55
Ile256	dI	2	-0.30	0.00
Ile256	dS	2	10.32	0.00
Ile256	R2I	2	45.34	1.60
Ile256	R2S	2	25.59	1.64
Val299	dI	2	0.67	0.00
Val299	dS	2	19.48	0.00
Val299	R2I	2	62.26	1.27
Val299	R2S	2	38.27	1.37
Val120	dI	2	0.43	0.00
Val120	dS	2	20.33	0.00
Val120	R2I	2	44.87	0.87
Val120	R2S	2	60.20	1.91
Ala268	dI	2	1.56	0.00
Ala268	dS	2	21.58	0.00
Ala268	R2I	2	63.93	4.66
Ala268	R2S	2	48.32	4.38
Leu339	dI	2	-0.28	0.00
Leu339	dS	2	22.98	0.00
Leu339	R2I	2	36.20	1.00
Leu339	R2S	2	23.86	1.04
Leu336	dI	2	0.33	0.00
Leu336	dS	2	23.13	0.00
Leu336	R2I	2	22.19	0.45
Leu336	R2S	2	94.67	2.01
Leu232	dI	2	0.31	0.00
Leu232	dS	2	23.27	0.00
Leu232	R2I	2	32.62	0.58
Leu232	R2S	2	71.79	1.68
Leu324	dI	2	1.08	0.00
Leu324	dS	2	26.01	0.00
Leu324	R2I	2	48.83	1.15
Leu324	R2S	2	62.64	1.90
Leu76	dI	2	1.63	0.00
Leu76	dS	2	25.91	0.00
Leu76	R2I	2	31.21	0.75
Leu76	R2S	2	38.90	1.33

Donor analog titrations with acceptor substrate- or analog-saturated GTB

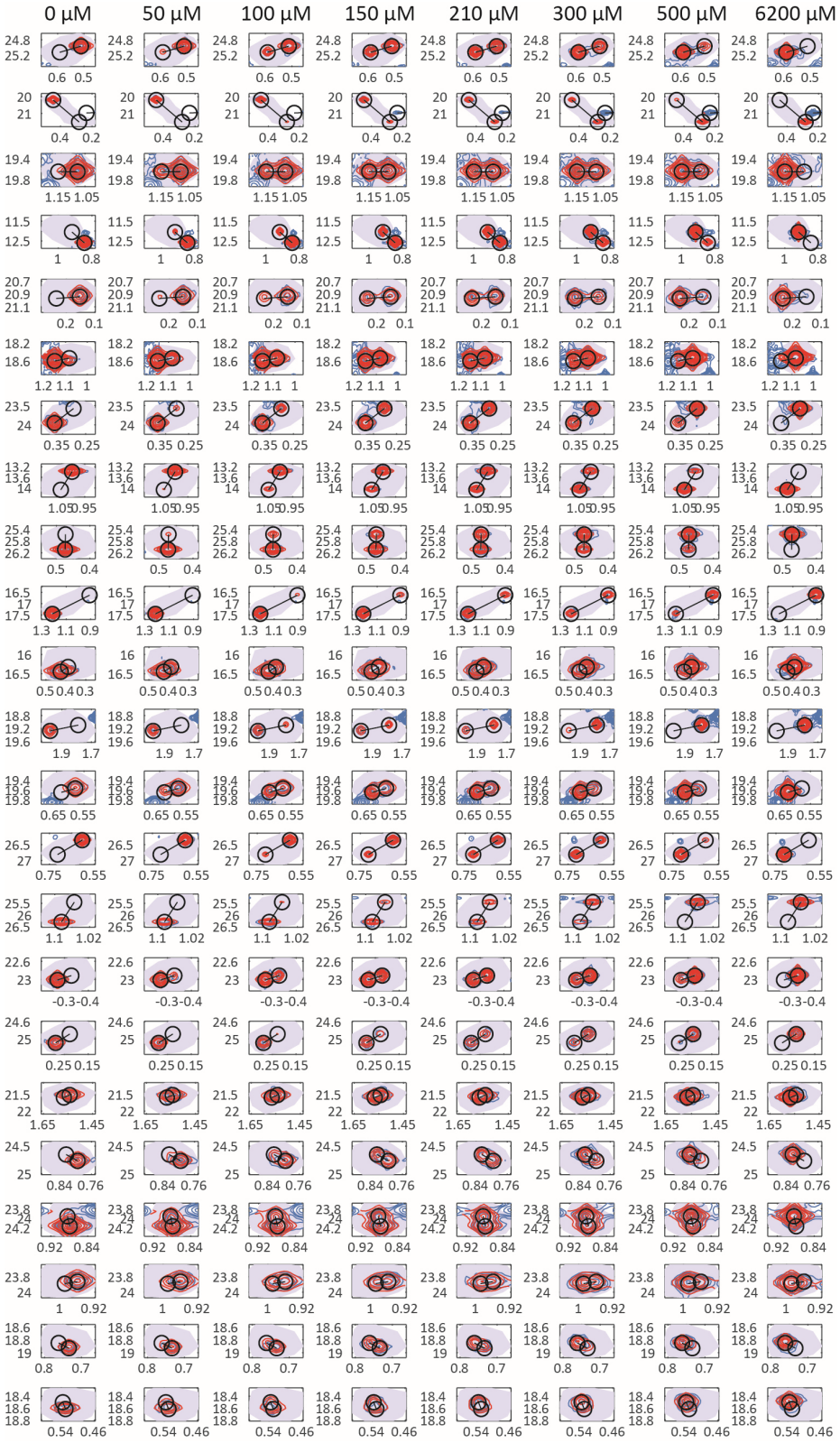


Fig. 14: Overlay of experimental (blue) and fitted (red) line shapes of the UDP titration to H-dis-saturated GTB. Each row corresponds to one fitted residue in the same order as in the following table.

Tab. 31: Line shape analysis results derived from the UDP titration to H-dis-saturated GTB. K_d is reported in units of µM. k_{off}, the transverse relaxation rates in the ^{1}H dimension (R2I), and the transverse relaxation rates in the ^{13}C dimension (R2S) are reported in units of s^{-1}. The chemical shifts (dI = ^{1}H; dS = ^{13}C) of the bound state (state 2) are reported in ppm.

Residue	Parameter	State	Fit result	Error
global	K_d		102.87	1.97
global	k_{off}		2.61	0.27
Ile118	dI	2	0.59	0.00
Ile118	dS	2	25.12	0.00
Ile118	R2I	2	29.85	1.10
Ile118	R2S	2	29.03	1.45
Val120	dI	2	0.28	0.00
Val120	dS	2	21.51	0.00
Val120	R2I	2	54.08	3.17
Val120	R2S	2	44.03	4.38
Ala122	dI	2	1.16	0.00
Ala122	dS	2	19.65	0.00
Ala122	R2I	2	49.89	0.82
Ala122	R2S	2	36.75	1.04
Ile123	dI	2	0.92	0.00
Ile123	dS	2	12.05	0.00
Ile123	R2I	2	27.12	0.55
Ile123	R2S	2	70.58	1.93
Leu134	dI	2	0.24	0.00
Leu134	dS	2	20.97	0.00
Leu134	R2I	2	43.41	2.25
Leu134	R2S	2	30.79	2.41
Ala128	dI	2	1.08	0.00
Ala128	dS	2	18.54	0.00
Ala128	R2I	2	45.56	0.54
Ala128	R2S	2	18.15	0.40
Leu173	dI	2	0.30	0.00
Leu173	dS	2	23.58	0.00
Leu173	R2I	2	35.71	1.07
Leu173	R2S	2	35.53	1.42
Ile192	dI	2	1.05	0.00
Ile192	dS	2	14.07	0.00
Ile192	R2I	2	52.25	2.12
Ile192	R2S	2	35.39	2.25
Leu207	dI	2	0.47	0.00
Leu207	dS	2	25.58	0.00
Leu207	R2I	2	30.12	1.06
Leu207	R2S	2	47.07	2.70
Met214	dI	2	0.91	0.00
Met214	dS	2	16.63	0.00
Met214	R2I	2	100.11	3.20

Residue	Parameter	State	Fit result	Error
Met214	R2S	2	60.85	4.40
Ala254	dI	2	0.39	0.00
Ala254	dS	2	16.32	0.00
Ala254	R2I	2	62.60	1.36
Ala254	R2S	2	36.87	1.20
Met266	dI	2	1.79	0.00
Met266	dS	2	19.10	0.00
Met266	R2I	2	45.85	1.93
Met266	R2S	2	43.86	2.44
Val299	dI	2	0.63	0.00
Val299	dS	2	19.65	0.00
Val299	R2I	2	31.24	1.04
Val299	R2S	2	30.07	1.50
Leu306	dI	2	0.71	0.00
Leu306	dS	2	26.81	0.00
Leu306	R2I	2	33.02	1.80
Leu306	R2S	2	32.75	2.19
Leu324	dI	2	1.06	0.00
Leu324	dS	2	25.45	0.01
Leu324	R2I	2	37.34	2.52
Leu324	R2S	2	51.51	5.72
Leu339	dI	2	-0.33	0.00
Leu339	dS	2	22.92	0.00
Leu339	R2I	2	28.85	0.85
Leu339	R2S	2	23.82	1.34
Leu280	dI	2	0.23	0.00
Leu280	dS	2	24.89	0.01
Leu280	R2I	2	52.87	3.85
Leu280	R2S	2	46.36	4.23
Ala268	dI	2	1.57	0.00
Ala268	dS	2	21.59	0.00
Ala268	R2I	2	50.83	1.58
Ala268	R2S	2	45.61	2.22
Leu130	dI	2	0.83	0.00
Leu130	dS	2	24.65	0.00
Leu130	R2I	2	27.31	1.89
Leu130	R2S	2	33.20	2.62
Val201	dI	2	0.88	0.00
Val201	dS	2	23.96	0.00
Val201	R2I	2	27.16	0.76
Val201	R2S	2	38.62	1.56
Val277	dI	2	0.99	0.00
Val277	dS	2	23.89	0.00
Val277	R2I	2	41.09	1.79
Val277	R2S	2	22.03	1.85

Residue	Parameter	State	Fit result	Error
Val204	dI	2	0.76	0.00
Val204	dS	2	18.85	0.00
Val204	R2I	2	31.14	2.46
Val204	R2S	2	18.90	2.55
Val222	dI	2	0.54	0.00
Val222	dS	2	18.50	0.00
Val222	R2I	2	33.43	2.65
Val222	R2S	2	29.10	3.30

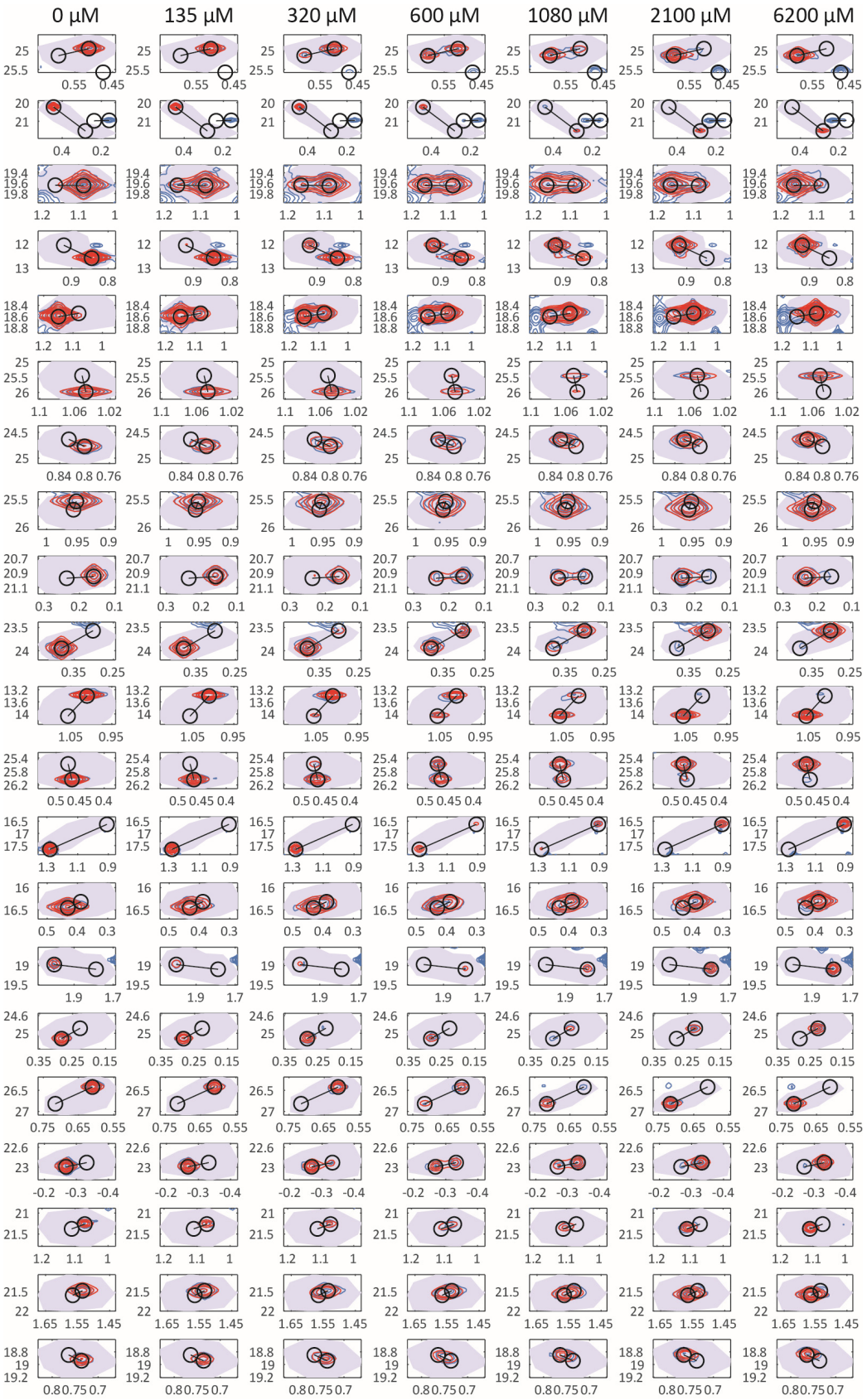
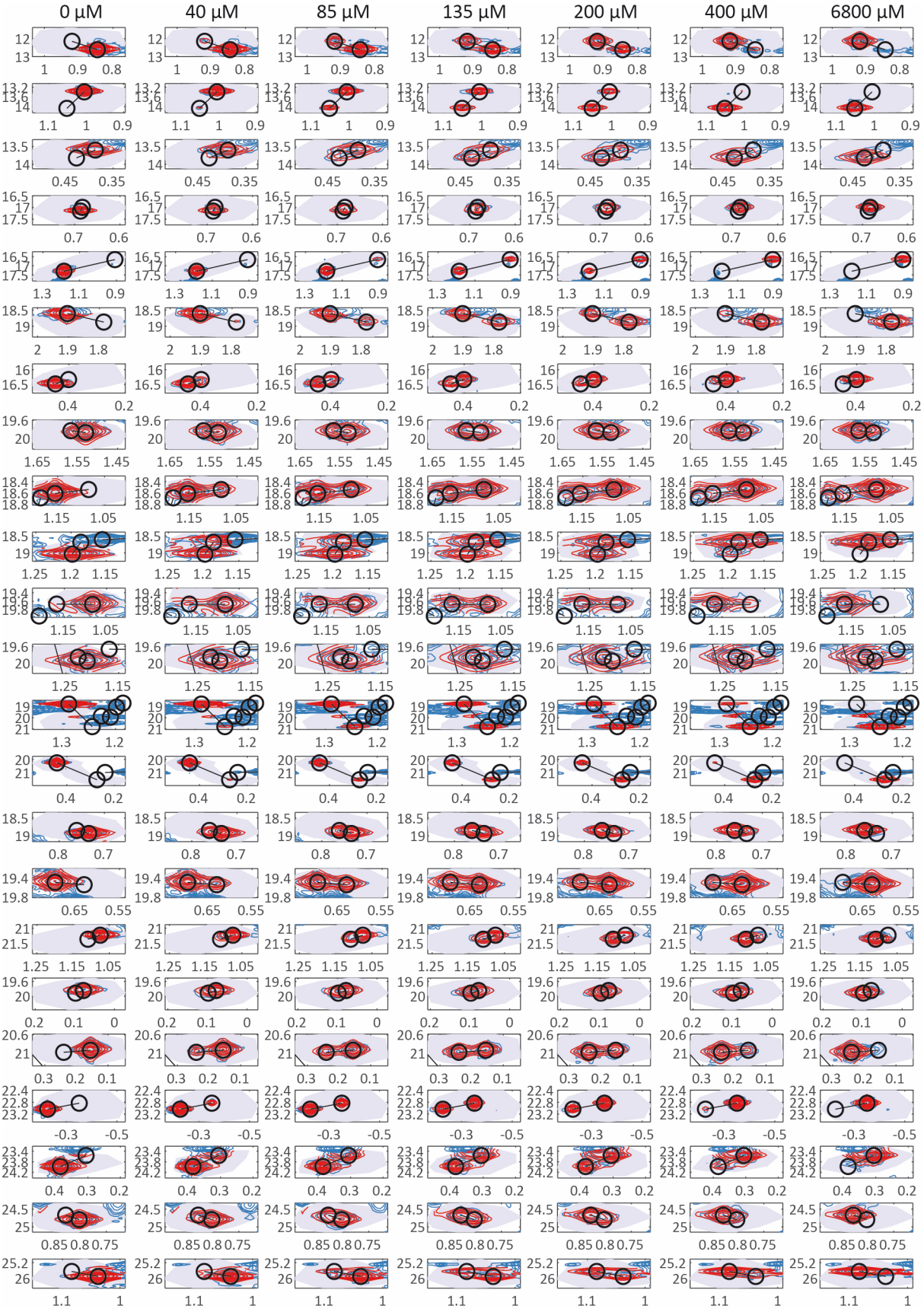


Fig. 15: Overlay of experimental (blue) and fitted (red) line shapes of the UDP titration to B-tris-saturated GTB. Each row corresponds to one fitted residue in the same order as in the following table.

Tab. 32: Line shape analysis results derived from the UDP titration to B-tris-saturated GTB. K_d is reported in units of µM. k_{off}, the transverse relaxation rates in the ^{1}H dimension (R2I), and the transverse relaxation rates in the ^{13}C dimension (R2S) are reported in units of s^{-1}. The chemical shifts (dI = ^{1}H; dS = ^{13}C) of the bound state (state 2) are reported in ppm.

Residue	Parameter	State	Fit result	Error
global	K_d		659.75	13.35
global	k_{off}		18.32	0.63
Leu118	dI	2	0.59	0.00
Leu118	dS	2	25.14	0.00
Leu118	R2I	2	34.95	2.03
Leu118	R2S	2	33.49	2.60
Val120	dI	2	0.28	0.00
Val120	dS	2	21.52	0.01
Val120	R2I	2	60.83	5.98
Val120	R2S	2	41.28	8.59
Ala122	dI	2	1.16	0.00
Ala122	dS	2	19.64	0.00
Ala122	R2I	2	56.31	1.75
Ala122	R2S	2	44.02	2.10
Ile123	dI	2	0.92	0.00
Ile123	dS	2	12.06	0.00
Ile123	R2I	2	24.87	1.02
Ile123	R2S	2	81.83	3.54
Ala128	dI	2	1.08	0.00
Ala128	dS	2	18.54	0.00
Ala128	R2I	2	34.74	0.89
Ala128	R2S	2	10.07	0.56
Leu324	dI	2	1.05	0.00
Leu324	dS	2	25.46	0.01
Leu324	R2I	2	66.38	6.53
Leu324	R2S	2	55.71	9.87
Leu130	dI	2	0.83	0.00
Leu130	dS	2	24.64	0.01
Leu130	R2I	2	28.16	2.75
Leu130	R2S	2	29.90	3.64
Leu132	dI	2	0.96	0.00
Leu132	dS	2	25.69	0.00
Leu132	R2I	2	38.23	1.50
Leu132	R2S	2	42.89	2.95
Leu134	dI	2	0.24	0.00
Leu134	dS	2	20.97	0.00
Leu134	R2I	2	54.41	5.69
Leu134	R2S	2	28.96	5.03
Leu173	dI	2	0.30	0.00
Leu173	dS	2	23.57	0.00
Leu173	R2I	2	34.99	2.34

Leu173	R2S	2	34.87	2.64
Ile192	dI	2	1.06	0.00
Ile192	dS	2	14.07	0.00
Ile192	R2I	2	41.86	2.34
Ile192	R2S	2	27.50	3.39
Leu207	dI	2	0.48	0.00
Leu207	dS	2	25.57	0.00
Leu207	R2I	2	34.08	1.87
Leu207	R2S	2	46.00	4.78
Met214	dI	2	0.91	0.00
Met214	dS	2	16.63	0.01
Met214	R2I	2	76.96	4.73
Met214	R2S	2	61.84	7.16
Ala254	dI	2	0.39	0.00
Ala254	dS	2	16.32	0.00
Ala254	R2I	2	67.74	2.57
Ala254	R2S	2	39.42	1.81
Met266	dI	2	1.79	0.00
Met266	dS	2	19.10	0.01
Met266	R2I	2	45.51	4.40
Met266	R2S	2	39.17	5.10
Leu280	dI	2	0.23	0.00
Leu280	dS	2	24.89	0.01
Leu280	R2I	2	51.52	6.37
Leu280	R2S	2	38.40	5.94
Leu306	dI	2	0.72	0.00
Leu306	dS	2	26.82	0.01
Leu306	R2I	2	31.78	3.73
Leu306	R2S	2	26.58	3.55
Leu339	dI	2	-0.33	0.00
Leu339	dS	2	22.91	0.00
Leu339	R2I	2	32.59	2.29
Leu339	R2S	2	30.81	3.16
Val208	dI	2	1.11	0.00
Val208	dS	2	21.38	0.00
Val208	R2I	2	34.42	4.53
Val208	R2S	2	28.86	5.22
Ala268	dI	2	1.57	0.00
Ala268	dS	2	21.59	0.00
Ala268	R2I	2	63.83	3.40
Ala268	R2S	2	45.88	3.32
Val204	dI	2	0.76	0.00
Val204	dS	2	18.85	0.00
Val204	R2I	2	31.62	3.05
Val204	R2S	2	14.07	3.28


0 µM
40 µM
85 µM
135 µM
200 µM
400 µM
6800 µM

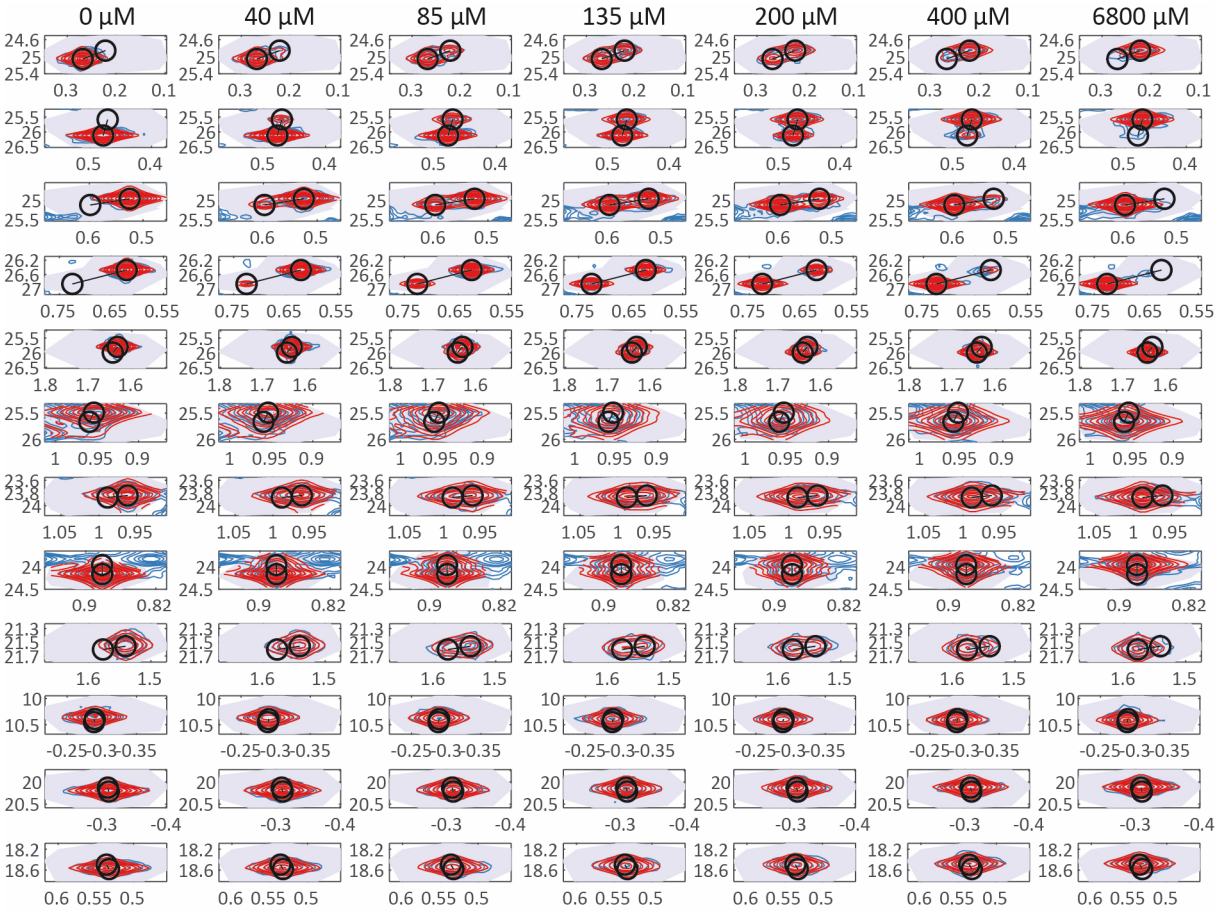


Fig. 16: Overlay of experimental (blue) and fitted (red) line shapes of the UDP titration to H-tris type I saturated GTB. Each row corresponds to one fitted residue in the same order as in the following table. This figure is spread over two pages.

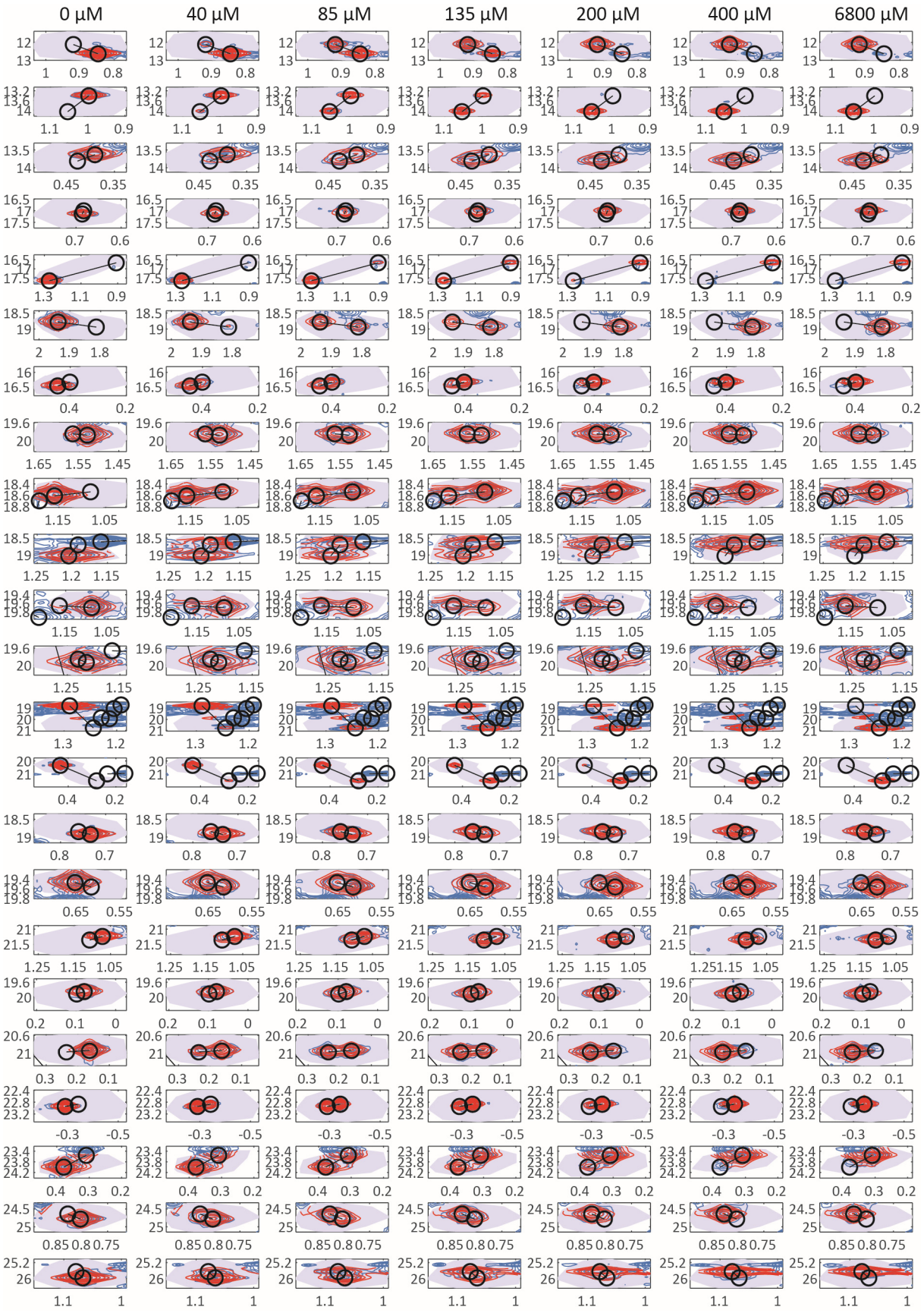
Tab. 33: Line shape analysis results derived from the UDP titration to H-tris type I saturated GTB.K_d is reported in units of µM. k_{off}, the transverse relaxation rates in the ^1H dimension (R2I), and the transverse relaxation rates in the ^{13}C dimension (R2S) are reported in units of s^{-1}. The chemical shifts (dI = ^1H; dS = ^{13}C) of the bound state (state 2) are reported in ppm.

Residue	Parameter	State	Fit result	Error
global	K_d		37.95	0.90
global	k_{off}		2.19	0.20
Ile123	dI	2	0.92	0.00
Ile123	dS	2	12.15	0.00
Ile123	R2I	2	48.91	1.30
Ile123	R2S	2	118.72	4.51
Ile192	dI	2	1.05	0.00
Ile192	dS	2	14.07	0.00
Ile192	R2I	2	62.07	2.91
Ile192	R2S	2	41.87	3.96
Ile224	dI	2	0.43	0.00

Residue	Parameter	State	Fit result	Error
Ile224	dS	2	13.82	0.00
Ile224	R2I	2	81.56	4.25
Ile224	R2S	2	59.85	5.54
Ile116	dI	2	0.68	0.00
Ile116	dS	2	16.99	0.01
Ile116	R2I	2	33.01	2.41
Ile116	R2S	2	54.50	4.97
Met214	dI	2	0.91	0.00
Met214	dS	2	16.66	0.00
Met214	R2I	2	123.10	4.48
Met214	R2S	2	54.74	4.73
Met266	dI	2	1.79	0.00
Met266	dS	2	18.87	0.00
Met266	R2I	2	106.72	2.81
Met266	R2S	2	59.76	2.98
Ala254	dI	2	0.40	0.00
Ala254	dS	2	16.34	0.00
Ala254	R2I	2	66.71	2.24
Ala254	R2S	2	36.11	2.42
Ala287	dI	2	1.57	0.00
Ala287	dS	2	19.83	0.00
Ala287	R2I	2	64.33	2.07
Ala287	R2S	2	42.04	2.12
Ala128	dI	2	1.08	0.00
Ala128	dS	2	18.54	0.00
Ala128	R2I	2	48.55	1.11
Ala128	R2S	2	19.95	0.78
Ala343	dI	2	1.18	0.00
Ala343	dS	2	18.67	0.00
Ala343	R2I	2	49.71	1.37
Ala343	R2S	2	41.99	1.87
Ala122	dI	2	1.17	0.00
Ala122	dS	2	19.68	0.00
Ala122	R2I	2	63.24	1.57
Ala122	R2S	2	51.81	2.56
Met142	dI	2	1.22	0.00
Met142	dS	2	19.83	0.00
Met142	R2I	2	61.81	1.68
Met142	R2S	2	65.02	2.76
Ala177	dI	2	1.24	0.00
Ala177	dS	2	20.80	0.00
Ala177	R2I	2	44.81	1.44
Ala177	R2S	2	81.60	3.54
Val120	dI	2	0.27	0.00
Val120	dS	2	21.52	0.00
Val120	R2I	2	72.26	2.62

Residue	Parameter	State	Fit result	Error
Val120	R2S	2	56.55	4.18
Val204	dI	2	0.76	0.00
Val204	dS	2	18.85	0.00
Val204	R2I	2	50.81	1.82
Val204	R2S	2	30.78	1.83
Val299	dI	2	0.63	0.00
Val299	dS	2	19.54	0.00
Val299	R2I	2	43.74	0.93
Val299	R2S	2	27.35	0.87
Val208	dI	2	1.11	0.00
Val208	dS	2	21.36	0.00
Val208	R2I	2	52.76	2.60
Val208	R2S	2	44.98	3.12
Leu225	dI	2	0.10	0.00
Leu225	dS	2	19.92	0.00
Leu225	R2I	2	55.59	3.22
Leu225	R2S	2	39.18	2.74
Leu134	dI	2	0.24	0.00
Leu134	dS	2	20.98	0.00
Leu134	R2I	2	58.41	1.57
Leu134	R2S	2	35.18	1.84
Leu339	dI	2	-0.35	0.00
Leu339	dS	2	22.83	0.00
Leu339	R2I	2	39.19	1.10
Leu339	R2S	2	32.28	1.30
Leu173	dI	2	0.31	0.00
Leu173	dS	2	23.56	0.00
Leu173	R2I	2	41.16	0.85
Leu173	R2S	2	42.32	1.15
Leu130	dI	2	0.83	0.00
Leu130	dS	2	24.67	0.00
Leu130	R2I	2	44.11	1.65
Leu130	R2S	2	46.99	2.16
Leu324	dI	2	1.08	0.00
Leu324	dS	2	25.64	0.00
Leu324	R2I	2	96.69	3.42
Leu324	R2S	2	54.63	3.64
Leu280	dI	2	0.22	0.00
Leu280	dS	2	24.86	0.00
Leu280	R2I	2	65.20	2.72
Leu280	R2S	2	48.53	2.84
Leu207	dI	2	0.47	0.00
Leu207	dS	2	25.58	0.00
Leu207	R2I	2	46.07	1.20
Leu207	R2S	2	63.49	2.69

Residue	Parameter	State	Fit result	Error
Leu118	dI	2	0.60	0.00
Leu118	dS	2	25.12	0.00
Leu118	R2I	2	44.79	1.05
Leu118	R2S	2	32.56	1.08
Leu306	dI	2	0.73	0.00
Leu306	dS	2	26.87	0.00
Leu306	R2I	2	49.36	1.40
Leu306	R2S	2	30.90	1.64
Val76	dI	2	1.64	0.00
Val76	dS	2	25.99	0.00
Val76	R2I	2	28.29	0.55
Val76	R2S	2	45.52	1.23
Leu132	dI	2	0.96	0.00
Leu132	dS	2	25.67	0.00
Leu132	R2I	2	50.90	1.02
Leu132	R2S	2	63.19	1.84
Leu277	dI	2	0.99	0.00
Leu277	dS	2	23.87	0.00
Leu277	R2I	2	48.66	1.13
Leu277	R2S	2	27.78	1.40
Leu201	dI	2	0.88	0.00
Leu201	dS	2	23.95	0.00
Leu201	R2I	2	30.52	0.46
Leu201	R2S	2	48.28	1.19
Ala268	dI	2	1.58	0.00
Ala268	dS	2	21.61	0.00
Ala268	R2I	2	62.39	3.33
Ala268	R2S	2	55.68	5.80
Ile256	dI	2	-0.29	0.00
Ile256	dS	2	10.45	0.00
Ile256	R2I	2	39.15	1.73
Ile256	R2S	2	31.53	1.92
Leu319	dI	2	-0.31	0.00
Leu319	dS	2	20.13	0.00
Leu319	R2I	2	47.02	1.40
Leu319	R2S	2	35.45	1.26
Val222	dI	2	0.54	0.00
Val222	dS	2	18.50	0.00
Val222	R2I	2	44.57	2.01
Val222	R2S	2	38.40	2.45


0 µM
40 µM
85 µM
135 µM
200 µM
400 µM
6800 µM

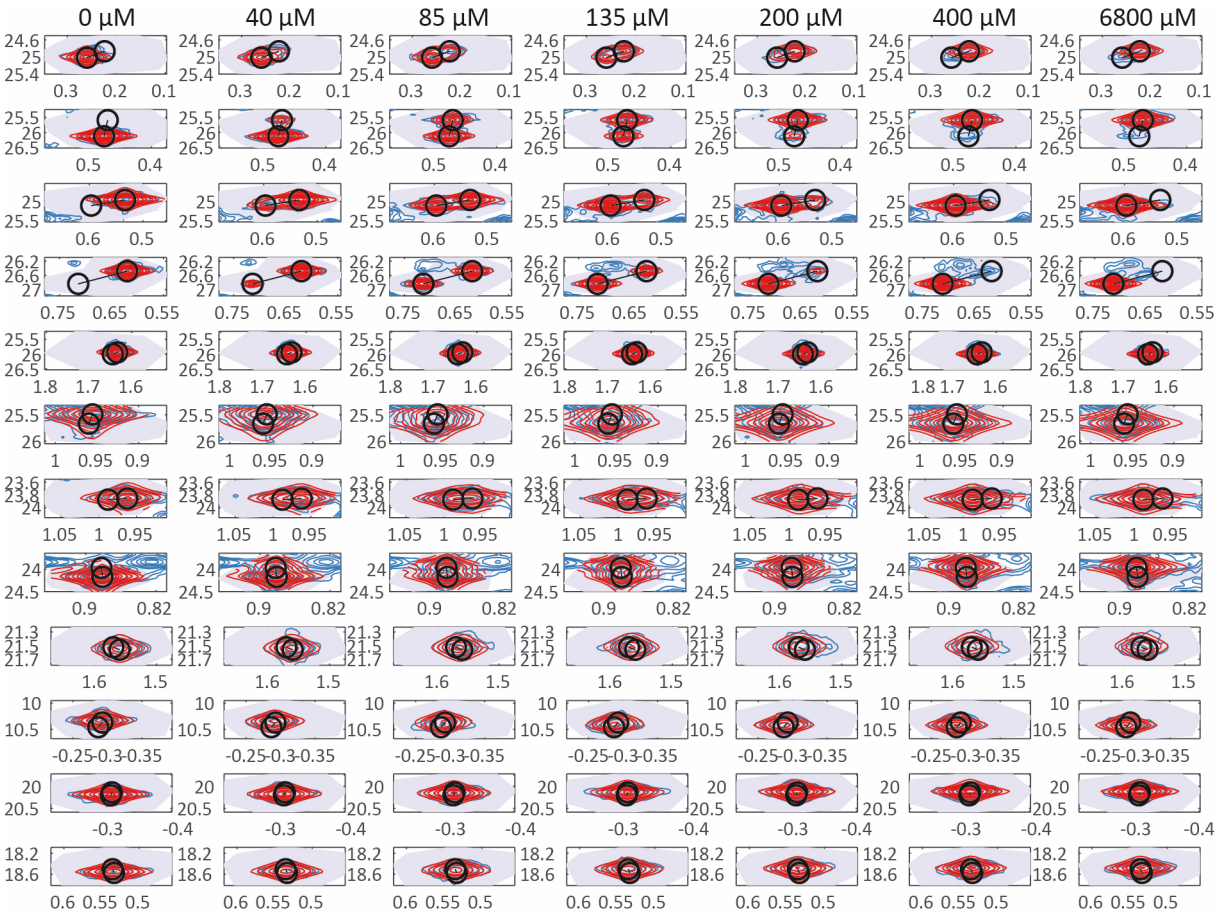


Fig. 17: Overlay of experimental (blue) and fitted (red) line shapes of the UDP titration to H-tris type II saturated GTB. Each row corresponds to one fitted residue in the same order as in the following table. This figure is spread over two pages.

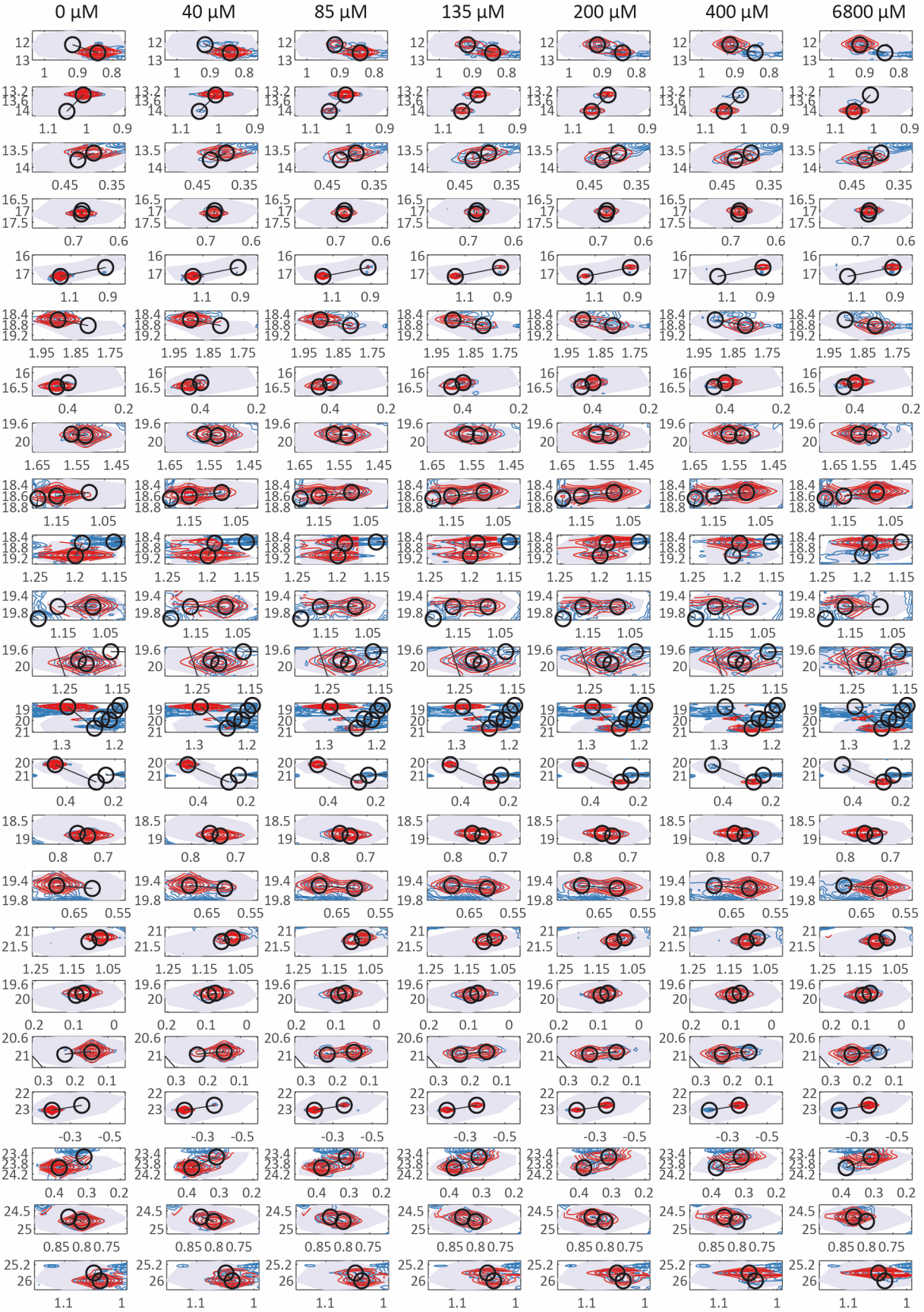
Tab. 34: Line shape analysis results derived from the UDP titration to H-tris type II saturated GTB.K_d is reported in units of µM. k_{off}, the transverse relaxation rates in the ^1H dimension (R2I), and the transverse relaxation rates in the ^{13}C dimension (R2S) are reported in units of s^{-1}. The chemical shifts (dI = ^1H; dS = ^{13}C) of the bound state (state 2) are reported in ppm.

Residue	Parameter	State	Fit result	Error
global	K_d		6.04	0.37
global	k_{off}		1.67	0.26
Ile123	dI	2	0.92	0.00
Ile123	dS	2	12.12	0.00
Ile123	R2I	2	56.19	1.48
Ile123	R2S	2	120.62	5.46
Ile192	dI	2	1.05	0.00
Ile192	dS	2	14.07	0.00
Ile192	R2I	2	55.34	2.81
Ile192	R2S	2	46.46	3.77
Ile224	dI	2	0.43	0.00

Residue	Parameter	State	Fit result	Error
Ile224	dS	2	13.82	0.00
Ile224	R2I	2	83.07	4.29
Ile224	R2S	2	65.00	5.54
Ile116	dI	2	0.68	0.00
Ile116	dS	2	17.00	0.00
Ile116	R2I	2	33.62	2.58
Ile116	R2S	2	53.65	5.13
Met214	dI	2	0.91	0.00
Met214	dS	2	16.67	0.01
Met214	R2I	2	168.80	6.57
Met214	R2S	2	50.48	5.90
Met266	dI	2	1.81	0.00
Met266	dS	2	18.94	0.01
Met266	R2I	2	92.26	3.57
Met266	R2S	2	83.26	6.59
Ala254	dI	2	0.40	0.00
Ala254	dS	2	16.33	0.00
Ala254	R2I	2	73.66	2.61
Ala254	R2S	2	37.49	2.56
Ala287	dI	2	1.57	0.00
Ala287	dS	2	19.84	0.00
Ala287	R2I	2	65.41	2.13
Ala287	R2S	2	42.07	2.26
Ala128	dI	2	1.08	0.00
Ala128	dS	2	18.54	0.00
Ala128	R2I	2	46.66	1.18
Ala128	R2S	2	18.76	0.70
Ala343	dI	2	1.19	0.00
Ala343	dS	2	18.69	0.00
Ala343	R2I	2	57.40	1.83
Ala343	R2S	2	50.54	2.51
Ala122	dI	2	1.17	0.00
Ala122	dS	2	19.67	0.00
Ala122	R2I	2	62.61	1.79
Ala122	R2S	2	53.63	2.74
Met142	dI	2	1.23	0.00
Met142	dS	2	19.84	0.00
Met142	R2I	2	65.90	1.76
Met142	R2S	2	79.99	3.56
Ala177	dI	2	1.24	0.00
Ala177	dS	2	20.77	0.01
Ala177	R2I	2	54.28	1.77
Ala177	R2S	2	118.44	6.19
Val120	dI	2	0.28	0.00
Val120	dS	2	21.50	0.00

Residue	Parameter	State	Fit result	Error
Val120	R2I	2	72.27	2.78
Val120	R2S	2	55.11	3.89
Val204	dI	2	0.76	0.00
Val204	dS	2	18.85	0.00
Val204	R2I	2	49.89	1.99
Val204	R2S	2	31.63	1.77
Val299	dI	2	0.62	0.00
Val299	dS	2	19.57	0.00
Val299	R2I	2	41.29	0.83
Val299	R2S	2	27.36	0.92
Val208	dI	2	1.11	0.00
Val208	dS	2	21.36	0.00
Val208	R2I	2	50.93	2.17
Val208	R2S	2	48.29	3.11
Leu225	dI	2	0.10	0.00
Leu225	dS	2	19.92	0.00
Leu225	R2I	2	57.16	3.09
Leu225	R2S	2	43.26	2.98
Leu134	dI	2	0.24	0.00
Leu134	dS	2	20.97	0.00
Leu134	R2I	2	59.87	1.87
Leu134	R2S	2	30.96	1.76
Leu339	dI	2	-0.34	0.00
Leu339	dS	2	22.87	0.00
Leu339	R2I	2	35.11	0.82
Leu339	R2S	2	26.23	1.06
Leu173	dI	2	0.31	0.00
Leu173	dS	2	23.56	0.00
Leu173	R2I	2	42.69	0.87
Leu173	R2S	2	46.50	1.22
Leu130	dI	2	0.83	0.00
Leu130	dS	2	24.64	0.00
Leu130	R2I	2	40.65	1.77
Leu130	R2S	2	49.18	2.70
Leu324	dI	2	1.08	0.00
Leu324	dS	2	25.65	0.00
Leu324	R2I	2	75.81	2.69
Leu324	R2S	2	61.58	3.32
Leu280	dI	2	0.22	0.00
Leu280	dS	2	24.87	0.00
Leu280	R2I	2	62.11	2.53
Leu280	R2S	2	50.36	2.66
Leu207	dI	2	0.47	0.00
Leu207	dS	2	25.59	0.00
Leu207	R2I	2	45.45	1.21
Leu207	R2S	2	64.69	2.84

Residue	Parameter	State	Fit result	Error
Leu118	dI	2	0.60	0.00
Leu118	dS	2	25.11	0.00
Leu118	R2I	2	47.69	1.06
Leu118	R2S	2	30.58	0.98
Leu306	dI	2	0.71	0.00
Leu306	dS	2	26.83	0.00
Leu306	R2I	2	44.18	1.43
Leu306	R2S	2	36.13	1.62
Val76	dI	2	1.64	0.00
Val76	dS	2	26.00	0.00
Val76	R2I	2	27.51	0.52
Val76	R2S	2	36.58	1.05
Leu132	dI	2	0.96	0.00
Leu132	dS	2	25.67	0.00
Leu132	R2I	2	48.13	1.03
Leu132	R2S	2	62.21	1.79
Leu277	dI	2	0.99	0.00
Leu277	dS	2	23.88	0.00
Leu277	R2I	2	48.89	1.20
Leu277	R2S	2	28.22	1.38
Leu201	dI	2	0.88	0.00
Leu201	dS	2	23.97	0.00
Leu201	R2I	2	29.05	0.44
Leu201	R2S	2	53.78	1.23
Ala268	dI	2	1.57	0.00
Ala268	dS	2	21.52	0.00
Ala268	R2I	2	68.93	3.85
Ala268	R2S	2	64.14	6.82
Ile256	dI	2	-0.29	0.00
Ile256	dS	2	10.46	0.00
Ile256	R2I	2	41.32	1.80
Ile256	R2S	2	36.40	1.96
Leu319	dI	2	-0.31	0.00
Leu319	dS	2	20.14	0.00
Leu319	R2I	2	48.50	1.39
Leu319	R2S	2	34.47	1.38
Val222	dI	2	0.54	0.00
Val222	dS	2	18.50	0.00
Val222	R2I	2	41.93	2.10
Val222	R2S	2	36.50	2.32


0 µM
40 µM
85 µM
135 µM
200 µM
400 µM
6800 µM

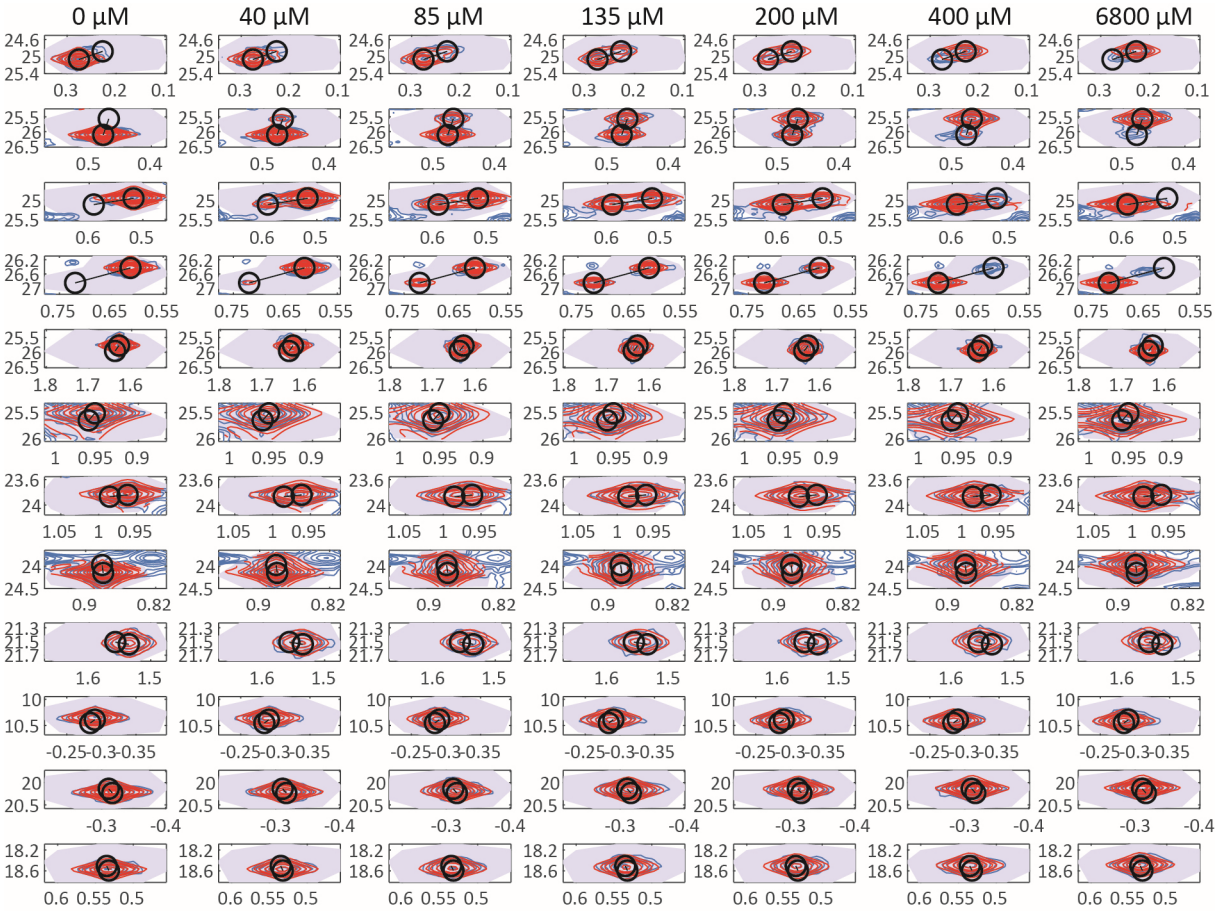


Fig. 18: Overlay of experimental (blue) and fitted (red) line shapes of the UDP titration to H-tris type III saturated GTB. Each row corresponds to one fitted residue in the same order as in the following table. This figure is spread over two pages.

Tab. 35: Line shape analysis results derived from the UDP titration to H-tris type III saturated GTB.K_d is reported in units of µM. k_{off}, the transverse relaxation rates in the ^1H dimension (R2I), and the transverse relaxation rates in the ^{13}C dimension (R2S) are reported in units of s^{-1}. The chemical shifts (dI = ^1H; dS = ^{13}C) of the bound state (state 2) are reported in ppm.

Residue	Parameter	State	Fit result	Error
global	K_d		29.24	1.42
global	k_{off}		3.60	0.53
Ile123	dI	2	0.92	0.00
Ile123	dS	2	12.15	0.01
Ile123	R2I	2	65.43	3.58
Ile123	R2S	2	147.19	10.84
Ile192	dI	2	1.05	0.00
Ile192	dS	2	14.07	0.01
Ile192	R2I	2	50.59	5.41
Ile192	R2S	2	59.54	10.32
Ile224	dI	2	0.42	0.00

Residue	Parameter	State	Fit result	Error
Ile224	dS	2	13.78	0.01
Ile224	R2I	2	85.42	12.18
Ile224	R2S	2	84.59	15.07
Ile116	dI	2	0.68	0.00
Ile116	dS	2	17.00	0.01
Ile116	R2I	2	30.43	4.26
Ile116	R2S	2	53.47	9.11
Met214	dI	2	0.92	0.00
Met214	dS	2	16.67	0.01
Met214	R2I	2	89.93	9.69
Met214	R2S	2	52.96	10.58
Met266	dI	2	1.82	0.00
Met266	dS	2	18.84	0.01
Met266	R2I	2	89.33	6.02
Met266	R2S	2	114.72	11.45
Ala254	dI	2	0.40	0.00
Ala254	dS	2	16.34	0.00
Ala254	R2I	2	70.55	5.42
Ala254	R2S	2	37.89	4.50
Ala287	dI	2	1.57	0.00
Ala287	dS	2	19.84	0.00
Ala287	R2I	2	73.74	4.93
Ala287	R2S	2	44.04	4.15
Ala128	dI	2	1.08	0.00
Ala128	dS	2	18.54	0.00
Ala128	R2I	2	68.88	7.45
Ala128	R2S	2	21.41	1.84
Ala343	dI	2	1.19	0.00
Ala343	dS	2	18.64	0.01
Ala343	R2I	2	56.90	3.26
Ala343	R2S	2	57.64	3.40
Ala122	dI	2	1.17	0.00
Ala122	dS	2	19.68	0.01
Ala122	R2I	2	91.69	7.29
Ala122	R2S	2	66.09	7.98
Met142	dI	2	1.22	0.00
Met142	dS	2	19.85	0.00
Met142	R2I	2	75.49	4.89
Met142	R2S	2	87.79	6.52
Ala177	dI	2	1.24	0.00
Ala177	dS	2	20.67	0.02
Ala177	R2I	2	48.82	4.00
Ala177	R2S	2	189.82	32.12
Val120	dI	2	0.28	0.00
Val120	dS	2	21.50	0.01
Val120	R2I	2	85.02	7.70

Residue	Parameter	State	Fit result	Error
Val120	R2S	2	65.27	10.34
Val204	dI	2	0.76	0.00
Val204	dS	2	18.86	0.00
Val204	R2I	2	49.97	3.92
Val204	R2S	2	26.21	2.83
Val299	dI	2	0.61	0.00
Val299	dS	2	19.56	0.00
Val299	R2I	2	63.08	3.30
Val299	R2S	2	31.14	2.73
Val208	dI	2	1.11	0.00
Val208	dS	2	21.35	0.00
Val208	R2I	2	46.85	4.27
Val208	R2S	2	43.61	6.21
Leu225	dI	2	0.10	0.00
Leu225	dS	2	19.91	0.01
Leu225	R2I	2	54.45	5.69
Leu225	R2S	2	41.83	4.84
Leu134	dI	2	0.24	0.00
Leu134	dS	2	20.98	0.00
Leu134	R2I	2	76.46	5.30
Leu134	R2S	2	38.26	3.22
Leu339	dI	2	-0.36	0.00
Leu339	dS	2	22.78	0.01
Leu339	R2I	2	57.74	4.80
Leu339	R2S	2	44.34	5.38
Leu173	dI	2	0.33	0.00
Leu173	dS	2	23.48	0.00
Leu173	R2I	2	82.86	2.43
Leu173	R2S	2	98.65	3.50
Leu130	dI	2	0.83	0.00
Leu130	dS	2	24.67	0.01
Leu130	R2I	2	41.53	3.72
Leu130	R2S	2	47.85	4.41
Leu324	dI	2	1.04	0.00
Leu324	dS	2	25.64	0.00
Leu324	R2I	2	90.83	6.65
Leu324	R2S	2	62.55	6.44
Leu280	dI	2	0.23	0.00
Leu280	dS	2	24.88	0.01
Leu280	R2I	2	70.14	8.09
Leu280	R2S	2	54.53	6.09
Leu207	dI	2	0.47	0.00
Leu207	dS	2	25.57	0.01
Leu207	R2I	2	46.45	2.74
Leu207	R2S	2	81.33	6.17

Residue	Parameter	State	Fit result	Error
Leu118	dI	2	0.59	0.00
Leu118	dS	2	25.11	0.00
Leu118	R2I	2	62.60	2.58
Leu118	R2S	2	36.37	2.32
Leu306	dI	2	0.72	0.00
Leu306	dS	2	26.85	0.00
Leu306	R2I	2	54.37	3.87
Leu306	R2S	2	35.75	3.45
Val76	dI	2	1.64	0.00
Val76	dS	2	25.95	0.00
Val76	R2I	2	27.22	1.07
Val76	R2S	2	61.51	2.59
Leu132	dI	2	0.96	0.00
Leu132	dS	2	25.65	0.00
Leu132	R2I	2	55.24	2.26
Leu132	R2S	2	57.22	3.05
Leu277	dI	2	0.98	0.00
Leu277	dS	2	23.87	0.00
Leu277	R2I	2	54.78	2.55
Leu277	R2S	2	30.47	2.33
Leu201	dI	2	0.88	0.00
Leu201	dS	2	23.97	0.00
Leu201	R2I	2	30.32	0.85
Leu201	R2S	2	59.82	2.09
Ala268	dI	2	1.56	0.00
Ala268	dS	2	21.51	0.01
Ala268	R2I	2	59.73	7.84
Ala268	R2S	2	51.27	9.99
Ile256	dI	2	-0.28	0.00
Ile256	dS	2	10.45	0.00
Ile256	R2I	2	40.74	3.07
Ile256	R2S	2	33.49	3.64
Leu319	dI	2	-0.31	0.00
Leu319	dS	2	20.14	0.00
Leu319	R2I	2	45.12	2.26
Leu319	R2S	2	36.86	2.25
Val222	dI	2	0.53	0.00
Val222	dS	2	18.51	0.00
Val222	R2I	2	40.84	3.25
Val222	R2S	2	38.42	4.22

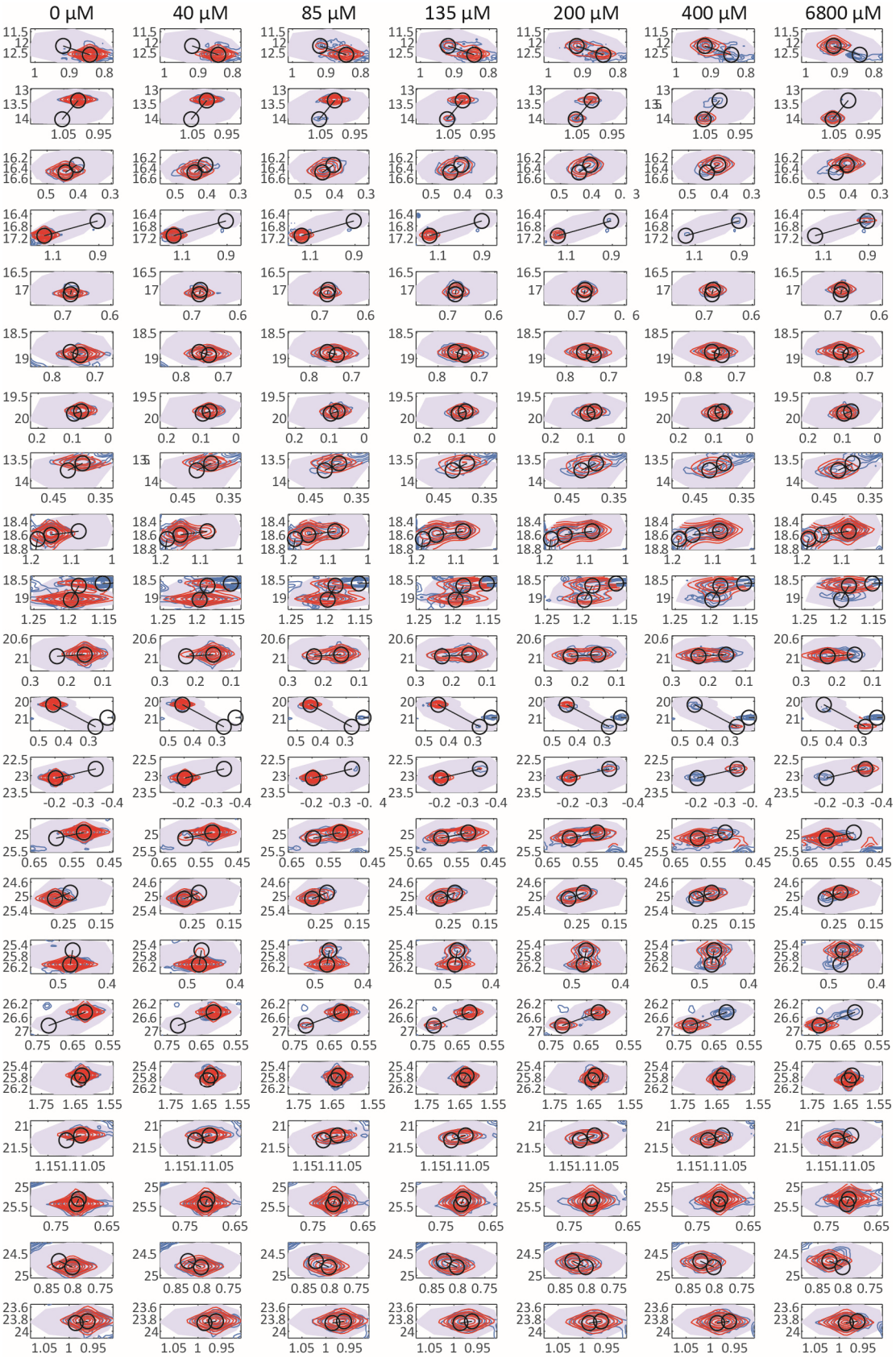


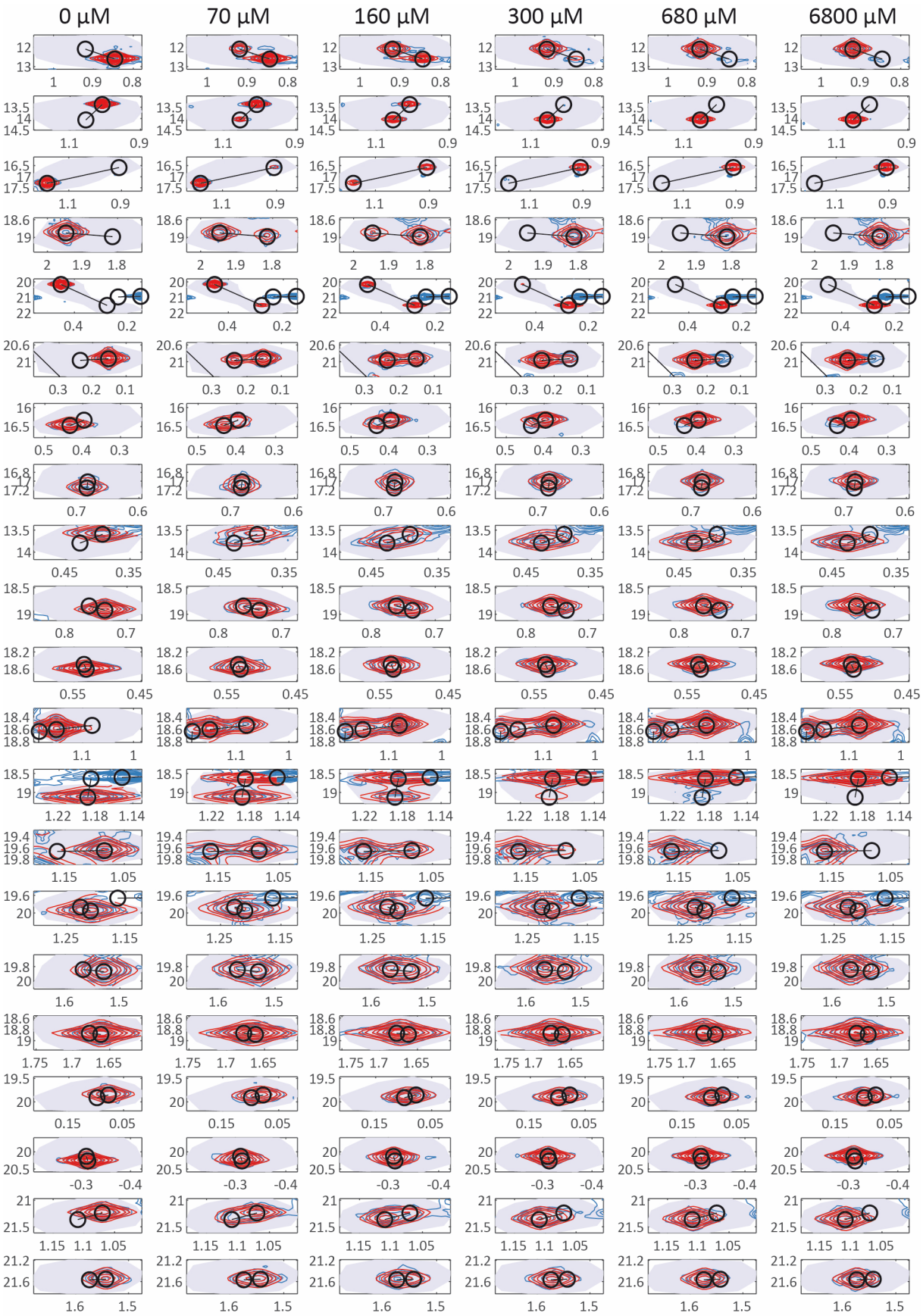
Fig. 19: Overlay of experimental (blue) and fitted (red) line shapes of the UDP titration to H-tris type III saturated GTB. Each row corresponds to one fitted residue in the same order as in the following table.

Tab. 36: Line shape analysis results derived from the UDP titration to H-tris type IV saturated GTB.K_d is reported in units of µM. k_{off}, the transverse relaxation rates in the ^1H dimension (R2I), and the transverse relaxation rates in the ^{13}C dimension (R2S) are reported in units of s^{-1}. The chemical shifts (dI = ^1H; dS = ^{13}C) of the bound state (state 2) are reported in ppm.

Residue	Parameter	State	Fit result	Error
global	K_d		65.53	2.05
global	k_{off}		12.26	0.69
Ile123	dI	2	0.92	0.00
Ile123	dS	2	12.19	0.01
Ile123	R2I	2	78.99	3.29
Ile123	R2S	2	166.28	8.88
Ile192	dI	2	1.05	0.00
Ile192	dS	2	14.04	0.01
Ile192	R2I	2	55.74	4.66
Ile192	R2S	2	98.83	13.08
Ala254	dI	2	0.41	0.00
Ala254	dS	2	16.35	0.00
Ala254	R2I	2	81.22	5.00
Ala254	R2S	2	43.89	4.13
Met214	dI	2	0.91	0.01
Met214	dS	2	16.64	0.01
Met214	R2I	2	184.09	14.90
Met214	R2S	2	42.68	14.27
Ile116	dI	2	0.68	0.00
Ile116	dS	2	17.01	0.01
Ile116	R2I	2	36.89	3.72
Ile116	R2S	2	59.66	7.55
Val204	dI	2	0.76	0.00
Val204	dS	2	18.87	0.00
Val204	R2I	2	57.01	3.06
Val204	R2S	2	29.65	2.29
Leu225	dI	2	0.10	0.00
Leu225	dS	2	19.90	0.00
Leu225	R2I	2	57.80	4.12
Leu225	R2S	2	47.61	4.58
Ile224	dI	2	0.42	0.00
Ile224	dS	2	13.75	0.01
Ile224	R2I	2	92.08	6.27
Ile224	R2S	2	106.96	10.63
Ala228	dI	2	1.09	0.00
Ala228	dS	2	18.55	0.00
Ala228	R2I	2	62.20	2.47
Ala228	R2S	2	20.95	1.36
Ala343	dI	2	1.18	0.00
Ala343	dS	2	18.63	0.00
Ala343	R2I	2	70.06	3.38

Residue	Parameter	State	Fit result	Error
Ala343	R2S	2	48.71	2.77
Leu134	dI	2	0.23	0.00
Leu134	dS	2	20.97	0.00
Leu134	R2I	2	91.39	3.94
Leu134	R2S	2	28.86	3.20
Val120	dI	2	0.27	0.01
Val120	dS	2	21.49	0.02
Val120	R2I	2	123.43	10.13
Val120	R2S	2	101.45	25.46
Leu339	dI	2	-0.34	0.00
Leu339	dS	2	22.79	0.01
Leu339	R2I	2	93.02	6.39
Leu339	R2S	2	62.67	8.47
Leu118	dI	2	0.59	0.00
Leu118	dS	2	25.12	0.00
Leu118	R2I	2	62.45	2.09
Leu118	R2S	2	43.48	1.98
Leu280	dI	2	0.23	0.00
Leu280	dS	2	24.90	0.01
Leu280	R2I	2	74.42	4.49
Leu280	R2S	2	54.75	4.94
Leu207	dI	2	0.47	0.00
Leu207	dS	2	25.60	0.01
Leu207	R2I	2	50.77	2.05
Leu207	R2S	2	127.19	7.90
Leu306	dI	2	0.72	0.00
Leu306	dS	2	26.84	0.00
Leu306	R2I	2	68.76	3.21
Leu306	R2S	2	49.92	3.68
Val76	dI	2	1.64	0.00
Val76	dS	2	25.90	0.00
Val76	R2I	2	29.95	0.88
Val76	R2S	2	66.18	2.52
Val208	dI	2	1.11	0.00
Val208	dS	2	21.34	0.00
Val208	R2I	2	51.34	3.40
Val208	R2S	2	47.92	4.75
Leu170	dI	2	0.71	0.00
Leu170	dS	2	25.31	0.00
Leu170	R2I	2	29.34	0.69
Leu170	R2S	2	42.03	1.20
Leu130	dI	2	0.83	0.00
Leu130	dS	2	24.67	0.00
Leu130	R2I	2	42.59	2.48
Leu130	R2S	2	53.09	3.08

Residue	Parameter	State	Fit result	Error
Leu277	dI	2	0.99	0.00
Leu277	dS	2	23.86	0.00
Leu277	R2I	2	51.81	1.71
Leu277	R2S	2	29.17	1.96


0 µM
70 µM
160 µM
300 µM
680 µM
6800 µM

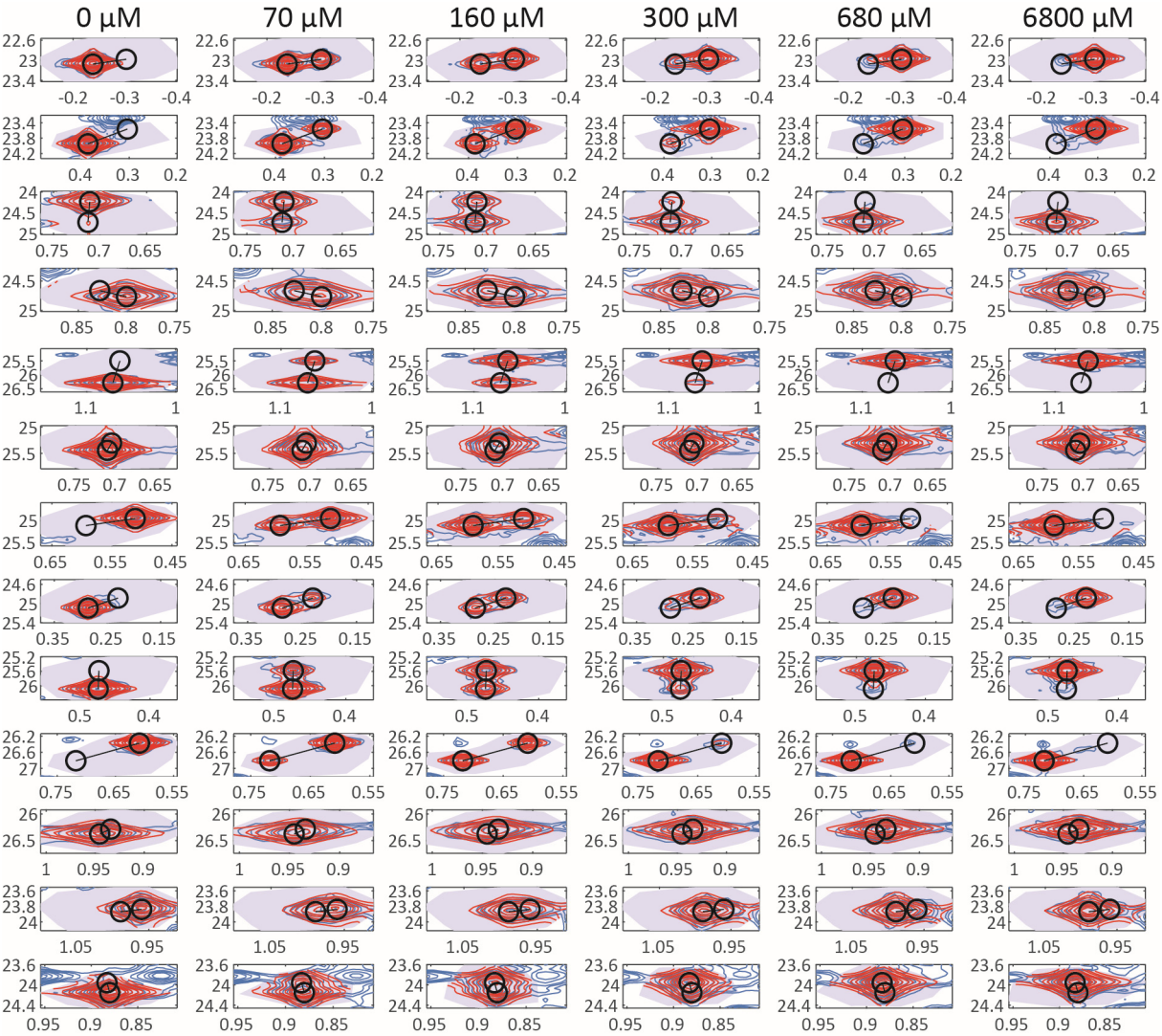


Fig. 20: Overlay of experimental (blue) and fitted (red) line shapes of the UDP titration to H-tris type V saturated GTB. Each row corresponds to one fitted residue in the same order as in the following table. This figure is spread over two pages.

Tab. 37: Line shape analysis results derived from the UDP titration to H-tris type V saturated GTB.K_d is reported in units of µM. k_{off}, the transverse relaxation rates in the ^1H dimension (R2I), and the transverse relaxation rates in the ^{13}C dimension (R2S) are reported in units of s^{-1}. The chemical shifts (dI = ^1H; dS = ^{13}C) of the bound state (state 2) are reported in ppm.

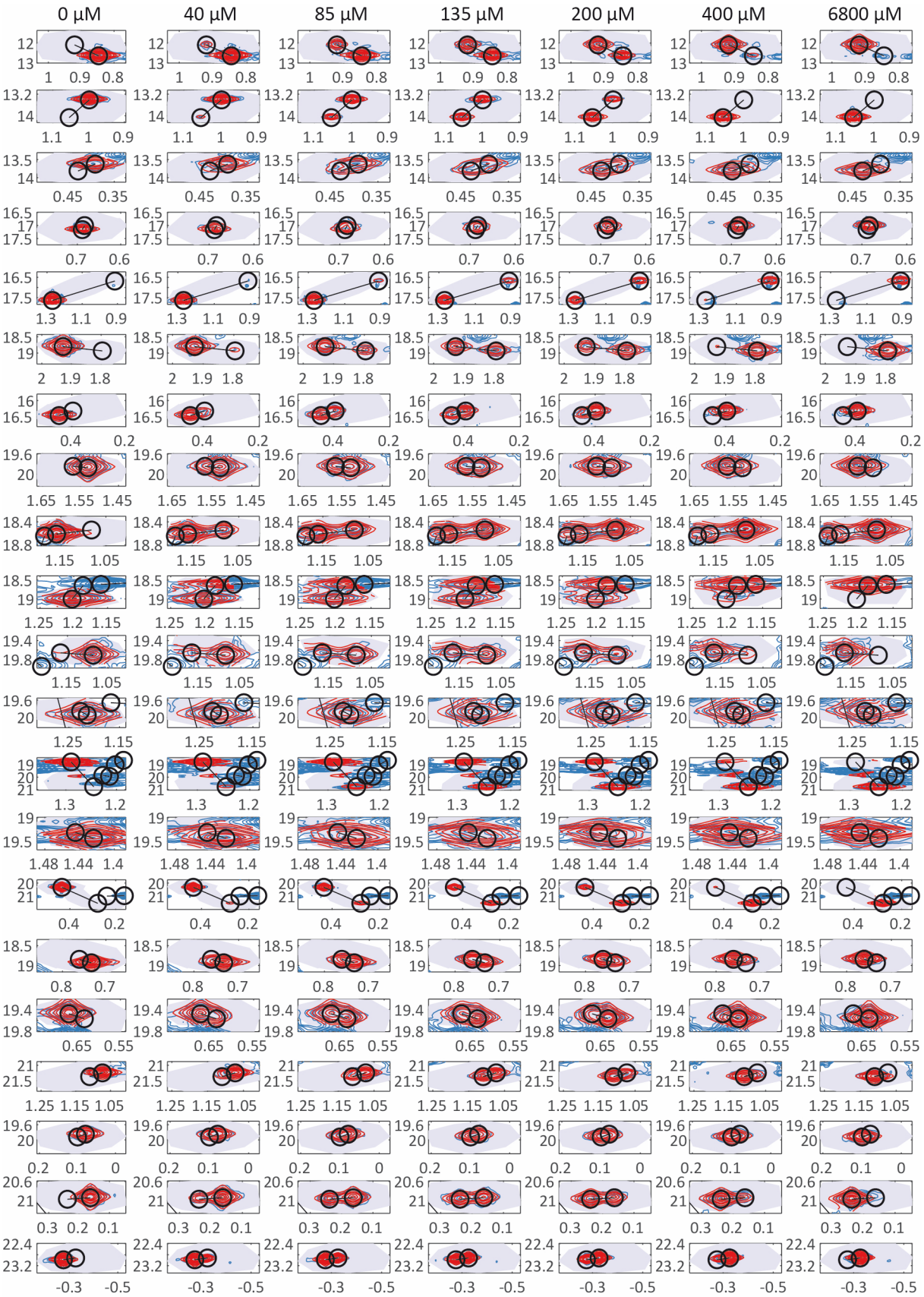
Residue	Parameter	State	Fit result	Error
global	K_d		30.73	0.88
global	k_{off}		3.37	0.28
Ile123	dI	2	0.92	0.00
Ile123	dS	2	12.10	0.00
Ile123	R2I	2	40.16	1.37
Ile123	R2S	2	108.87	3.94
Ile192	dI	2	1.06	0.00

Residue	Parameter	State	Fit result	Error
Ile192	dS	2	14.06	0.00
Ile192	R2I	2	41.74	2.17
Ile192	R2S	2	37.73	2.92
Met214	dI	2	0.91	0.00
Met214	dS	2	16.59	0.00
Met214	R2I	2	64.73	4.31
Met214	R2S	2	48.10	5.06
Met266	dI	2	1.82	0.00
Met266	dS	2	18.97	0.00
Met266	R2I	2	74.12	3.24
Met266	R2S	2	82.39	4.99
Met189	dI	2	1.84	0.00
Met189	dS	2	18.18	0.00
Met189	R2I	2	42.27	1.30
Met189	R2S	2	99.54	3.10
Met69	dI	2	2.08	0.00
Met69	dS	2	16.93	0.00
Met69	R2I	2	53.02	0.79
Met69	R2S	2	47.57	0.80
Val120	dI	2	0.28	0.00
Val120	dS	2	21.51	0.00
Val120	R2I	2	62.61	3.01
Val120	R2S	2	46.07	3.43
Leu134	dI	2	0.24	0.00
Leu134	dS	2	20.97	0.00
Leu134	R2I	2	56.88	2.31
Leu134	R2S	2	30.79	1.88
Ala254	dI	2	0.40	0.00
Ala254	dS	2	16.33	0.00
Ala254	R2I	2	63.21	2.39
Ala254	R2S	2	35.15	2.30
Ile116	dI	2	0.68	0.00
Ile116	dS	2	17.02	0.00
Ile116	R2I	2	37.83	2.99
Ile116	R2S	2	48.54	4.26
Ile224	dI	2	0.43	0.00
Ile224	dS	2	13.79	0.00
Ile224	R2I	2	79.51	4.90
Ile224	R2S	2	60.93	5.00
Val204	dI	2	0.76	0.00
Val204	dS	2	18.84	0.00
Val204	R2I	2	39.05	1.74
Val204	R2S	2	27.34	1.85
Val222	dI	2	0.54	0.00
Val222	dS	2	18.50	0.00

Residue	Parameter	State	Fit result	Error
Val222	R2I	2	40.33	1.90
Val222	R2S	2	33.57	2.46
Ala128	dI	2	1.08	0.00
Ala128	dS	2	18.54	0.00
Ala128	R2I	2	53.23	1.80
Ala128	R2S	2	18.52	0.80
Ala343	dI	2	1.18	0.00
Ala343	dS	2	18.63	0.00
Ala343	R2I	2	70.51	2.70
Ala343	R2S	2	35.31	1.60
Ala122	dI	2	1.17	0.00
Ala122	dS	2	19.68	0.00
Ala122	R2I	2	61.94	2.52
Ala122	R2S	2	66.94	3.98
Met142	dI	2	1.22	0.00
Met142	dS	2	19.86	0.00
Met142	R2I	2	84.57	3.17
Met142	R2S	2	75.25	3.37
Ala287	dI	2	1.57	0.00
Ala287	dS	2	19.84	0.00
Ala287	R2I	2	61.85	2.16
Ala287	R2S	2	32.76	1.61
Ala283	dI	2	1.68	0.00
Ala283	dS	2	18.87	0.00
Ala283	R2I	2	44.08	1.14
Ala283	R2S	2	22.26	1.05
Leu225	dI	2	0.10	0.00
Leu225	dS	2	19.91	0.00
Leu225	R2I	2	51.33	2.70
Leu225	R2S	2	34.91	2.65
Leu319	dI	2	-0.31	0.00
Leu319	dS	2	20.13	0.00
Leu319	R2I	2	43.83	1.41
Leu319	R2S	2	35.88	1.67
Val208	dI	2	1.11	0.00
Val208	dS	2	21.36	0.00
Val208	R2I	2	48.21	2.47
Val208	R2S	2	39.20	2.28
Ala268	dI	2	1.57	0.00
Ala268	dS	2	21.57	0.00
Ala268	R2I	2	56.77	3.46
Ala268	R2S	2	48.08	4.80
Leu339	dI	2	-0.30	0.00
Leu339	dS	2	22.98	0.00
Leu339	R2I	2	35.57	1.01
Leu339	R2S	2	26.62	1.20

Residue	Parameter	State	Fit result	Error
Leu173	dI	2	0.30	0.00
Leu173	dS	2	23.56	0.00
Leu173	R2I	2	41.56	0.90
Leu173	R2S	2	38.35	1.06
Leu329	dI	2	0.71	0.00
Leu329	dS	2	24.73	0.00
Leu329	R2I	2	48.10	2.58
Leu329	R2S	2	77.18	5.36
Leu130	dI	2	0.83	0.00
Leu130	dS	2	24.67	0.00
Leu130	R2I	2	45.78	1.96
Leu130	R2S	2	50.81	2.21
Leu324	dI	2	1.06	0.00
Leu324	dS	2	25.50	0.00
Leu324	R2I	2	62.10	2.67
Leu324	R2S	2	68.25	4.15
Leu170	dI	2	0.71	0.00
Leu170	dS	2	25.30	0.00
Leu170	R2I	2	25.73	0.42
Leu170	R2S	2	35.28	0.85
Leu118	dI	2	0.59	0.00
Leu118	dS	2	25.11	0.00
Leu118	R2I	2	46.98	1.28
Leu118	R2S	2	34.94	1.21
Leu280	dI	2	0.23	0.00
Leu280	dS	2	24.89	0.00
Leu280	R2I	2	53.75	2.70
Leu280	R2S	2	41.51	2.90
Leu207	dI	2	0.47	0.00
Leu207	dS	2	25.58	0.00
Leu207	R2I	2	38.25	1.02
Leu207	R2S	2	56.45	2.23
Leu306	dI	2	0.72	0.00
Leu306	dS	2	26.81	0.00
Leu306	R2I	2	38.87	1.32
Leu306	R2S	2	31.14	1.55
Leu228	dI	2	0.93	0.00
Leu228	dS	2	26.29	0.00
Leu228	R2I	2	54.16	2.14
Leu228	R2S	2	40.01	2.22
Val277	dI	2	0.99	0.00
Val277	dS	2	23.87	0.00
Val277	R2I	2	50.35	1.66
Val277	R2S	2	29.06	1.37
Leu201	dI	2	0.88	0.00

Residue	Parameter	State	Fit result	Error
Leu201	dS	2	23.96	0.00
Leu201	R2I	2	28.58	0.54
Leu201	R2S	2	45.08	1.02


0 µM
40 µM
85 µM
135 µM
200 µM
400 µM
6800 µM

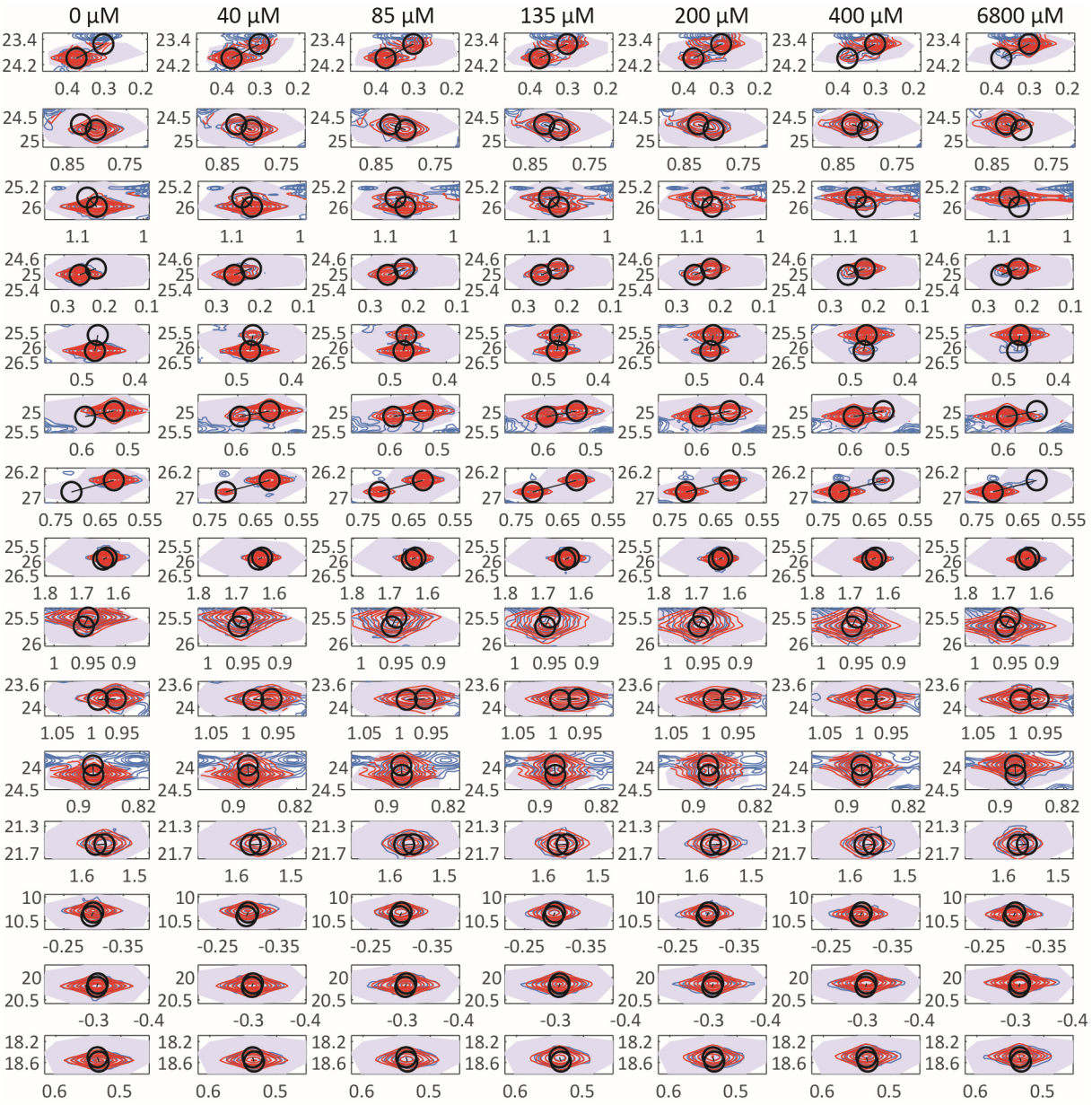


Fig. 21: Overlay of experimental (blue) and fitted (red) line shapes of the UDP titration to H-tris type VI saturated GTB. Each row corresponds to one fitted residue in the same order as in the following table. This figure is spread over two pages.

Tab. 38: Line shape analysis results derived from the UDP titration to H-tris type VI saturated GTB.K_d is reported in units of µM. k_{off}, the transverse relaxation rates in the ^{1}H dimension (R2I), and the transverse relaxation rates in the ^{13}C dimension (R2S) are reported in units of s^{-1}. The chemical shifts (dI = ^{1}H; dS = ^{13}C) of the bound state (state 2) are reported in ppm.

Residue	Parameter	State	Fit result	Error
global	K_d		31.89	0.67
global	k_{off}		2.16	0.15
Ile123	dI	2	0.92	0.00

Residue	Parameter	State	Fit result	Error
Ile123	dS	2	12.09	0.00
Ile123	R2I	2	43.07	0.90
Ile123	R2S	2	104.45	3.46
Ile192	dI	2	1.05	0.00
Ile192	dS	2	14.07	0.00
Ile192	R2I	2	57.29	1.95
Ile192	R2S	2	42.28	2.63
Ile224	dI	2	0.43	0.00
Ile224	dS	2	13.81	0.00
Ile224	R2I	2	87.18	3.44
Ile224	R2S	2	58.92	4.86
Ile116	dI	2	0.68	0.00
Ile116	dS	2	17.00	0.00
Ile116	R2I	2	33.77	1.93
Ile116	R2S	2	52.64	3.95
Met214	dI	2	0.91	0.00
Met214	dS	2	16.68	0.01
Met214	R2I	2	139.23	4.31
Met214	R2S	2	70.21	4.73
Met266	dI	2	1.80	0.00
Met266	dS	2	18.93	0.00
Met266	R2I	2	93.41	2.43
Met266	R2S	2	65.59	3.65
Ala254	dI	2	0.40	0.00
Ala254	dS	2	16.32	0.00
Ala254	R2I	2	64.77	1.94
Ala254	R2S	2	36.77	2.02
Ala287	dI	2	1.57	0.00
Ala287	dS	2	19.84	0.00
Ala287	R2I	2	64.11	1.57
Ala287	R2S	2	39.87	1.59
Ala128	dI	2	1.08	0.00
Ala128	dS	2	18.54	0.00
Ala128	R2I	2	48.95	1.09
Ala128	R2S	2	19.10	0.66
Ala343	dI	2	1.18	0.00
Ala343	dS	2	18.64	0.00
Ala343	R2I	2	53.67	1.15
Ala343	R2S	2	29.25	0.99
Ala122	dI	2	1.17	0.00
Ala122	dS	2	19.67	0.00
Ala122	R2I	2	55.80	1.28
Ala122	R2S	2	48.13	2.14
Met142	dI	2	1.23	0.00
Met142	dS	2	19.84	0.00

Residue	Parameter	State	Fit result	Error
Met142	R2I	2	66.20	1.51
Met142	R2S	2	67.97	2.49
Ala177	dI	2	1.24	0.00
Ala177	dS	2	20.78	0.00
Ala177	R2I	2	45.89	1.06
Ala177	R2S	2	88.46	3.38
Ala158	dI	2	1.44	0.00
Ala158	dS	2	19.31	0.00
Ala158	R2I	2	65.67	1.21
Ala158	R2S	2	35.41	0.95
Val120	dI	2	0.28	0.00
Val120	dS	2	21.50	0.00
Val120	R2I	2	71.39	2.10
Val120	R2S	2	56.64	3.03
Val204	dI	2	0.76	0.00
Val204	dS	2	18.84	0.00
Val204	R2I	2	46.00	1.49
Val204	R2S	2	27.62	1.54
Val299	dI	2	0.64	0.00
Val299	dS	2	19.57	0.00
Val299	R2I	2	38.54	0.85
Val299	R2S	2	27.01	0.86
Val208	dI	2	1.11	0.00
Val208	dS	2	21.36	0.00
Val208	R2I	2	56.18	2.20
Val208	R2S	2	41.45	2.66
Leu225	dI	2	0.10	0.00
Leu225	dS	2	19.92	0.00
Leu225	R2I	2	52.33	2.19
Leu225	R2S	2	36.92	2.12
Leu134	dI	2	0.24	0.00
Leu134	dS	2	20.97	0.00
Leu134	R2I	2	56.60	1.39
Leu134	R2S	2	29.96	1.23
Leu339	dI	2	-0.33	0.00
Leu339	dS	2	22.92	0.00
Leu339	R2I	2	33.80	0.59
Leu339	R2S	2	27.08	0.73
Leu173	dI	2	0.31	0.00
Leu173	dS	2	23.56	0.00
Leu173	R2I	2	36.57	0.63
Leu173	R2S	2	39.05	0.90
Leu130	dI	2	0.83	0.00
Leu130	dS	2	24.66	0.00
Leu130	R2I	2	38.92	1.33
Leu130	R2S	2	45.93	1.62

Residue	Parameter	State	Fit result	Error
Leu324	dI	2	1.09	0.00
Leu324	dS	2	25.64	0.00
Leu324	R2I	2	70.02	2.05
Leu324	R2S	2	63.38	3.29
Leu280	dI	2	0.22	0.00
Leu280	dS	2	24.86	0.00
Leu280	R2I	2	56.47	1.89
Leu280	R2S	2	41.89	1.94
Leu207	dI	2	0.47	0.00
Leu207	dS	2	25.58	0.00
Leu207	R2I	2	41.96	0.83
Leu207	R2S	2	56.45	1.99
Leu118	dI	2	0.60	0.00
Leu118	dS	2	25.11	0.00
Leu118	R2I	2	40.75	0.69
Leu118	R2S	2	29.90	0.79
Leu306	dI	2	0.72	0.00
Leu306	dS	2	26.84	0.00
Leu306	R2I	2	43.43	1.14
Leu306	R2S	2	34.72	1.49
Val76	dI	2	1.64	0.00
Val76	dS	2	25.96	0.00
Val76	R2I	2	27.28	0.44
Val76	R2S	2	36.14	0.72
Leu132	dI	2	0.96	0.00
Leu132	dS	2	25.67	0.00
Leu132	R2I	2	41.07	0.74
Leu132	R2S	2	45.15	1.19
Leu277	dI	2	0.99	0.00
Leu277	dS	2	23.88	0.00
Leu277	R2I	2	45.65	1.02
Leu277	R2S	2	27.23	1.25
Leu201	dI	2	0.88	0.00
Leu201	dS	2	23.96	0.00
Leu201	R2I	2	29.59	0.42
Leu201	R2S	2	44.48	0.88
Ala268	dI	2	1.58	0.00
Ala268	dS	2	21.58	0.00
Ala268	R2I	2	59.18	2.47
Ala268	R2S	2	59.66	4.37
Ile256	dI	2	-0.30	0.00
Ile256	dS	2	10.40	0.00
Ile256	R2I	2	39.45	1.23
Ile256	R2S	2	31.33	1.74
Leu319	dI	2	-0.31	0.00

Residue	Parameter	State	Fit result	Error
Leu319	dS	2	20.14	0.00
Leu319	R2I	2	46.21	1.27
Leu319	R2S	2	33.10	1.12
Val222	dI	2	0.54	0.00
Val222	dS	2	18.50	0.00
Val222	R2I	2	38.46	1.35
Val222	R2S	2	34.92	1.86

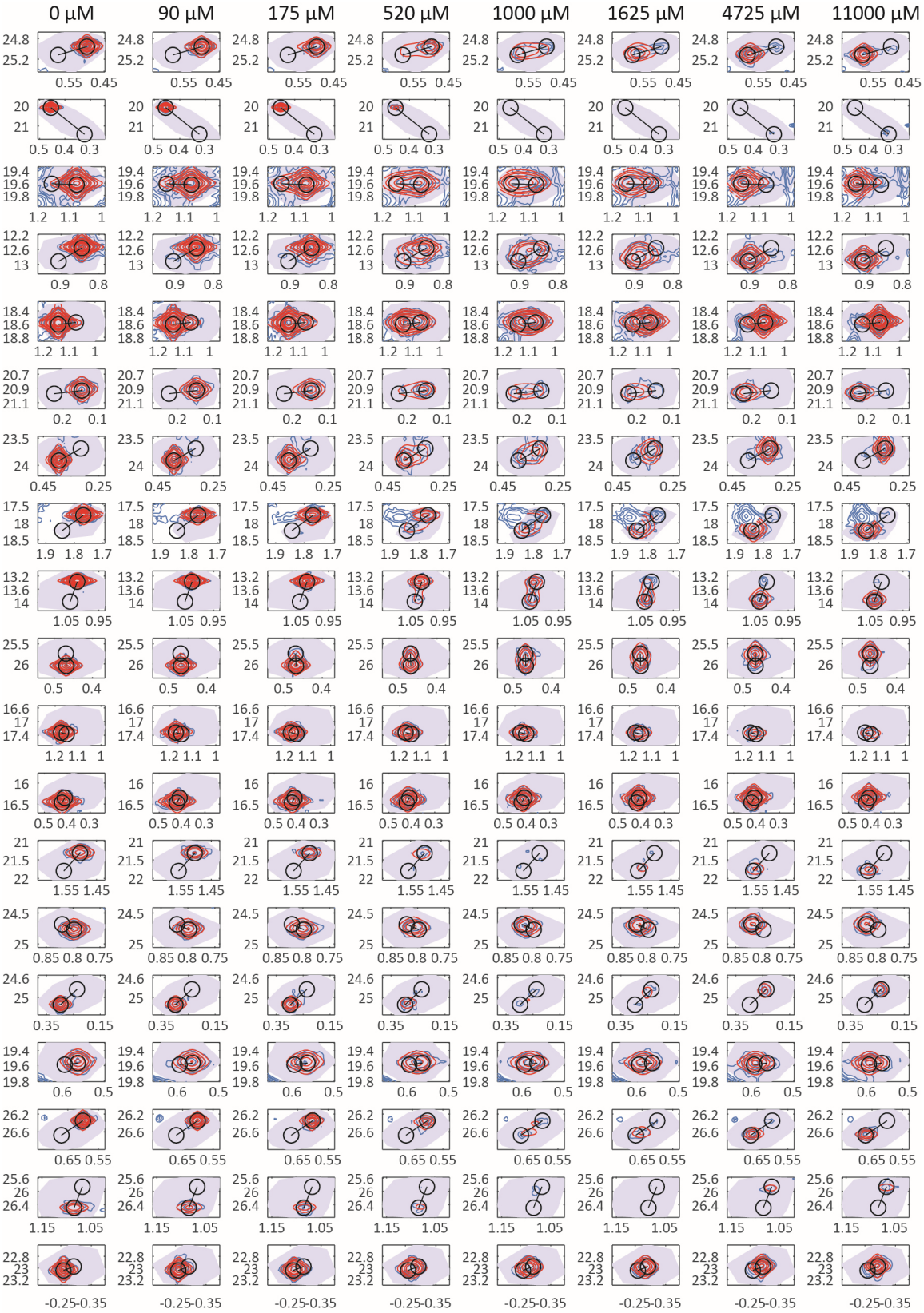


Fig. 22: Overlay of experimental (blue) and fitted (red) line shapes of the UDP-Glc titration to 3DD-saturated GTB. Each row corresponds to one fitted residue in the same order as in the following table.

Tab. 39: Line shape analysis results derived from the UDP-Glc titration to 3DD-saturated GTB.K_d is reported in units of μM. k_{off}, the transverse relaxation rates in the ^{1}H dimension (R2I), and the transverse relaxation rates in the ^{13}C dimension (R2S) are reported in units of s^{-1}. The chemical shifts (dI = ^{1}H; dS = ^{13}C) of the bound state (state 2) are reported in ppm.

Residue	Parameter	State	Fit result	Error
global	K_d		580.64	11.48
global	k_{off}		49.85	1.57
Leu118	dI	2	0.58	0.00
Leu118	dS	2	25.12	0.00
Leu118	R2I	2	48.74	2.79
Leu118	R2S	2	48.92	3.94
Val120	dI	2	0.32	0.01
Val120	dS	2	21.39	0.03
Val120	R2I	2	104.87	13.53
Val120	R2S	2	108.68	43.23
Ala122	dI	2	1.16	0.00
Ala122	dS	2	19.61	0.00
Ala122	R2I	2	87.88	2.16
Ala122	R2S	2	52.75	2.31
Ile123	dI	2	0.91	0.00
Ile123	dS	2	12.92	0.00
Ile123	R2I	2	62.89	1.98
Ile123	R2S	2	102.68	4.34
Ala128	dI	2	1.08	0.00
Ala128	dS	2	18.57	0.00
Ala128	R2I	2	60.94	0.98
Ala128	R2S	2	17.70	0.69
Leu134	dI	2	0.23	0.00
Leu134	dS	2	20.97	0.01
Leu134	R2I	2	83.07	5.87
Leu134	R2S	2	38.51	5.47
Leu173	dI	2	0.32	0.00
Leu173	dS	2	23.69	0.00
Leu173	R2I	2	51.79	2.50
Leu173	R2S	2	85.90	5.96
Met189	dI	2	1.84	0.00
Met189	dS	2	18.22	0.01
Met189	R2I	2	66.00	2.70
Met189	R2S	2	134.54	7.65
Ile192	dI	2	1.04	0.00
Ile192	dS	2	13.97	0.01
Ile192	R2I	2	60.61	3.14
Ile192	R2S	2	106.09	8.54
Leu207	dI	2	0.47	0.00
Leu207	dS	2	25.74	0.01
Leu207	R2I	2	39.36	1.76

Residue	Parameter	State	Fit result	Error
Leu207	R2S	2	112.37	6.79
Met214	dI	2	1.15	0.00
Met214	dS	2	17.37	0.01
Met214	R2I	2	142.41	5.52
Met214	R2S	2	110.96	8.98
Ala254	dI	2	0.41	0.00
Ala254	dS	2	16.35	0.00
Ala254	R2I	2	69.60	1.59
Ala254	R2S	2	52.12	1.78
Ala268	dI	2	1.56	0.00
Ala268	dS	2	21.80	0.01
Ala268	R2I	2	98.76	8.77
Ala268	R2S	2	103.98	15.95
Leu170	dI	2	0.82	0.00
Leu170	dS	2	24.68	0.01
Leu170	R2I	2	37.32	3.46
Leu170	R2S	2	60.16	7.15
Leu280	dI	2	0.24	0.00
Leu280	dS	2	24.84	0.01
Leu280	R2I	2	70.17	7.77
Leu280	R2S	2	84.60	11.93
Val299	dI	2	0.60	0.00
Val299	dS	2	19.59	0.00
Val299	R2I	2	69.20	4.04
Val299	R2S	2	37.52	3.57
Leu306	dI	2	0.67	0.00
Leu306	dS	2	26.67	0.01
Leu306	R2I	2	70.41	5.63
Leu306	R2S	2	46.82	7.30
Leu324	dI	2	1.07	0.00
Leu324	dS	2	25.87	0.02
Leu324	R2I	2	70.96	9.15
Leu324	R2S	2	92.18	20.64
Leu339	dI	2	-0.29	0.00
Leu339	dS	2	22.98	0.00
Leu339	R2I	2	50.19	2.01
Leu339	R2S	2	40.56	2.50

Acceptor substrate and analog titrations with donor analog-saturated GTB

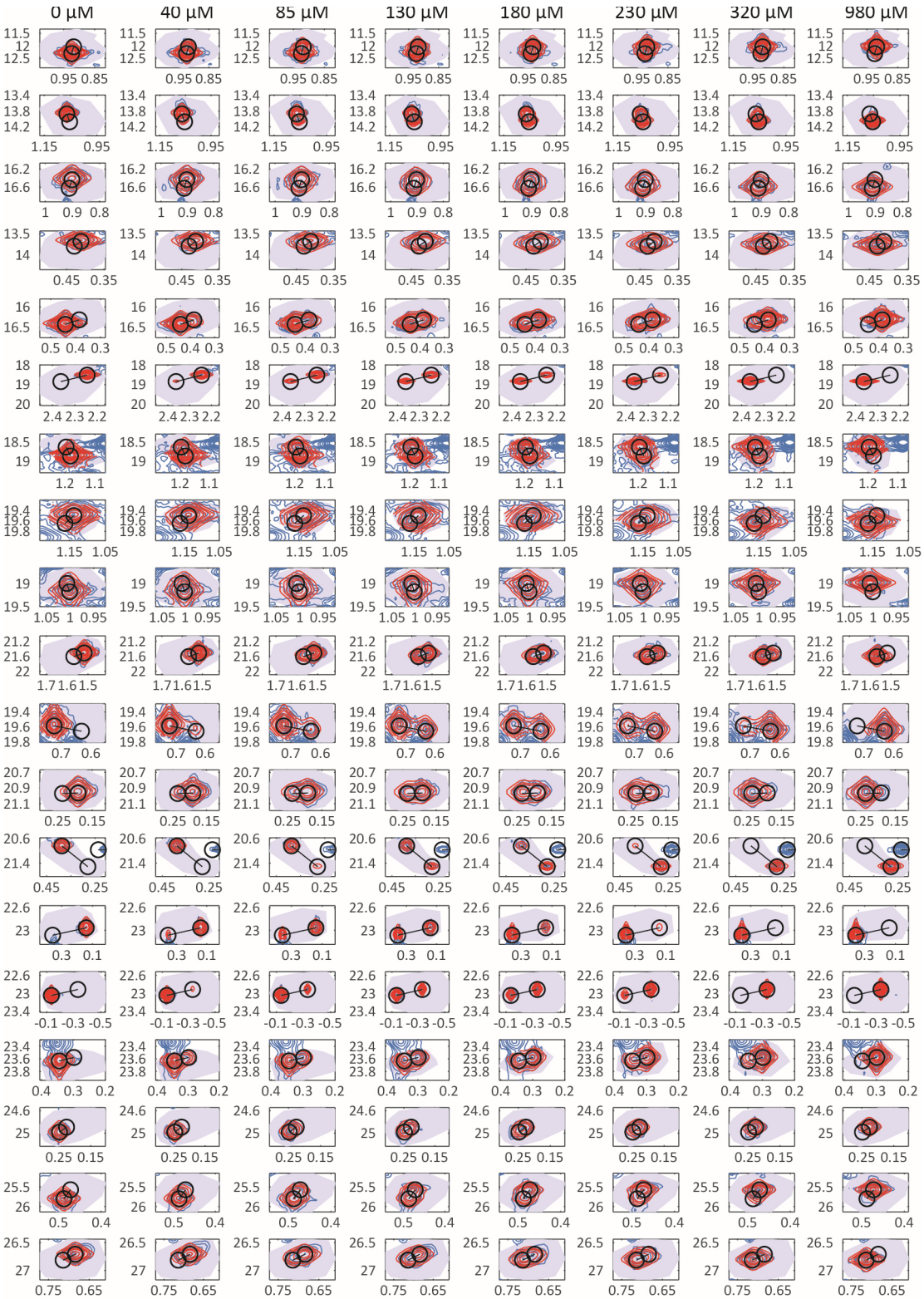


Fig. 23: Overlay of experimental (blue) and fitted (red) line shapes of the H-dis titration to UDP-saturated GTB. Each row corresponds to one fitted residue in the same order as in the following table.

Tab. 40: Line shape analysis results derived from the H-dis titration to UDP-saturated GTB.K_d is reported in units of μM. k_{off}, the transverse relaxation rates in the ^{1}H dimension (R2I), and the transverse relaxation rates in the ^{13}C dimension (R2S) are reported in units of s^{-1}. The chemical shifts (dI = ^{1}H; dS = ^{13}C) of the bound state (state 2) are reported in ppm.

Residue	Parameter	State	Fit result	Error
global	K_d		28.40	1.16
global	k_{off}		6.93	0.36
Ile123	dI	2	0.92	0.00
Ile123	dS	2	12.04	0.00
Ile123	R2I	2	30.18	0.54
Ile123	R2S	2	71.19	1.67
Ile192	dI	2	1.05	0.00
Ile192	dS	2	14.07	0.00
Ile192	R2I	2	38.40	1.32
Ile192	R2S	2	24.13	1.49
Met214	dI	2	0.91	0.00
Met214	dS	2	16.62	0.00
Met214	R2I	2	84.59	2.39
Met214	R2S	2	52.84	2.97
Ile224	dI	2	0.43	0.00
Ile224	dS	2	13.79	0.00
Ile224	R2I	2	72.65	2.13
Ile224	R2S	2	47.37	2.62
Ala254	dI	2	0.39	0.00
Ala254	dS	2	16.32	0.00
Ala254	R2I	2	62.16	1.12
Ala254	R2S	2	37.51	1.15
Met191	dI	2	2.36	0.00
Met191	dS	2	18.85	0.00
Met191	R2I	2	49.77	1.60
Met191	R2S	2	25.19	1.25
Ala343	dI	2	1.20	0.00
Ala343	dS	2	18.64	0.00
Ala343	R2I	2	59.70	0.90
Ala343	R2S	2	36.06	0.94
Ala122	dI	2	1.16	0.00
Ala122	dS	2	19.65	0.00
Ala122	R2I	2	61.28	0.77
Ala122	R2S	2	37.67	0.93
Val127	dI	2	1.01	0.00
Val127	dS	2	18.99	0.00
Val127	R2I	2	44.02	1.30
Val127	R2S	2	41.96	1.77
Ala268	dI	2	1.57	0.00
Ala268	dS	2	21.61	0.00
Ala268	R2I	2	66.87	1.52

Residue	Parameter	State	Fit result	Error
Ala268	R2S	2	46.77	2.01
Val299	dI	2	0.63	0.00
Val299	dS	2	19.66	0.00
Val299	R2I	2	49.09	1.29
Val299	R2S	2	40.74	1.76
Leu134	dI	2	0.24	0.00
Leu134	dS	2	20.97	0.00
Leu134	R2I	2	50.30	2.17
Leu134	R2S	2	31.88	2.44
Val120	dI	2	0.28	0.00
Val120	dS	2	21.51	0.00
Val120	R2I	2	57.86	2.62
Val120	R2S	2	41.38	3.63
Leu336	dI	2	0.36	0.00
Leu336	dS	2	23.09	0.00
Leu336	R2I	2	28.51	1.17
Leu336	R2S	2	30.43	1.62
Leu339	dI	2	-0.33	0.00
Leu339	dS	2	22.92	0.00
Leu339	R2I	2	35.18	1.06
Leu339	R2S	2	26.50	1.42
Leu173	dI	2	0.30	0.00
Leu173	dS	2	23.58	0.00
Leu173	R2I	2	34.23	0.99
Leu173	R2S	2	37.04	1.32
Leu280	dI	2	0.23	0.00
Leu280	dS	2	24.89	0.00
Leu280	R2I	2	47.25	2.65
Leu280	R2S	2	37.01	3.20
Leu207	dI	2	0.47	0.00
Leu207	dS	2	25.57	0.00
Leu207	R2I	2	35.18	1.04
Leu207	R2S	2	45.38	2.31
Leu306	dI	2	0.71	0.00
Leu306	dS	2	26.81	0.00
Leu306	R2I	2	39.65	1.62
Leu306	R2S	2	31.24	1.72

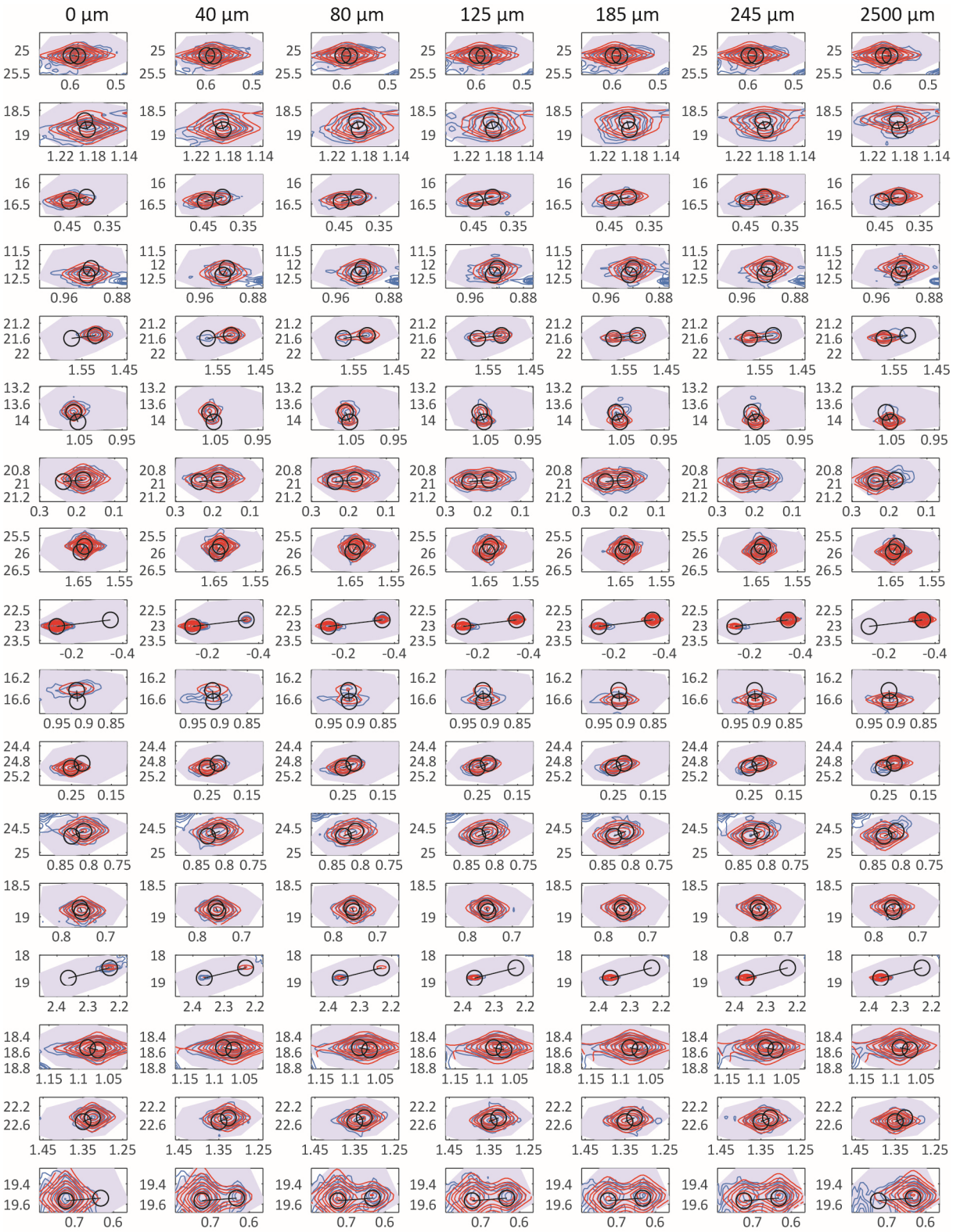


Fig. 24: Overlay of experimental (blue) and fitted (red) line shapes of the H-tris type I titration to UDP-saturated GTB.Each row corresponds to one fitted residue in the same order as in the following table.

Tab. 41: Line shape analysis results derived from the H-tris type I titration to UDP-saturated GTB.K_d is reported in units of µM. k_{off}, the transverse relaxation rates in the ^1H dimension (R2I), and the transverse relaxation rates in the ^{13}C dimension (R2S) are reported in units of s^{-1}. The chemical shifts (dI = ^1H; dS = ^{13}C) of the bound state (state 2) are reported in ppm.

Residue	Parameter	State	Fit result	Error
global	K_d		44.13	2.30
global	k_{off}		0.26	0.38
Leu118	dI	2	0.60	0.00
Leu118	dS	2	25.12	0.00
Leu118	R2I	2	69.09	1.78
Leu118	R2S	2	40.40	1.67
Ala343	dI	2	1.19	0.00
Ala343	dS	2	18.70	0.01
Ala343	R2I	2	63.05	3.26
Ala343	R2S	2	84.28	5.88
Ala254	dI	2	0.40	0.00
Ala254	dS	2	16.34	0.00
Ala254	R2I	2	81.83	4.21
Ala254	R2S	2	46.08	3.66
Ile123	dI	2	0.92	0.00
Ile123	dS	2	12.15	0.01
Ile123	R2I	2	40.30	1.65
Ile123	R2S	2	118.06	6.57
Ala268	dI	2	1.57	0.00
Ala268	dS	2	21.60	0.01
Ala268	R2I	2	71.07	4.71
Ala268	R2S	2	51.35	6.03
Ile192	dI	2	1.05	0.00
Ile192	dS	2	14.05	0.00
Ile192	R2I	2	42.06	3.18
Ile192	R2S	2	47.09	4.65
Leu134	dI	2	0.24	0.00
Leu134	dS	2	20.98	0.00
Leu134	R2I	2	80.61	3.27
Leu134	R2S	2	38.36	2.61
Val76	dI	2	1.64	0.00
Val76	dS	2	25.98	0.00
Val76	R2I	2	31.48	0.80
Val76	R2S	2	63.63	1.93
Leu339	dI	2	-0.35	0.00
Leu339	dS	2	22.83	0.00
Leu339	R2I	2	49.56	2.06
Leu339	R2S	2	38.77	2.46
Met214	dI	2	0.91	0.00
Met214	dS	2	16.66	0.00
Met214	R2I	2	70.18	5.47

Residue	Parameter	State	Fit result	Error
Met214	R2S	2	37.91	5.24
Leu288	dI	2	0.22	0.00
Leu288	dS	2	24.87	0.00
Leu288	R2I	2	64.68	3.36
Leu288	R2S	2	53.63	4.01
Leu130	dI	2	0.83	0.00
Leu130	dS	2	24.67	0.00
Leu130	R2I	2	44.05	2.22
Leu130	R2S	2	69.52	3.61
Val204	dI	2	0.76	0.00
Val204	dS	2	18.86	0.00
Val204	R2I	2	60.37	3.02
Val204	R2S	2	33.52	2.41
Met191	dI	2	2.36	0.00
Met191	dS	2	18.85	0.00
Met191	R2I	2	40.49	3.33
Met191	R2S	2	23.54	3.07
Ala228	dI	2	1.09	0.00
Ala228	dS	2	18.55	0.00
Ala228	R2I	2	46.73	1.56
Ala228	R2S	2	22.65	1.04
Val220	dI	2	1.35	0.00
Val220	dS	2	22.55	0.00
Val220	R2I	2	60.32	1.89
Val220	R2S	2	51.56	2.28
Val299	dI	2	0.63	0.00
Val299	dS	2	19.54	0.00
Val299	R2I	2	85.39	2.34
Val299	R2S	2	37.21	1.71

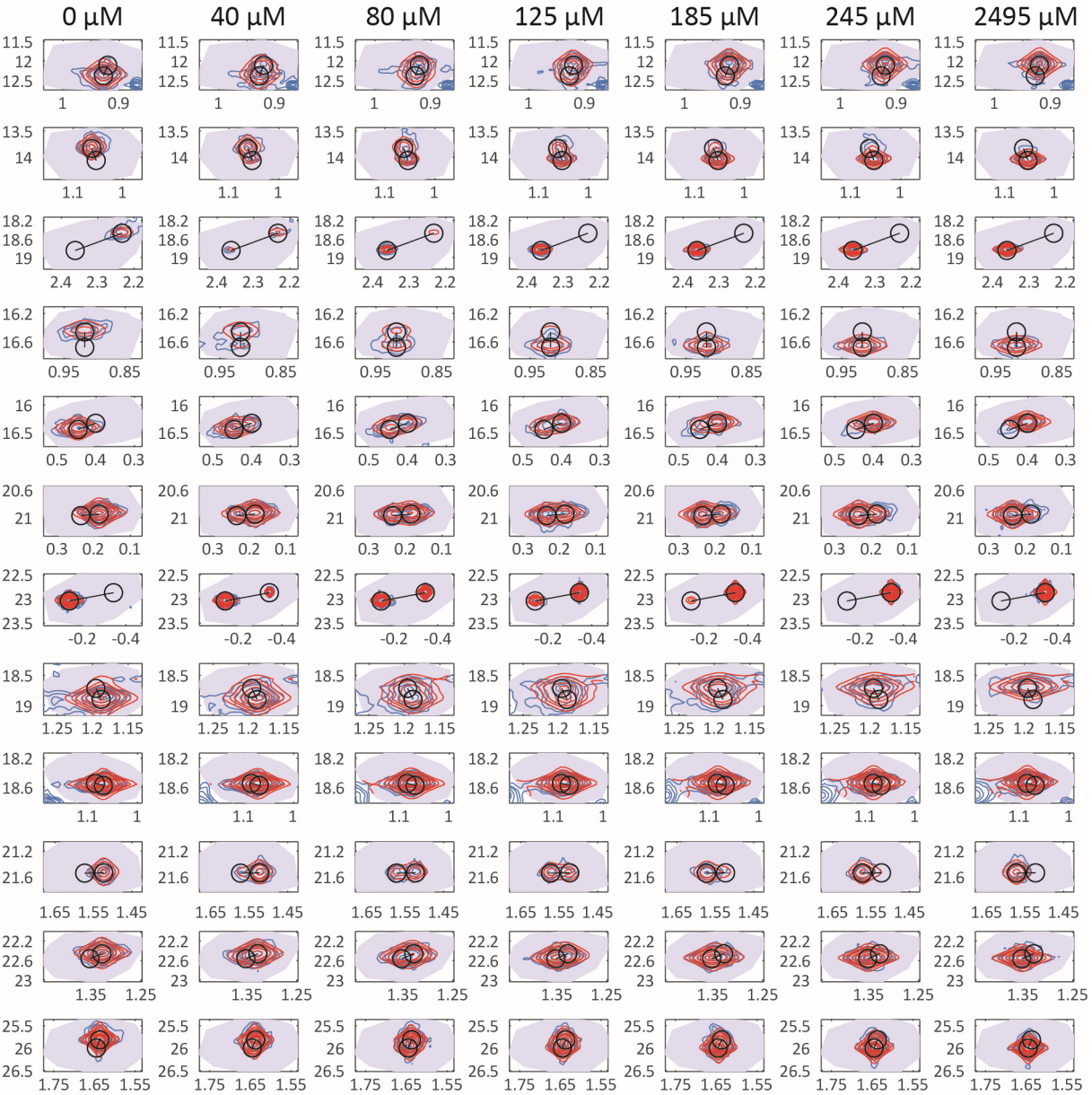


Fig. 25: Overlay of experimental (blue) and fitted (red) line shapes of the H-tris type II titration to UDP-saturated GTB. Each row corresponds to one fitted residue in the same order as in the following table.

Tab. 42: Line shape analysis results derived from the H-tris type II titration to UDP-saturated GTB.K_d is reported in units of µM. k_{off}, the transverse relaxation rates in the ^1H dimension (R2I), and the transverse relaxation rates in the ^{13}C dimension (R2S) are reported in units of s^{-1}. The chemical shifts (dI = ^1H; dS = ^{13}C) of the bound state (state 2) are reported in ppm.

Residue	Parameter	State	Fit result	Error
global	K_d		9.51	0.89
global	k_{off}		1.68	0.49
Ile123	dI	2	0.92	0.00
Ile123	dS	2	12.11	0.00
Ile123	R2I	2	42.24	1.53

Residue	Parameter	State	Fit result	Error
Ile123	R2S	2	110.70	5.23
Ile192	dI	2	1.05	0.00
Ile192	dS	2	14.06	0.00
Ile192	R2I	2	40.56	2.23
Ile192	R2S	2	39.69	2.90
Met191	dI	2	2.36	0.00
Met191	dS	2	18.85	0.00
Met191	R2I	2	43.62	2.50
Met191	R2S	2	26.01	2.36
Met214	dI	2	0.92	0.00
Met214	dS	2	16.68	0.00
Met214	R2I	2	68.00	4.52
Met214	R2S	2	37.63	4.09
Ala254	dI	2	0.40	0.00
Ala254	dS	2	16.33	0.00
Ala254	R2I	2	80.28	3.18
Ala254	R2S	2	43.51	2.61
Leu134	dI	2	0.24	0.00
Leu134	dS	2	20.97	0.00
Leu134	R2I	2	77.24	2.63
Leu134	R2S	2	33.83	1.77
Leu339	dI	2	-0.34	0.00
Leu339	dS	2	22.87	0.00
Leu339	R2I	2	39.94	1.12
Leu339	R2S	2	34.04	1.27
Ala343	dI	2	1.19	0.00
Ala343	dS	2	18.71	0.00
Ala343	R2I	2	75.89	2.84
Ala343	R2S	2	64.67	3.93
Ala128	dI	2	1.08	0.00
Ala128	dS	2	18.55	0.00
Ala128	R2I	2	46.39	1.15
Ala128	R2S	2	22.53	0.85
Ala268	dI	2	1.57	0.00
Ala268	dS	2	21.54	0.00
Ala268	R2I	2	61.96	3.71
Ala268	R2S	2	67.31	6.08
Val220	dI	2	1.35	0.00
Val220	dS	2	22.56	0.00
Val220	R2I	2	55.48	1.33
Val220	R2S	2	46.89	1.74
Val76	dI	2	1.65	0.00
Val76	dS	2	26.00	0.00
Val76	R2I	2	32.55	0.59
Val76	R2S	2	49.55	1.31

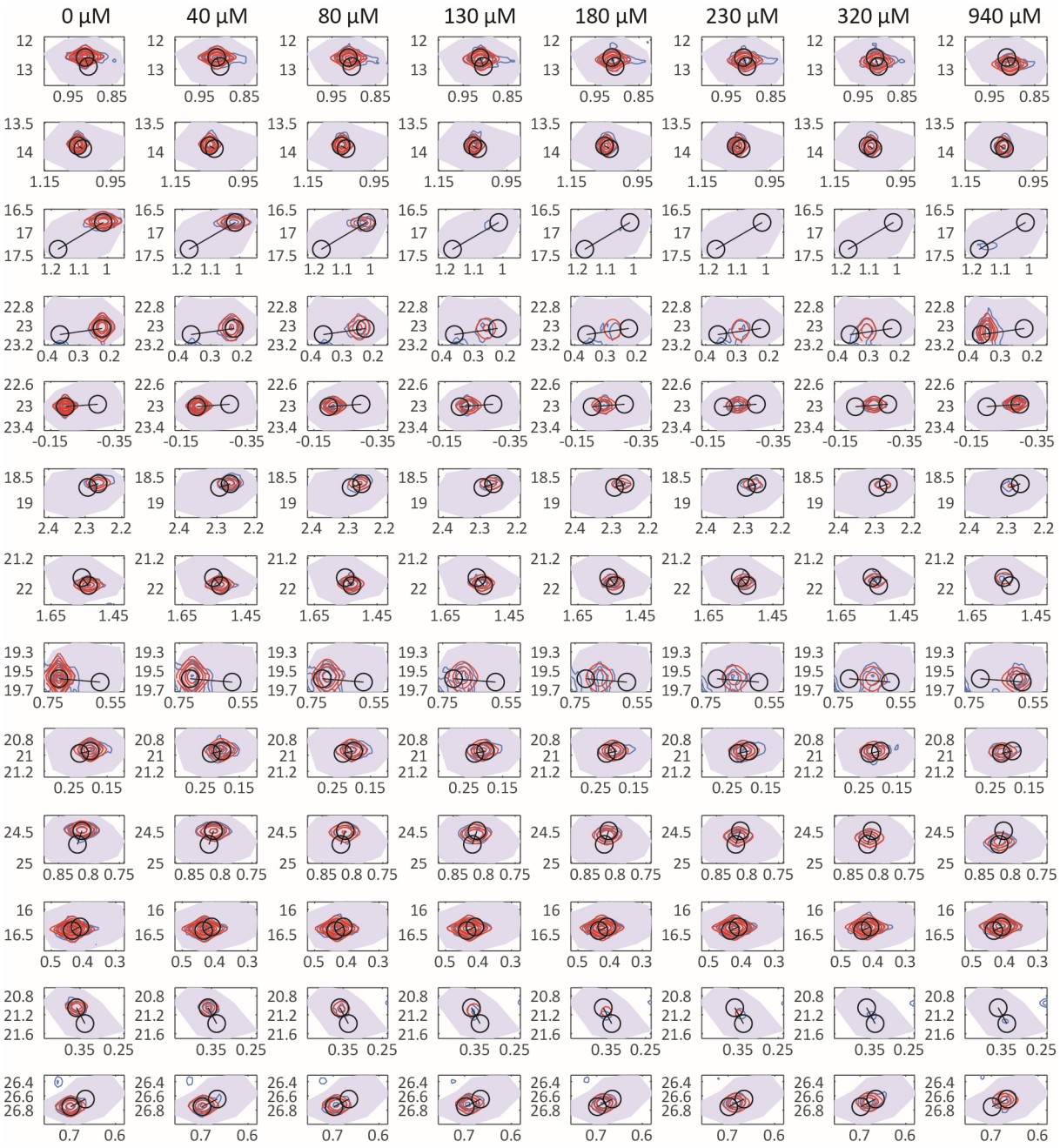


Fig. 26: Overlay of experimental (blue) and fitted (red) line shapes of the 3DD titration to UDP-Glc-saturated GTB. Each row corresponds to one fitted residue in the same order as in the following table.

Tab. 43: Line shape analysis results derived from the 3DD titration to UDP-Glc-saturated GTB.K_d is reported in units of µM. k_{off}, the transverse relaxation rates in the ^{1}H dimension (R2I), and the transverse relaxation rates in the ^{13}C dimension (R2S) are reported in units of s^{-1}. The chemical shifts (dI = ^{1}H; dS = ^{13}C) of the bound state (state 2) are reported in ppm.

Residue	Parameter	State	Fit result	Error
global	K_d		116.67	5.65
global	k_{off}		392.85	16.36

Residue	Parameter	State	Fit result	Error
Ile123	dI	2	0.90	0.00
Ile123	dS	2	12.91	0.01
Ile123	R2I	2	56.75	1.33
Ile123	R2S	2	112.62	4.28
Ile192	dI	2	1.04	0.00
Ile192	dS	2	13.95	0.01
Ile192	R2I	2	44.80	2.56
Ile192	R2S	2	77.64	3.87
Met214	dI	2	1.18	0.01
Met214	dS	2	17.38	0.01
Met214	R2I	2	222.46	12.46
Met214	R2S	2	44.60	16.12
Leu336	dI	2	0.36	0.00
Leu336	dS	2	23.10	0.00
Leu336	R2I	2	31.37	2.45
Leu336	R2S	2	48.65	5.36
Leu339	dI	2	-0.30	0.00
Leu339	dS	2	22.98	0.00
Leu339	R2I	2	56.52	2.98
Leu339	R2S	2	35.38	3.52
Met191	dI	2	2.29	0.00
Met191	dS	2	18.71	0.01
Met191	R2I	2	115.61	7.98
Met191	R2S	2	85.58	9.88
Ala268	dI	2	1.55	0.00
Ala268	dS	2	21.72	0.01
Ala268	R2I	2	111.01	4.92
Ala268	R2S	2	145.03	11.17
Val299	dI	2	0.58	0.00
Val299	dS	2	19.62	0.00
Val299	R2I	2	102.90	4.72
Val299	R2S	2	47.04	5.85
Leu134	dI	2	0.22	0.00
Leu134	dS	2	20.98	0.00
Leu134	R2I	2	91.33	4.46
Leu134	R2S	2	44.19	4.64
Leu130	dI	2	0.82	0.00
Leu130	dS	2	24.70	0.01
Leu130	R2I	2	47.52	3.86
Leu130	R2S	2	63.33	5.88
Ala254	dI	2	0.41	0.00
Ala254	dS	2	16.35	0.00
Ala254	R2I	2	72.74	1.48
Ala254	R2S	2	48.09	1.67
Val120	dI	2	0.33	0.00
Val120	dS	2	21.35	0.03

Residue	Parameter	State	Fit result	Error
Val120	R2I	2	93.56	9.27
Val120	R2S	2	209.47	29.11
Leu306	dI	2	0.67	0.00
Leu306	dS	2	26.64	0.01
Leu306	R2I	2	61.42	4.27
Leu306	R2S	2	61.33	6.20

Ligand titrations with GTA

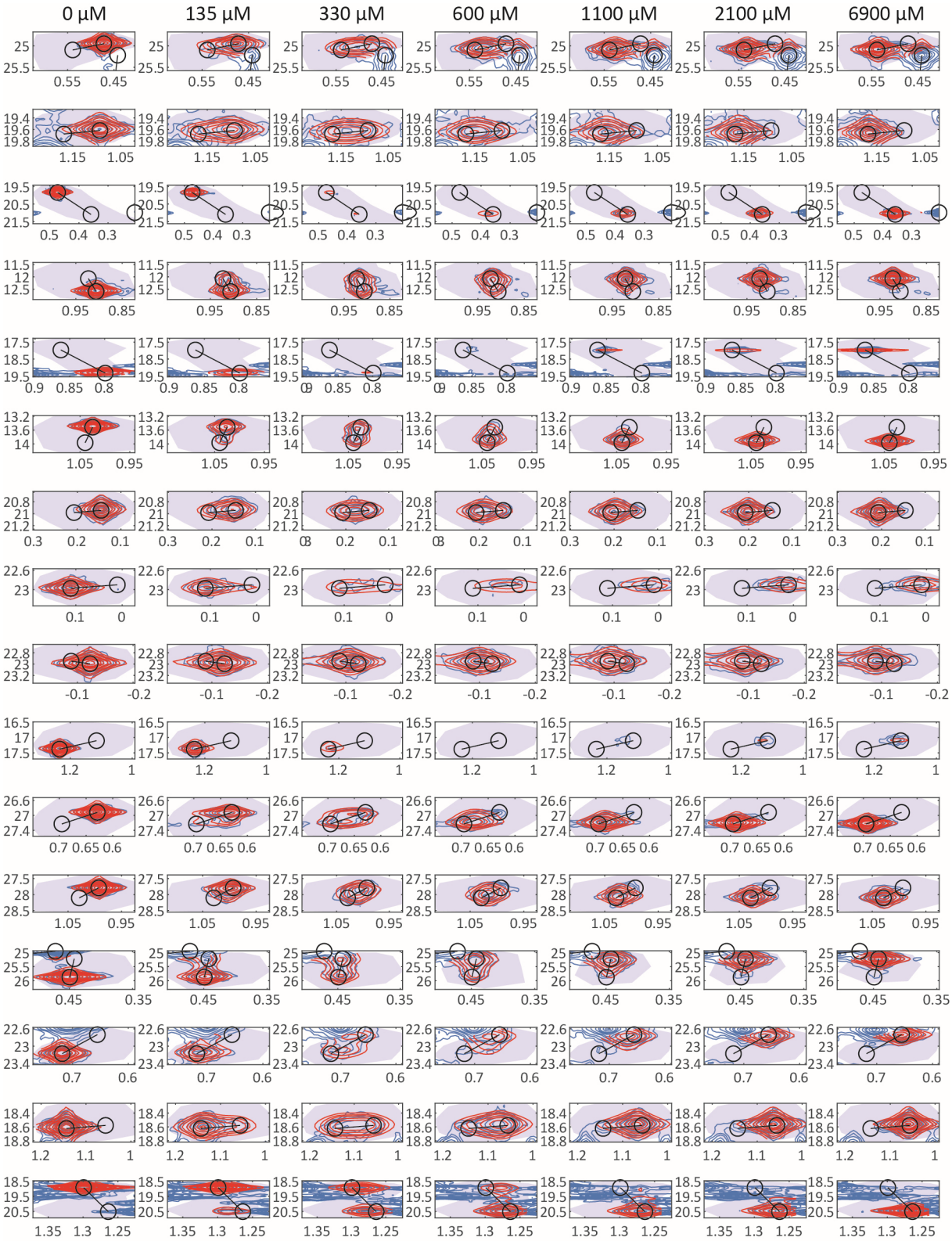


Fig. 27: Overlay of experimental (blue) and fitted (red) line shapes of the UDP-Gal titration to GTA. Each row corresponds to one fitted residue in the same order as in the following table.

Tab. 44: Line shape analysis results derived from the UDP-Gal titration to GTA.K_d is reported in units of µM. k_{off}, the transverse relaxation rates in the ^{1}H dimension (R2I), and the transverse relaxation rates in the ^{13}C dimension (R2S) are reported in units of s^{-1}. The chemical shifts (dI = ^{1}H; dS = ^{13}C) of the bound state (state 2) are reported in ppm.

Residue	Parameter	State	Fit result	Error
global	K_d		236.86	3.67
global	k_{off}		64.24	1.49
Leu118	dI	2	0.54	0.00
Leu118	dS	2	25.10	0.00
Leu118	R2I	2	49.32	1.36
Leu118	R2S	2	32.41	1.26
Ala122	dI	2	1.17	0.00
Ala122	dS	2	19.68	0.00
Ala122	R2I	2	59.03	1.50
Ala122	R2S	2	48.84	2.03
Val120	dI	2	0.36	0.00
Val120	dS	2	21.08	0.01
Val120	R2I	2	60.17	2.56
Val120	R2S	2	59.45	4.62
Ile123	dI	2	0.92	0.00
Ile123	dS	2	12.07	0.00
Ile123	R2I	2	36.69	0.93
Ile123	R2S	2	80.00	3.26
Val175	dI	2	0.87	0.01
Val175	dS	2	17.96	0.01
Val175	R2I	2	187.17	10.29
Val175	R2S	2	7.03	4.91
Ile192	dI	2	1.04	0.00
Ile192	dS	2	13.96	0.00
Ile192	R2I	2	49.78	2.08
Ile192	R2S	2	37.20	2.60
Leu134	dI	2	0.21	0.00
Leu134	dS	2	20.98	0.00
Leu134	R2I	2	48.30	1.81
Leu134	R2S	2	27.83	1.75
Leu336	dI	2	0.01	0.00
Leu336	dS	2	22.91	0.01
Leu336	R2I	2	116.48	5.91
Leu336	R2S	2	58.80	6.66
Leu339	dI	2	-0.09	0.00
Leu339	dS	2	22.95	0.00
Leu339	R2I	2	64.72	1.74
Leu339	R2S	2	46.10	1.66
Met214	dI	2	1.11	0.01
Met214	dS	2	17.11	0.01
Met214	R2I	2	202.62	13.41

Residue	Parameter	State	Fit result	Error
Met214	R2S	2	49.47	11.37
Leu306	dI	2	0.69	0.00
Leu306	dS	2	27.23	0.00
Leu306	R2I	2	36.58	0.97
Leu306	R2S	2	27.24	1.33
Leu324	dI	2	1.03	0.00
Leu324	dS	2	28.10	0.00
Leu324	R2I	2	47.27	1.44
Leu324	R2S	2	81.93	3.54
Leu207	dI	2	0.44	0.00
Leu207	dS	2	25.21	0.00
Leu207	R2I	2	38.27	0.95
Leu207	R2S	2	63.34	2.58
Leu266	dI	2	0.66	0.00
Leu266	dS	2	22.73	0.00
Leu266	R2I	2	56.96	1.81
Leu266	R2S	2	41.84	2.72
Ala228	dI	2	1.06	0.00
Ala228	dS	2	18.58	0.00
Ala228	R2I	2	46.28	0.91
Ala228	R2S	2	15.67	0.70

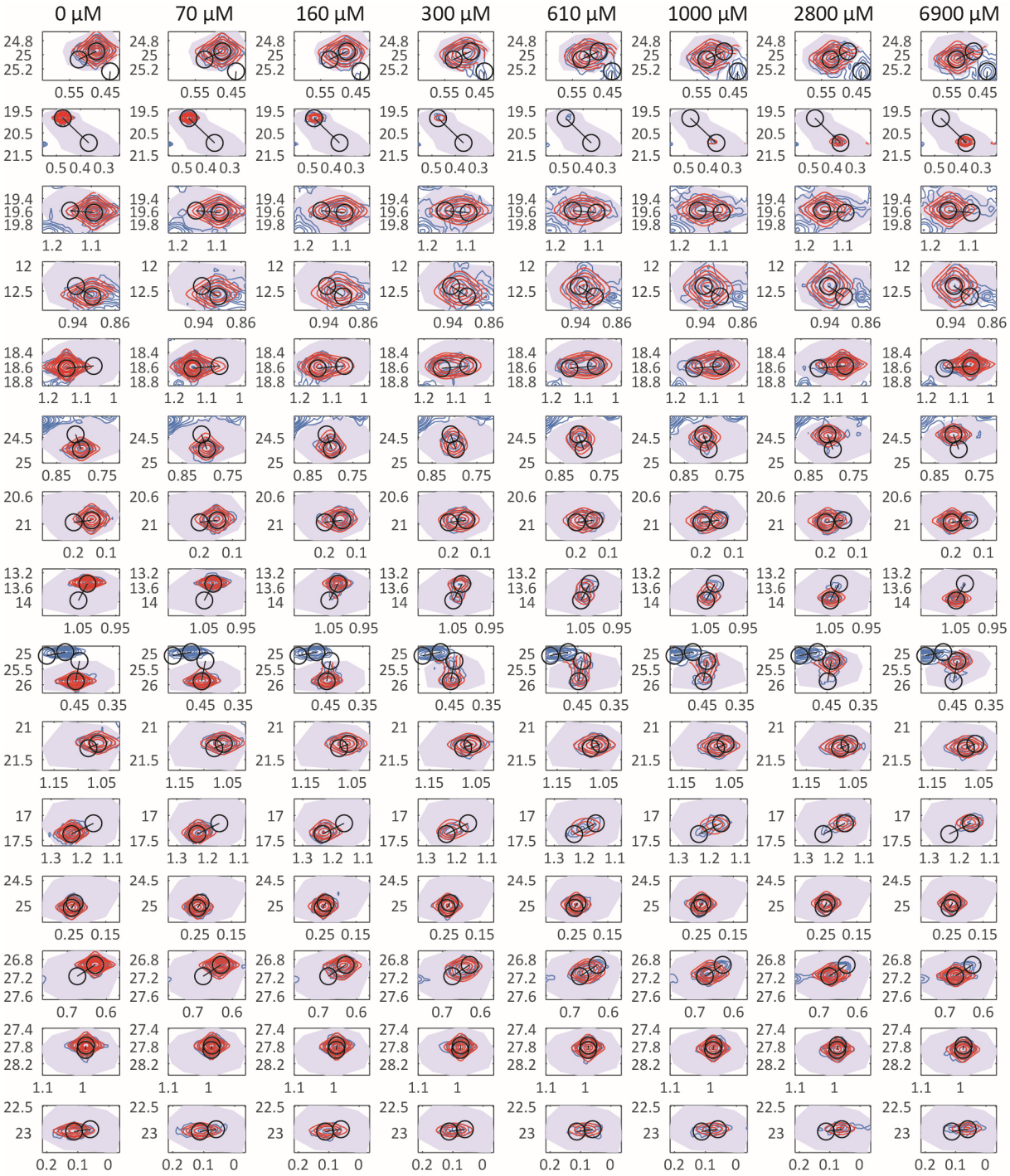


Fig. 28: Overlay of experimental (blue) and fitted (red) line shapes of the UDP-Glc titration to GTA. Each row corresponds to one fitted residue in the same order as in the following table.

Tab. 45: Line shape analysis results derived from the UDP-Glc titration to GTA.K_d is reported in units of µM. k_{off}, the transverse relaxation rates in the ^{1}H dimension (R2I), and the transverse relaxation rates in the ^{13}C dimension (R2S) are reported in units of s^{-1}. The chemical shifts (dI = ^{1}H; dS = ^{13}C) of the bound state (state 2) are reported in ppm.

Residue	Parameter	State	Fit result	Error
global	K_d		374.93	5.96
global	k_{off}		77.80	2.21
Leu118	dI	2	0.52	0.00
Leu118	dS	2	25.07	0.00
Leu118	R2I	2	79.13	1.87
Leu118	R2S	2	43.43	1.27
Val120	dI	2	0.36	0.00
Val120	dS	2	20.96	0.00
Val120	R2I	2	63.78	2.73
Val120	R2S	2	60.39	4.95
Ala122	dI	2	1.15	0.00
Ala122	dS	2	19.59	0.00
Ala122	R2I	2	102.04	2.68
Ala122	R2S	2	65.66	2.23
Ile123	dI	2	0.93	0.00
Ile123	dS	2	12.41	0.00
Ile123	R2I	2	56.13	1.52
Ile123	R2S	2	141.42	4.16
Ala128	dI	2	1.06	0.00
Ala128	dS	2	18.59	0.00
Ala128	R2I	2	57.51	0.90
Ala128	R2S	2	13.82	0.57
Leu130	dI	2	0.81	0.00
Leu130	dS	2	24.44	0.00
Leu130	R2I	2	52.91	1.69
Leu130	R2S	2	59.01	2.33
Leu134	dI	2	0.20	0.00
Leu134	dS	2	20.97	0.00
Leu134	R2I	2	69.64	2.08
Leu134	R2S	2	28.17	1.51
Ile192	dI	2	1.05	0.00
Ile192	dS	2	13.96	0.00
Ile192	R2I	2	47.98	2.03
Ile192	R2S	2	56.47	2.75
Val207	dI	2	0.44	0.00
Val207	dS	2	25.20	0.00
Val207	R2I	2	63.53	1.49
Val207	R2S	2	123.35	4.46
Val208	dI	2	1.08	0.00
Val208	dS	2	21.33	0.00
Val208	R2I	2	60.31	2.75

Residue	Parameter	State	Fit result	Error
Val208	R2S	2	39.74	2.42
Met214	dI	2	1.16	0.00
Met214	dS	2	17.16	0.01
Met214	R2I	2	88.47	3.65
Met214	R2S	2	69.04	4.74
Leu280	dI	2	0.24	0.00
Leu280	dS	2	24.95	0.00
Leu280	R2I	2	48.12	1.80
Leu280	R2S	2	50.07	2.27
Leu306	dI	2	0.67	0.00
Leu306	dS	2	27.17	0.00
Leu306	R2I	2	46.73	1.21
Leu306	R2S	2	38.98	1.66
Leu324	dI	2	0.99	0.00
Leu324	dS	2	27.88	0.00
Leu324	R2I	2	39.13	0.96
Leu324	R2S	2	60.25	1.69
Leu336	dI	2	0.06	0.00
Leu336	dS	2	22.94	0.01
Leu336	R2I	2	155.39	8.20
Leu336	R2S	2	54.23	3.74

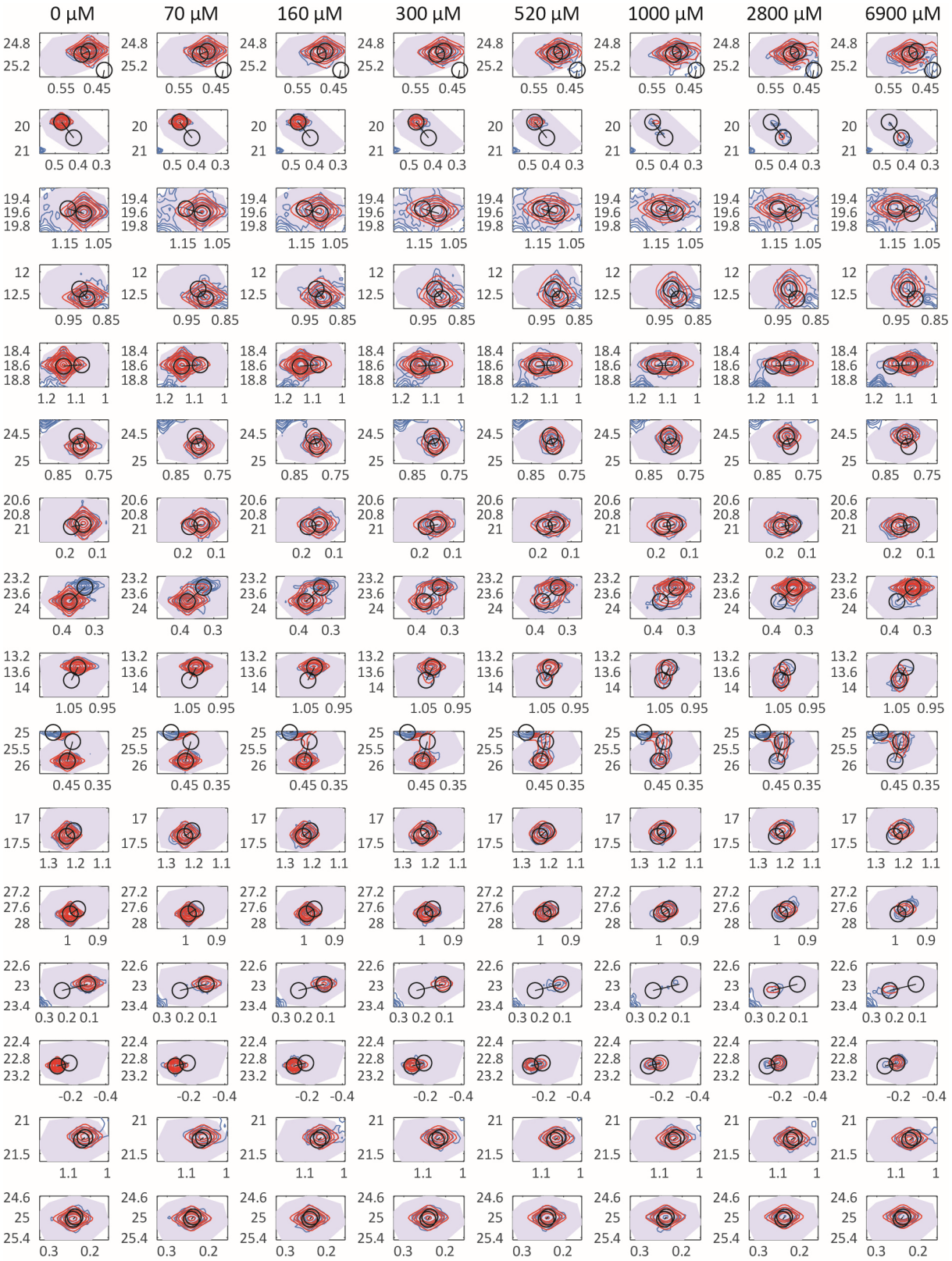


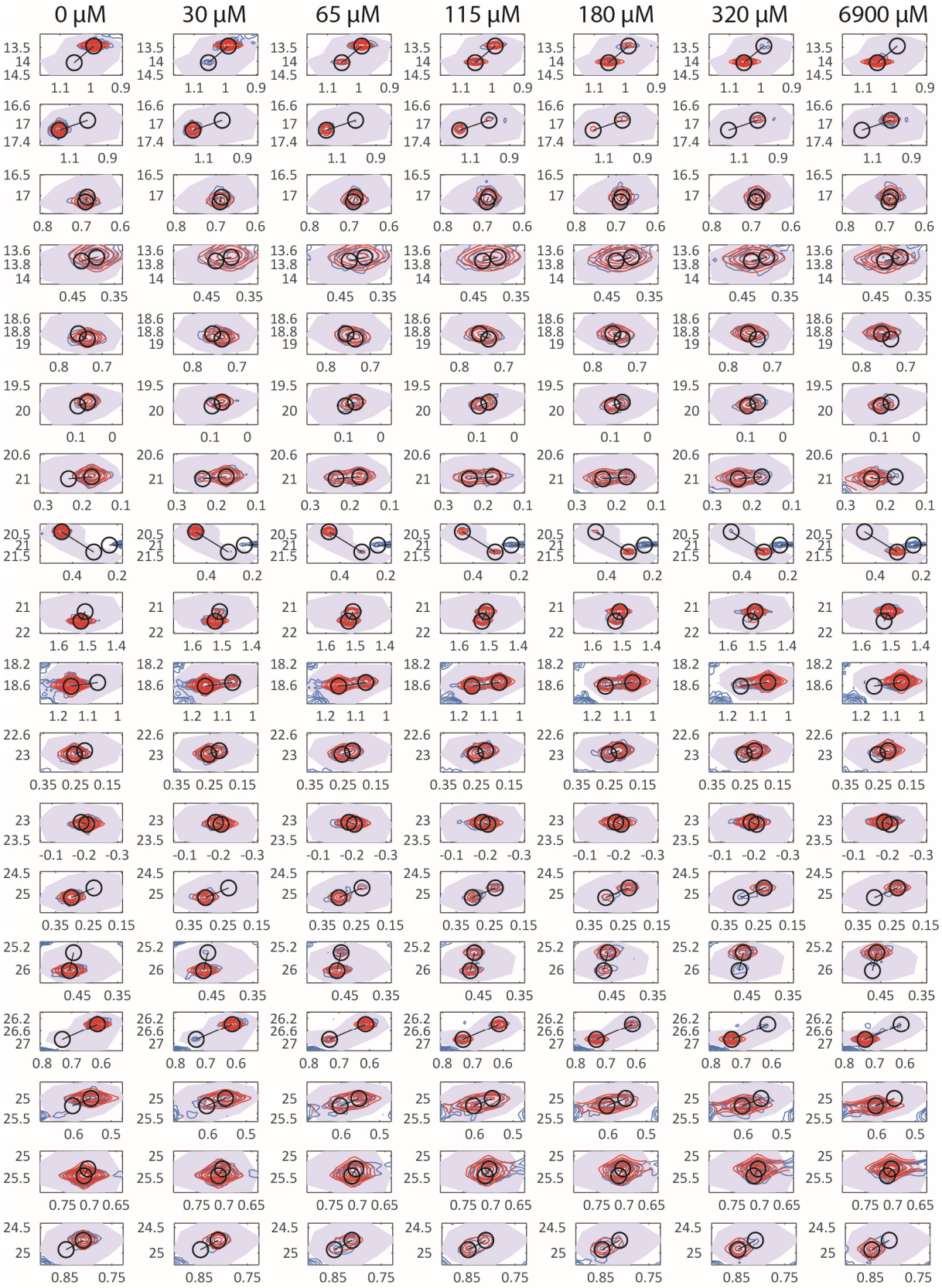
Fig. 29: Overlay of experimental (blue) and fitted (red) line shapes of the UDP-GlcNAc titration to GTA. Each row corresponds to one fitted residue in the same order as in the following table.

Tab. 46: Line shape analysis results derived from the UDP-GlcNAc titration to GTA.K_d is reported in units of µM. k_{off}, the transverse relaxation rates in the ^{1}H dimension (R2I), and the transverse relaxation rates in the ^{13}C dimension (R2S) are reported in units of s^{-1}. The chemical shifts (dI = ^{1}H; dS = ^{13}C) of the bound state (state 2) are reported in ppm.

Residue	Parameter	State	Fit result	Error
global	K_d		373.84	13.15
global	k_{off}		22.06	1.52
Leu118	dI	2	0.49	0.00
Leu118	dS	2	25.01	0.00
Leu118	R2I	2	62.54	2.25
Leu118	R2S	2	40.03	2.33
Val120	dI	2	0.42	0.00
Val120	dS	2	20.50	0.05
Val120	R2I	2	95.22	9.29
Val120	R2S	2	262.80	50.45
Ala122	dI	2	1.14	0.00
Ala122	dS	2	19.55	0.00
Ala122	R2I	2	93.30	3.24
Ala122	R2S	2	44.58	3.88
Ile123	dI	2	0.92	0.00
Ile123	dS	2	12.39	0.01
Ile123	R2I	2	71.89	3.10
Ile123	R2S	2	178.73	12.79
Ala128	dI	2	1.08	0.00
Ala128	dS	2	18.60	0.00
Ala128	R2I	2	85.07	2.95
Ala128	R2S	2	15.57	1.73
Leu130	dI	2	0.80	0.00
Leu130	dS	2	24.55	0.01
Leu130	R2I	2	47.19	3.10
Leu130	R2S	2	65.16	7.39
Leu134	dI	2	0.18	0.00
Leu134	dS	2	20.98	0.00
Leu134	R2I	2	82.20	4.11
Leu134	R2S	2	37.53	3.98
Leu173	dI	2	0.33	0.00
Leu173	dS	2	23.46	0.00
Leu173	R2I	2	41.64	1.12
Leu173	R2S	2	41.19	2.00
Ile192	dI	2	1.04	0.00
Ile192	dS	2	13.82	0.03
Ile192	R2I	2	49.71	4.01
Ile192	R2S	2	186.32	22.63
Leu207	dI	2	0.44	0.00
Leu207	dS	2	25.14	0.02
Leu207	R2I	2	52.22	2.36

Residue	Parameter	State	Fit result	Error
Leu207	R2S	2	179.98	13.99
Met214	dI	2	1.21	0.00
Met214	dS	2	17.26	0.01
Met214	R2I	2	90.72	5.25
Met214	R2S	2	82.16	11.06
Leu324	dI	2	0.97	0.00
Leu324	dS	2	27.66	0.01
Leu324	R2I	2	79.22	5.15
Leu324	R2S	2	100.33	10.91
Leu336	dI	2	0.23	0.01
Leu336	dS	2	23.11	0.02
Leu336	R2I	2	150.75	12.57
Leu336	R2S	2	63.07	16.69
Leu339	dI	2	-0.19	0.00
Leu339	dS	2	22.92	0.01
Leu339	R2I	2	101.91	7.43
Leu339	R2S	2	64.59	8.35
Val208	dI	2	1.07	0.00
Val208	dS	2	21.30	0.00
Val208	R2I	2	64.21	4.46
Val208	R2S	2	38.00	3.95
Leu280	dI	2	0.24	0.00
Leu280	dS	2	25.00	0.00
Leu280	R2I	2	55.80	2.69
Leu280	R2S	2	54.57	4.32

Ligand titrations with AAGlyB



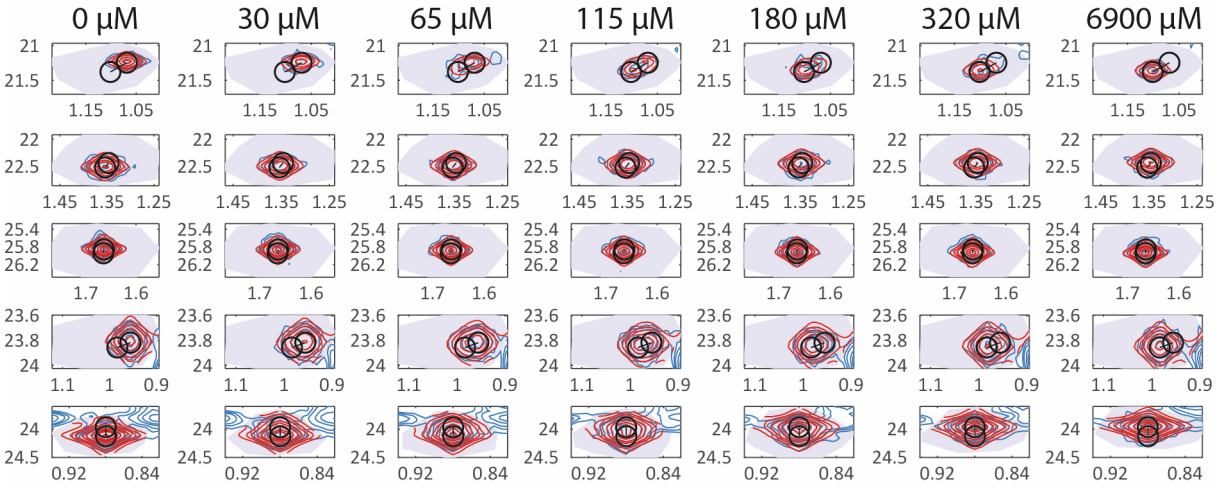


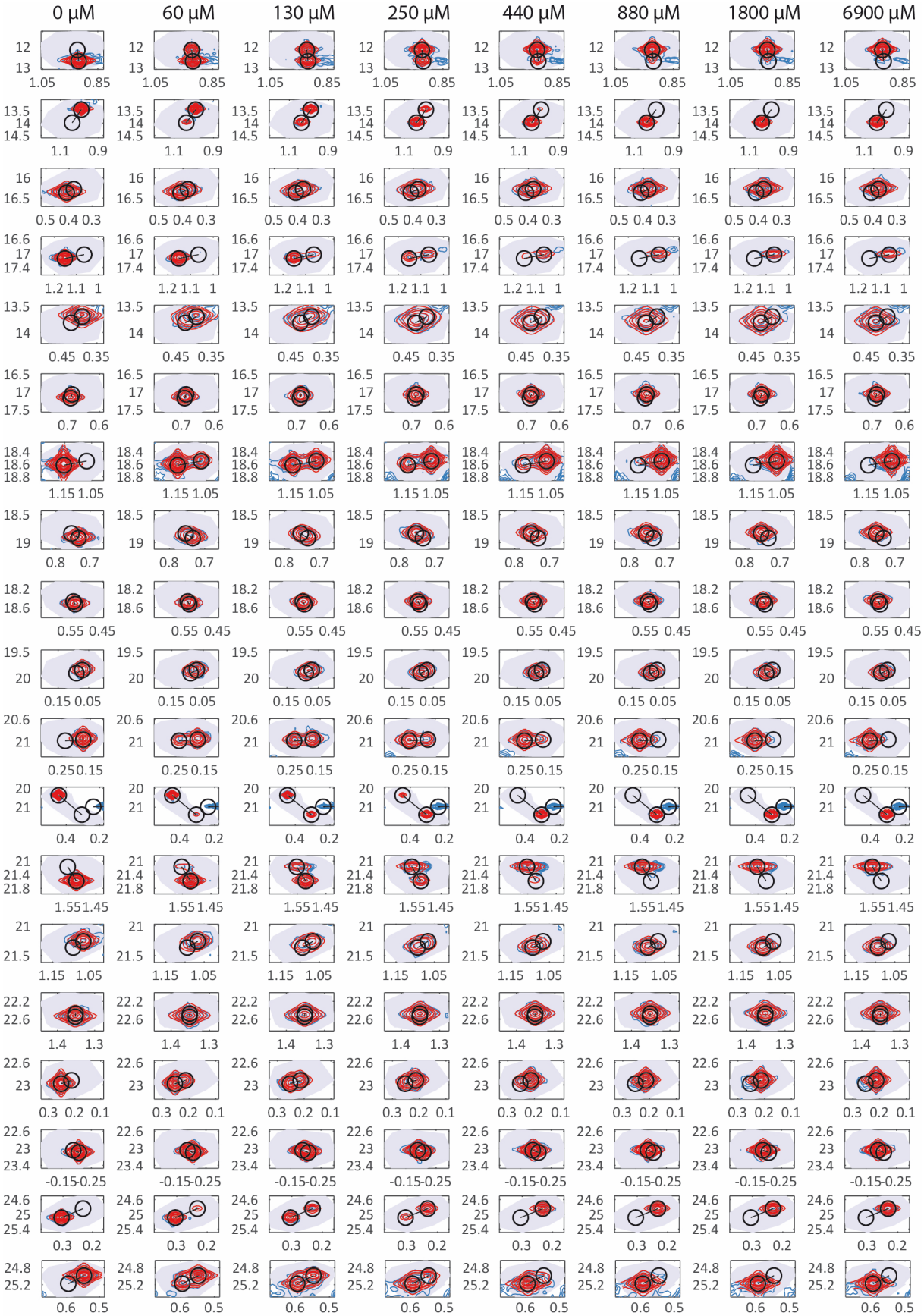
Fig. 30: Overlay of experimental (blue) and fitted (red) line shapes of the UDP titration to AAGlyB. Each row corresponds to one fitted residue in the same order as in the following table. This figure is spread over two pages.

Tab. 47: Line shape analysis results derived from the UDP titration to AAGlyB.K_d is reported in units of µM. k_{off}, the transverse relaxation rates in the ^{1}H dimension (R2I), and the transverse relaxation rates in the ^{13}C dimension (R2S) are reported in units of s^{-1}. The chemical shifts (dI = ^{1}H; dS = ^{13}C) of the bound state (state 2) are reported in ppm.

Residue	Parameter	State	Fit result	Error
global	K_d		37.26	1.09
global	k_{off}		6.77	0.41
Ile192	dI	2	1.05	0.00
Ile192	dS	2	14.05	0.00
Ile192	R2I	2	59.61	2.12
Ile192	R2S	2	37.08	2.31
Met214	dI	2	1.00	0.00
Met214	dS	2	16.93	0.01
Met214	R2I	2	127.60	7.35
Met214	R2S	2	22.43	3.54
Ile116	dI	2	0.69	0.00
Ile116	dS	2	17.04	0.00
Ile116	R2I	2	41.14	2.01
Ile116	R2S	2	74.89	5.00
Ile224	dI	2	0.43	0.00
Ile224	dS	2	13.75	0.00
Ile224	R2I	2	96.81	3.39
Ile224	R2S	2	47.00	2.74
Val204	dI	2	0.76	0.00
Val204	dS	2	18.84	0.00
Val204	R2I	2	54.86	3.11
Val204	R2S	2	26.65	2.53
Leu225	dI	2	0.09	0.00
Leu225	dS	2	19.91	0.00

Residue	Parameter	State	Fit result	Error
Leu225	R2I	2	52.09	3.69
Leu225	R2S	2	42.53	3.89
Leu134	dI	2	0.24	0.00
Leu134	dS	2	21.00	0.00
Leu134	R2I	2	63.69	2.73
Leu134	R2S	2	32.12	2.25
Val120	dI	2	0.30	0.00
Val120	dS	2	21.31	0.00
Val120	R2I	2	80.20	4.26
Val120	R2S	2	58.27	5.26
Ala268	dI	2	1.51	0.00
Ala268	dS	2	21.18	0.00
Ala268	R2I	2	51.36	1.69
Ala268	R2S	2	54.95	2.35
Ala128	dI	2	1.07	0.00
Ala128	dS	2	18.55	0.00
Ala128	R2I	2	48.73	1.00
Ala128	R2S	2	17.53	0.64
Leu336	dI	2	0.22	0.00
Leu336	dS	2	22.92	0.00
Leu336	R2I	2	53.92	1.98
Leu336	R2S	2	34.71	1.80
Leu339	dI	2	-0.19	0.00
Leu339	dS	2	23.05	0.00
Leu339	R2I	2	49.98	1.26
Leu339	R2S	2	29.71	1.34
Leu280	dI	2	0.23	0.00
Leu280	dS	2	24.85	0.01
Leu280	R2I	2	65.00	4.25
Leu280	R2S	2	48.32	4.34
Leu207	dI	2	0.46	0.00
Leu207	dS	2	25.39	0.01
Leu207	R2I	2	52.47	2.45
Leu207	R2S	2	99.09	7.24
Leu306	dI	2	0.73	0.00
Leu306	dS	2	26.87	0.00
Leu306	R2I	2	53.97	2.10
Leu306	R2S	2	40.26	2.45
Leu118	dI	2	0.60	0.00
Leu118	dS	2	25.19	0.00
Leu118	R2I	2	83.05	2.70
Leu118	R2S	2	45.92	2.01
Leu170	dI	2	0.70	0.00
Leu170	dS	2	25.29	0.00
Leu170	R2I	2	31.70	0.72

Residue	Parameter	State	Fit result	Error
Leu170	R2S	2	44.44	1.31
Leu130	dI	2	0.85	0.00
Leu130	dS	2	24.93	0.01
Leu130	R2I	2	36.11	2.52
Leu130	R2S	2	61.66	5.19
Val208	dI	2	1.10	0.00
Val208	dS	2	21.38	0.00
Val208	R2I	2	49.82	3.25
Val208	R2S	2	41.15	4.40
Val220	dI	2	1.35	0.00
Val220	dS	2	22.44	0.00
Val220	R2I	2	56.83	1.95
Val220	R2S	2	61.02	3.44
Val76	dI	2	1.66	0.00
Val76	dS	2	25.94	0.00
Val76	R2I	2	35.27	0.98
Val76	R2S	2	58.76	1.83
Val277	dI	2	0.98	0.00
Val277	dS	2	23.86	0.00
Val277	R2I	2	64.18	2.33
Val277	R2S	2	36.95	2.22
Leu201	dI	2	0.88	0.00
Leu201	dS	2	23.96	0.00
Leu201	R2I	2	34.56	0.66
Leu201	R2S	2	54.04	1.63


0 µM
60 µM
130 µM
250 µM
440 µM
880 µM
1800 µM
6900 µM

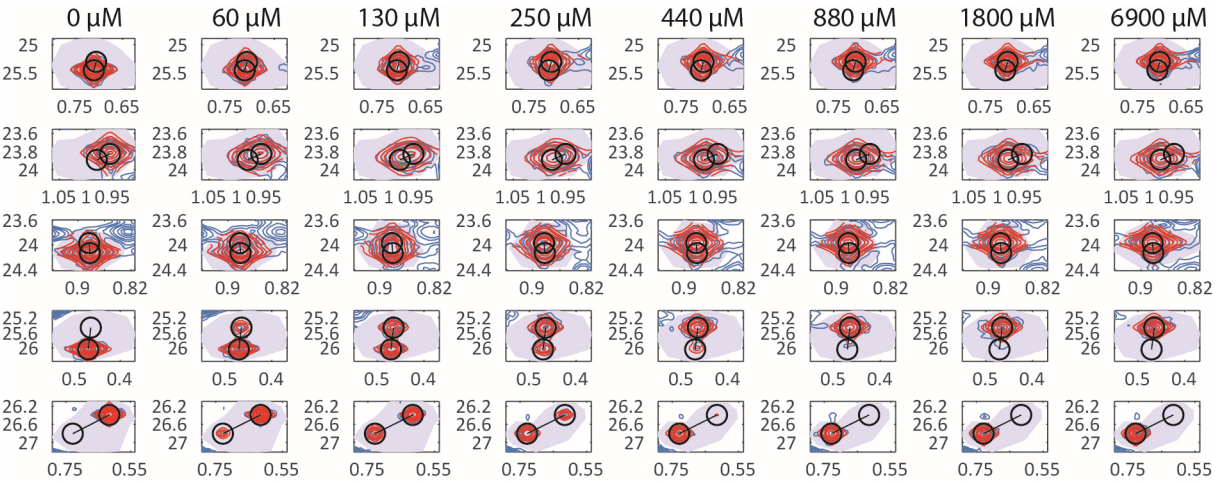


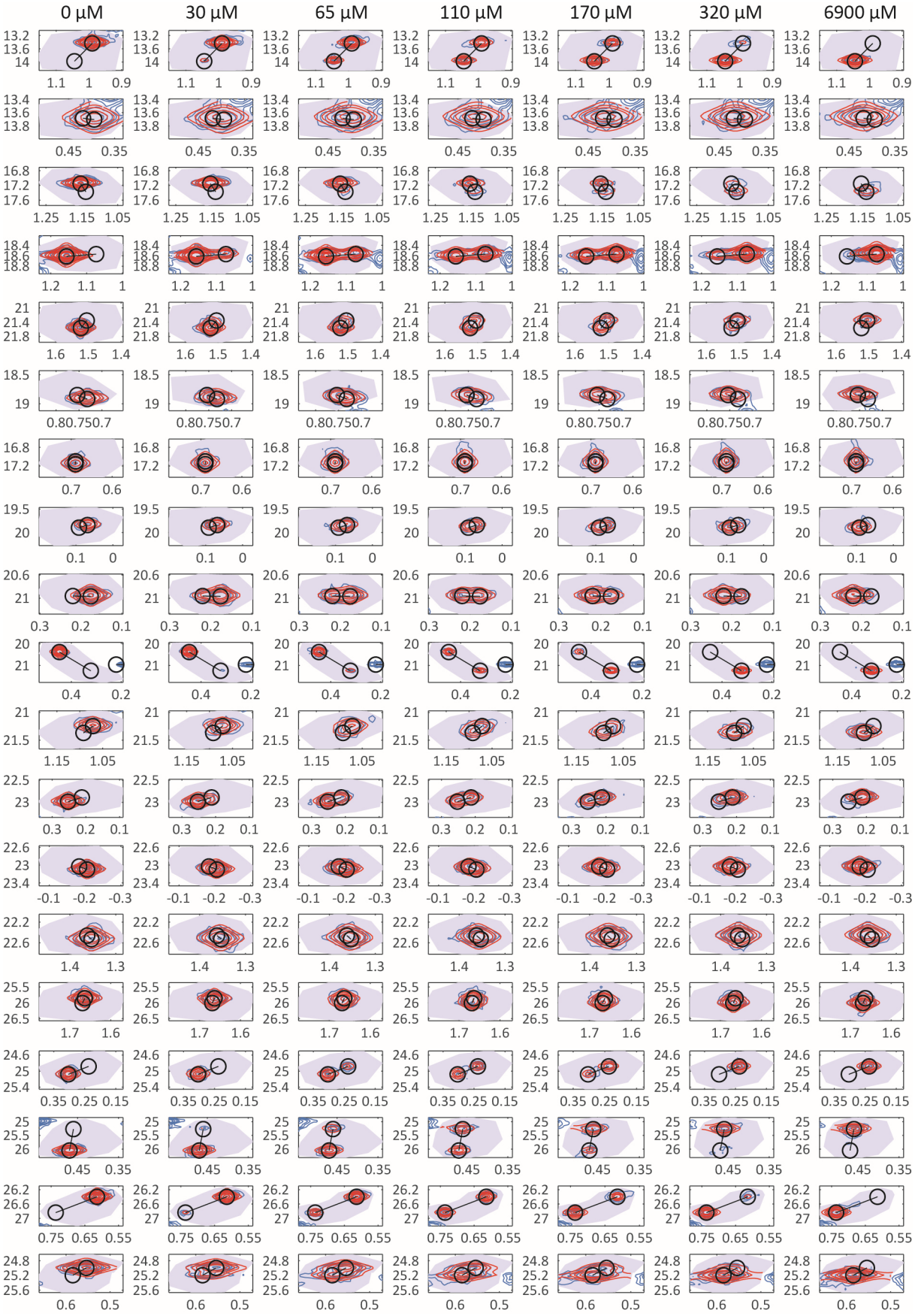
Fig. 31: Overlay of experimental (blue) and fitted (red) line shapes of the UDP-Gal titration to AAGlyB. Each row corresponds to one fitted residue in the same order as in the following table. This figure is spread over two pages.

Tab. 48: Line shape analysis results derived from the UDP-Gal titration to AAGlyB.K_d is reported in units of µM. k_{off}, the transverse relaxation rates in the ^{1}H dimension (R2I), and the transverse relaxation rates in the ^{13}C dimension (R2S) are reported in units of s^{-1}. The chemical shifts (dI = ^{1}H; dS = ^{13}C) of the bound state (state 2) are reported in ppm.

Residue	Parameter	State	Fit result	Error
global	K_d		64.14	1.06
global	k_{off}		5.30	0.23
Ile123	dI	2	0.92	0.00
Ile123	dS	2	12.15	0.00
Ile123	R2I	2	33.85	0.53
Ile123	R2S	2	78.95	1.54
Ile192	dI	2	1.04	0.00
Ile192	dS	2	13.99	0.00
Ile192	R2I	2	53.61	1.56
Ile192	R2S	2	41.19	1.80
Ala254	dI	2	0.38	0.00
Ala254	dS	2	16.28	0.00
Ala254	R2I	2	82.60	1.88
Ala254	R2S	2	40.36	1.05
Met214	dI	2	1.06	0.00
Met214	dS	2	17.04	0.00
Met214	R2I	2	120.03	5.05
Met214	R2S	2	38.32	3.59
Ile224	dI	2	0.43	0.00
Ile224	dS	2	13.81	0.00
Ile224	R2I	2	70.59	2.27
Ile224	R2S	2	62.12	2.45
Ile116	dI	2	0.69	0.00
Ile116	dS	2	17.07	0.00

Residue	Parameter	State	Fit result	Error
Ile116	R2I	2	37.06	1.10
Ile116	R2S	2	50.93	2.01
Ala128	dI	2	1.07	0.00
Ala128	dS	2	18.55	0.00
Ala128	R2I	2	37.89	0.56
Ala128	R2S	2	15.55	0.40
Val204	dI	2	0.75	0.00
Val204	dS	2	18.84	0.00
Val204	R2I	2	43.40	1.51
Val204	R2S	2	26.49	1.50
Val222	dI	2	0.54	0.00
Val222	dS	2	18.47	0.00
Val222	R2I	2	40.36	1.32
Val222	R2S	2	29.15	1.39
Leu225	dI	2	0.09	0.00
Leu225	dS	2	19.91	0.00
Leu225	R2I	2	52.04	2.47
Leu225	R2S	2	36.18	2.28
Leu134	dI	2	0.24	0.00
Leu134	dS	2	20.98	0.00
Leu134	R2I	2	47.07	1.41
Leu134	R2S	2	28.18	1.33
Val120	dI	2	0.31	0.00
Val120	dS	2	21.40	0.00
Val120	R2I	2	51.95	1.94
Val120	R2S	2	65.15	2.95
Ala268	dI	2	1.55	0.00
Ala268	dS	2	21.17	0.00
Ala268	R2I	2	101.43	2.75
Ala268	R2S	2	36.64	2.24
Val208	dI	2	1.09	0.00
Val208	dS	2	21.37	0.00
Val208	R2I	2	52.29	2.29
Val208	R2S	2	34.31	2.25
Val220	dI	2	1.35	0.00
Val220	dS	2	22.47	0.00
Val220	R2I	2	47.97	1.00
Val220	R2S	2	47.86	1.52
Leu336	dI	2	0.21	0.00
Leu336	dS	2	22.92	0.00
Leu336	R2I	2	43.04	0.84
Leu336	R2S	2	25.96	0.89
Leu339	dI	2	-0.19	0.00
Leu339	dS	2	23.05	0.00
Leu339	R2I	2	32.86	0.54

Residue	Parameter	State	Fit result	Error
Leu339	R2S	2	23.36	0.53
Leu280	dI	2	0.23	0.00
Leu280	dS	2	24.85	0.00
Leu280	R2I	2	46.46	2.13
Leu280	R2S	2	35.78	2.21
Leu118	dI	2	0.59	0.00
Leu118	dS	2	25.18	0.00
Leu118	R2I	2	45.50	0.96
Leu118	R2S	2	35.78	0.88
Leu170	dI	2	0.71	0.00
Leu170	dS	2	25.31	0.00
Leu170	R2I	2	28.03	0.45
Leu170	R2S	2	34.13	0.74
Val277	dI	2	0.98	0.00
Val277	dS	2	23.89	0.00
Val277	R2I	2	51.94	1.49
Val277	R2S	2	30.54	1.03
Leu201	dI	2	0.88	0.00
Leu201	dS	2	23.97	0.00
Leu201	R2I	2	26.75	0.44
Leu201	R2S	2	37.35	0.73
Leu207	dI	2	0.47	0.00
Leu207	dS	2	25.46	0.00
Leu207	R2I	2	40.53	1.10
Leu207	R2S	2	71.44	2.33
Leu306	dI	2	0.73	0.00
Leu306	dS	2	26.81	0.00
Leu306	R2I	2	36.98	1.01
Leu306	R2S	2	49.55	1.35


0 µM
30 µM
65 µM
110 µM
170 µM
320 µM
6900 µM

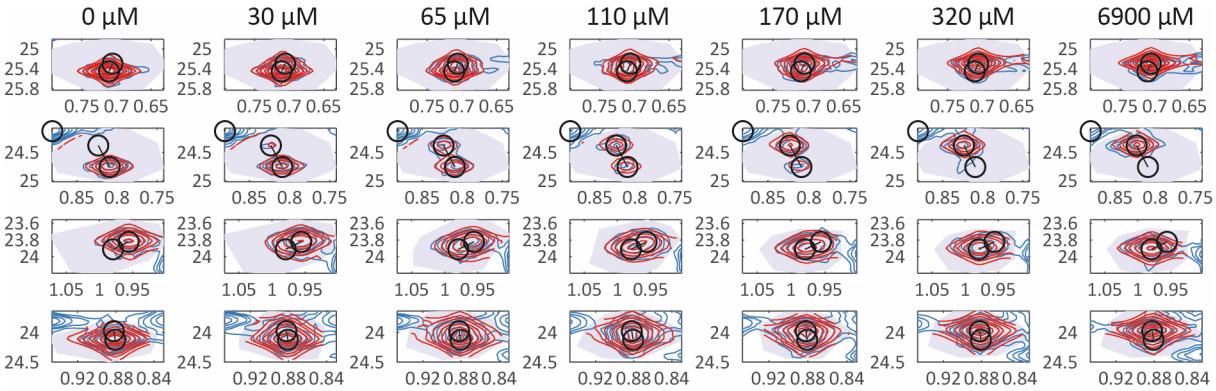


Fig. 32: Overlay of experimental (blue) and fitted (red) line shapes of the UDP-Glc titration to AAGlyB. Each row corresponds to one fitted residue in the same order as in the following table. This figure is spread over two pages.

Tab. 49: Line shape analysis results derived from the UDP-Glc titration to AAGlyB. K_d is reported in units of µM. k_{off}, the transverse relaxation rates in the ^{1}H dimension (R2I), and the transverse relaxation rates in the ^{13}C dimension (R2S) are reported in units of s^{-1}. The chemical shifts (dI = ^{1}H; dS = ^{13}C) of the bound state (state 2) are reported in ppm.

Residue	Parameter	State	Fit result	Error
global	K_d		38.82	1.40
global	k_{off}		0.86	0.34
Ile192	dI	2	1.04	0.00
Ile192	dS	2	13.98	0.00
Ile192	R2I	2	59.81	2.29
Ile192	R2S	2	38.57	2.30
Ile224	dI	2	0.42	0.00
Ile224	dS	2	13.69	0.00
Ile224	R2I	2	103.02	3.97
Ile224	R2S	2	55.87	2.42
Met214	dI	2	1.14	0.00
Met214	dS	2	17.37	0.01
Met214	R2I	2	101.83	6.88
Met214	R2S	2	77.46	8.21
Ala228	dI	2	1.07	0.00
Ala228	dS	2	18.57	0.00
Ala228	R2I	2	57.81	1.38
Ala228	R2S	2	19.53	0.88
Ala268	dI	2	1.51	0.00
Ala268	dS	2	21.35	0.00
Ala268	R2I	2	78.39	3.76
Ala268	R2S	2	66.02	6.03
Val204	dI	2	0.75	0.00
Val204	dS	2	18.85	0.00
Val204	R2I	2	59.71	3.18
Val204	R2S	2	28.96	2.47

Residue	Parameter	State	Fit result	Error
Ile116	dI	2	0.69	0.00
Ile116	dS	2	17.10	0.01
Ile116	R2I	2	35.66	2.06
Ile116	R2S	2	85.25	5.31
Leu225	dI	2	0.09	0.00
Leu225	dS	2	19.90	0.00
Leu225	R2I	2	48.99	3.56
Leu225	R2S	2	42.70	4.57
Leu134	dI	2	0.22	0.00
Leu134	dS	2	20.96	0.00
Leu134	R2I	2	58.93	2.27
Leu134	R2S	2	32.88	2.60
Val120	dI	2	0.32	0.00
Val120	dS	2	21.25	0.01
Val120	R2I	2	66.78	3.34
Val120	R2S	2	59.79	4.35
Val208	dI	2	1.09	0.00
Val208	dS	2	21.37	0.00
Val208	R2I	2	64.52	4.24
Val208	R2S	2	38.68	4.12
Leu336	dI	2	0.21	0.00
Leu336	dS	2	22.89	0.00
Leu336	R2I	2	60.68	2.45
Leu336	R2S	2	38.57	2.48
Leu339	dI	2	-0.18	0.00
Leu339	dS	2	23.03	0.00
Leu339	R2I	2	46.66	1.41
Leu339	R2S	2	33.78	1.82
Val220	dI	2	1.36	0.00
Val220	dS	2	22.46	0.00
Val220	R2I	2	59.29	2.27
Val220	R2S	2	55.23	3.12
Val76	dI	2	1.67	0.00
Val76	dS	2	26.01	0.00
Val76	R2I	2	35.74	1.20
Val76	R2S	2	62.52	2.89
Leu280	dI	2	0.24	0.00
Leu280	dS	2	24.88	0.00
Leu280	R2I	2	60.40	3.58
Leu280	R2S	2	43.39	3.50
Leu207	dI	2	0.46	0.00
Leu207	dS	2	25.25	0.01
Leu207	R2I	2	62.58	2.97
Leu207	R2S	2	77.67	4.56
Leu306	dI	2	0.74	0.00

Residue	Parameter	State	Fit result	Error
Leu306	dS	2	26.84	0.00
Leu306	R2I	2	50.07	1.97
Leu306	R2S	2	43.30	2.40
Leu118	dI	2	0.58	0.00
Leu118	dS	2	25.20	0.00
Leu118	R2I	2	85.92	2.51
Leu118	R2S	2	45.11	1.76
Leu170	dI	2	0.71	0.00
Leu170	dS	2	25.29	0.00
Leu170	R2I	2	33.87	0.86
Leu170	R2S	2	45.68	1.46
Leu130	dI	2	0.82	0.00
Leu130	dS	2	24.37	0.01
Leu130	R2I	2	38.43	2.75
Leu130	R2S	2	70.38	6.07
Val277	dI	2	0.98	0.00
Val277	dS	2	23.91	0.00
Val277	R2I	2	63.85	2.81
Val277	R2S	2	40.06	2.37
Leu201	dI	2	0.88	0.00
Leu201	dS	2	23.98	0.00
Leu201	R2I	2	35.94	0.77
Leu201	R2S	2	58.29	1.85

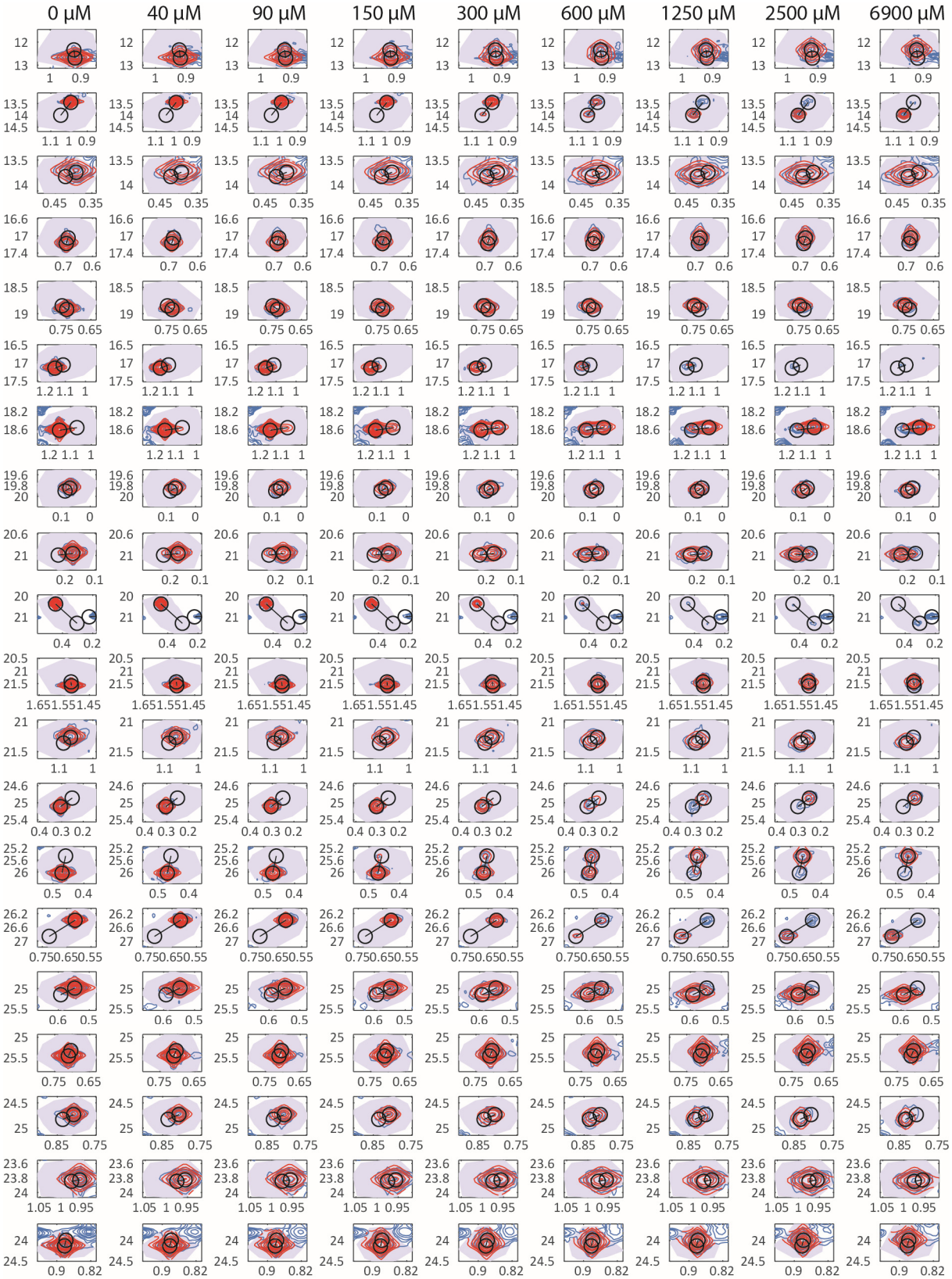


Fig. 33: Overlay of experimental (blue) and fitted (red) line shapes of the UDP-GlcNAc titration to AAGlyB. Each row corresponds to one fitted residue in the same order as in the following table.

Tab. 50: Line shape analysis results derived from the UDP-GlcNAc titration to AAGlyB.K_d is reported in units of µM. k_{off}, the transverse relaxation rates in the ^{1}H dimension (R2I), and the transverse relaxation rates in the ^{13}C dimension (R2S) are reported in units of s^{-1}. The chemical shifts (dI = ^{1}H; dS = ^{13}C) of the bound state (state 2) are reported in ppm.

Residue	Parameter	State	Fit result	Error
global	K_d		296.87	8.80
global	k_{off}		22.27	1.26
Ile123	dI	2	0.92	0.00
Ile123	dS	2	12.34	0.01
Ile123	R2I	2	70.74	2.27
Ile123	R2S	2	171.09	8.49
Ile192	dI	2	1.05	0.00
Ile192	dS	2	13.99	0.01
Ile192	R2I	2	86.14	5.20
Ile192	R2S	2	81.34	9.03
Ile224	dI	2	0.42	0.00
Ile224	dS	2	13.77	0.00
Ile224	R2I	2	96.57	4.28
Ile224	R2S	2	53.83	3.72
Ile116	dI	2	0.69	0.00
Ile116	dS	2	17.05	0.00
Ile116	R2I	2	38.30	2.23
Ile116	R2S	2	78.46	5.89
Val204	dI	2	0.75	0.00
Val204	dS	2	18.85	0.00
Val204	R2I	2	59.32	3.72
Val204	R2S	2	28.30	2.82
Met214	dI	2	1.11	0.01
Met214	dS	2	17.05	0.17
Met214	R2I	2	274.07	28.59
Met214	R2S	2	23.49	65.34
Ala128	dI	2	1.07	0.00
Ala128	dS	2	18.56	0.00
Ala128	R2I	2	82.78	2.82
Ala128	R2S	2	13.18	1.35
Leu225	dI	2	0.09	0.00
Leu225	dS	2	19.90	0.01
Leu225	R2I	2	58.93	5.09
Leu225	R2S	2	42.96	5.64
Leu134	dI	2	0.22	0.00
Leu134	dS	2	20.99	0.00
Leu134	R2I	2	79.00	4.07
Leu134	R2S	2	28.36	3.29
Val120	dI	2	0.30	0.01
Val120	dS	2	21.27	0.04
Val120	R2I	2	143.15	16.46

Residue	Parameter	State	Fit result	Error
Val120	R2S	2	79.52	28.95
Ala268	dI	2	1.52	0.00
Ala268	dS	2	21.43	0.01
Ala268	R2I	2	55.79	2.44
Ala268	R2S	2	115.19	6.26
Val208	dI	2	1.09	0.00
Val208	dS	2	21.36	0.01
Val208	R2I	2	68.58	5.76
Val208	R2S	2	57.52	8.27
Leu280	dI	2	0.25	0.00
Leu280	dS	2	24.90	0.01
Leu280	R2I	2	84.00	7.47
Leu280	R2S	2	80.27	10.46
Leu207	dI	2	0.46	0.00
Leu207	dS	2	25.45	0.01
Leu207	R2I	2	52.86	3.27
Leu207	R2S	2	128.93	11.74
Leu306	dI	2	0.72	0.00
Leu306	dS	2	26.86	0.01
Leu306	R2I	2	97.53	7.02
Leu306	R2S	2	54.59	7.78
Leu118	dI	2	0.59	0.00
Leu118	dS	2	25.15	0.00
Leu118	R2I	2	62.51	2.28
Leu118	R2S	2	43.85	2.60
Leu170	dI	2	0.70	0.00
Leu170	dS	2	25.32	0.00
Leu170	R2I	2	29.41	0.83
Leu170	R2S	2	56.05	2.15
Leu130	dI	2	0.84	0.00
Leu130	dS	2	24.83	0.01
Leu130	R2I	2	45.73	4.03
Leu130	R2S	2	95.93	10.73
Val277	dI	2	0.97	0.00
Val277	dS	2	23.85	0.00
Val277	R2I	2	63.88	2.85
Val277	R2S	2	35.57	2.66
Leu201	dI	2	0.88	0.00
Leu201	dS	2	23.99	0.00
Leu201	R2I	2	30.01	0.69
Leu201	R2S	2	65.08	1.68

Ligand titrations with GTB Trp[181]mutants

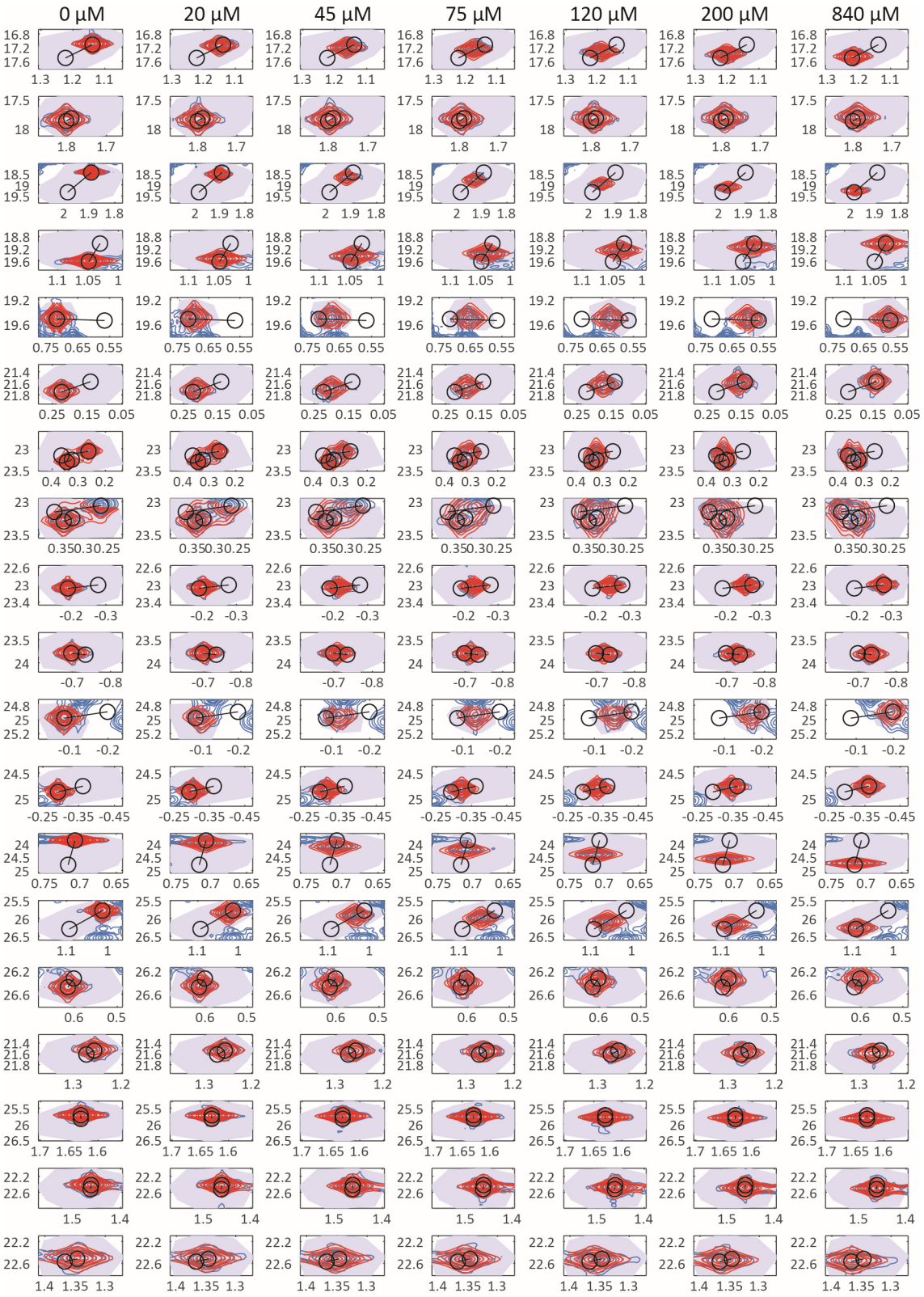


Fig. 34: Overlay of experimental (blue) and fitted (red) line shapes of the H-dis titration to GTB W181E. Each row corresponds to one fitted residue in the same order as in the following table.

Tab. 51: Line shape analysis results derived from the H-dis titration to GTB W181E.K_d is reported in units of µM. k_{off}, the transverse relaxation rates in the ^{1}H dimension (R2I), and the transverse relaxation rates in the ^{13}C dimension (R2S) are reported in units of s^{-1}. The chemical shifts (dI = ^{1}H; dS = ^{13}C) of the bound state (state 2) are reported in ppm. ILMV methyl-labeled protein was used in the titration. Some L/V pro-R methyl resonances (r) are not assigned. They are indicated by a question mark.

Residue	Parameter	State	Fit result	Error
global	K_d		35.02	0.50
global	koff		1291.26	32.67
Met214	dI	2	1.22	0.00
Met214	dS	2	17.50	0.00
Met214	R2I	2	55.69	1.53
Met214	R2S	2	41.24	2.25
Met189	dI	2	1.79	0.00
Met189	dS	2	17.82	0.00
Met189	R2I	2	49.47	1.40
Met189	R2S	2	33.38	1.64
Met266	dI	2	1.98	0.00
Met266	dS	2	19.31	0.01
Met266	R2I	2	94.85	3.85
Met266	R2S	2	62.68	5.46
Val?r	dI	2	1.03	0.00
Val?r	dS	2	19.04	0.00
Val?r	R2I	2	36.39	1.59
Val?r	R2S	2	59.02	3.35
Val299	dI	2	0.57	0.00
Val299	dS	2	19.54	0.00
Val299	R2I	2	60.45	1.98
Val299	R2S	2	29.61	1.98
Val?r	dI	2	0.14	0.00
Val?r	dS	2	21.58	0.00
Val?r	R2I	2	44.12	2.19
Val?r	R2S	2	35.60	2.61
Leu336	dI	2	0.36	0.00
Leu336	dS	2	23.22	0.00
Leu336	R2I	2	29.58	0.96
Leu336	R2S	2	83.93	2.93
Leu332	dI	2	0.33	0.00
Leu332	dS	2	23.18	0.00
Leu332	R2I	2	29.89	0.88
Leu332	R2S	2	92.96	3.18
Leu339	dI	2	-0.28	0.00
Leu339	dS	2	23.01	0.00
Leu339	R2I	2	33.33	1.23
Leu339	R2S	2	22.41	1.39
Leu336r	dI	2	-0.73	0.00

Residue	Parameter	State	Fit result	Error
Leu336r	dS	2	23.82	0.00
Leu336r	R2I	2	39.79	1.46
Leu336r	R2S	2	26.94	1.62
Leu339r	dI	2	-0.20	0.00
Leu339r	dS	2	24.89	0.00
Leu339r	R2I	2	46.85	2.13
Leu339r	R2S	2	43.86	3.17
Leu?r	dI	2	-0.36	0.00
Leu?r	dS	2	24.76	0.00
Leu?r	R2I	2	33.36	1.03
Leu?r	R2S	2	19.62	1.07
Leu329	dI	2	0.72	0.00
Leu329	dS	2	24.77	0.01
Leu329	R2I	2	62.64	3.17
Leu329	R2S	2	55.54	6.01
Leu324	dI	2	1.09	0.00
Leu324	dS	2	26.29	0.00
Leu324	R2I	2	53.36	2.12
Leu324	R2S	2	50.01	3.54
Leu306	dI	2	0.60	0.00
Leu306	dS	2	26.33	0.00
Leu306	R2I	2	35.38	1.41
Leu306	R2S	2	36.66	1.87
Val?r	dI	2	1.27	0.00
Val?r	dS	2	21.61	0.00
Val?r	R2I	2	44.63	2.36
Val?r	R2S	2	28.90	2.55
Leu76	dI	2	1.63	0.00
Leu76	dS	2	25.83	0.00
Leu76	R2I	2	29.77	0.75
Leu76	R2S	2	29.18	1.35
Leu76r	dI	2	1.46	0.00
Leu76r	dS	2	22.52	0.00
Leu76r	R2I	2	36.92	0.86
Leu76r	R2S	2	29.77	1.04
Val220	dI	2	1.37	0.00
Val220	dS	2	22.56	0.00
Val220	R2I	2	55.32	1.79
Val220	R2S	2	35.45	2.05

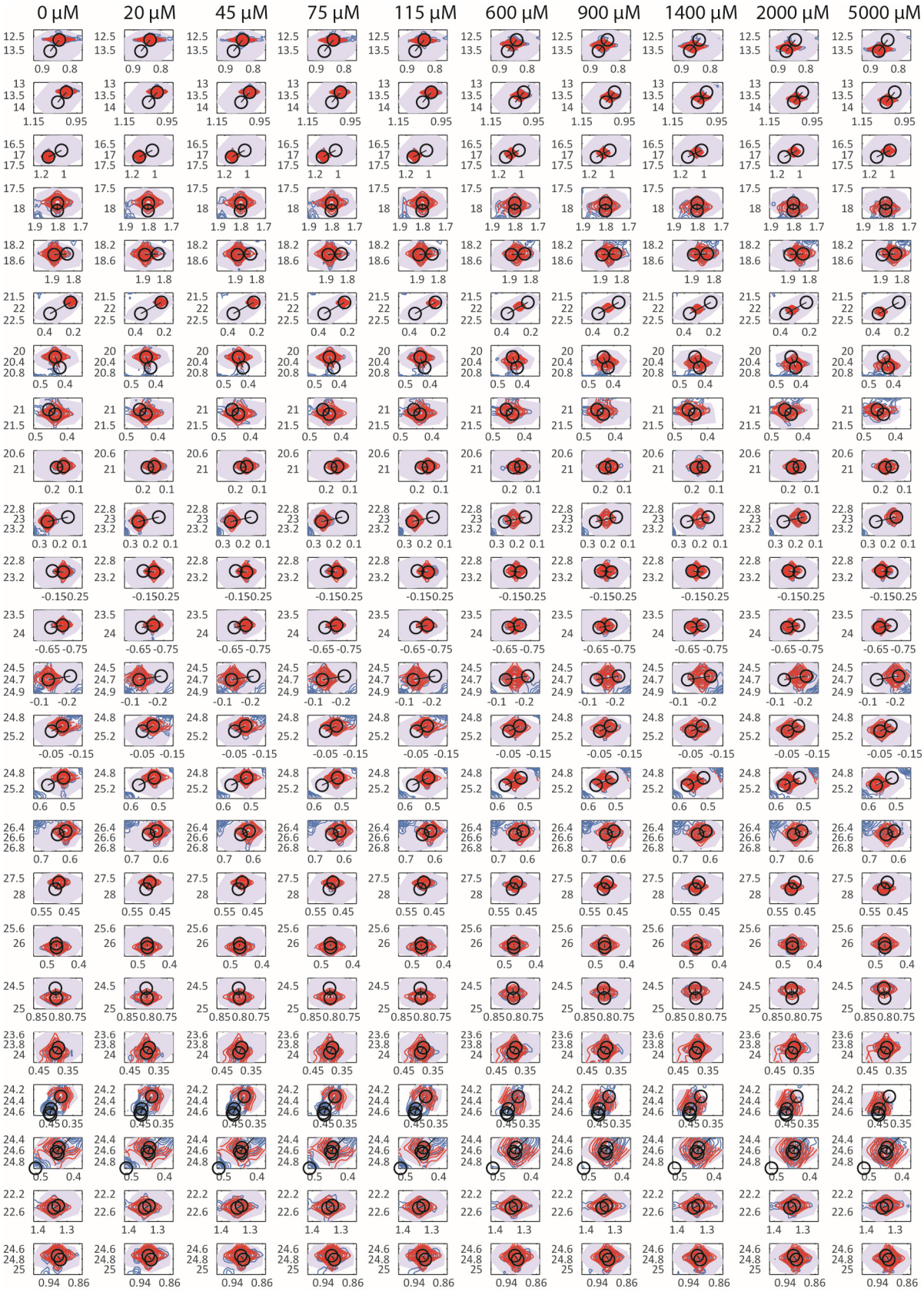


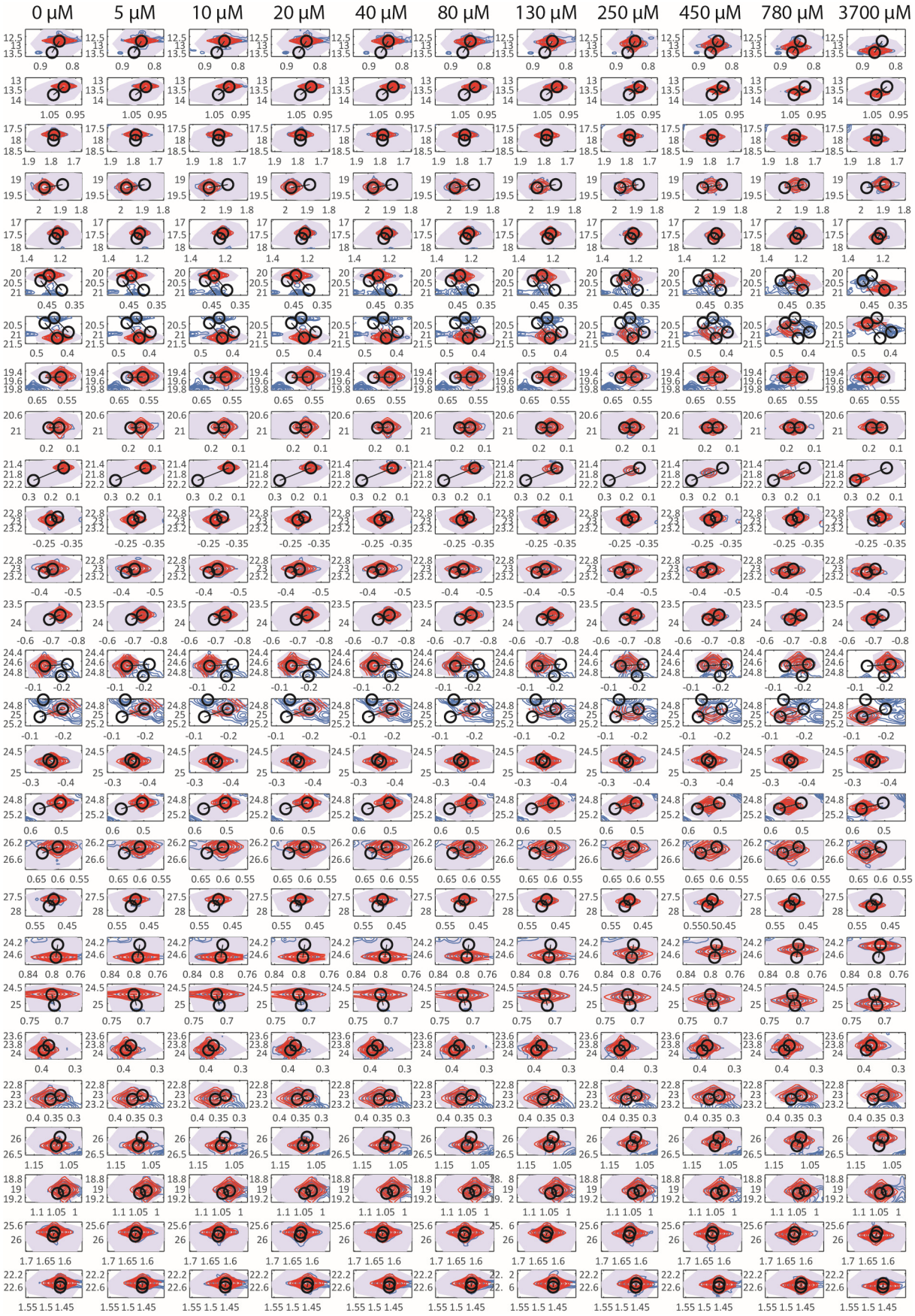
Fig. 35: Overlay of experimental (blue) and fitted (red) line shapes of the UDP titration to GTB W181E. Each row corresponds to one fitted residue in the same order as in the following table.

Tab. 52: Line shape analysis results derived from the UDP titration to GTB W181E. K_d is reported in units of µM. k_{off}, the transverse relaxation rates in the ^{1}H dimension (R2I), and the transverse relaxation rates in the ^{13}C dimension (R2S) are reported in units of s^{-1}. The chemical shifts (dI = ^{1}H; dS = ^{13}C) of the bound state (state 2) are reported in ppm. ILMV methyl-labeled protein was used in the titration. Some L/V pro-R methyl resonances (r) are not assigned. They are indicated by a question mark.

Residue	Parameter	State	Fit result	Error
global	K_d		738.00	6.33
global	k_{off}		1704.01	71.71
Ile123	dI	2	0.87	0.00
Ile123	dS	2	13.56	0.00
Ile123	R2I	2	33.67	0.76
Ile123	R2S	2	68.98	2.40
Ile192	dI	2	1.04	0.00
Ile192	dS	2	13.78	0.00
Ile192	R2I	2	37.63	1.11
Ile192	R2S	2	35.66	1.83
Met214	dI	2	1.02	0.00
Met214	dS	2	16.82	0.00
Met214	R2I	2	74.12	2.32
Met214	R2S	2	48.99	2.50
Met189	dI	2	1.81	0.00
Met189	dS	2	18.06	0.00
Met189	R2I	2	60.11	1.47
Met189	R2S	2	45.70	1.59
Met266	dI	2	1.83	0.00
Met266	dS	2	18.43	0.00
Met266	R2I	2	44.70	0.90
Met266	R2S	2	35.64	0.95
Val?r	dI	2	0.36	0.00
Val?r	dS	2	22.22	0.01
Val?r	R2I	2	56.72	3.91
Val?r	R2S	2	41.79	4.57
Val120	dI	2	0.42	0.00
Val120	dS	2	20.61	0.00
Val120	R2I	2	38.00	0.98
Val120	R2S	2	56.20	2.04
Val120r	dI	2	0.46	0.00
Val120r	dS	2	21.00	0.00
Val120r	R2I	2	40.24	0.93
Val120r	R2S	2	52.92	1.62
Leu134	dI	2	0.18	0.00
Leu134	dS	2	20.97	0.00
Leu134	R2I	2	42.11	1.61
Leu134	R2S	2	27.02	1.92
Leu336	dI	2	0.16	0.00
Leu336	dS	2	22.97	0.00

Residue	Parameter	State	Fit result	Error
Leu336	R2I	2	52.93	3.04
Leu336	R2S	2	33.41	3.53
Leu339	dI	2	-0.14	0.00
Leu339	dS	2	23.06	0.00
Leu339	R2I	2	32.49	1.07
Leu339r	R2S	2	21.46	1.26
Leu339r	dI	2	-0.64	0.00
Leu339r	dS	2	23.85	0.00
Leu339r	R2I	2	40.72	1.53
Leu339r	R2S	2	32.45	1.86
Leu?r	dI	2	-0.21	0.00
Leu?r	dS	2	24.64	0.00
Leu?r	R2I	2	37.27	1.07
Leu?r	R2S	2	28.79	1.16
Leu330r	dI	2	-0.05	0.00
Leu330r	dS	2	25.09	0.00
Leu330r	R2I	2	38.33	1.50
Leu330r	R2S	2	29.06	1.66
Leu118	dI	2	0.57	0.00
Leu118	dS	2	25.11	0.00
Leu118	R2I	2	28.87	1.08
Leu118	R2S	2	27.61	1.50
Leu306	dI	2	0.64	0.00
Leu306	dS	2	26.54	0.00
Leu306	R2I	2	37.79	1.34
Leu306	R2S	2	36.78	1.80
Leu?r	dI	2	0.50	0.00
Leu?r	dS	2	27.84	0.00
Leu?r	R2I	2	37.43	1.73
Leu?r	R2S	2	32.22	2.50
Leu207	dI	2	0.47	0.00
Leu207	dS	2	26.02	0.00
Leu207	R2I	2	33.69	1.14
Leu207	R2S	2	39.25	2.06
Leu130	dI	2	0.80	0.00
Leu130	dS	2	24.56	0.00
Leu130	R2I	2	32.51	1.53
Leu130	R2S	2	36.04	2.79
Leu173	dI	2	0.39	0.00
Leu173	dS	2	23.87	0.00
Leu173	R2I	2	30.71	0.78
Leu173	R2S	2	24.35	1.00
Leu207r	dI	2	0.46	0.00
Leu207r	dS	2	24.67	0.00
Leu207r	R2I	2	26.22	0.57

Residue	Parameter	State	Fit result	Error
Leu207r	R2S	2	50.52	1.52
Leu?r	dI	2	0.44	0.00
Leu?r	dS	2	24.60	0.00
Leu?r	R2I	2	19.96	0.51
Leu?r	R2S	2	66.80	1.45
Val220	dI	2	1.33	0.00
Val220	dS	2	22.47	0.00
Val220	R2I	2	53.20	2.03
Val220	R2S	2	29.65	1.87
Leu?r	dI	2	0.91	0.00
Leu?r	dS	2	24.81	0.00
Leu?r	R2I	2	18.36	0.45
Leu?r	R2S	2	26.06	0.79


0 µM
5 µM
10 µM
20 µM
40 µM
80 µM
130 µM
250 µM
450 µM
780 µM
3700 µM

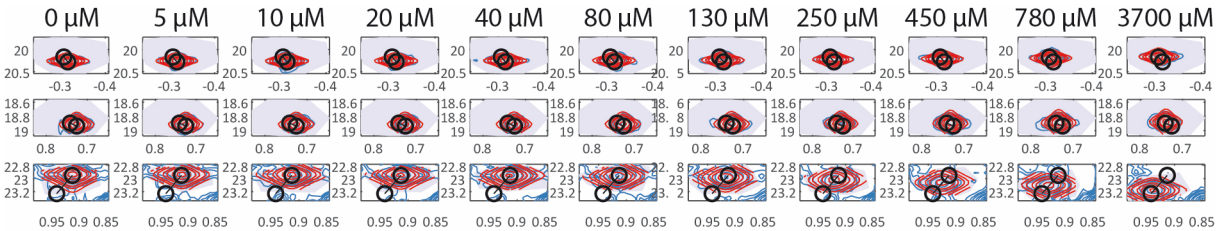


Fig. 36: Overlay of experimental (blue) and fitted (red) line shapes of the UDP titration to H-dis-saturated GTB W181E. Each row corresponds to one fitted residue in the same order as in the following table. This figure is spread over two pages.

Tab. 53: Line shape analysis results derived from the UDP titration to H-dis-saturated GTB W181E.K_d is reported in units of µM. k_{off}, the transverse relaxation rates in the ^{1}H dimension (R2I), and the transverse relaxation rates in the ^{13}C dimension (R2S) are reported in units of s^{-1}. The chemical shifts (dI = ^{1}H; dS = ^{13}C) of the bound state (state 2) are reported in ppm. ILMV methyl-labeled protein was used in the titration. Some L/V pro-R methyl resonances (r) are not assigned. They are indicated by a question mark.

Residue	Parameter	State	Fit result	Error
global	K_d		498.91	3.64
global	k_{off}		647.42	11.76
Ile123	dI	2	0.86	0.00
Ile123	dS	2	13.49	0.00
Ile123	R2I	2	37.09	1.04
Ile123	R2S	2	53.47	2.71
Ile192	dI	2	1.04	0.00
Ile192	dS	2	13.78	0.00
Ile192	R2I	2	45.04	1.63
Ile192	R2S	2	35.64	2.30
Met189	dI	2	1.79	0.00
Met189	dS	2	18.05	0.00
Met189	R2I	2	56.94	1.55
Met189	R2S	2	36.70	1.83
Met266	dI	2	1.89	0.00
Met266	dS	2	19.19	0.00
Met266	R2I	2	64.77	2.82
Met266	R2S	2	53.50	4.52
Met214	dI	2	1.23	0.00
Met214	dS	2	17.68	0.00
Met214	R2I	2	70.24	2.33
Met214	R2S	2	77.02	3.71
Val120	dI	2	0.40	0.00
Val120	dS	2	20.93	0.00
Val120	R2I	2	44.19	1.26
Val120	R2S	2	52.86	2.74
Val120r	dI	2	0.47	0.00
Val120r	dS	2	20.45	0.00

Residue	Parameter	State	Fit result	Error
Val120r	R2I	2	42.31	1.23
Val120r	R2S	2	65.95	3.25
Val299	dI	2	0.63	0.00
Val299	dS	2	19.55	0.00
Val299	R2I	2	41.47	1.43
Val299	R2S	2	28.87	1.86
Leu134	dI	2	0.19	0.00
Leu134	dS	2	20.95	0.00
Leu134	R2I	2	50.34	1.80
Leu134	R2S	2	24.31	2.01
Val?r	dI	2	0.28	0.00
Val?r	dS	2	22.08	0.00
Val?r	R2I	2	56.22	3.24
Val?r	R2S	2	37.86	4.80
Leu339	dI	2	-0.30	0.00
Leu339	dS	2	22.93	0.00
Leu339	R2I	2	29.80	0.93
Leu339	R2S	2	23.50	1.21
Leu319r	dI	2	-0.41	0.00
Leu319r	dS	2	23.13	0.00
Leu319r	R2I	2	50.68	2.27
Leu319r	R2S	2	33.03	2.56
Leu336r	dI	2	-0.69	0.00
Leu336r	dS	2	23.94	0.00
Leu336r	R2I	2	37.84	1.29
Leu336r	R2S	2	23.78	1.62
Leu?r	dI	2	-0.22	0.00
Leu?r	dS	2	24.67	0.00
Leu?r	R2I	2	37.74	1.21
Leu?r	R2S	2	33.42	1.64
Leu330r	dI	2	-0.13	0.00
Leu330r	dS	2	25.07	0.00
Leu330r	R2I	2	71.73	2.72
Leu330r	R2S	2	51.79	4.16
Leu339r	dI	2	-0.35	0.00
Leu339r	dS	2	24.71	0.00
Leu339r	R2I	2	28.32	0.88
Leu339r	R2S	2	18.85	1.12
Leu118	dI	2	0.57	0.00
Leu118	dS	2	25.08	0.00
Leu118	R2I	2	32.23	1.17
Leu118	R2S	2	20.74	1.59
Leu306	dI	2	0.64	0.00
Leu306	dS	2	26.48	0.00
Leu306	R2I	2	38.46	1.49

Residue	Parameter	State	Fit result	Error
Leu306	R2S	2	50.26	2.75
Leu?r	dI	2	0.51	0.00
Leu?r	dS	2	27.85	0.00
Leu?r	R2I	2	39.64	1.83
Leu?r	R2S	2	29.74	2.51
Leu130	dI	2	0.79	0.00
Leu130	dS	2	24.32	0.00
Leu130	R2I	2	44.76	2.77
Leu130	R2S	2	50.32	5.36
Leu329	dI	2	0.71	0.00
Leu329	dS	2	25.06	0.01
Leu329	R2I	2	41.74	3.15
Leu329	R2S	2	64.09	5.42
Leu173	dI	2	0.38	0.00
Leu173	dS	2	23.84	0.00
Leu173	R2I	2	27.41	0.74
Leu173	R2S	2	23.54	1.28
Leu336	dI	2	0.33	0.00
Leu336	dS	2	23.04	0.00
Leu336	R2I	2	41.60	1.67
Leu336	R2S	2	32.59	1.99
Leu324	dI	2	1.08	0.00
Leu324	dS	2	25.98	0.00
Leu324	R2I	2	41.06	1.80
Leu324	R2S	2	57.59	3.82
Val?r	dI	2	1.05	0.00
Val?r	dS	2	19.11	0.00
Val?r	R2I	2	30.89	1.14
Val?r	R2S	2	34.56	1.64
Val76	dI	2	1.63	0.00
Val76	dS	2	25.92	0.00
Val76	R2I	2	27.46	0.67
Val76	R2S	2	28.59	1.25
Val76r	dI	2	1.46	0.00
Val76r	dS	2	22.62	0.00
Val76r	R2I	2	36.45	0.79
Val76r	R2S	2	27.33	1.12
Leu319	dI	2	-0.31	0.00
Leu319	dS	2	20.17	0.00
Leu319	R2I	2	42.74	2.02
Leu319	R2S	2	33.13	2.46
Val204	dI	2	0.74	0.00
Val204	dS	2	18.90	0.00
Val204	R2I	2	36.33	1.99
Val204	R2S	2	29.51	2.45
Val?r	dI	2	0.94	0.00

Residue	Parameter	State	Fit result	Error
Val?r	dS	2	23.23	0.00
Val?r	R2I	2	75.15	2.55
Val?r	R2S	2	57.73	3.45

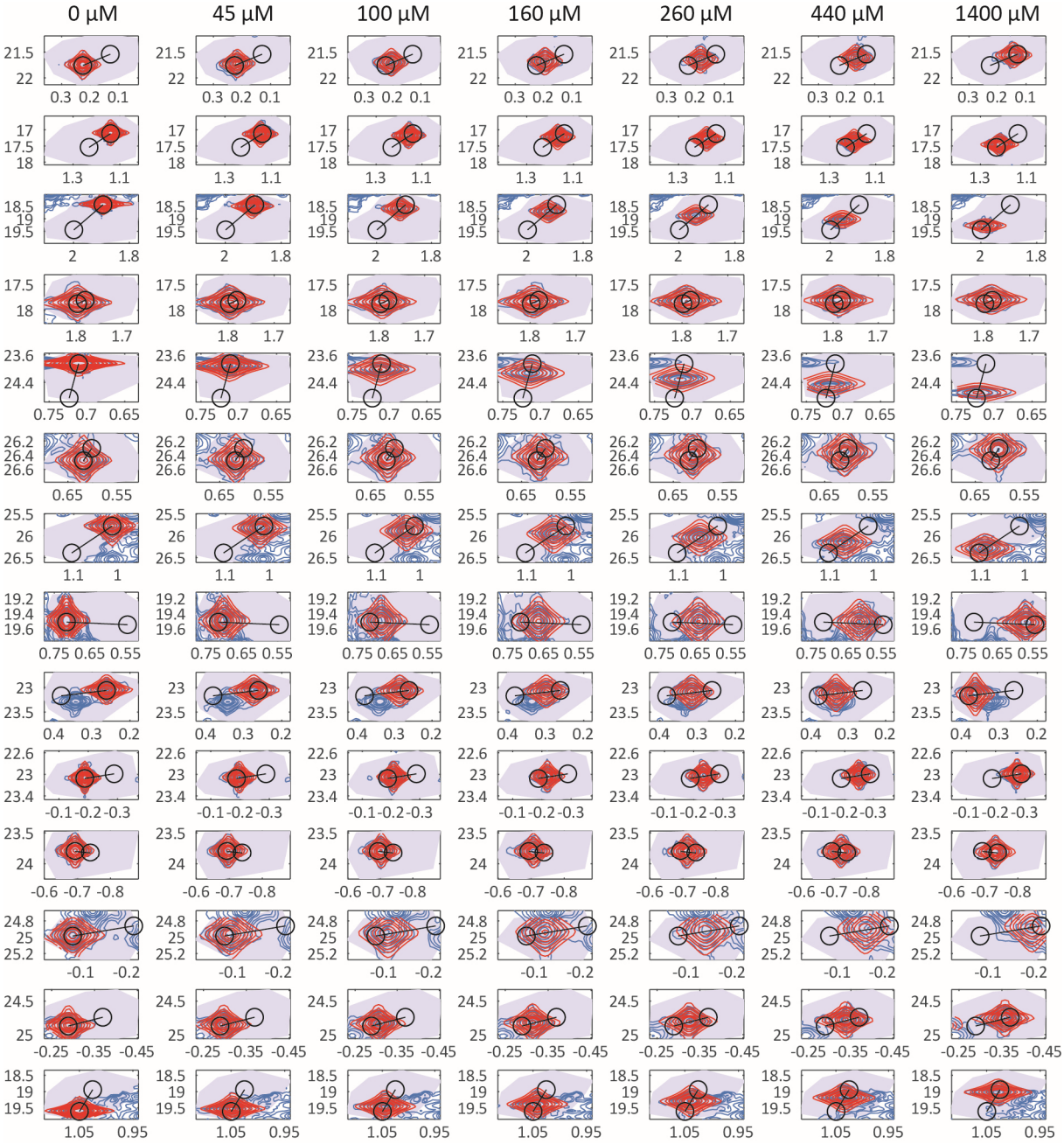


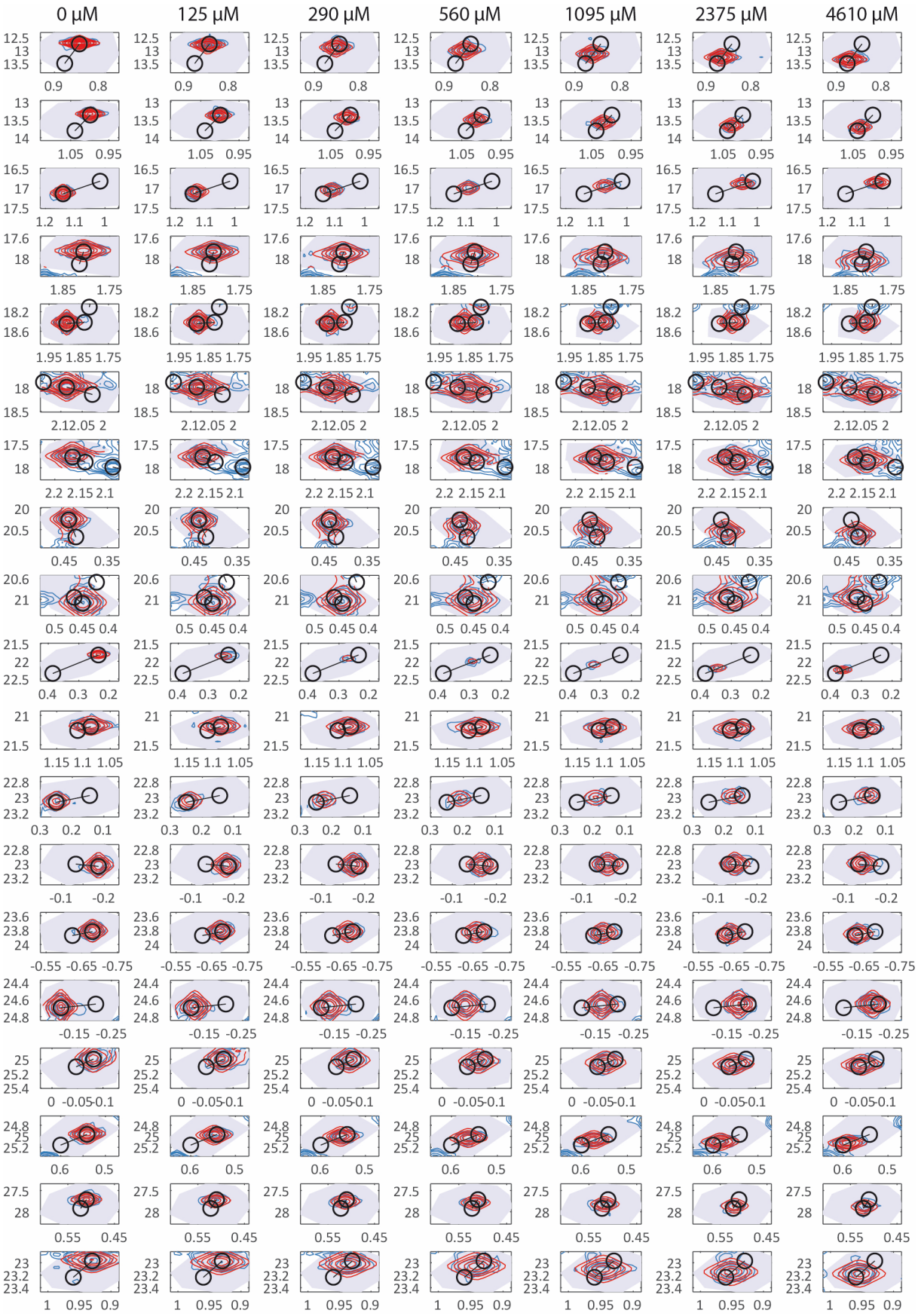
Fig. 37: Overlay of experimental (blue) and fitted (red) line shapes of the H-dis titration to GTB W181M. Each row corresponds to one fitted residue in the same order as in the following table.

Tab. 54: Line shape analysis results derived from the H-dis titration to GTB W181M.K_d is reported in units of µM. k_{off}, the transverse relaxation rates in the ^{1}H dimension (R2I), and the transverse relaxation rates in the ^{13}C dimension (R2S) are reported in units of s^{-1}. The chemical shifts (dI = ^{1}H; dS = ^{13}C) of the bound state (state 2) are reported in ppm. ILMV methyl-labeled protein was used in the titration. Some L/V pro-R methyl resonances (r) are not assigned. They are indicated by a question mark.

Residue	Parameter	State	Fit result	Error
global	K_d		215.57	3.98

Residue	Parameter	State	Fit result	Error
global	k_{off}		1524.01	64.70
Val?r	dI	2	0.13	0.00
Val?r	dS	2	21.54	0.01
Val?r	R2I	2	61.24	5.18
Val?r	R2S	2	35.95	5.23
Met214	dI	2	1.23	0.00
Met214	dS	2	17.54	0.00
Met214	R2I	2	63.45	3.45
Met214	R2S	2	40.55	3.89
Met266	dI	2	2.00	0.00
Met266	dS	2	19.44	0.02
Met266	R2I	2	124.65	8.16
Met266	R2S	2	74.28	13.70
Met189	dI	2	1.78	0.00
Met189	dS	2	17.81	0.00
Met189	R2I	2	68.95	3.21
Met189	R2S	2	39.47	3.64
Val329	dI	2	0.72	0.00
Val329	dS	2	24.86	0.02
Val329	R2I	2	89.45	7.10
Val329	R2S	2	96.19	18.49
Leu306	dI	2	0.60	0.00
Leu306	dS	2	26.30	0.00
Leu306	R2I	2	42.12	2.35
Leu306	R2S	2	41.87	3.32
Leu324	dI	2	1.10	0.00
Leu324	dS	2	26.39	0.01
Leu324	R2I	2	72.65	4.45
Leu324	R2S	2	68.85	9.44
Val299	dI	2	0.55	0.00
Val299	dS	2	19.55	0.00
Val299	R2I	2	63.66	3.85
Val299	R2S	2	26.95	3.10
Leu336	dI	2	0.38	0.00
Leu336	dS	2	23.17	0.01
Leu336	R2I	2	33.17	2.41
Leu336	R2S	2	75.53	5.77
Leu339	dI	2	-0.29	0.00
Leu339	dS	2	22.99	0.00
Leu339	R2I	2	37.98	2.84
Leu339	R2S	2	21.29	3.53
Leu336R	dI	2	-0.74	0.00
Leu336R	dS	2	23.82	0.00
Leu336R	R2I	2	46.75	3.12
Leu336R	R2S	2	28.34	2.70

Residue	Parameter	State	Fit result	Error
Leu339R	dI	2	-0.22	0.00
Leu339R	dS	2	24.86	0.01
Leu339R	R2I	2	61.51	5.61
Leu339R	R2S	2	65.37	9.04
Leu?r	dI	2	-0.37	0.00
Leu?r	dS	2	24.74	0.00
Leu?r	R2I	2	43.83	2.59
Leu?r	R2S	2	18.78	2.41
Val?r	dI	2	1.02	0.00
Val?r	dS	2	18.94	0.01
Val?r	R2I	2	48.37	2.42
Val?r	R2S	2	56.36	4.31


0 µM
125 µM
290 µM
560 µM
1095 µM
2375 µM
4610 µM

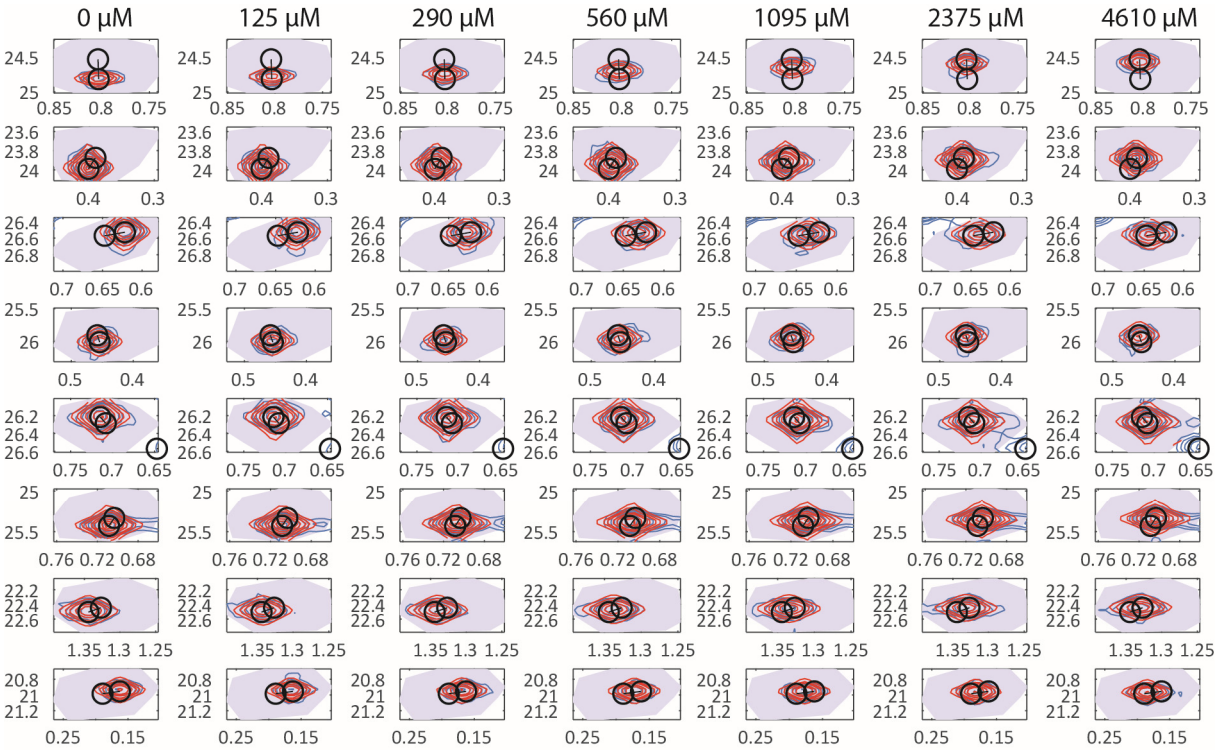


Fig. 38: Overlay of experimental (blue) and fitted (red) line shapes of the UDP titration to GTB W181M. Each row corresponds to one fitted residue in the same order as in the following table. This figure is spread over two pages.

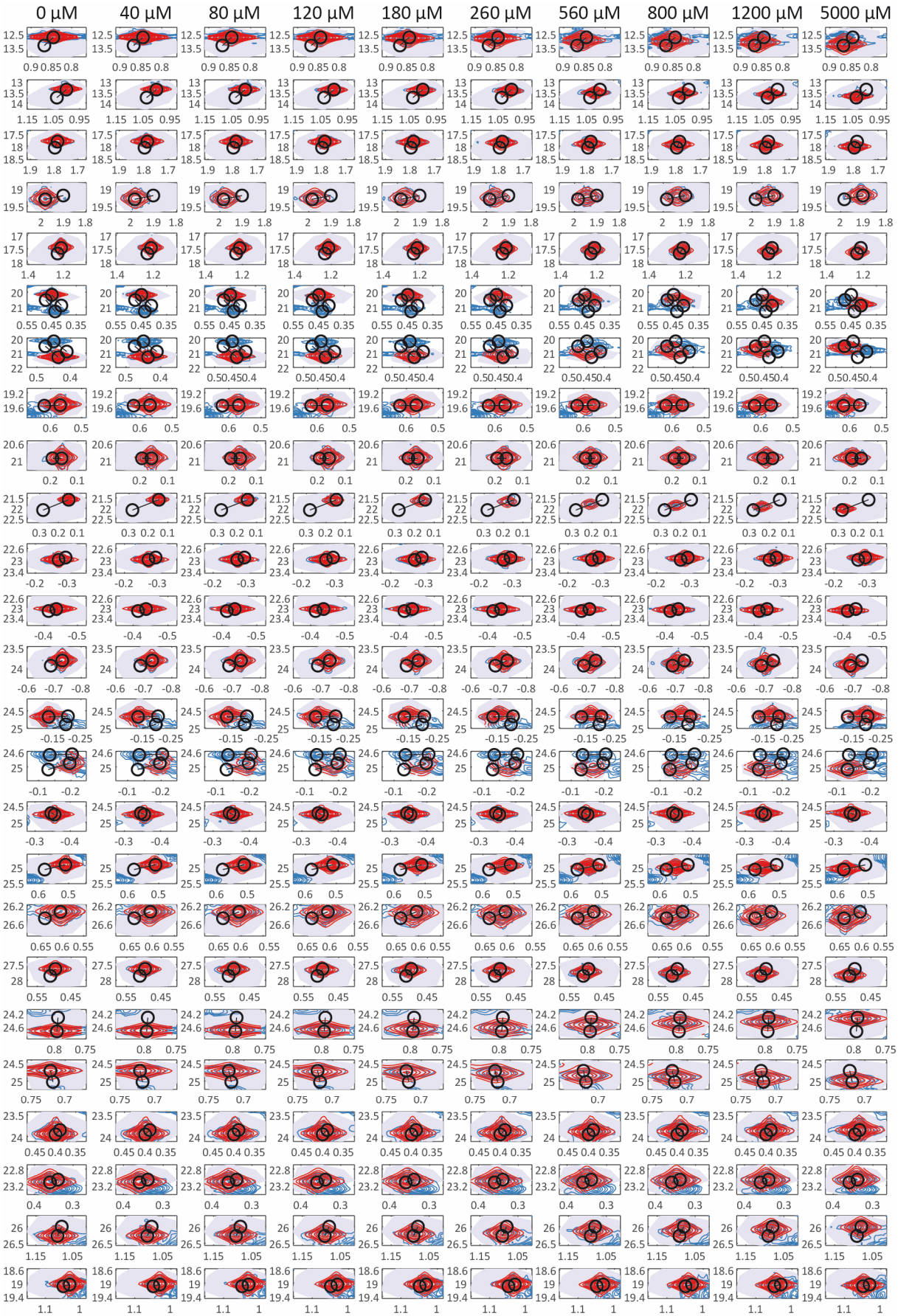
Tab. 55: Line shape analysis results derived from the UDP titration to GTB W181M.K_d is reported in units of µM. k_{off}, the transverse relaxation rates in the ^{1}H dimension (R2I), and the transverse relaxation rates in the ^{13}C dimension (R2S) are reported in units of s^{-1}. The chemical shifts (dI = ^{1}H; dS = ^{13}C) of the bound state (state 2) are reported in ppm. ILMV methyl-labeled protein was used in the titration. Some L/V pro-R methyl resonances (r) are not assigned. They are indicated by a question mark.

Residue	Parameter	State	Fit Result	Error
global	K_d		887.76	12.99
global	k_{off}		1047.40	53.41
Ile123	dI	2	0.88	0.00
Ile123	dS	2	13.51	0.00
Ile123	R2I	2	38.34	1.54
Ile123	R2S	2	66.56	4.43
Ile192	dI	2	1.04	0.00
Ile192	dS	2	13.81	0.01
Ile192	R2I	2	41.96	2.62
Ile192	R2S	2	57.41	5.20
Met214	dI	2	1.02	0.00
Met214	dS	2	16.82	0.00
Met214	R2I	2	74.09	5.16
Met214	R2S	2	34.95	5.12
Met189	dI	2	1.82	0.00
Met189	dS	2	18.12	0.00

Residue	Parameter	State	Fit Result	Error
Met189	R2I	2	60.81	2.46
Met189	R2S	2	63.93	3.70
Met266	dI	2	1.83	0.00
Met266	dS	2	18.41	0.00
Met266	R2I	2	50.43	1.79
Met266	R2S	2	47.07	2.40
Met191	dI	2	2.03	0.00
Met191	dS	2	18.14	0.00
Met191	R2I	2	74.98	1.78
Met191	R2S	2	47.68	2.15
Met288	dI	2	2.14	0.00
Met288	dS	2	17.88	0.00
Met288	R2I	2	51.86	1.65
Met288	R2S	2	61.04	3.01
Val120	dI	2	0.43	0.00
Val120	dS	2	20.69	0.01
Val120	R2I	2	49.56	1.86
Val120	R2S	2	79.18	4.23
Val120r	dI	2	0.46	0.00
Val120r	dS	2	20.94	0.01
Val120r	R2I	2	53.96	2.16
Val120r	R2S	2	93.29	5.41
Val?r	dI	2	0.39	0.00
Val?r	dS	2	22.34	0.01
Val?r	R2I	2	66.16	7.80
Val?r	R2S	2	33.22	9.19
Val208	dI	2	1.11	0.00
Val208	dS	2	21.26	0.00
Val208	R2I	2	50.76	2.86
Val208	R2S	2	35.03	3.31
Leu336	dI	2	0.15	0.00
Leu336	dS	2	22.98	0.01
Leu336	R2I	2	92.32	9.03
Leu336	R2S	2	30.92	7.40
Leu339	dI	2	-0.13	0.00
Leu339	dS	2	23.01	0.00
Leu339	R2I	2	42.64	2.68
Leu339	R2S	2	29.58	3.48
Leu336r	dI	2	-0.62	0.00
Leu336r	dS	2	23.88	0.00
Leu336r	R2I	2	59.99	3.84
Leu336r	R2S	2	27.41	3.46
Leu?r	dI	2	-0.21	0.00
Leu?r	dS	2	24.65	0.00
Leu?r	R2I	2	56.31	2.50
Leu?r	R2S	2	18.24	2.00

Residue	Parameter	State	Fit Result	Error
Leu330r	dI	2	-0.05	0.00
Leu330r	dS	2	25.10	0.00
Leu330r	R2I	2	60.30	4.31
Leu330r	R2S	2	24.63	3.17
Leu118	dI	2	0.60	0.00
Leu118	dS	2	25.16	0.00
Leu118	R2I	2	56.85	3.04
Leu118	R2S	2	24.46	3.20
Leu?r	dI	2	0.52	0.00
Leu?r	dS	2	27.92	0.01
Leu?r	R2I	2	50.46	3.80
Leu?r	R2S	2	64.06	7.23
Val?r	dI	2	0.96	0.00
Val?r	dS	2	23.23	0.01
Val?r	R2I	2	58.02	2.88
Val?r	R2S	2	61.16	3.96
Leu130	dI	2	0.80	0.00
Leu130	dS	2	24.53	0.01
Leu130	R2I	2	21.92	2.41
Leu130	R2S	2	40.18	5.03
Leu173	dI	2	0.39	0.00
Leu173	dS	2	23.87	0.00
Leu173	R2I	2	35.14	1.38
Leu173	R2S	2	21.98	1.60
Leu306	dI	2	0.65	0.00
Leu306	dS	2	26.57	0.00
Leu306	R2I	2	46.68	3.35
Leu306	R2S	2	43.20	4.86
Leu207	dI	2	0.46	0.00
Leu207	dS	2	25.91	0.01
Leu207	R2I	2	45.13	3.08
Leu207	R2S	2	67.73	5.58
Leu232r	dI	2	0.71	0.00
Leu232r	dS	2	26.29	0.00
Leu232r	R2I	2	30.56	1.51
Leu232r	R2S	2	36.65	2.85
Leu170	dI	2	0.70	0.00
Leu170	dS	2	25.33	0.00
Leu170	R2I	2	25.21	1.03
Leu170	R2S	2	26.34	2.05
Val220	dI	2	1.33	0.00
Val220	dS	2	22.45	0.00
Val220	R2I	2	56.58	3.41
Val220	R2S	2	35.15	3.44
Leu134	dI	2	0.19	0.00
Leu134	dS	2	20.98	0.00

Residue	Parameter	State	Fit Result	Error
Leu134	R2I	2	41.30	2.26
Leu134	R2S	2	22.34	2.59


0 µM
40 µM
80 µM
120 µM
180 µM
260 µM
560 µM
800 µM
1200 µM
5000 µM

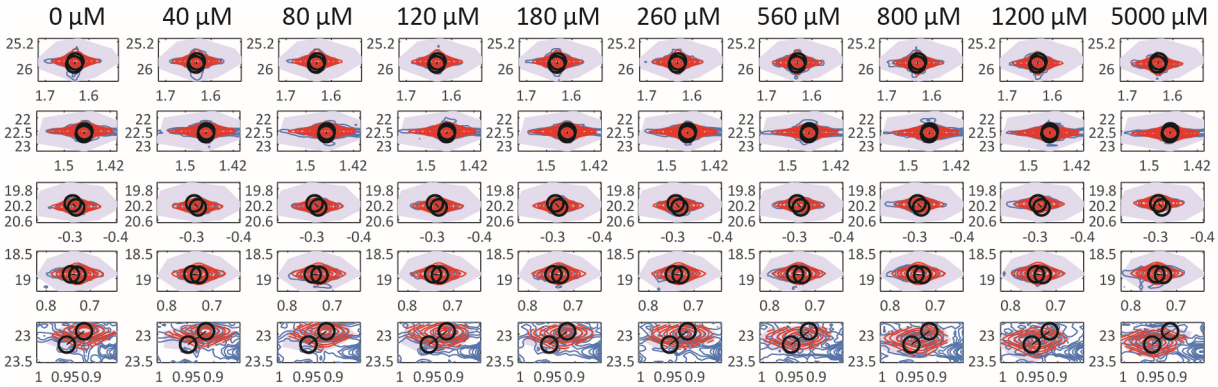


Fig. 39: Overlay of experimental (blue) and fitted (red) line shapes of the UDP titration to H-dis-saturated GTB W181M. Each row corresponds to one fitted residue in the same order as in the following table. This figure is spread over two pages.

Tab. 56: Line shape analysis results derived from the UDP titration to H-dis-saturated GTB W181M.K_d is reported in units of µM. k_{off}, the transverse relaxation rates in the ^{1}H dimension (R2I), and the transverse relaxation rates in the ^{13}C dimension (R2S) are reported in units of s^{-1}. The chemical shifts (dI = ^{1}H; dS = ^{13}C) of the bound state (state 2) are reported in ppm. ILMV methyl-labeled protein was used in the titration. Some L/V pro-R methyl resonances (r) are not assigned. They are indicated by a question mark.

Residue	Parameter	State	Fit Result	Error
global	K_d		486.07	6.54
global	k_{off}		556.15	14.35
Ile123	dI	2	0.87	0.00
Ile123	dS	2	13.32	0.01
Ile123	R2I	2	39.72	1.23
Ile123	R2S	2	152.20	5.63
Ile192	dI	2	1.04	0.00
Ile192	dS	2	13.74	0.00
Ile192	R2I	2	47.54	1.87
Ile192	R2S	2	35.97	2.62
Met189	dI	2	1.80	0.00
Met189	dS	2	18.06	0.00
Met189	R2I	2	63.70	2.28
Met189	R2S	2	42.57	2.67
Met266	dI	2	1.90	0.00
Met266	dS	2	19.20	0.01
Met266	R2I	2	85.94	4.71
Met266	R2S	2	59.36	5.82
Met214	dI	2	1.23	0.00
Met214	dS	2	17.67	0.00
Met214	R2I	2	81.53	3.06
Met214	R2S	2	63.46	3.90
Val120	dI	2	0.42	0.00
Val120	dS	2	20.89	0.00

Residue	Parameter	State	Fit Result	Error
Val120	R2I	2	47.37	1.56
Val120	R2S	2	54.01	2.57
Val120r	dI	2	0.47	0.00
Val120r	dS	2	20.52	0.01
Val120r	R2I	2	44.44	1.18
Val120r	R2S	2	78.19	4.13
Val299	dI	2	0.62	0.00
Val299	dS	2	19.56	0.00
Val299	R2I	2	49.34	1.70
Val299	R2S	2	34.10	2.29
Leu134	dI	2	0.19	0.00
Leu134	dS	2	20.95	0.00
Leu134	R2I	2	55.66	2.04
Leu134	R2S	2	26.48	2.09
Val?r	dI	2	0.28	0.00
Val?r	dS	2	22.08	0.01
Val?r	R2I	2	70.34	5.37
Val?r	R2S	2	48.33	6.86
Leu339	dI	2	-0.29	0.00
Leu339	dS	2	22.92	0.00
Leu339	R2I	2	31.44	1.10
Leu339	R2S	2	24.08	1.42
Leu319r	dI	2	-0.41	0.00
Leu319r	dS	2	23.13	0.00
Leu319r	R2I	2	54.78	2.13
Leu319r	R2S	2	34.31	2.49
Leu336r	dI	2	-0.69	0.00
Leu336r	dS	2	23.94	0.00
Leu336r	R2I	2	38.68	1.35
Leu336r	R2S	2	27.01	1.94
Leu?r	dI	2	-0.20	0.00
Leu?r	dS	2	24.67	0.00
Leu?r	R2I	2	43.78	1.17
Leu?r	R2S	2	42.62	1.90
Leu330r	dI	2	-0.13	0.00
Leu330r	dS	2	25.05	0.00
Leu330r	R2I	2	80.07	3.65
Leu330r	R2S	2	67.04	5.49
Leu339r	dI	2	-0.35	0.00
Leu339r	dS	2	24.72	0.00
Leu339r	R2I	2	30.14	1.06
Leu339r	R2S	2	17.62	1.17
Leu118	dI	2	0.58	0.00
Leu118	dS	2	25.08	0.00
Leu118	R2I	2	42.19	1.27
Leu118	R2S	2	23.80	1.78

Residue	Parameter	State	Fit Result	Error
Leu306	dI	2	0.64	0.00
Leu306	dS	2	26.47	0.00
Leu306	R2I	2	44.47	1.49
Leu306	R2S	2	45.02	2.27
Leu?r	dI	2	0.51	0.00
Leu?r	dS	2	27.85	0.00
Leu?r	R2I	2	46.20	2.90
Leu?r	R2S	2	44.31	4.04
Leu130	dI	2	0.79	0.00
Leu130	dS	2	24.33	0.01
Leu130	R2I	2	55.82	3.92
Leu130	R2S	2	60.60	6.00
Leu329	dI	2	0.72	0.00
Leu329	dS	2	25.02	0.01
Leu329	R2I	2	49.87	4.07
Leu329	R2S	2	63.24	7.89
Leu173	dI	2	0.39	0.00
Leu173	dS	2	23.85	0.00
Leu173	R2I	2	31.80	0.84
Leu173	R2S	2	27.86	1.21
Leu336	dI	2	0.34	0.00
Leu336	dS	2	23.06	0.00
Leu336	R2I	2	41.67	1.49
Leu336	R2S	2	61.25	3.00
Leu324	dI	2	1.08	0.00
Leu324	dS	2	26.00	0.00
Leu324	R2I	2	51.36	2.40
Leu324	R2S	2	61.88	4.27
Val?r	dI	2	1.05	0.00
Val?r	dS	2	19.09	0.00
Val?r	R2I	2	37.31	0.98
Val?r	R2S	2	38.41	1.31
Val76	dI	2	1.63	0.00
Val76	dS	2	25.91	0.00
Val76	R2I	2	28.89	0.75
Val76	R2S	2	29.46	1.10
Val76r	dI	2	1.47	0.00
Val76r	dS	2	22.61	0.00
Val76r	R2I	2	36.58	0.83
Val76r	R2S	2	28.98	1.18
Leu319	dI	2	-0.30	0.00
Leu319	dS	2	20.18	0.00
Leu319	R2I	2	46.38	2.35
Leu319	R2S	2	29.91	2.79
Val204	dI	2	0.74	0.00

Residue	Parameter	State	Fit Result	Error
Val204	dS	2	18.92	0.00
Val204	R2I	2	50.91	2.67
Val204	R2S	2	28.00	2.82
Val?r	dI	2	0.95	0.00
Val?r	dS	2	23.20	0.00
Val?r	R2I	2	81.81	2.93
Val?r	R2S	2	65.21	3.90

Pulse programs

Listed are pulse programs that are not included in the standard Bruker pulse program library.

Methyl-TROSY

```
;metr-hmqcph_new.tb
;avance-version (09/04/17)
;Methyl-TROSY HMQC with optional Water supression
;2D H-1/X correlation via heteronuclear zero and double quantum
;   coherence
;phase sensitive
;with decoupling during acquisition
;
;V. Tugarinov, P.W. Hwang, J.E. Ollerenshaw & L.E. Kay,
;                  J. Magn. Reson. 125, 10420-10428 (2003)
;
;$CLASS=HighRes
;$DIM=2D
;$TYPE=
;$SUBTYPE=
;$COMMENT=


#include <Avance.incl>
#include <Grad.incl>
#include <Delay.incl>


"p2=p1*2"
"d2=3.6m"
"d11=30m"
"d12=20u"
"d13=4u"


"d0=3u"

"in0=inf1/2"

"DELTA1=d2-p19-d16-d13"



1 ze
2 d11 do:f2
3 4u

# ifdef WATER
  d11 fq=cnst20 (bf ppm) :f1
  d11 pl9:f1
  d1 cw:f1 ph29
  d13 do:f1
  d13 pl2:f2
# else
  d1 pl2:f2
# endif

  p3:f2 ph0
  d13 UNBLKGRAD

# ifdef WATER
  4u
```

```
  p16:gp1
  d16 fq=0 :f1
# else
  4u
  p16:gp1
  d16
# endif

  d12 pl1:f1
  p1 ph1
  d13
  p19:gp2
  d16
  DELTA1
  p3:f2 ph3
  d0
  p2 ph2
  d0
  p3:f2 ph4
  DELTA1
  p19:gp2
  d16 pl12:f2
  d13 BLKGRAD
  go=2 ph31 cpd2:f2
  d11 do:f2 mc #0 to 2 F1PH(calph(ph3, +90) & calph(ph29, +90), caldel(d0, +in0))
exit


ph0=0
ph1=0
ph2=0
ph3=0 2
ph4=0 0 2 2
ph29=0
ph31=0 2 2 0


;pl1 : f1 channel - power level for pulse (default)
;pl2 : f2 channel - power level for pulse (default)
;pl9 : f1 channel - power level for presaturation
;pl12: f2 channel - power level for CPD/BB decoupling
;p1 : f1 channel -  90 degree high power pulse
;p2 : f1 channel - 180 degree high power pulse
;p3 : f2 channel -  90 degree high power pulse
;p16: homospoil/gradient pulse                         [1 msec]
;p19: gradient pulse 2                                 [500 usec]
;d0 : incremented delay (2D)                          [3 usec]
;d1 : relaxation delay; 1-5 * T1
;d2 : 1/(2J)XH                                        [3.6 ms]
;d11: delay for disk I/O                              [30 msec]
;d12: delay for power switching                       [20 usec]
;d13: short delay                                     [4 usec]
;d16: delay for homospoil/gradient recovery
;cnst20: chemical shift of residual Water peak (in ppm)   [4.7 ppm]
;inf1: 1/SW(X) = 2 * DW(X)
;in0: 1/(2 * SW(X)) = DW(X)
;nd0: 2
;NS: 4 * n
;DS: 16
;td1: number of experiments
;FnMODE: States-TPPI, TPPI, States or QSEQ
;cpd2: decoupling according to sequence defined by cpdprg2
;pcpd2: f2 channel - 90 degree pulse for decoupling sequence

;for z-only gradients:
;gpz1: 30%
```

```
;gpz2: 40%

;use gradient files:
;gpnam1: SMSQ10.100
;gpnam2: SMSQ10.100

                                          ;preprocessor-flags-start
;WATER: for optional Watersupression start experiment with
;             option -DWATER (eda: ZGOPTNS)
                                          ;preprocessor-flags-end

;$Id: hmqcphpr,v 1.5 2009/07/02 16:40:44 ber Exp $
```

3D NOESY HMQC

```
;noesyhmqcf3gpph3d
;avance-version (12/01/11)
;NOESY-HMQC
;3D sequence with
;   homonuclear correlation via dipolar coupling
;   dipolar coupling may be due to noe or chemical exchange.
;   H-1/X correlation via double inept transfer
;phase sensitive (t1)
;phase sensitive (t2)
;with decoupling during acquisition
;water suppression using 3-9-19 pulse sequence with gradients
;(use parameterset NOESYHMQCF3GPPH3D)
;
;$CLASS=HighRes
;$DIM=3D
;$TYPE=
;$SUBTYPE=
;$COMMENT=


prosol relations=<triple>


#include <Avance.incl>
#include <Grad.incl>
#include <Delay.incl>


"p2=p1*2"
"p4=p3*2"
"d11=30m"
"d21=1s/(cnst4*2)"


"in0=inf1/2"
"in10=inf2"

"d0=3u"
"d10=in10/2-p3*4/3.1415"


"DELTA1=d21-p16-d16"

"DELTA=p14+d0*2"

"TAU=d8-p16-d16"
"TAU1=de+4u"
"TAU2=p1*2/3.1416"
```

```
"acqt0=0"
baseopt_echo


aqseq 312


1 d11 ze
  d11 pl12:f2
2 d11 do:f2
3 d1 pl1:f1 pl2:f2
  50u UNBLKGRAD

  p3:f2 ph0
  4u
  p16:gp1
  d16

  (p1 ph2)
  DELTA
  (p2 ph2)
  d0 pl0:f2

  (p14:sp3 ph2):f2

  d0
  (p1 ph1)

  TAU
  p16:gp2
  d16

  (p1 ph1)
  TAU1 pl2:f2
  p16:gp3
  d16

  (center (p2 ph5):f1 (DELTA1 p3 ph3 d10 p3 ph4 DELTA1):f2 )

  p16:gp3
  d16 pl12:f2
  TAU2
  4u BLKGRAD
  go=2 ph31 cpd2:f2
  d11 do:f2 mc #0 to 2
     F1PH(calph(ph2, +90), caldel(d0, +in0))
     F2PH(calph(ph3, +90), caldel(d10, +in10))
exit


ph0=0
ph1=0
ph2=0 0 2 2
ph3=0 2
ph4=0 0 0 0 0 0 0 0 2 2 2 2 2 2 2 2
ph5=0 0 0 0 2 2 2 2
ph6=2
ph7=2 2 2 2 0 0 0 0
ph31=0 2 2 0 0 2 2 0 2 0 0 2 2 0 0 2


;pl1 : f1 channel - power level for pulse (default)
;pl3 : f3 channel - power level for pulse (default)
;pl16: f3 channel - power level for CPD/BB decoupling
```

```
;sp3: f2 channel - shaped pulse (180degree inversion)
;spnam3: Crp60,0.5,20.1
;p1 : f1 channel -  90 degree high power pulse
;p2 : f1 channel - 180 degree high power pulse
;p3 : f2 channel - 90 degree high power pulse
;p14 : f2 channel - 180 degree shaped pulse for inversion
;     = 500usec for Crp60,0.5,20.1
;p16: homospoil/gradient pulse
;d0 : incremented delay (F1 in 3D)                      [3 usec]
;d1 : relaxation delay; 1-5 * T1
;d8 : mixing time
;d10: incremented delay (F2 in 3D) = in10/2-p21*4/3.1415
;d11: delay for disk I/O                                [30 msec]
;d16: delay for homospoil/gradient recovery
;d21: 1/(2J)CH
;cnst4: = J(CH)
;inf1: 1/SW(H) = 2 * DW(H)
;inf2: 1/SW(C) = 2 * DW(C)
;in0: 1/(2 * SW(H)) = DW(H)
;nd0: 2
;in10: 1/(2 * SW(C)) = DW(C)
;nd10: 2
;ns: 8 * n
;ds: 32
;td1: number of experiments in F1
;td2: number of experiments in F2
;FnMODE: States-TPPI (or TPPI) in F1
;FnMODE: States-TPPI (or TPPI) in F2
;cpd2: decoupling according to sequence defined by cpdprg3
;pcpd2: f3 channel - 90 degree pulse for decoupling sequence


;for z-only gradients:
;gpz1: 30%
;gpz2: 50%
;gpz3: 31%

;use gradient files:
;gpnam1: SMSQ10.100
;gpnam2: SMSQ10.100
;gpnam3: SMSQ10.100


                                          ;preprocessor-flags-start
;LABEL_CN: for C-13 and N-15 labeled samples start experiment with
;             option -DLABEL_CN (eda: ZGOPTNS)
                                          ;preprocessor-flags-end


;Processing

;PHC0(F2): 90
;PHC1(F2): -180
;FCOR(F2): 1



;$Id: noesyhmqcf3gpph3d,v 1.3 2012/01/31 17:49:27 ber Exp $
```

4D HMQC NOESY HMQC

```
;hmqcnoesyhmqc4d.tb
;avance-version (12/01/11)
;(C13)HMQC-NOESY-(C13)HMQC
;4D 13C/13C-separated HMQC-NOESY-HMQC
;   homonuclear correlation via dipolar coupling
;   dipolar coupling may be due to noe or chemical exchange.
;   H-1/X correlation via heteronuclear zero and double quantum coherence
;phase sensitive (t1)
;phase sensitive (t2)
;phase sensitive (t3)
;with decoupling during acquisition
;using shaped pulses for inversion on f2 - channel
;
;G.W. Vuister, M.G. Clore, A.M. Gronenborn, R. Powers, D.S. Garret,
; R. Tschudin & A. Bax J. Magn. Reson., B101, 210-213 (1993).
;
;$CLASS=HighRes
;$DIM=4D
;$TYPE=
;$SUBTYPE=
;$COMMENT=


prosol relations=<triple>


#include <Avance.incl>
#include <Grad.incl>
#include <Delay.incl>


"p2=p1*2"
"p4=p3*2"
"d11=30m"
"d12=20u"
"d21=1s/(cnst4*2)"

"d31=3u"
"d32=3u"
"d33=3u"

"in31=inf1/2"
"in32=inf2/2"
"in33=inf3/2"

"DELTA1=d21-p29-d16"

"TAU=d8-p30-p3-p31-2*d16"

"acqt0=0"
baseopt_echo


1 ze
  d11 pl12:f2
2 d11 do:f2
3 d12 ;pl9:f1 falls Wasserunterdrückung nötig sein sollte, können diese Teile wieder
aktiviert werden

  d1 ;cw:f1 ph29
  4u ;do:f1
  d12 pl2:f2
  50u UNBLKGRAD
```

```
  (p3 ph0):f2
  p16:gp1
  d16 pl1:f1
  (p1 ph1)
  p29:gp2
  d16
  DELTA1 ;Wartezeit 1/2J, Gradientenlänge abziehen, müssen Pulslängen abgezogen
werden?
  (p3 ph2):f2
  d31 ;erste Hälfte von t1, der mittlere 180er muss zur Hälfte abgezogen werden
  p2 ph1
  d31 ;zweite Hälfte von t1, der mittlere 180er muss zur Hälfte abgezogen werden
  (p3 ph6):f2
  DELTA1 ;Wartezeit 1/2J, Gradientenlänge abziehen, müssen Pulslängen abgezogen
werden?
  p29:gp2

;-----------Variante Composite-Pulse ?Auswahl über ZGOPTNS?--------
  d16
  d32
  (p3 ph4 p4 ph6 p3 ph4):f2 ;composite 13C-Pulse, hier alternativ adiabatischen
inversion-Puls einfügen?
  d32
  (p1 ph5)
  p30:gp2
  d16
;-----------Variante Composite-Pulse--------

;-----------Variante adiabatic-Pulse 500µs CRP60,0.5,20.1--------
  ;d16 pl0:f2
  ;d32
  ;(p14:sp3 ph8):f2
  ;d32
  ;(p1 ph5)
  ;p30:gp2
  ;d16 pl2:f2
;-----------Variante adiabatic-Pulse--------

  (p3 ph6):f2
  p31:gp2
  d16
  TAU
  (p1 ph5)
  p29:gp2*-1
  d16
  DELTA1
  (p3 ph3):f2
  d33
  (p2 ph5)
  d33
  (p3 ph6):f2
  DELTA1
  p29:gp2*-1
  d16 pl12:f2

  4u BLKGRAD
  go=2 ph31 cpd2:f2
  d11 do:f2 mc #0 to 2
     F1PH(calph(ph2, +90), caldel(d31, +in31))
     F2PH(calph(ph1, +90), caldel(d32, +in32))
     F3PH(calph(ph3, +90), caldel(d33, +in33))
exit


ph0=0
ph1=0
```

```
ph2=0 2
ph3=0
;-----------Variante Composite-Pulse--------
ph4=1
;-----------Variante Composite-Pulse--------
ph5=0
ph6=0
;-----------Variante adiabatic-Pulse 500µs CRP60,0.5,20.1--------
ph8=0
;-----------Variante adiabatic-Pulse--------
ph29=0
ph31=0 2



;pl1 : f1 channel - power level for pulse (default)
;pl2 : f2 channel - power level for pulse (default)
;pl9: f1 channel - power level for low power presaturation
;pl12: f2 channel - power level for CPD/BB decoupling
;sp3: f2 channel - shaped pulse (180degree inversion)
;spnam3: Crp60,0.5,20.1
;p1 : f1 channel -  90 degree high power pulse
;p2 : f1 channel - 180 degree high power pulse
;p3 : f2 channel -  90 degree high power pulse
;p4 : f2 channel - 180 degree high power pulse
;p14 : f2 channel - 180 degree shaped pulse for inversion (adiabatic)
;     = 500usec for Crp60,0.5,20.1
;p16: homospoil/gradient pulse                         [1 msec]
;p29: homospoil/gradient pulse                         [750 usec]
;p30: homospoil/gradient pulse                         [2 msec]
;p31: homospoil/gradient pulse                         [4 msec]
;d1 : relaxation delay; 1-5 * T1
;d8 : mixing time
;d11: delay for disk I/O                               [30 msec]
;d12: delay for power switching                        [20 usec]
;d16: delay for homospoil/gradient recovery            [200 usec]
;d21: 1/(2J(NH))
;d31: incremented delay (F1 in 4D)                     [3 usec]
;d32: incremented delay (F2 in 4D)                     [3 usec]
;d33: incremented delay (F3 in 4D)                     [3 usec]
;cnst4: = J(CH)
;inf1: 1/SW(C) = 2 * DW(N)
;inf2: 1/SW(H) = 2 * DW(H)
;inf3: 1/SW(C) = 2 * DW(N)
;ns: 2 * n
;ds: >= 16
;td1: number of experiments in F1
;td2: number of experiments in F2
;td3: number of experiments in F3
;FnMODE: States-TPPI (or TPPI) in F1
;FnMODE: States-TPPI (or TPPI) in F2
;FnMODE: States-TPPI (or TPPI) in F3
;cpd2: decoupling according to sequence defined by cpdprg2
;pcpd2: f2 channel - 90 degree pulse for decoupling sequence


;for z-only gradients:
;gpz1: 30%
;gpz2: 14%


;use gradient files:
;gpnam1: SMSQ10.100
;gpnam2: SMSQ10.100

;$Id: hmqcnoesyhmqcnngp4d,v 1.4 2012/01/31 17:49:23 ber Exp $
```

ZZ-exchange auto experiment

```
#include <Avance.incl>
#include <Grad.incl>
#include <rs.incl>

; version 24-08-2009, remco
; version 26-08-2009, realized that this is the auto and not the cross experiment.
; version 12-05-2010, changed the water flages:
;                                                                    l0=0: no water pulses
;                                                                    l0=1: presat
;                                                                    l0=2: water purge pulse
;                                                              l0=3: water flip back

;This sequence runs an IzCz exechange experiment on methyl groups.
; mixing time is before 13C and 1H evolution times. The relaxation rate of the auto
peaks can thus be determined.
; No cross peaks should appear
;Chemical shift in carbon is of the HMQC type

; adjust o2p for the carbon offset
; adjust sw to get right sw in carbon
; adjust td to get right time domain size in carbon
; offset jumps from water to methyl groups

;### Parameters to set ###
;p1 = 90 degree proton hard pulse
;pl1 = power for hard proton
;p3 = 90 degree carbon hard pulse
;pl2 = power for hard carbon
;pl9 = presat power during d1


;p11 = pulselength of waterselective pulse sel3
;sp11 = water selctive pulse power sel3
;spnam11 = shape of the water selective pulse sel3

;d1 = relaxation delay, 1-5 * T1
;NS = total number of scans

;p20 gradient pulse
;p21 gradient during MIX

;d21 Taua

;cnst0 0 (water on resonance)
;cnst1 difference in Hz between water and methyl groups (-3700 @ 800)

; calculate delays
"in0=inf1/2"
"d0=(in0*0.5 -p1 -p3*0.637)"
"d21 = 1.80m"                ; Taua
"d22= d21 -p20 - 2u -500u"
"d23= d21 -p20 - 500u -p3 + 0.5*(p3-p1) + p1*0.637"
"d24= d21 -p20 - 2u -500u"

"d11=5m"
"l3=(td1/2)"
"prompt=10u+l0*10u"
"l2=td2"
;l2 number of delays in VDLIST
;"d28=1m"


1 ze
```

```
2 10u
  d11 do:f2
  d11 do:f3
3 d11*3.0
4 10u fq=cnst0:f1
  1m BLKGRAD
  if (l0 == 1)
  {                ; presat flag
  d12 pl9:f1
  d1 cw:f1 ph29
  4u do:f1
  }
  else
  {                ; no presat
  d1
  }
  1m UNBLKGRAD
  "d28 = vd - p21 - 150u"    ; mixing time

  if (l0 == 3)
  {                ; waterflag
  "d28 = vd - p21 - 150u - p11 - p11 - 4u -4u" ; mixing time
 }


  10u pl2:f2
  10u pl3:f3
  10u pl1:f1

  (p3 ph0):f2           ; purge carbon magn.
  if (l0 == 2)
  {                ; waterflag
  2u pl11:f1
  (p11:sp11 ph11:r):f1
  }
  2u
  p20:gp0
  200u pl1:f1
  10u fq=cnst1:f1                       ; offset at methyl protons

  if (l0 == 3)
  {                ; waterflag
  10u fq=cnst0:f1
  4u pl11:f1
  (p11:sp12 ph12:r):f1
  4u pl1:f1
  }

;-----------real start of experiment
  (p1 ph0):f1                    ; start
  2u
  p20:gp1
  500u
  d22
  (center (p3*2 ph0):f2 (p1*2 ph0):f1)
  d22
  2u
  p20:gp1
  500u
  (p1 ph1):f1
;-------------- HzCz
; ----------- TMIX

  (p3 ph0):f2
  (p3 ph21):f2
```

```
  if (l0 == 3)
  {                ; waterflag
  4u pl11:f1
  (p11:sp12 ph13:r):f1
  4u pl1:f1
  }

  d28
  p21:gp3
  150u

  if (l0 == 3)
  {                ; waterflag
  4u pl11:f1
  (p11:sp12 ph14:r):f1
  4u pl1:f1
  }

; ----------- t1 evolution in carbon
  (center (p1 ph0):f1 (p3 ph22):f2)
  d0
  (p1*2 ph23):f1
  d0
  (p3 ph0):f2
;------------- back to protons
  d23
  p20:gp4
  500u
  (center (p1*2 ph0):f1 (p3*2 ph0):f2)
  d24
  p20:gp4
  500u pl12:f2

;*******************************

  go=2 ph31 cpd2:f2
  10u do:f2 do:f3
  d11 wr #0 if #0 zd
  d11 ivd
  lo to 2 times l2
  d11 ip22
  lo to 3 times 2

  d11 ip31
  d11 ip31

  d11 id0
  lo to 4 times l3

1m BLKGRAD
exit

ph0=0
ph1=1
ph11=0
ph12=2
ph13=3
ph14=2
ph21=0 0 2 2
ph22=0 0 0 0 2 2 2 2
ph23=0 1
ph29=0
ph31=0 2 2 0 2 0 0 2
```

ZZ-exchange cross experiment

```
#include <Avance.incl>
#include <Grad.incl>
#include <rs.incl>

; version 24-08-2009, remco
; version 26-08-2009, remco. modified from rs_Chmqc_HzCz, that is the auto experiment.
; version 12-05-2010, remco, changed the waterflag:
;                                     l0=0: no water pulses etc.
;                                          l0=1: presat
;                                          l0=2: water purge pulse
;                                          l0=3: water flip back (no frequency jump)

;This sequence runs an IzCz exechange experiment on methyl groups.
; 1H -> 13C(t1) -> Mix -> 1H(t2)
;Chemical shift in carbon is of the HMQC type

; adjust o2p for the carbon offset
; adjust sw to get right sw in carbon
; adjust td to get right time domain size in carbon
; offset jumps from water to methyl groups

;### Parameters to set ###
;p1 = 90 degree proton hard pulse
;pl1 = power for hard proton
;p3 = 90 degree carbon hard pulse
;pl2 = power for hard carbon
;pl9 = presat power during d1


;p11 = pulselength of waterselective pulse sel3
;sp11 = water selctive pulse power sel3
;spnam11 = shape of the water selective pulse sel3

;d1 = relaxation delay, 1-5 * T1
;NS = total number of scans

;p20 gradient pulse
;p21 gradient during MIX

;d21 Taua

;l0 l0=0: no presat; l0=1: presat

;cnst0 0 (water on resonance)
;cnst1 difference in Hz between water and methyl groups (-3700 @ 800)



; calculate delays
"in0=inf1/2"
"d0=(in0*0.5 -p1 -p3*0.637)"
"d21 = 1.80m"                ; Taua
"d22= d21 -p20 - 2u -500u"
"d23= d21 -p20 - 500u -p3 + 0.5*(p3-p1) + p1*0.637"
"d24= d21 -p20 - 2u -500u"
"d26= d21 -p20 - 2u -500u + p1*0.637 -p3 + 0.5*(p3-p1)+ p1*0.637 "

"d11=5m"
"l3=(td1/2)"
"prompt=10u+l0*10u+10u"
"l2=td2"
;l2 number of delays in VDLIST
;"d28=400m"
```

```
1 ze
2 10u
  d11 do:f2
  d11 do:f3
3 d11*3.0
4 10u fq=cnst0:f1
  1m BLKGRAD
  if (l0 == 1)
  {                ; presat flag
  d12 pl9:f1
  d1 cw:f1 ph29
  4u do:f1
  }
  else
  {                ; no presat
  d1
  }

  1m UNBLKGRAD
  "d28 = vd - p21 - 150u"    ; mixing time

  if (l0 == 3)
  {
  "d28 = vd - p21 - 150u - p11 - p11 -4u -4u"  ; mixing time
  }

  10u pl2:f2
  10u pl3:f3
  10u pl1:f1

  (p3 ph0):f2           ; purge carbon magn.
  if (l0 == 2)
  {                ; waterflag
  4u pl11:f1
  (p11:sp11 ph11:r):f1
  }
  2u
  p20:gp0
  200u pl1:f1
  10u fq=cnst1:f1                       ; offset at methyl protons

  if (l0 == 3)
  {                ; waterflag
  10u fq=cnst0:f1
  4u pl11:f1
  (p11:sp12 ph12:r):f1
  4u pl1:f1
  }

;-----------real start of experiment
  (p1 ph0):f1                   ; start
  2u
  p20:gp1
  500u
  d22
  (center (p3*2 ph0):f2 (p1*2 ph0):f1)
  d26
  2u
  p20:gp1
  500u
; ----------- t1 evolution in carbon
  (p3 ph21):f2
  d0
```

```
  (p1*2 ph22):f1
  d0
  (center (p1 ph1):f1 (p3 ph0):f2)
; ----------- TMIX

  if (l0 == 3)
  {                ; waterflag
  4u pl11:f1
  (p11:sp12 ph13:r):f1
  4u pl1:f1
  }

  d28
  p21:gp3
  150u

  if (l0 == 3)
  {                ; waterflag
  4u pl11:f1
  (p11:sp12 ph14:r):f1
  4u pl1:f1
  }

; ----------- back to protons
  (p1 ph23):f1
  d23
  p20:gp4
  500u
  (center (p1*2 ph0):f1 (p3*2 ph0):f2)
  d24
  p20:gp4
  500u pl12:f2

;*******************************

  go=2 ph31 cpd2:f2
  10u do:f2 do:f3
  d11 wr #0 if #0 zd
  d11 ivd
  lo to 2 times l2
  d11 ip21
  lo to 3 times 2

  d11 ip31
  d11 ip31

  d11 id0
  lo to 4 times l3

1m BLKGRAD
exit

ph0=0
ph1=1
ph11=0
ph12=2
ph13=3
ph14=2 2 2 2 0 0 0 0
ph21=0 2
ph22=0 0 1 1
ph23=0 0 0 0 2 2 2 2
ph29=0
ph31=0 2 2 0 2 0 0 2
```

Literature

Agafonov R V, Wilson C, Otten R, et al (2014) Energetic dissection of Gleevec's selectivity toward human tyrosine kinases. Nat Struct Mol Biol 21:848–53. doi: 10.1038/nsmb.2891

Akimoto M, McNicholl ET, Ramkissoon A, et al (2015) Mapping the Free Energy Landscape of PKA Inhibition and Activation: A Double-Conformational Selection Model for the Tandem cAMP-Binding Domains of PKA RIα. PLoS Biol 13:1–21. doi: 10.1371/journal.pbio.1002305

Albesa-Jové D, Mendoza F, Rodrigo-Unzueta A, et al (2015) A Native Ternary Complex Trapped in a Crystal Reveals the Catalytic Mechanism of a Retaining Glycosyltransferase. Angew Chemie - Int Ed 54:9898–9902. doi: 10.1002/anie.201504617

Alfaro J a, Zheng RB, Persson M, et al (2008) ABO(H) blood group A and B glycosyltransferases recognize substrate via specific conformational changes. J Biol Chem 283:10097–10108. doi: 10.1074/jbc.M708669200

Allegrozzi M, Bertini I, Janik MBL, et al (2000) Lanthanide-induced pseudocontact shifts for solution structure refinements of macromolecules in shells up to 40 Å from the metal ion. J Am Chem Soc 122:4154–4161. doi: 10.1021/ja993691b

Amero C, Asunción Durá M, Noirclerc-Savoye M, et al (2011) A systematic mutagenesis-driven strategy for site-resolved NMR studies of supramolecular assemblies. J Biomol NMR 50:229–236. doi: 10.1007/s10858-011-9513-5

Amero C, Schanda P, Asunción Durá M, et al (2009) Fast Two-Dimensional NMR Spectroscopy of High Molecular Weight Protein Assemblies. J Am Chem Soc 131:3448–3449. doi: 10.1021/ja809880p

Angulo J, Langpap B, Blume A, et al (2006) Blood group B galactosyltransferase: Insights into substrate binding from NMR experiments. J Am Chem Soc 128:13529–13538. doi: 10.1021/ja063550r

Ardèvol A, Iglesias-Fernández J, Rojas-Cervellera V, Rovira C (2016) The reaction mechanism of retaining glycosyltransferases. Biochem Soc Trans 44:51–60. doi: 10.1042/BST20150177

Ardèvol A, Rovira C (2015) Reaction Mechanisms in Carbohydrate-Active Enzymes: Glycoside Hydrolases and Glycosyltransferases. Insights from ab Initio Quantum Mechanics/Molecular Mechanics Dynamic Simulations. J Am Chem Soc 137:7528–7547. doi: 10.1021/jacs.5b01156

Ayala I, Sounier R, Usé N, et al (2009) An efficient protocol for the complete incorporation of methyl-protonated alanine in perdeuterated protein. J Biomol NMR 43:111–119. doi: 10.1007/s10858-008-9294-7

Berg JM, Tymoczko JL, Stryer L (2007) Carbohydrates. In: Biochemistry, 6th edn. W. H. Freeman and Company, pp 303–325

Blackler RJ, Gagnon SML, Polakowski R, et al (2017) Glycosyltransfer in mutants of putative catalytic residue Glu303 of the human ABO(H) A and B blood group glycosyltransferases GTA and GTB proceeds through a labile active site. Glycobiology 27:370–380. doi: 10.1093/glycob/cww117

Blume A, Angulo J, Biet T, et al (2006) Fragment-based screening of the donor substrate specificity of human blood group B galactosyltransferase using saturation transfer difference NMR. J Biol Chem 281:32728–32740. doi: 10.1074/jbc.M600424200

Bobovská A, Tvaroška I, Kóňa J (2015) Theoretical study of enzymatic catalysis explains why the trapped

covalent intermediate in the E303C mutant of glycosyltransferase GTB was not detected in the wild-type enzyme. Glycobiology 25:3–7. doi: 10.1093/glycob/cwu085

Boix E, Swaminathan GJ, Zhang Y, et al (2001) Structure of UDP Complex of UDP-galactose:β-Galactoside-α -1,3-galactosyltransferase at 1.53-Å Resolution Reveals a Conformational Change in the Catalytically Important C Terminus. J Biol Chem 276:48608–48614. doi: 10.1074/jbc.M108828200

Boix E, Zhang Y, Swaminathan GJ, et al (2002) Structural basis of ordered binding of donor and acceptor substrates to the retaining glycosyltransferase, alpha-1,3-galactosyltransferase. J Biol Chem 277:28310–28318. doi: 10.1074/jbc.M202631200

Boulton S, Akimoto M, Selvaratnam R, et al (2014) A tool set to map allosteric networks through the NMR chemical shift covariance analysis. Sci Rep 4:7306. doi: 10.1038/srep07306

Bouvignies G, Kay LE (2012) A 2D 13C-CEST experiment for studying slowly exchanging protein systems using methyl probes: An application to protein folding. J Biomol NMR 53:303–310. doi: 10.1007/s10858-012-9640-7

Brockhausen I, Stanley P (2017) O-GalNAc Glycans. In: Essentials of Glycobiology, 3rd edition. Cold Spring Harbor (NY): Cold Spring Harbor Laboratory Press; 2015-2017, p Chapter 10

Campbell J a, Davies GJ, Bulone V, Henrissat B (1997) A classification of nucleotide-diphospho-sugar glycosyltransferases based on amino acid sequence similarities. Biochem J 326:929–39. doi: 10.1042/bj2800309

Cantarel BI, Coutinho PM, Rancurel C, et al (2009) The Carbohydrate-Active EnZymes database (CAZy): An expert resource for glycogenomics. Nucleic Acids Res. doi: 10.1093/nar/gkn663

Caramelo JJ, Parodi AJ (2015) A sweet code for glycoprotein folding. FEBS Lett 589:3379–3387. doi: 10.1016/j.febslet.2015.07.021

Cembran A, Kim J, Gao J, Veglia G (2014) NMR mapping of protein conformational landscapes using coordinated behavior of chemical shifts upon ligand binding. Phys Chem Chem Phys 16:6508–18. doi: 10.1039/c4cp00110a

Chan PHW, Cheung AH, Okon M, et al (2013) Investigating the Structural Dynamics of alpha-1,4-Galactosyltransferase C from Neisseria meningitidis by Nuclear Magnetic Resonance Spectroscopy. Biochemistry 52:320–332. doi: 10.1021/Bi301317d

Chan PHW, Weissbach S, Okon M, et al (2012) Nuclear magnetic resonance spectral assignments of α-1,4-galactosyltransferase LgtC from Neisseria meningitidis: substrate binding and multiple conformational states. Biochemistry 51:8278–92. doi: 10.1021/bi3010279

Christiansen MN, Chik J, Lee L, et al (2014) Cell surface protein glycosylation in cancer. Proteomics 14:525–546. doi: 10.1002/pmic.201300387

Chung BC, Zhao J, Gillespie RA, et al (2013) Crystal structure of MraY, an essential membrane enzyme for bacterial cell wall synthesis. Science (80-) 341:1012–1016. doi: 10.1126/science.1236501

Cornilescu G, Marquardt JL, Ottiger M, Bax A (1998) Validation of protein structure from anisotropic carbonyl chemical shifts in a dilute liquid crystalline phase. J Am Chem Soc 120:6836–6837. doi: 10.1021/ja9812610

Coutinho PM, Deleury E, Davies GJ, Henrissat B (2003) An evolving hierarchical family classification

for glycosyltransferases. J Mol Biol 328:307–317. doi: 10.1016/S0022-2836(03)00307-3

Decastello A von, Sturli A (1902) Über die Isoagglutinine im Serum gesunder und kranker Menschen. Münchener Medizinische Wochenschrift 49:1090–1095.

Delaglio F, Grzesiek S, Vuister GW, et al (1995) NMRPipe: A multidimensional spectral processing system based on UNIX pipes. J Biomol NMR 6:277–293. doi: 10.1007/BF00197809

DeLano WL (2002) The PyMOL Molecular Graphics System. Schrödinger LLC Version 1.:http://www.pymol.org.

Dube DH, Bertozzi CR (2005) Glycans in cancer and inflammation--potential for therapeutics and diagnostics. Nat Rev Drug Discov 4:477–488. doi: 10.1038/nrd1751

Farrow NA, Zhang O, Forman-Kay JD, Kay LE (1994) A heteronuclear correlation experiment for simultaneous determination of 15N longitudinal decay and chemical exchange rates of systems in slow equilibrium. J Biomol NMR 4:727–734. doi: 10.1007/BF00404280

Farrow NA, Zhang O, Forman-Kay JD, Kay LE (1995) Comparison of the backbone dynamics of a folded and an unfolded SH3 domain existing in equilibrium in aqueous buffer. Biochemistry 34:868–878. doi: 10.1021/bi00003a021

Fersht A (1999) Structure and mechanism in protein science: a guide to enzyme catalysis and protein folding. W. H. Freeman and Company, New York

Fesik SW, Zuiderweg ER. (1988) Heteronuclear three-dimensional nmr spectroscopy. A strategy for the simplification of homonuclear two-dimensional NMR spectra. J Magn Reson 78:588–593. doi: 10.1016/0022-2364(88)90144-8

Finne J (1980) Identification of the Blood-Group ABH-Active Glycoprotein Components of Human Erythrocyte Membrane. Eur J Biochem 104:181–189. doi: 10.1111/j.1432-1033.1980.tb04414.x

Finne J, Krusius T, Rauvala H (1978) Alkali-stable blood group A- and B-active poly(glycosyl)-peptides from human erythrocyte membrane. FEBS Lett 89:111–115. doi: 10.1016/0014-5793(78)80534-1

Fiser A, Sali A (2003) ModLoop: Automated modeling of loops in protein structures. Bioinformatics 19:2500–2501. doi: 10.1093/bioinformatics/btg362

Flügge F (2014) "Hot spot" Tryptophan Residues as Reporters of Protein Dynamics of Human Blood Group Glycosyltransferases. Master's thesis. Universität zu Lübeck

Freeze HH, Kinoshita T, Schnaar RL (2017a) Genetic Disorders of Glycan Degradation. In: Essentials of Glycobiology, 3rd edition. Cold Spring Harbor (NY): Cold Spring Harbor Laboratory Press; 2015-2017, p Chapter 44

Freeze HH, Kinoshita T, Varki A (2017b) Glycans in Acquired Human Diseases. In: Essentials of Glycobiology, 3rd edition. Cold Spring Harbor (NY): Cold Spring Harbor Laboratory Press; 2015-2017, p Chapter 46

Freeze HH, Schachter H, Kinoshita T (2017c) Genetic Disorders of Glycosylation. In: Essentials of Glycobiology, 3rd edition. Cold Spring Harbor (NY): Cold Spring Harbor Laboratory Press; 2015-2017, p Chapter 45

Gagnon SML, Legg MSG, Sindhuwinata N, et al (2017) High-resolution crystal structures and STD NMR mapping of human ABO(H) blood group glycosyltransferases in complex with trisaccharide reaction products suggest a molecular basis for product release. Glycobiology 27:966–977. doi:

10.1093/glycob/cwx053

Gagnon SML, Meloncelli PJ, Zheng RB, et al (2015) High resolution structures of the human ABO(H) blood group enzymes in complex with donor analogs reveal that the enzymes utilize multiple donor conformations to bind substrates in a stepwise manner. J Biol Chem 290:27040–27052. doi: 10.1074/jbc.M115.682401

Gans P, Hamelin O, Sounier R, et al (2010) Stereospecific Isotopic Labeling of Methyl Groups for NMR Spectroscopic Studies of High-Molecular-Weight Proteins. Angew Chemie Int Ed 49:1958–1962. doi: 10.1002/anie.200905660

Gardner KH, Kay LE (1997) Production and Incorporation of 15N, 13C, 2H (1H-δ1 Methyl) Isoleucine into Proteins for Multidimensional NMR Studies. J Am Chem Soc 239:7599–7600. doi: 10.1021/ja9706514

Gelis I, Bonvin AMJJ, Keramisanou D, et al (2007) Structural Basis for Signal Sequence Recognition by the 204-kDa Translocase Motor SecA as Determined by NMR. Cell 131:756–769. doi: 10.1016/j.cell.2007.09.039

Gómez H, Lluch JM, Masgrau L (2013) Substrate-assisted and nucleophilically assisted catalysis in bovine α1,3-galactosyltransferase. Mechanistic implications for retaining glycosyltransferases. J Am Chem Soc 135:7053–7063. doi: 10.1021/ja4024447

Gómez H, Polyak I, Thiel W, et al (2012) Retaining glycosyltransferase mechanism studied by QM/MM methods: Lipopolysaccharyl-α-1,4-galactosyltransferase C transfers α-galactose via an oxocarbenium ion-like transition state. J Am Chem Soc 134:4743–4752. doi: 10.1021/ja210490f

Goto NK, Gardner KH, Mueller GA, et al (1999) A robust and cost-effective method for the production of Val, Leu, Ile (δ1) methyl-protonated 15N-, 13C-, 2H-labeled proteins. J Biomol NMR 13:369–374. doi: 10.1023/A:1008393201236

Grimm LL (2015) Ligandenbindung und Proteindynamik bei humaner Blutgruppe B Galactosyltransferase und West-Nil Virus Protease NS2B-NS3. PhD thesis. Universität zu Lübeck

Grimm LL, Weissbach S, Flügge F, et al (2017) Protein NMR Studies of Substrate Binding to Human Blood Group A and B Glycosyltransferases. ChemBioChem 18:1260–1269. doi: 10.1002/cbic.201700025

Guerin ME, Kordulakova J, Schaeffer F, et al (2007) Molecular recognition and interfacial catalysis by the essential phosphatidylinositol mannosyltransferase PimA from mycobacteria. J Biol Chem 282:20705–20714. doi: 10.1074/jbc.M702087200

Günther UL, Schaffhausen B, Gunther UL, Schaffhausen B (2002) NMRKIN: Simulating line shapes from two-dimensional spectra of proteins upon ligand binding. J Biomol Nmr 22:201–209. doi: 10.1023/A:1014985726029

Han B, Liu Y, Ginzinger SW, Wishart DS (2011) SHIFTX2: Significantly improved protein chemical shift prediction. J Biomol NMR 50:43–57. doi: 10.1007/s10858-011-9478-4

Harrington PR, Vinjé J, Moe CL, Baric RS (2004) Norovirus capture with histo-blood group antigens reveals novel virus-ligand interactions. J Virol 78:3035–3045. doi: 10.1128/JVI.78.6.3035-3045.2004

Heggelund JE, Varrot A, Imberty A, Krengel U (2017) Histo-blood group antigens as mediators of infections. Curr Opin Struct Biol 44:190–200. doi: 10.1016/j.sbi.2017.04.001

Hinou H, Nishimura S-I (2009) Mechanism-based probing, characterization, and inhibitor design of glycosidases and glycosyltransferases. Curr Top Med Chem 9:106–116. doi: 10.2174/156802609787354298

Hurtado-Guerrero R, Davies GJ (2012) Recent structural and mechanistic insights into post-translational enzymatic glycosylation. Curr Opin Chem Biol 16:479–487. doi: 10.1016/j.cbpa.2012.10.013

Isaacson RL, Simpson PJ, Liu M, et al (2007) A new labeling method for methyl transverse relaxation-optimized spectroscopy NMR spectra of alanine residues. J Am Chem Soc 129:15428–15429. doi: 10.1021/ja0761784

Järnefelt J, Rush J, Li YT, Laine RA (1978) Erythroglycan, a high molecular weight glycopeptide with the repeating structure [galactosyl-(1→4)-2-deoxy-2-acetamido-4)-2-deoxy-2-acetamido-glucosyl(1→3)] comprising more than one-third of the protein-bound carbohydrate of human erythrocyte stroma. J Biol Chem 253:8006–8009.

Johal AR, Blackler RJ, Alfaro JA, et al (2014) PH-induced conformational changes in human ABO(H) blood group glycosyltransferases confirm the importance of electrostatic interactions in the formation of the semi-closed state. Glycobiology 24:237–246. doi: 10.1093/glycob/cwt098

John M, Schmitz C, Ah YP, et al (2007) Sequence-specific and stereospecific assignment of methyl groups using paramagnetic lanthanides. J Am Chem Soc 129:13749–13757. doi: 10.1021/ja0744753

Jørgensen R, Pesnot T, Lee HJ, et al (2013) Base-modified donor analogues reveal novel dynamic features of a glycosyltransferase. J Biol Chem 288:26201–26208. doi: 10.1074/jbc.M113.465963

Kamath VP, Seto NOL, Compston CA, et al (1999) Synthesis of the acceptor analog αFuc(1→2)αGal-O(CH2)7 CH3: A probe for the kinetic mechanism of recombinant human blood group B glycosyltransferase. Glycoconj J 16:599–606. doi: 10.1023/A:1007072832421

Kay LE (2011) Solution NMR spectroscopy of supra-molecular systems, why bother? A methyl-TROSY view. J Magn Reson 210:159–170. doi: 10.1016/j.jmr.2011.03.008

Keeler J (2010) Understanding NMR Spectroscopy, 2nd ed. John Wiley & Sons, New York

Keizers PHJ, Mersinli B, Reinle W, et al (2010) A solution model of the complex formed by adrenodoxin and adrenodoxin reductase determined by paramagnetic NMR spectroscopy. Biochemistry 49:6846–6855. doi: 10.1021/bi100598f

Kleckner IR, Foster MP (2011) An introduction to NMR-based approaches for measuring protein dynamics. Biochim Biophys Acta-Proteins Proteomics 1814:942–968. doi: DOI 10.1016/j.bbapap.2010.10.012

Kloiber K, Spitzer R, Grutsch S, et al (2011) Longitudinal exchange: An alternative strategy towards quantification of dynamics parameters in ZZ exchange spectroscopy. J Biomol NMR 51:123–129. doi: 10.1007/s10858-011-9547-8

Kobata A, Grollman EF, Ginsburg V (1968a) An enzymatic basis for blood type B in humans. Biochem Biophys Res Commun 124:272–277. doi: 10.1016/0006-291X(68)90380-X

Kobata A, Grollman EF, Ginsburg V (1968b) An enzymic basis for blood type A in humans. Arch Biochem Biophys 124:609–612. doi: https://doi.org/10.1016/0003-9861(68)90373-1

Korzhnev DM, Religa TL, Banachewicz W, et al (2010) A transient and low-populated protein-folding

intermediate at atomic resolution. Science (80-) 329:1312–1316. doi: 10.1126/science.1191723

Korzhnev DM, Salvatella X, Vendruscolo M, et al (2004) Low-populated folding intermediates of Fyn SH3 characterized by relaxation dispersion NMR. Nature 430:586–590. doi: 10.1038/nature02655

Kovrigin EL (2012) NMR line shapes and multi-state binding equilibria. J Biomol NMR 53:257–270. doi: 10.1007/s10858-012-9636-3

Krusius T, Finne J, Rauvala H (1978) The Poly(glycosyl) Chains of Glycoproteins. Characterisation of a Novel Type of Glycoprotein Saccharides from Human Erythrocyte Membrane. Eur J Biochem 92:289–300. doi: 10.1111/j.1432-1033.1978.tb12747.x

Kwan DH, Withers SG (2011) Toward Efficient Enzymatic Glycan Synthesis: Directed Evolution and Enzyme Engineering. J Carbohydr Chem 30:181–205. doi: 10.1080/07328303.2011.604457

Lairson LL, Henrissat B, Davies GJ, Withers SG (2008) Glycosyltransferases: structures, functions, and mechanisms. Annu Rev Biochem 77:521–555. doi: 10.1146/annurev.biochem.76.061005.092322

Lamriben L, Graham JB, Adams BM, et al (2016) N-glycan based ER molecular chaperone and protein quality control system: the calnexin binding cycle. Traffic 17:308–326. doi: 10.1111/tra.12358

Landsteiner K (1900) Zur Kenntnis der antifermentativen, lytischen und agglutinierenden Wirkungen des Blutserums und der Lymphe. Zentralblatt für Bakteriol 27:357–362.

Lee SS, Hong SY, Errey JC, et al (2011) Mechanistic evidence for a front-side, S(N)i-type reaction in a retaining glycosyltransferase. Nat Chem Biol 7:631–638. doi: 10.1038/nchembio.628

Lescanne M, Skinner SP, Blok A, et al (2017) Methyl group assignment using pseudocontact shifts with PARAssign. J Biomol NMR 0:0. doi: 10.1007/s10858-017-0136-3

Letts JA, Rose NL, Fang YR, et al (2006) Differential Recognition of the Type I and II H Antigen Acceptors by the Human ABO(H) Blood Group A and B Glycosyltransferases. J Biol Chem 281:3625–3632. doi: 10.1074/jbc.M507620200

Li Y, Palmer AG (2009) TROSY-selected ZZ-exchange experiment for characterizing slow chemical exchange in large proteins. J Biomol NMR 45:357–360. doi: 10.1007/s10858-009-9385-0

Liu WM, Overhand M, Ubbink M (2014) The application of paramagnetic lanthanoid ions in NMR spectroscopy on proteins. Coord. Chem. Rev. 273–274:2–12.

London R (1993) Chemical-shift and linewidth characteristics of reversibly bound ligands. J Magn Reson Ser A 104:190–196. doi: 10.1006/jmra.1993.1208

Long D, Marshall CB, Bouvignies G, et al (2013) A Comparative CEST NMR Study of Slow Conformational Dynamics of Small GTPases Complexed with GTP and GTP Analogues. Angew Chemie-International Ed 52:10771–10774. doi: 10.1002/anie.201305434

Lovering AL, De Castro LH, Lim D, Strynadka NCJ (2007) Structural insight into the transglycosylation step of bacterial cell-wall biosynthesis. Science (80-) 315:1402–1405. doi: 10.1126/science.1136611

Lowary TL, Hindsgaul O (1994) Recognition of synthetic O-methyl, epimeric, and amino analogues of the acceptor α-L-Fucp-(1 → 2)-β-D-Galp-OR glycosyltransferases. Carbohydr Res 251:33–67. doi: 10.1016/0008-6215(94)84275-2

Marcus SL, Polakowski R, Seto NOL, et al (2003) A single point mutation reverses the donor specificity of human blood group B-synthesizing galactosyltransferase. J Biol Chem 278:12403–12405. doi: 10.1074/jbc.M212002200

Masterson LR, Mascioni A, Traaseth NJ, et al (2008) Allosteric cooperativity in protein kinase A. Proc Natl Acad Sci U S A 105:506–511. doi: 10.1073/pnas.0709214104

McConnell HM (1958) Reaction Rates by Nuclear Magnetic Resonance. J Chem Phys 28:430. doi: 10.1063/1.1744152

Meloncelli PJ, Lowary TL (2010) Synthesis of ABO histo-blood group type I and II antigens. Carbohydr Res 345:2305–2322. doi: 10.1016/j.carres.2010.08.012

Milland J, Sandrin MS (2006) ABO blood group and related antigens, natural antibodies and transplantation. Tissue Antigens 68:459–466.

Mittag T, Schaffhausen B, Gunther UL (2004) Tracing kinetic intermediates during ligand binding. J Am Chem Soc 126:9017–9023. doi: 10.1021/Ja0392519

Monegal A, Planas A (2006) Chemical rescue of α3-galactosyltransferase. Implications in the mechanism of retaining glycosyltransferases. J Am Chem Soc 128:16030–16031. doi: 10.1021/ja0659931

Morgan WTJ, Watkins WM (1959) Some aspects of the biochemistry of the human blood-group substances. Br Med Bull 15:109–112.

Morgan WTJ, Watkins WM (1969) Genetic and biochemical aspects of human blood group A-, B-, H-, Le-a- and Le-b-specificity. Br Med Bull 25:30–34.

Nagai M, Davè V, Kaplan BE, Yoshida A (1978a) Human Blood Group Glycosyltransferases I. Purification of N-Acetylgalactosaminyltransferase. J Biol Chem 253:377–379.

Nagai M, Davè V, Kaplan BE, Yoshida A (1978b) Human Blood Group Glycosyltransferase II. Purification of Galactosyltransferase. J Biol Chem 253:380–381.

Neudecker P, Lundstrom P, Kay LE (2009) Relaxation Dispersion NMR Spectroscopy as a Tool for Detailed Studies of Protein Folding. Biophys J 96:2045–2054. doi: 10.1016/j.bpj.2008.12.3907

Ollerenshaw JE, Tugarinov V, Kay LE (2003) Methyl TROSY: explanation and experimental verification. Magn Reson Chem 41:843–852. doi: 10.1002/mrc.1256

Otting G (2010) Protein NMR using paramagnetic ions. Annu Rev Biophys 39:387–405. doi: 10.1146/annurev.biophys.093008.131321

Palcic M, Heerze L, Pierce M, Hindsgaul O (1988) The use of hydrophobic synthetic glycosides as acceptors in glycosyltransferase assays. Glycoconj J 5:49–63. doi: 10.1007/BF01048331

Palmer AG (2014) Chemical exchange in biomacromolecules: Past, present, and future. J Magn Reson 241:3–17. doi: 10.1016/j.jmr.2014.01.008

Palmer AG, Kroenke CD, Loria JP (2001) Nuclear magnetic resonance methods for quantifying microsecond-to-millisecond motions in biological macromolecules. Methods Enzymol 339:204–238. doi: 10.1016/S0076-6879(01)39315-1

Pan YZ, Quade B, Brewer KD, et al (2016) Sequence-specific assignment of methyl groups from the neuronal SNARE complex using lanthanide-induced pseudocontact shifts. J Biomol NMR 66:281–293. doi: 10.1007/s10858-016-0078-1

Parodi A, Cummings RD, Aebi M (2017) Glycans in Glycoprotein Quality Control. In: Essentials of Glycobiology, 3rd edition. Cold Spring Harbor (NY): Cold Spring Harbor Laboratory Press; 2015-2017, p Chapter 39

Patenaude SI, Seto NOL, Borisova SN, et al (2002) The structural basis for specificity in human ABO(H) blood group biosynthesis. Nat Struct Biol 9:685–90. doi: 10.1038/nsb832

Paulson JC, Colley KJ (1989) Glycosyltransferases. Structure, localization, and control of cell type-specific glycosylation. J Biol Chem 264:17615–17618.

Persson K, Ly HD, Dieckelmann M, et al (2001) Crystal structure of the retaining galactosyltransferase LgtC from Neisseria meningitidis in complex with donor and acceptor sugar analogs. Nat Struct Biol 8:166–175. doi: 10.1038/84168

Persson M, Letts JA, Hosseini-Maaf B, et al (2007) Structural effects of naturally occurring human blood group B galactosyltransferase mutations adjacent to the DXD motif. J Biol Chem 282:9564–9570. doi: 10.1074/jbc.M610998200

Pesnot T, Jørgensen R, Palcic MM, et al (2010) Structural and mechanistic basis for a new mode of glycosyltransferase inhibition. Nat Chem Biol 6:321–323. doi: 10.1038/nchembio.343

Pham TTK, Stinson B, Thiyagarajan N, et al (2014) Structures of complexes of a metal-independent glycosyltransferase GT6 from Bacteroides ovatus with UDP-N-acetylgalactosamine (UDP-GalNAc) and its hydrolysis products. J Biol Chem 289:8041–8050. doi: 10.1074/jbc.M113.545384

Pintacuda G, John M, Su X-C, Otting G (2007) NMR Structure Determination of Protein-Ligand Complexes by Lanthanide Labeling. Acc Chem Res 40:206–212. doi: 10.1021/ar050087z

Pintacuda G, Keniry M a, Huber T, et al (2004) Fast structure-based assignment of 15N HSQC spectra of selectively 15N-labeled paramagnetic proteins. J Am Chem Soc 126:2963–2970. doi: 10.1021/ja039339m

Pol A, Barends TRM, Dietl A, et al (2014) Rare earth metals are essential for methanotrophic life in volcanic mudpots. Environ Microbiol 16:255–264. doi: 10.1111/1462-2920.12249

Prestegard JH, Liu J, Widmalm G (2017) Oligosaccharides and Polysaccharides. In: Essentials of Glycobiology, 3rd edition. Cold Spring Harbor (NY): Cold Spring Harbor Laboratory Press; 2015-2017, p Chapter 3

Proudfoot A, Frank AO, Ruggiu F, et al (2016) Facilitating unambiguous NMR assignments and enabling higher probe density through selective labeling of all methyl containing amino acids. J Biomol NMR 65:15–27. doi: 10.1007/s10858-016-0032-2

Ramakrishnan B, Boeggeman E, Ramasamy V, Qasba PK (2004) Structure and catalytic cycle of beta-1,4-galactosyltransferase. Curr Opin Struct Biol 14:593–600. doi: 10.1016/j.sbi.2004.09.006

Religa TL, Sprangers R, Kay LE (2010) Dynamic regulation of archaeal proteasome gate opening as studied by TROSY NMR. Science 328:98–102. doi: 10.1126/science.1184991

Rennella E, Huang R, Velyvis A, Kay LE (2015) 13CHD2-CEST NMR spectroscopy provides an avenue for studies of conformational exchange in high molecular weight proteins. J Biomol NMR 63:187–199. doi: 10.1007/s10858-015-9974-z

Rini JM, Esko JD (2017) Glycosyltransferases and Glycan-Processing Enzymes. In: Essentials of Glycobiology, 3rd edition. Cold Spring Harbor (NY): Cold Spring Harbor Laboratory Press; 2015-2017, p Chapter 6

Rojas-Cervellera V, Ardèvol A, Boero M, et al (2013) Formation of a covalent glycosyl-enzyme species in a retaining glycosyltransferase. Chemistry 19:14018–14023. doi: 10.1002/chem.201302898

Rosenzweig R, Kay LE (2014) Bringing Dynamic Molecular Machines into Focus by Methyl-TROSY NMR. Annu Rev Biochem 83:291–315. doi: 10.1146/annurev-biochem-060713-035829

Sahakyan AB, Vranken WF, Cavalli A, Vendruscolo M (2011) Structure-based prediction of methyl chemical shifts in proteins. J Biomol NMR 50:331–346. doi: 10.1007/s10858-011-9524-2

Sahu D, Clore GM, Iwahara J (2007) TROSY-based z-exchange spectroscopy: Application to the determination of the activation energy for intermolecular protein translocation between specific sites on different DNA molecules. J Am Chem Soc 129:13232–13237. doi: 10.1021/ja074604f

Schanda P, Kupĉe E, Brutscher B (2005) SOFAST-HMQC experiments for recording two-dimensional deteronuclear correlation spectra of proteins within a few seconds. J Biomol NMR 33:199–211. doi: 10.1007/s10858-005-4425-x

Schmitz C, Stanton-Cook MJ, Su XC, et al (2008) Numbat: An interactive software tool for fitting ΔX-tensors to molecular coordinates using pseudocontact shifts. J Biomol NMR 41:179–189. doi: 10.1007/s10858-008-9249-z

Schmitz C, Vernon R, Otting G, et al (2012) Protein structure determination from pseudocontact shifts using ROSETTA. J Mol Biol 416:668–677. doi: 10.1016/j.jmb.2011.12.056

Schuman B, Evans S V., Fyles TM (2013) Geometric Attributes of Retaining Glycosyltransferase Enzymes Favor an Orthogonal Mechanism. PLoS One. doi: 10.1371/journal.pone.0071077

Schuman B, Persson M, Landry RC, et al (2010) Cysteine-to-serine mutants dramatically reorder the active site of human ABO(H) blood group B glycosyltransferase without affecting activity: Structural insights into cooperative substrate binding. J Mol Biol 402:399–411. doi: 10.1016/j.jmb.2010.07.036

Secundino I, Lizcano A, Wang X, et al (2016) Host and Pathogen Hyaluronan Signal Through Human Siglec-9 to Suppress Neutrophil Activation. J Mol Med 94:219–233. doi: 10.1007/s00109-015-1341-8.

Seeberger PH, Cummings RD (2017) Glycans in Biotechnology and the Pharmaceutical Industry. In: Essentials of Glycobiology, 3rd edition. p Chapter 57

Selvaratnam R, Chowdhury S, VanSchouwen B, Melacini G (2011) Mapping allostery through the covariance analysis of NMR chemical shifts. Proc Natl Acad Sci 108:6133–6138. doi: 10.1073/pnas.1017311108

Selvaratnam R, Vanschouwen B, Fogolari F, et al (2012) The projection analysis of NMR chemical shifts reveals extended EPAC autoinhibition determinants. Biophys J 102:630–639. doi: 10.1016/j.bpj.2011.12.030

Seto N, Compston C, Szpacenko A, Palcic M (2000) Enzymatic synthesis of blood group A and B trisaccharide analogues. Carbohydr Res 324:161–169. doi: 10.1016/S0008-6215(99)00297-9

Seto NO, Palcic MM, Compston CA, et al (1997) Sequential interchange of four amino acids from blood group B to blood group A glycosyltransferase boosts catalytic activity and progressively modifies substrate recognition in human recombinant enzymes. J Biol Chem 272:14133–14138. doi: 10.1074/jbc.272.22.14133

Seto NO, Palcic MM, Hindsgaul O, et al (1995) Expression of a recombinant human glycosyltransferase from a synthetic gene and its utilization for synthesis of the human blood group B trisaccharide.

Eur J Biochem 234:323–328. doi: 10.1111/j.1432-1033.1995.323_c.x

Seto NOL, Compston CA, Evans S V., et al (1999) Donor substrate specificity of recombinant human blood group A, B and hybrid A/B glycosyltransferases expressed in Escherichia coli. Eur J Biochem 259:770–775. doi: 10.1046/j.1432-1327.1999.00086.x

Shinya S, Ghinet MG, Brzezinski R, et al (2017) NMR line shape analysis of a multi-state ligand binding mechanism in chitosanase. J Biomol NMR 0:0. doi: 10.1007/s10858-017-0109-6

Shoemaker GK, Kitova EN, Palcic MM, Klassen JS (2007) Equivalency of binding sites in protein-ligand complexes revealed by time-resolved tandem mass spectrometry. J Am Chem Soc 129:8674–8675. doi: 10.1021/ja068421p

Shoemaker GK, Soya N, Palcic MM, Klassen JS (2008) Temperature-dependent cooperativity in donor-acceptor substrate binding to the human blood group glycosyltransferases. Glycobiology 18:587–592. doi: 10.1093/glycob/cwn043

Sindhuwinata N (2012) Zum Katalysemechanismus der humanen Blutgruppe B Galactosyltransferase. PhD thesis. Universität zu Lübeck

Sindhuwinata N, Grimm LL, Weissbach S, et al (2013) Thermodynamic signature of substrates and substrate analogs binding to human blood group B galactosyltransferase from isothermal titration calorimetry experiments. Biopolymers 99:784–795. doi: 10.1002/bip.22297

Sindhuwinata N, Munoz E, Munoz FJ, et al (2010) Binding of an acceptor substrate analog enhances the enzymatic activity of human blood group B galactosyltransferase. Glycobiology 20:718–723. doi: cwq019 [pii]10.1093/glycob/cwq019

Skinner SP, Moshev M, Hass MAS, Ubbink M (2013) PARAssign - Paramagnetic NMR assignments of protein nuclei on the basis of pseudocontact shifts. J Biomol NMR 55:379–389. doi: 10.1007/s10858-013-9722-1

Soya N, Fang Y, Palcic MM, Klassen JS (2011) Trapping and characterization of covalent intermediates of mutant retaining glycosyltransferases. Glycobiology 21:547–552. doi: 10.1093/glycob/cwq190

Soya N, Shoemaker GK, Palcic MM, Klassen JS (2009) Comparative study of substrate and product binding to the human ABO(H) blood group glycosyltransferases. Glycobiology 19:1224–1234. doi: 10.1093/glycob/cwp114

Sprangers R, Kay LE (2007) Quantitative dynamics and binding studies of the 20S proteasome by NMR. Nature 445:618–622. doi: 10.1038/nature05512

Sprangers R, Velyvis A, Kay LE (2007) Solution NMR of supramolecular complexes: providing new insights into function. Nat Methods 4:697–703. doi: 10.1038/nmeth1080

Stanley P, Taniguchi N, Aebi M (2017) N-Glycans. In: Essentials of Glycobiology, 3rd edition. Cold Spring Harbor (NY): Cold Spring Harbor Laboratory Press; 2015-2017, p Chapter 9

Stellner K, Hakomori SI (1974) A ceramide pentasaccharide of human erythrocyte membrane. J Biol Chem 249:1022–1025.

Stoffregen MC, Schwer MM, Renschler F a, Wiesner S (2012) Methionine scanning as an NMR tool for detecting and analyzing biomolecular interaction surfaces. Structure 20:573–81. doi: 10.1016/j.str.2012.02.012

Su XC, Otting G (2010) Paramagnetic labelling of proteins and oligonucleotides for NMR. J Biomol

NMR 46:101–112. doi: 10.1007/s10858-009-9331-1

Szymanski CM, Schnaar RL, Aebi M (2017) Bacterial and Viral Infections. In: Essentials of Glycobiology, 3rd edition. Cold Spring Harbor (NY): Cold Spring Harbor Laboratory Press; 2015-2017, p Chapter 42

Tang C, Schwieters CD, Clore GM (2007) Open-to-closed transition in apo maltose-binding protein observed by paramagnetic NMR. Nature 449:1078–1082. doi: 10.1038/nature06232

Tugarinov V, Hwang PM, Ollerenshaw JE, Kay LE (2003) Cross-correlated relaxation enhanced 1H-13C NMR spectroscopy of methyl groups in very high molecular weight proteins and protein complexes. J Am Chem Soc 125:10420–10428. doi: 10.1021/ja030153x

Tugarinov V, Kay LE (2004) An isotope labeling strategy for methyl TROSY spectroscopy. J Biomol NMR 28:165–172. doi: 10.1023/B:JNMR.0000013824.93994.1f

Tugarinov V, Kay LE (2003a) Ile, Leu, and Val Methyl Assignments of the 723-Residue Malate Synthase G Using a New Labeling Strategy and Novel NMR Methods. J Am Chem Soc 125:13868–13878. doi: 10.1021/ja030345s

Tugarinov V, Kay LE (2003b) Quantitative NMR studies of high molecular weight proteins: Application to domain orientation and ligand binding in the 723 residue enzyme malate synthase G. J Mol Biol 327:1121–1133. doi: 10.1016/S0022-2836(03)00238-9

Tugarinov V, Kay LE, Ibraghimov I, Orekhov VY (2005) High-resolution four-dimensional 1H-13C NOE spectroscopy using methyl-TROSY, sparse data acquisition, and multidimensional decomposition. J Am Chem Soc 127:2767–2775. doi: 10.1021/ja044032o

Tuppy H, Staudenbauer WL (1966) Microsomal incorporation of N-acetyl-D-galactosamine into blood group substance. Nature 210:316–317. doi: 10.1038/210316a0

Vallurupalli P, Bouvignies G, Kay LE (2012) Studying "Invisible" Excited Protein States in Slow Exchange with a Major State Conformation. J Am Chem Soc 134:8148–8161. doi: 10.1021/Ja3001419

Vallurupalli P, Sekhar A, Yuwen T, Kay LE (2017) Probing conformational dynamics in biomolecules via chemical exchange saturation transfer: a primer. J Biomol NMR 67:243–271. doi: 10.1007/s10858-017-0099-4

Varki A (1993) Biological roles of oligosaccharides: all of the theories are correct. Glycobiology 3:97–130. doi: 10.1093/glycob/3.2.97

Varki A, Esko JD, Colley KJ (2017a) Cellular Organization of Glycosylation. In: Essentials of Glycobiology, 3rd edition. Cold Spring Harbor (NY): Cold Spring Harbor Laboratory Press; 2015-2017, p Chapter 4

Varki A, Gagneux P (2017) Biological Functions of Glycans. In: Essentials of Glycobiology, 3rd edition. Cold Spring Harbor (NY): Cold Spring Harbor Laboratory Press; 2015-2017, p Chapter 7

Varki A, Kannagi R, Toole B, Stanley P (2017b) Glycosylation changes in cancer. In: Essentials of Glycobiology, 3rd edition. Cold Spring Harbor (NY): Cold Spring Harbor Laboratory Press; 2015-2017, p Chapter 47

Varki A, Sharon N (2017) Historical Background and Overview. In: Essentials of Glycobiology, 3rd edition. Cold Spring Harbor (NY): Cold Spring Harbor Laboratory Press; 2015-2017, p Chapter 1

Velyvis A, Ruschak AM, Kay LE (2012) An Economical Method for Production of 2H,13CH3-Threonine for Solution NMR Studies of Large Protein Complexes: Application to the 670 kDa Proteasome. PLoS One 7:1–8. doi: 10.1371/journal.pone.0043725

Vranken WF, Boucher W, Stevens TJ, et al (2005) The CCPN data model for NMR spectroscopy: Development of a software pipeline. Proteins Struct Funct Genet 59:687–696. doi: 10.1002/prot.20449

Wagner GK, Pesnot T, Palcic MM, Jørgensen R (2015) Novel UDP-GalNAc Derivative Structures Provide Insight into the Donor Specificity of Human Blood Group Glycosyltransferase. J Biol Chem 290:31162–31172. doi: 10.1074/jbc.M115.681262

Watkins W, Morgan WTJ (1957) Specific Inhibition Studies Relating to the Lewis Blood-Group System. Nature 180:1038.

Watkins WM (1991) Chemical structure, biosynthesis and genetic regulation of carbohydrate antigens: retrospect and prospect. Pure Appl Chem 63:561–568. doi: 10.1351/pac199163040561

Waudby CA, Ramos A, Cabrita LD, Christodoulou J (2016) Two-Dimensional NMR Lineshape Analysis. Sci Rep 6:24826. doi: 10.1038/srep24826

Weissbach S (2016) Einfluss der Ligandenbindung auf Struktur und Dynamik von Glycosyltransferasen und Norovirus-Kapsidproteinen. PhD thesis. Universität zu Lübeck

Weissbach S, Flügge F, Peters T (2018) Substrate binding drives active site closing of human blood group B galactosyltransferase as revealed by hot-spot labeling and NMR experiments. ChemBioChem Accepted Author Manuscript. doi: 10.1002/cbic.201800019

Wiesner S, Sprangers R (2015) Methyl groups as NMR probes for biomolecular interactions. Curr Opin Struct Biol 35:60–67. doi: 10.1016/j.sbi.2015.08.010

Williamson MP (2013) Using chemical shift perturbation to characterise ligand binding. Prog Nucl Magn Reson Spectrosc 73:1–16. doi: 10.1016/j.pnmrs.2013.02.001

Xu J, Sarma AVS, Wei Y, et al (2017) Multiple Ligand-Bound States of a Phosphohexomutase Revealed by Principal Component Analysis of NMR Peak Shifts. Sci Rep 7:1–11. doi: 10.1038/s41598-017-05557-w

Xu Y, Matthews S (2013) MAP-XSII: An improved program for the automatic assignment of methyl resonances in large proteins. J Biomol NMR 55:179–187. doi: 10.1007/s10858-012-9700-z

Yamamoto F (2004) ABO blood group system—ABH oligosaccharide antigens, anti-A and anti-B,A and B glycosyltransferases, and ABO genes. Immunohematology 20:3–77.

Yamamoto F, Clausen H, White T, et al (1990a) Molecular genetic basis of the histo-blood group ABO system. Nature 345:229–233. doi: 10.1038/345229a0

Yamamoto F, Hakomori S (1990) Sugar-nucleotide Donor Specificity of Histo-blood Group A and B Transferases Is Based on Amino Acid Substitutions. J Biol Chem 265:19257–19262.

Yamamoto F, Marken J, Tsutomu T, et al (1990b) Cloning and characterization of DNA complementary to human UDP-GalNAc : Fuc alpha 1-2Gal alpha 1-3GalNAc. J Biol Chem 265:1146–1151.

Yamamoto F, McNeill PD (1996) Amino Acid Residue at Codon 268 Determines Both Activity and Nucleotide-Sugar Donor Substrate Specificity of Human Histo-blood Group A and B Transferases Histo-blood group A transferase produces A antigens and transfers GalNAc to the acceptor

substrate ,. J Biol Chem 271:10515–10520.

Yamamoto M, Lin X-H, Kominato Y, et al (2001) Murine equivalent of the human histo-blood group ABO gene is a cis-AB gene and encodes a glycosyltransferase with both A and B transferase activity. J Biol Chem 276:13701–8. doi: 10.1074/jbc.M010805200

Yazer MH, Palcic MM (2005) The importance of disordered loops in ABO glycosyltransferases. Transfus. Med. Rev. 19:210–216.

Zhang Y, Wang PG, Brew K (2001) Specificity and Mechanism of Metal Ion Activation in UDP-galactose:β-Galactoside-α-1,3-galactosyltransferase. J Biol Chem 276:11567–11574. doi: 10.1074/jbc.M006530200

Curriculum Vitae

Acknowledgment

My deepest gratitude goes to Prof. Dr. Thomas Peters for giving me the opportunity to work on this fascinating project, for his support, and for the freedom to develop my own ideas. I would also like to thank for the opportunity to attend several conferences.

Many thanks to Dr. Alvaro Mallagaray for the long and fruitful discussions and substantial support in all stages of this project. His expertise in paramagnetic NMR was particularly helpful. Furthermore, he revised this manuscript.

Dr. Hanne Peters, Dr. Lena Lisbeth Grimm and Dr. Sophie Weißbach introduced me to this project. I acknowledge their preliminary work as well as the studies of Dr. Nora Begemann (geb. Sindhuwinata) as an outstanding basis for my investigations.

Furthermore, I acknowledge the work of Julian Revenstorff who synthesized ILMV methyl-labeled GTB W181 mutants, and executed the NMR-monitored ligand titrations with these enzymes.

I want to thank Dr. Thorsten Biet for the implementation of nontrivial NMR pulse programs that were crucial to realize this thesis. Furthermore, I thank Dr. Hans Wienk for the acquisition of the 4D methyl-methyl NOESY experiment at the NMR facility in Utrecht.

I thank Dr. Todd L. Lowary and Dr. David R. Bundle from the University of Alberta, Edmonton, Dr. Beat Ernst from the University of Basel, and Wilfried Hellebrandt from the University of Lübeck for the supply with precious carbohydrate samples.

In addition to the previously mentioned members of the Institute of Chemistry, I want to thank the whole staff for the inspiring and motivating atmosphere: Christiane Blunk, Robert Creutznacher, Thies Köhli, Petra Lipp, Dr. Rosa Pulz, Barbara Richer, Tobias Schöne, Dr. Karsten Seeger and Dr. Thomas Weimar.

I thank the *Deutsche Forschungsgemeinschaft* for the financial support.

Finally, I owe my heartfelt gratitude to my family, to my friends, and especially to my wife Ulrike for encouragement and the continuous support.